

Biochemical studies on nucleic acid modifying enzymes and inhibition of metallo-β-lactamases

A thesis submitted to the Board of the Faculty of Physical Sciences of the University of Oxford in partial fulfilment of the requirements for the degree of Doctor of Philosophy

Dong Zhang

St. Cross College

Trinity Term 2019

Authors Declaration

The work presented in this thesis was conducted at the Chemistry Research Laboratory at the University of Oxford between Michaelmas Term 2014 and Michaelmas Term 2018 under the supervision of Professor Christopher J. Schofield. All the work is my own, except where otherwise stated, and has not been submitted for any other degree at this or any other university.

Dong Zhang

October 2019

Abstract

Dong Zhang D.Phil

St Cross College Trinity Term 2019

The work described in this thesis concerns inhibition and mechanisms of two classes of metallo-enzymes of biomedical importance. The first class is Fe(II)- and 2-oxoglutarate (2OG)-dependent oxygenases involved in modifications of nucleic acids. The second class is Zn(II)-ion-dependent β-lactamases (metallo-β-lactamases, MBLs), which are involved in antibacterial resistance.

A new generation of small-molecule inhibitors of the fat mass and obesity-associated protein (FTO) was developed using structure-based design. Initial inhibition data proved inadequate due to inhibition-assay limitations. Various FTO inhibition assays were then developed. These included assays based on matrix-assisted laser desorption ionisation (MALDI), liquid chromatography-mass spectrometry (LC-MS) and RapidFire mass spectrometry (RF-MS). RF-MS is preferred owing to its high-throughput capacity and reliability. New enzyme kinetic parameters were determined using RF-MS. This work led to significantly improved inhibition data, which resulted in the identification of a potent and selective FTO inhibitor.

An apparently hydroxylated product instead of a demethylated product was observed during the optimisation of the FTO RF-MS inhibition assay. Potential FTO-catalysed hydroxylation was investigated, comparing the results with those for related enzymes, i.e. AlkB and ABH5, as well as the mouse homologue of FTO (mFTO). The studies revealed direct evidence, derived from nuclear magnetic resonance (NMR) and MS studies, for the formation of N-6-hydroxymethyl adenosine as a product of FTO-catalysed hydroxylation of RNA that contains a m^6A modification.

Biochemical characterisations were performed on a novel FTO variant, p.(Ser319Phe), which correlates with congenital malformations. NMR and MS analyses revealed that p.(Ser319Phe) FTO manifests reduced 2OG turnover and catalytic activity. The substitution also affected enzyme refolding. These findings may relate to previous reports that homozygous mutations in FTO can lead to a rare growth-retardation and developmental-delay syndrome. The results support the proposal that FTO plays an important role in early development of human central nervous and cardiovascular systems.

MBLs employ one or two Zn(II) ions to catalyse the hydroxylation of nearly all classes of β-lactam antibiotics, including the carbapenems, which are often considered to be antibiotics of last resort. After a report that rhodanine-derived enethiols could be potent MBL inhibitors, extensive SAR studies were carried out on rhodanines and enethiols as MBL inhibitors. Highly potent enethiol-based MBL inhibitors were identified. The results support the proposal that rhodanines have potential as promiscuous enzyme inhibitors/protein binders, in part owing to their tendency to undergo reaction to give products, including enethiols, which have the potential to inhibit the multiple metallo-enzymes present in cells. These enzymes include related MBL-fold enzymes with biological roles beyond antibiotic resistance, including in nucleic-acid repair and metabolism. These results imply that any medicinal-chemistry studies that employ rhodanine inhibitors should include tests of their degradation products.

The overall results provide insights into the reaction mechanisms, and inhibition of two classes of metallo-enzymes that are of interest from a medicinal perspective. In the longer term, it is hoped that the results will enable manipulation of these enzymes for therapeutic benefits.

Acknowledgements

Firstly, I would like to thank my supervisor, Professor Christopher Schofield for providing me with support, inspiration and the opportunity to pursue my research interest and further develop a passion for chemical biology.

The work detailed in this thesis could not have been completed without the help of many co-workers within the University. I would like to especially express my gratitude to Dr Michael McDonough for his advice and guidance on multiple occasions through my time in Oxford. I would like to thank Dr Marina Demetriades for providing me with an initial platform for FTO inhibitors, biochemical assays and the guidance during the beginning of my research. I thank Dr Jürgen Brem for providing me with invaluable advice and guidance on MBL inhibition studies, which form a major part of my work.

Thanks to Shifali Shishodia for providing me with materials and being a great member of FTO team, I also formed a close friendship with her during the time we worked together; Dr Anthony Tumber for helping me developing RF-MS assay and being the "magical co-factor"; Dr James Wickens for helping developing LC-MS assays and allowing me to use his precious instruments; Jos Kamp for his advice and running of NMR times-course experiments. I would also like to thank Roman Belle, Lennart Brewitz, Md Saiful Islam, Robert Leśniak, Tongri Liu, Christopher Lohans, Jame Holt-Martyn, Tharindi Panduwawala, Klaus-Daniel Umland, David Yuxin Wang, Yijia Zhang and Zhihong Zhang for their invaluable support, guidance and friendship. Furthermore, I would like to thank all members of the Schofield group, past and present, for pormiting a kind, friendly and truly inspirational working environment which had made the lab a great place to work. Adam Hardy, Herminio Manso Jubier, Jennyt Houlsby, Zahn Gowar and Wendy Sobey deserve a huge thanks for keeping the lab running as efficiently as possible.

Most importantly, I would like to thanks my parents and my wife for providing love, support and encouragement throughout my D.Phil at Oxford, and without which I could not have achieved what I have today. Special thanks to my lovely wife, Yaoyue Zhang. She gave birth to our child Albert Zhang at the closing stages of my D.Phil, which has given me the much need boost at difficult times during thesis writing.

General Contents

1. Introduction 3

1.1. 2-oxoglutarate-dependent oxygenases 3

1.2. Structures of 2-oxoglutarate-dependent oxygenases 5

1.2.1. The double stranded β-helix fold 5

1.2.2. The iron-binding motif 7

1.2.3. 2OG binding site 8

1.2.4. Substrate recognition region 9

1.3. Mechanistic properties of 2-oxoglutarate-dependent oxygenases 10

1.3.1. The Fe(II) complex and 2OG binding 11

1.3.2. Substrate and oxygen binding 12

1.3.3. Substrate hydroxylation and release 12

1.4. 2-Oxoglutarate dependent oxygenases in nucleic acid modification 13

1.4.1. AlkB and its subfamily of human homologues 16

1.4.2. TET enzymes 22

1.4.3. TYW5 23

1.5. RNA epigenetics 23

1.6. Thesis outline 27

References 28

2. Inhibition studies and assay optimisation for the nucleic-acid demethylase FTO 47

2.1. Introduction 47

2.2. Previous studies 49

2.1.1 Inhibition studies 49

2.1.2 Screening (demethylation) assay 53

2.3. Objectives 54

2.4. FTO-inhibitor development 55
2.5. Production and purification of enzymes 58
2.6. *In vitro* assay optimisation 60
2.6.1. FTO assay based on matrix-assisted laser desorption/ionisation 60
2.6.2. Inhibition of FTO by second-generation inhibitors 65
2.6.3. Assay based on liquid chromatography-mass spectrometry 69
2.6.4. RapidFire® Mass Spectrometry- (RF-MS)-based assays 76
2.6.5. Inhibition of FTO with new RF-MS assay 90
2.7. Discussion and future work 95
Acknowledgements 98
References 99
3. Mechanistic studies of FTO using mass spectrometry 109
3.1. Previous studies 109
3.2. Objectives 112
3.3. Is FTO a demethylase or a hydroxylase? 113
3.4. Investigation of FTO activity 117
3.4.1. FTO compared with ABH5 117
3.4.2. FTO catalysis investigation with inhibitor 2,4-PDCA 129
3.4.3. Human FTO compared with mouse FTO 133
3.4.4. FTO compared with AlkB 135
3.5. Discussion and future work 139
Acknowledgements 143
References 144
4. Biochemical studies on an FTO variant 151
4.1. Introduction 151
4.2. Objectives 152

4.3. Production of FTO variants 153
4.4. Structural rationalisation 154
4.5. Circular dichroism (CD) 156
4.6. LC-MS demethylation assays 157
4.7. 2OG turnover assay by NMR 158
4.8. Discussion and future work 160
Acknowledgements 163
References 164
5. Metallo-β-lactamases and their inhibition 170
5.1. Introduction 170
5.1.1. The β-lactam antibiotics and their history 173
5.1.2. Mechanism of β-lactam antibiotics 181
5.1.3. Antibiotic resistance 182
5.1.4. Serine β-lactamases 186
5.1.5. Inhibition of serine β-lactamases 190
5.1.6. Metallo-β-lactamases 194
5.1.7. Mechanisms of metallo-β-lactamases 201
5.1.8. Inhibition of metallo-β-lactamases 208
5.1.9. Summary 211
5.2. Previous studies on rhodanines as MBL inhibitors 212
5.3. Chapter objectives 216
5.4. MBL inhibition 217
5.4.1. Design and synthesis of rhodanine and rhodanine-derivative inhibitors of MBLs 217
5.4.2. Protein production 224
5.4.3. Inhibition and structure activity relationship studies 224
5.4.4. Investigation of the binding/inhibiting motif 232

5.4.5. Synergistic inhibition studies 234
5.4.6. Structural studies 237
5.4.7. Susceptibility of clinical isolates to rhodanines and enethiols 243
5.4.8. Hydrolysis/degradation of rhodanine amides 245
5.5. SBL inhibition 249
5.6. A serendipitous finding 252
5.6.1. Emerging instability 252
5.6.2. Solvent screening 254
5.6.3. Product structure elucidation 257
5.7. Discussion and future work 269
Acknowledgements 272
References 273
6. Summary 303
References 306
7. Materials and Methods 312
7.1. Sourcing of materials 312
7.2. Competent Cells 313
7.3. pH Measurement for Buffer Solutions 313
7.4. Determination of DNA Concentration 313
7.5. Determination of Protein Concentration 313
7.6. Cell Density Measurements 314
7.7. Centrifugation of Samples 314
7.8. Buffer Exchange 314
7.9. Media and Antibiotic Plate Preparation 315
7.9.1. 1000x Antibiotic Stocks for Cell Growth and Agar Plates 315
7.9.2. Preparation of 2TY Medium 315

7.9.3. Preparation of Super Optimal Catabolite Repression (SOC) Outgrowth Medium... 315
7.10. SDS-PAGE Electrophoresis ... 316
7.10.1. SDS-PAGE Gel Preparation ... 316
7.10.2. Running of SDS-PAGE Experiments ... 317
7.11. Site Directed Mutagenesis ... 318
7.12. DNA Digests ... 319
7.13. Plasmid Purification ... 320
7.14. Protein Production and Purification ... 320
7.14.1. Competent Cell Transformations ... 320
7.14.2. Starter Cultures ... 321
7.14.3. Large Scale Cell Growths ... 321
7.14.4. Cell Lysate Preparation ... 322
7.14.5. Fast Protein Liquid Chromatography (FPLC) ... 322
7.15. Denaturing Mass-Spectrometry ... 323
7.16. *In Vitro* Biochemical Assays for 2OG oxygenases ... 324
7.16.1. LC-MS Based Demethylation Assays ... 324
7.16.2. MALDI-MS Based Assays ... 325
7.16.3. RapidFire-MS (RF-MS) Based Assays ... 326
7.16.4. K_M Determination ... 327
7.16.5. Inhibition Assays ... 327
7.17. MBL Inhibition assays ... 328
7.18. Standard Error Calculation ... 329
7.19. Circular Dichroism (CD) Analyses ... 329
7.20. Computational Modelling of the Ser319Phe FTO Substitution ... 330
7.21. Nuclear Magnetic Resonance Spectroscopy ... 330
7.21.1. NMR time course for 2OG Turnover Assays ... 331
7.21.2. NMR (^{1}H-^{13}C-HSQC) Time Course on FTO catalysis Product Degradation ... 331
7.21.3. NMR Time Course for Rhodanine Degradation ... 332

7.22. Organic synthesis 332
7.22.1. Synthesis and compound characterisation 333
References 359

Abbreviations

2,4-PDCA	2,4-Pyridinedicarboxylic acid
2OG	2-Oxoglutarate
5caC	5-Carboxylcytosine
5fC	5-Formylcytosine
5hmC	5-Hydroxymethylcyotosine
5mC	5-Methylcytosine
6-APA	6-Aminopenicillanic acid
7-ACA	7-Aminocephalosporanic acid
ABH	AlkB Homologue
ACE	Angiotensin-converting enzyme
AcOH	Acetic acid
Ac_2O	Acetic anhydride
AmpCs	Ambler class C serine-β-lactamases
ASCC3	Activating signal cointegrator 1 complex subunit 3
BcII	*Bacillus cereus* metallo-β-lactamase II
BOP-Cl	Bis(2-oxo-3-oxazolidinyl)phosphinic Chloride
CAS	Clavaminic acid synthase
CcrA	Cefoxitin and carbapenem resistant metallo-β-lactamase
CDI	Carbonyldiimidazole
cm^5U	5-Carboxymethyluridine
CPH	Collagen prolyl hydroxylase
CphA	Carbapenem hydrolysing enzyme from *Aeromonas hydrophila*
CTX-M	Cefotaxime hydrolase from Munich
DAOCS	Deacetoxycephalosporin-C synthase

DBO	Diazabicyclooctane
DCM	Dichloromethane
DEPC	Diethyl pyrocarbonate
DHP-1	Human renal dehydropeptidase-1
DIPEA	N,N-Diisopropylethylamine
DMA	Dimethylacetamide
DMAP	4-Dimethylaminopyridine
DNA	Deoxyribonucleic acid
DSBH	Double stranded β-helix
εA	N-6-ethenoadenine
εC	3,N-4-ethenocytosine
EDTA	Ethylenediaminetetraacetic acid
ESACs	Extended spectrum AmpC
ESBLs	Extended-spectrum serine-β-lactamases
EtOH	Ethanol
f^6A	N-6-formyl adenosine
FEZ-1	*Fluoribacter (Legionella) gormanii* endogenous zinc β-lactamase
FMMH	Five-membered multiheterocyclic
FTO	Fat mass and obesity-associated protein
GOB-1	*Chryseobacterium meningosepticum* β-lactamase
HATU	1-[Bis(dimethylamino)methylene]-1H-1,2,3-triazolo[4,5-b]pyridinium 3-oxid hexafluorophosphate
HCl	Hydrochloric acid
HIF	Hypoxia inducible factor
HFIP	1,1,1,3,3,3-Hexafluoro-2-propanol
hm^6A	N-6-hydroxymethyl adenosine

HPLC	High performance liquid chromatography
IMI	Imipenem-hydrolysing enzyme
ImiS	Imipenemase from *Aeromonas veronii bv. Sobria*
IMP	MBL imipenemase
IPNS	Isopenicillin N synthase
IRX3	Iroquois-class homeodomain protein-3
JmjC	Jumanji C
KDM4	Lysine-specific demethylase 4
KO^tBu	Potassium butyl oxide
KSAc	Potassium thioacetate
KSCN	Potassium thiocyanate
L1	Labile enzyme from *Stenotrophomonas maltophilia*
LC-MS	Liquid chromatography-mass spectrometry
K_2CO_3	Potassium carbonate
K_3PO_4	Potassium phosphate
K_m	Michaelis–Menten constant
KOH	Potassium hydroxide
KPC	*Klebsiella pneumoniae* carbapenemase
m^1A	*N*-1-methyladenosine
m^1G	1-Methylguanine
m^3T	3-Methylthymine
m^3U	3-Methyluracil
m^6A	*N*-6-methyladenosine
m^6A_m	N^6,2-O-dimethyladenosine
MBL	Metallo-β-lactamases
mcm^5U	5-Methoxycarbonylmethyluridine
MeOH	Methanol

MES	2-(*N*-morpholino)ethanesulfonic acid
METTL3/14	Methyltransferase like 3/14
MIC	Minimum inhibitory concentration
MMS	Methylmethanesulfonate
mRNA	Messenger RNA
MRSA	Methicillin resistant *Staphylococcus aureus*
MS	Mass spectrometry
MT	Methyltransferase
m/z	Mass to charge
Na	Sodium
$NaBH_4$	Sodium borohydride
NaOAc	Sodium acetate
NaOH	Sodium hydroxide
NDM	New Delhi metallo-β-lactamase
NH_4HCO_3	Ammonium bicarbonate
NH_4OAc	Ammonium acetate
NMR	Nuclear magnetic resonance
OXA	Oxacillinases
P99	β-Lactamase from *E. cloacae* strain P99
PBPs	Penicillin-binding proteins
Pd	Palladium
PHD	HIF-prolyl hydroxylases
PMA	Phosphomolybdic acid
ppm	Parts per million
PyBOP	Benzotriazol-1-yl-oxytripyrrolidinophosphonium hexafluorophosphate
qTOF	Quadrupole time of flight
RF	RapidFire®

RNA	Ribonucleic acid
RRM	RNA recognition motif
rRNA	Ribosomal ribonucleic acid
S-mchm^{5}U	S-5-(methoxycarbonylhydroxymethyl)uracil
SAM	S-adenosylmethionine
SAH	S-adenosylhomocysteine
SAR	Structure activity relationship
SBL	Serine-β-lactamases
SDS-PAGE	Sodium dodecyl sulfate polyacrylamide gel electrophoresis
Sfh-1	*Serratia fonticola* carbapenem hydrolase
SHV	Sulfhydryl reagent variable β-lactamases
SNP	Single nucleotide polymorphism
SPE	Solid-phase extraction
SPM	São Paulo metallo-β-lactamase
ssDNA	Single stranded DNA
ssRNA	Single stranded RNA
T3P	Propylphosphonic anhydride
TauD	Taurine dioxygenase
TCA	Tricarboxylic acid
TEA	Triethylamine
TEM	Temoneira β-lactamases
TDG	Thymine DNA glycosylase
THF	Tetrahydrofuran
TLC	Thin layer chromatography
TMS	Tetramethylsilane
TMSI	Trimethylsilyl iodide
TOF	Time of flight

TYW5	tRNA wybutosine-synthesizing protein 5
Tris	Tris(hydroxymethyl)aminomethane
YTHDF	YTH domain-containing family protein
UPLC	Ultra-performance liquid chromatography
UV	Ultraviolet
VIM	Verona integron-encoded metallo-β-lactamase
v/v	Volume to volume
WTAP	Wilms' tumor 1-associating protein

Chapter 1

Introduction

Table of Contents

1. Introduction **3**

1.1. 2-oxoglutarate dependent oxygenases 3

1.2. Structures of 2-oxoglutarate dependent oxygenases 5

1.2.1. The double stranded β-helix (DSBH) fold 5

1.2.2. The iron-binding motif 7

1.2.3. 2OG binding site 8

1.2.4. Substrate recognition region 9

1.3. Mechanistic properties of 2-oxoglutarate dependent oxygenases 10

1.3.1. The Fe(II) complex and 2OG binding 11

1.3.2. Substrate and oxygen binding 12

1.3.3. Substrate hydroxylation and release 12

1.4. 2-Oxoglutarate dependent oxygenases in nucleic acid modification 13

1.4.1. AlkB and its subfamily human homologues 16

1.4.2. TET enzymes 22

1.4.3. TYW5 23

1.5. RNA epigenetics 23

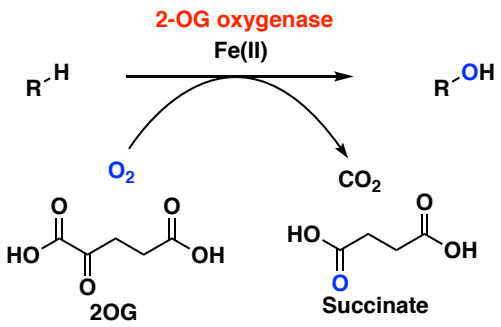
1.6. Thesis outline 27

Reference **28**

1. Introduction

1.1. 2-oxoglutarate-dependent oxygenases

The discovery of collagen prolyl hydroxylase (CPH) in the 1960s identified the first known 2-oxoglutarate-dependent oxygenases (2OG oxygenases), which were shown subsequently to be members of a large superfamily[1]. Members of the 2OG oxygenase superfamily catalyse a diverse set of oxidation reactions, possibly a greater number than any other enzyme family[2]. These 2OG oxygenases are found in almost all aerobic organisms, with the probable exception of archaea[3]. Sequence analyses suggest that there are more than 60 2OG oxygenases in humans, with many more in microorganisms and plants[3-4]. 2OG oxygenases catalyse substrate oxidation coupled with the reaction of oxygen and 2-oxoglutarate, an intermediate in the tricarboxylic acid (TCA) cycle[5]. Iron(II) is used as a cofactor, and some 2OG oxygenases (e.g. CPH) employ ascorbate for optimal activity (Scheme 1.1)[6-7]; succinate and carbon dioxide are byproducts[8]. Reactions catalysed by 2OG oxygenases include demethylations[9-10], desaturations[11], hydroxylations[12], halogenations[13-14] and ring closures[15]. In animals, reported reactions catalysed by 2OG oxygenases are restricted to hydroxylations and demethylations (which likely proceed *via* hydroxylation)[3]. In humans, reactions that are catalysed by 2OG oxygenases are involved in important biological processes including oxygen sensing, nucleic acid alkylation lesion repair, lipid metabolism and epigenetic modifications (Figure 1.1)[3-4, 16].



Scheme 1.1: *General reaction scheme for 2-OG oxygenases.*

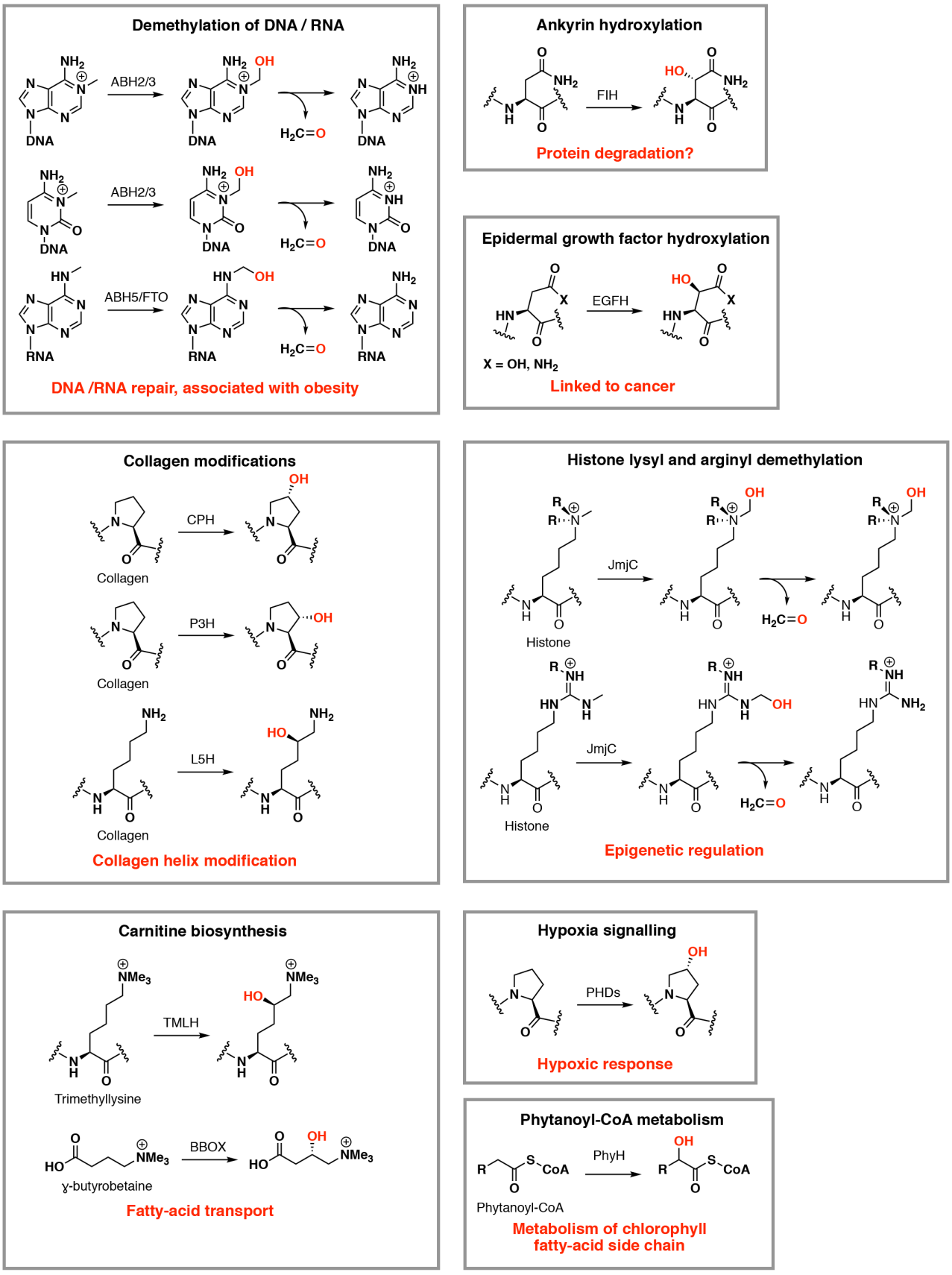


Figure 1.1: *Outline summary of reactions catalysed by human 2OG oxygenases. Assigned or potential roles are listed at the bottom of each box.*

1.2. Structures of 2-oxoglutarate-dependent oxygenases

The reactions that are catalysed by 2OG oxygenases, in particular the activation of inert C-H bonds, are often challenging to achieve synthetically. Therefore their catalytic mechanisms are of chemical interest. Given that 2OG oxygenases are involved in many biological processes, extensive structural and mechanical studies have been carried out. Efforts have also been made to develop 2OG oxygenases inhibitors for medicinal chemistry puroposes[17-20].

1.2.1. The double stranded β-helix fold

All 2OG oxygenases that have been characterised display a conserved distorted double stranded β-helix (DSBH) fold, sometimes known as a jelly-roll fold.[8, 21-23] The first 2OG oxygenase-related enzyme to be crystallised with a DSBH fold was isopenicillin N synthase (IPNS)[24]. IPNS structurally is related to 2OG oxygenases, but does not utilise 2OG as a co-substrate. Crystallographic analysis of IPNS showed that the DSBH core involved three iron-binding residues (Figure 1.2)[24]. Other studies revealed that the DSBH fold is not limited to 2OG oxygenases[25]. The plant cupin-fold proteins, c-nucleoside monophosphate kinase-(cNMP)-binding domain and copper monooxygenases[25]; and the Jumonji C (JmjC) domain-containing proteins each contain a modified DSBH[26-27].

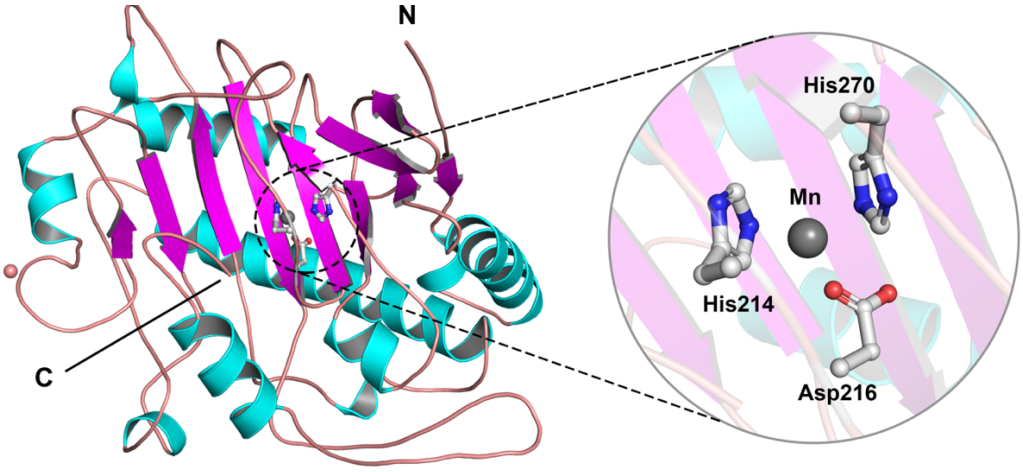


Figure 1.2: *View from a crystal structure of IPNS in complex with manganese (Mn), in which the DSBH was first characterised (PDB ID: 1IPS)[24]. The DSBH core is represented in magenta, and the metal-chelating residues (His214, Asp216, His270) are highlighted in the expanded active site view (white ball-and-stick models).*

The DSBH (jelly-roll) core of 2OG oxygenases has eight β-strands that form two anti-parallel β-sheets. The major sheet consists of strands I, VIII, III and VI; and the minor sheet consists of strands II, VII, IV and V[28-29]. The β-sheets are coiled to form a right-handed helix that takes the shape of a distorted barrel. The active site is sandwiched between the first and second beta strands (β-I and β-II) (Figure 1.3). The DSBH core usually has a conserved *N*-terminal extension that consists of a mixed α/β secondary structure, in which one or two α-helices flank the major β-sheet[28-29]. The active site is typically located at the open end of the DSBH barrel; differences in this region differentiate the 2OG oxygenase superfamily from other proteins that contain the DSBH fold (Figure 1.3). *C*-terminal extensions from the DSBH core are less well conserved. Depending on the specific 2OG oxygenase subfamily, these residues may form loops (after strand VIII) or α-helices, which can be important for substrate binding (e.g. AlkB) or dimerisation (e.g. JmjC hydroxylases)[29]. Residues between DSBH β-IV and β-V strand, known as the βIV-V insert, are frequently involved in substrate recognition[26, 28].

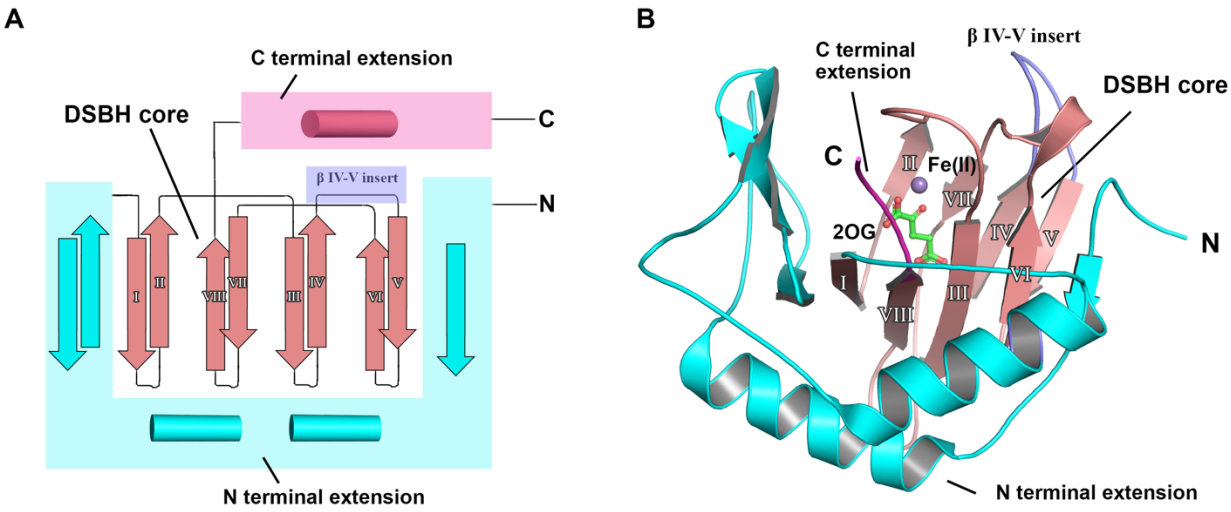


Figure 1.3: *(A) General two-dimensional topology of a 2OG oxygenases. (B) Crystal structure of a 2OG oxygenase adapted from the structure of AlkB, representing three-dimensional structure (PDB ID: 3BIE)[30].*

1.2.2. The iron-binding motif

Since the iron-binding residues of IPNS were characterised, subsequent structural studies have revealed that the non-haem iron [Fe(II)] binding site is highly (but not universally) conserved in 2OG oxygenases[8, 11-12, 22, 28-29]. The metal-binding triad in 2OG oxygenases normally resemble that in IPNS. A HXD/E…H motif (generally, two histidine and one carboxylate facial triad), with aspartate occurring more commonly than glutamate in the triad (i.e. in 80% of structurally characterised 2OG oxygenases)[8, 28-29]. As exemplified by deacetoxycephalosporin-C synthase (DAOCS)[24], a 2OG oxygenase that is involved in cephalosporin biosynthesis, the catalytic Fe(II) is coordinated octahedrally by an HXD/E…H triad (His183, Asp185, His243) and three water molecules in the resting state (Figure 1.4). The binding affinity of Fe(II) to 2OG oxygenases (which are non-haem enzymes) is sometimes relatively low, for instance in comparison with Fe(II)-haem oxygenases, although there is variation of Fe(II)-binding affinity within the 2OG oxygenases[31-32].

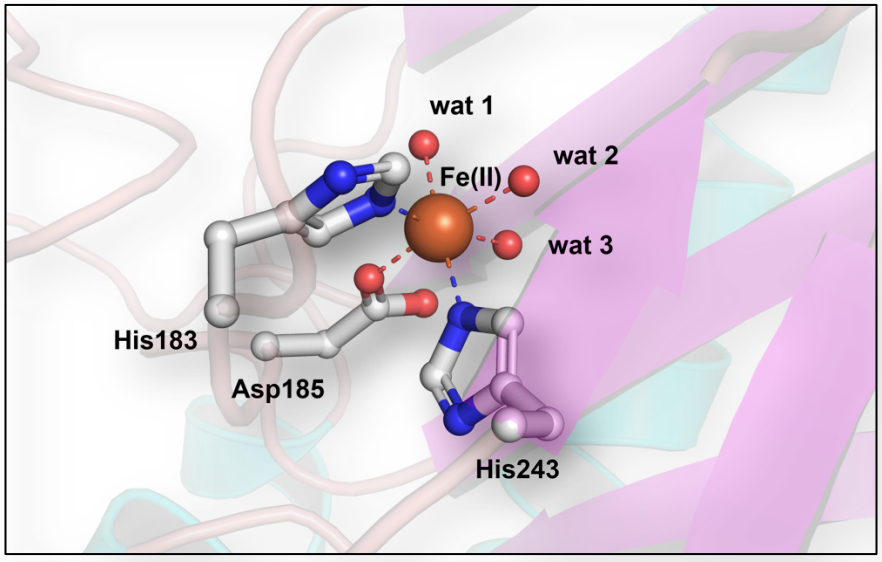


Figure 1.4: *View from a crystal structure of the 2OG oxygenase deacetoxycephalosporin-C synthase (DAOCS), in complex with Fe(II) (PDB ID: 1RXF)[33]. The metal is bound by His183, Asp185 and His243, and three water molecules in an octahedral coordination state.*

1.2.3. 2OG binding site

The (co-substrate) 2OG-binding region is buried within the DSBH core between the major and minor β-sheets. Although adjacent to the Fe(II) binding site, it is away from the active site opening[8, 28-29]. The 2OG coordinates with Fe(II) ion *in* a bidentate manner: the carbonyl and carboxylate oxygens from the oxalyl group replace two of the water molecules bound to the Fe(II) ion (from the resting state), which leaves the remaining coordination site free for an oxygen molecule to bind[8, 28-29] (Figure 1.5). The non-coordinating oxygen atom on the C-1 carboxylate of 2OG forms electrostatic interactions with residues such as arginine, histidine or asparagine. The distal (C-5) carboxylate of 2OG interacts electrostatically with either a (conserved) arginyl or lysyl residue at the back of the active site, and is supported by additional interactions with at least one residue that contains a hydroxyl group (usually threonine, serine or tyrosine). Most nucleic acid demethylases (e.g. the fat mass and obesity associated enzyme FTO), utilise an arginine from the *N*-terminal end of β-VIII to interact with the 2OG C-5 carboxylate[30, 34-35], while most JmjC histone demethylases utilise a lysine from the *C*-terminal end of β-IV to achieve this, except in the human UTX/JMJD3 subfamily, in which the lysine residue is on β-I[36-37].

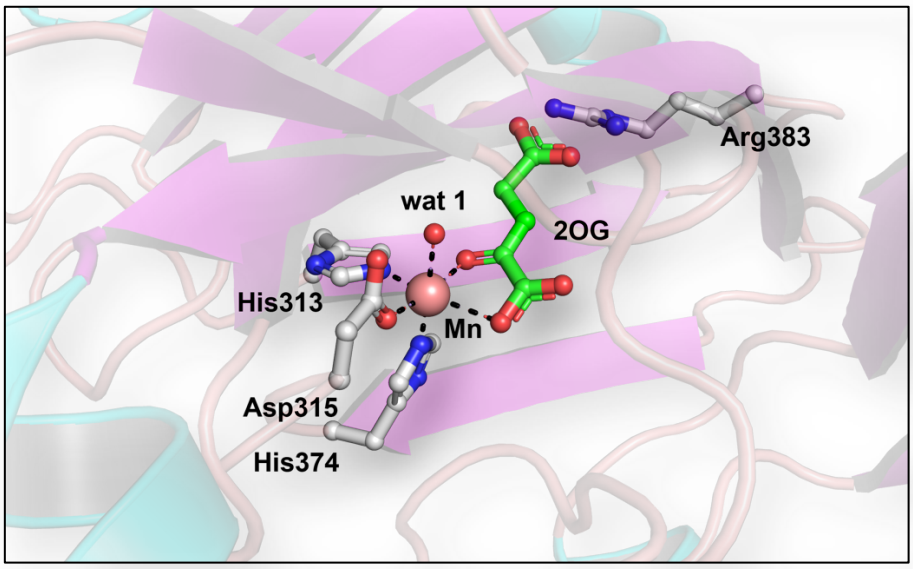


Figure 1.5: *View from a crystal structure of a 2OG oxygenase, hypoxia-inducible factors-prolyl hydroxylases domain-2 (PHD2), in complex with manganese (Mn) (PDB ID: 3HQR)[38]. His313, Asp315 and His374 coordinate the metal. The oxalyl group of 2OG replaces two water molecules in the resting enzyme. The C-5 2OG carboxylate forms an electrostatic interaction with Arg383.*

1.2.4. Substrate recognition region

Despite the presence in all known 2OG oxygenases of a common DSBH fold, which contains the highly (but not universally) conserved Fe(II)- and 2OG-binding sites, the 2OG oxygenases have evolved to recognise a multitude of substrates[2, 8, 28]. Substrates recognised by 2OG oxygenases range from small molecule (primary and secondary) metabolites, including cofactor derivatives (e.g. acyl CoA), to macromolecules such as nucleic acids and peptides[29]. Members of the 2OG oxygenase superfamily probably evolved into distinct subfamilies with characteristic substrate-recognition components. Substrate selectivity is often achieved by engagement of α-helices and β-strands (from the *N*-terminal extension) to bind substrates in the active site. In some cases, a mobile loop in the form of a βIV-V insert may aid to position or 'hold' substrates. The nucleotide recognition lid (NRL) found in members of the AlkB subfamily is able selectively to recognise double- or single-stranded DNA/RNA (dsDNA/RNA or ssDNA/RNA)[39]. Some of the multi-domain JmjC histone demethylases, such as JMJD3, JMJD2A and PHF8, use additional *N*- and/or *C*-terminal domains (outside the DSBH core) for

substrate recognition[32, 40-41]. Substrate binding may involve hydrogen bonding, electrostatic and hydrophobic interactions, provided that the C-H bond (for activation, hence oxidative hydroxylation catalysed by 2OG oxygenases) on the substrate is held in close proximity to the active site Fe(II) ion[29].

1.3. Mechanistic properties of 2-oxoglutarate-dependent oxygenases

Mechanistic studies of the first identified 2OG oxygenases, i.e. the CPHs, led to the proposal that an oxygen molecule bound to Fe(II) in the active site to give an Fe(II)-2OG-substrate ternary complex, with subsequent formation of a peroxide-Fe(III) intermediate[42]. Spectroscopic and crystallographic studies of many other 2OG oxygenases support these proposals [11-12, 15, 21-22, 28, 43-47]. In most cases, 2OG oxygenases catalyse the two-electron oxidation of substrates, coupled with oxidative decarboxylation of 2OG, to give succinate and carbon dioxide (Figure 1.6).

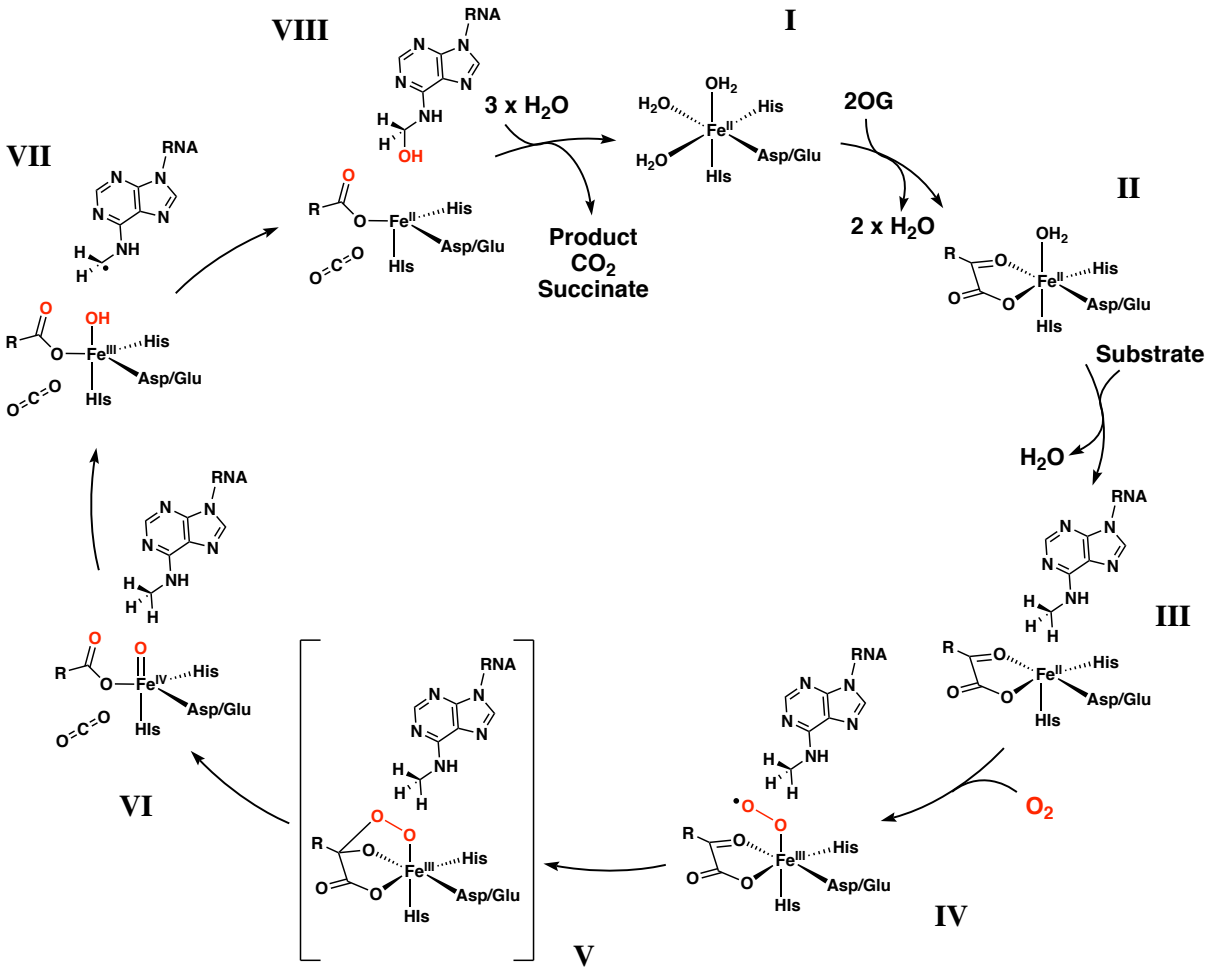


Figure 1.6: *General mechanism for the 2OG oxygenase catalytic cycle. The example illustrated for substrate shows the conversion of N-6-adenosine (m^6A) to an N-6-hydroxymethyl adenosine (hm^6A) in an oligonucleotide.*

1.3.1. The Fe(II) complex and 2OG binding

In the resting state prior to 2OG binding, the Fe(II) ion coordinates with the HxD/E…H triad of the protein and two or three water molecules to form an octahedral coordination complex (Figure 1.6 I)[33]. The catalytic process is initiated by the binding of 2OG to the Fe(II) ion centre. The carbonyl and carboxylate oxygens from the oxalyl group replace two of the water molecules bound to the Fe(II) ion in a bidentate manner (Figure 1.6 II)[8, 28-29]. This leaves one coordination site free to bind oxygen[8, 26]. The oxalyl carboxylate may coordinate (*trans*) either to the axial histidine or to the equatorial histidine of the HxD/E…H triad. The coordination position depends on the specific subfamily (2OG oxygenases)[8, 28, 48].

1.3.2. Substrate and oxygen binding

Spectroscopic and structural studies reveal that the close proximity of the active-site-bound substrate to the Fe(II)-2OG complex activates the Fe(II) centre for oxygen binding, possibly through the β sheets of the DSBH core[49], and displaces a water molecule[8, 15, 28]. Binding of oxygen to the Fe(II)-2OG-substrate complex is reported to oxidise the Fe(II) ion centre to a Fe(III)-superoxo intermediate (Figure 1.6 IV)[45]. The nucleophilic (distal) oxygen of the superoxo intermediate then attacks the C-2 carbonyl carbon of 2OG, and generates a peroxide transition-state species (Figure 1.6 V)[43-44, 50]. Although not structurally observed, computational analysis supports the formation of this peroxide[50]. The delayed binding of oxygen prevents formation of a highly oxidising Fe(IV)=O species until the substrate is coordinated/bound to the metal centre, so the accidental oxidation of the active site residues, which could lead to inactivation, is minimised. Sometimes oxygen binding proceeds prior to substrate coordination, which results in uncoupled 2OG turnover to succinate[51]. Decarboxylation (oxidative) of the cyclic peroxide transition-state (of 2OG) to succinate and carbon dioxide (CO_2) produces a five-coordinated Fe(IV)=O intermediate (Figure 1.6 VI)[44, 47, 52-53].

1.3.3. Substrate hydroxylation and release

The ferryl Fe(IV)=O intermediate is highly oxidising and can abstracts an appropriately aligned hydrogen atom from an inert C-H bond of a substrate, which results in the formation of a radical and spontaneous reduction of the Fe(IV)=O intermediate to Fe(III)-OH (Figure 1.6 VII)[54]. The substrate radical subsequently reacts with the Fe(III)-OH radical in a rebound-type reaction, with concomitant reduction of the Fe(III) ion to Fe(II) and departure of the hydroxylated substrate. This final process restores the enzyme to its resting state (Figure 1.6 VIII)[43, 55-57]. The two oxygen atoms from the oxygen molecule are incorporated separately into succinate

and the hydroxylated product. Evidence from labelled oxygen studies shows that the hydroxyl group oxygen is at least partially derived from dioxygen[58].

1.4. 2-Oxoglutarate dependent oxygenases in nucleic acid modification

A subset of the 2OG oxygenases acts on nucleic acids, known as the nucleic acid oxygenases (NAOXs). To date, members from three subfamilies have been reported to modify nucleic acids: they are AlkB[59-66]; Ten-eleven translocation methylcytosine dioxygenase, TET[67-69]; and the Jumonji C (JmjC) subfamily (specifically, tRNA wybutosine-synthesising protein 5, TYW5)[20, 25, 70]. Reactions that are catalysed by NAOXs include DNA and/or RNA demethylation, RNA hydroxylation and DNA oxidation[71]. Several diseases are linked to malfunction of these enzymes, for instance cancer to AlkBH2, known as ABH2, and ABH8, and obesity to FTO[20].

Nucleic acids carry a diverse range of modifications, which may act as markers to regulate cellular processes in eukaryotic organisms[72]. Among the various modifications, alkylation of nucleic acid bases is the most common. Cellular DNA and RNA are exposed to non-enzymatic and non-specific alkylation (e.g. methylation), by methylation agents such as endogenous S-adenosylmethionine (SAM) or exogenous methyl halides[73]. Accidental methylation at unwanted sites can cause damage or be lethal to the cells[74]. To prevent such damage, organisms have evolved repair mechanisms that involve DNA/RNA repair proteins. *Escherichia coli* respond to alkylation by expressing the *Ada*, *AlkA* and *AlkB* genes[75-77]. Ada removes methyl groups from S_p-methyl-phosphotriester and O^6-methylguanaine[78-79]. AlkA is a glycosylase that cleaves methylated bases from DNA *via* base-excision repair[80-81]. AlkB is a 2OG oxygenase that directly reverses DNA/RNA alkylation *via* oxidative hydroxylation followed by fragmentation to produce demethylated DNA/RNA and formaldehyde[59, 82-87].

Human AlkB homologues, ABH1 and ABH3 are strongly selective for ssDNA/RNA that contains m^1A or m^3C[61-62]. ABH2 displays a preference towards dsDNA that contains m^1A or m^3C[62]. ABH4 has been shown to demethylate K84me1 on actin and plays a regulatory role on the actin–myosin interaction[64]. ABH7 has not yet been demonstrated to show nucleic acid demethylase activity, although it is reported to be involved in programmed cell necrosis[66]. ABH8 is reported to catalyse the hydroxylation of 5-methoxycarbonylmethyluridine in tRNA[65]. A summary of reactions catalysed by NAOXs is given in Figure 1.7.

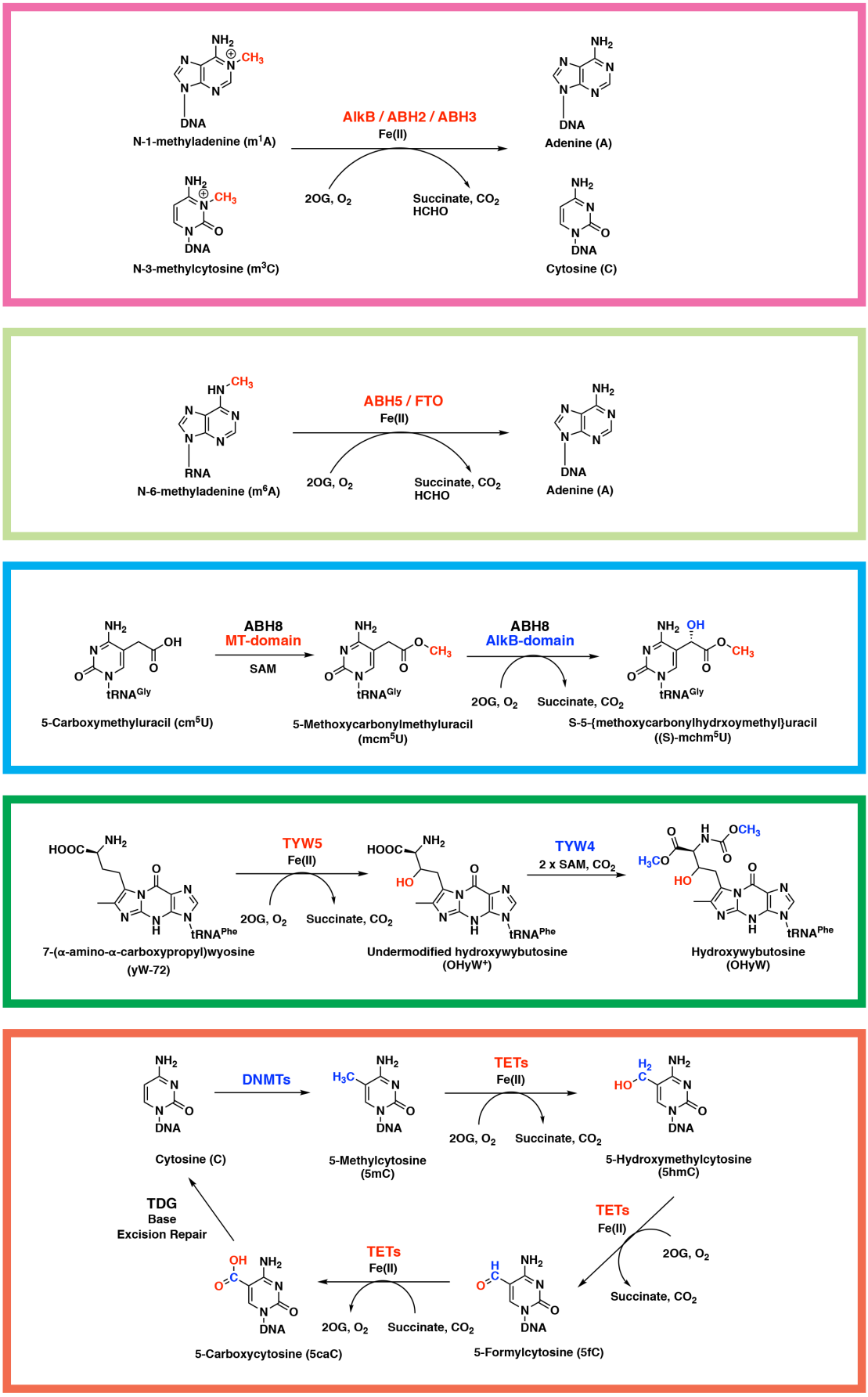


Figure 1.7: *Summary reactions catalysed by nucleic acid oxygenases (NAOXs).*

1.4.1. AlkB and its subfamily of human homologues

1.4.1.1. AlkB

The *E. coli* enzyme AlkB was the first in its 2OG oxygenase subfamily to be reported as a DNA-repair enzyme[59]. AlkB and all its subfamily members share the common DSBH fold that is characteristic of 2OG oxygenases. In addition, the HXD…H Fe(II)-binding residues (His131, Asp133 and His187 for AlkB) and two arginine (Arg204 and Arg210 for AlkB) 2OG-binding residues are strictly conserved across the AlkB subfamily members (Figure 1.8). The first arginine residue, Arg204, has been observed to interact with the C-5 carboxylate on 2OG, while Arg210 is proposed to be involved in substrate binding[30].

```
AlkB            RYAPGAKLSLHQDKDEPDLR--APIVSVSLGLPAIFQFGGLKRND--------------- 163
ABH1            YYRLDSTLGIHVD--RSELDHSKPLLSFSFGQSAIFLLGGLQRD---------------E 188
ABH2            YKDGCDHIGEHRD-DERELAPGSPIASVSFGACRDFVFRH-KDSRG------KSPSRR-V 211
ABH3            YRNEKDSVDWHSD-DEPSLGRCPIIASLSFGATRTFEMRK-KPPPE------ENGDYTYV 232
ABH4            CPERGSAIDPHLD-DAWLWG--ERLVSLNLLSPTVLSMCR-EAPGSL--LLCSAPSAAPE 212
ABH5            DYQPGGCIVSHVD---PIHIFERPIVSVSFFSDSALCFGCKFQFKP---------IRVSE 241
ABH6            QYLPGEGIMPHED-GPLYYP---TVSTISLGSHTVLDFYEPRRPEDD--DPTEQPRPPPR 88
ABH7            DLEARGYIKPHVD-SIKFCG--ATIAGLSLLSPSVMRLVH-TQE--------------PG 152
ABH8*           QYEPGQGIPAHID---THSAFEDEIVSLSLGSEIVMDFKHPDG----------------- 267

AlkB            PLKRLLLEHG-----------------DVVVWGGESRLFY-HGIQPLKAG---------- 195
ABH1            APPPMFMHSG-----------------DIMIMSGFSRLLN-HAVPRVLPNPEGEGLPHCL 230
ABH2            AVVRLPLAHG-----------------SLLMMNHPTNTHWYHSLPVR------------- 241
ABH3            ERVKIPLDHG-----------------TLLIMEGATQADWQHRVPKE------------- 262
ABH4            ALVDSVIAPSRSVLCQEVEVAIPLPARSLLVLTGAARHQWKHAIHR-------------- 258
ABH5            PVLSLPVRRG-----------------SVTVLSGYAADEITHCIRPQ------------- 271
ABH6            PTTSLLLEPR-----------------SLLVLRGPAYTRLLHGIAAARVDALDAASSPPN 131
ABH7            EWLELLLEPG-----------------SLYILRGSARYDFSHEILRDEESFFGER----- 190
ABH8*           TAVPVMLPRR-----------------SLLVMTGESRYLWTHGITCRKFDTVQASENHKS 310

AlkB            ------------------------FHPLTTDCRYNLTFRQAGKKE----  216
ABH1            EAPLPAVLPRDSMVEPCSMEDWQVCASYLKTARVNMTVRQVLATDQNFP  279
ABH2            --------------------------KKVLAPRVNLTFRKILLTKK---  261
ABH3            --------------------------YHSREPRVNLTFRTVYPDPRGAP  285
ABH4            --------------------------RHIEARRVCVTFRELSAEFGPGG  281
ABH5            --------------------------DIKERRAVIILRKTRLDAPRLE  293
ABH6            AAACP---------------SARPGACLVRGTRVSLTIRRVPRVLRAGL  165
ABH7            --------------------------RIPRGRRISVICRSLPEGMGPGE  213
ABH8*           ---------------GIITSDVGDLTLSKRGLRTSFTFRKVRQTPCNCS  344
```

Figure 1.8: *Sequence alignment of the enzymes in the AlkB subfamily. ABH1-7 are human homologues; ABH8* is the sequence from* Macaca fascicularis*. The conserved Fe(II)-binding residues (HXD…H) are highlighted in yellow, and two conserved arginine residues are highlighted in blue. The RXXXXXR motif is characteristic of the AlkB subfamily proteins. Sequence alignment was performed using Clustal Omega[88].*

AlkB directly reverses alkylated DNA/RNA lesions on N-1-methyladenosine (m^1A), N-3-methylthymine (m^3T), 1-methylguanine (m^1G) and N-6-methyladenosine (m^6A) *via* oxidative demethylation (Figure 1.7)[82-85, 89]. AlkB also eliminates etheno DNA lesions including N-6-ethenoadenine (εA), 3,N-4-ethenocytosine (εC) and 1,N-6-ethanoadenosine (ε^1A) *via* a related oxidative mechanism[86-87, 90]. AlkB shows a preference towards positively charged substrates, such as DNA/RNA-containing m^1A and εC. Structural studies show that AlkB utilises the negatively charged residue Asp135 to achieve the apparent substrate selectivity (Figure 1.9)[39]. It is suggested that Thr51, Tyr55, Lys127 and Ser129 act as substrate anchor points, as they interact with the phosphodiester backbone of the nucleic acid substrates[39].

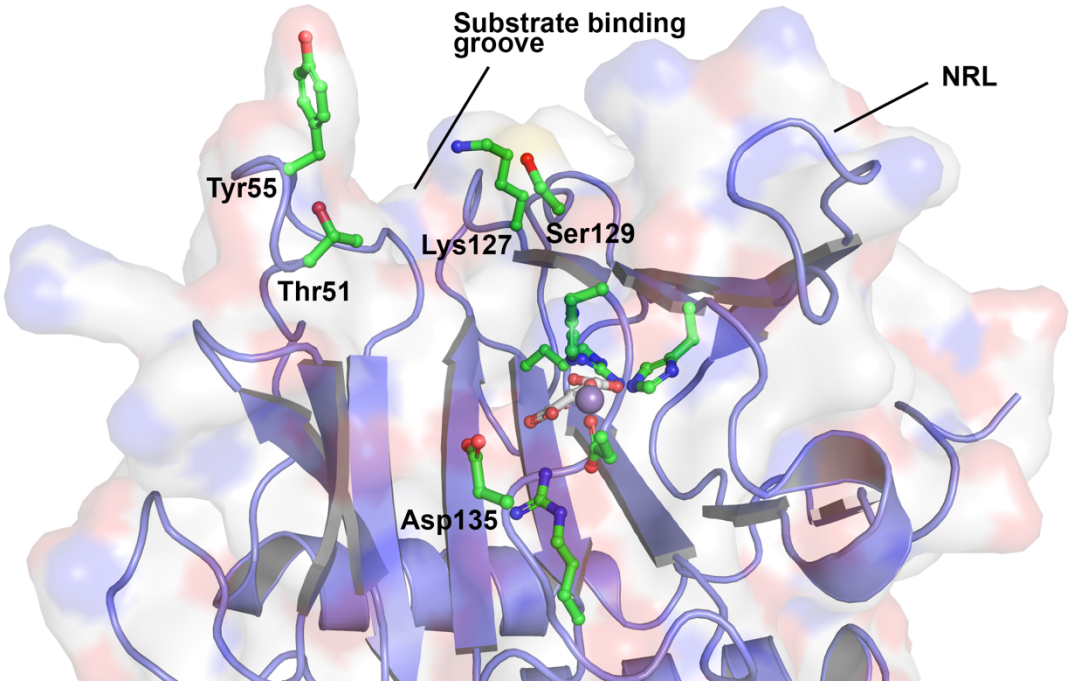


Figure 1.9: *View from a crystal structure of AlkB showing the electropositive (substrate) binding groove. The residues involved in the phosphodiester backbone of the binding groove are labelled (PDB ID: 3BIE)[30]. The residue Asp135, which interacts with the alkylated DNA/RNA base, is also labelled. NRL: nucleic-acid recognition lid.*

1.4.1.2. ABH1

ABH1 is one of the nine human homologues of *E. coli* AlkB, and it is ubiquitously expressed in the human body, although its biological function is still debated[61-62, 91]. ABH1 shares 34% of its sequence identity and 59% similarity with AlkB[92]. Initially it was proposed that ABH1

acted as a DNA-repair enzyme in the same way as AlkB; however, treatment with MMS did not stimulate ABH1 expression, as it did with AlkB[62]. Subsequent studies have revealed that ABH1 exhibits m^3C demethylase activity *in vitro*[61]. More recently ABH1 has been reported to be a histone H2A demethylase that has a functional role in neural differentiation[91]. Other reports show that ABH1 cleaves DNA at apurine/aprymidine (AP) sites in the absence of 2OG and iron[93-94]. The conflicting reports on ABH1's biological role cast doubts on its role as a nucleic acid demethylase. Definitive knowledge should be sought for this enzyme.

1.4.1.3. ABH2 and ABH3

ABH2 was shown to demethylate the cytotoxic m^1A and m^3C from dsDNA, and exhibits moderate (demethylation) activity towards m^3T[35, 62]. It has been proposed that ABH3 acts similarly to ABH2 as a DNA-repair enzyme on substrates with the same base modifications. However, ABH3 shows preference towards ssDNA[95]. Owing to its preference towards single-stranded nucleic acids, ABH3 has been considered to play a role in RNA repair[84]. Subsequent studies have reported that ABH3 associates with 3'-5' helicase activating signal co-integrator 1 complex subunit 3 (ASCC3), which unwinds dsDNA to enable ABH3 to repair alkylation damage in ssDNA. This indicates that ABH3 plays a role predominantly in DNA repair with the help of a helicase[96].

Crystal structures of ABH2 in complex with dsDNA reveal that a phenylalanine 'finger' (Phe102) from the NRL is involved in flipping the alkylated base into the active site for repair[30]. By contrast, AlkB, which lacks an analogous finger, flips an alkylated base *via* a direct stacking mechanism[30, 39]. A crystal structure of ABH3 in the absence of a primary substrate has been reported[97]. ABH3 is shown in this report to exhibit a more polar protein surface than AlkB or ABH2, and this narrows its substrate specificity[97]. ABH3 also lacks the phenylalanine finger found in ABH2. It utilises a slightly longer loop (a β-hairpin), which forms part of the nucleic

acid recognition lid 1 (NRL 1), which is involved in single-stranded nucleic acid selectivity (Figure 1.10). ABH3 is highly expressed in prostate-cancer cells, so it is a potential drug target for therapeutic research.

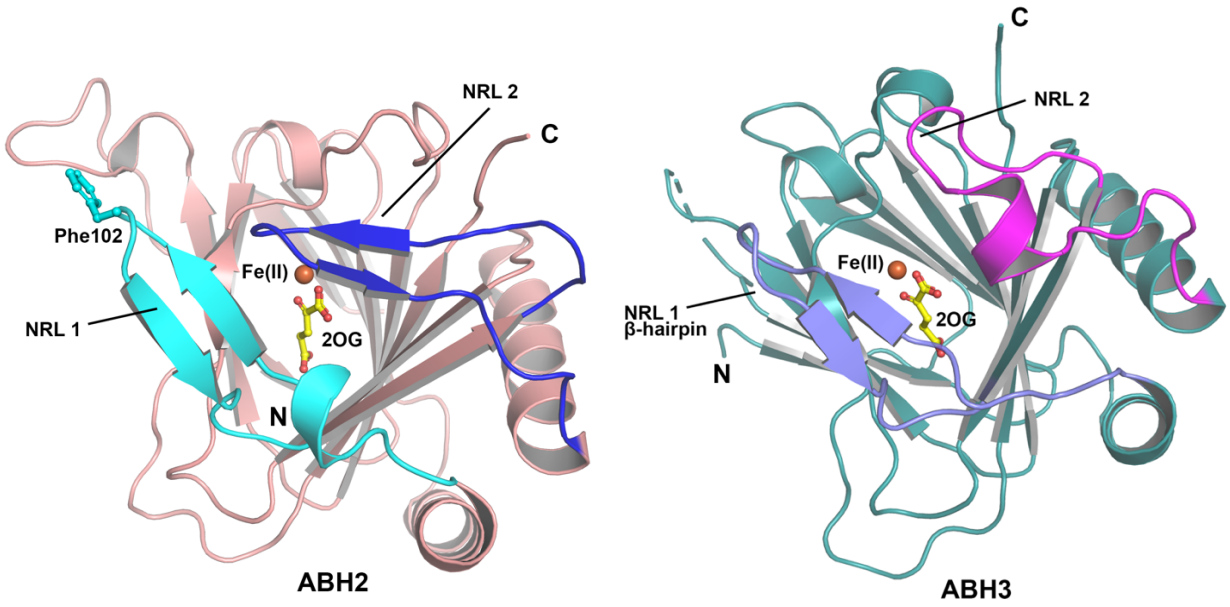


Figure 1.10: *Views from crystal structures of human AlkB homologues 2 and 3 (ABH2 and ABH3). The Phe102 finger (cyan) in ABH2 is observed to flip an alkylated base into the active site, while the β-hairpin in NRL1 (slate) from ABH3 is thought to confer single-stranded DNA selectivity. It is proposed that the extra-long loop in NRL2 with antiparallel β sheets from ABH2 interacts with dsDNA. (PDB ID: [30]for ABH2, 2IUW for ABH3[98]). Fe(II), orange sphere; 2OG, yellow sticks; NRL2, blue on ABH2, magenta on ABH3.*

1.4.1.4. ABH4, ABH6 and ABH7

The biological roles of ABH4, ABH6 and ABH7 are unclear. In particular, no functional studies on ABH6 have been reported to date. ABH4 has been reported to demethylate a monomethylated lysine (K84me1) on actin, and may regulate actin-myosin interaction[64]. ABH7 is localised in the mitochondria[66, 99]. Its alkylation repair activity towards nucleic acid has not been observed[64]. Interestingly, ABH7 deletion in mice has been observed to increase their body weight[100]; this suggests that ABH7 has a regulatory role in fatty-acid metabolism.

1.4.1.5. ABH5

ABH5 is a nuclear protein and is ubiquitously expressed in various tissues. Its highest expression has been observed in the lung and testis[63, 101]. ABH5 has been reported to be up-

regulated *via* the hypoxia inducible factor (HIF) pathway during hypoxia[102]. In the same study it showed no demethylase activity against m^1A and m^3C in ssDNA[102]. However, ABH5 was later reported to demethylate m^6A in mRNA (Figure 1.7), and ABH5 deficiency caused impaired fertility in mice as a result of compromised spermatogenesis[63]. It was further illustrated that ABH5 localises with SC35 splice factor in nuclear speckles, which indicates that ABH5 may play a role in mRNA processing[63]. Additionally, ABH5 was found to show preference toward ssRNA substrate (compared with dsRNA and stem-loop RNA); its activity was found to be dependent on a sequence, in which m^6A in a consensus motif GG(m^6A)CU resulted in the highest demethylation efficiency. Crystallographic studies revealed that a highly mobile loop on the β IV-V insert (NRL 1) blocked double-stranded nucleic acids from binding to the substrate binding region, supporting its selectivity toward single-stranded RNA[103].

1.4.1.6. ABH8

ABH8 was the first enzyme that has been reported to act as a nucleic acid hydroxylase in the AlkB subfamily, and the first member found to be involved in tRNA modification[65]. Unlike its subfamily members, ABH8 contains three domains: an AlkB-like domain, an *N*-terminal RNA recognition motif (RRM), and a *C*-terminal methyltransferase (MT) domain[104]. The MT domain of ABH8 alkylates 5-carboxymethyluridine (cm^5U) to 5-methoxycarbonylmethyluridine (mcm^5U)[105-106]. An ABH8 knockout study showed that the mcm^5U was important for recoding the UGA stop codon for the integration of selenocysteine[106]. Although an early report that the AlkB domain of ABH8 performed as a demethylase[65], it was later revealed that it hydroxylated mcm^5U to S-5-(methoxycarbonylhydroxymethyl)uracil (S-$mchm^5U$)[107]. Despite the observation of both diastereomers *R*- and *S*-$mchm^5U$ diastereomers in mammalian tRNA[107], ABH8 has been observed to catalyse only the formation of the *S*-diastereomer[105, 107]. This observation has led to the proposal that formation of the *R*-diastereomer may be catalysed by another 2OG

oxygenase[107]. ABH8 is linked to cancer as many cancer cell lines have been observed to show ABH8 over-expression, and a siRNA knockdown study has shown that ABH8 is involved in bladder-cancer progression[108].

1.4.1.7. The fat mass and obesity-associated protein (FTO)

The *Fto* gene, which encodes for the fat mass and obesity-associated protein (FTO), was first identified in a genome-wide association study. This established that single nucleotide polymorphisms (SNPs) in the first intron of the *Fto* gene were associated with increased risk of obesity[109]. Inactivation of the *Fto* gene resulted in protection from obesity[110], thus, the prospect that inhibition of FTO activity offered a potential anti-obesity treatment attracted much attention.

FTO is ubiquitously expressed in the human body. Its highest expression level is found in the hypothalamus of the brain, which is important for energy homeostasis[60]. FTO knockout studies on mice demonstrated lean phenotype[110]; this observation was attributed to elevated energy expenditure, and supported the proposal that alteration of FTO levels had an impact on energy homeostasis[110]. Over-expression of FTO in mice correlated with increased food intake, which resulted in increased overall body weight of mice and especially increased fat mass[111]. Recently, a non-coding sequence within the *Fto* gene (i.e. an intron) was reported to interact with the promoter of Iroquois-class homeodomain protein (IRX3) in humans. A single nucleotide polymorphism (SNP) in FTO enhanced IRX3 expression, which affected body mass and composition[112]. This finding suggests that FTO may not be directly associated to (fat) body mass. In addition, FTO has been reported to be associated with melanoma[113], and mutation of the active site residue Arg96 causes retardation of postnatal growth, facial dysmorphism and certain brain malfunctions in human[114].

Among the assigned human analogues of AlkB (ABH1-8), FTO was one of the first RNA demethylases to be discovered[60]; this followed its initial assignment as a 2OG oxygenase/demethylase[10]. FTO was initially reported to demethylate m^3U in ssRNA and m^3T in ssDNA[10]. Subsequent biochemical analyses showed that it preferentially demethylated m^6A over other previously proposed substrates[9]. FTO's preferred substrate, m^6A, is the most abundant modified nucleoside in mRNA[115].

Although all the AlkB subfamily members share the same highly conserved 2OG oxygenase DSBH fold, which supports strictly conserved 2OG and Fe(II) binding residues, their substrate selectivities differ, although they sometimes overlap.

Notably, FTO and ABH5 are the only AlkB homologous enzymes that are reported to preferentially demethylate m^6A-containing ssRNA (exclusively for ABH5). FTO also accepts m^3T-containing ssDNA as a substrate (albeit to a lesser extent than m^6A-containing ssRNA)[9-10, 63]. FTO and ABH5 levels vary substantially in the human body. The ABH5 protein is reported to be highly expressed in the lung and testis, less so in pancreas, spleen and ovary[101]. By contrast, the FTO protein is expressed ubiquitously across multiple tissues, while it is most highly expressed in the hypothalamus of the brain[60]. Modulation of FTO levels in the arcuate nucleus (ARC) of the hypothalamus can influence food intake[116], whereas alternation of ABH5 levels leads to impaired fertility and decreased RNA metabolism[63]. Given these observations regarding the biological roles of ABH5 and FTO, study of their molecular functions is of interest.

1.4.2. TET enzymes

The human ten-level-translocation enzymes, TET1-3, were the first mammalian proteins identified as DNA 5-methylcytosine (5mC) hydroxylases. They hydroxylate 5mC on CG islands to give 5-hydroxymethylcytosine (5hmC)[67]. The TET enzymes were then reported to

also catalyse sequential oxidations of 5hmC first to 5-formylcytosine (5fC) and subsequently to 5-carboxycytosine (5caC) (Figure 1.7)[68-69]. The 5caC is then repaired by thymine DNA glycosylase (TDG) *via* base excision, thus removing the methylation on cytosine[69]. The TETs are reported to play a role in stem-cell differentiation and cancer[20, 117]. A reduced level of 5hmC has been linked to various types of cancers, such as skin[118], lung[119] and myeloid[120]. The mechanism is partially attributed to TET enzyme activity in the alteration of cytosine-specific epigenetic markers[20, 117].

1.4.3. TYW5

The tRNA wybutosine-synthesising protein 5 (TYW5) is the only identified member of the JmjC subfamily that takes nucleic acid as substrate. TYW5 hydroxylates a wybutosine precursor in the hydroxywybutosine biosynthesis pathway, which is located near the wobble uridine base of $tRNA^{Phe}$.[121]

1.5. RNA epigenetics

The discoveries of catalytic RNAs, non-coding RNAs and pseudouridine[122] have shifted nucleic-acid research from DNA towards RNA[123]. More than 100 types of post-transcriptional modifications have been identified, including ribosomal RNA (rRNA), transfer RNA (tRNA), messenger RNA (mRNA) and long non-coding RNA (lcRNA)[124]. Many modifications involve alkylation (in particular, methylation) of side-chain bases or 2'-hydroxyl group of the ribose sugar in RNA[124], while others involve more complex enzyme catalysed modifications[125]. It has been proposed that modifications of rRNA control ribosome assembly quality[126]. Modifications of tRNA are involved in tRNA stability and folding[127]. Internal modifications in mRNA (except splicing) have not been well studied until recently[123, 128-134]. The most prevalent mRNA modification is m^6A, present on average in approximately three sites per mRNA

molecule (Figure 1.11 A)[135-138]. Modifications such as m^5C or 2'-O-methylated nucleotides (Nm) have also been identified in mRNA (Figure 1.11 B, C)[139-140].

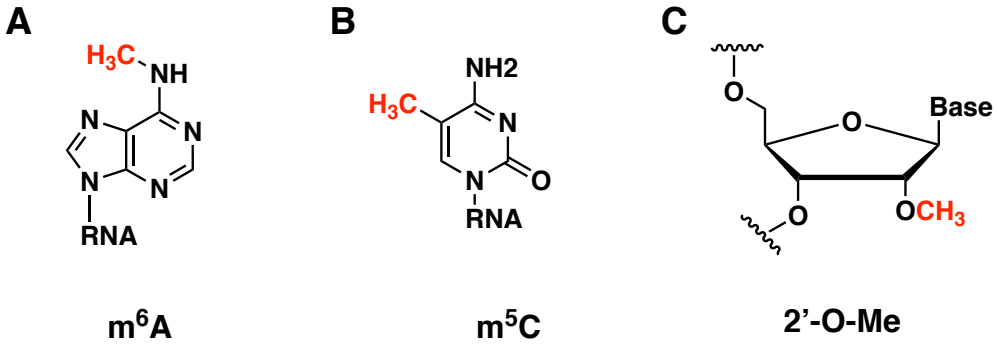


Figure 1.11: *Chemical structures of common internal mRNA modifications (A) m^6A; (B) m^5C; (C) Nm.*

The discovery of the m^6A demethylase activity of FTO [9] sparked interest in research into mRNA modifications, due to the implication that physiologically relevant m^6A modification may be dynamically regulated[141]. This discovery suggested that RNA methylation might be involved in post-transcriptional regulation process, analogous to DNA methylation and histone modification[123, 142]. Indeed, subsequent studies reported that m^6A was involved in the regulation of gene expression, mRNA splicing and transport[136, 143-144]. The heterodimeric methyltransferase-like 3 and 14 proteins (METTL3/14) catalyse methylation of mammalian nuclear RNA[145-146]. The Wilms' tumour 1-associating protein (WTAP) is also involved as a regulatory protein in mammalian cells[147]. METTL3/14 are reported to transfer methyl groups from S-adenosylmethionine (SAM) to a consensus RNA sequence Pu[G>A]AC[A/C/U][136], wherein the central adenosine is methylated. METTL3 alone exhibits reduced efficiency in the transfer of the methyl group compared with its efficiency in the METTL3/14 complex[145-147]. The METTL3/14-WTAP complexes are thus dubbed the m^6A 'epigenetic writers'[148-149].

FTO along with another AlkB subfamily member, ABH5, demethylates m^6A. Thus these 2OG oxygenases are proposed to act as 'RNA epigenetic erasers'[63]. YTH domain containing proteins

(YTHDF1–3), which are involved in regulation of mRNA degradation, are reported to display specific binding preference for m^{6}A in ssRNA and have been designated as 'RNA epigenetic readers'[144, 150]. It is proposed that these enzymes form a dynamic and highly versatile complex for mRNA epigenetic regulation (Figure 1.12).

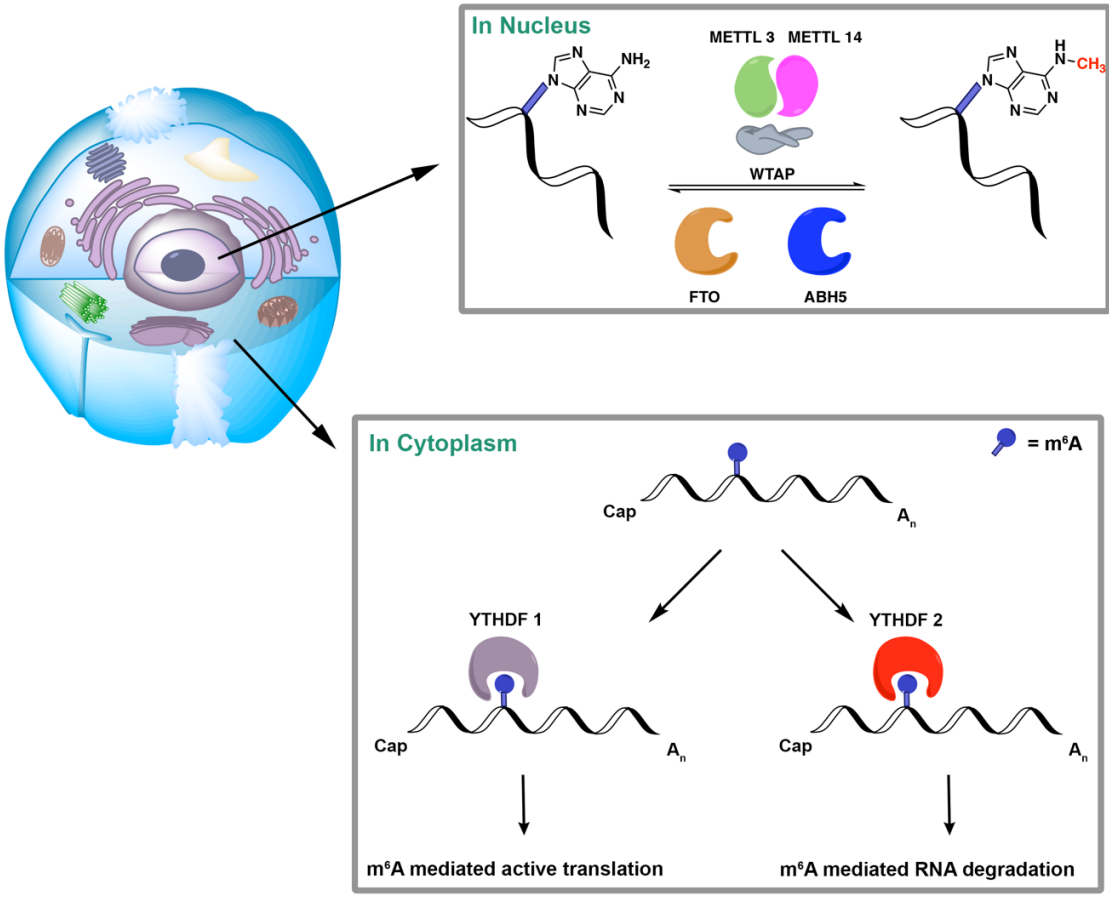


Figure 1.12: *Scheme showing N-6-methyladenosine (m^{6}A) in mRNA and Its biological significance. It is proposed that reversible methylation and demethylation occur in the nucleus, catalysed by methyltransferase 'writers' and demethylase 'erasers'. The m^{6}A modification affects the fate of mRNA: it is recognised by YTHDF 1, which switches on mRNA translation, or by YTHDF 2, which accelerates mRNA degradation. Figure adapted from Liu et al.[141].*

The m^{6}A modification is involved in the regulation of a diverse range of biological processes, and dysregulation of m^{6}A has been linked to many diseases. The m^{6}A methyltransferases METTL3 and METTL14 are crucial for cell development, and their inactivation results in cell death[151-152]. Diseases associated with METTL3 and METTL14 include prostatitis, Aicardi syndrome and alcohol dependence[151-152]. Variants within the non-coding sequence of the m^{6}A demethylase gene *Fto* have been associated with increased risk of obesity and diabetes[60, 111,

[153]. Later studies have reported that the *Fto* gene forms long-range functional connections with the homeobox gene *Irx3*, which may be linked to obesity[112]. Over-expression of the *Fto* gene causes a decrease in global m^6A levels, which could disrupt neural processes including dopaminergic signalling in the mouse midbrain[154], neurogenesis in adult mice[155], learning, and memory[156]. These observations suggest that m^6A is closely linked with brain activity. Recently, down-regulation of m^6A mRNA methylation (*via* over-expression of FTO) has also been observed to be involved in dopaminergic neuronal death[157], a biological marker for Parkinson's disease.

Although mRNA modifications have been well known since the 1970s, their functional importance in mRNA metabolism and their effects on human biology have not been widely studied. The discovery of the m^6A-demethylase FTO in 2011 directly linked m^6A modification in mRNA to disease, which stimulated work in the field. Given the extensive involvement of different enzymes in (acting on m^6A) mRNA regulation, e.g. FTO and METTL3/14; attenuation (inhibition or activation) of their activity may be a desirable prospect for therapeutic purposes.

1.6. Thesis outline

The principal aim of the first part of the work described in this thesis was to contribute to biochemical characterisation of the nucleic acid demethylases and their inhibition. Specific objectives were:

- Design of second-generation inhibitors for FTO (**Chapter 2**).
- Develop a robust and accurate assay platform for high-throughput FTO inhibitor screening (**Chapter 2**)
- Biochemical characterisation of FTO and comparison of its products with other subfamily members (**Chapter 3**).
- Biochemical characterisation of a pathological variant of human FTO (**Chapter 4**).

In addition to these studies, investigations have been initiated in order to study the inhibition of metallo-β-lactamases and stability of their enethiol inhibitors (**Chapter 5**).

References

1. Hutton, J. J., Jr.; Kaplan, A.; Udenfriend, S., Conversion of the amino acid sequence gly-pro-pro in protein to gly-pro-hyp by collagen proline hydroxylase. *Arch Biochem Biophys* **1967,** *121* (2), 384-91.

2. Flashman, E.; Schofield, C. J., The most versatile of all reactive intermediates? *Nat Chem Biol* **2007,** *3* (2), 86-7.

3. Loenarz, C.; Schofield, C. J., Expanding chemical biology of 2-oxoglutarate oxygenases. *Nat Chem Biol* **2008,** *4* (3), 152-6.

4. Prescott, A. G.; Lloyd, M. D., The iron(II) and 2-oxoacid-dependent dioxygenases and their role in metabolism. *Nat Prod Rep* **2000,** *17* (4), 367-83.

5. Kelly, D. J.; Hughes, N. J., The Citric Acid Cycle and Fatty Acid Biosynthesis. In *Helicobacter pylori: Physiology and Genetics*, Mobley, H. L. T.; Mendz, G. L.; Hazell, S. L., Eds. Washington (DC), 2001.

6. Ozer, A.; Bruick, R. K., Non-heme dioxygenases: cellular sensors and regulators jelly rolled into one? *Nat Chem Biol* **2007,** *3* (3), 144-53.

7. Costas, M.; Mehn, M. P.; Jensen, M. P.; Que, L., Dioxygen activation at mononuclear nonheme iron active sites: rnzymes, models, and intermediates. *Chem Rev* **2004,** *104* (2), 939-86.

8. Clifton, I. J.; McDonough, M. A.; Ehrismann, D.; Kershaw, N. J.; Granatino, N.; Schofield, C. J., Structural studies on 2-oxoglutarate oxygenases and related double-stranded beta-helix fold proteins. *J Inorg Biochem* **2006,** *100* (4), 644-69.

9. Jia, G.; Fu, Y.; Zhao, X.; Dai, Q.; Zheng, G.; Yang, Y.; Yi, C.; Lindahl, T.; Pan, T.; Yang, Y.-G.; He, C., N6-Methyladenosine in nuclear RNA is a major substrate of the obesity-associated FTO. *Nat Chem Biol* **2011,** *7*, 885-7.

10. Jia, G.; Yang, C. G.; Yang, S.; Jian, X.; Yi, C.; Zhou, Z.; He, C., Oxidative demethylation of 3-methylthymine and 3-methyluracil in single-stranded DNA and RNA by mouse and human FTO. *FEBS Lett* **2008,** *582* (23-24), 3313-9.

11. Zhang, Z.; Ren, J. S.; Clifton, I. J.; Schofield, C. J., Crystal structure and mechanistic implications of 1-aminocyclopropane-1-carboxylic acid oxidase--the ethylene-forming enzyme. *Chem Biol* **2004,** *11* (10), 1383-94.

12. Schofield, C. J.; Zhang, Z., Structural and mechanistic studies on 2-oxoglutarate-dependent oxygenases and related enzymes. *Curr Opin Struct Biol* **1999,** *9* (6), 722-31.

13. Vaillancourt, F. H.; Yeh, E.; Vosburg, D. A.; Garneau-Tsodikova, S.; Walsh, C. T., Nature's inventory of halogenation catalysts: oxidative strategies predominate. *Chem Rev* **2006,** *106* (8), 3364-78.

14. Butler, A.; Sandy, M., Mechanistic considerations of halogenating enzymes. *Nature* **2009,** *460* (7257), 848-54.

15. Zhou, J.; Kelly, W. L.; Bachmann, B. O.; Gunsior, M.; Townsend, C. A.; Solomon, E. I., Spectroscopic studies of substrate interactions with clavaminate synthase 2, a multifunctional alpha-KG-dependent non-heme iron enzyme: correlation with mechanisms and reactivities. *J Am Chem Soc* **2001,** *123* (30), 7388-98.

16. Ryle, M. J.; Hausinger, R. P., Non-heme iron oxygenases. *Curr Opin Chem Biol* **2002,** *6* (2), 193-201.

17. Thinnes, C. C.; England, K. S.; Kawamura, A.; Chowdhury, R.; Schofield, C. J.; Hopkinson, R. J., Targeting histone lysine demethylases - progress, challenges, and the future. *Biochim Biophys Acta* **2014,** *1839* (12), 1416-32.

18. Rose, N. R.; McDonough, M. A.; King, O. N. F.; Kawamura, A.; Schofield, C. J., Inhibition of 2-oxoglutarate dependent oxygenases. *Chemical Society Reviews* **2011,** *40* (8), 4364-97.

19. Yan, L.; Colandrea, V. J.; Hale, J. J., Prolyl hydroxylase domain-containing protein inhibitors as stabilizers of hypoxia-inducible factor: small molecule-based therapeutics for anemia. *Expert Opin Ther Pat* **2010,** *20* (9), 1219-45.

20. Thalhammer, A.; Aik, W.; Bagg, E. A. L.; Schofield, C. J., The potential of 2-oxoglutarate oxygenases acting on nucleic acids as therapeutic targets. *Drug Discov Today Ther Strateg* **2012,** *9* (2), e91-e100.

21. Clifton, I. J.; Hsueh, L. C.; Baldwin, J. E.; Harlos, K.; Schofield, C. J., Structure of proline 3-hydroxylase. Evolution of the family of 2-oxoglutarate dependent oxygenases. *Eur J Biochem* **2001,** *268* (24), 6625-36.

22. Elkins, J. M.; Ryle, M. J.; Clifton, I. J.; Dunning Hotopp, J. C.; Lloyd, J. S.; Burzlaff, N. I.; Baldwin, J. E.; Hausinger, R. P.; Roach, P. L., X-ray crystal structure of

Escherichia coli taurine/α-ketoglutarate dioxygenase complexed to ferrous iron and substrates. *Biochemistry* **2002,** *41* (16), 5185-92.

23. Zhang, Z.; Ren, J.; Stammers, D. K.; Baldwin, J. E.; Harlos, K.; Schofield, C. J., Structural origins of the selectivity of the trifunctional oxygenase clavaminic acid synthase. *Nat Struct Biol* **2000,** *7* (2), 127-33.

24. Valegard, K.; van Scheltinga, A. C.; Lloyd, M. D.; Hara, T.; Ramaswamy, S.; Perrakis, A.; Thompson, A.; Lee, H. J.; Baldwin, J. E.; Schofield, C. J.; Hajdu, J.; Andersson, I., Structure of a cephalosporin synthase. *Nature* **1998,** *394* (6695), 805-9.

25. Iyer, L. M.; Abhiman, S.; de Souza, R. F.; Aravind, L., Origin and evolution of peptide-modifying dioxygenases and identification of the wybutosine hydroxylase/hydroperoxidase. *Nucleic Acids Res* **2010,** *38* (16), 5261-79.

26. Aik, W. S.; Chowdhury, R.; Clifton, I. J.; Hopkinson, R. J.; Leissing, T.; al, e., *2-Oxoglutarate-dependent oxygenases*. The Royal Society of Chemistry: 2015; p 59-94.

27. Clissold, P. M.; Ponting, C. P., JmjC: cupin metalloenzyme-like domains in jumonji, hairless and phospholipase A2beta. *Trends Biochem Sci* **2001,** *26* (1), 7-9.

28. McDonough, M. A.; Loenarz, C.; Chowdhury, R.; Clifton, I. J.; Schofield, C. J., Structural studies on human 2-oxoglutarate dependent oxygenases. *Curr Opin Struct Biol* **2010,** *20* (6), 659-72.

29. Aik, W.; McDonough, M. A.; Thalhammer, A.; Chowdhury, R.; Schofield, C. J., Role of the jelly-roll fold in substrate binding by 2-oxoglutarate oxygenases. *Curr Opin Struct Biol* **2012,** *22* (6), 691-700.

30. Yang, C. G.; Yi, C.; Duguid, E. M.; Sullivan, C. T.; Jian, X.; Rice, P. A.; He, C., Crystal structures of DNA/RNA repair enzymes AlkB and ABH2 bound to dsDNA. *Nature* **2008,** *452* (7190), 961-5.

31. Hopkinson, R. J.; Tumber, A.; Yapp, C.; Chowdhury, R.; Aik, W.; Che, K. H.; Li, X. S.; Kristensen, J. B. L.; King, O. N. F.; Chan, M. C.; Yeoh, K. K.; Choi, H.; Walport, L. J.; Thinnes, C. C.; Bush, J. T.; Lejeune, C.; Rydzik, A. M.; Rose, N. R.; Bagg, E. A.; McDonough, M. A.; Krojer, T.; Yue, W. W.; Ng, S. S.; Olsen, L.; Brennan, P. E.; Oppermann, U.; Muller-Knapp, S.; Klose, R. J.; Ratcliffe, P. J.; Schofield, C. J.; Kawamura, A., 5-Carboxy-8-hydroxyquinoline is a broad spectrum 2-oxoglutarate oxygenase inhibitor which causes iron translocation. *Chem Sci* **2013,** *4* (8), 3110-7.

32. Kruidenier, L.; Chung, C.-w.; Cheng, Z.; Liddle, J.; Che, K.; Joberty, G.; Bantscheff, M.; Bountra, C.; Bridges, A.; Diallo, H.; Eberhard, D.; Hutchinson, S.; Jones, E.; Katso, R.; Leveridge, M.; Mander, P. K.; Mosley, J.; Ramirez-Molina, C.; Rowland, P.; Schofield, C. J.; Sheppard, R. J.; Smith, J. E.; Swales, C.; Tanner, R.; Thomas, P.; Tumber, A.; Drewes, G.; Oppermann, U.; Patel, D. J.; Lee, K.; Wilson, D. M., A selective jumonji H3K27 demethylase inhibitor modulates the proinflammatory macrophage response. *Nature* **2012,** *488* (7411), 404-8.

33. Valegård, K.; van Scheltinga, A. C. T.; Lloyd, M. D.; Hara, T.; Ramaswamy, S.; Perrakis, A.; Thompson, A.; Lee, H.-J.; Baldwin, J. E.; Schofield, C. J.; Hajdu, J.; Andersson, I., Structure of a cephalosporin synthase. *Nature* **1998,** *394* (6695), 805-9.

34. Yi, C.; Jia, G.; Hou, G.; Dai, Q.; Zhang, W.; Zheng, G.; Jian, X.; Yang, C. G.; Cui, Q.; He, C., Iron-catalysed oxidation intermediates captured in a DNA repair dioxygenase. *Nature* **2010,** *468* (7321), 330-3.

35. Aas, P. A.; Otterlei, M.; Falnes, P. Ø.; Vågbø, C. B.; Skorpen, F.; Akbari, M.; Sundheim, O.; Bjørås, M.; Slupphaug, G.; Seeberg, E.; Krokan, H. E., Human and bacterial oxidative demethylases repair alkylation damage in both RNA and DNA. *Nature* **2003,** *421* (6925), 859-863.

36. Sengoku, T.; Yokoyama, S., Structural basis for histone H3 Lys 27 demethylation by UTX/KDM6A. *Genes Dev* **2011,** *25* (21), 2266-77.

37. Ng, S. S.; Kavanagh, K. L.; McDonough, M. A.; Butler, D.; Pilka, E. S.; Lienard, B. M.; Bray, J. E.; Savitsky, P.; Gileadi, O.; von Delft, F.; Rose, N. R.; Offer, J.; Scheinost, J. C.; Borowski, T.; Sundstrom, M.; Schofield, C. J.; Oppermann, U., Crystal structures of histone demethylase JMJD2A reveal basis for substrate specificity. *Nature* **2007,** *448* (7149), 87-91.

38. Chowdhury, R.; McDonough, M. A.; Mecinovic, J.; Loenarz, C.; Flashman, E.; Hewitson, K. S.; Domene, C.; Schofield, C. J., Structural basis for binding of hypoxia-inducible factor to the oxygen-sensing prolyl hydroxylases. *Structure* **2009,** *17* (7), 981-9.

39. Yu, B.; Edstrom, W. C.; Benach, J.; Hamuro, Y.; Weber, P. C.; Gibney, B. R.; Hunt, J. F., Crystal structures of catalytic complexes of the oxidative DNA/RNA repair enzyme AlkB. *Nature* **2006,** *439* (7078), 879-84.

40. Horton, J. R.; Upadhyay, A. K.; Qi, H. H.; Zhang, X.; Shi, Y.; Cheng, X., Enzymatic and structural insights for substrate specificity of a family of jumonji histone lysine demethylases. *Nat Struct Mol Biol* **2010,** *17* (1), 38-43.

41. Chen, Z.; Zang, J.; Kappler, J.; Hong, X.; Crawford, F.; Wang, Q.; Lan, F.; Jiang, C.; Whetstine, J.; Dai, S.; Hansen, K.; Shi, Y.; Zhang, G., Structural basis of the recognition of a methylated histone tail by JMJD2A. *Proc Natl Acad Sci USA* **2007,** *104* (26), 10818-23.

42. Hanauske-Abel, H. M.; Günzler, V., A stereochemical concept for the catalytic mechanism of prolylhydroxylase: Applicability to classification and design of inhibitors. *J. Theor. Biol.* **1982,** *94* (2), 421-455.

43. Grzyska, P. K.; Appelman, E. H.; Hausinger, R. P.; Proshlyakov, D. A., Insight into the mechanism of an iron dioxygenase by resolution of steps following the Fe=O species. *Proc Natl Acad Sci USA* **2010,** *107* (9), 3982-9.

44. Price, J. C.; Barr, E. W.; Hoffart, L. M.; Krebs, C.; Bollinger, J. M., Jr., Kinetic dissection of the catalytic mechanism of taurine:alpha-ketoglutarate dioxygenase (TauD) from Escherichia coli. *Biochemistry* **2005,** *44* (22), 8138-47.

45. Bollinger, J. M., Jr.; Krebs, C., Stalking intermediates in oxygen activation by iron enzymes: motivation and method. *J Inorg Biochem* **2006,** *100* (4), 586-605.

46. Koehntop, K. D.; Emerson, J. P.; Que, L., Jr., The 2-His-1-carboxylate facial triad: a versatile platform for dioxygen activation by mononuclear non-heme iron(II) enzymes. *J Biol Inorg Chem* **2005,** *10* (2), 87-93.

47. Krebs, C.; Galonic Fujimori, D.; Walsh, C. T.; Bollinger, J. M., Jr., Non-heme Fe(IV)-oxo intermediates. *Acc Chem Res* **2007,** *40* (7), 484-92.

48. Hangasky, J. A.; Taabazuing, C. Y.; Valliere, M. A.; Knapp, M. J., Imposing function down a (cupin)-barrel: secondary structure and metal stereochemistry in the alphaKG-dependent oxygenases. *Metallomics* **2013,** *5* (4), 287-301.

49. Zhang, Z.; Ren, J.; Harlos, K.; McKinnon, C. H.; Clifton, I. J.; Schofield, C. J., Crystal structure of a clavaminate synthase-Fe(II)-2-oxoglutarate-substrate-NO complex: evidence for metal centered rearrangements. *FEBS Lett* **2002,** *517* (1-3), 7-12.

50. Borowski, T.; Bassan, A.; Siegbahn, P. E., Mechanism of dioxygen activation in 2-oxoglutarate-dependent enzymes: a hybrid DFT study. *Chemistry* **2004,** *10* (4), 1031-41.

51. Henshaw, T. F.; Feig, M.; Hausinger, R. P., Aberrant activity of the DNA repair enzyme AlkB. *J Inorg Biochem* **2004,** *98* (5), 856-61.

52. Price, J. C.; Barr, E. W.; Glass, T. E.; Krebs, C.; Bollinger, J. M., Jr., Evidence for hydrogen abstraction from C1 of taurine by the high-spin Fe(IV) intermediate detected during oxygen activation by taurine:alpha-ketoglutarate dioxygenase (TauD). *J Am Chem Soc* **2003,** *125* (43), 13008-9.

53. Price, J. C.; Barr, E. W.; Tirupati, B.; Bollinger, J. M., Jr.; Krebs, C., The first direct characterization of a high-valent iron intermediate in the reaction of an alpha-ketoglutarate-dependent dioxygenase: a high-spin FeIV complex in taurine/alpha-ketoglutarate dioxygenase (TauD) from Escherichia coli. *Biochemistry* **2003,** *42* (24), 7497-508.

54. Hoffart, L. M.; Barr, E. W.; Guyer, R. B.; Bollinger, J. M., Jr.; Krebs, C., Direct spectroscopic detection of a C-H-cleaving high-spin Fe(IV) complex in a prolyl-4-hydroxylase. *Proc Natl Acad Sci USA* **2006,** *103* (40), 14738-43.

55. Puistola, U.; Turpeenniemi-Hujanen, T. M.; Myllyla, R.; Kivirikko, K. I., Studies on the lysyl hydroxylase reaction. II. Inhibition kinetics and the reaction mechanism. *Biochim Biophys Acta* **1980,** *611* (1), 51-60.

56. Holme, E., A kinetic study of thymine 7-hydroxylase from neurospora crassa. *Biochemistry* **1975,** *14* (22), 4999-5003.

57. Walport, L. J.; Hopkinson, R. J.; Schofield, C. J., Mechanisms of human histone and nucleic acid demethylases. *Curr Opin Chem Biol* **2012,** *16* (5-6), 525-34.

58. Hausinger, R. P., FeII/alpha-ketoglutarate-dependent hydroxylases and related enzymes. *Crit Rev Biochem Mol Biol* **2004,** *39* (1), 21-68.

59. Aravind, L.; Koonin, E. V., The DNA-repair protein AlkB, EGL-9, and leprecan define new families of 2-oxoglutarate- and iron-dependent dioxygenases. *Genome Biol* **2001,** *2* (3), RESEARCH0007.

60. Gerken, T.; Girard, C. A.; Tung, Y. C.; Webby, C. J.; Saudek, V.; Hewitson, K. S.; Yeo, G. S.; McDonough, M. A.; Cunliffe, S.; McNeill, L. A.; Galvanovskis, J.; Rorsman, P.; Robins, P.; Prieur, X.; Coll, A. P.; Ma, M.; Jovanovic, Z.; Farooqi, I. S.; Sedgwick, B.; Barroso, I.; Lindahl, T.; Ponting, C. P.; Ashcroft, F. M.; O'Rahilly, S.; Schofield, C. J., The obesity-associated FTO gene encodes a 2-oxoglutarate-dependent nucleic acid demethylase. *Science* **2007,** *318* (5855), 1469-72.

61. Westbye, M. P.; Feyzi, E.; Aas, P. A.; Vågbø, C. B.; Talstad, V. A.; Kavli, B.; Hagen, L.; Sundheim, O.; Akbari, M.; Liabakk, N.-B.; Slupphaug, G.; Otterlei, M.; Krokan, H. E., Human AlkB homolog 1 is a mitochondrial protein that demethylates 3-methylcytosine in DNA and RNA. *J Biol Chem* **2008,** *283* (36), 25046-56.

62. Duncan, T.; Trewick, S. C.; Koivisto, P.; Bates, P. A.; Lindahl, T.; Sedgwick, B., Reversal of DNA alkylation damage by two human dioxygenases. *Proc Natl Acad Sci USA* **2002,** *99* (26), 16660-5.

63. Zheng, G.; Dahl, John A.; Niu, Y.; Fedorcsak, P.; Huang, C.-M.; Li, Charles J.; Vågbø, Cathrine B.; Shi, Y.; Wang, W.-L.; Song, S.-H.; Lu, Z.; Bosmans, Ralph P. G.; Dai, Q.; Hao, Y.-J.; Yang, X.; Zhao, W.-M.; Tong, W.-M.; Wang, X.-J.; Bogdan, F.; Furu, K.; Fu, Y.; Jia, G.; Zhao, X.; Liu, J.; Krokan, Hans E.; Klungland, A.; Yang, Y.-G.; He, C., ALKBH5 is a mammalian RNA demethylase that impacts RNA metabolism and mouse fertility. *Mol Cell* **2013,** *49* (1), 18-29.

64. Li, M. M.; Nilsen, A.; Shi, Y.; Fusser, M.; Ding, Y. H.; Fu, Y.; Liu, B.; Niu, Y.; Wu, Y. S.; Huang, C. M.; Olofsson, M.; Jin, K. X.; Lv, Y.; Xu, X. Z.; He, C.; Dong, M. Q.; Rendtlew Danielsen, J. M.; Klungland, A.; Yang, Y. G., ALKBH4-dependent demethylation of actin regulates actomyosin dynamics. *Nat Commun* **2013,** *4*, 1832.

65. Fu, Y.; Dai, Q.; Zhang, W.; Ren, J.; Pan, T.; He, C., The AlkB domain of mammalian ABH8 catalyzes hydroxylation of 5-methoxycarbonylmethyluridine at the wobble position of tRNA. *Angew Chem* **2010,** *49* (47), 8885-8888.

66. Fu, D.; Jordan, J. J.; Samson, L. D., Human ALKBH7 is required for alkylation and oxidation-induced programmed necrosis. *Genes & Development* **2013,** *27* (10), 1089-1100.

67. Tahiliani, M.; Koh, K. P.; Shen, Y.; Pastor, W. A.; Bandukwala, H.; Brudno, Y.; Agarwal, S.; Iyer, L. M.; Liu, D. R.; Aravind, L.; Rao, A., Conversion of 5-methylcytosine to 5-hydroxymethylcytosine in mammalian DNA by MLL partner TET1. *Science* **2009,** *324* (5929), 930-5.

68. Ito, S.; Shen, L.; Dai, Q.; Wu, S. C.; Collins, L. B.; Swenberg, J. A.; He, C.; Zhang, Y., Tet proteins can convert 5-methylcytosine to 5-formylcytosine and 5-carboxylcytosine. *Science* **2011,** *333* (6047), 1300.

69. He, Y. F.; Li, B. Z.; Li, Z.; Liu, P.; Wang, Y.; Tang, Q.; Ding, J.; Jia, Y.; Chen, Z.; Li, L.; Sun, Y.; Li, X.; Dai, Q.; Song, C. X.; Zhang, K.; He, C.; Xu, G. L., Tet-mediated formation of 5-carboxylcytosine and its excision by TDG in mammalian DNA. *Science* **2011,** *333* (6047), 1303-7.

70. Kato, M.; Araiso, Y.; Noma, A.; Nagao, A.; Suzuki, T.; Ishitani, R.; Nureki, O., Crystal structure of a novel JmjC-domain-containing protein, TYW5, involved in tRNA modification. *Nucleic Acids Res* **2011,** *39* (4), 1576-85.

71. Zheng, G.; Fu, Y.; He, C., Nucleic acid oxidation in DNA damage repair and epigenetics. *Chem Rev* **2014,** *114* (8), 4602-20.

72. Chen, K.; Zhao, B. S.; He, C., Nucleic acid modifications in regulation of gene expression. *Cell Chem Biol* **2016,** *23* (1), 74-85.

73. Sedgwick, B., Repairing DNA-methylation damage. *Nat Rev Mol Cell Biol* **2004,** *5* (2), 148-57.

74. Janion, C., Mechanisms of action of methyl methanesulfonate on Escherichia coli: mutagenesis, DNA damage and repair. *Postepy Biochem* **1995,** *41* (5 Suppl), 308-13.

75. Lindahl, T.; Sedgwick, B.; Sekiguchi, M.; Nakabeppu, Y., Regulation and expression of the adaptive response to alkylating agents. *Annu Rev Biochem* **1988,** *57*, 133-57.

76. Teo, I.; Sedgwick, B.; Kilpatrick, M. W.; McCarthy, T. V.; Lindahl, T., The intracellular signal for induction of resistance to alkylating agents in E. coli. *Cell* **1986,** *45* (2), 315-24.

77. Sakumi, K.; Sekiguchi, M., Regulation of expression of the ada gene controlling the adaptive response. Interactions with the ada promoter of the Ada protein and RNA polymerase. *J Mol Biol* **1989,** *205* (2), 373-85.

78. Sedgwick, B.; Robins, P.; Totty, N.; Lindahl, T., Functional domains and methyl acceptor sites of the Escherichia coli ada protein. *J Biol Chem* **1988,** *263* (9), 4430-3.

79. He, C.; Hus, J. C.; Sun, L. J.; Zhou, P.; Norman, D. P.; Dotsch, V.; Wei, H.; Gross, J. D.; Lane, W. S.; Wagner, G.; Verdine, G. L., A methylation-dependent electrostatic switch controls DNA repair and transcriptional activation by E. coli ada. *Mol Cell* **2005,** *20* (1), 117-29.

80. Larson, K.; Sahm, J.; Shenkar, R.; Strauss, B., Methylation-induced blocks to in vitro DNA replication. *Mutat Res* **1985,** *150* (1-2), 77-84.

81. Labahn, J.; Scharer, O. D.; Long, A.; Ezaz-Nikpay, K.; Verdine, G. L.; Ellenberger, T. E., Structural basis for the excision repair of alkylation-damaged DNA. *Cell* **1996,** *86* (2), 321-9.

82. Falnes, P. O.; Johansen, R. F.; Seeberg, E., AlkB-mediated oxidative demethylation reverses DNA damage in Escherichia coli. *Nature* **2002,** *419* (6903), 178-82.

83. Koivisto, P.; Robins, P.; Lindahl, T.; Sedgwick, B., Demethylation of 3-methylthymine in DNA by bacterial and human DNA dioxygenases. *J Biol Chem* **2004,** *279* (39), 40470-4.

84. Falnes, P. O., Repair of 3-methylthymine and 1-methylguanine lesions by bacterial and human AlkB proteins. *Nucleic Acids Res* **2004,** *32* (21), 6260-7.

85. Delaney, J. C.; Essigmann, J. M., Mutagenesis, genotoxicity, and repair of 1-methyladenine, 3-alkylcytosines, 1-methylguanine, and 3-methylthymine in alkB Escherichia coli. *Proc Natl Acad Sci USA* **2004,** *101* (39), 14051-6.

86. Mishina, Y.; Yang, C. G.; He, C., Direct repair of the exocyclic DNA adduct 1,N6-ethenoadenine by the DNA repair AlkB proteins. *J Am Chem Soc* **2005,** *127* (42), 14594-5.

87. Delaney, J. C.; Smeester, L.; Wong, C.; Frick, L. E.; Taghizadeh, K.; Wishnok, J. S.; Drennan, C. L.; Samson, L. D.; Essigmann, J. M., AlkB reverses etheno DNA lesions caused by lipid oxidation in vitro and in vivo. *Nat Struct Mol Biol* **2005,** *12* (10), 855-60.

88. Sievers, F.; Wilm, A.; Dineen, D.; Gibson, T. J.; Karplus, K.; Li, W.; Lopez, R.; McWilliam, H.; Remmert, M.; Söding, J.; Thompson, J. D.; Higgins, D. G., Fast, scalable generation of high-quality protein multiple sequence alignments using Clustal Omega. *Mol Syst Biol* **2011,** *7* (1), 539-42.

89. Li, D.; Delaney, J. C.; Page, C. M.; Yang, X.; Chen, A. S.; Wong, C.; Drennan, C. L.; Essigmann, J. M., Exocyclic carbons adjacent to the N6 of adenine are targets for oxidation by the Escherichia coli adaptive response protein AlkB. *J Am Chem Soc* **2012,** *134* (21), 8896-901.

90. Maciejewska, A. M.; Poznanski, J.; Kaczmarska, Z.; Krowisz, B.; Nieminuszczy, J.; Polkowska-Nowakowska, A.; Grzesiuk, E.; Kusmierek, J. T., AlkB dioxygenase preferentially repairs protonated substrates: specificity against exocyclic adducts and molecular mechanism of action. *J Biol Chem* **2013,** *288* (1), 432-41.

91. Ougland, R.; Lando, D.; Jonson, I.; Dahl, J. A.; Moen, M. N.; Nordstrand, L. M.; Rognes, T.; Lee, J. T.; Klungland, A.; Kouzarides, T.; Larsen, E., ALKBH1 is a histone H2A dioxygenase involved in neural differentiation. *Stem Cells* **2012,** *30* (12), 2672-82.

92. Wei, Y. F.; Carter, K. C.; Wang, R. P.; Shell, B. K., Molecular cloning and functional analysis of a human cDNA encoding an Escherichia coli AlkB homolog, a protein involved in DNA alkylation damage repair. *Nucleic Acids Res* **1996,** *24* (5), 931-37.

93. Müller, T. A.; Yu, K.; Hausinger, R. P.; Meek, K., ALKBH1 is dispensable for abasic site cleavage during base excision repair and class switch recombination. *PLoS One* **2013,** *8* (6), e67403.

94. Müller, Tina A.; Andrzejak, Megan M.; Hausinger, Robert P., A covalent protein–DNA 5′-product adduct is generated following AP lyase activity of human ALKBH1 (AlkB homologue 1). *Biochem J* **2013,** *452* (3), 509-17.

95. Yi, C.; Jia, G.; Hou, G.; Dai, Q.; Zhang, W.; Zheng, G.; Jian, X.; Yang, C.-G.; Cui, Q.; He, C., Iron-catalysed oxidation intermediates captured in a DNA repair dioxygenase. *Nature* **2010,** *468* (7321), 330-3.

96. Dango, S.; Mosammaparast, N.; Sowa, Mathew E.; Xiong, L.-J.; Wu, F.; Park, K.; Rubin, M.; Gygi, S.; Harper, J. W.; Shi, Y., DNA unwinding by ASCC3 helicase is coupled to ALKBH3-dependent DNA alkylation repair and cancer cell proliferation. *Mol Cell* **2011,** *44* (3), 373-84.

97. Sundheim, O.; Vagbo, C. B.; Bjoras, M.; Sousa, M. M.; Talstad, V.; Aas, P. A.; Drablos, F.; Krokan, H. E.; Tainer, J. A.; Slupphaug, G., Human ABH3 structure and key residues for oxidative demethylation to reverse DNA/RNA damage. *EMBO J* **2006,** *25* (14), 3389-97.

98. Sundheim, O.; Vågbø, C. B.; Bjørås, M.; Sousa, M. M. L.; Talstad, V.; Aas, P. A.; Drabløs, F.; Krokan, H. E.; Tainer, J. A.; Slupphaug, G., Human ABH3 structure and key residues for oxidative demethylation to reverse DNA/RNA damage. *EMBO J* **2006,** *25* (14), 3389-97.

99. Rhee, H.-W.; Zou, P.; Udeshi, N. D.; Martell, J. D.; Mootha, V. K.; Carr, S. A.; Ting, A. Y., Proteomic mapping of mitochondria in living cells via spatially restricted enzymatic tagging. *Science* **2013,** *339* (6125), 1328.

100. Solberg, A.; Robertson, A. B.; Aronsen, J. M.; Rognmo, O.; Sjaastad, I.; Wisloff, U.; Klungland, A., Deletion of mouse Alkbh7 leads to obesity. *J Mol Cell Biol* **2013,** *5* (3), 194-203.

101. Tsujikawa, K.; Koike, K.; Kitae, K.; Shinkawa, A.; Arima, H.; Suzuki, T.; Tsuchiya, M.; Makino, Y.; Furukawa, T.; Konishi, N.; Yamamoto, H., Expression and sub-cellular localization of human ABH family molecules. *J Cell Mol Med* **2007,** *11* (5), 1105-16.

102. Thalhammer, A.; Bencokova, Z.; Poole, R.; Loenarz, C.; Adam, J.; O'Flaherty, L.; Schödel, J.; Mole, D.; Giaslakiotis, K.; Schofield, C. J.; Hammond, E. M.; Ratcliffe, P. J.; Pollard, P. J., Human AlkB homologue 5 Is a nuclear 2-oxoglutarate dependent oxygenase and a direct target of hypoxia-inducible factor 1α (HIF-1α). *PLoS One* **2011,** *6* (1), e16210.

103. Aik, W.; Scotti, J. S.; Choi, H.; Gong, L.; Demetriades, M.; Schofield, C. J.; McDonough, M. A., Structure of human RNA N6-methyladenine demethylase ALKBH5 provides insights into its mechanisms of nucleic acid recognition and demethylation. *Nucleic Acids Res* **2014,** *42* (7), 4741-54.

104. Pastore, C.; Topalidou, I.; Forouhar, F.; Yan, A. C.; Levy, M.; Hunt, J. F., Crystal structure and RNA binding properties of the RNA recognition motif (RRM) and AlkB domains in human AlkB homolog 8 (ABH8), an enzyme catalyzing tRNA hypermodification. *J Biol Chem* **2012,** *287* (3), 2130-43.

105. Songe-Moller, L.; van den Born, E.; Leihne, V.; Vagbo, C. B.; Kristoffersen, T.; Krokan, H. E.; Kirpekar, F.; Falnes, P. O.; Klungland, A., Mammalian ALKBH8 possesses tRNA methyltransferase activity required for the biogenesis of multiple wobble uridine modifications implicated in translational decoding. *Mol Cell Biol* **2010,** *30* (7), 1814-27.

106. Fu, D.; Brophy, J. A. N.; Chan, C. T. Y.; Atmore, K. A.; Begley, U.; Paules, R. S.; Dedon, P. C.; Begley, T. J.; Samson, L. D., Human AlkB Homolog ABH8 Is a tRNA Methyltransferase Required for Wobble Uridine Modification and DNA Damage Survival. *Mol Cell Biol* **2010,** *30* (10), 2449-55.

107. van den Born, E.; Vagbo, C. B.; Songe-Moller, L.; Leihne, V.; Lien, G. F.; Leszczynska, G.; Malkiewicz, A.; Krokan, H. E.; Kirpekar, F.; Klungland, A.; Falnes, P. O., ALKBH8-mediated formation of a novel diastereomeric pair of wobble nucleosides in mammalian tRNA. *Nat Commun* **2011,** *2*, 172-5.

108. Shimada, K.; Nakamura, M.; Anai, S.; De Velasco, M.; Tanaka, M.; Tsujikawa, K.; Ouji, Y.; Konishi, N., A novel human AlkB homologue, ALKBH8, contributes to human bladder cancer progression. *Cancer Res* **2009,** *69* (7), 3157-64.

109. Frayling, T. M.; Timpson, N. J.; Weedon, M. N.; Zeggini, E.; Freathy, R. M.; Lindgren, C. M.; Perry, J. R.; Elliott, K. S.; Lango, H.; Rayner, N. W.; Shields, B.; Harries, L. W.; Barrett, J. C.; Ellard, S.; Groves, C. J.; Knight, B.; Patch, A. M.; Ness, A. R.; Ebrahim, S.; Lawlor, D. A.; Ring, S. M.; Ben-Shlomo, Y.; Jarvelin, M. R.; Sovio, U.; Bennett, A. J.; Melzer, D.; Ferrucci, L.; Loos, R. J.; Barroso, I.; Wareham, N. J.; Karpe, F.; Owen, K. R.; Cardon, L. R.; Walker, M.; Hitman, G. A.; Palmer, C. N.; Doney, A. S.; Morris, A. D.; Smith, G. D.; Hattersley, A. T.; McCarthy, M. I., A common variant in the FTO gene is associated with body mass index and predisposes to childhood and adult obesity. *Science* **2007,** *316* (5826), 889-94.

110. Fischer, J.; Koch, L.; Emmerling, C.; Vierkotten, J.; Peters, T.; Bruning, J. C.; Ruther, U., Inactivation of the Fto gene protects from obesity. *Nature* **2009,** *458* (7240), 894-8.

111. Church, C.; Moir, L.; McMurray, F.; Girard, C.; Banks, G. T.; Teboul, L.; Wells, S.; Bruning, J. C.; Nolan, P. M.; Ashcroft, F. M.; Cox, R. D., Overexpression of Fto leads to increased food intake and results in obesity. *Nat Genet* **2010,** *42* (12), 1086-92.

112. Smemo, S.; Tena, J. J.; Kim, K.-H.; Gamazon, E. R.; Sakabe, N. J.; Gómez-Marín, C.; Aneas, I.; Credidio, F. L.; Sobreira, D. R.; Wasserman, N. F.; Lee, J. H.; Puviindran, V.; Tam, D.; Shen, M.; Son, J. E.; Vakili, N. A.; Sung, H.-K.; Naranjo, S.; Acemel, R. D.; Manzanares, M.; Nagy, A.; Cox, N. J.; Hui, C.-C.; Gomez-Skarmeta, J. L.; Nóbrega, M. A., Obesity-associated variants within FTO form long-range functional connections with IRX3. *Nature* **2014,** *507*, 371-82.

113. the Geno, M. E. L. C.; Iles, M. M.; Law, M. H.; Stacey, S. N.; Han, J.; Fang, S.; Pfeiffer, R.; Harland, M.; MacGregor, S.; Taylor, J. C.; Aben, K. K.; Akslen, L. A.; Avril, M.-F.; Azizi, E.; Bakker, B.; Benediktsdottir, K. R.; Bergman, W.; Scarrà, G. B.; Brown, K. M.; Calista, D.; Chaudru, V.; Fargnoli, M. C.; Cust, A. E.; Demenais, F.; de Waal, A. C.; Dębniak, T.; Elder, D. E.; Friedman, E.; Galan, P.; Ghiorzo, P.; Gillanders, E. M.; Goldstein, A. M.; Gruis, N. A.; Hansson, J.; Helsing, P.; Hočevar, M.; Höiom, V.; Hopper, J. L.; Ingvar, C.; Janssen, M.; Jenkins, M. A.; Kanetsky, P. A.; Kiemeney, L. A.; Lang, J.; Lathrop, G. M.; Leachman, S.; Lee, J. E.; Lubiński, J.; Mackie, R. M.; Mann, G. J.; Martin, N. G.; Mayordomo, J. I.; Molven, A.; Mulder, S.; Nagore, E.; Novaković, S.; Okamoto, I.; Olafsson, J. H.; Olsson, H.; Pehamberger, H.; Peris, K.; Grasa, M. P.; Planelles, D.; Puig, S.; Puig-Butille, J. A.; Randerson-Moor, J.; Requena, C.; Rivoltini, L.; Rodolfo, M.; Santinami, M.; Sigurgeirsson, B.; Snowden, H.; Song, F.; Sulem, P.; Thorisdottir, K.; Tuominen, R.; Van Belle, P.; van der Stoep, N.; van Rossum, M. M.; Wei, Q.; Wendt, J.; Zelenika, D.; Zhang, M.; Landi, M. T.; Thorleifsson, G.; Bishop, D. T.; Amos, C. I.; Hayward, N. K.; Stefansson, K.; Bishop, J. A. N.; Barrett, J. H., A variant in FTO shows association with melanoma risk not due to BMI. *Nat Genet* **2013,** *45*, 428-32.

114. Boissel, S.; Reish, O.; Proulx, K.; Kawagoe-Takaki, H.; Sedgwick, B.; Yeo, G. S.; Meyre, D.; Golzio, C.; Molinari, F.; Kadhom, N.; Etchevers, H. C.; Saudek, V.; Farooqi, I. S.; Froguel, P.; Lindahl, T.; O'Rahilly, S.; Munnich, A.; Colleaux, L., Loss-of-function mutation in the dioxygenase-encoding FTO gene causes severe growth retardation and multiple malformations. *Am J Hum Genet* **2009,** *85* (1), 106-11.

115. Desrosiers, R.; Friderici, K.; Rottman, F., Identification of methylated nucleosides in messenger RNA from Novikoff hepatoma cells. *Proc Natl Acad Sci USA* **1974,** *71* (10), 3971-5.

116. Tung, Y. C.; Ayuso, E.; Shan, X.; Bosch, F.; O'Rahilly, S.; Coll, A. P.; Yeo, G. S., Hypothalamic-specific manipulation of Fto, the ortholog of the human obesity gene FTO, affects food intake in rats. *PLoS One* **2010,** *5* (1), e8771.

117. Bacher, U.; Haferlach, C.; Schnittger, S.; Kohlmann, A.; Kern, W.; Haferlach, T., Mutations of the TET2 and CBL genes: novel molecular markers in myeloid malignancies. *Ann Hematol* **2010,** *89* (7), 643-52.

118. Rasmussen, K. D.; Helin, K., Role of TET enzymes in DNA methylation, development, and cancer. *Genes & development* **2016,** *30* (7), 733-750.

119. Imielinski, M.; Berger, A. H.; Hammerman, P. S.; Hernandez, B.; Pugh, T. J.; Hodis, E.; Cho, J.; Suh, J.; Capelletti, M.; Sivachenko, A.; Sougnez, C.; Auclair, D.; Lawrence, M. S.; Stojanov, P.; Cibulskis, K.; Choi, K.; de Waal, L.; Sharifnia, T.; Brooks, A.; Greulich, H.; Banerji, S.; Zander, T.; Seidel, D.; Leenders, F.; Ansen, S.; Ludwig, C.; Engel-Riedel, W.; Stoelben, E.; Wolf, J.; Goparju, C.; Thompson, K.; Winckler, W.; Kwiatkowski, D.; Johnson, B. E.; Janne, P. A.; Miller, V. A.; Pao, W.; Travis, W. D.; Pass, H. I.; Gabriel, S. B.; Lander, E. S.; Thomas, R. K.; Garraway, L. A.; Getz, G.; Meyerson, M., Mapping the hallmarks of lung adenocarcinoma with massively parallel sequencing. *Cell* **2012,** *150* (6), 1107-20.

120. Ko, M.; Huang, Y.; Jankowska, A. M.; Pape, U. J.; Tahiliani, M.; Bandukwala, H. S.; An, J.; Lamperti, E. D.; Koh, K. P.; Ganetzky, R.; Liu, X. S.; Aravind, L.; Agarwal, S.; Maciejewski, J. P.; Rao, A., Impaired hydroxylation of 5-methylcytosine in myeloid cancers with mutant TET2. *Nature* **2010,** *468* (7325), 839-43.

121. Noma, A.; Ishitani, R.; Kato, M.; Nagao, A.; Nureki, O.; Suzuki, T., Expanding role of the Jumonji C domain as an RNA hydroxylase. *J Biol Chem* **2010,** *285* (45), 34503-7.

122. Cohn, W. E.; Volkin, E., Nucleoside-5′-phosphates from ribonucleic acid. *Nature* **1951,** *167* (4247), 483-4.

123. He, C., Grand challenge commentary: RNA epigenetics? *Nat Chem Biol* **2010,** *6* (12), 863-5.

124. Boccaletto, P.; Machnicka, M. A.; Purta, E.; Piatkowski, P.; Baginski, B.; Wirecki, T. K.; de Crecy-Lagard, V.; Ross, R.; Limbach, P. A.; Kotter, A.; Helm, M.; Bujnicki, J. M., MODOMICS: a database of RNA modification pathways. 2017 update. *Nucleic Acids Res* **2018,** *46* (D1), D303-D307.

125. Grosjean, H.; de Crecy-Lagard, V.; Marck, C., Deciphering synonymous codons in the three domains of life: co-evolution with specific tRNA modification enzymes. *FEBS Lett* **2010,** *584* (2), 252-64.

126. Song, X.; Nazar, R. N., Modification of rRNA as a 'quality control mechanism' in ribosome biogenesis. *FEBS Letters* **2002,** *523* (1-3), 182-186.

127. Agris, P. F., Decoding the genome: a modified view. *Nucleic Acids Res* **2004,** *32* (1), 223-38.

128. Grosjean, H. *Fine-Tuning Of RNA Functions By Modification And Editing*. Topics In Current Genetics, Volume 12; Springer, **2005**.

129. Roundtree, I. A.; He, C., RNA epigenetics--chemical messages for posttranscriptional gene regulation. *Curr Opin Chem Biol* **2016,** *30*, 46-51.

130. Mauer, J.; Luo, X.; Blanjoie, A.; Jiao, X.; Grozhik, A. V.; Patil, D. P.; Linder, B.; Pickering, B. F.; Vasseur, J. J.; Chen, Q.; Gross, S. S.; Elemento, O.; Debart, F.; Kiledjian, M.; Jaffrey, S. R., Reversible methylation of m(6)Am in the 5' cap controls mRNA stability. *Nature* **2017,** *541* (7637), 371-5.

131. Fustin, J. M.; Doi, M.; Yamaguchi, Y.; Hida, H.; Nishimura, S.; Yoshida, M.; Isagawa, T.; Morioka, M. S.; Kakeya, H.; Manabe, I.; Okamura, H., RNA-methylation-dependent RNA processing controls the speed of the circadian clock. *Cell* **2013,** *155* (4), 793-806.

132. Holoch, D.; Moazed, D., RNA-mediated epigenetic regulation of gene expression. *Nat Rev Genet* **2015,** *16* (2), 71-84.

133. Saikia, M.; Fu, Y.; Pavon-Eternod, M.; He, C.; Pan, T., Genome-wide analysis of N1-methyl-adenosine modification in human tRNAs. *RNA* **2010,** *16* (7), 1317-27.

134. Lee, M.; Kim, B.; Kim, V. N., Emerging roles of RNA modification: m(6)A and U-tail. *Cell* **2014,** *158* (5), 980-7.

135. Wei, C.; Gershowitz, A.; Moss, B., N6, O2'-dimethyladenosine a novel methylated ribonucleoside next to the 5' terminal of animal cell and virus mRNAs. *Nature* **1975,** *257* (5523), 251-3.

136. Harper, J. E.; Miceli, S. M.; Roberts, R. J.; Manley, J. L., Sequence specificity of the human mRNA N6-adenosine methylase in vitro. *Nucleic Acids Res* **1990,** *18* (19), 5735-41.

137. Narayan, P.; Rottman, F. M., An in vitro system for accurate methylation of internal adenosine residues in messenger RNA. *Science* **1988,** *242* (4882), 1159-62.

138. Horowitz, S.; Horowitz, A.; Nilsen, T. W.; Munns, T. W.; Rottman, F. M., Mapping of N6-methyladenosine residues in bovine prolactin mRNA. *Proc Natl Acad Sci USA* **1984,** *81* (18), 5667-71.

139. Perry, R. P.; Kelley, D. E.; Friderici, K.; Rottman, F., The methylated constituents of L cell messenger RNA: Evidence for an unusual cluster at the 5′ terminus. *Cell* **1975,** *4* (4), 387-394.

140. Dubin, D. T.; Taylor, R. H., The methylation state of poly A-containing messenger RNA from cultured hamster cells. *Nucleic Acids Res* **1975,** *2* (10), 1653-68.

141. Liu, N.; Pan, T., RNA epigenetics. *Transl Res* **2015,** *165* (1), 28-35.

142. Yi, C.; Pan, T., Cellular dynamics of RNA modification. *Acc Chem Res* **2011,** *44* (12), 1380-8.

143. Meyer, K. D.; Saletore, Y.; Zumbo, P.; Elemento, O.; Mason, C. E.; Jaffrey, S. R., Comprehensive analysis of mRNA methylation reveals enrichment in 3' UTRs and near stop codons. *Cell* **2012,** *149* (7), 1635-46.

144. Dominissini, D.; Moshitch-Moshkovitz, S.; Schwartz, S.; Salmon-Divon, M.; Ungar, L.; Osenberg, S.; Cesarkas, K.; Jacob-Hirsch, J.; Amariglio, N.; Kupiec, M.; Sorek, R.; Rechavi, G., Topology of the human and mouse m6A RNA methylomes revealed by m6A-seq. *Nature* **2012,** *485* (7397), 201-6.

145. Wang, X.; Feng, J.; Xue, Y.; Guan, Z.; Zhang, D.; Liu, Z.; Gong, Z.; Wang, Q.; Huang, J.; Tang, C.; Zou, T.; Yin, P., Structural basis of N(6)-adenosine methylation by the METTL3-METTL14 complex. *Nature* **2016,** *534* (7608), 575-8.

146. Liu, J.; Yue, Y.; Han, D.; Wang, X.; Fu, Y.; Zhang, L.; Jia, G.; Yu, M.; Lu, Z.; Deng, X.; Dai, Q.; Chen, W.; He, C., A METTL3-METTL14 complex mediates mammalian nuclear RNA N6-adenosine methylation. *Nat Chem Biol* **2014,** *10* (2), 93-5.

147. Ping, X.-L.; Sun, B.-F.; Wang, L.; Xiao, W.; Yang, X.; Wang, W.-J.; Adhikari, S.; Shi, Y.; Lv, Y.; Chen, Y.-S.; Zhao, X.; Li, A.; Yang, Y.; Dahal, U.; Lou, X.-M.; Liu, X.; Huang, J.; Yuan, W.-P.; Zhu, X.-F.; Cheng, T.; Zhao, Y.-L.; Wang, X.; Danielsen, J. M. R.; Liu, F.; Yang, Y.-G., Mammalian WTAP is a regulatory subunit of the RNA N6-methyladenosine methyltransferase. *Cell* **2014,** *24* (2), 177-89.

148. Bokar, J. A.; Rath-Shambaugh, M. E.; Ludwiczak, R.; Narayan, P.; Rottman, F., Characterization and partial purification of mRNA N6-adenosine methyltransferase from HeLa cell nuclei. Internal mRNA methylation requires a multisubunit complex. *J Biol Chem* **1994,** *269* (26), 17697-704.

149. Liu, J.; Yue, Y.; Han, D.; Wang, X.; Fu, Y.; Zhang, L.; Jia, G.; Yu, M.; Lu, Z.; Deng, X.; Dai, Q.; Chen, W.; He, C., A METTL3–METTL14 complex mediates mammalian nuclear RNA N6-adenosine methylation. *Nat Chem Biol* **2013,** *10*, 93.

150. Wang, X.; Lu, Z.; Gomez, A.; Hon, G. C.; Yue, Y.; Han, D.; Fu, Y.; Parisien, M.; Dai, Q.; Jia, G.; Ren, B.; Pan, T.; He, C., N6-methyladenosine-dependent regulation of messenger RNA stability. *Nature* **2014,** *505* (7481), 117-20.

151. Wang, Y.; Li, Y.; Toth, J. I.; Petroski, M. D.; Zhang, Z.; Zhao, J. C., N6-methyladenosine modification destabilizes developmental regulators in embryonic stem cells. *Nat Cell Biol* **2014,** *16* (2), 191-8.

152. Niu, Y.; Zhao, X.; Wu, Y. S.; Li, M. M.; Wang, X. J.; Yang, Y. G., N6-methyl-adenosine (m6A) in RNA: an old modification with a novel epigenetic function. *Genomics Proteomics Bioinformatics* **2013,** *11* (1), 8-17.

153. Dina, C.; Meyre, D.; Gallina, S.; Durand, E.; Korner, A.; Jacobson, P.; Carlsson, L. M.; Kiess, W.; Vatin, V.; Lecoeur, C.; Delplanque, J.; Vaillant, E.; Pattou, F.; Ruiz, J.; Weill, J.; Levy-Marchal, C.; Horber, F.; Potoczna, N.; Hercberg, S.; Le Stunff, C.; Bougneres, P.; Kovacs, P.; Marre, M.; Balkau, B.; Cauchi, S.; Chevre, J. C.; Froguel, P., Variation in FTO contributes to childhood obesity and severe adult obesity. *Nat Genet* **2007,** *39* (6), 724-6.

154. Hess, M. E.; Hess, S.; Meyer, K. D.; Verhagen, L. A.; Koch, L.; Bronneke, H. S.; Dietrich, M. O.; Jordan, S. D.; Saletore, Y.; Elemento, O.; Belgardt, B. F.; Franz, T.; Horvath, T. L.; Ruther, U.; Jaffrey, S. R.; Kloppenburg, P.; Bruning, J. C., The fat mass and obesity associated gene (Fto) regulates activity of the dopaminergic midbrain circuitry. *Nat Neurosci* **2013,** *16* (8), 1042-8.

155. Li, L.; Zang, L.; Zhang, F.; Chen, J.; Shen, H.; Shu, L.; Liang, F.; Feng, C.; Chen, D.; Tao, H.; Xu, T.; Li, Z.; Kang, Y.; Wu, H.; Tang, L.; Zhang, P.; Jin, P.; Shu, Q.; Li, X., Fat mass and obesity-associated (FTO) protein regulates adult neurogenesis. *Hum Mol Genet* **2017,** *26* (13), 2398-411.

156. Shi, H.; Zhang, X.; Weng, Y.-L.; Lu, Z.; Liu, Y.; Lu, Z.; Li, J.; Hao, P.; Zhang, Y.; Zhang, F.; Wu, Y.; Delgado, J. Y.; Su, Y.; Patel, M. J.; Cao, X.; Shen, B.; Huang, X.; Ming, G.-l.; Zhuang, X.; Song, H.; He, C.; Zhou, T., m6A facilitates hippocampus-dependent learning and memory through YTHDF1. *Nature* **2018,** *563* (7730), 249-53.

157. Chen, X.; Yu, C.; Guo, M.; Zheng, X.; Ali, S.; Huang, H.; Zhang, L.; Wang, S.; Huang, Y.; Qie, S.; Wang, J., Down-regulation of m6A mRNA methylation is involved in dopaminergic neuronal death. *ACS Chem Neurosci* **2019,** *10* (5), 2355-2363.

Chapter 2

Inhibition studies and assay optimisation for the nucleic-acid demethylase FTO

Table of Contents

2.1 Introduction 47

2.2 Previous studies 49

2.2.1 Inhibition studies 49

2.2.2 Screening (demethylation) assay 53

2.3 Objectives 54

2.4 FTO-inhibitor development 55

2.5 Production and purification of enzymes 58

2.6 *In vitro* assay optimisation 60

2.6.1. FTO assay based on matrix-assisted laser desorption/ionisation 60

2.6.2. Inhibition of FTO by second-generation inhibitors 65

2.6.3. Assay based on liquid chromatography-mass spectrometry 69

2.6.4. RapidFire® Mass Spectrometry- (RF-MS)-based assays 76

2.6.5. Inhibition of FTO with new RF-MS assay 90

2.7. Discussion and future work 95

Acknowledgements **98**

References **98**

2. Inhibition studies and assay optimisation for the nucleic-acid demethylase FTO

2.1. Introduction

A pioneering genome-wide association study reported in 2007 that single-nucleotide polymorphisms (SNPs) in the first intron of the human *Fto* gene were associated with increased body mass.[1] Subsequent studies apparently confirmed the correlation of FTO polymorphisms/mutations with obesity in Asian, European, and African populations[2-3]. This seemingly direct link between increased body mass and SNPs in the *Fto* gene was supported by several subsequent mouse-model studies[4-5]. *Fto* gene-knockout mice demonstrated a leaner phenotype; by contrast, over-expression of *Fto* led to increased food intake that resulted in obesity[4-5]. The *Fto* gene encodes for the fat mass and obesity-associated protein (FTO), which is a 2-oxoglutarate (2OG) and Fe(II)-dependent oxygenase (2OG oxygenase) that acts on nucleic acids (NAs). It belongs to the AlkB subfamily of 2OG oxygenases, of which there are eight other assigned human homologues (ABH1-8)[6].

Although the precise biochemical and physiological roles of FTO are not well understood, some of its bacterial and human homologues are reported to be involved in the repair of alkylated DNA and RNA damage by oxidative demethylation, e.g. in order to remove N-methyl group lesions[7-8]. FTO has been shown to demethylate 3-methyluracil (m^3U) in single-strand RNA (ssRNA) and 3-methylthymine (m^3T) in single-strand DNA (ssDNA)[9]. Subsequent reports reveal that FTO and ABH5 preferentially demethylate *N*-6-methyladenine (m^6A) in RNA (Figure 2.1)[10-11]. The m^6A modification is present in many types of RNA including mRNA. This indicates that m^6A in mRNA could potentially be a regulatory marker in epigenetic regulation of gene expression[10]. Indeed, studies have shown that FTO regulates levels of the hunger hormone, ghrelin, through m^6A demethylation in ghrelin mRNA[12]. Over-expression of *Fto* results in an increase in ghrelin mRNA and peptide levels; hence, m^6A

abundance in mRNA is inversely correlated to total mRNA levels. Furthermore, FTO has been linked with other diseases such as polycystic ovary syndrome[13], breast cancer[14] and Alzheimer's disease[15]. Due to the strong association of FTO SNPs with obesity and other biological pathologies relevant to FTO, it is desirable to develop small-molecule inhibitors that target FTO to probe the biological functions of FTO and potentially lead to treatments for obesity and/or related diseases, such as diabetes and cardiovascular diseases.

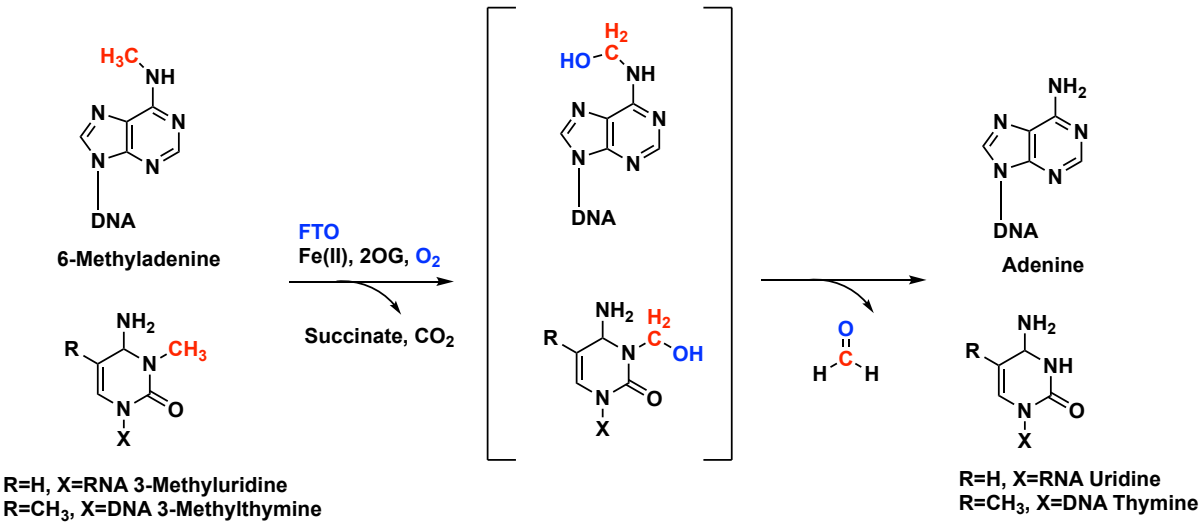


Figure 2.1: *The demethylation mechanism of ssDNA/ssRNA as catalysed by FTO.*

Although studies have been conducted on FTO inhibition[16-23], prior to the work described here, a lack of reliable and high-throughput screening (HTS) assay techniques has hampered structure-activity relationship (SAR) studies and hence inhibitor development. The common co-substrates (O_2 and 2OG) and co-products (CO_2 and succinate) that are produced in nearly all 2OG oxygenase catalysis have enabled development of generic assays[24], which often rely on measurement of isotopically labelled co-substrates/products. These assay methods include quantification of $^{14}CO_2$ released during decarboxylation of ^{14}C-labelled 2OG[25]; separation and measurement of [1-^{14}C]succinate concentration from ^{14}C-labelled 2OG by precipitation or by liquid chromatography-mass spectrometry (LC-MS)[26], and by ion-exchange chromatography[27]. These assays assume that 2OG consumption/succinate production is

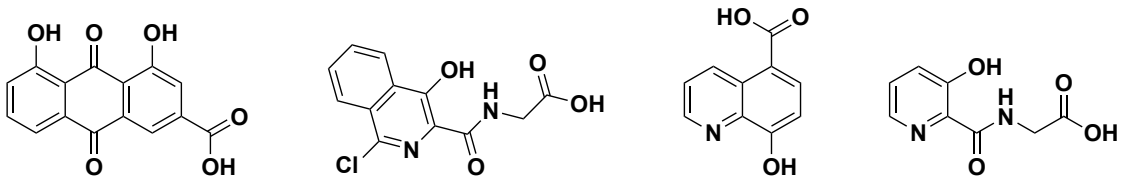
coupled to true enzyme activity (i.e. primary-substrate/oxidation-substrate turnover, e.g. methyl-group oxidation in the case of FTO). However, this assumption is not always valid, as non-enzymatic conversion from 2OG to succinate can occur, and enzymatic conversion may not be coupled to product formation[28]. Fluorescence assays, based on measurement of fluorescently derivatised 2OG[28] or formaldehyde[29] release, and spectrophotometric assays that rely on measurement of remaining 2OG in solution[30], have also been developed. However, interference from other fluorescent components that are added to the reaction mixture can render these assays non-robust and generate false positive/negative results. Mass spectrometry (MS) and nuclear magnetic resonance- (NMR)-based assays are considered the most reliable methods for measurement of 2OG oxygenases, including FTO. However, NMR is time and material consuming and, like certain types of MS, i.e. traditional LC-MS, is thus low throughput. Hence, it was considered that a high-throughput and more user-friendly MS-based assay was desirable for FTO. Note, the inhibition work described in this chapter was initiated in 2014, prior to more recently reported FTO inhibition studies.

2.2. Previous studies

2.1.1 Inhibition studies

Due to the highly conserved double-stranded β-helix (DSBH) core fold in 2OG oxygenases and utilisation of Fe(II), 2OG and O_2 as co-substrates[31-32], 'generic' (i.e. broad spectrum) inhibitors such as metal chelators and 2OG analogues have been identified[30, 33-36]. One of the first potent FTO inhibitors to be reported was rhein (Figure 2.2,)[16]. Interestingly, rhein is present in rhubarb, which also produces the 2OG analogue N-oxalylglycine and a variety of other oxalo-acids[17]. Subsequent structural studies have revealed that rhein inhibits FTO, not as a 2OG mimic or ion chelator as originally proposed, but as a competitive primary substrate (nucleic acid) analogue[17]. These studies also showed that rhein was not selective for FTO over

other members of the nucleic acid oxygenase (NAOX) subfamily, including AlkB and ABH5[17, 37]. Structure-based design led to the development of FTO inhibitors at the University of Oxford (by Dr Marina Demetriades and Dr WeiShen Aik, Figure 2.2)[17]. Further, some known inhibitors of 2OG oxygenases (including compounds in clinical development), i.e. the human hypoxia inducible factor-prolyl hydroxylase 1-3 (PHD1-3) inhibitor **FG2216**[38], and the non-specific lysine-specific demethylase 4 (KDM4) inhibitor **IOX-1**[39], have been found also to be relatively potent inhibitors of FTO (Figure 2.2).



IC_{50} (μM)				
FTO	**9.0**	**2.8**	**3.3**	**15**
PHD2	**—**	**0.3**	**14.3**	**400**
KDM4C	**—**	**>20**	**0.6**	**>>20**

Figure 2.2: *FTO inhibitors that were initially reported at the University of Oxford. Their potency is comparable with that of other 2OG oxygenases, i.e. PHD2 and KDM4C.*

Despite the low potency and lack of selectivity of these inhibitors, structural and inhibition information have revealed that further development of FTO-selective inhibitors should be possible. It was envisaged that occupation of both the substrate-binding site and 2OG-binding pocket may lead to more selective and potent FTO inhibitors.

In 2014, meclofenamic acid (Figure 2.3) was reported as an 8.0 μM (IC_{50}) inhibitor for FTO; it was also reported to selectively inhibit FTO over another assigned human m^6A demethylase, ABH5[18]. This was the first reported FTO-selective inhibitor that competed with NA substrate binding rather than 2OG[18]. In 2015, FTO inhibitor **2** (IC_{50} 4.9 μM, Figure 2.3) with a binding site that overlapped that of meclofenamic acid was reported[19]; further development led to inhibitor **3** (IC_{50} 39.3 μM, Figure 2.3), which was reported a year later. Again it exploited

competitive inhibition at the NA substrate-binding site[20]. FTO inhibitor **4**, reported in 2014 (IC_{50} 4.9 μM, Figure 2.3)[21], was based on the mimicking of ascorbate, a cofactor that stimulated the activity of many 2OG oxygenases *in vitro*, though its *in vivo* relevance, other than in collagen biosynthesis, is unclear. To date, the most potent FTO inhibitor **5** is a fumarate derivative (IC_{50} 0.8 μM, Figure 2.3)[22], which is reported to have apparent 100-fold selectivity for FTO over its subfamily counterpart ABH5, a notable observation given the structural similarity of these enzymes. In such selectivity screens, however, it is important to appreciate that different assay conditions were used for the two enzymes. However, compound **5** also manifests potent inhibition towards at least one other 2OG oxygenase (KDM2A, IC_{50} 0.06 μM), which may render it unsuitable as a selective FTO inhibitor for use in cells/animals.

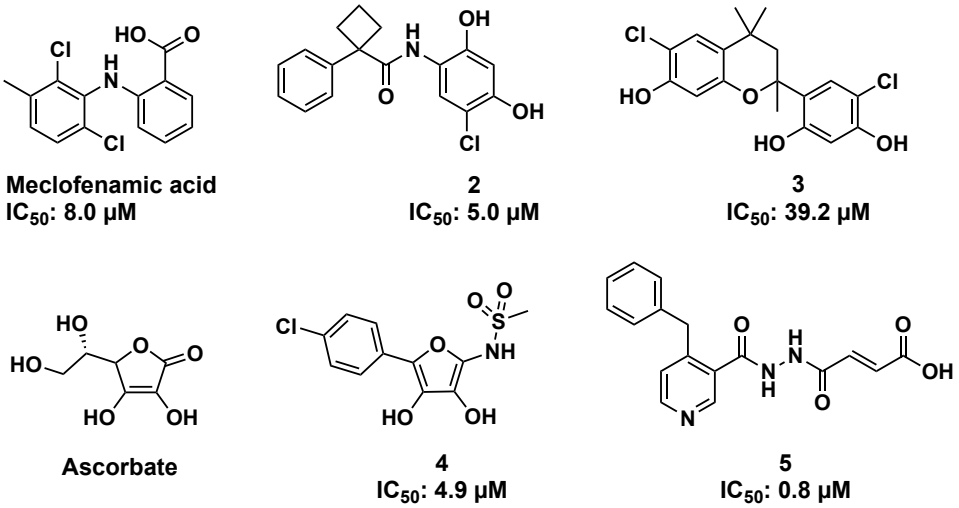


Figure 2.3: *Reported inhibitors of FTO and their IC_{50} values against FTO from literature.*

Structural and biochemical information regarding the mode of FTO inhibition by **1** (IC_{50} 15 μM) and rhein (IC_{50} 9.0 μM) promoted the structure-based design of a second generation of FTO inhibitors (Figure 2.4). The overlaying of images of crystal structures of FTO in complex with 2OG (PDB ID: 5DAB), **1** (PDB ID: 4IE5), m^3T (PDB ID: 3LFM) and rhein (PDB ID: 4IE7) suggested that occupation of both the NA substrate and 2OG-binding pockets could produce an inhibitor of high affinity and specificity for FTO (Figure 2.5). Four compounds

were designed and synthesised *via* Suzuki coupling (Figure 2.4, work conducted by Caitlin Clunie-O'Connor), and a crystal structure was obtained of the most potent inhibitor, **7** (PDB ID: 4QHO, crystal production and structure refinement by Dr WeiShen Aik). Overlays of the structure of **7** with **1** and rhein showed almost complete overlap of the inhibitor-binding modes (Figure 2.5). Both the NA substrate and 2OG-binding pockets were occupied as intended, which explained the markedly improved potency of **7** towards FTO (IC_{50} 4 μM).

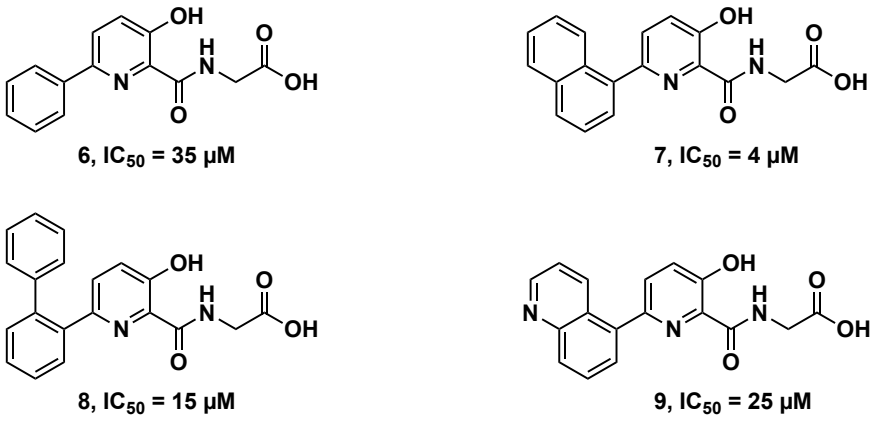


Figure 2.4: *Structures of the second-generation FTO inhibitors.*

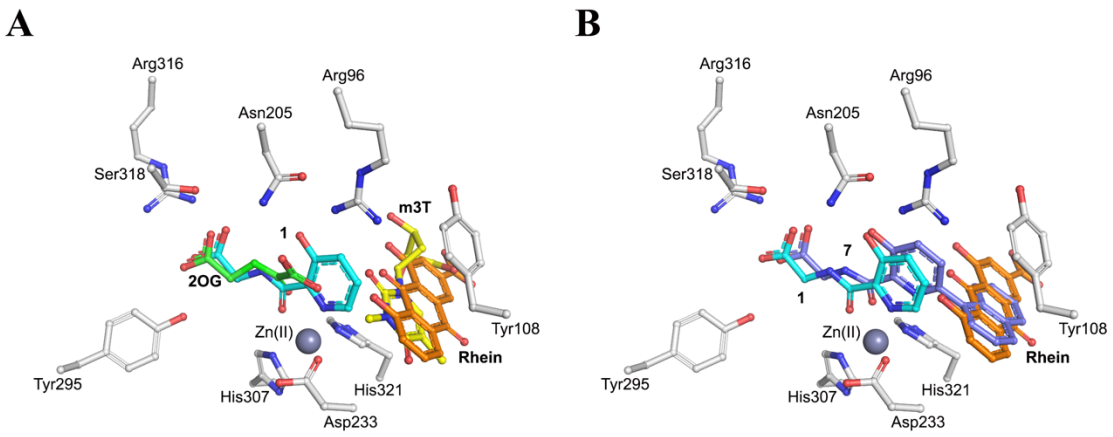


Figure 2.5: *Superimposition of the active sites of (A) m^3T (yellow, PDB ID: 3LFM), 2OG (green, PDB ID: 5DAB), **1** (cyan, PDB ID: 4IE5) and rhein (orange, PDB ID: 4IE7); and (B) **1** (cyan, PDB ID: 4IE5), **7** (purple, PDB ID: 4QHO) and rhein (orange, PDB ID: 4IE7). Note: the binding mode of the second-generation FTO inhibitor **7** overlaps with **1** and rhein, with both occupying both the 2OG- and substrate-binding sites. FTO residue side chains C (white), O (red), N(blue), Zn(II) (grey sphere).*

2.1.2 Screening (demethylation) assay

A LC-MS based assay was developed for inhibitor screening of 2OG oxygenase and FTO at the University of Oxford[17]. The assay utilises m^3T as substrate and a reverse phase (ethylene bridged hybrid) C18 column (Waters ACQUITY UPLC BEH) to separate substrate (3-methylthymine, m^3T) and product (thymidine, T); quantification is achieved by integration of UV-trace peak areas. The optimised conditions are summarised in Table 2.1.

Table 2.1: Optimised conditions of FTO *in vitro* inhibition assay based on the K_m of reagents.

Component	K_m (μM)	Optimised conditions
Enzyme, FTO		3 μM
m^3T nucleoside	62.9	70 μM
2OG	151.2	160 μM
L-ascorbate	491.0	500 μM
Fe(II)	94.3	100 μM
Buffer		50mM MES (pH 6.3)
Incubation time at 25 ˚C		1 hour

A matrix-assisted laser desorption/ionisation-time of flight (MALDI-TOF) MS assay[40] was also developed for the closely related ABH5 (by Dr WeiShen Aik in conjunction with Dr Marina Demetriades). The substrate used in this assay was a 5-mer oligonucleotide (ssRNA) with the modified m^6A base positioned in the middle of the sequence [5'-GG(m^6A)CU-3']. This sequence was chosen due to its biological relevance, as it has been reported to be the consensus motif involved in mRNA stability regulation via YTH domain-containing family proteins, YTHDF2 and YTHDF3, which specifically recognise and bind to m^6A in mRNA[41-42]. Quantification was achieved by integration of the MS peak intensity of each species. The MS-based assay was chosen due to its reliability and sensitivity, even though it was relatively time consuming. The optimised conditions are summarised in Table 2.2.

Table 2.2: Optimised conditions of ABH5 *in vitro* inhibition assay based on the K_m of reagents.

Component	K_m (μM)	Optimised conditions
Enzyme, ABH5		0.7 μM
5-mer ssRNA	0.89±0.16	3 μM
2OG	1.29±0.14	3 μM
L-ascorbate	Not dependent	1000 μM
Fe(II)	4.58±1.0	100 μM
Buffer		50 mM Tris (pH 7.5)
Incubation time at 25 ˚C		20 mins

2.3. Objectives

With the apparent success of structure-based inhibitor design, i.e. through identification of molecules that compete for both 2OG- and substrate-binding sites, the goal of the work described in this chapter was to design and synthesise potent and selective FTO inhibitors by building on previous results in Oxford. Further, it was also considered desirable to develop an FTO assay platform that was both reliable and high-throughput. MS-based assays have proved to provide the most robust and meaningful methods in this lab (for nucleic acid and peptide substrates), hence MS was considered the best method to develop into a higher throughput assay platform.

2.4. FTO-inhibitor development

Functionalisation at the 6-position on the pyridine ring of **1** had led to the discovery of **7** (Figure 2.6); it was envisaged that the C-5 position on **1** offered another potential site for exploration. Two prolyl hydroxylase 2 (PHD2) inhibitors, **10** and **11**, which are both 5-substituted, were tested against FTO (Figure 2.6). Unsurprisingly perhaps, the 5-substituted inhibitors (Figure 2.6, **10** and **11**) displayed little inhibition toward FTO compared with the 6-substituted inhibitor, **7**. Previous inhibition data indicated that the hydroxyl group on the 3-position was important for binding, so it was decided to retain this in future inhibitors.

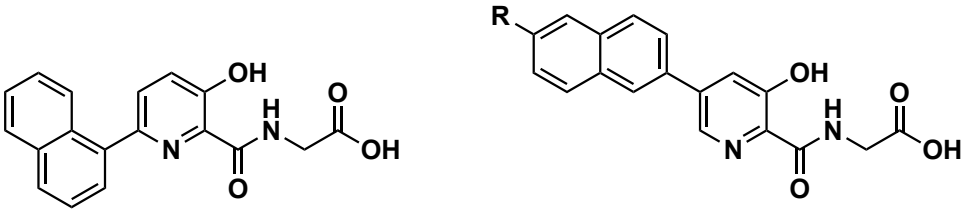


Figure 2.6: *IC_{50} values of pyridinyl inhibitors that display 5- or 6-substituted functional groups.*

Drawing inspiration from **7**, it was envisaged that inhibitors that contained:

1. Novel substitutions at the 6-position of the pyridine ring;
2. Hydroxyl substitutions at the 3-position of the pyridine ring; and
3. A glycinamide side chain to occupy the 2OG-binding site,

could provide potent and selective inhibition against FTO. Closer inspection of the FTO-**7** structural complex (Figure 2.7, PDB ID: 4QHO) suggested that several polar residues involved in substrate binding by FTO might be exploited in inhibition; it was proposed that replacement of the carbon-carbon bond at C-6 with a carbon-heteroatom bond would lead to more favourable electrostatic/hydrogen bond interactions between the inhibitor and the surrounding residues, hence improve binding and/or potency. This led to the hypothesis that Buchwald-Hartwig coupling could be employed instead of Suzuki coupling to incorporate a heteroatom.

This approach could also introduce a higher degree of flexibility to the molecule, which could enable improved induced fit during the formation of the ligand-enzyme complex.

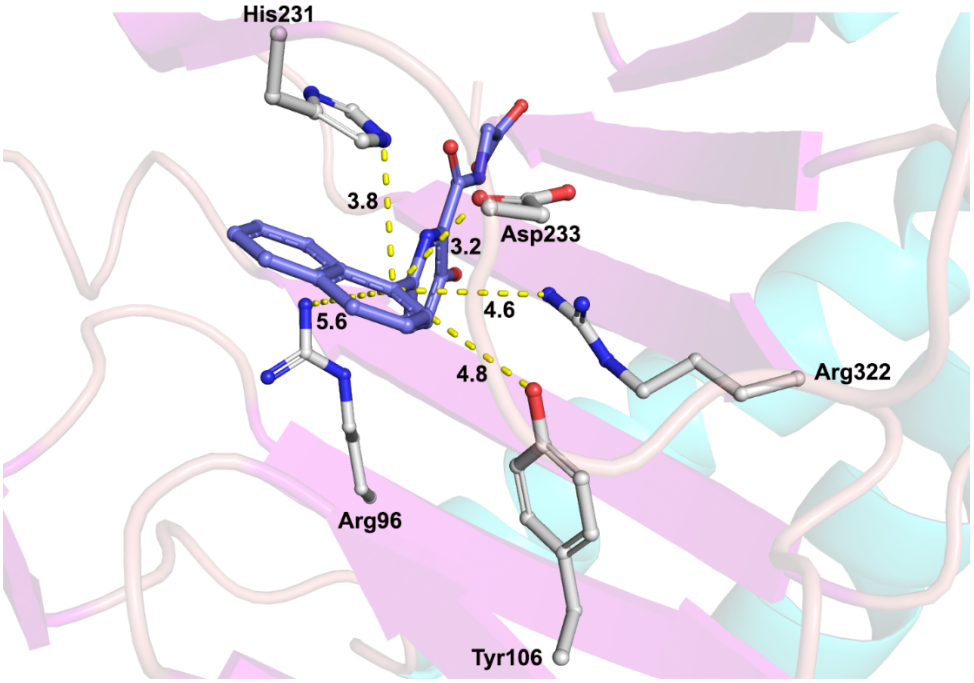
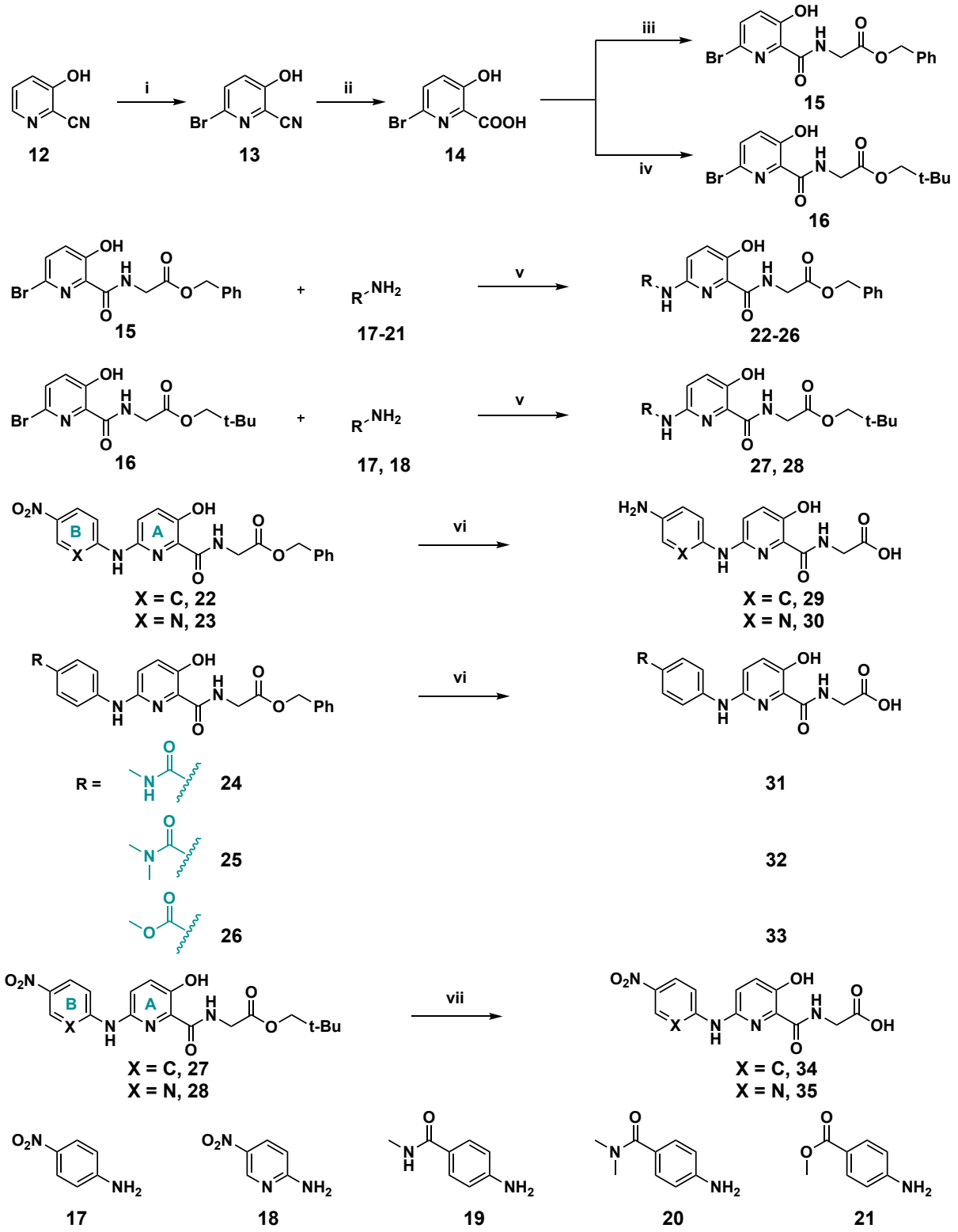


Figure 2.7: *View from a crystal structure of the FTO-**7** complex (PDB ID: 4QHO) showing formation of potential electrostatic/hydrogen-bond interactions through replacement of the C-6 carbon-carbon bond with a carbon-heteroatom bond. Potential electrostatic/hydrogen-bond interactions are represented by yellow dashed lines. FTO residue side chains C (white), O (red), N(blue), Zn(II) (grey sphere).*

The FTO inhibitors used in this study were synthesised by Dr Shifali Shishodia (D. Phil thesis, Oxford University). The synthetic route employed is outlined in Scheme 2.1. Both benzyl and *t*-butyl esters were used as orthogonal glycine ester protecting groups, so that two chemically different functional groups (-NO_2 and -NH_2) at the 4-position of ring B (Scheme 2.1) could be investigated through the use of different deprotection methods. It was envisaged that palladium on charcoal (Pd/C) would reduce both the benzyl and nitro groups on **22** and **23** to produce **29** and **30**, whilst use of potassium hydroxide (KOH) would hydrolyse only the *t*-butyl ester (**27**, **28**), but leave the –NO_2 group intact to provide **34** and **35**.



Scheme 2.1: *Reaction conditions: i) Br_2 (1.1 eq, H_2O, 3 days; ii) NaOH (30%) in MeOH, reflux, 12 hr; iii) $GlyOCH_2Ph.HCl$ (1.5 eq), T3P (1.5 eq), DIPEA (4 eq), mw, 120 ºC, 4 hr; iv) GlyOt-Bu.HCl (1.5 eq), DIPEA (4 eq), mw, 120 ºC, 4 hr; v) R-NH_2 (1.1 eq), K_3PO_4 (1.2 eq), BrettPhos (13.5 eq), G1 Pd catalyst (9 eq), mw, 120 ºC, 8 hr; vi) Pd/C, H_2, THF, r.t., 24 hr; vii) KOH (excess), THF, r.t., 2 days.*

2.5. Production and purification of enzymes

For *in vitro* biochemical assays, recombinant hexahistidine-tagged full-length FTO (pET28a_hFTO construct) and $ABH5_{66-292}$ (pNIC28_Bsa4 construct) proteins were produced using a modified version of a previously reported method[17, 43]. FTO and $ABH5_{66-292}$ encoding vectors were expressed in *E. coli* BL21 (DE3). Purification by nickel-affinity chromatography (HisTrap) was followed by heparin-affinity chromatography as described in the Chapter 7 (Materials and methods). For X-ray crystallography, a recombinant truncated FTOΔ31 (pET28a_hFTOΔ31 construct, hexahistidine-tagged human FTO with residues 2−31 deleted from the *N*-terminus) was produced using a method that was previously reported[17]. The FTOΔ31 encoding vector was expressed in *E. coli* BL21 (DE3) cells. The resultant recombinant protein was purified sequentially using nickel-affinity chromatography (HisTrap), heparin-affinity chromatography and MonoQ anion-exchange chromatography as described in Chapter 7 (Materials and methods). At each stage in the purification of these enzymes, protein purity was determined by sodium dodecyl sulphate-polyacrylamide gel electrophoresis (SDS-PAGE) (Figure 2.8). Once purification was complete, the molecular weights of purified proteins were confirmed by electrospray ionisation-mass spectrometry (ESI-MS) (Figure 2.9).

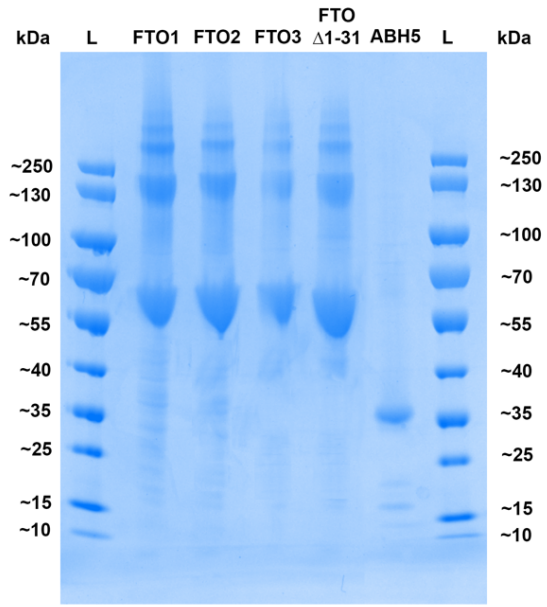
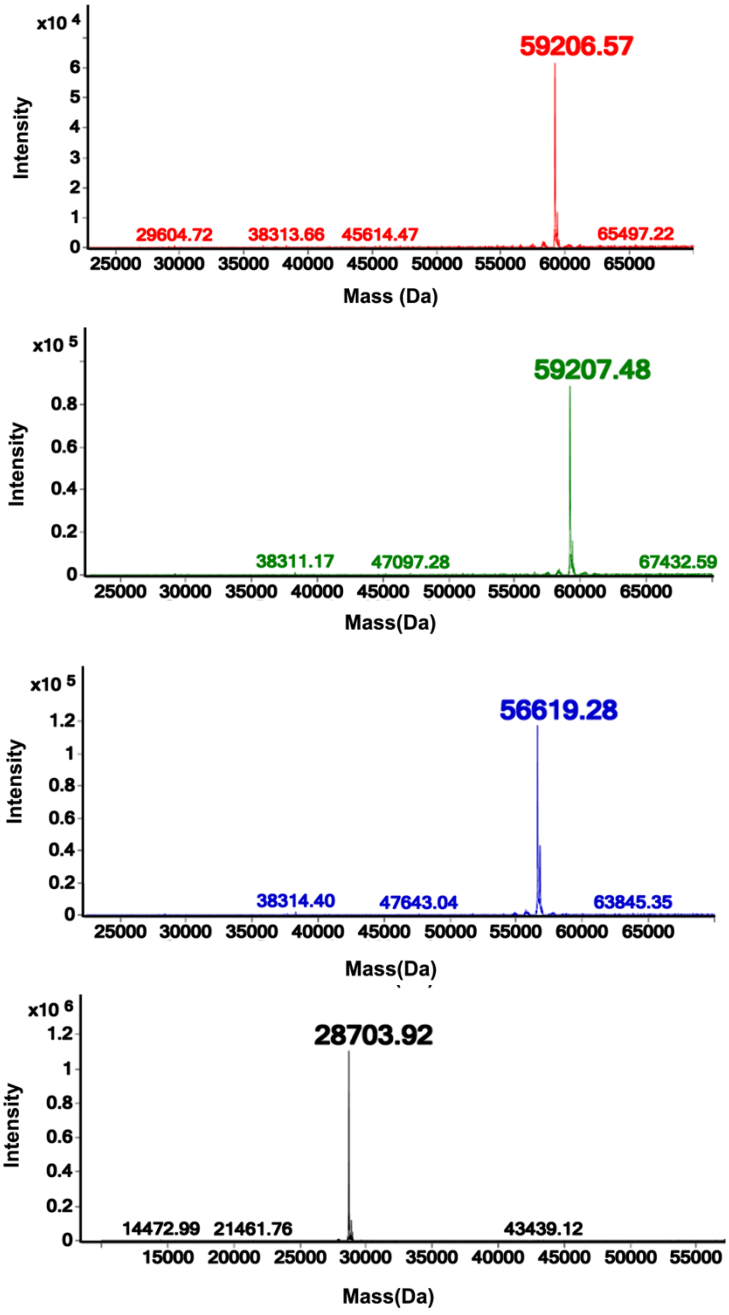


Figure 2.8: *SDS-PAGE Gel of FTO after one (FTO1), two (FTO2) or three (FTO3) rounds, respectively, of metal ion affinity purification by elution from an immobilised nickel column (HisTrap) with a gradient of 0-0.5 M imidazole, heparin affinity purification by elution from an immobilised heparin column (Heparin) with a gradient of 0-2 M NaCl, and anion exchange purification by elution from an monoQ column with a gradient of 0-2 M NaCl at pH 7.5. FTO Δ31 and ABH5 were prepared using three rounds of purification (HisTrap + Heparin + monoQ). All enzyme purification steps were carried out at 4 °C.*



Enzyme	Predicted mass (Da)	Measured mass (Da)
FTO (HisTrap)	59204.91	59206.57
FTO (HisTrap + Heparin)	59204.91	59207.48
FTO Δ31 (HisTrap + Heparin + MonoQ)	56617.95	56617.28
ABH5$_{66-292}$	28631.46	28703.92

Figure 2.9: *Masses of enzymes newly purified for this study as determined by electrospray ionisation mass spectrometry (ESI-MS). Enzymes were assayed at c.a. 10 μM in 50 mM Tris buffer, pH 7.5. The predicted masses, based on amino acid sequences, are also provided. Red, FTO (Histrap). Green, FTO (HisTrap + Heparin). Blue, FTO Δ31 (HisTrap + Heparin + MonoQ). Black, ABH5$_{66-292}$.*

2.6. *In vitro* assay optimisation

2.6.1. FTO assay based on matrix-assisted laser desorption/ionisation

A good inhibition assay should ideally reconstitute the approximate biologically relevant conditions of the target enzymes, while consuming the minimum amount of enzyme and offering the most efficiency/cost-effectiveness as possible. During enzyme assays, the catalytic reaction should be carried out at substrate concentrations near to or slightly above (e.g. multiplied two-fold) co-substrate/substrate K_m values. This is so that the reaction can be easily monitored at a moderate rate while ensuring adequate product formation. MALDI is a robust and potentially high-throughput technique[44-45]. Thus, since oligonucleotide (ssRNA) that contains m^6A is the preferred identified substrate for FTO[10], and a MALDI-based assay that utilises 5-mer ssRNA substrate has been optimised for ABH5 (Dr WeiShen Aik, D. Phil thesis, Oxford University), it seems sensible to attempt to translate this assay to FTO inhibition screening.

Initially, FTO activities with 5-mer ssDNA [dGdG(dm^6A)dCdT] (ELLA Biotech, Munich, Germany) and 5-mer ssRNA [GG(m^6A)CU] (ELLA Biotech, Munich, Germany) substrates were tested at different pH values, using the previously optimised reaction conditions for m^3T[17] (FTO 3 μM, substrate 70 μM, 1 hr, Figure 2.10).

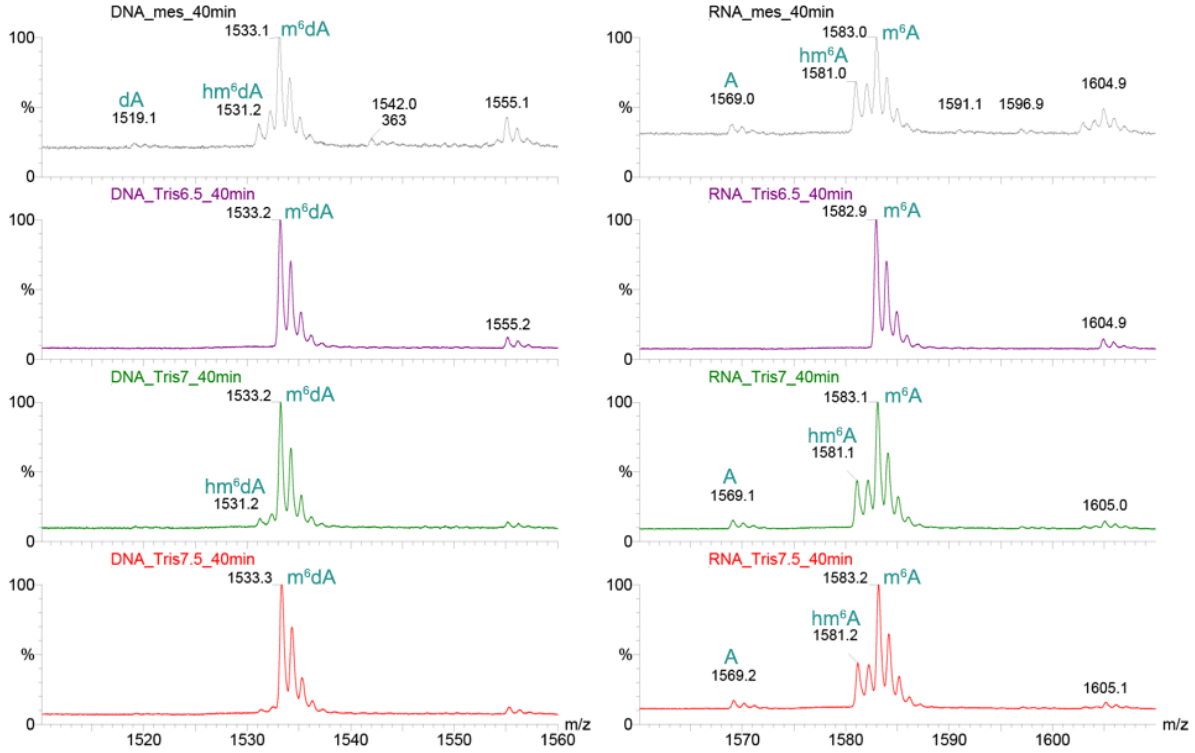


Figure 2.10: *FTO activity tests with ssDNA and ssRNA at different pH values (6.3, 6.5, 7.0, and 7.5). The substrates are marked as* ***m⁶dA*** *(5-mer ssDNA) or* ***m⁶A*** *(5-mer ssRNA), intermediates are marked as* ***hm⁶dA*** *(5-mer ssDNA)* ***or hm⁶A*** *(5-mer ssRNA), and products are marked as* ***dA*** *(5-mer ssDNA) or* ***A*** *(5-mer ssRNA).*

The strongest activity was achieved with the ssRNA substrate in MES buffer at pH 6.3. However, when the FTO and substrate concentrations were reduced, the mass spectra quality deteriorated considerably. To improve the spectrum quality, various buffers, quenching reagents, and matrices were screened with 6 µM ssRNA as standard substrate (Figure 2.11). The quality of the MS spectra was improved using 50 mM Tris buffer (pH 6.5); as shown in Figure 2.10, the activity of FTO using this buffer at pH 7.5 was comparable with the activity observed using MES, pH 6.3. Tris buffer at pH 7.5 was thus selected for further FTO assays. Of the quench reagents tested, 1 mM EDTA diluted in Tris buffer provided a much cleaner spectrum than use of methanol (MeOH) or formic acid (FA). The optimal matrix was determined to be 0.5 M 2,4,6-trihydroxyacetophenone in EtOH with 0.1 M ammonium citrate in H_2O. To ensure that 1 mM EDTA was adequate to quench the reaction, the activity was tested after 20 min with both 1 mM and 2 mM EDTA; results showed the same loss of activity.

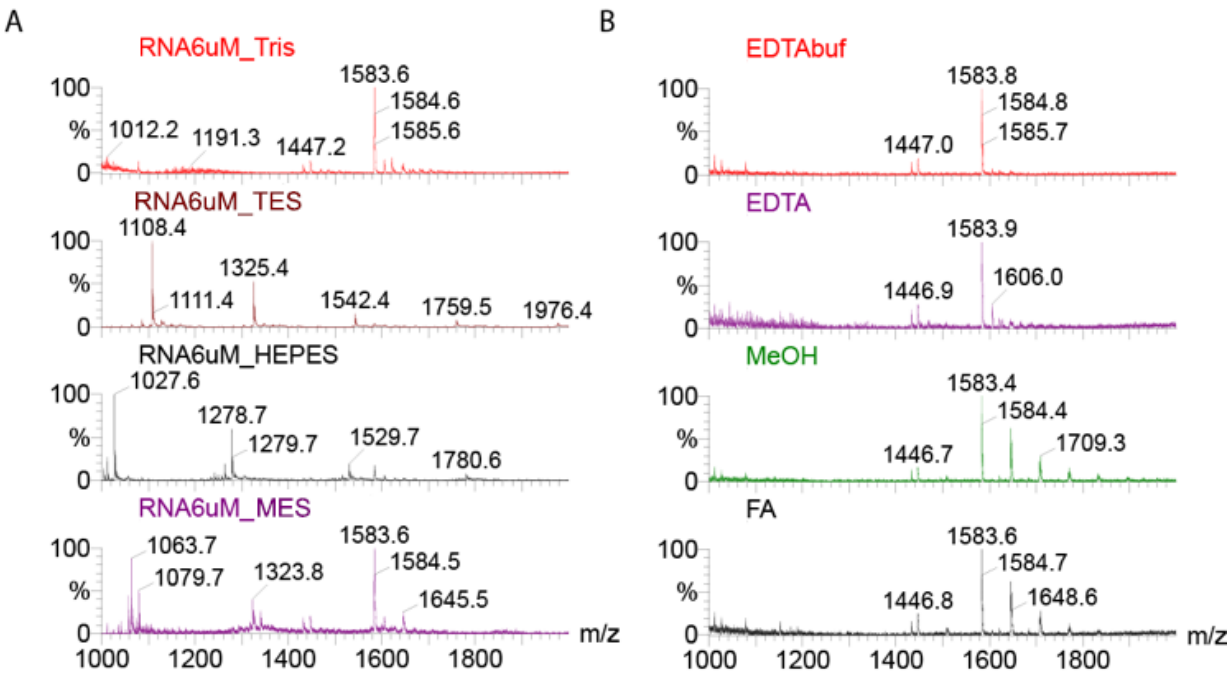


Figure 2.11: *Mass spectra of 6μM ssRNA with (A) buffers at pH 6.5 and (B) quench solvents at 1:1 ratio.*

It was noted that at different stages of its purification, FTO showed varied levels of activity. Thus, FTO proteins of different purities were investigated with the MALDI assay. FTO after purification through only the HisTrap column was very active, but of low purity, which likely caused lower quality MS spectra. FTO purified via either HisTrap + Heparin, or HisTrap + Heparin + MonoQ, column chromatography were tested under the same conditions. A drop in activity was observed when the purer forms of FTO were used, but spectral quality was improved consistent with the increased purity.

The effect of ascorbate added to the reaction was investigated using HisTrap + Heparin and/or HisTrap + Heparin + MonoQ purified FTO. The best results were obtained from HisTrap + Heparin purified FTO with ascorbic acid (AscOH) (Figure 2.12).

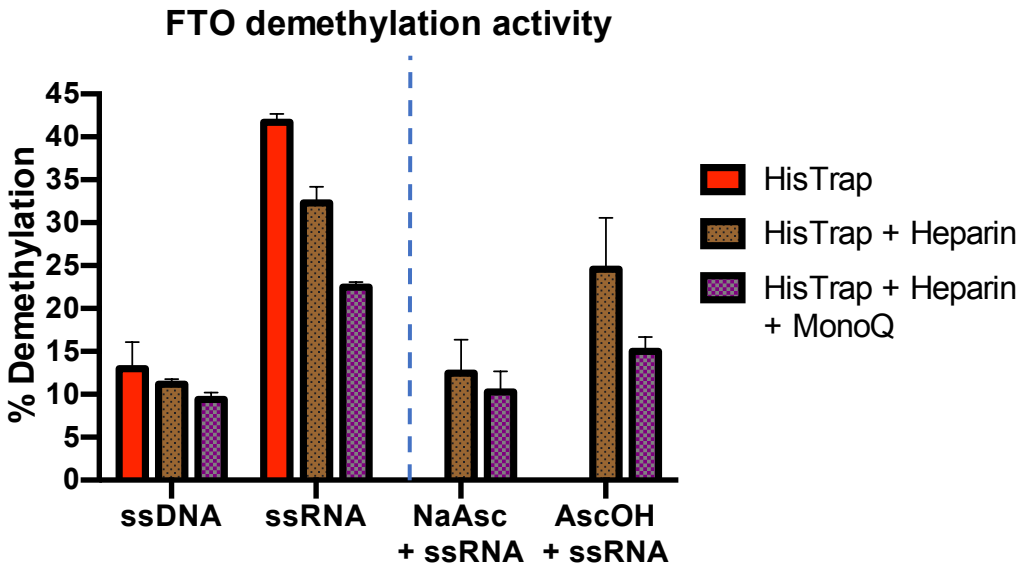


Figure 2.12: *FTO-catalysed demethylation of 5-mer ssDNA and 5-mer ssRNA at different stages of the purification process. The best results were achieved with ssRNA as a substrate and FTO prepared by HisTrap chromatography alone. Demethylation reactions were carried out in 50 mM Tris buffer pH 7.5, 3 µM FTO, 70 µM substrates; reaction was quenched with 1mM EDTA after 20 min incubation at 25 ºC. Data were plotted as the mean of technical triplicates using GraphPad Prism® software. AscOH: ascorbic acid, NaAsc: sodium ascorbate.*

After identification of the appropriate buffer, quenching reagents and FTO purification level for assays, a time course at two different concentrations of FTO was attempted (1.3 µM, 1.5 µM) to ensure use of the minimum amount of enzyme. Activity was observed to be satisfactory at 1.3 µM of FTO after 30 min (Figure 2.13). Thus a 30 min reaction time (and 1.3 µM enzyme concentration) was used for subsequent optimisation steps with other co-factors/substrates.

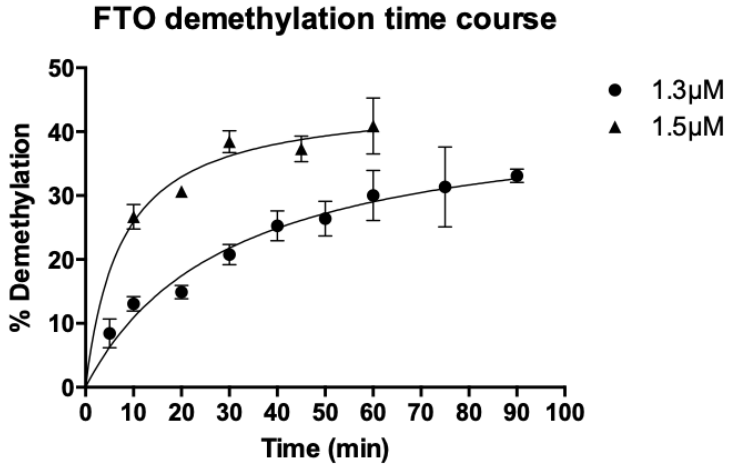


Figure 2.13: *A time course experiment of FTO-catalysed demethylation of 5-mer ssRNA at two enzyme concentrations, 1.3 µM, 1.5 µM. Data were plotted as the mean of technical triplicates using GraphPad Prism® software.*

Kinetic investigations were then carried out for FTO by varying the 2OG, Fe(II), ascorbic acid and 5-mer ssRNA concentrations. The Michaelis–Menten constant, K_m, which shows the concentration of the substrate when the reaction velocity is half of the maximal velocity (V_{max}), was determined by plotting the initial rate of reaction against the concentration of each varying component (Figure 2.14). The determined K_m values are given in Table 2.3.

Table 2.3: Optimised conditions of FTO for MALDI assay based on the K_m values of reagents. Note difference from previous LC-MS assay results (Table 2.2).

Reagent	LC-MS (µM)	K_m (µM)	MALDI (µM)
Asc	NaAsc/500	119 ± 16	L-ascorbic acid/500
2OG	160	7.2 ± 1	10
$(NH_4)_2Fe(SO_4)_2 \cdot 6H_2O$	100	0.44 ± 0.09	10
Substrate	m^3T/70	20 ± 5	ssRNA-GG(m^6A)CU/20
hFTO	3		1.3
Buffer	50 mM Mes. pH 6.3		50 mM Tris, pH 7.5
Incubation time/T	1 h/r.t		30 min/r.t
Final Volume	50 µL		25 µL

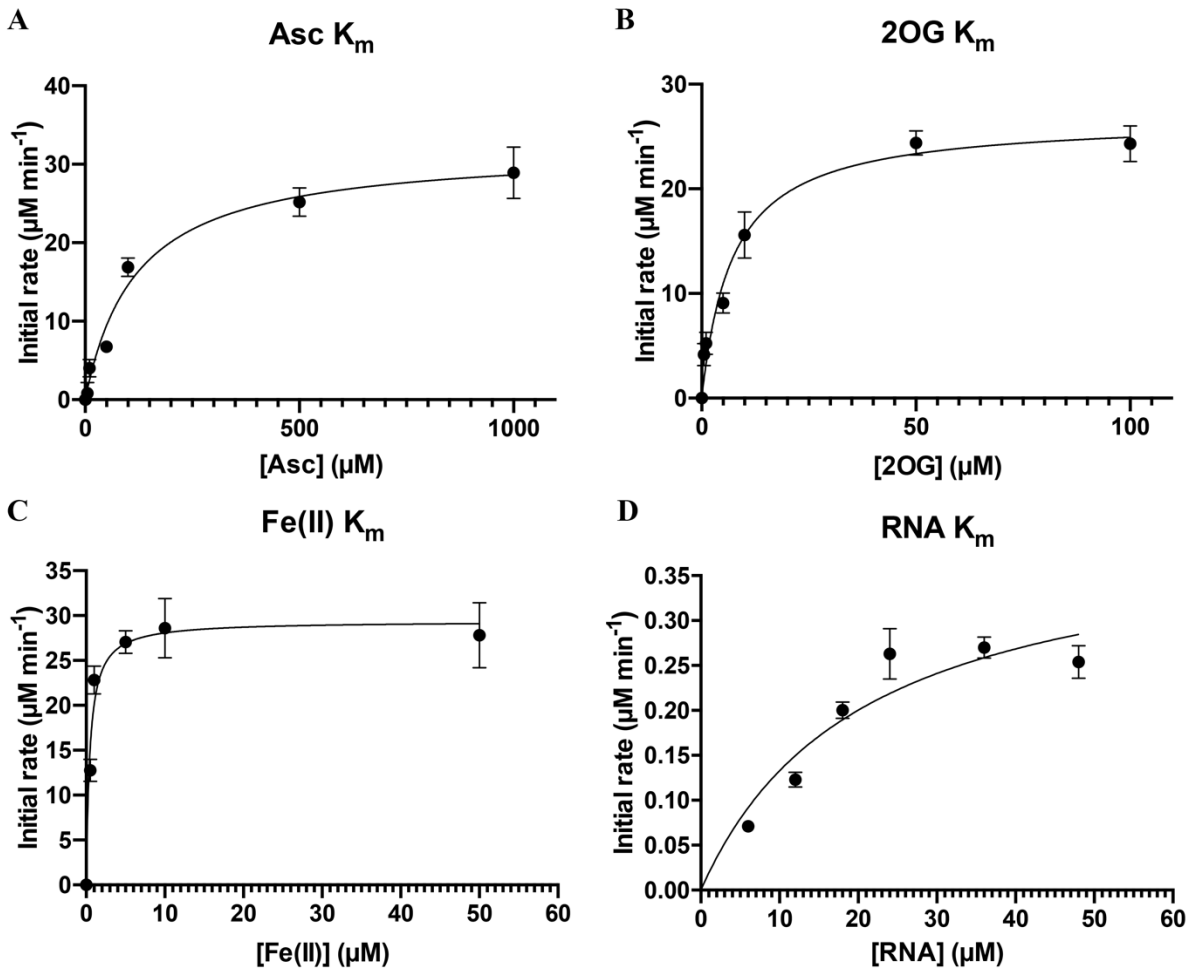
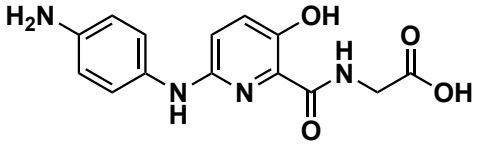
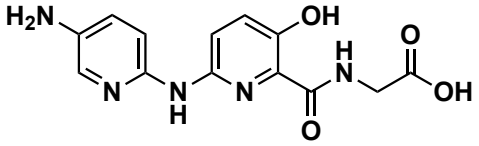
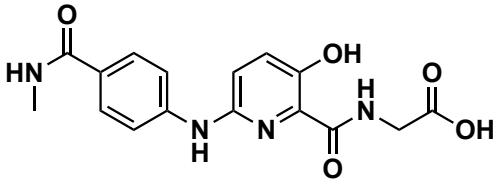
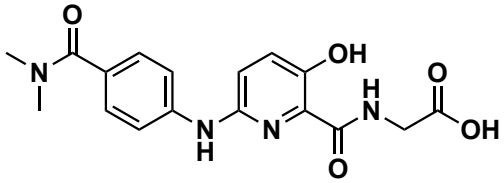
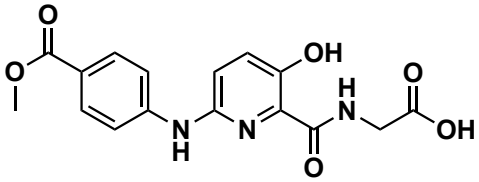
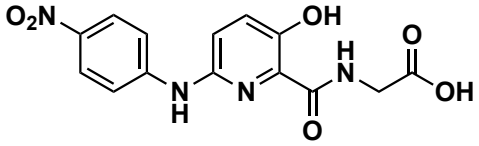
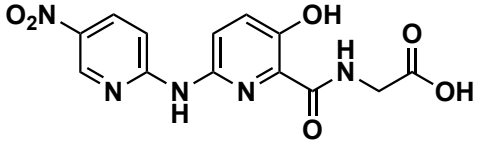


Figure 2.14: *FTO kinetic parameters. Michaelis-Menten curves of initial rate (μM/min) versus (A) concentration of ascorbic acid (Asc, μM); (B) concentration of 2-oxoglutarate (2OG, μM); (C) concentration of Fe(II) (μM)); and (D) concentration of 5-mer RNA (5'-GGm^{6}ACU-3') substrate (μM). Data were plotted as the mean of technical triplicates using GraphPad Prism® software.*

2.6.2. Inhibition of FTO by second-generation inhibitors

Using the optimised MALDI assay conditions, the inhibitors (**29-35**) were initially screened against FTO. Residual activity, through the demethylation of 5-mer ssRNA (5'-GGm^{6}ACU-3'), was measured *via* MALDI-TOF MS for a range of inhibitor concentrations. All measurements were performed at 25 °C and pH 7.5. Note that the enzyme was not incubated with inhibitors prior to the addition of substrate (Figure 2.15 & Table 2.4).

Table 2.4: IC_{50} values for the inhibition of FTO by second-generation inhibitors. Errors were calculated as standard deviation of the mean of technical triplicates.

Compound	Structural Formula	FTO IC_{50} (μM)
29		29.3 ± 2.9
30		5.6 ± 0.5
31		5.8 ± 0.4
32		37.6 ± 3.1
33		5.2 ± 0.4
34		3.2 ± 0.4
35		8.0 ± 0.7

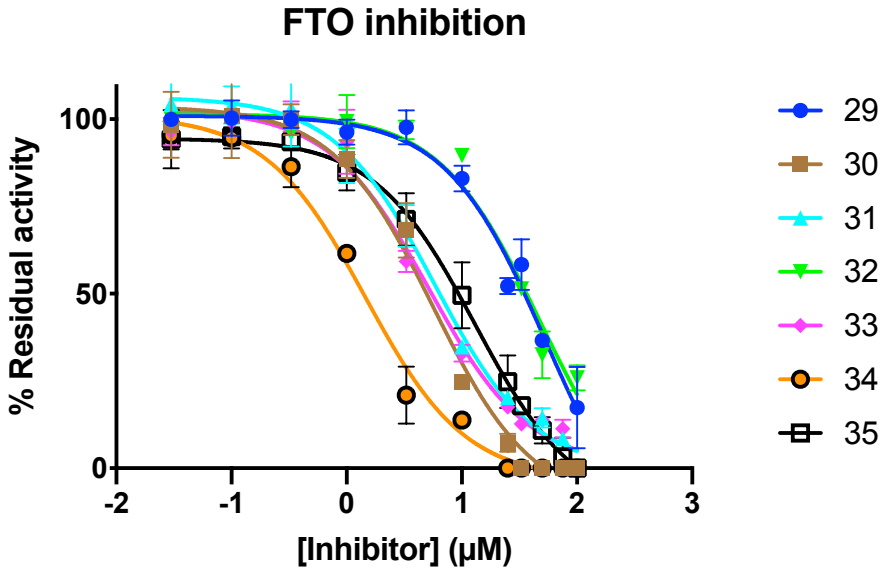


Figure 2.15: *IC_{50} curves for the inhibition of FTO. Inhibition assays were carried out at 25 °C and pH 7.5.*

The initial results for the second-generation FTO inhibitors revealed some trends. Most compounds, except for **29** and **32,** showed low micromolar potency. Compound **34** was the most potent inhibitor (IC_{50} 3.2 ± 0.4 μM), which is close to the enzyme concentration employed in the assays (1.3 μM) and indicated strong binding and hence inhibition. The results indicate that the substitution of a carbon-heteroatom bond for a carbon-carbon bond at the 6-position of ring A may result in improved potency. The most potent second-generation inhibitor, compound **34** (IC_{50} 3.2 ± 0.4 μM), exhibits similar potency within error as its counterpart from the first-generation inhibitors, i.e. compound **7** (IC_{50} 4 μM). It was inconclusive whether the presence of a heteroatom on ring B (Scheme 2.1) increased potency, as compound **30** (IC_{50} 5.6 ± 0.5 μM), with a pyridinyl ring B, showed five-fold more potency than its phenyl counterpart, **29** (IC_{50} 29.3 ± 2.9 μM). Compound **34** (IC_{50} 3.2 ± 0.4 μM), with a phenyl ring B, exhibited more than three-fold greater potency than the pyridinyl-containing compound **35** (IC_{50} 8.0 ± 0.7 μM). It should be noted that **29** showed poor solubility under the inhibition assay conditions, which is thought to have contributed to its observed relatively high IC_{50} value. It is apparent, however, that increasing steric bulk at the 4-position of ring B decreases inhibition

(**31** and **32**), which is likely to be due to steric clash with the incoming NA substrate (Figure 2.16).

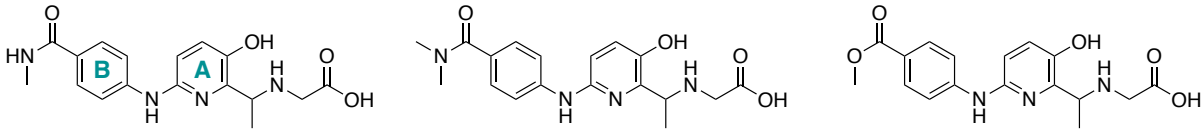


Figure 2.16: *FTO inhibitors that show increased steric bulk (in the cases of 31 and 32) hamper potency against FTO.*

Having established the activity of the second-generation compounds against FTO, their inhibitory activity towards other 2OG oxygenases was considered. Thus, **29-35** were screened for inhibitory activity against a panel of human 2OG oxygenases, which included the histone demethylases KDM5B, KDM5D, KDM3A, KDM6B, KDM2A, KDM4C and the clinically relevant HIF-PHD2 (inhibition screening performed by Dr Anthony Tumber) (Table 2.5).

Table 2.5: IC_{50} values for the inhibition of a panel of 2OG oxygenases by second-generation FTO inhibitors. NI – No inhibition at 100 μM inhibitor concentration. Note: the inhibition data for PHD2 KDMs were determined at enzyme concentration 0.1 μM (FTO concentration 1.3 μM); for KDM and PHD2 inhibition screen, duplicates were used, hence no error is given.

Cpd	IC_{50} (μM)							
	FTO	KDM5B/ JARID1B	KDM5D/ JARID1D	KDM3A/ JMJD1A	KDM6B/ JMJD3	KDM2A/ FBXL11	KDM4C/ JMJD2C	PHD2
29	29.3 ± 2.9	53.44	NI	NI	NI	NI	NI	21.28
30	5.6 ± 0.5	39.85	NI	51.3	NI	81.04	63.86	10.11
31	5.8 ± 0.4	17.74	57.84	69.44	47.83	NI	NI	7.85
32	37.6 ± 3.1	63.06	85.07	52.01	89.74	NI	100.6	10.94
33	5.2 ± 0.4	NI	NI	NI	89.73	NI	NI	6.05
34	3.2 ± 0.4	46.34	27.47	NI	19.55	NI	NI	2.25
35	8.0 ± 0.7	87.82	NI	41.9	38.45	NI	44.41	2.57

The results demonstrated that the FTO inhibitors were relatively selective for FTO (at least 3-fold more selective) over, at least some, KDMs. Most of the second-generation FTO inhibitors (**29-35**) showed no selectivity for FTO over PHD2 (under the tested conditions) compared with **FG2216** and previously reported FTO inhibitors[17] (Figures 2.2 and 2.4). This is attributed to

the different enzyme concentrations used (0.1 μM for PHD2 and 1.3 μM for FTO), and this further supported the need for an assay platform that required lower enzyme concentration.

2.6.3. Assay based on liquid chromatography-mass spectrometry

Despite the promising inhibition and selectivity results (over KDMs but not PHD2), it was noted that the most potent inhibitor **34** (IC_{50} value 3.2 ± 0.4 μM) was not as effective at inhibition of FTO as some inhibitors reported in the literature, e.g. compound **5** (IC_{50} value 0.8 μM)[22]. It was proposed that the inherent assay condition was a limit to IC_{50} measurements, i.e. the enzyme concentration used (1.3 μM) limited the lowest possible IC_{50} value to half [E] of 0.65 μM. Moreover, the MALDI-based assay had additional caveats. The substrate used for the MALDI assay was a 5-mer oligonucleotide ssRNA [GG(m^6A)CU] (MW: 1582.2 Da), which could be observed by MALDI-TOF MS in the positive-ion mode (1583.2 m/z). However, the hydroxylated intermediate/hemiaminal does not manifest at 1599.2 m/z (+ 16 Da), but was observed as its apparently dehydrated (imine) species (1581.2 m/z, - 2 Da) (Figure 2.17). This was thought to be due to laser ionisation or matrix effects associated with the MALDI technique[46]. Separation and measurement of substrate and product peaks was difficult due to overlapping peaks. Additionally, as the 5-mer ssRNA substrate was commercially sourced, the cost was significant given the amount of substrate (20 μM) required in the MALDI assay.

In search of a more efficient solution, attention was turned to the development of a new assay platform. Florescence-based techniques were ruled out due to complications outlined earlier (Section 2.1). NMR-based assays were considered. However, NMR methods require relatively large amounts of material (0.1 mM range)[47] and are not suitable for large-scale inhibitor screening. Given the limited amount of oligonucleotide substrate available, an assay that was both sensitive and accurate was desired. Hence, following on from prior work that used nucleoside substrate (m^3T), the LC-MS-based assay was revisited using oligonucleotides.

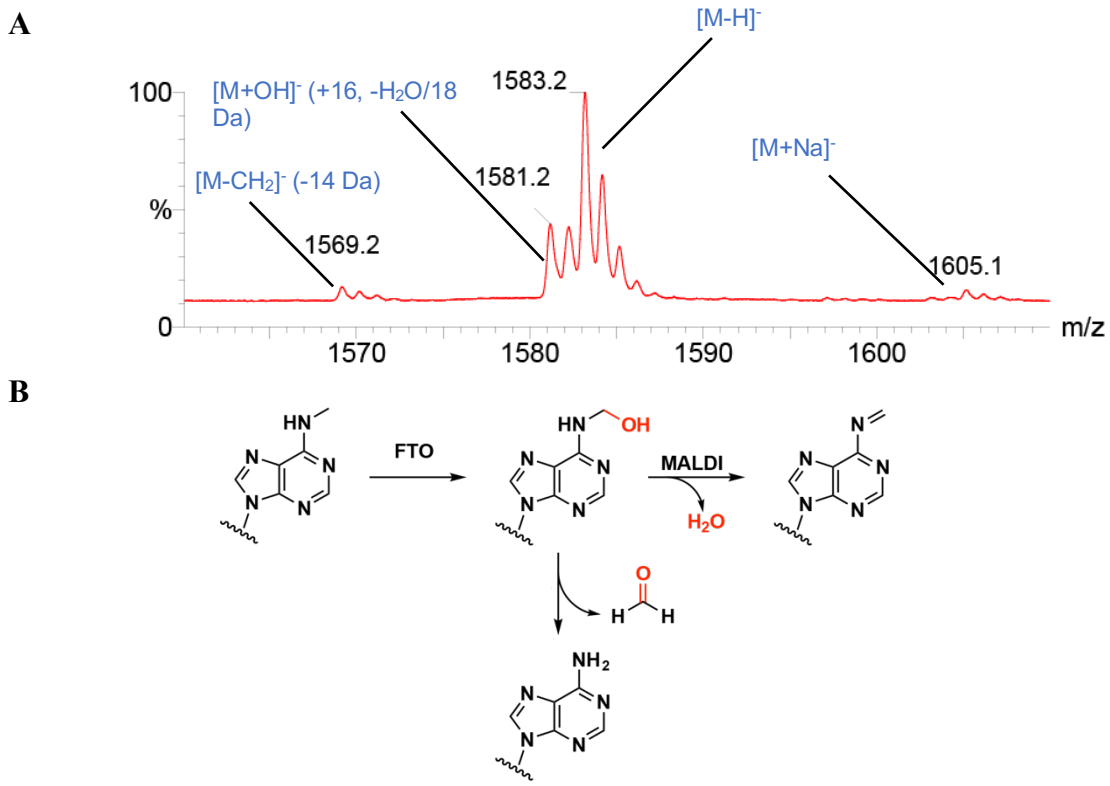


Figure 2.17: *A) MALDI-TOF MS spectrum of an FTO-catalysed reaction showing the 5-mer ssRNA substrate, m^{6}A (1583.2 m/z), demethylated product, A (1569.2 m/z, -14 Da) and a peak at 1581.2 m/z, complying to the hemiaminal with loss of water, hm^{6}A. B) The proposed MALDI observed product, hemiaminal, is dehydrated to form an imine/iminium ion.*

LC-MS based assays are used extensively in oligonucleotide research[48-49]. LC-MS can overcome issues with quantification inaccuracy observed with the MALDI based assay by direct injection of samples in solution, which is then separated by liquid chromatography and monitored by UV-Vis directly, prior to injection into a mass spectrometer for accurate mass measurement and identification of peaks. Standards of substrate and product were prepared in Milli-Q purified water, separated using a Waters® ACQUITY UPLC Oligonucleotide BEH C18 Column, and analysed using a Bruker Daltonics, microTOF MS in negative-ion mode. An ion-pairing buffer of 1,1,1,3,3,3-Hexafluoro-2-propanol (HFIP) and triethylamine (TEA) was used for better separation and retention of RNA substrate[49]. Calibration curves of standards for unmodified and modified 5-mer ssRNA oligonucleotide, [GGACU] and [GG(m^{6}A)CU],

respectively, demonstrated a linear dependence on integrated peak area of the concentration of oligos, from 100 μM to the limit of detection at 0.1 μM.

Initially, the UV trace of peaks for [GGACU] (labelled as a demethylated peak in Figure 2.18, $[M\text{-}CH_2]^-$ 1567.2 m/z) and for [GG(m^6A)CU] (labelled as a methylated peak in Figure 2.18, $[M\text{-}H]^-$ 1581.3 m/z) were found to overlap, which meant that quantification of product formation was difficult (Figure 2.18, C). The conditions of the analysis were then optimised. Among changes made were alteration of the LC mobile-phase solvents and variation of the elution gradients. Although partial separation of [GGACU] and [GG(m^6A)CU] standards (from co-injection) at different ratios (Figure 2.18, D, E) was observed, further improvements were required, as baseline separation of the different signals was essential for accurate quantification.

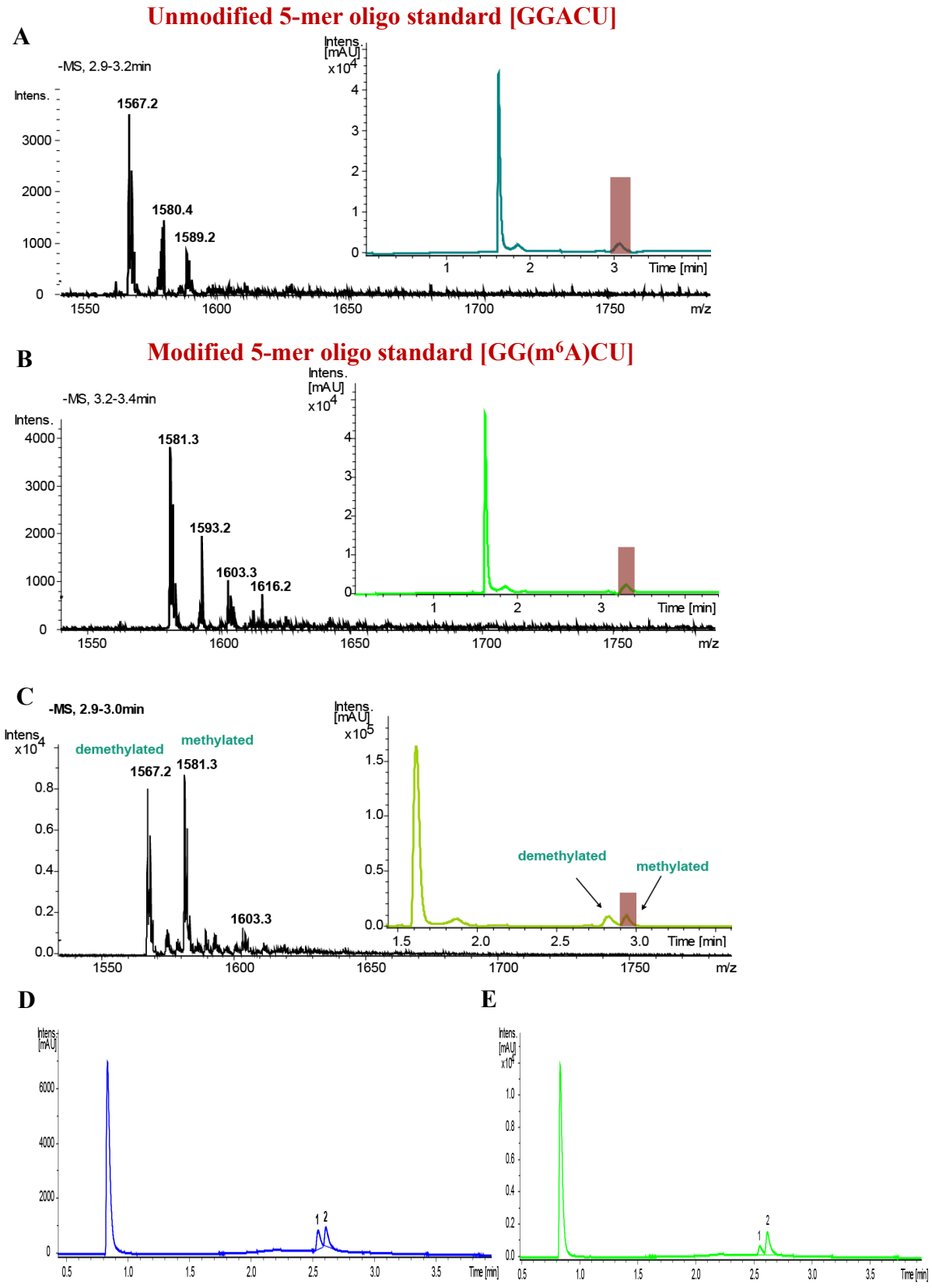


Figure 2.18: *LC-MS trace of (A) demethylated oligonucleotide [GGACU], (B) methylated oligo nucleotide [GG(m^{6}A)CU] and (C) both oligo nucleotides at equal concentration, but the UV peaks overlap, showing poor separation. (D) and (E) show UV traces of demethylated and methylated oligo nucleotides at 1:1 and 1:3 ratios, respectively. The [GGACU] peak is marked as **1** and the [GG(m^{6}A)CU] peak is marked as **2**. Shading indicates the peak of interest.*

Close inspection of the UV chromatogram revealed that the initial 'dead volume', which referred to the sample that was first injected onto the column, contained a significant amount of sample material, i.e. material that had not bound to the column (Figure 2.20, A). It was postulated that samples may not have been retained on the column due to the high concentration of organic solvent used in the injection needle-wash cycles. The needle-washing solvents were thus varied for optimisation; significant separation of the methylated substrate and unmethylated product was only observed when water was used for the needle wash (Figure 2.20, B). It was also found that the commercially purchased 5-mer oligonucleotide (Ella Biotech, Germany) was impure, with two peaks that represented methylated substrate observed in the LC (UV-Vis visualised) trace with the same apparent mass (Figure. 2.20, C, D). The observed separation by LC indicated that chemically/structurally distinctive entities were present; the apparently identical mass indicated the presence of structural isomers. Indeed, m^6A is known to undergo Dimroth-type rearrangement to form m^1A[50-52] (Figure 2.19), which could happen during oligo and/or phosphoramidite synthesis. Dimroth rearrangement would explain the observation by LC-MS of two separate species with the same mass. Despite these difficulties, the assay was deemed satisfactory, as the m^6A to m^1A ratio was constant at different concentrations, and the peaks of interest were well separated.

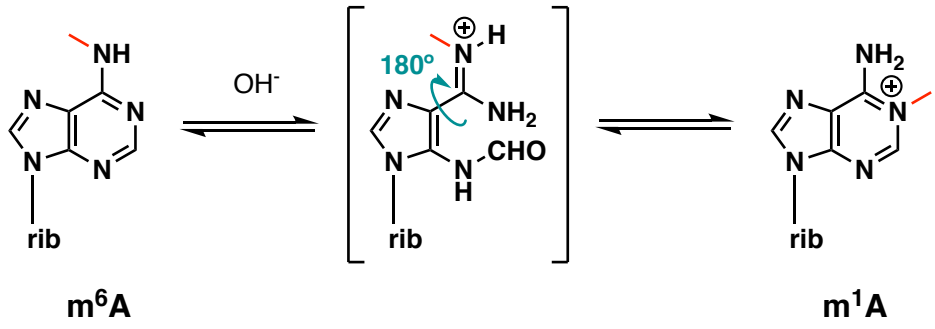


Figure 2.19: *Scheme showing Dimroth rearrangement from m^6A to m^1A in the presence of OH^- ion/basic condition*[51].

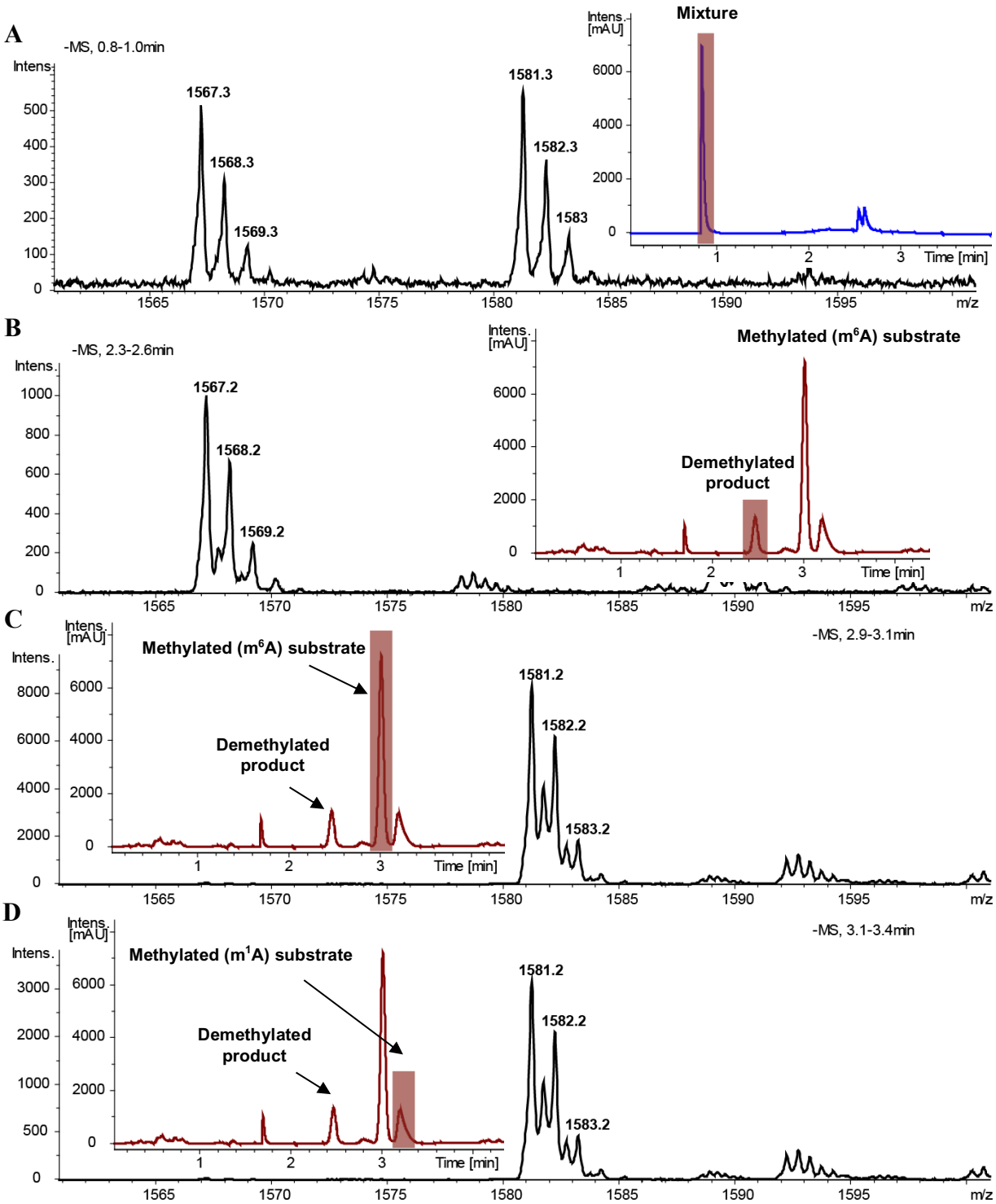


Figure 2.20: *(A) UV chromatogram and MS spectrum showing elution of both standards in the 'dead volume' when using a Waters® ACQUITY UPLC Oligonucleotide BEH C18 column; UV chromatogram and MS spectra showing good separation of the (B) demethylated species, from (C) and (D), which are methylated species. (D) exhibits the same mass as (C), indicating it is an impurity. Shading indicates the peak of interest.*

One drawback of LC-MS-based assays was that the protocol was time- and labour-intensive, in particular because the enzyme had to be removed from the reaction mixture. In LC-MS, MeOH is often used as a quenching reagent as it causes the protein to precipitate, and this can subsequently be removed by centrifugation. The supernatant is collected for analysis and MeOH is removed by heating under vacuum, e.g. using a Speedvac Vacuum Concentrator. The final step is to reconstitute the resultant material with water. This process not only consumes a large amount of time, but is also prone to human error and loss of material.

Inhibition assays are often carried out in 96-well or 384-well plates. Thus it was highly desirable to find an alternative method to remove FTO/ABH5 protein that did not require the addition of quenching reagent. It was envisaged that filtration of the enzyme from the reaction mixture using a membrane with a specific cut-off size could provide the desired effect. Such filters commonly exist in spin 'columns' (i.e., columns used in centrifugation). The Seahorse® polypropylene 96-well filter microplates with 10-30 KDa molecular weight cut-off polyethersulphone membrane were considered suitable ($M.W._{FTO}$: 59 KDa). To screen ABH5 (mass of recombinant $ABH5_{66\text{-}292}$: 25 KDa), plates with a 10 KDa cut-off membrane were obtained. Given the observed sensitivity, lower enzyme and substrate concentrations were used for inhibition screening (Table 2.6). Compound **34** was used to test the sensitivity of the LC-MS-based assay (Figure 2.21), with lower enzyme concentration. However, the Bruker Daltonics, microTOF MS was decommissioned after the inhibition assay had been optimised, therefore screening of the remaining inhibitors could not be performed using this instrument. Fortunately, the Bruker Daltonics, microTOF was replaced by a RapidFire 365® sampling robot coupled to an Agilent 6550 accurate mass qTOF.

Table 2.6: Optimised conditions of FTO for oligo LC-MS assay based on the K_m of reagents (adopted from MALDI assay).

Reagent	Oligo LC-MS (µM)
L-ascorbic acid	500
2OG	10
$(NH_4)_2Fe(SO_4)_2 \cdot 6H_2O$	10
Substrate, ssRNA-GG(m^6A)CU	10
FTO	0.8
Buffer	Tris 50 mM pH 7.5
Incubation time/T	30 min/r.t
Final Volume	25 µL

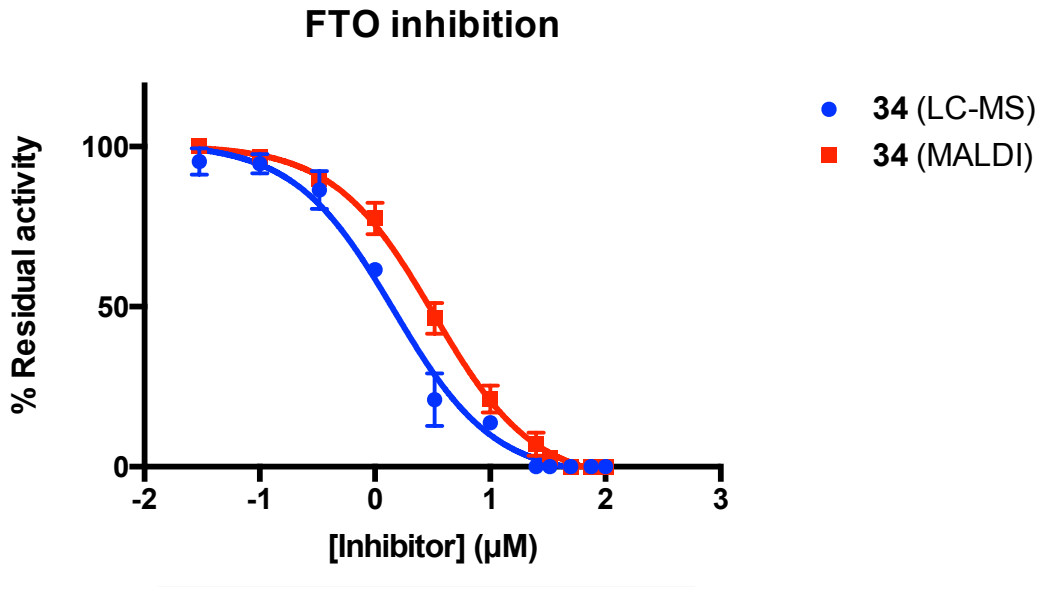


Figure 2.21: *Inhibition curve (IC_{50}) for compound **34** against FTO using LC-MS assay (blue) and MALDI assay (red). Note the slight decrease in IC_{50} value through use of the LC-MS assay.*

2.6.4. RapidFire® Mass Spectrometry- (RF-MS)-based assays

The RapidFire® mass spectrometry (RF-MS) system (Agilent Technologies) as set up at the University of Oxford comprises a high-throughput robotic sample preparation and injection system coupled to a quadrupole time of flight (qTOF) mass spectrometer. This assay platform has been extensively used in drug discovery programmes in the pharmaceutical industry[53-56]. In RF-MS, a conventional LC unit is replaced by the RF in-line solid-phase extraction (SPE) cartridge system; this overcomes the problem of time-consuming and labour-intensive sample

separation by use of SPE for sample clean-up and analyte concentration. The washing of cartridges, elution of sample and eluent injection directly into the MS system are achieved automatically. The current LC-MS assay requires a 10-minute run per well/sample after sample preparation, which usually exceeds 30 minutes). By contrast the RF-MS assays typically require approximately 10-12 seconds per well/sample, which enables analysis of a 384-well plate to be completed in 90 minutes. It was desirable to establish a RF-MS assay system, since accurate high-throughput assays for inhibitor screening against FTO and ABH5 had not been achieved thus far.

Having observed an impurity in the commercially sourced 5-mer ssRNA [GG(m^6A)CU] (ELLA Biotech, Munich, Germany, Figure 2.20), it was decided to synthesise oligonucleotide substrates in house (phosphoramidite, m^6A, was synthesised by Miss Shifali Shishodia, and the oligonucleotide was synthesised by Dr Afaf El-Sagheer). Two ssRNAs of different length were synthesised, a 15-mer [AUUGUGG(m^6A)CUGCAGC] and a 5-mer [GG(m^6A)CU], the purity of which was confirmed by MS (Figure 2.22).

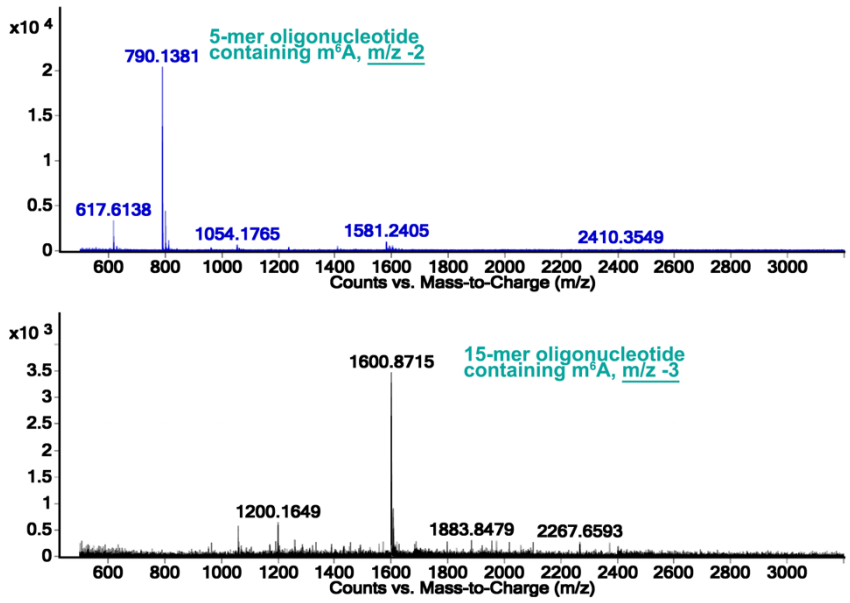


Figure 2.22: *MS spectra of purified (A) 5-mer RNA [GG(m^6A)CU], observed as 790.1381 (m/z -2), and (B) 15-mer RNA oligo [AUUGUGG(m^6A)CUGCAGC], observed as 1600.8715 (m/z -3).*

2.6.4.1. RapidFire® system optimisation

To successfully monitor demethylation/hydroxylation reactions (from FTO or ABH5) using the RF-MS system, it was essential to determine the suitability of substrates and/or products for SPE purification. HFIP and TEA were initially used in the form of an ion-pairing buffer for the ssRNA oligomers due to their successful use in the LC-MS assay; however, no signal was detected in either positive-ion mode or negative-ion modes using this buffer. It was concluded that the HFIP/TEA combination did not enable RNA retention on the SPE cartridge. Ion-pairing agent octylammonium acetate (OAA) was tested as it was used for separation of sugar-phosphates in prior chromatography studies[57]. To achieve optimal sample retention while minimising use of OAA, mobile-phase solvents were optimised to include 6 mM OAA in LC-MS grade water as aqueous buffer/binding buffer (buffer A); 80% (v/v) acetonitrile with 20% LC-MS grade water was used as the preferred organic buffer/elution buffer (buffer B). The OAA was prepared by mixing 0.1 M of octylamine and 0.1 M of acetic acid with 100 mL diethyl ether on ice. This solution was stirred and cooled to -40 ºC. resulting in OAA crystallisation. The ether was removed, and the OAA salt was washed three times with 50 mL of cold cyclohexane. After successful detection of the oligo signals (15-mer [AUUGUGG(m^6A)CUGCAGC] and 5-mer [GG(m^6A)CU]) using OAA, calibration curves were constructed. These showed a linear dependence on the integrated peak area with respect to the concentration of oligonucleotides.

Parameters of the RF system were systematically optimised for sensitivity and sample purification. Initially, 10 µM of the oligo standards in 50 mM Tris buffer pH 7.5 (15-mer and 5-mer) were used to select the most suitable SPE cartridge (Figure 2.23). The available cartridges included: C-4, C-8, C-18 reverse phase; and cyano and phenyl as speciality cartridges. Both these speciality cartridges were not optimal for oligo retention; the phenyl cartridge showed a considerable amount of sample carry-over between injections, and the

cyano cartridge gave a poor signal (likely caused by poor sample retention). However, the phenyl cartridge provided the cleanest signal as it gave the lowest sodium-adduct peaks, which could reduce parent-peak intensity and hence interfere with data analysis. It was noted that sample was carried over between injections during use of the C-4 cartridge, and this could interfere with screening results and accuracy during extended use, i.e. running compound-screening plates. An increase in pH (7.0 – 8.0) had a positive effect on sample carry-over, as the higher pH (pH 8.0) reduced carry-over (Figure 2.23). Alteration of the ratio of organic:aqueous in the wash/eluent buffers did not affect sample purification or sensitivity.

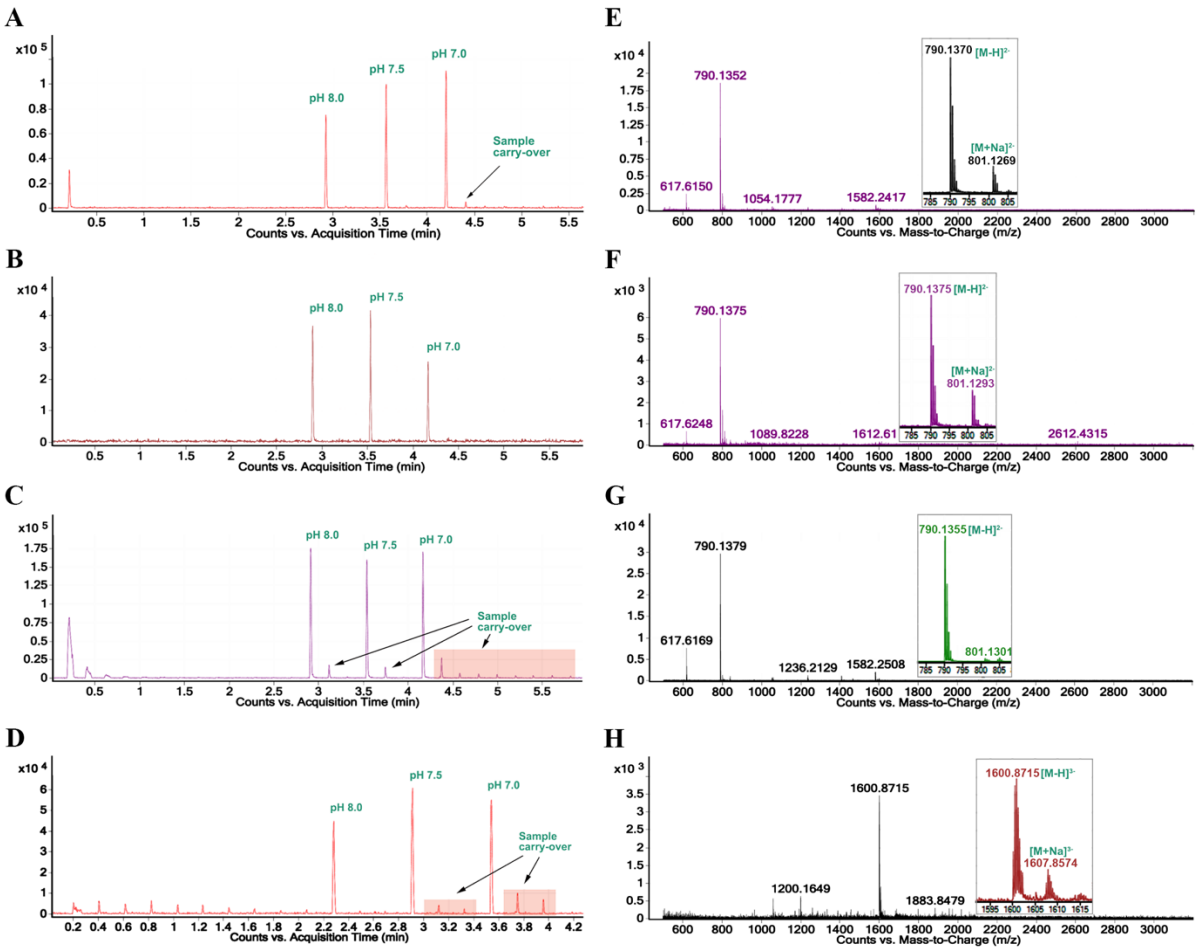


Figure 2.23: *Extracted chromatogram of 5-mer RNA (m/z 790.1) using (A) C-4, (B) cyano and (C) phenyl cartridges. Note: the signal intensity varies: phenyl > C-4 > cyano. Sample carry-over was an issue for the phenyl cartridge, but improved with increasing pH (7.0, 7.5, 8.0) for all cartridges. Mass spectrum of (E) C-4, (F) cyano and (G) phenyl cartridge showing sodium adducts; phenyl cartridge does not contain any sodium adducts. Similar chromatogram (D) and mass spectrum (H) data for 15-mer (m/z 1600.9) can be observed.*

The sample retention by the C-4 reverse-phase cartridge was compared with that of C-8 and C-18 cartridges (Figure 2.24). The signal intensity more than doubled as the carbon-chain length in the cartridge increased (from C-4 to C-8 to C-18), although the sample carry-over between injections also increased for the C-18 cartridge. It was decided to select the C-8 reverse-phase cartridge for further optimisation as the chromatogram and spectral data quality was superior to that of the other cartridges.

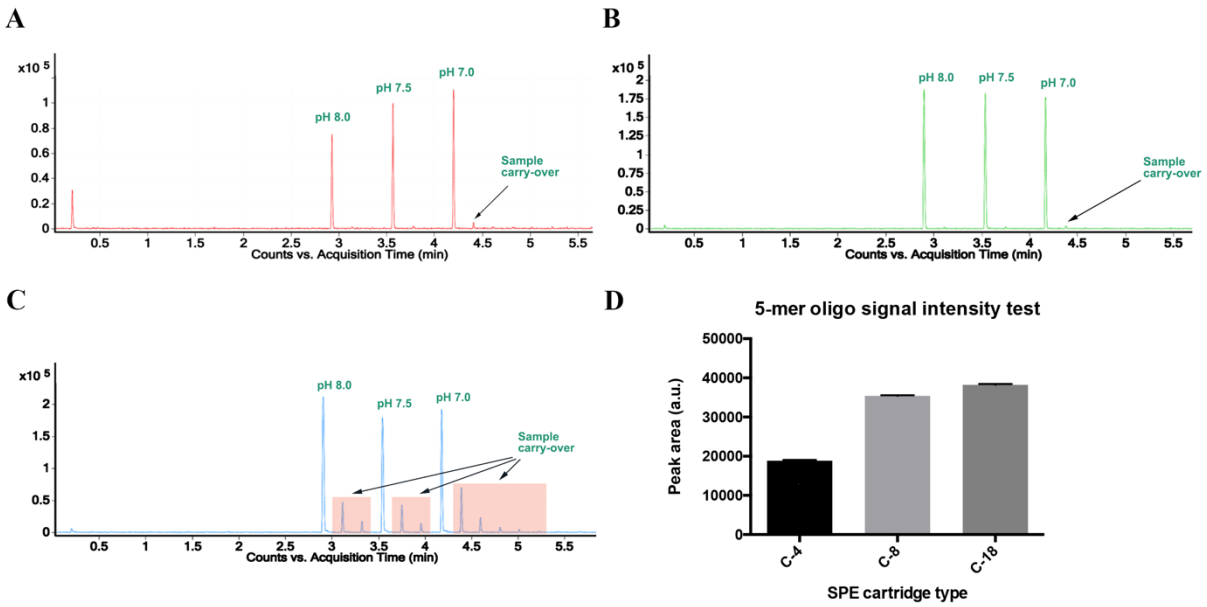


Figure 2.24: *Extracted chromatogram of 5-mer (m/z 790.1) using (A) C-4, (B) C-8 and (C) C-18 reverse-phase cartridge at varying pH range (7.0, 7.5, 8.0). The C-18 cartridge provided more than double the signal intensity compared with the C-4 cartridge. However, the significant sample carry-over rendered the C-18 cartridge unacceptable for further optimisation. The C-8 cartridge was considered the most suitable due to its signal intensity and lack of sample carry-over, especially at pH 7.5 and pH 8.0. Signal intensity data (D) were plotted as the mean of technical triplicates using GraphPad Prism® software.*

The RF methods were also optimised for chromatogram clarity. The initial method generated chromatograms that showed split peaks, which made data analysis difficult and inaccurate since signal intensity is calculated as peak area. Addition of an extra wash significantly improved the chromatogram quality; however, signal intensity decreased by more than half. The optimised RF methods are presented in Figure 2.25

A

State	Time (milliseconds)
Aspirate	*350*
Load/wash	*4000*
Extra wash	*0*
Elute	*6000*
Reequilibrate	*350*

State	Time (milliseconds)
Aspirate	*600*
Load/wash	*5500*
Extra wash	*0*
Elute	*5500*
Reequilibrate	*500*

B

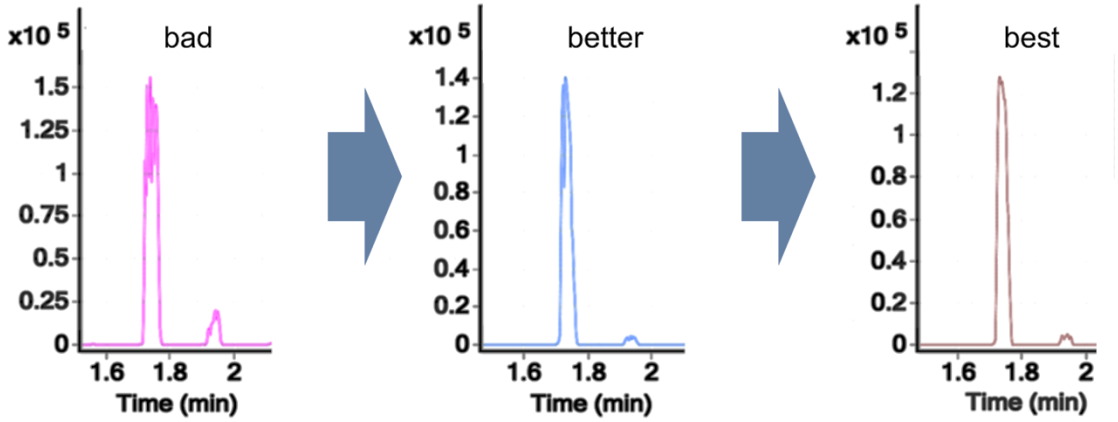


Figure 2.25: *(A) Summarised RF parameters for optimal peak intensity and (B) progress in spectral quality. Note the improvement from the initial split peak to the uniform peak.*

2.6.4.2. Optimisation of qTOF mass spectrometer

Having optimised the RF methods and selected the optimal SPE cartridge, attention turned to the optimisation of MS parameters to increase signal detection further, due to the inherent low sensitivity of MS for oligonucleotides compared with other material, i.e. peptides.

The Agilent 6550 qTOF MS is fitted with an Agilent Jet Stream Ion Source (AJS), which uses superheated nitrogen (sheathed around the analyte) to improve ion generation and de-solvation. This combined with a hexabore sampling capillary and innovative ion funnel technology results in a stronger signal and reduced noise. Among the many parameters, three are of crucial influence in sample sensitivity; gas temperature, sheath gas temperature and fragmentor voltage[58]. However, only variation of the fragmentor voltage made a noticeable difference/improvement (Figure 2.26). Unexpectedly, it was found that decreased nozzle voltage of the ion-spray source significantly improved signal intensity/sensitivity (Figure 2.26). The marked increase in sample sensitivity with decreased nozzle voltage could be attributed to the detection of more intact ions, and suggests that high voltage at the skimmer-nozzle may cause fragmentation of oligonucleotides[59-60]. The optimised MS parameters are summarised in Table 2.7.

Table 2.7: Optimised MS parameters of optimal oligonucleotide detection.

Parameter name	Parameter condition
Gas temperature	280 ºC
Drying gas	13 L/min
Nebuliser	40 psi
Sheath gas temperature	350 ºC
Sheath gas flow	12 L/min
Nozzle voltage	0 V
Fragmentor voltage	250 V

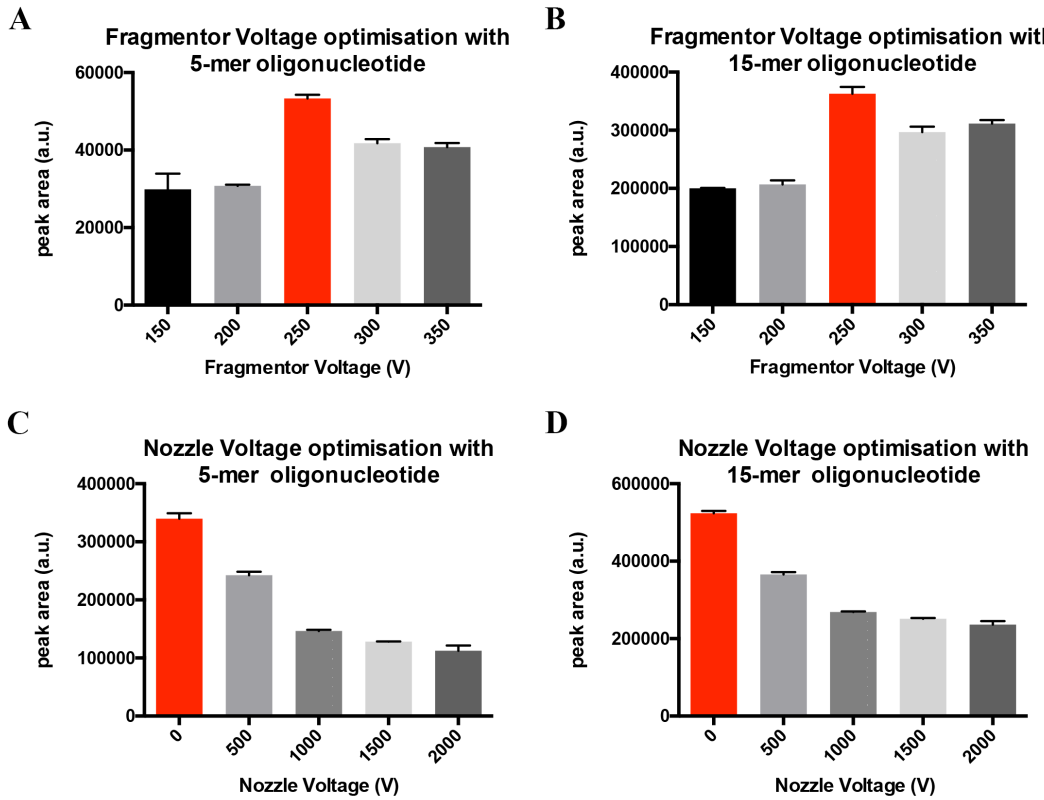


Figure 2.26: *MS-parameter optimisation for oligonucleotide detection. Fragmentor voltage optimisation of (A) 5-mer and (B) 15-mer; nozzle voltage optimisation of (C) 5-mer and (D) 15-mer. Data were plotted as the mean of technical triplicates using GraphPad Prism® software.*

2.6.4.3. Assay condition optimisation

Another advantage of the use of assays based on RF-MS is that enzymatic reactions can be monitored in real-time, and the absence of quenching reagents results in the observation of accurate apparent kinetics.

The final factor to be investigated was the *in vitro* assay conditions. FTO activities against 5-mer RNA oligo [GG(m^6A)CU] and 15-mer RNA oligo [AUUGUGG(m^6A)CUGCAGC] were tested and monitored in real-time using conditions adopted from the LC-MS assay (section 2.6.3). From the time course experiments it was apparent that the 15-mer oligo showed better substrate performance and it was selected for future assays (Figure 2.27). Surprisingly, no demethylation was observed under the assay conditions; instead the hemiaminal/hydroxylated intermediate was the only observed product for both 5-mer and 15-mer oligo substrates. This

led to the hypothesis that FTO might not catalyse nucleotide demethylation, but rather hydroxylation, at least for m^6A (discussed in Chapter 3).

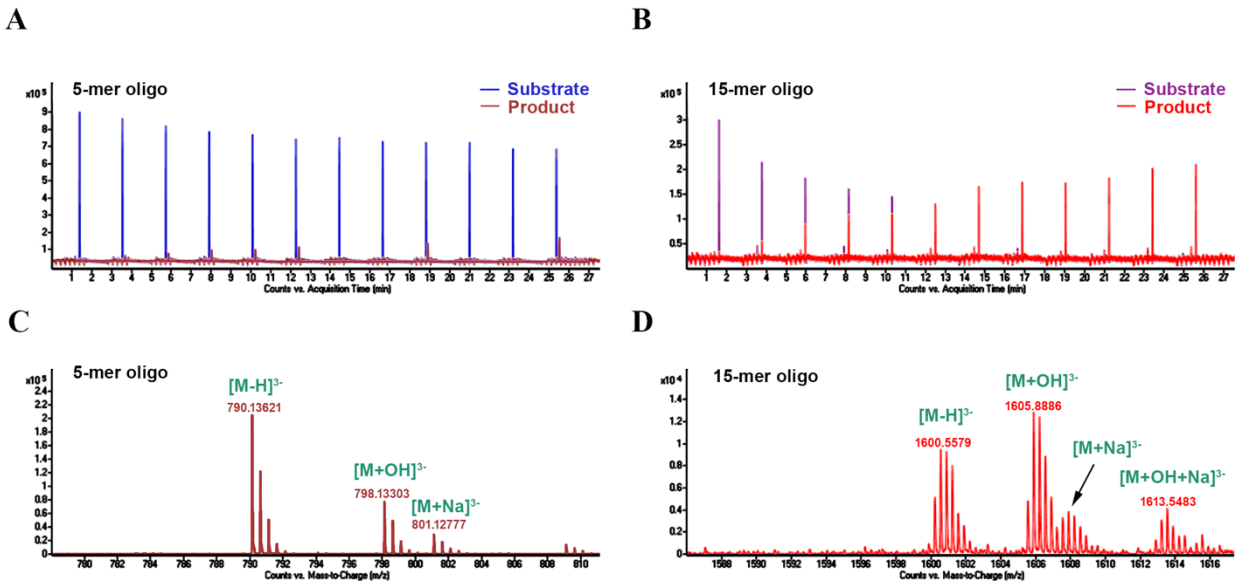


Figure 2.27: *FTO-catalysed reaction with (A) 5-mer and (B) 15-mer RNA oligomer. Mass spectra of both (C) 5-mer oligo and (D) 15-mer oligo show only hydroxylation, not demethylation.*

During subsequent time-course analyses, substrate degradation was observed. It was postulated that due to the inherent sensitivity of RNA oligonucleotides to nucleases, the substrate was being degraded/digested by contaminating nucleases. It was decided to add 1 unit of RNasin® (Promega) to each reaction well. RNasin® is a broad-spectrum ribonuclease inhibitor that protects RNA oligonucleotides from degradation by RNases A, B and C[61]. The addition of RNAsin reduced degradation. However, it required a substantial amount of manual handling/pipetting that may introduce error, and hence hampering assay accuracy and reliability. It was then decided to treat water with a small-molecule ribonuclease (RNase) inhibitor, diethyl pyrocarbonate (DEPC), prior to preparation of the buffer. DEPC covalently modifies histidine (most strongly), tyrosine, cysteine and lysine residues of the RNase enzymes, and inactivates them[62-63]. By preparing the buffer with 0.1% (v/v) DEPC, the inactivation of RNases was apparent, and this expedited sample preparation.

The pH dependence of FTO-catalysed hydroxylation was then tested using the 15-mer RNA oligo substrate and the partially optimised conditions described above (Figure 2.28). Although the greatest amount of conversion was observed at pH 8.0, the buffer pH was kept at 7.5, close to physiological condition. The extent of demethylation increased with pH, consistent with the formation of a hemiaminal, as the hemiaminal carbon-nitrogen bond is prone to fragmentation under basic conditions.

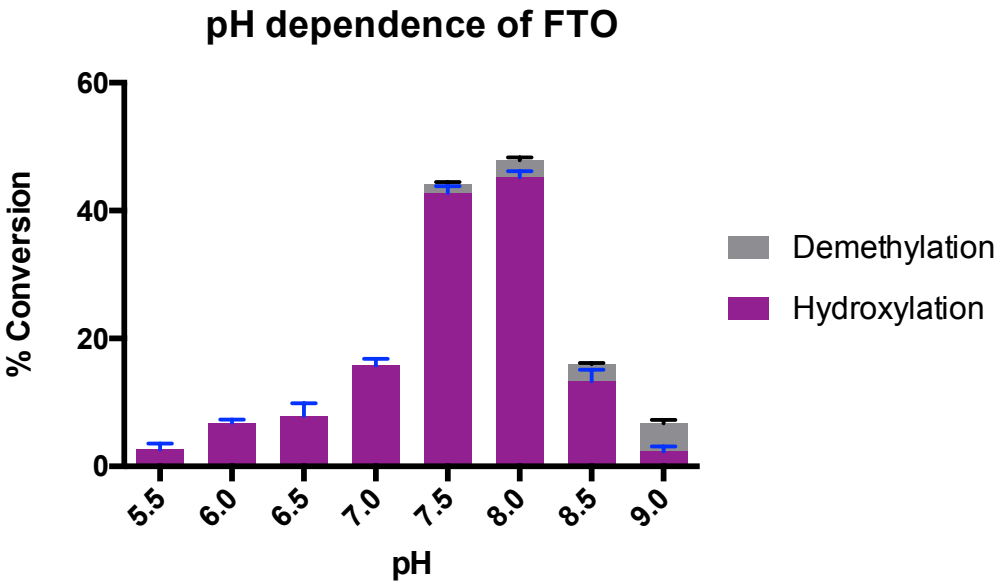


Figure 2.28: *FTO catalysis of 15-mer RNA oligo in MES (pH 5.5 – pH 6.5) or Tris (pH 7.0 – pH 9.0) buffer. Reactions were carried out in real-time for 30 minutes at room temperature (25 ºC). The extent of hydroxylation or demethylation (percentage) was analysed by RF-MS. Data were plotted as the mean of technical triplicates using GraphPad Prism® software. Note: demethylation can be observed at 30 minutes at pHs higher than 7.0, and the extent of demethylation increases with pH.*

Due to the high sensitivity of the RF-MS assay, ion suppression was observed when the enzyme was added to the reaction mixture. Therefore it was decided to reduce the enzyme concentration as much as possible. A time course at two different FTO concentrations (0.1 µM, 0.2 µM) was attempted to ensure that the minimum amount of enzyme was used to generate observable product. Activity was observed also at 0.1 µM of FTO after 20 min (Figure 2.29). Thus, 0.1 µM enzyme concentration was used for subsequent optimisation steps with other co-factors/substrates.

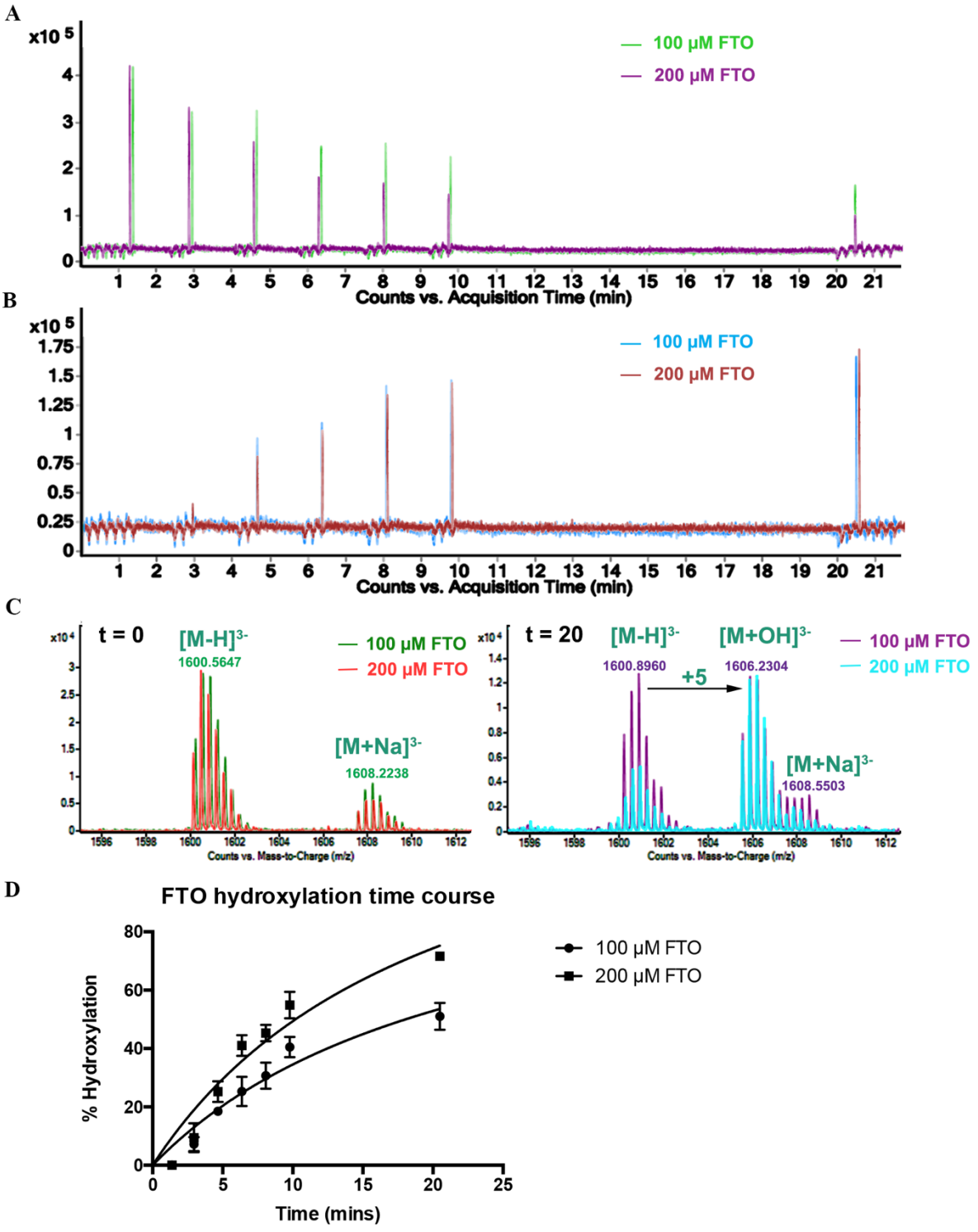


Figure 2.29: *FTO-catalysed hydroxylation of 15-mer RNA oligo (1 µM) was monitored in real-time for 20 minutes at 100 µM and 200 µM enzyme concentration; 2OG (disodium salt, 20 µM), $(NH_4)_2Fe(SO_4)_2$ (20 µM) and ascorbic acid (200 µM) were in excess to ensure maximum enzymatic activity. (A) Extracted chromatogram of m/z 1600.9, which represented $[M\text{-}H]^{3-}$, and (B) extracted chromatogram of m/z 1606.2, which represented $[M+OH]^{3-}$. (C) Δm/z of +5.3 (-3 charge state) was observed, which indicated hydroxylation (+16 Da) of RNA oligo substrate as a stable product. (D) Product formation as percentage is plotted as the mean of technical triplicates using GraphPad Prism® software.*

FTO assays (MALDI, LC-MS) investigated until this point did not include sodium chloride (NaCl) in the assay buffer. However, added sodium chloride was shown to significantly affect other 2OG oxygenases (i.e. improving KDM demethylation activities)[64]; it might thus have a similar effect on FTO-catalysed reactions. Time courses were carried out using 0.1 µM FTO and 1 µM 15-mer RNA substrate with varying NaCl concentrations (0 mM, 50 mM, 100 mM, 200 mM). The level of hydroxylation was monitored at 30 min (Figure 2.30). Contrary to the observed increase in KDM activities[64], addition of NaCl decreased FTO activity. The data in Figure 2.30 suggest that NaCl inhibits FTO activity, and that concentrations of over 100 mM completely ablate FTO activity. Furthermore, buffers that contain NaCl have a significant impact on the MS spectrum quality, as the additional Na^+ ion-adduct peaks reduce the parent-peak intensities and complicate data analysis.

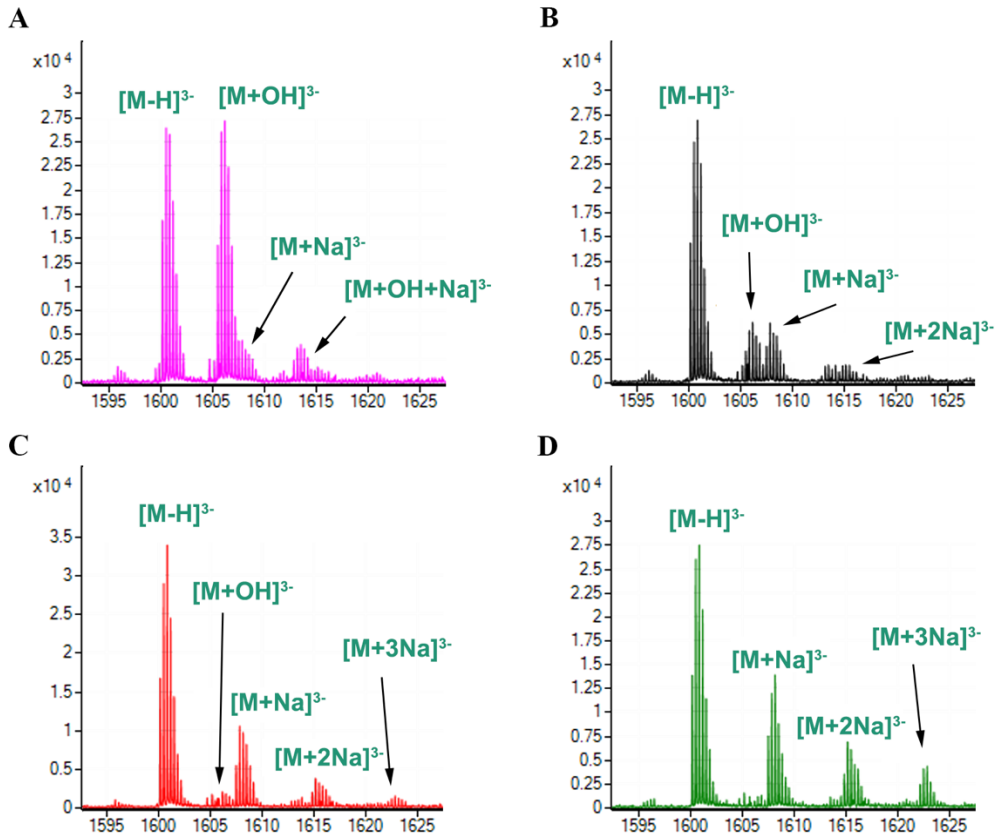


Figure 2.30: *Mass spectra of FTO (0.1 µM) incubated with 15-mer oligo (1 µM); 2OG (disodium salt, 20 µM), $(NH_4)_2Fe(SO_4)_2$ (20 µM) and ascorbic acid (200 µM) were in excess to ensure maximum enzymatic activity. NaCl was added to test the extent of its influence on enzyme activity, (A) 0 mM NaCl, (B) 50 mM NaCl, (C) 100 mM NaCl, (D) 200 mM NaCl. Note: the quality of MS spectra deteriorates as NaCl concentration increases.*

Having optimised the instrumental parameters and assay conditions, determination of kinetic parameters was carried out for FTO by independently varying 2OG, Fe(II), ascorbic acid or 15-mer ssRNA concentrations. Using the RF-MS-based assay for real-time kinetics was possible. Instead of quenching the reaction at specific time points, it was possible to measure time courses without interrupting the reaction, hence increasing data reliability. The Michaelis–Menten constant K_m, the concentration of the substrate [s] when the reaction velocity V_0 equals half of the maximal velocity (V_{max}) for the reaction, was determined by plotting the initial rate of reaction against the concentration for each varying component (Figure 2.31). The determined K_m values and optimised assay conditions are summarised in Table 2.8.

Table 2.8: Optimised conditions of FTO for RF-MS assay based on the K_m of reagents. Note the significant reduction in the amount of reagents required compared with the MALDI assay.

Reagent	MALDI (µM)	K_m (µM)	RapidFire (µM)
L-ascorbic acid	500	120.3 ± 13	200
2OG	10	0.81 ± 0.11	1
$(NH_4)_2Fe(SO_4)_2 \cdot 6H_2O$	10	0.28 ± 0.03	0.5
Substrate	ssRNA-GG(m^6A)CU/20	0.33 ± 0.10	15-mer ssRNA/0.6
FTO	1.3		0.1
Buffer	Tris 25mM pH 7.5		Tris 25mM pH 7.5
Incubation time/T	30min/r.t		10min/r.t
Final Volume	25 µL		25 µL

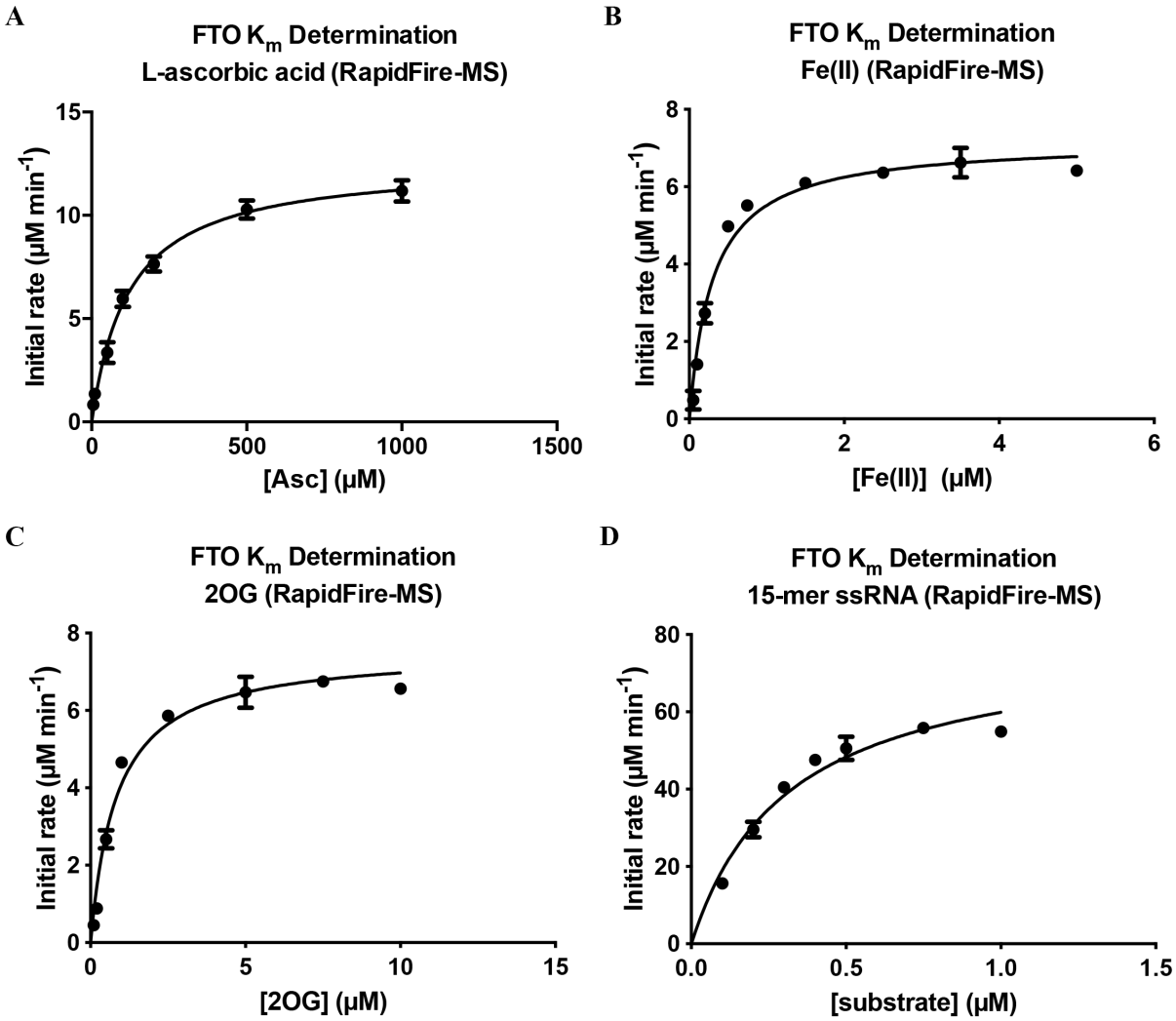


Figure 2.31: *FTO kinetic parameter determination for varying (co-)substrates and cofactors. Michaelis-Menten curve of initial rate (μM/min) versus (A) concentration of ascorbic acid (Asc, μM); (B) concentration of Fe(II) (μM); (C) concentration of 2-oxoglutarate (2OG, μM)); and (D) concentration of 15-mer RNA (5'-AUUGUGGm^{6}ACUGCAGC-3') substrate (μM). Data were plotted as the mean of technical triplicates using GraphPad Prism® software.*

Use of the RF-MS assay ensured lower enzyme concentration was possible to determine kinetic parameters, while maintaining minimal impact on reaction outcome. By contrast with previously reported kinetic parameters (on 15-mer RNA substrate and 2OG, using LC-MS digestion or fluorescence-based assays)[65-66], RF-MS assay produced lower K_m values on 15-mer RNA substrate and 2OG, possibly due to lowered enzyme concentration and sensitivity of the RF-MS instrument. The K_m values are summarised in Table 2.9.

Table 2.9: Kinetic parameters determined by RF-MS assay in comparison with reported kinetic parameters (on 15-mer RNA substrate and 2OG) by fluorescence or LC-MS digestion-based assays.

	K_m (μM)		
Reagent	**RF-MS**	**Fluorescence based[66]**	**LC-MS digestion[65]**
2OG	0.81 ± 0.11	2.88	
15-mer RNA	0.33 ± 0.10		0.60 ± 0.12

2.6.5. Inhibition of FTO with new RF-MS assay

Although the assay based on RF-MS has real-time monitoring capacity, the end point (quenched) reaction is still preferred for inhibition screening, because by this method multiple plate-screening assays can be carried out, stored and eventually analysed separately.

The previously optimised quenching reagent for the MALDI (Section 2.6.1) and LC-MS assays (Section 2.6.3) was 1 mM EDTA diluted in Tris buffer, and therefore this was also used for the RF-MS assay. However, addition of EDTA (10 mM) abolished the 15-mer oligo (1 μM) signal in the RF-MS assays. This could have been a result of ion suppression due to the influx of EDTA ions, since the substrate:EDTA ratio was 1:10,000, although the wash cycle during the RF protocol should have been sufficient to remove any EDTA ions. EDTA is a negatively charged metal-chelating agent, which may compete with the negatively charged phosphate backbone on the oligo substrate to bind to the SPE cartridge and prevent substrate retention.

In order to find a suitable quenching reagent, two 'classic' quenching reagents were tested: MeOH and 1% (v/v) aqueous formic acid. Inspired by the NaCl result discussed in Section 2.6.4.3 (Figure 2.30), 10 mM magnesium chloride ($MgCl_2$) was also tested as a FTO quenching reagent. 2,4-Pyridinedicarboxylic acid (2,4-PDCA) is a broad-spectrum 2OG oxygenase inhibitor[67], which may also be used as quenching reagent. Addition of formic acid severely hampered the oligonucleotide signal, as had happened with EDTA. The presence of formic acid introduces an influx of H^+ ions, which may preferentially bind to phosphate groups on the

RNA oligonucleotide to neutralise the negative charge and hence prevent the RNA substrate binding to the SPE cartridge and reduce signal intensity. Both 2,4-PDCA (100 μM) and $MgCl_2$ (10mM) were suitable quenching reagents since they did not affect spectral quality or intensity, while they almost completely inhibited FTO activity. In comparison, addition of MeOH moderately reduced peak intensity. The results are presented in Figure 2.32.

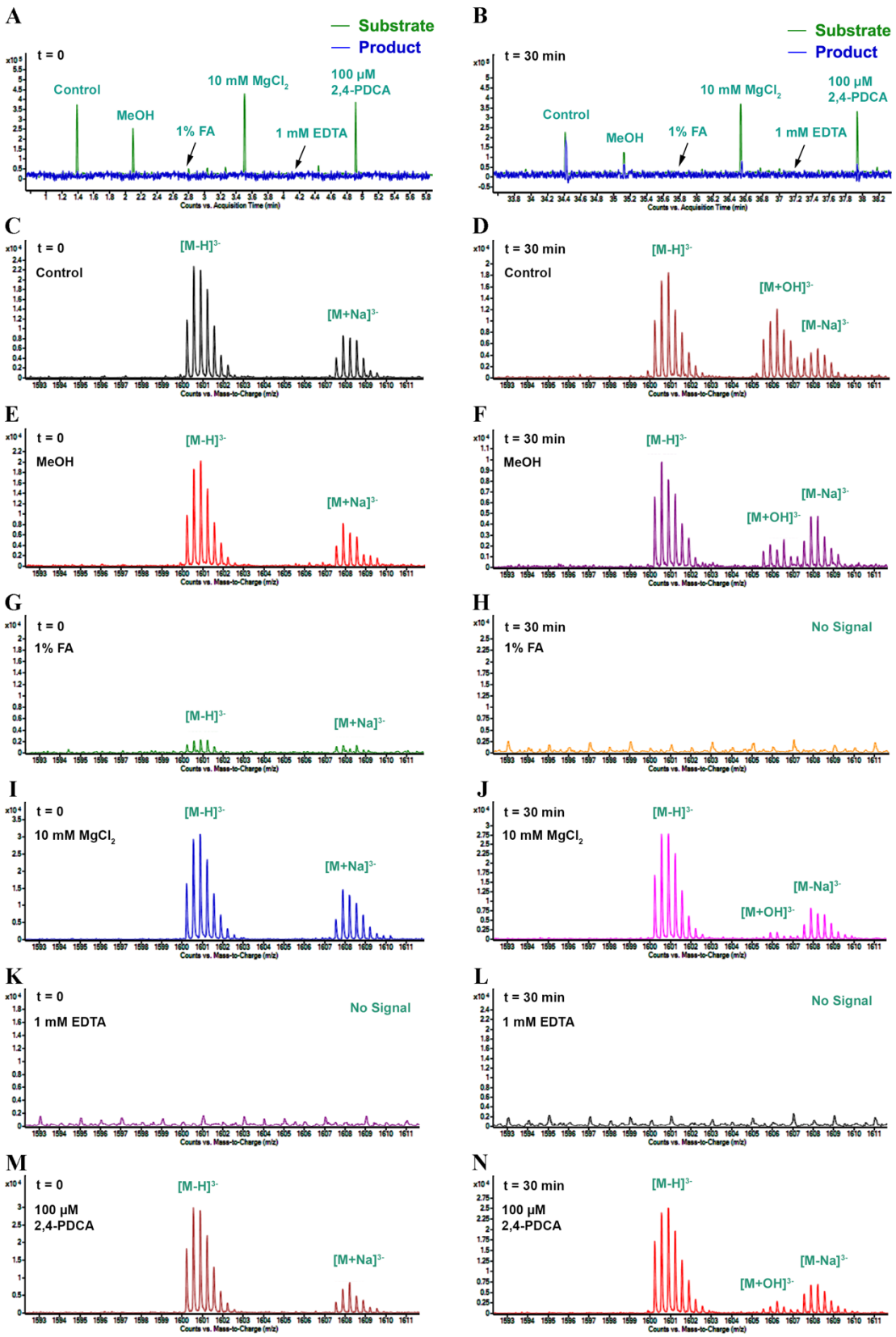
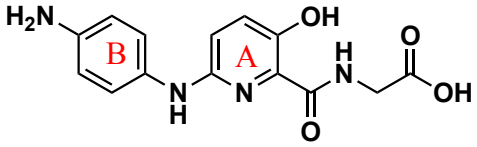
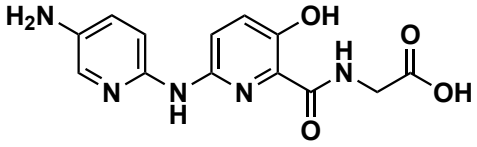
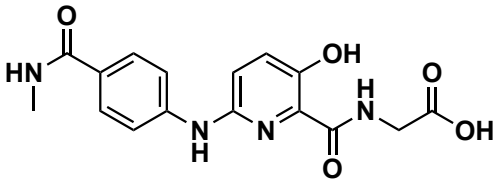
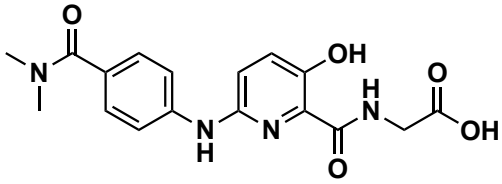
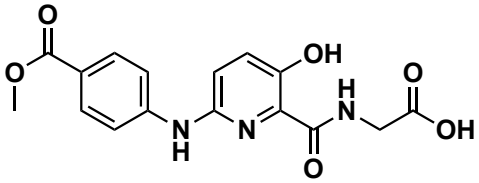
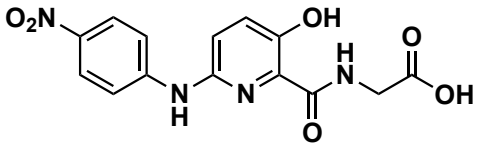
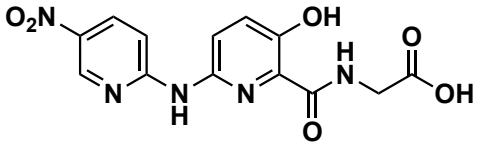


Figure 2.32: *Extracted chromatograms (A, B) and mass spectra (D-N) of 15-mer RNA oligo substrate (1 µM) incubated with FTO (0.1 µM), 2OG (disodium salt, 20 µM), $(NH_4)_2Fe(SO_4)_2$ (20 µM) and ascorbic acid (200 µM). Quenching reagents were added at the beginning of the reactions to compare them as a control for effectiveness (A, C, E, G, I, K, M). Note: a time course was carried out, only the t=0 and t=30 spectra are presented here.*

Compounds **29-35** were tested using the optimised RF-MS assay; the results are presented in Table 2.10 and Figure 2.33.

Table 2.10: IC_{50} values for the inhibition of FTO by second-generation inhibitors using RF-MS assay. Errors were calculated as standard deviation of the mean of technical duplicates.

Compound	Structural Formula	FTO IC_{50} (μM)
29		5.10 ± 0.63
30		0.17 ± 0.02
31		0.43 ± 0.09
32		1.36 ± 0.69
33		0.86 ± 0.08
34		0.08 ± 0.005
35		0.33 ± 0.05

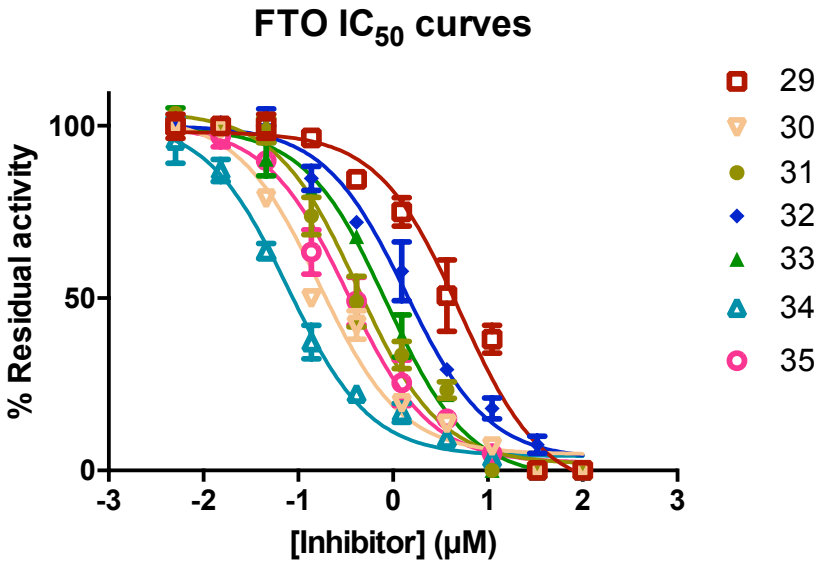


Figure 2.33: *IC_{50} curves for the inhibition of FTO. Inhibition assays were carried out at 25 °C and pH 7.5.*

The potent FTO inhibitor **34** (IC_{50} 0.08 ± 0.005 μM) was tested against ABH5 and found to have an IC_{50} of 65.7 ± 8.9 μM using the optimised RF-MS assay conditions (for FTO). These results reveal the potential for selectivity in this series, even against a closely related enzyme (at least based on the tested assay conditions) (Figure 2.34). Thus, the IC_{50} values suggest that the second-generation FTO inhibitors are potent and selective; further understanding of their binding modes could be achieved by structural analyses.

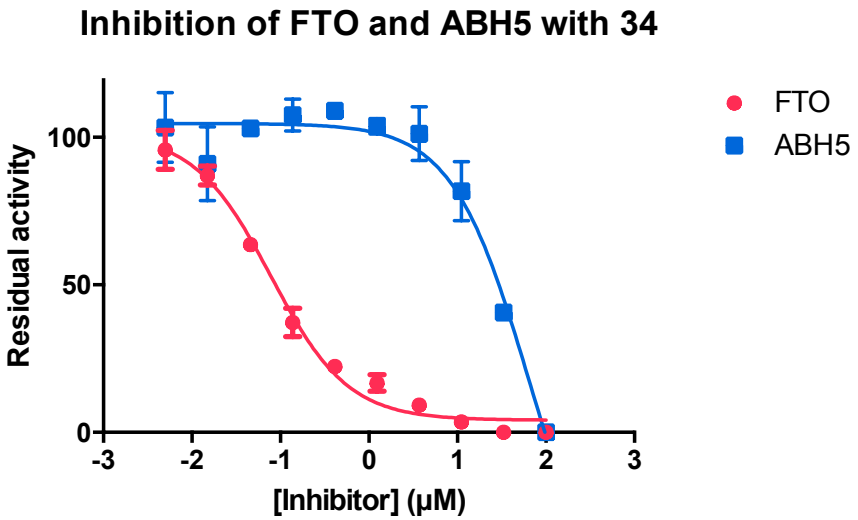


Figure 2.34: *IC_{50} curves for the inhibition of FTO (0.1 μM) and ABH5 (0.1 μM) with **34** in the presence of 15-mer oligo substrate (1 μM). Inhibition assays were carried out at 25 °C and pH 7.5.*

2.7. Discussion and future work

Following the development of second-generation FTO inhibitors (**29-35**) based on structure activity relationship (SAR) studies conducted previously at the University of Oxford, IC_{50} values were determined (Tables 2.4 and 2.9). One of the objectives was to demonstrate the selectivity of these compounds toward FTO over other 2OG oxygenases. Different MS-based assay platforms were sequentially developed and optimised to monitor FTO-catalysed reactions, including assays based on MALDI-MS, LC-MS and RF-MS. It is important to note that potency of a compound should not be judged solely on IC_{50} value, since the enzyme concentration and assay conditions has significant effects on the IC_{50}, as is evident from the work described in this chapter. The compounds **29-35** were designed using existing structures (PDB ID: 4QHO), and were selective towards FTO (under the same assay conditions) compared with other 2OG oxygenases, such as KDMs and PHD2. The most potent compound **34** (IC_{50} 0.08 ± 0.005 μM) was apparently almost three orders of magnitude more selective for FTO than another m^6A-modifying enzyme from the same sub-family, ABH5 (65.7 ± 8.9 μM).

An initial screening assay that employed MALDI-MS was optimised using a 5-mer RNA oligonucleotide substrate [GGm^6ACU]. Buffer conditions, quenching reagents, protein preparation sequence and constitution of co-substrates were investigated. Kinetic parameters based on a 1.3 μM final enzyme (FTO) concentration were established. IC_{50} determinations for **29-35** were carried out using the MALDI-MS assay; most compounds, except **29** and **32,** had IC_{50} values in the micromolar range. Note that compound **29** showed poor solubility in DMSO, which might have altered its observed potency. Increasing the steric bulk at the 4-position on ring B apparently results in a reduction of potency when compared with the secondary amide (**30**, IC_{50} 5.8 ± 0.4 μM) and tertiary amide (**31**, IC_{50} 37.6 ± 3.1 μM) (Figure 2.16), possibly due to a steric clash with polar residues in the substrate-binding pocket. Modification of the polarity

of the ring (B), however, did not significantly influence potency (i.e. **34**, IC_{50} 3.2 ± 0.4 μM; **35**, IC_{50} 8.0 ± 0.7 μM). Although the MALDI-MS assay was sufficient as a medium-throughput screening method, this assay platform was deemed too inaccurate because of instrument specific artefacts[46] (Figure 2.17).

The developed assay based on LC-MS was not suitable for high-throughput screening (HTS), because of the extremely labour-intensive nature of this platform. Moreover, the lengthy protocol of this assay makes it prone to accuracy issues and loss of material, although the sensitivity and inherent accuracy of this assay cannot be denied.

Finally, RF-MS-based FTO assay was optimised and chosen for future screening, owing to the high-throughput capability of the Rapidfire® system and high accuracy of the qTOF MS. A 15-mer RNA oligonucleotide substrate [AUUGUGG(m^6A)CUGCAGC] was used instead of the 5-mer [GG(m^6A)CU], which resulted in shorter reaction times and improved monitoring of the FTO-catalysed reaction. Interestingly, the previously reported hemiaminal/hydroxylated intermediate[10] was observed as a stable product under the RF-MS assay conditions (discussed in detail in Chapter 3). Since the optimised RF-MS assay reaction conditions required only low concentrations of enzyme and substrate, the IC_{50} values determined were orders of magnitude lower than those for MALDI-MS or LC-MS-based assays (Figure 2.35).

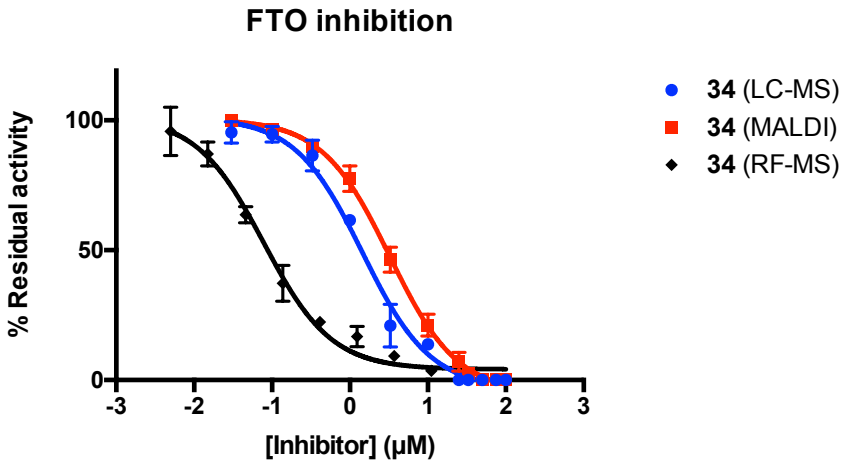


Figure 2.35: *Inhibition curve (IC_{50}) for **34** against FTO using MALDI assay (red), LC-MS assay (blue) and RF-MS assay (black).*

Having established a robust and accurate high-throughput assay platform, which resulted in the identification of a potent and selective compound (**34**), next-generation selective FTO inhibitors are likely to be identified. To improve selectivity over other 2OG oxygenases, elimination of the glycinamide moiety would be useful. The glycinamide moiety mimics 2OG and binds in the 2OG binding pocket; the 2OG co-substrate is required by all 2OG-dependent oxygenases, hence avoidance of the targeting of this pocket may lead to selective inhibitors. Potent and selective PHD2 inhibitors without the 2OG pocket 'anchoring' glycinamide moiety have been reported[68], which demonstrates that 2OG pocket binding is not essential for potent inhibition. It should be noted that the apparent FTO assay dependence on IC_{50} values for the same compound, **34**, raises questions regarding the potency of FTO inhibitors reported elsewhere[18-22].

Structural studies on FTOΔ31 in complex with **34** were attempted. Crystals were obtained through hanging drop co-crystallisation trials, and X-ray diffraction data were collected. However, the best quality data-sets obtained had a resolution of 3.3 Å, and at this poor resolution the ring B of **34** could not be observed in the electron-density map. These initial studies were a promising starting point from which to optimise crystallisation conditions.

Acknowledgements

Compounds **29-35** were synthesised by Dr Shifali Shishodia, who also contributed to compound design under the supervision of Dr Marina Demetriades. Dr Anthony Tumber conducted the IC_{50} determinations for PHD2, KDM5B/JARID1B, KDM5D/JARID1D, KDM3A/JMJD1A, KDM6B/JMJD3, KDM2A/FBXL11 and KDM4C/JMJD2C, who also contributed to the development of the Rapidfire-MS assay. Dr Michael McDonough guided crystallisation design, collected and processed diffraction data and solved the crystal structure of the FTO complex with **34**.

References

1. Frayling, T. M.; Timpson, N. J.; Weedon, M. N.; Zeggini, E.; Freathy, R. M.; Lindgren, C. M.; Perry, J. R.; Elliott, K. S.; Lango, H.; Rayner, N. W.; Shields, B.; Harries, L. W.; Barrett, J. C.; Ellard, S.; Groves, C. J.; Knight, B.; Patch, A. M.; Ness, A. R.; Ebrahim, S.; Lawlor, D. A.; Ring, S. M.; Ben-Shlomo, Y.; Jarvelin, M. R.; Sovio, U.; Bennett, A. J.; Melzer, D.; Ferrucci, L.; Loos, R. J.; Barroso, I.; Wareham, N. J.; Karpe, F.; Owen, K. R.; Cardon, L. R.; Walker, M.; Hitman, G. A.; Palmer, C. N.; Doney, A. S.; Morris, A. D.; Smith, G. D.; Hattersley, A. T.; McCarthy, M. I., A common variant in the FTO gene is associated with body mass index and predisposes to childhood and adult obesity. *Science* **2007,** *316* (5826), 889-94.

2. Scott, L. J.; Mohlke, K. L.; Bonnycastle, L. L.; Willer, C. J.; Li, Y.; Duren, W. L.; Erdos, M. R.; Stringham, H. M.; Chines, P. S.; Jackson, A. U.; Prokunina-Olsson, L.; Ding, C. J.; Swift, A. J.; Narisu, N.; Hu, T.; Pruim, R.; Xiao, R.; Li, X. Y.; Conneely, K. N.; Riebow, N. L.; Sprau, A. G.; Tong, M.; White, P. P.; Hetrick, K. N.; Barnhart, M. W.; Bark, C. W.; Goldstein, J. L.; Watkins, L.; Xiang, F.; Saramies, J.; Buchanan, T. A.; Watanabe, R. M.; Valle, T. T.; Kinnunen, L.; Abecasis, G. R.; Pugh, E. W.; Doheny, K. F.; Bergman, R. N.; Tuomilehto, J.; Collins, F. S.; Boehnke, M., A genome-wide association study of type 2 diabetes in Finns detects multiple susceptibility variants. *Science* **2007,** *316* (5829), 1341-5.

3. Fawcett, K. A.; Barroso, I., The genetics of obesity: FTO leads the way. *Trends Genet.* **2010,** *26* (6), 266-74.

4. Church, C.; Moir, L.; McMurray, F.; Girard, C.; Banks, G. T.; Teboul, L.; Wells, S.; Bruning, J. C.; Nolan, P. M.; Ashcroft, F. M.; Cox, R. D., Overexpression of Fto leads to increased food intake and results in obesity. *Nat. Genet.* **2010,** *42* (12), 1086-92.

5. Fischer, J.; Koch, L.; Emmerling, C.; Vierkotten, J.; Peters, T.; Bruning, J. C.; Ruther, U., Inactivation of the Fto gene protects from obesity. *Nature* **2009,** *458* (7240), 894-8.

6. Gerken, T.; Girard, C. A.; Tung, Y. C.; Webby, C. J.; Saudek, V.; Hewitson, K. S.; Yeo, G. S.; McDonough, M. A.; Cunliffe, S.; McNeill, L. A.; Galvanovskis, J.; Rorsman, P.; Robins, P.; Prieur, X.; Coll, A. P.; Ma, M.; Jovanovic, Z.; Farooqi, I. S.; Sedgwick, B.; Barroso, I.; Lindahl, T.; Ponting, C. P.; Ashcroft, F. M.; O'Rahilly, S.; Schofield, C. J., The obesity-associated FTO gene encodes a 2-oxoglutarate-dependent nucleic acid demethylase. *Science* **2007,** *318* (5855), 1469-72.

7. Falnes, P. O.; Johansen, R. F.; Seeberg, E., AlkB-mediated oxidative demethylation reverses DNA damage in Escherichia coli. *Nature* **2002,** *419* (6903), 178-82.

8. Koivisto, P.; Robins, P.; Lindahl, T.; Sedgwick, B., Demethylation of 3-methylthymine in DNA by bacterial and human DNA dioxygenases. *J. Biol. Chem.* **2004,** *279* (39), 40470-4.

9. Jia, G.; Yang, C. G.; Yang, S.; Jian, X.; Yi, C.; Zhou, Z.; He, C., Oxidative demethylation of 3-methylthymine and 3-methyluracil in single-stranded DNA and RNA by mouse and human FTO. *FEBS Lett.* **2008,** *582* (23-24), 3313-9.

10. Jia, G.; Fu, Y.; Zhao, X.; Dai, Q.; Zheng, G.; Yang, Y.; Yi, C.; Lindahl, T.; Pan, T.; Yang, Y.-G.; He, C., N6-Methyladenosine in nuclear RNA is a major substrate of the obesity-associated FTO. *Nat. Chem. Biol.* **2011,** *7*, 885-7.

11. Zheng, G.; Dahl, John A.; Niu, Y.; Fedorcsak, P.; Huang, C.-M.; Li, Charles J.; Vågbø, Cathrine B.; Shi, Y.; Wang, W.-L.; Song, S.-H.; Lu, Z.; Bosmans, Ralph P. G.; Dai, Q.; Hao, Y.-J.; Yang, X.; Zhao, W.-M.; Tong, W.-M.; Wang, X.-J.; Bogdan, F.; Furu, K.; Fu, Y.; Jia, G.; Zhao, X.; Liu, J.; Krokan, Hans E.; Klungland, A.; Yang, Y.-G.; He, C., ALKBH5 is a mammalian RNA demethylase that impacts RNA metabolism and mouse fertility. *Mol. Cell* **2013,** *49* (1), 18-29.

12. Karra, E.; O'Daly, O. G.; Choudhury, A. I.; Yousseif, A.; Millership, S.; Neary, M. T.; Scott, W. R.; Chandarana, K.; Manning, S.; Hess, M. E.; Iwakura, H.; Akamizu, T.; Millet, Q.; Gelegen, C.; Drew, M. E.; Rahman, S.; Emmanuel, J. J.; Williams, S. C. R.; Rüther, U. U.; Brüning, J. C.; Withers, D. J.; Zelaya, F. O.; Batterham, R. L., A link between FTO, ghrelin, and impaired brain food-cue responsivity. *J Clin Invest* **2013,** *123* (8), 3539-51.

13. Wehr, E.; Schweighofer, N.; Moller, R.; Giuliani, A.; Pieber, T. R.; Obermayer-Pietsch, B., Association of FTO gene with hyperandrogenemia and metabolic parameters in women with polycystic ovary syndrome. *Metabolism* **2010,** *59* (4), 575-80.

14. Kaklamani, V.; Yi, N.; Sadim, M.; Siziopikou, K.; Zhang, K.; Xu, Y.; Tofilon, S.; Agarwal, S.; Pasche, B.; Mantzoros, C., The role of the fat mass and obesity associated gene (FTO) in breast cancer risk. *BMC Med Genet* **2011,** *12*, 52-8.

15. Keller, L.; Xu, W.; Wang, H. X.; Winblad, B.; Fratiglioni, L.; Graff, C., The obesity related gene, FTO, interacts with APOE, and is associated with Alzheimer's disease risk: a prospective cohort study. *J Alzheimers Dis* **2011,** *23* (3), 461-9.

16. Chen, B.; Ye, F.; Yu, L.; Jia, G.; Huang, X.; Zhang, X.; Peng, S.; Chen, K.; Wang, M.; Gong, S.; Zhang, R.; Yin, J.; Li, H.; Yang, Y.; Liu, H.; Zhang, J.; Zhang, H.; Zhang, A.; Jiang, H.; Luo, C.; Yang, C. G., Development of cell-active N6-methyladenosine RNA demethylase FTO inhibitor. *J Am Chem Soc* **2012,** *134* (43), 17963-71.

17. Aik, W.; Demetriades, M.; Hamdan, M. K.; Bagg, E. A.; Yeoh, K. K.; Lejeune, C.; Zhang, Z.; McDonough, M. A.; Schofield, C. J., Structural basis for inhibition of the fat mass and obesity associated protein (FTO). *J med chem* **2013,** *56* (9), 3680-8.

18. Huang, Y.; Yan, J.; Li, Q.; Li, J.; Gong, S.; Zhou, H.; Gan, J.; Jiang, H.; Jia, G. F.; Luo, C.; Yang, C. G., Meclofenamic acid selectively inhibits FTO demethylation of m6A over ALKBH5. *Nucleic Acids Res.* **2015,** *43* (1), 373-84.

19. He, W.; Zhou, B.; Liu, W.; Zhang, M.; Shen, Z.; Han, Z.; Jiang, Q.; Yang, Q.; Song, C.; Wang, R.; Niu, T.; Han, S.; Zhang, L.; Wu, J.; Guo, F.; Zhao, R.; Yu, W.; Chai, J.; Chang, J., Identification of a novel small-molecule binding site of the fat mass and obesity associated protein (FTO). *J med chem* **2015,** *58* (18), 7341-8.

20. Qiao, Y.; Zhou, B.; Zhang, M.; Liu, W.; Han, Z.; Song, C.; Yu, W.; Yang, Q.; Wang, R.; Wang, S.; Shi, S.; Zhao, R.; Chai, J.; Chang, J., A Novel Inhibitor of the Obesity-Related Protein FTO. *Biochemistry* **2016,** *55* (10), 1516-22.

21. Zheng, G.; Cox, T.; Tribbey, L.; Wang, G. Z.; Iacoban, P.; Booher, M. E.; Gabriel, G. J.; Zhou, L.; Bae, N.; Rowles, J.; He, C.; Olsen, M. J., Synthesis of a FTO inhibitor with anticonvulsant activity. *ACS Chem Neurosci* **2014,** *5* (8), 658-65.

22. Toh, J. D. W.; Sun, L.; Lau, L. Z. M.; Tan, J.; Low, J. J. A.; Tang, C. W. Q.; Cheong, E. J. Y.; Tan, M. J. H.; Chen, Y.; Hong, W.; Gao, Y. G.; Woon, E. C. Y., A strategy based on nucleotide specificity leads to a subfamily-selective and cell-active inhibitor of N(6)-methyladenosine demethylase FTO. *Chem Sci* **2015,** *6* (1), 112-22.

23. McMurray, F.; Demetriades, M.; Aik, W.; Merkestein, M.; Kramer, H.; Andrew, D. S.; Scudamore, C. L.; Hough, T. A.; Wells, S.; Ashcroft, F. M.; McDonough, M. A.; Schofield, C. J.; Cox, R. D., Pharmacological inhibition of FTO. *PLoS One* **2015,** *10* (4), e0121829.

24. Martinez, S.; Hausinger, R. P., Catalytic mechanisms of Fe(II)- and 2-oxoglutarate-dependent oxygenases. *J Biol Chem* **2015,** *290* (34), 20702-11.

25. Rhoads, R. E.; Udenfriend, S., Decarboxylation of alpha-ketoglutarate coupled to collagen proline hydroxylase. *Proc Natl Acad Sci USA* **1968,** *60* (4), 1473-8.

26. Kaule, G.; Gunzler, V., Assay for 2-oxoglutarate decarboxylating enzymes based on the determination of [1-14C]succinate: application to prolyl 4-hydroxylase. *Anal. Biochem.* **1990,** *184* (2), 291-7.

27. Cunliffe, C. J.; Franklin, T. J.; Gaskell, R. M., Assay of prolyl 4-hydroxylase by the chromatographic determination of [14C]succinic acid on ion-exchange minicolumns. *Biochem J* **1986,** *240* (2), 617-9.

28. McNeill, L. A.; Bethge, L.; Hewitson, K. S.; Schofield, C. J., A fluorescence-based assay for 2-oxoglutarate-dependent oxygenases. *Anal Biochem* **2005,** *336* (1), 125-31.

29. Roy, T. W.; Bhagwat, A. S., Kinetic studies of Escherichia coli AlkB using a new fluorescence-based assay for DNA demethylation. *Nucleic Acids Res* **2007,** *35* (21), e147-e147.

30. Rose, N. R.; Ng, S. S.; Mecinovic, J.; Lienard, B. M.; Bello, S. H.; Sun, Z.; McDonough, M. A.; Oppermann, U.; Schofield, C. J., Inhibitor scaffolds for 2-oxoglutarate-dependent histone lysine demethylases. *J med chem* **2008,** *51* (22), 7053-6.

31. Schofield, C. J.; Zhang, Z., Structural and mechanistic studies on 2-oxoglutarate-dependent oxygenases and related enzymes. *Curr Opin Struct Biol* **1999,** *9* (6), 722-31.

32. Clifton, I. J.; McDonough, M. A.; Ehrismann, D.; Kershaw, N. J.; Granatino, N.; Schofield, C. J., Structural studies on 2-oxoglutarate oxygenases and related double-stranded beta-helix fold proteins. *J Inorg Biochem* **2006,** *100* (4), 644-69.

33. Conejo-Garcia, A.; McDonough, M. A.; Loenarz, C.; McNeill, L. A.; Hewitson, K. S.; Ge, W.; Lienard, B. M.; Schofield, C. J.; Clifton, I. J., Structural basis for binding of cyclic 2-oxoglutarate analogues to factor-inhibiting hypoxia-inducible factor. *Bioorg Med Chem Lett* **2010,** *20* (20), 6125-8.

34. Mole, D. R.; Schlemminger, I.; McNeill, L. A.; Hewitson, K. S.; Pugh, C. W.; Ratcliffe, P. J.; Schofield, C. J., 2-oxoglutarate analogue inhibitors of HIF prolyl hydroxylase. *Bioorg Med Chem Lett* **2003,** *13* (16), 2677-80.

35. Welford, R. W.; Schlemminger, I.; McNeill, L. A.; Hewitson, K. S.; Schofield, C. J., The selectivity and inhibition of AlkB. *J Biol Chem* **2003,** *278* (12), 10157-61.

36. Hamada, S.; Suzuki, T.; Mino, K.; Koseki, K.; Oehme, F.; Flamme, I.; Ozasa, H.; Itoh, Y.; Ogasawara, D.; Komaarashi, H.; Kato, A.; Tsumoto, H.; Nakagawa, H.; Hasegawa, M.; Sasaki, R.; Mizukami, T.; Miyata, N., Design, synthesis, enzyme-inhibitory activity, and effect on human cancer cells of a novel series of jumonji domain-containing protein 2 histone demethylase inhibitors. *J Med Chem* **2010,** *53* (15), 5629-38.

37. Li, Q.; Huang, Y.; Liu, X.; Gan, J.; Chen, H.; Yang, C. G., Rhein inhibits AlkB repair enzymes and sensitizes cells to methylated DNA damage. *J Biol Chem* **2016,** *291* (21), 11083-93.

38. Bernhardt, W. M.; Wiesener, M. S.; Scigalla, P.; Chou, J.; Schmieder, R. E.; Günzler, V.; Eckardt, K.-U., Inhibition of prolyl hydroxylases increases erythropoietin production in ESRD. *J Am Soc Nephrol* **2010,** *21* (12), 2151-6.

39. King, O. N. F.; Li, X. S.; Sakurai, M.; Kawamura, A.; Rose, N. R.; Ng, S. S.; Quinn, A. M.; Rai, G.; Mott, B. T.; Beswick, P.; Klose, R. J.; Oppermann, U.; Jadhav, A.; Heightman, T. D.; Maloney, D. J.; Schofield, C. J.; Simeonov, A., Quantitative high-throughput screening identifies 8-hydroxyquinolines as cell-active histone demethylase inhibitors. *PLoS One* **2010,** *5* (11), e15535.

40. Hillenkamp, F.; Karas, M.; Beavis, R. C.; Chait, B. T., Matrix-assisted laser desorption/ionization mass spectrometry of biopolymers. *Anal Chem* **1991,** *63* (24), 1193A-1203A.

41. Dominissini, D.; Moshitch-Moshkovitz, S.; Schwartz, S.; Salmon-Divon, M.; Ungar, L.; Osenberg, S.; Cesarkas, K.; Jacob-Hirsch, J.; Amariglio, N.; Kupiec, M.; Sorek, R.; Rechavi, G., Topology of the human and mouse m6A RNA methylomes revealed by m6A-seq. *Nature* **2012,** *485* (7397), 201-6.

42. Wang, X.; Lu, Z.; Gomez, A.; Hon, G. C.; Yue, Y.; Han, D.; Fu, Y.; Parisien, M.; Dai, Q.; Jia, G.; Ren, B.; Pan, T.; He, C., N6-methyladenosine-dependent regulation of messenger RNA stability. *Nature* **2014,** *505* (7481), 117-20.

43. Aik, W.; Scotti, J. S.; Choi, H.; Gong, L.; Demetriades, M.; Schofield, C. J.; McDonough, M. A., Structure of human RNA N(6)-methyladenine demethylase ALKBH5 provides insights into its mechanisms of nucleic acid recognition and demethylation. *Nucleic Acids Res.* **2014,** *42* (7), 4741-54.

44. Rajakaruna, L.; Hallas, G.; Molenaar, L.; Dare, D.; Sutton, H.; Encheva, V.; Culak, R.; Innes, I.; Ball, G.; Sefton, A. M.; Eydmann, M.; Kearns, A. M.; Shah, H. N., High throughput identification of clinical isolates of Staphylococcus aureus using MALDI-TOF-MS of intact cells. *Infect, Genet Evol* **2009,** *9* (4), 507-513.

45. Singhal, N.; Kumar, M.; Kanaujia, P. K.; Virdi, J. S., MALDI-TOF mass spectrometry: an emerging technology for microbial identification and diagnosis. *Front Microbiol* **2015,** *6*, 791-3.

46. Porta, T.; Lesur, A.; Varesio, E.; Hopfgartner, G., Quantification in MALDI-MS imaging: what can we learn from MALDI-selected reaction monitoring and what can we expect for imaging? *Anal Bioanal Chem* **2015,** *407* (8), 2177-87.

47. Loenarz, C.; Schofield, C. J., Expanding chemical biology of 2-oxoglutarate oxygenases. *Nat Chem Biol* **2008,** *4* (3), 152-6.

48. Bhatt, D. P.; Chen, X.; Geiger, J. D.; Rosenberger, T. A., A sensitive HPLC-based method to quantify adenine nucleotides in primary astrocyte cell cultures. *J Chromatogr B Analyt Technol Biomed Life Sci* **2012,** *889-90*, 110-5.

49. Gong, L.; McCullagh, J. S., Comparing ion-pairing reagents and sample dissolution solvents for ion-pairing reversed-phase liquid chromatography/electrospray ionization mass spectrometry analysis of oligonucleotides. *Rapid Commun Mass Spectrom* **2014,** *28* (4), 339-50.

50. Macon, J. B.; Wolfenden, R., 1-Methyladenosine. Dimroth rearrangement and reversible reduction. *Biochemistry* **1968,** *7* (10), 3453-58.

51. Engel, J. D., Mechanism of the dimroth rearrangement in adenosine. *Biochem Biophys Res Commun* **1975,** *64* (2), 581-6.

52. Fujii, T.; Itaya, T., The Dimroth rearrangement in the adenine series: A review updated. *Heterocycles* **1998,** *48* (2), 359-90.

53. Hutchinson, S. E.; Leveridge, M. V.; Heathcote, M. L.; Francis, P.; Williams, L.; Gee, M.; Munoz-Muriedas, J.; Leavens, B.; Shillings, A.; Jones, E.; Homes, P.; Baddeley, S.; Chung, C.-w.; Bridges, A.; Argyrou, A., Enabling lead discovery for histone lysine demethylases by high-throughput RapidFire mass spectrometry. *J Biomol Screen* **2011,** *17* (1), 39-48.

54. Lu, H.; Kopcho, L.; Ghosh, K.; Witmer, M.; Parker, M.; Gupta, S.; Paul, M.; Krishnamurthy, P.; Laksmaiah, B.; Xie, D.; Tredup, J.; Zhang, L.; Abell, L. M., Development of a RapidFire mass spectrometry assay and a fluorescence assay for the discovery of kynurenine aminotransferase II inhibitors to treat central nervous system disorders. *Anal Biochem* **2016,** *501*, 56-65.

55. Gordon, L. J.; Allen, M.; Artursson, P.; Hann, M. M.; Leavens, B. J.; Mateus, A.; Readshaw, S.; Valko, K.; Wayne, G. J.; West, A., Direct measurement of intracellular compound concentration by RapidFire mass spectrometry offers insights into cell permeability. *J Biomol Screen* **2015,** *21* (2), 156-64.

56. Takamiya, M.; Sakurai, M.; Teranishi, F.; Ikeda, T.; Kamiyama, T.; Asai, A., Lead discovery for mammalian elongation of long chain fatty acids family 6 using a combination of high-throughput fluorescent-based assay and RapidFire mass spectrometry assay. *Biochem Biophys Res Commun* **2016,** *480* (4), 721-6.

57. Huck, J. H. J.; Struys, E. A.; Verhoeven, N. M.; Jakobs, C.; van der Knaap, M. S., Profiling of pentose phosphate pathway intermediates in blood spots by tandem mass spectrometry: application to transaldolase deficiency. *Clin Chem* **2003,** *49* (8), 1375-80.

58. Ni, J. S.; Pomerantz, S. C.; Rozenski, J.; Zhang, Y. H.; McCloskey, J. A., Interpretation of oligonucleotide mass spectra for determination of sequence using electrospray ionization and tandem mass spectrometry. *Anal Chem* **1996,** *68* (13), 1989-99.

59. Barry, J. P.; Vouros, P.; Van Schepdael, A.; Law, S.-J., Mass and sequence verification of modified oligonucleotides using electrospray tandem mass spectrometry. *J Mass Spectrom* **1995,** *30* (7), 993-1006.

60. Banerjee, S.; Mazumdar, S., Electrospray ionization mass spectrometry: A technique to access the information beyond the molecular weight of the analyte. *Int J Anal Chem* **2012,** *2012*, 1-40.

61. Dickson, K. A.; Haigis, M. C.; Raines, R. T., Ribonuclease inhibitor: structure and function. *Prog Nucleic Acid Res Mol Biol* **2005,** *80*, 349-74.

62. Chirgwin, J. M.; Przybyla, A. E.; MacDonald, R. J.; Rutter, W. J., Isolation of biologically active ribonucleic acid from sources enriched in ribonuclease. *Biochemistry* **1979,** *18* (24), 5294-99.

63. Wolf, B.; Lesnaw, J. A.; Reichmann, M. E., A Mechanism of the ireversible inactivation of bovine pancreatic ribonuclease by diethylpyrocarbonate. *Eur J Biochem* **1970,** *13* (3), 519-25.

64. Wigle, T. J.; Swinger, K. K.; Campbell, J. E.; Scholle, M. D.; Sherrill, J.; Admirand, E. A.; Boriack-Sjodin, P. A.; Kuntz, K. W.; Chesworth, R.; Moyer, M. P.; Scott, M. P.; Copeland, R. A., A high-throughput mass spectrometry assay coupled with redox activity testing reduces artifacts and false positives in lysine demethylase screening. *J Biomol Screen* **2015,** *20* (6), 810-20.

65. Zhu, C.; Yi, C., Switching demethylation activities between AlkB family RNA/DNA demethylases through exchange of active-site residues. *Angew Chem* **2014,** *53* (14), 3659-62.

66. Ma, M.; Harding, Heather P.; Rahilly, S.; Ron, D.; Yeo, Giles S. H., Kinetic analysis of FTO (fat mass and obesity-associated) reveals that it is unlikely to function as a sensor for 2-oxoglutarate. *Biochem J* **2012,** *444* (2), 183-7.

67. Rose, N. R.; McDonough, M. A.; King, O. N. F.; Kawamura, A.; Schofield, C. J., Inhibition of 2-oxoglutarate dependent oxygenases. *Chem Soc Rev* **2011,** *40* (8), 4364-97.

68. Holt-Martyn, J. P.; Tumber, A.; Rahman, M. Z.; Lippl, K.; Figg, W.; McDonough, M. A.; Chowdhury, R.; Schofield, C. J., Studies on spiro[4.5]decanone prolyl hydroxylase domain inhibitors. *MedChemComm* **2019,** *10* (4), 500-4.

Chapter 3

Mechanistic studies of FTO using mass spectrometry

Table of Contents

3. Mechanistic studies of FTO using mass spectrometry **109**

3.1. Previous studies 109

3.2. Objectives 112

3.3. Is FTO a demethylase or a hydroxylase? 113

3.4. Investigation of FTO activity 117

3.4.1. FTO compared with ABH5 117

3.4.2. FTO catalysis investigation with inhibitor 2,4-PDCA 129

3.4.3. Human FTO compared with mouse FTO 133

3.4.4. FTO compared with AlkB 135

3.5. Discussion and future work 139

Acknowledgements **143**

References **144**

3. Mechanistic studies of FTO using mass spectrometry

3.1. Previous studies

Following the initial report of FTO catalysed N-methyl DNA demethylation[1], FTO was reported as an RNA demethylase, converting N-6-methylated adenosine (m^6A) to adenosine (A) in RNA oligonucleotides (Figure 3.1)[2]. The latter study employed an assay based on high-performance liquid chromatography-mass spectrometry (HPLC-MS), in which a ssRNA oligonucleotide was incubated with FTO. The incubated mixture was then digested using nuclease P1 and alkaline phosphatase to single nucleosides, before being analysed by ultraviolet light with liquid chromatography-mass spectrometry (UV/LC-MS)[2]. It was apparent from the UV chromatogram that m^6A had disappeared under the reaction conditions[2]. Substitution of the Fe(II) or 2OG-binding residues in FTO supported the proposal that the demethylation was catalysed by FTO in a 2OG and Fe(II)-dependent manner[2]. In 2013, Fu *et al.* reported evidence that FTO catalyses formation of a "meta-stable intermediate", N-6-hydroxymethyl adenosine (hm^6A) intermediate, which is further oxidised by FTO to form N-6-formyl adenosine (f^6A). The hm^6A can react to give adenosine and formaldehyde, and f^6A can react to give formic acid and adenosine (Figure 3.1)[3].

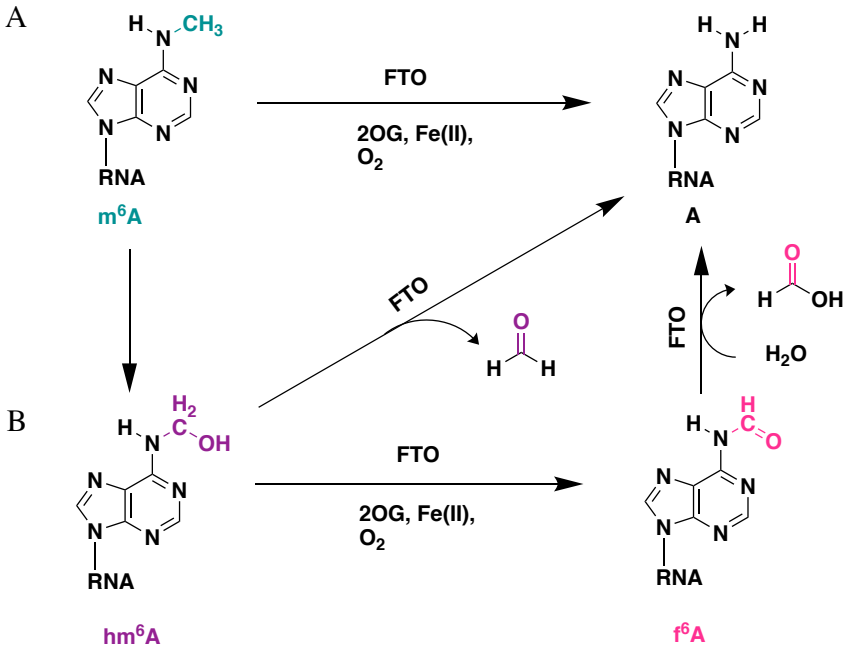


Figure 3.1: *Scheme showing the FTO-catalysed midification of m^{6}A in ssRNA. (A) FTO was initially reported to catalyse the direct demethylation of m^{6}A to adenosine; (B) further studies demonstrated that FTO catalyses the formation of two other species, i.e. N-6-hydroxymethyl adenosine (hm^{6}A) and N-6-formyl adenosine (f^{6}A).*

Cellular studies demonstrated that m^{6}A content is affected by FTO[4], with hm^{6}A and f^{6}A being detected in mammalian cells[3]. These observations indicate that the catalytic activities of FTO are related to those of other 2OG oxygenases, e.g. the Ten-eleven translocation methylcytosine dioxygenases (TETs) (Figure 3.2A). The TETs perform sequential oxidations on C-methylated DNA[5-7]. The TETs were initially reported to catalyse the oxidation of 5-methylcytosine (5mC) to 5-hydroxymethylcyotosine (5hmC) in mammalian genomic DNA[5]. Subsequent studies showed that TETs further oxidise 5hmC to 5-formylcytosine (5fC) and 5-carboxylcytosine (5caC)[6-7].

Prior to the FTO study by Fu *et al.*[3], the demethylation mechanism of FTO was thought to be similar to that of the Jumonji-C histone lysine demethylases (JmjC KDMs). KDMs, also members of the 2OG oxygenase superfamily, catalyse the demethylation of N$^{\varepsilon}$-methylated lysyl or arginyl residues on histone[8]. The JmjC KDMs are proposed to catalyse the hydroxylation of N$^{\varepsilon}$-methylated lysine (or arginine) residues in a typical 2OG-dependent

manner, although the hemiaminal intermediate has not been observed, which implies that it is unstable[9-10].

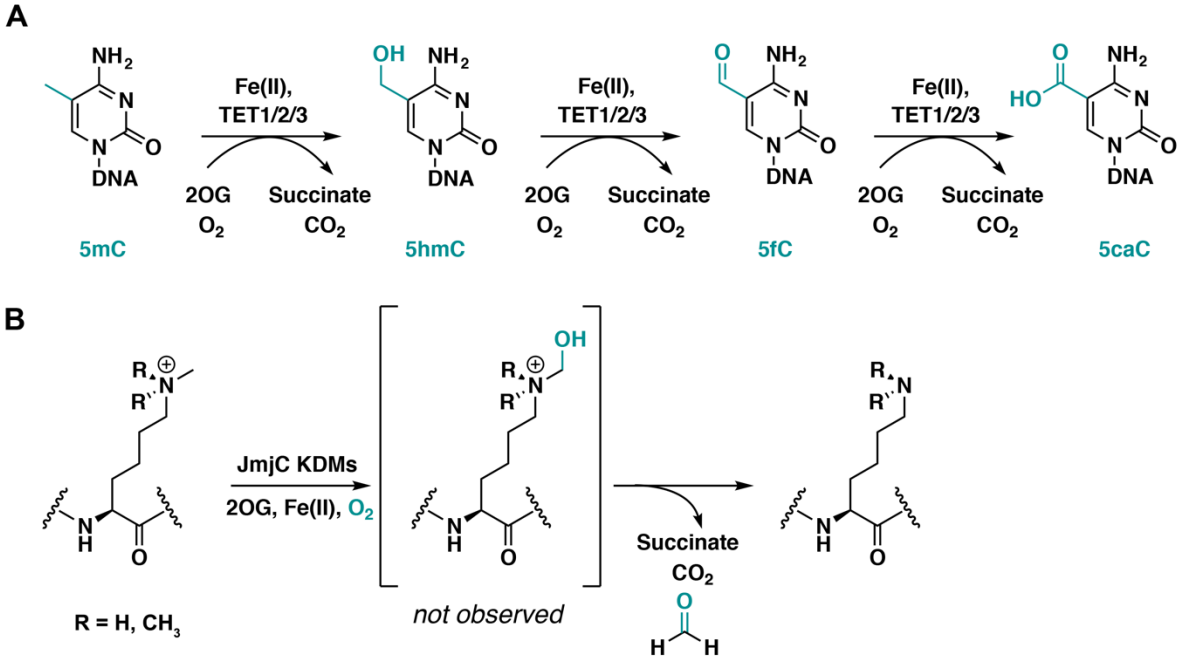


Figure 3.2: *Schemes showing demethylation activities of two different types of 2OG oxygenases. (A) Successive oxidation of DNA with 5mC modification by the TET enzymes[5-7]. (B) Demethylation co-catalysed by the Jumonji-C histone lysine demethylases (JmjC KDMs); the methylated lysine is first hydroxylated to produce a hemiaminal, which is unstable and thus fragments to demethylated product and formaldehyde. Note: the hemiaminal intermediate has not been observed in KDM-catalysed demethylation[9-10].*

Both those FTO studies employed MALDI-MS and/or LC-MS based assays, and required sequential use of nuclease P1 and alkaline phosphatase to digest the intact oligonucleotides before analysis[2-3]. However, the hm^{6}A and f^{6}A likely did not survive sequential treatment with the P1 nuclease and alkaline phosphatase[2]. To take account of this in the latter FTO study[3], only the P1 nuclease was used, at neutral pH for oligonucleotide digestion, so apparently enabling detection of hm^{6}A and f^{6}A. However, having additional enzymatic reactions after the FTO-catalysed reaction may still introduce modifications to the oligonucleotide substrate. Therefore, an assay with minimal impact on the substrate/product(s) is desirable to monitor FTO catalysis.

3.2. Objectives

In light of the unexpected observation that an apparently stable hydroxylated (hemiaminal) product apparently results from FTO catalysis, it was considered that further investigations should be carried out to better understand the biochemistry and function of FTO. The goal of the work described in the current chapter was to assess whether FTO indeed catalyses m^6A demethylation *via* a two-step oxidation that proceeds *via* a hemiaminal[3, 11]. It was envisaged that other AlkB subfamily member proteins would be used for comparative studies, i.e. ABH5 and AlkB. As described in Chapter 2, Rapidfire-MS based assays were successful for the assaying of FTO catalysis; hence this technique was employed, along with MALDI-MS and LC-MS, to investigate the products of FTO catalysis.

Please note, part of the work detailed in this chapter has been reported in the academic literature in: '*NMR analyses on N-hydroxymethylated nucleobases – implications for formaldehyde toxicity and nucleic acid demethylases*', doi: 10.1039/C8OB00734A.

3.3. Is FTO a demethylase or a hydroxylase?

Initially, the FTO-catalysed modification of a 5-mer ssRNA oligonucleotide, GG(m^6A)CU (1582 Da), was studied by MALDI-MS. The results were consistent with those previously reported (Figure 3.2)[2]. A low-intensity peak for the demethylated product at m/z 1569.2 (-14Da) was observed after 20 mins of FTO-catalysed reaction, while a more intense peak was observed at m/z 1581.2 (-2 Da). The peak at m/z 1581.2 (-2 Da) corresponds to a dehydrated hemiaminal, i.e. an imine/iminium ion (+16 Da - 18 Da = -2 Da). This observation is in agreement with general 2OG oxygenase-catalysed demethylation reactions (e.g. KDM catalysed reactions) that proceed *via* formation of an unstable hemiaminal intermediate (e.g. hm^{6}A), which decomposes to afford the demethylated product and formaldehyde as a by-product[9, 12].

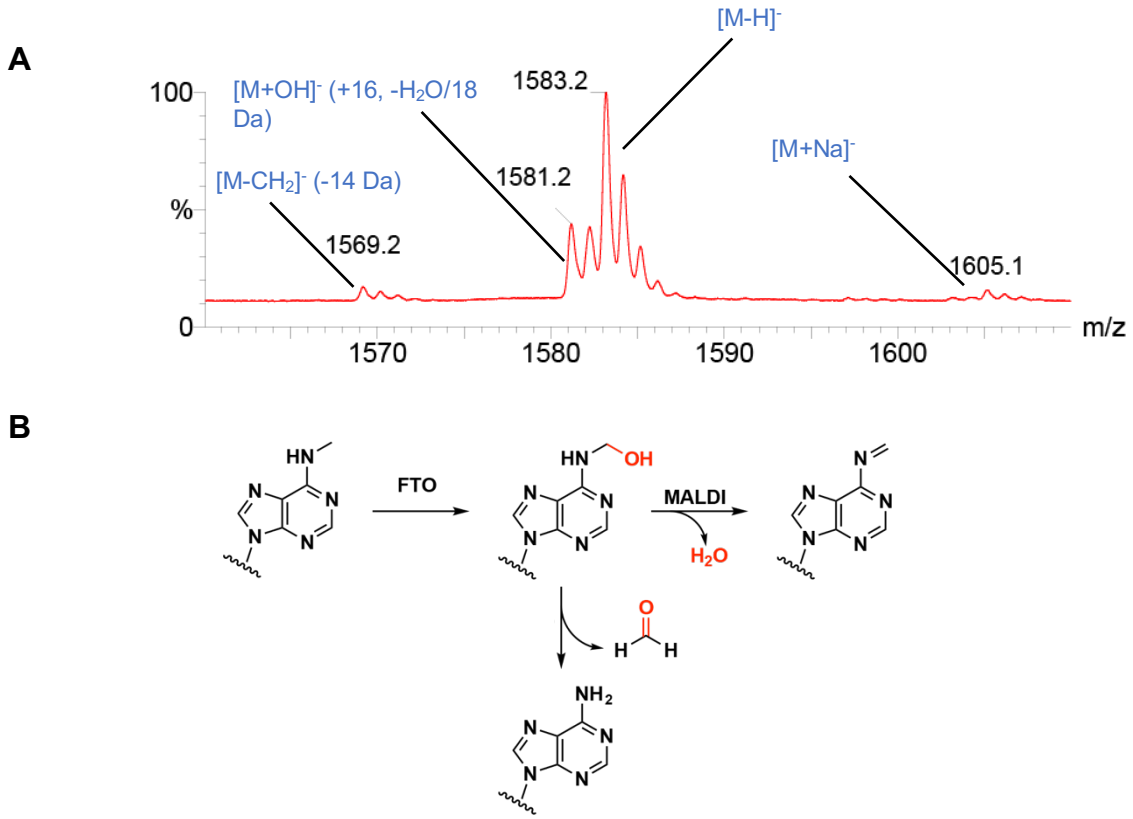


Figure 3.2: *(A) MALDI-TOF MS spectrum of an FTO-catalysed reaction showing the 5-mer ssRNA substrate containing m^{6}A (m/z 1583.2), the demethylated product, A (m/z 1569.2, -14 Da) and a peak at 1581.2 m/z, which corresponds to an imine, i.e., dehydrated hm^{6}A. (B) The hemiaminal is dehydrated to form an imine/iminium ion, which is observed by MALDI-MS.*

The evidence for hm^{6}A stability was initially not considered to be of significance, because the peak at m/z 1581.2 was thought to be an artefact of the MALDI assay (Chapter 2)[13]. Based on the work with JmjC KDMs[9] and the FTO research reported in the literature, it was considered possible that degradation of hm^{6}A might proceed rapidly in water to give the demethylated product.

During the optimisation of the LC-MS based assay (Chapter 2), evidence for a hydroxylated hemiaminal was observed (Figure 3.3). However, spectral data from the LC-MS based assay with the 5-mer ssRNA oligonucleotide [GG(m^{6}A)CU] (1582 Da), were not consistent with the MALDI-MS data, i.e. the m/z 1581 peak (+16 Da, - 18 Da) was not observed. Some of the LC-MS screening plates were not analysed immediately after quenching and were instead stored at 4ºC for an extended time (over one week). Upon LC-MS analysis of these plates, the apparent presence of hm^{6}A was still observed (Figure 3.3). Furthermore, the LC-MS based assay required lengthy handling after reaction quenching, including extended heating (30 mins at 40 ºC), which could have accelerated degradation of the hm^{6}A intermediate. This observation led to the proposal that hm^{6}A may not be a transient intermediate, but instead a hydroxylated FTO product[3]. Notably, the presence of f^{6}A was not observed.

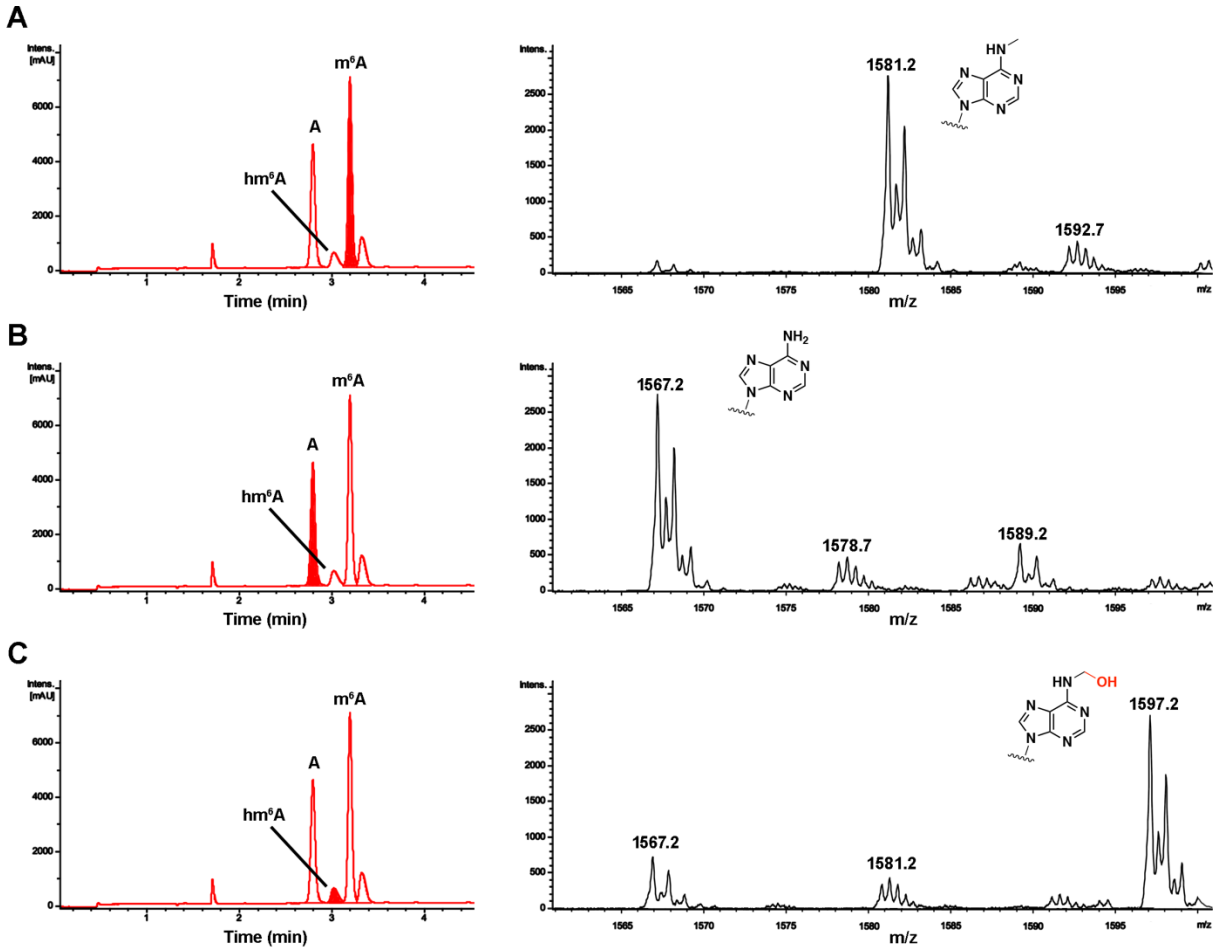


Figure 3.3: *UV trace from LC type chromatogram and mass spectrum (MS) of FTO-catalysed reactions with 5-mer ssRNA oligonucleotide (intact) from LC-MS based assay. Peak of interest is highlighted in red and the corresponding spectrum is shown on the right. (A) LC and MS showing RNA substrate containing m^6A modification; (B)) LC and MS showing RNA with demethylated adenosine; (C)) LC and MS showing RNA with hm^6A.*

The potential of FTO-catalysed formation of f^6A was not supported by the Rapidfire-MS (RF-MS) studies (Chapter 2). The LC-MS based assay employed an intact 5-mer ssRNA oligonucleotide substrate [GG(m^6A)CU] (1582 Da); similarly, an intact 15-mer ssRNA oligonucleotide [AUUGUGG(m^6A)CUGCAGC] (4805 Da) was used as a substrate in the RF-MS assays. The FTO-catalysed reaction was monitored in real-time without any chemical and/or biological treatment, with the aim that potential modifications to the products/intermediates would be minimised. The results (Figure 3.4) indicate that the m^6A-containing 15-mer RNA oligomer substrate has been converted to hm^6A, which is stable over the time course of the monitored reaction. Contrary to previous reports[3], these results suggest

that (under the assay conditions) hm^{6}A is not a substrate for FTO. This observation raises the possibility that hydroxylation of m^{6}A to give hm^{6}A, at least in ssRNA, may be the biologically relevant reaction of FTO, at least in terms of the initial product formed.

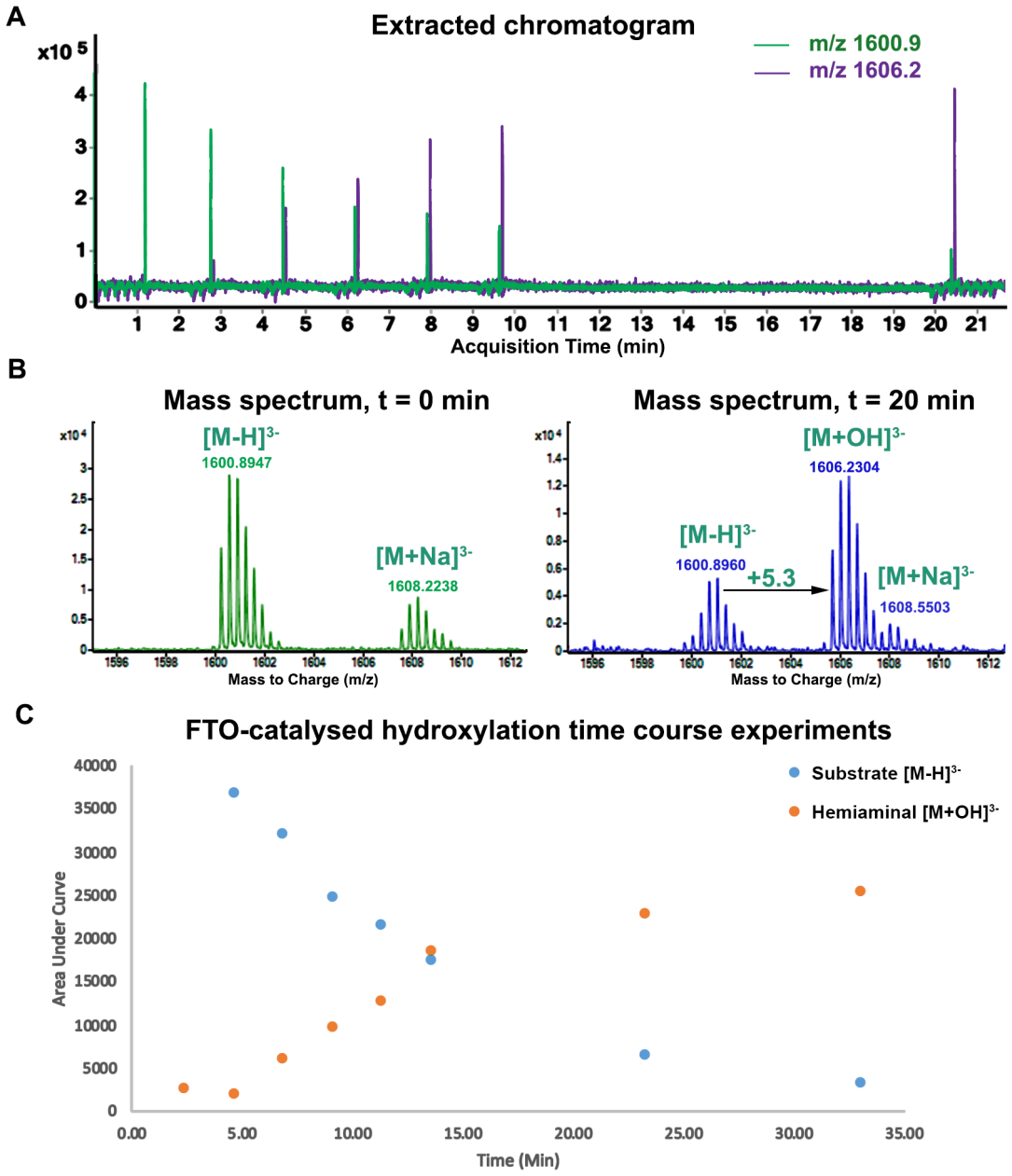


Figure 3.4: *RapidFire-MS analysis of FTO catalysis. Extracted ion chromatograms indicate that (A) 15-mer oligomer containing m^{6}A (m/z 1600.9) is converted to hm^{6}A (m/z 1606.2), + m/z 5.3 (at -3 charge state), implying formation of a hydroxylated product (+ 16 Da). No other products were observed. (B) The mass spectrum at 20 mins indicates formation of RNA oligomer containing hm^{6}A. (C) The consumption of substrate (i.e., 15-mer oligomer containing m^{6}A) was directly proportional to the formation of product (i.e., 15-mer oligomer containing hm^{6}A).*

3.4. Investigation of FTO activity

3.4.1. FTO compared with ABH5

3.4.1.1. Rapidfire-MS time course study of ABH5

Given that hemiaminal type intermediates have not been observed in JmjC KDM catalysis[8, 9], and that hm^{6}A was observed in these FTO catalysis studies, it was of interest to investigate whether such intermediates would be observed with another AlkB homologue. ABH5 is reported to demethylate ssRNA that contains N-6-methyladenosine (as is FTO)[14]. Both 5-mer and 15-mer RNA oligomers containing m^{6}A were used to test the activity of ABH5 using the RF-MS based assay (Figure 3.5). The ABH5-catalysed reaction was carried out in 50 mM Tris buffer under the same conditions as the FTO-catalysed reaction (i.e. 25 ºC, 20 mins, 0.1 μM ABH5, 1 μM RNA substrate, 20 μM 2OG, 20 μM $(NH_4)_2Fe(SO_4)_2$, 200 μM ascorbic acid).

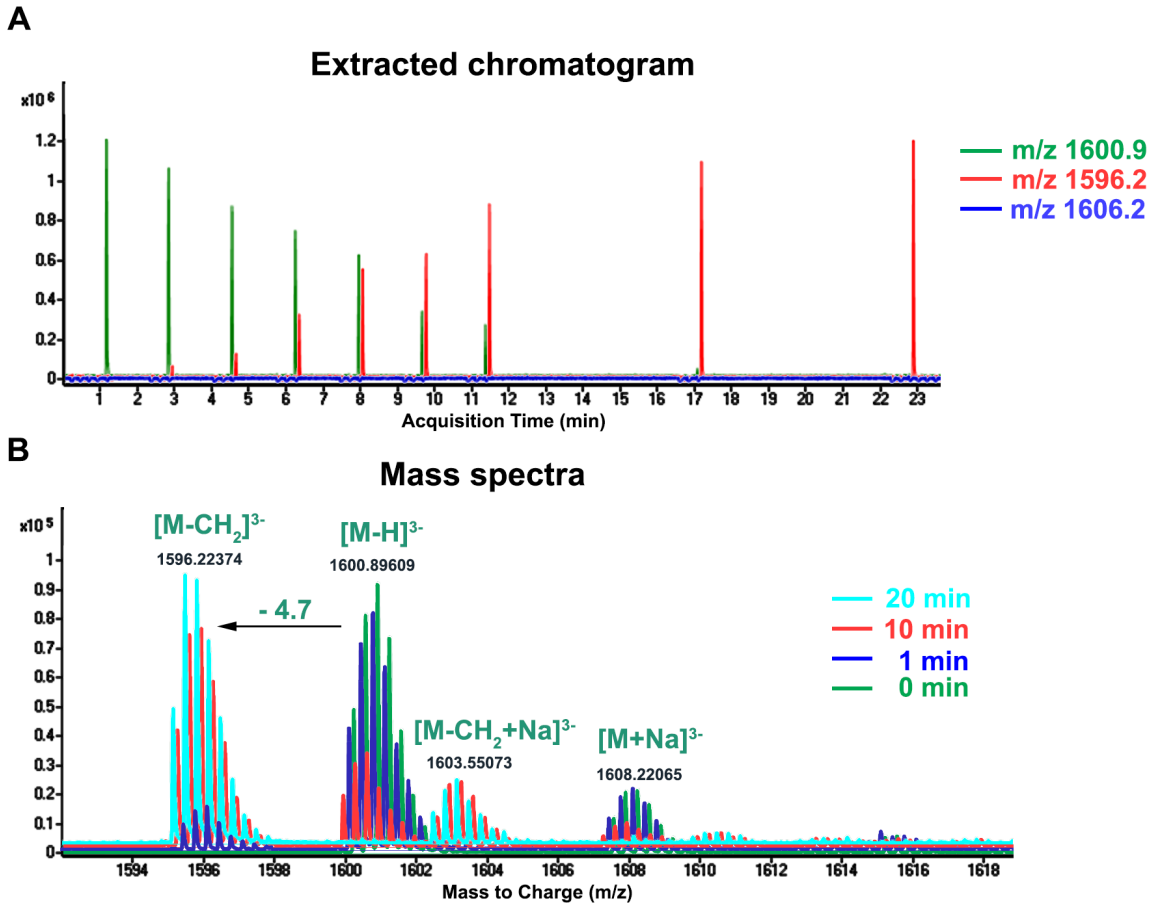


Figure 3.5: *Rapidfire-MS data (time course) showing ABH5-catalysed reaction with 15-mer ssRNA oligomer. The extracted chromatograms (A) show the 15-mer oligomer substrate (m/z 1600.9, -3 charge state) is converted to the demethylated product (m/z 1596.2). The putative hemiaminal (hm^{6}A, m/z 1606.2) intermediate was not observed. Mass spectra taken at different time points are shown in (B).*

At 20 min, a signal corresponding to hm^{6}A (-3 charge state, m/z 1606.2), which was observed in the FTO-catalysed reaction, is not observed in the reaction with ABH5. Instead, the demethylated product (from m^{6}A to A; m/z 1596.2) is observed. It is possible that the ABH5-catalysed demethylation proceeds *via* a hemiaminal intermediate, which degrades to formaldehyde and the demethylated product whilst bound to the protein[14]. The hm^{6}A signal (m/z 1606.2) is not observed at any time point of the ABH5-catalysed reaction, which indicates that the hydroxylated hm^{6}A intermediate is not released.

3.4.1.2. Comparison of the pH profiles of FTO and ABH5

It was considered that catalysis by FTO and ABH5 might vary as a function of pH. To investigate this, reactions were carried out in the same conditions as before, using the 15-mer oligomer substrate. The reaction was analysed after 15 min without quenching, with no more than 50% substrate being converted into product. The results imply that the enzymes exhibit different pH profiles; FTO was most active at pH 8.0, while ABH5 was most active at pH 7.0 (Figure 3.6). Although demethylation was observed with FTO-catalysed reaction at pH values above 7.5, this is like due to the chemical instability of hemiaminal at high pH[15]. This observations suggest that the different pH profiles suggest that FTO and ABH5 interact with their common substrate differently; leading to hydroxylation with FTO, i.e. production of hm^{6}A, or demethylation with ABH5.

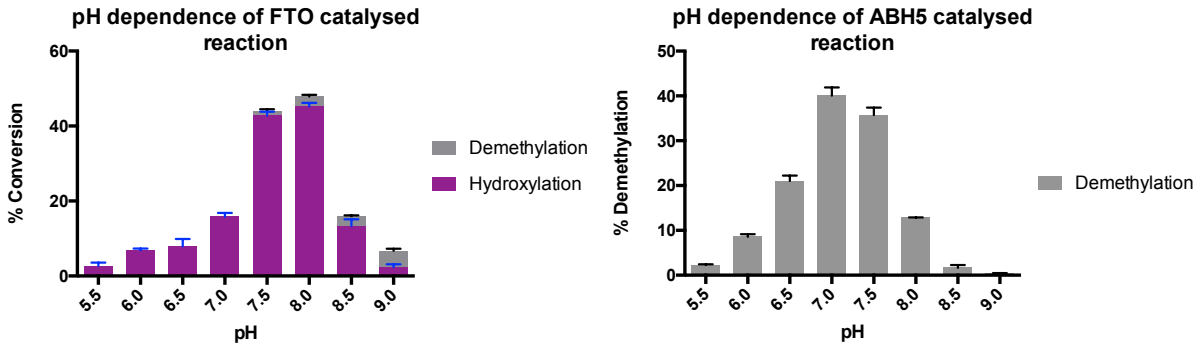


Figure 3.6: *FTO- and ABH5-catalysed hydroxylation/demethylation of 15-mer RNA oligomers in MES (pH 5.5 – pH 6.5) or Tris (pH 7.0 – pH 9.0) buffer. Reactions were carried out for 15 minutes at room temperature (25 ºC). The extent of hydroxylation/demethylation (percentage) was analysed by RF-MS. Data were plotted as the mean of technical triplicates using GraphPad Prism®. Note: demethylation was observed for FTO-catalysed hydroxylation at 30 minutes and at pH values above pH 7.5. The extent of demethylation was observed to increases with pH. Only demethylation was observed for the ABH5-catalysed reaction. FTO is most active at pH 8.0 and ABH5 is most active at pH 7.0.*

3.4.1.3. Investigation of reaction pathways

To further investigate the products of reactions catalysed by FTO and ABH5, reactions with the 15-mer RNA oligomer containing hemiaminal were carried out with each enzyme (Figure 3.7). The hm^{6}A-containing oligomer was generated *via* FTO-catalysed hydroxylation. Thus, in a 1 mL reaction mixture, the 2 µM 15-mer RNA oligomer was incubated with 1 µM FTO at 37

ºC for 30 mins to enable conversion of m^6A to hm^6A (Figure 3.7 A). Then 2OG (20 μM), $(NH_4)_2Fe(SO_4)_2$ (20 μM) and ascorbic acid (200 μM) were added in excess. After the initial hydroxylation reaction, FTO was removed by filtration using a Seahorse® polypropylene 96-well filter microplate with 30 kDa polyethersulfone membrane (Chapter 2, section 2.6.3). The resultant reaction mixture was divided into three separate wells, treated with (i) Tris buffer (as control), (ii) 1 μM FTO, or (iii) 1 μM ABH5, respectively. Each reaction was run for a further 20 mins at 37 ºC before RF-MS analysis.

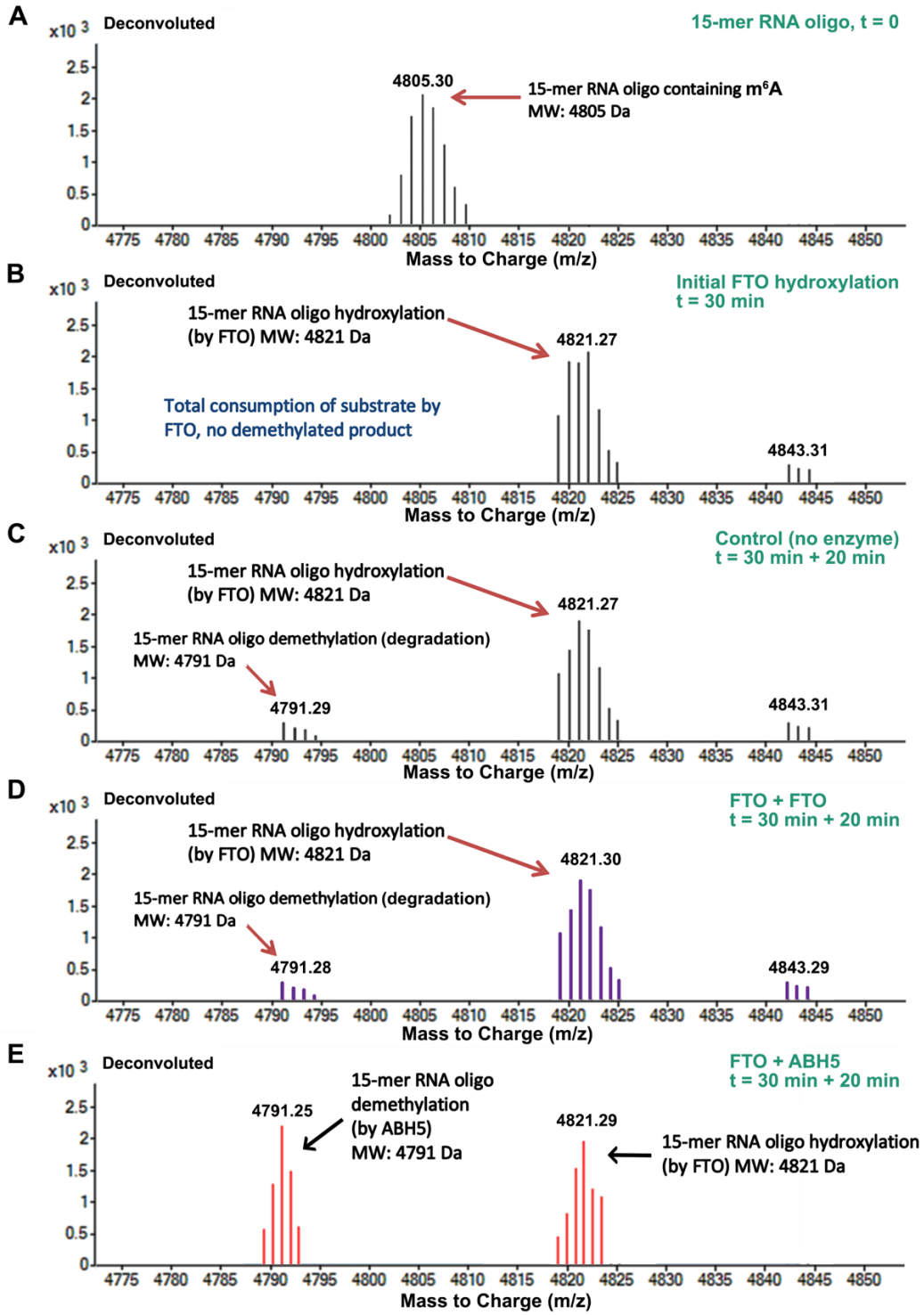


Figure 3.7: *Deconvoluted MS spectra showing the progress of FTO- and/or ABH5-catalysed reactions. (A) The 15-mer RNA substrate containing m^{6}A (4805 Da) at t = 0. (B) Initial hydroxylation after 30 mins, as catalysed by FTO. The substrate (4805 Da) is converted to a hemiaminal (hm^{6}A, 4821 Da). After removal of FTO enzyme, the reaction mixture was divided into three samples and treated with (i) Tris buffer (control), (iI) FTO (1 μM), or (iii) ABH5 (1 μM). These reactions were run for a further 20 mins at 37 ºC. The control (C) showed slight hemiaminal (hm^{6}A) degradation to form demethylated RNA (4791 Da); the FTO-treated sample (D) showed the same level of hemiaminal (hm^{6}A) degradation, suggesting that RNA with hm^{6}A modification is not an FTO substrate. (E) The ABH5-treated sample displayed conversion of hemiaminal (hm^{6}A, 4821 Da) to demethylated RNA (4791 Da), indicating that hm^{6}A is an ABH5 substrate.*

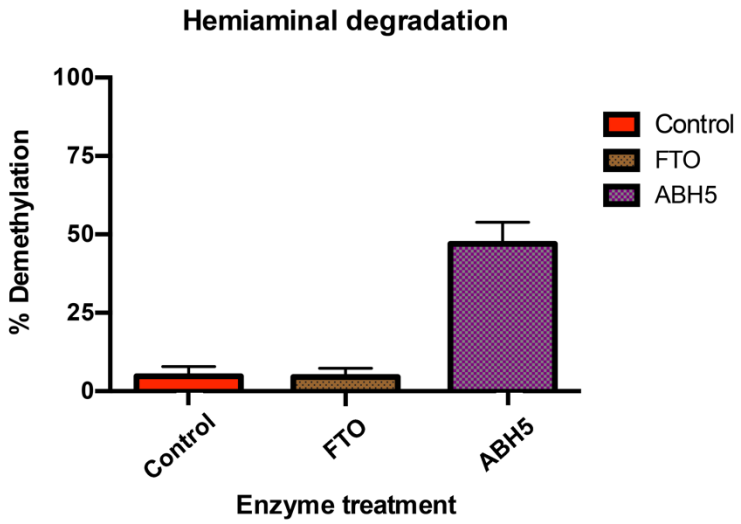


Figure 3.8: *RF-MS analysis of FTO- and ABH5-catalysed degradation of hm^{6}A after 20 mins incubation at 37ºC. The level of hemiaminal degradation in the sample treated with FTO is the same as the no enzyme control, within error; however, the ABH5-treated sample shows a significant level of hemiaminal degradation. These observations suggest that FTO does not take hm^{6}A as a substrate, but ABH5 does.*

RNA with an hm^{6}A modification is reported as a substrate for FTO, in which hm^{6}A is oxidised (by FTO) to give f^{6}A[3]. It is apparent (Figure 3.7) that FTO catalyses conversion of RNA that contains m^{6}A (4805 Da) to a hydroxylated product (the stable hemiaminal, hm^{6}A, 4821 Da). However, no further oxidation to formylated product was observed, which suggests that FTO does not take hm^{6}A as a substrate, under the tested conditions. Although demethylation (from hm^{6}A-containing RNA oligomer) was observed in the sample treated with FTO, the rate of demethylation was the same as the no enzyme control, i.e. it is likely due to non-enzymatic reaction (Figure 3.8).

When ABH5 was added to the hm^{6}A product generated by FTO, a significant level of demethylation was observed relative to the control (Figures 3.7 and 3.8). This implies that ABH5 takes RNA with the hm^{6}A modification as a substrate, albeit that the rate of demethylation, or rather the fragmentation of hemiaminal, is lower than in reactions with m^{6}A substrate. This observation is consistent with the proposal that ABH5 does not release hm^{6}A, i.e. fragmentation to give formaldehyde occurs, whilst the RNA remains bound to ABH5, and

the product being released after demethylation. RNA that contains hm^{6}A still binds to ABH5, but binding is less favourable compared with RNA that contains a m^{6}A modification.

To test the proposal that hemiaminal (hm^{6}A) is not a substrate for FTO, nuclear magnetic resonance (NMR) analyses of FTO-catalysed reactions were carried out with ^{13}C-labelled nucleoside m^{6}A (^{13}C-labelled on its 6-methyl group). These analyses were conducted by Shifali Shishodia[11, 16].

FTO-catalysed reaction of m^{6}A was analysed: samples containing (^{13}C-labelled) m^{6}A (400 μM), 2OG (5 mM), sodium ascorbate (1 mM), $(NH_4)_2Fe(SO_4)_2$ (20 μM) and FTO (20 μM) were prepared in ammonium formate buffer (D_2O, pH 7.5), then immediately analysed by ^{1}H NMR (700 MHz) and 1-dimensional heteronuclear single quantum correlation NMR (1D-^{1}H–^{13}C-HSQC) for 19 hours at 37 ºC. The 1D-^{1}H–^{13}C-HSQC analysis enhances detection of resonances of ^{1}H attached to ^{13}C-labels. Thus in this case it was employed to enrich resonance signals from ^{13}C-labelled N-6-methyl group on m^{6}A. FTO-catalysed hydroxylation of m^{6}A was observed, as evidenced by loss of the N-6-methyl group ^{1}H-resonance (doublet at δ_H 3.3 ppm, $J_{C\text{-}H}$ = 145 Hz), and appearance of ^{13}C-labelled hm^{6}A resonance (doublet at δ_H 5.3 ppm, $J_{C\text{-}H}$ = 165 Hz). It was apparent that, during the first six hours, ^{13}C-labelled hm^{6}A is formed as the major FTO-catalysed product; this then gradually fragments to adenosine and formaldehyde (HCHO) (Figures 4.9 and 4.10). After the first hour, no significant further formation of succinate was observed by ^{1}H NMR (Figure 3.9), which indicated that catalysis by FTO was complete and the formation of HCHO (from hm^{6}A fragmentation) was non-enzymatic. This observation is consistent with the RF-MS results.

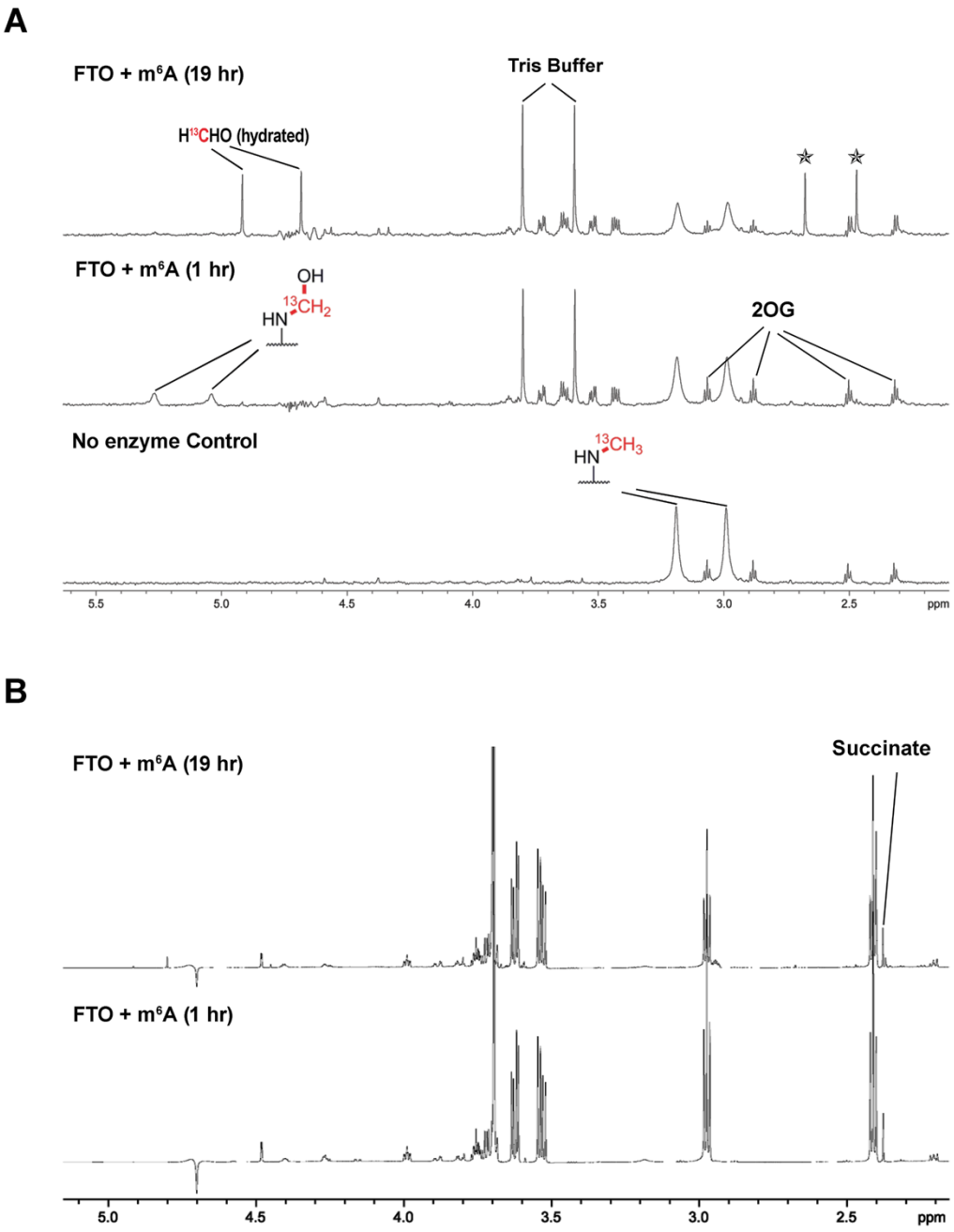


Figure 3.9: *NMR analyses of FTO-catalysed hydroxylation of m6A.[11] (A) 1-Dimensional ^{1}H–^{13}C heteronuclear single quantum correlation (1D-^{1}H–^{13}C-HSQC, ^{13}C-coupled) spectra showing FTO-catalysed hydroxylation of m^6A. A sample containing ^{13}C-labelled (on N-6-methyl group) m^6A (400 µM), was incubated with 2OG (5 mM), ascorbate (1 mM), $(NH_4)_2Fe(SO_4)_2$ (20 µM) and FTO (20 µM) in deuterated ammonium formate buffer in D_2O at pH 7.5; the reaction was monitored by ^{1}H and 1D-^{1}H–^{13}C-HSQC NMR (over 19 hours, 37 ºC). Using 1D-^{1}H-^{13}C-HSQC, ^{1}H-resonances attached to ^{13}C-labelled carbon appear as doublets due to ^{1}H–^{13}C coupling. After one hour, the major product of the reaction was ^{13}C-labelled hm^6A (middle). Formation of hm^6A coincided with decreased amounts of m^6A and formation of succinate, confirming FTO-catalysed hydroxylation of m^6A to hm^6A. Over time, hm^6A levels decreased with concomitant $H^{13}CHO$ formation (top). Evidence for formation of ^{13}C-labelled methylamine was observed in the 1D-^{1}H–^{13}C-HSQC spectrum after 19 hours (stars), likely as a consequence of hm^6A deamination. Tris buffer signal observed was from enzyme stock buffer. (B) No substantial increase in succinate was observed after one hour, indicating conclusion of 2OG-dependent catalysis, at least. Figure adapted from Shishodia et al.[11]*

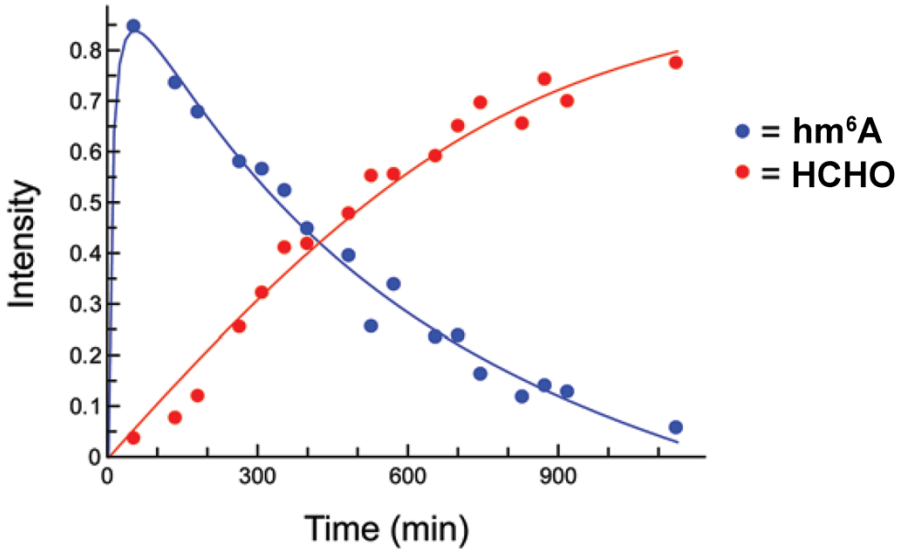


Figure 3.10: *1D-^{1}H–^{13}C-HSQC time-course analysis of FTO-catalysed hydroxylation of m^{6}A[11]. Levels of hm^{6}A were highest at the first time-point (one hour) before fragmenting to form (^{13}C-labelled) HCHO. However, under the test conditions, hm^{6}A was more prevalent than HCHO for six hours after FTO addition. Figure adapted from Shishodia et al.* [11]

3.4.1.4. Sequence alignment

Having observed the apparently different reaction pathways followed and products formed during FTO and ABH5 catalysis, it was envisaged that specific residues at the active site may be involved in distinct reactions. The amino acid sequences of the catalytic domains of *E. coli* AlkB, human FTO and ABH5 were aligned using Clustal Omega[17]. The results show that the characteristic 2OG oxygenase residues, e.g. the HxD/E…H motif used to bind Fe(II) (Figure 3.11, highlighted in red), are conserved[18], as are the 2OG-binding residues (Asn120, Arg206, Arg212 on AlkB; Asn205, Arg316, Arg322 on FTO; and Asn193, Arg277, Arg283 on ABH5). A distinctive feature of FTO is an unusually long loop located between beta sheets β7 and β8 (which correspond to β4 and β5 in ABH5), referred to as the L1 Loop. It is proposed that the role of this loop is to block the binding of double-stranded DNA/RNA to FTO[19]. The sequence alignments do not indicate an obvious reason for the different reaction outcomes observed with FTO and ABH5.

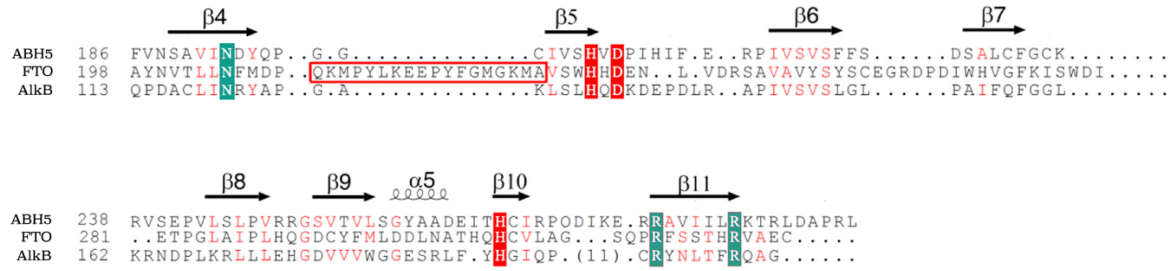


Figure 3.11: *Sequence alignment of the catalytic domains (double-stranded β helix, DSBH) of human ABH5, FTO and AlkB. The conserved 2OG-binding residues are shown in green and metal-binding residues are highlighted in red. Residues on the L1 Loop of FTO are indicated with a red box. The alignment was performed using Clustal Omega[17].*

3.4.1.5. Structural rationalisation

An FTO structure complexed with ssDNA that contains N-6-adenosine (6mA, PDB ID: 5ZMD) offers information that can help to rationalise the observed different mechanisms of reaction of FTO and ABH5[20]. When a ABH5 (PDB ID: 4OCT) structure is superimposed on that of FTO-ssDNA structure, conformational variation in substrate binding by the two enzymes is indicated (Figure 3.12). FTO utilises two pairs of positively charged residues from two loops to bind the oligonucleotide. A lysine residue (Lys88) located on a short loop between the β2 and β3 strands of the double-stranded β-helix (DSBH) core of FTO is positioned to interact with the phosphate backbone of the oligonucleotide. A second lysine residue (Lys216) on the L1 loop (present in FTO but not in ABH5) is positioned to interact with the same backbone phosphate, but from a different direction. It is proposed that these residues stabilise the oligonucleotide complex in a clamp-like manner. A second pair of residues, Lys88 and Lys306 (glutamine in wild-type FTO), bind to the oligonucleotide in a similar fashion. Lys86 is located on the same short loop next to Lys88 and can interact with oxygen and/or nitrogen atoms on the oligonucleotide, while Lys306 is positioned to bind to the phosphate backbone (Figure 3.12). These clamp-like bindings of the oligonucleotide to FTO are apparently missing from the corresponding region of ABH5 (Figure 3.12).

A long, flexible loop between the β3 and β4 strands of the DSBH core of ABH5 (residues 141-153) is positioned to sterically clash with the oligonucleotide (Figure 3.12C). However, it is likely that this loop is mobile in solution and may adopt other conformations to accommodate incoming oligonucleotides. It is reported that, in cells, FTO demethylates RNA with internal m^6A, capped N^6,2-O-dimethyladenosine (m^6A_m) and N-1-methyladenosine (m^1A) modifications[4, 21]. ABH5 has been reported to recognise and demethylate RNA with the m^6A modification only[14]. The different residues located at the entrances of the substrate binding regions of FTO and ABH5 may play roles in substrate recognition and/or catalysis.

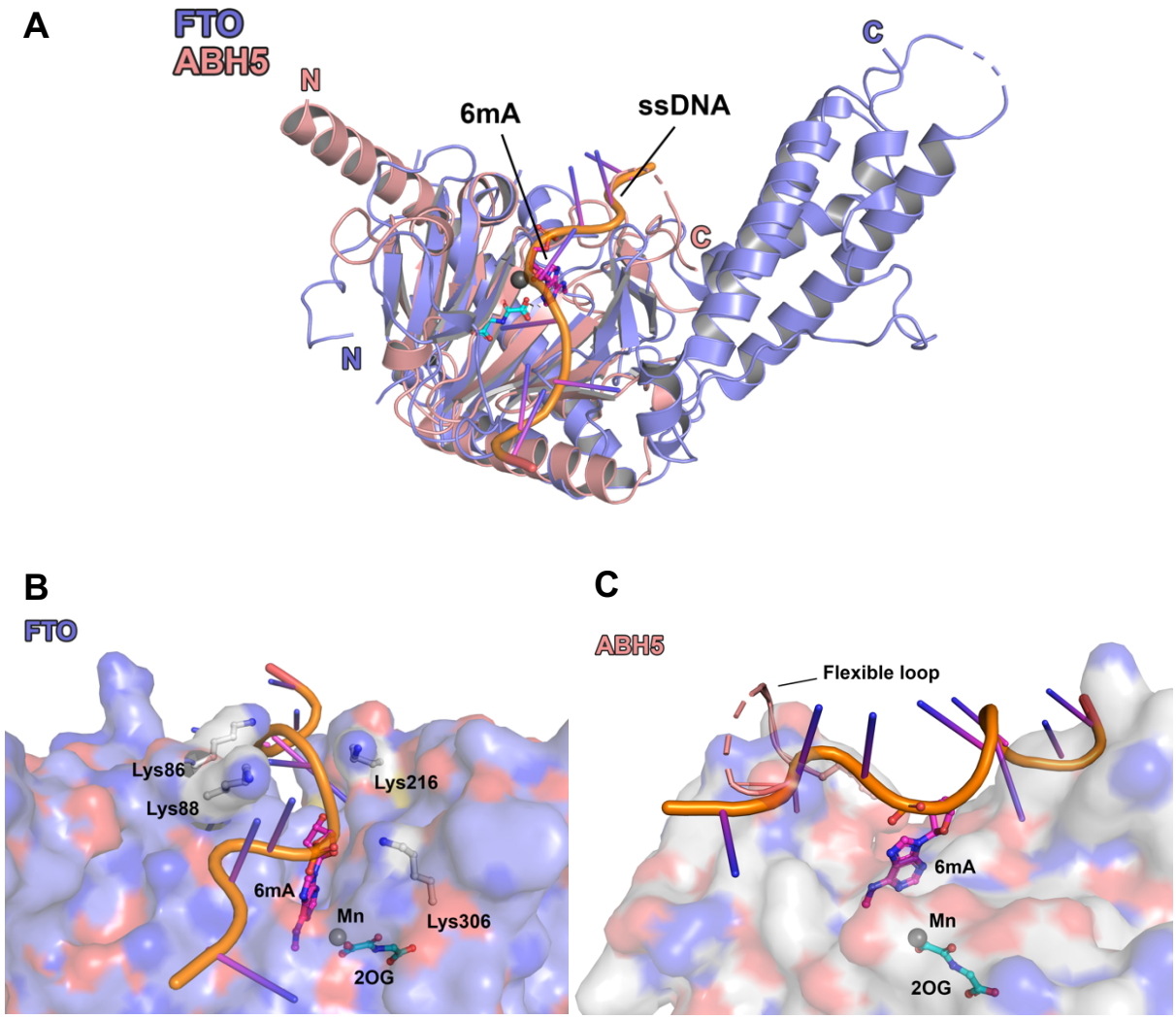


Figure 3.12: *Overlaid views of structures of FTO (purple, PDB ID: 5ZMD[20]) bound to ssDNA (orange) and ABH5 (salmon, PDB ID: 4OCT[22]). (A) The superimposed structures show overall similarities between the two enzymes. (B) Views of the positively charged oligonucleotide-binding residues present in FTO but not ABH5. (C) Views of the corresponding substrate-binding region on ABH5. Note: there is steric clash caused by the flexible loop (residues 141-153 between β4 and β5).*

Residues from the 'hydrophobic cage' which interacts with the purine ring of 6mA are similar in FTO and ABH5. In the FTO structure, the pyrimidine ring from 6mA (or m^6A for RNA) is sandwiched between a conserved histidine (His 231 on FTO, His204 on ABH5) and a tyrosine (Tyr108 on FTO, Tyr139 on ABH5); a third residue (Leu109 on FTO, Tyr141 on ABH5) completes the hydrophobic cage. Two polar residues that are positioned in FTO to interact with N^6 of 6mA (or m^6A for RNA) are not present in ABH5. These variations may contribute to the

observed differences in their reaction outcomes. A polar residue (Glu234) in FTO is essential for its catalytic activity[20]; this is replaced by Pro207 in ABH5, a substitution which may lead to loss of polar interaction with N^6 and the hydroxyl group of the hemiaminal product/intermediate. Arg96 of FTO is substituted by Lys132 on ABH5, possibly also affecting reaction outcome. These polar residues on FTO may contribute to the stabilisation of the hemiaminal, as the hydrogen bond interactions may prevent further oxidation and/or fragmentation at the active site.

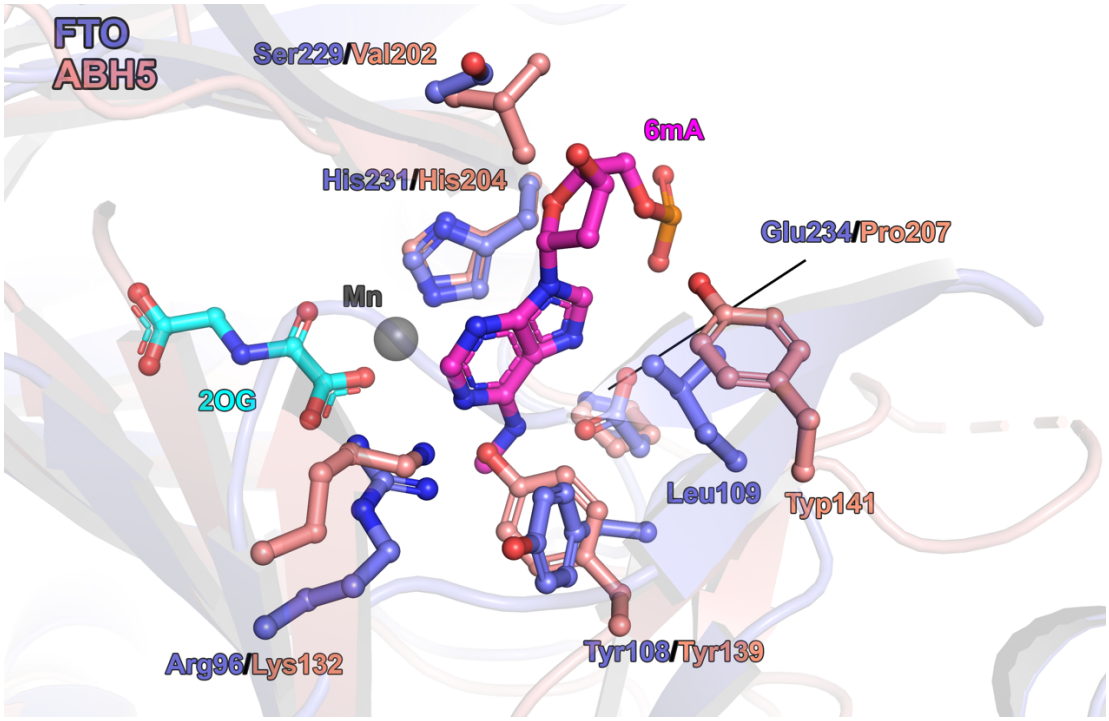


Figure 3.13: *Views from structures of FTO (purple, PDB ID: 5ZMD[20]) bound to ssDNA (orange) overlaid to a reported ABH5 structure (salmon, PDB ID: 4OCT[22]). Residue Glu234, which recognises the substrate and is catalytically essential on FTO, is not conserved in ABH5 (Pro207); residue Arg96 in FTO is believed to interact with N^6 of 6mA (or m^6A) for substrate recognition and stabilisation, and it also is not conserved in ABH5.*

3.4.2. FTO catalysis investigation with inhibitor 2,4-PDCA

The results described above imply that FTO catalyses hydroxylation of RNA that contains a m^6A modification. However, the possibility of slow demethylation cannot be ruled out, (compared with that observed in reactions that use ABH5 (Figures 4.4, 4.5 and 4.7). To further investigate FTO catalysis, a broad-spectrum 2OG oxygenase inhibitor, 2,4-

pyridinedicarboxylic acid (2,4-PDCA) (IC_{50} for FTO 8.3 μM ± 1.1)[23], was used to determine whether the observed demethylation was catalysed by FTO. If the formation of demethylated adenosine was generated from the natural degradation of hm^6A-containing product, then the rate of demethylation would be the same with or without the presence of the FTO inhibitor. A reaction (1 mL) was set up, in which 15-mer RNA oligomer with m^6A modification (2 μM) was incubated with FTO (0.1 μM), 2OG (20 μM), $(NH_4)_2Fe(SO_4)_2$ (20 μM) and ascorbic acid (200 μM) for 15 mins at 37 ºC, so that approximately 50% of substrate was hydroxylated. The resultant reaction mixture was divided equally between two wells; one was treated with 10 mM 2,4-PDCA, while the other was untreated as control. Samples were kept at 37 ºC and the reactions were monitored at hourly intervals (Figure 3.14).

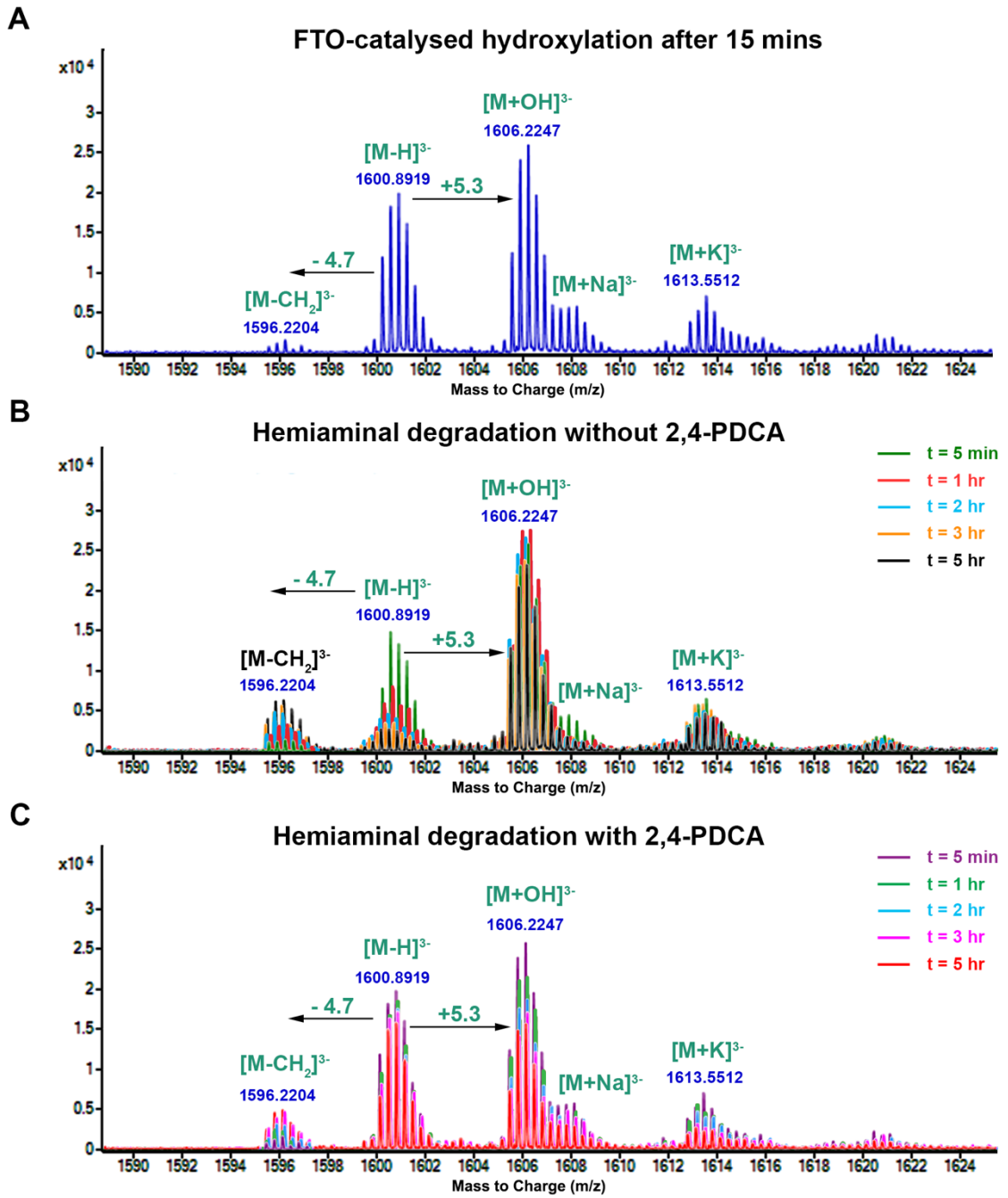


Figure 3.14: *Mass spectrometric data showing the extent of FTO-catalysed hydroxylation and the non-enzymatic degradation of hemiaminal product of 15-mer RNA oligonucleotide over a five-hour period. (A) Mass spectrum of the initial FTO-catalysed hydroxylation; (B) overlaid mass spectra of hemiaminal (hm^{6}A) degradation to adenosine and continued FTO-catalysed hydroxylation without addition of 2,4-PDCA; (C) overlaid mass spectra of hemiaminal (hm^{6}A) degradation to adenosine with addition of 2,4-PDCA. Note the complete inhibition of FTO activity by 2,4-PDCA; formation of new hemiaminal product (hm^{6}A) is not observed in the inhibitor-treated sample.*

After the initial FTO reaction, slightly more than 50% of the m^{6}A-containing RNA oligomer was hydroxylated (with negligible demethylation). After division of the sample into two, the

reactions, with or without 2,4-PDCA, were analysed. The results show increasing levels of demethylated RNA as reaction progresses. Hydroxylation catalysed by FTO continued in the inhibitor-free sample, while in the 2,4-PDCA sample, no further reaction was observed. This is thought to be due to FTO inhibition (Figure 3.15).

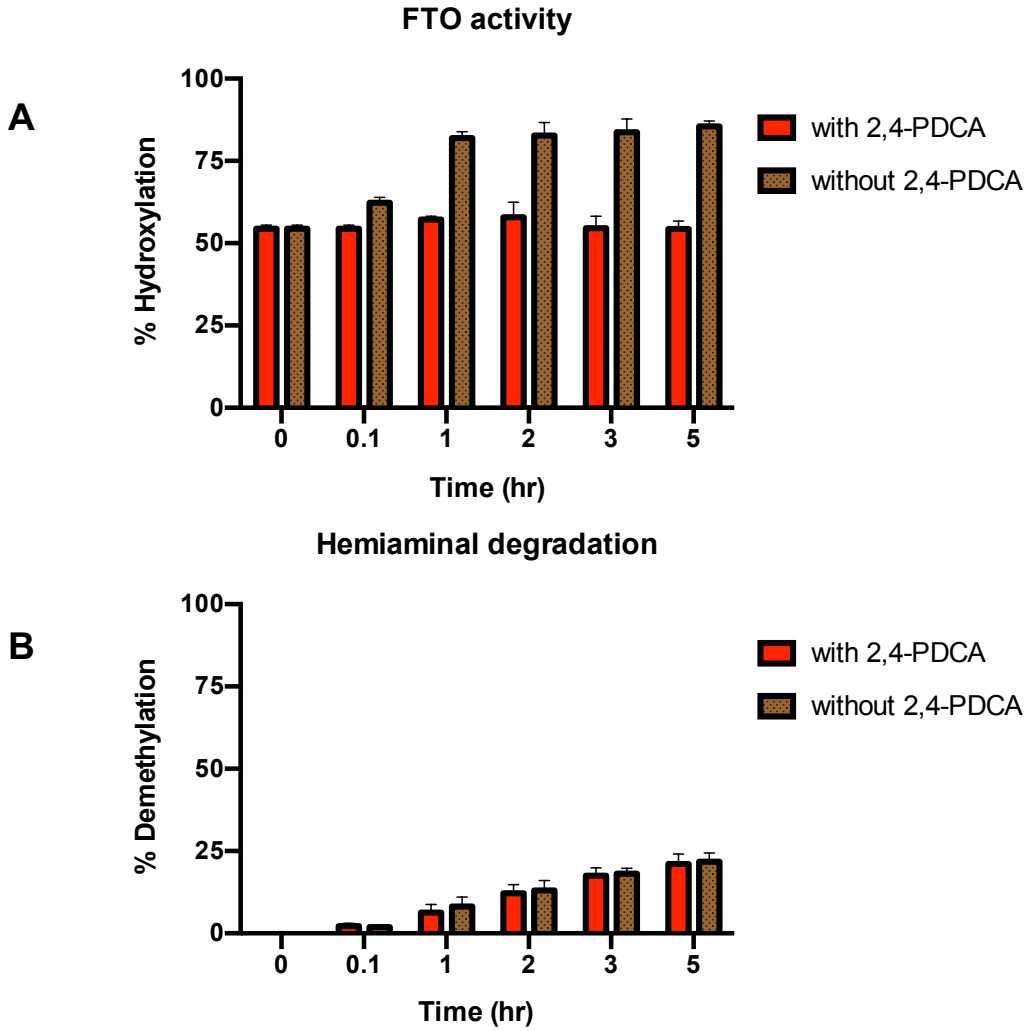


Figure 3.15: *After initial FTO catalysis, which resulted in ~50% RNA-substrate hydroxylation, the sample was divided into two, and the reaction progress was monitored in the presence and absence of 2,4-PDCA. (A) FTO continued to catalyse hydroxylation in the absence of 2,4-PDCA, while no further hydroxylation was observed in the presence of 2,4-PDCA, over a five-hour period. (B) Extent of hemiaminal degradation over the five-hour period with or without 2,4-PDCA was comparable. Note: the rate of demethylation/degradation from hydroxylated product was not affected by 2,4-PDCA, indicating that demethylation/degradation was non-enzymatic. Data were plotted as the means of technical triplicates using GraphPad Prism® software.*

Formation of demethylated RNA was observed in both samples (with or without 2,4-PDCA), and the levels of demethylated RNA increased with time (Figure 3.15B). however, the rate of

demethylation was the same for both samples, with or without inhibitor. These observations indicate that degradation of the hemiaminal (hm^{6}A) is not catalysed by FTO (or at least not *via* a typical 2OG oxygenase manner). The reported oxidised product (f^{6}A)[3] was not observed under the assay conditions.

3.4.3. Human FTO compared with mouse FTO

To test whether such mechanisms (i.e., hydroxylation of RNA that contains m^{6}A) occur in other homologues of FTO, mouse FTO (mFTO) was used. A time-course experiment was performed using 15-mer RNA oligomer that contained m^{6}A as substrate; assay conditions were the same as those used with hFTO (Figure 3.16).

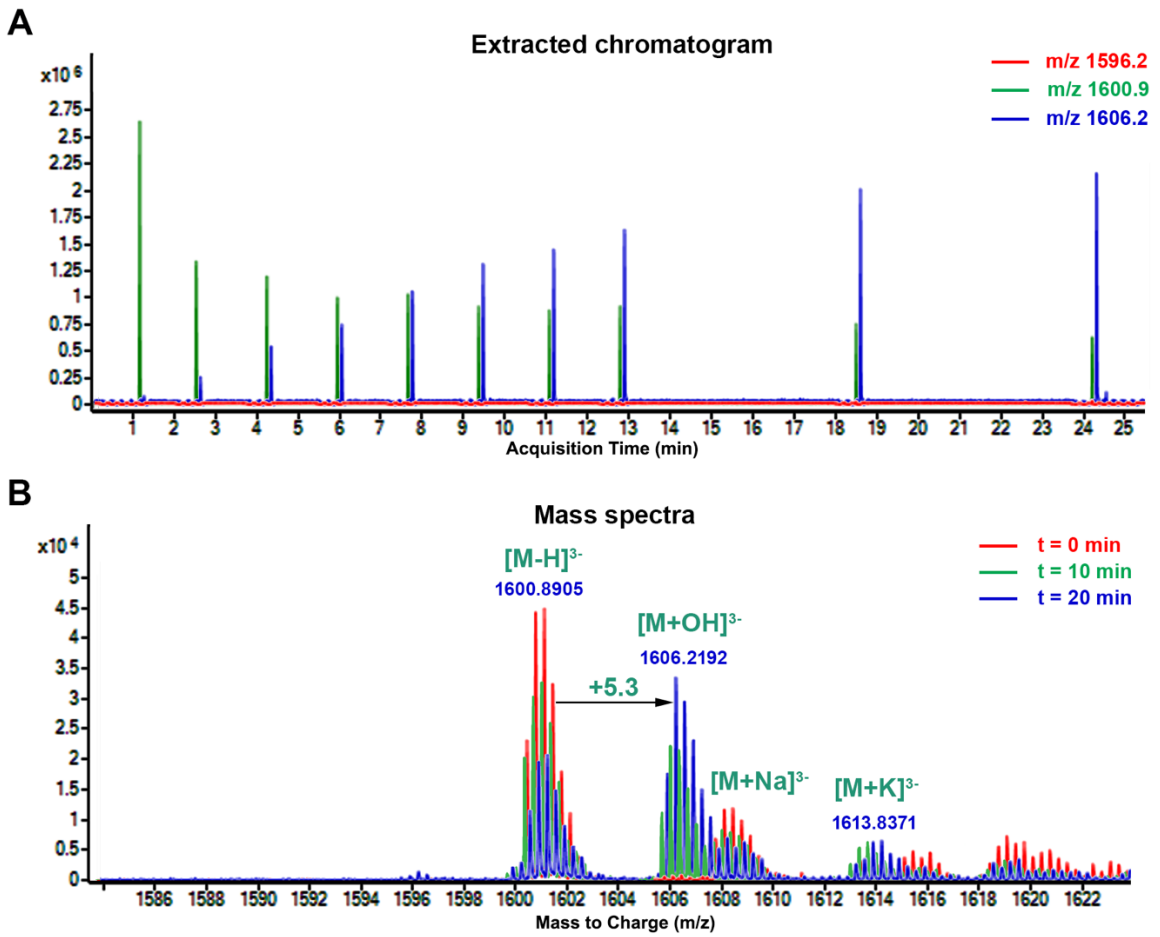


Figure 3.16: *Time-course experiments of extracted-ion chromatograms indicate that (A) 15-mer oligomer that contains m^{6}A (m/z 1600.9, -3 charge state) is converted to hm^{6}A (m/z 1606.2, -3 charge state) by FTO catalysis. (B) The mass spectrum at 20 mins shows apparent (and exclusive) formation of RNA oligomer that contains hm^{6}A; presence of f^{6}A was not observed.*

As observed with hFTO, mFTO catalyses conversion of m^6A to hm^6A, at least for the 15-mer RNA oligomer tested. mFTO shares approximately 87% identity with hFTO, and the metal-binding, 2OG-binding and substrate-binding residues are substantially conserved, which probably explains the observed identical reaction outcomes (Figure 3.17). The observation of the same reaction outcome with FTOs from different species supports the proposal that the observed hFTO-catalysed hydroxylation is not an artefact related to protein preparation/purification.

```
hFTO    MKRTPTAEEREREAKKLRLLEELEDTWLPYLTPKDDEFYQQWQLKYPKLILREASSVSEE 60
mFTO    MKRVQTAEEREREAKKLRLLEELEDTWLPYLTPKDDEFYQQWQLKYPKLVFREAGSIPEE 60

hFTO    LHKEVQEAFLTLHKHGCLFRDLVRIQGKDLLTPVSRILIGNPGCTYKYINTRLFTVPWPV 120
mFTO    LHKEVPEAFLTLHKHGCLFRDVVRIQGKDVLTPVSRILIGDPGCTYKYINTRLFTVPWPV 120

hFTO    KGSNIKHTEAEIAAACETFLKLNDYLQIETIQALEELAAKEKANEDAVPLCMSADFPRVG 180
mFTO    KGCTVKYTEAEIAAACQTFLKLNDYLQVETIQALEELAVREKANEDAVPLCMA-EFPRAG 179

hFTO    MGSSYNGQDEVDIKSRAAYNVTLLNFMDPQKMPYLKEEPYFGMGKMAVSWHHDENLVDRS 240
mFTO    VGPSC--DDEVDLKSRAAYNVTLLNFMDPQKMPYLKEEPYFGMGKMAVSWHHDENLVDRS 237

hFTO    AVAVYSYSCEGPEEESEDDSHLEGRDPDIWHVGFKISWDIETPGLAIPLHQGDCYFMLDD 300
mFTO    AVAVYSYSCEGSEDESEDESSFEGRDPDTWHVGFKISWDIETPGLTIPLHQGDCYFMLDD 297

hFTO    LNATHQHCVLAGSQPRFSSTHRVAECSTGTLDYILQRCQLALQNVCDDVDNDDVSLKSFE 360
mFTO    LNATHQHCVLAGSQPRFSSTHRVAECSTGTLDYILERCQLALQNVLNDSDDGDVSLKSFD 357

hFTO    PAVLKQGEEIHNEVEFEWLRQFWFQGNRYRKCTDWWCQPMAQLEALWKKMEGVTNAVLHE 420
mFTO    PAVLKQGEEIHNEVEFEWLRQFWFQGNRYKLCTDWWCEPMTHLEGLWKKMESMTNAVLRE 417

hFTO    VKREGLPVEQRNEILTAILASLTARQNLRREWHARCQSRIARTLPADQKPECRPYWEKDD 480
mFTO    VKREGLPVEQRSEILSAILVPLTVRQNLRKEWHARCQSRVVRTLPVQQKPDCRPYWEKDD 477

hFTO    ASMPLPFDLTDIVSELRGQLLEAKP 505
mFTO    PSMPLPFDLTDVVSELRGQLLEARS 502
```

Figure 3.17: *Sequence alignment of human (h) and mouse (m) FTO proteins. The active site is highlighted in grey with conserved 2OG-binding residues highlighted in green, iron-binding residues in red, and substrate-binding residues in cyan. The alignment was performed using Clustal Omega[17].*

The observation of different reaction outcomes when FTO and ABH5 are reacted separately with the same substrate indicates that the intrinsic stability of the hydroxylated product (hemiaminal) ion is not an issue. The apparent demethylation observed with ABH5 is likely to be effectively irreversible because the formaldehyde product is sequestered by further reactions with nucleophiles.

3.4.4. FTO compared with AlkB

Among the AlkB subfamily, ABH1 to ABH5 are reported to be nucleic acid demethylases[14, 24-27], while ABH8 is reported to be a tRNA hydroxylase[28]. AlkB has only been reported as a direct DNA/RNA methylated lesion-repair enzyme (demethylase)[24, 29-31]. The present work supports the proposal that FTO might more suitably be considered as a hydroxylase.

To test whether AlkB shows hydroxylase activity, separate reactions that involved AlkB with either a 15-mer ssRNA oligonucleotide with (that contained m^6A), [AUUGUGG(m^6A)CUGCAGC], or trimeric ssDNA oligomer (that contained m^1A), [T(m^1A)T], were carried out. AlkB has been reported to demethylate oligonucleotide with both m^1A and m^6A modifications[24, 32]. AlkB (0.2 μM) was incubated with either 15-mer RNA (containing m^6A, 1 μM) or trimer DNA (containing m^1A, 1 μM), 2OG (20 μM), $(NH_4)_2Fe(SO_4)_2$ (20 μM) and ascorbic acid (200 μM) at 25ºC. Reaction progress was monitored in real-time by Rapidfire mass spectrometry (RF-MS). The mass spectra were recorded initially in one-minute intervals for 10 mins, then every five minutes for 35 mins (Figures 4.18 and 4.19).

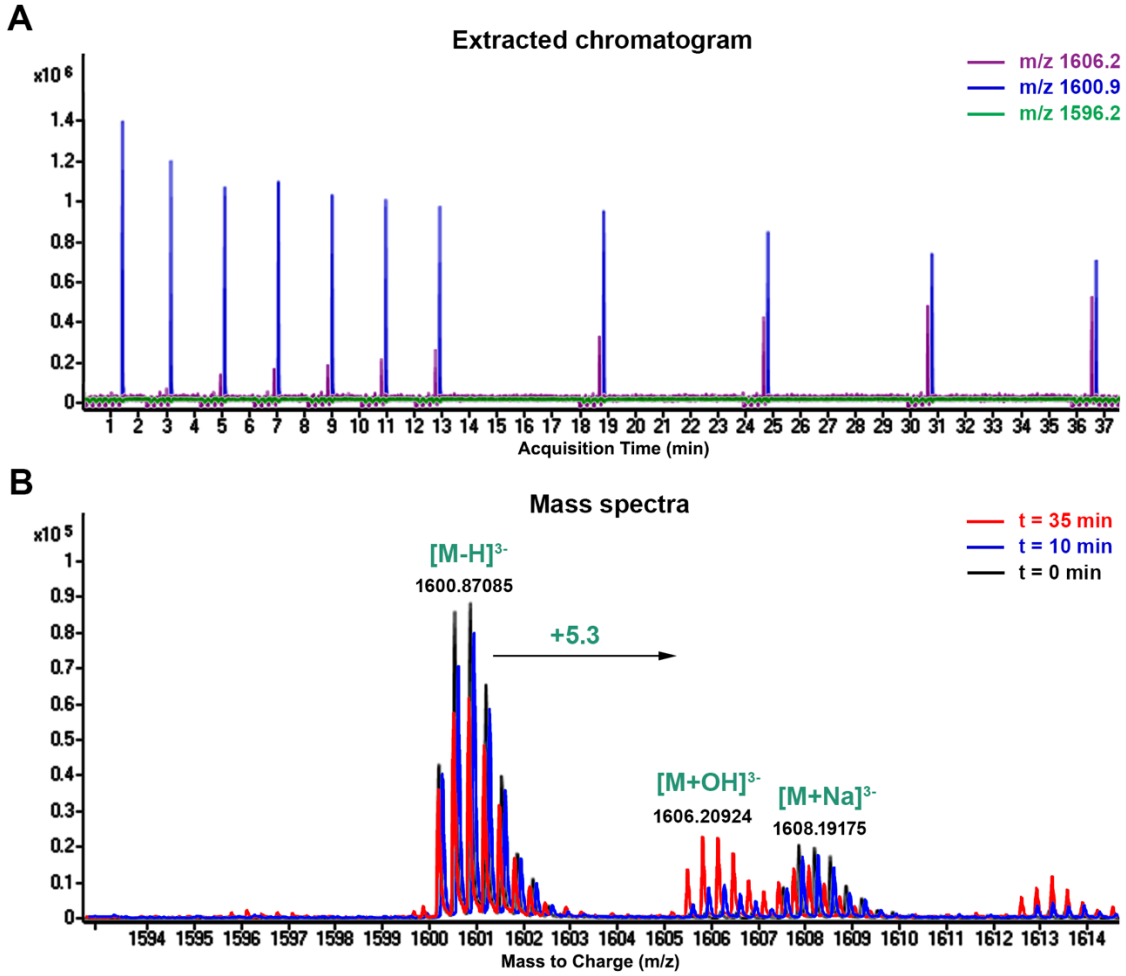


Figure 3.18: *RF-MS data showing AlkB-catalysed reaction with 15-mer RNA. (A) The extracted ion chromatograms show that the 15-mer oligomer substrate (m/z 1600.9, -3 charge state) is converted to a hydroxylated product (m/z 1606.2, -3 charge state). Mass spectra taken at different time points are shown in (B).*

For AlkB with the 15-mer RNA oligomer substrate, the demethylated product was not observed under the RF-MS assay conditions. Instead only hydroxylation was observed, albeit at a very low level. No evidence for oxidation from hm^{6}A to f^{6}A was observed, but cannot be ruled out given the low level of conversion to hm^{6}A. This observation is consistent with the proposed scheme of FTO-catalysed hydroxylation, although the rate of hydroxylation is significantly slower compared with the FTO-catalysed reaction. Note that this reaction outcome might reflect the fact that the m^{6}A RNA is a poor AlkB substrate[33].

A contrast was observed when using a trimeric DNA substrate [T(m^1A)T]; the assay results (Figure 3.19) are consistent with previous reports[24] that AlkB is a demethylase, i.e. demethylation was observed with no evidence for formation of a hemiaminal/hydroxylation intermediate. Thus, consistent with the literature at least with methylated DNA, AlkB directly reverses m^1A alkylation *via* demethylation, probably *via* a transient hemiaminal (hm^1A) intermediate. NMR evidence[11] shows that hydroxymethyl hemiaminals on endocyclic nitrogen nucleobases, as observed with thymidine and uridine monophosphates, are less stable in solution compared with their exocyclic nitrogen nucleobase counterparts, i.e. with adenine, guanine and cytosine[11, 16]. Since the AlkB derived hydroxymethyl hemiaminal (hm^1A) would be on a endocyclic nitrogen, it is proposed that m^1A demethylation may be a product from resultant hemiaminal (hm^1A) product catalysed by AlkB, which is unstable in solution. These observations (Figures 4.18 and 4.19) indicate that AlkB has the ability to catalyse reactions to produce different outcomes depending on the substrate.

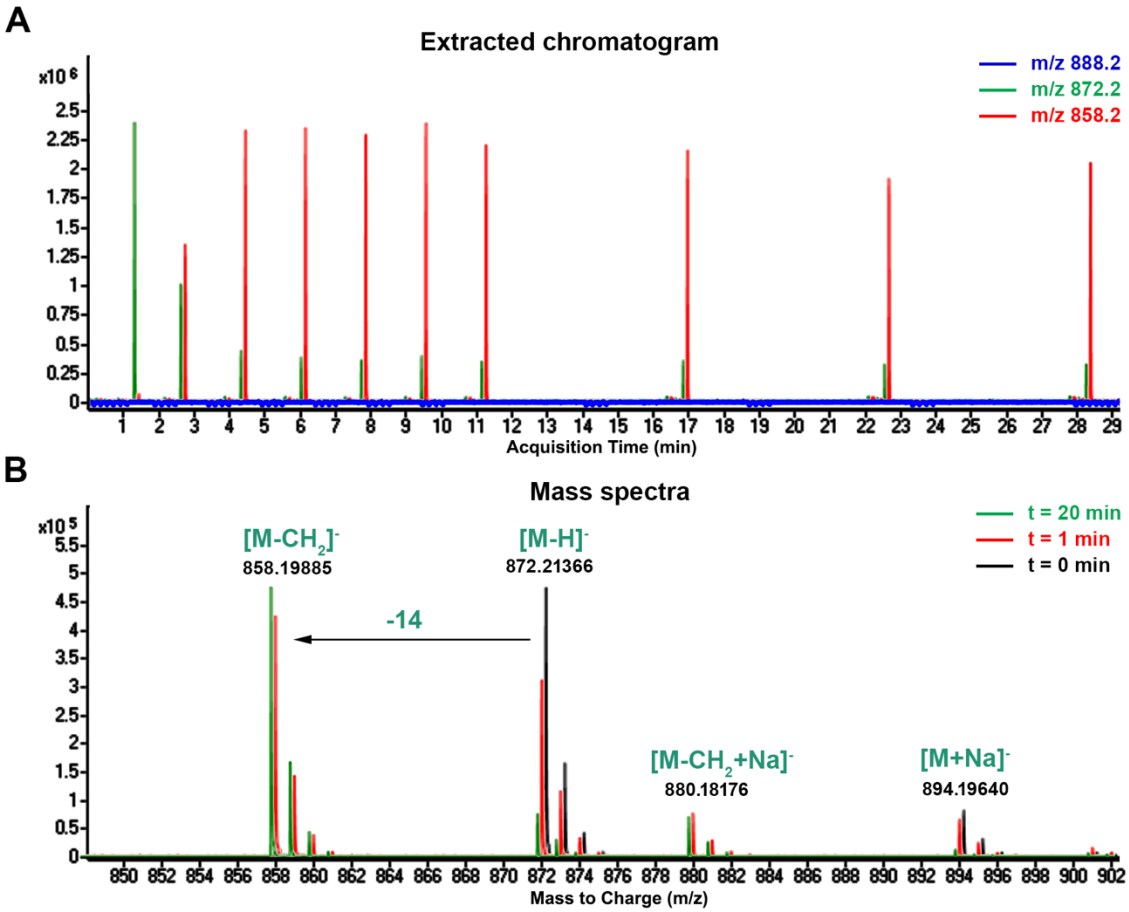


Figure 3.19: *RF-MS data showing AlkB-catalysed reaction with a ssDNA trimer, T(m¹A)T. The extracted ion chromatograms (A) show that the trimeric substrate (m/z 872, -1 charge state) is converted to the demethylated product (m/z 858.2, -1 charge state). A putative hemiaminal (hm¹A, m/z 888.2, -1 charge state) intermediate was not observed. Mass spectra taken at different time points are shown in (B).*

Studies with FTO and DNA trimer (T(m^{1}A)T) under the same conditions over 35 mins revealed no reaction (Figure 3.20), contrary to a previous report[4]. It is possible that the trimeric DNA, T(m^{1}A)T, is not a good substrate for FTO, which would explain this result.

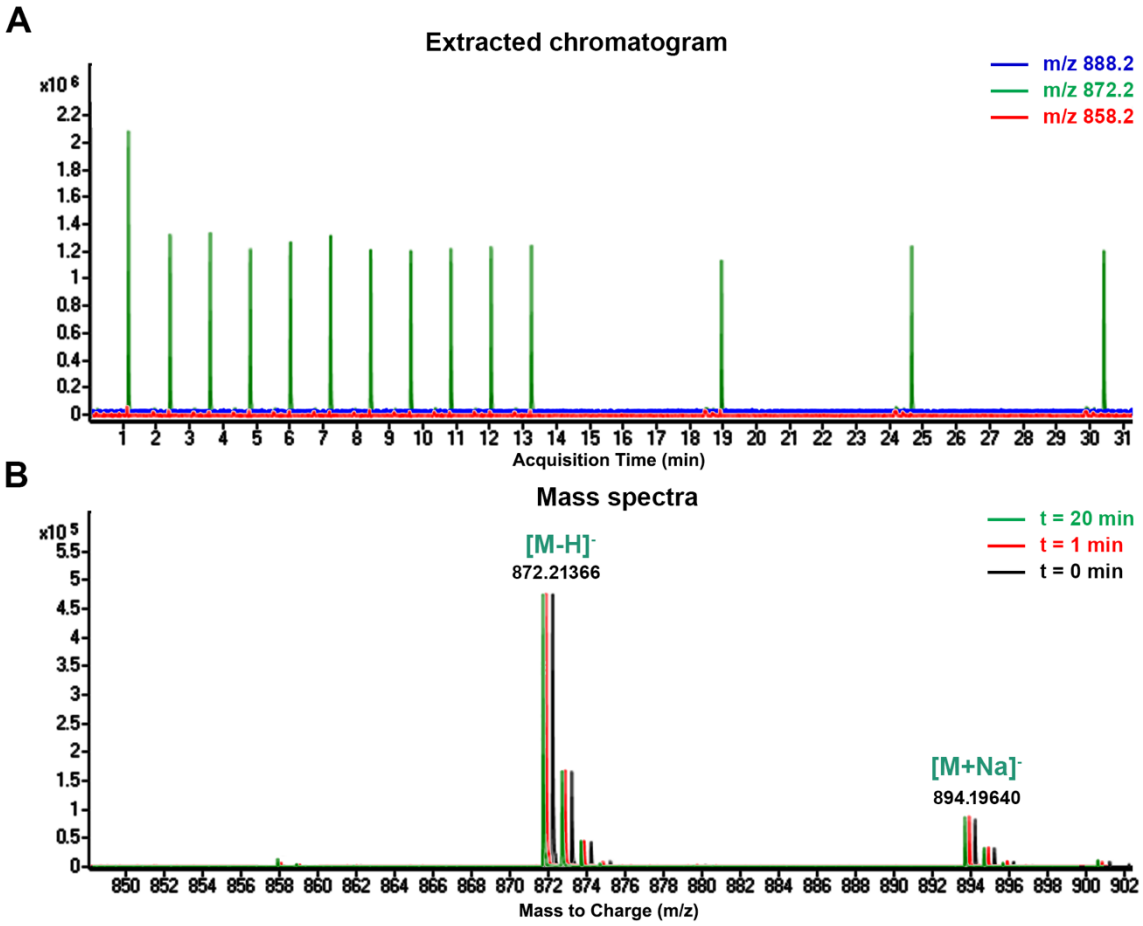


Figure 3.20: *RF-MS data showing FTO-catalysed reaction with a ssDNA trimer, T(m^{1}A)T. The extracted-ion chromatograms (A) show that the trimeric substrate (m/z 872, -1 charge state) is not converted and neither demethylation nor hydroxylation was observed. Mass spectra taken at different time points are shown in (B).*

3.5. Discussion and future work

Inspired by the observations of FTO-catalysed hydroxylation in Chapter 2, catalysis by FTO was investigated by MS-based assays, the development of which was described in the previous chapter. The observation of the presence of stable hemiaminal in the LC-MS based assays and a literature report[3] led to the proposal that FTO might better be considered a hydroxylase rather than a demethylase. One of the objectives of this work was to examine differences between FTO and closely related subfamily members, i.e. AlkB and ABH5.

RF-MS monitored real-time experiments on FTO and ABH5 under the same reaction conditions produced different outcomes; FTO produced hydroxylated product and ABH5

produced a demethylated product (Figure 3.7). The two enzymes have distinctive pH profiles (Figure 3.6), which suggests that they operate by subtly different mechanisms. FTO and ABH5 also have different biological roles: FTO-deficient mice exhibit a lean body mass and retarded growth, while male mice that are ABH5-deficient have impaired fertility[14, 34-35]. Whether or not these observations are related to the different biochemistry of the two enzymes remains to be determined. Although low levels of a demethylated species were observed during FTO-catalysed reaction, the rate of demethylation was found to be the same (within error) as that observed in the presence of the FTO inhibitor 2,4-PDCA. This observation implies that in the case of FTO, the formation of the demethylated product arises from non-enzymatic degradation of the hemiaminal rather than FTO catalysis.

Sequence alignment of the ABH5, FTO and AlkB proteins suggest that most active site residues are conserved. This implies that residues involved in nucleic acid binding determine the different outcomes of catalysis. In light of recently published data regarding the FTO-ssDNA structure[20], the superimposition of FTO and ABH5 structures reveals significant variations between the two structures (Figure 3.12); residues that are important in substrate binding by FTO are not conserved in ABH5. Furthermore, under the tested assay conditions, FTO did not accept RNA that contains hm^{6}A as a substrate to produce f^{6}A, as described in the literature[3]. By contrast, ABH5 catalysed the fragmentation of RNA that contained hm^{6}A to produce a demethylated product (Figure 3.7). NMR analyses supported the observations from MS studies, in which FTO catalysed hydroxylation of ^{13}C-labelled m^{6}A to give the hm^{6}A product. Although the FTO-catalysed hm^{6}A product fragmented to formaldehyde over time, formation of substantial amounts of succinate was not observed. This suggested that hm^{6}A fragmentation was non-enzyme catalysed.

Despite the reported catalysis by FTO of m^1A tRNA demethylation[4], no reaction was observed with the trimer ssDNA tested (AlkB against FTO) (Figure 3.20). By contrast, AlkB catalysed apparent hydroxylation of 15-mer RNA oligomer that contained m^6A modification at a low level, but catalysed demethylation of trimer DNA oligomer that contained m^1A modification. The observations support the proposal that FTO functions as a hydroxylase, while ABH5 functions as a demethylase, at least under same conditions. This was supported by studies with mouse FTO (mFTO), which showed an identical reaction outcome of hFTO, i.e. production of the hydroxylated (hm^6A) product.

Overall, the comparative studies on FTO and its related 2OG oxygenase subfamily members strongly support the proposal that isolated FTO principally functions as a hydroxylase rather than demethylase, at least on the tested substrates. These results also support the proposal that hm^6A is a stable modification in RNA. Note that the stability of hm^6A is likely to reflect the electron-rich nature of the exocyclic N^6 nitrogen of adenosine when compared with the unstable hemiaminal adduct (hm^1A) on endocyclic nitrogen[11].

It should be noted that owing to its ability to monitor reactions in real-time without interference, the RF-MS based assay employed only manifested hydroxylated FTO product (hm^6A), which contrasted with reported results[1-3]. All previous studies on FTO (and ABH5) have involved additional enzymatic treatment (digestion assay) post FTO (and ABH5) reaction[1-4, 14].

Knowledge regarding the hydroxylase activity of recombinant FTO may aid investigations into its function in cellular contexts. FTO and the methyltransferase proteins (METTLs), which catalyse hydroxylation and methylation respectively, determine the modification status of mRNA (both are localised in nuclear speckles[2]). Formation of the hydroxymethyl group on the N^6 position of adenosine may act as a blockade, through which the hydroxylated RNA could be exported/diffused out of the nucleus for down-stream processing. This may be in part

regulated by pH as well as catalytic deformylation. m^6A "reader" proteins, such as YTHDF2, may or may not recognise hm^6A, and the hm^6A modification could serve as a marker to recruit a different set of RNA-binding proteins. Silencing of m^6A methyltransferase METTL3 can lead to varied circadian rhythm and delayed RNA processing[36]. Therefore, FTO may be involved in the regulation of circadian rhythm, as its hydroxylated product (hm^6A) intrinsically decomposes over time to regenerate A (adenosine) on which methyltransferases can act.

Acknowledgements

NMR analyses were carried out by Miss Shifali Shishodia, under the supervision of Dr Richard J. Hopkinson and Prof Timothy D.W. Claridge; Shifali Shishodia also synthesised m^6A phosphoramidite and ^{13}C-labelled m^6A nucleoside. The 15-mer RNA oligonucleotide that contained the m^6A modification was synthesised by Dr Afaf H. El-Sagheer. The RF-MS assay of FTO compared with ABH5 was conducted in collaboration with Dr Anthony Tumber.

References

1. Jia, G.; Yang, C. G.; Yang, S.; Jian, X.; Yi, C.; Zhou, Z.; He, C., Oxidative demethylation of 3-methylthymine and 3-methyluracil in single-stranded DNA and RNA by mouse and human FTO. *FEBS Lett* **2008,** *582* (23-24), 3313-9.

2. Jia, G.; Fu, Y.; Zhao, X.; Dai, Q.; Zheng, G.; Yang, Y.; Yi, C.; Lindahl, T.; Pan, T.; Yang, Y.-G.; He, C., N6-methyladenosine in nuclear RNA is a major substrate of the obesity-associated FTO. *Nat Chem Biol* **2011,** *7*, 885-7.

3. Fu, Y.; Jia, G.; Pang, X.; Wang, R. N.; Wang, X.; Li, C. J.; Smemo, S.; Dai, Q.; Bailey, K. A.; Nobrega, M. A.; Han, K.-L.; Cui, Q.; He, C., FTO-mediated formation of N6-hydroxymethyladenosine and N6-formyladenosine in mammalian RNA. *Nature Commun* **2013,** *4*, 1798-801.

4. Wei, J.; Liu, F.; Lu, Z.; Fei, Q.; Ai, Y.; He, P. C.; Shi, H.; Cui, X.; Su, R.; Klungland, A.; Jia, G.; Chen, J.; He, C., Differential m(6)A, m(6)Am, and m(1)A demethylation mediated by FTO in the cell nucleus and cytoplasm. *Mol Cell* **2018,** *71* (6), 973-985 e5.

5. Tahiliani, M.; Koh, K. P.; Shen, Y.; Pastor, W. A.; Bandukwala, H.; Brudno, Y.; Agarwal, S.; Iyer, L. M.; Liu, D. R.; Aravind, L.; Rao, A., Conversion of 5-methylcytosine to 5-hydroxymethylcytosine in mammalian DNA by MLL partner TET1. *Science* **2009,** *324* (5929), 930-5.

6. He, Y. F.; Li, B. Z.; Li, Z.; Liu, P.; Wang, Y.; Tang, Q.; Ding, J.; Jia, Y.; Chen, Z.; Li, L.; Sun, Y.; Li, X.; Dai, Q.; Song, C. X.; Zhang, K.; He, C.; Xu, G. L., Tet-mediated formation of 5-carboxylcytosine and its excision by TDG in mammalian DNA. *Science* **2011,** *333* (6047), 1303-7.

7. Ito, S.; Shen, L.; Dai, Q.; Wu, S. C.; Collins, L. B.; Swenberg, J. A.; He, C.; Zhang, Y., Tet proteins can convert 5-methylcytosine to 5-formylcytosine and 5-carboxylcytosine. *Science* **2011,** *333* (6047), 1300-3.

8. Walport, L. J.; Hopkinson, R. J.; Schofield, C. J., Mechanisms of human histone and nucleic acid demethylases. *Curr Opin Chem Biol* **2012,** *16* (5-6), 525-34.

9. Hopkinson, R. J.; Hamed, R. B.; Rose, N. R.; Claridge, T. D. W.; Schofield, C. J., Monitoring the activity of 2-oxoglutarate dependent histone demethylases by NMR spectroscopy: direct observation of formaldehyde. *ChemBioChem* **2010,** *11* (4), 506-510.

10. Walport, L. J.; Hopkinson, R. J.; Chowdhury, R.; Zhang, Y.; Bonnici, J.; Schiller, R.; Kawamura, A.; Schofield, C. J., Mechanistic and structural studies of KDM-catalysed demethylation of histone 1 isotype 4 at lysine 26. *FEBS Letters* **2018,** *592* (19), 3264-3273.

11. Shishodia, S.; Zhang, D.; El-Sagheer, A. H.; Brown, T.; Claridge, T. D. W.; Schofield, C. J.; Hopkinson, R. J., NMR analyses on N-hydroxymethylated nucleobases - implications for formaldehyde toxicity and nucleic acid demethylases. *Org Biomol Chem* **2018,** *16* (21), 4021-32.

12. Mishina, Y.; He, C., Oxidative dealkylation DNA repair mediated by the mononuclear non-heme iron AlkB proteins. *J Inorg Biochem* **2006,** *100* (4), 670-8.

13. Porta, T.; Lesur, A.; Varesio, E.; Hopfgartner, G., Quantification in MALDI-MS imaging: what can we learn from MALDI-selected reaction monitoring and what can we expect for imaging? *Anal Bioanal Chem* **2015,** *407* (8), 2177-2187.

14. Zheng, G.; Dahl, John A.; Niu, Y.; Fedorcsak, P.; Huang, C.-M.; Li, Charles J.; Vågbø, Cathrine B.; Shi, Y.; Wang, W.-L.; Song, S.-H.; Lu, Z.; Bosmans, Ralph P. G.; Dai, Q.; Hao, Y.-J.; Yang, X.; Zhao, W.-M.; Tong, W.-M.; Wang, X.-J.; Bogdan, F.; Furu, K.; Fu, Y.; Jia, G.; Zhao, X.; Liu, J.; Krokan, Hans E.; Klungland, A.; Yang, Y.-G.; He, C., ALKBH5 Is a mammalian RNA demethylase that impacts RNA metabolism and mouse fertility. *Mol Cell* **2013,** *49* (1), 18-29.

15. Iwasawa, T.; Hooley, R. J.; Rebek, J., Stabilization of labile carbonyl addition intermediates by a synthetic receptor. *Science* **2007,** *317* (5837), 493-6.

16. Shishodia, S., DPhil Thesis: Inhibition and mechanistic studies of FTO. *University of Oxford*, Oxford, **2017**.

17. Sievers, F.; Wilm, A.; Dineen, D.; Gibson, T. J.; Karplus, K.; Li, W.; Lopez, R.; McWilliam, H.; Remmert, M.; Söding, J.; Thompson, J. D.; Higgins, D. G., Fast, scalable generation of high-quality protein multiple sequence alignments using Clustal Omega. *Mol Syst Biol* **2011,** *7* (1), 539.

18. McDonough, M. A.; Loenarz, C.; Chowdhury, R.; Clifton, I. J.; Schofield, C. J., Structural studies on human 2-oxoglutarate dependent oxygenases. *Curr Opin Struct Biol* **2010,** *20* (6), 659-672.

19. Han, Z.; Niu, T.; Chang, J.; Lei, X.; Zhao, M.; Wang, Q.; Cheng, W.; Wang, J.; Feng, Y.; Chai, J., Crystal structure of the FTO protein reveals basis for its substrate specificity. *Nature* **2010,** *464*, 1205-9.

20. Zhang, X.; Wei, L.-H.; Wang, Y.; Xiao, Y.; Liu, J.; Zhang, W.; Yan, N.; Amu, G.; Tang, X.; Zhang, L.; Jia, G., Structural insights into FTO's catalytic mechanism for the demethylation of multiple RNA substrates. *Proc Natl Acad Sci USA* **2019,** *116* (8), 2919-24.

21. Mauer, J.; Luo, X.; Blanjoie, A.; Jiao, X.; Grozhik, A. V.; Patil, D. P.; Linder, B.; Pickering, B. F.; Vasseur, J. J.; Chen, Q.; Gross, S. S.; Elemento, O.; Debart, F.; Kiledjian, M.; Jaffrey, S. R., Reversible methylation of m(6)Am in the 5' cap controls mRNA stability. *Nature* **2017,** *541* (7637), 371-375.

22. Xu, C.; Liu, K.; Tempel, W.; Demetriades, M.; Aik, W.; Schofield, C. J.; Min, J., Structures of human ALKBH5 demethylase reveal a unique binding mode for specific single-stranded N6-methyladenosine RNA demethylation. *J Biol Chem* **2014,** *289* (25), 17299-311.

23. Aik, W.; Demetriades, M.; Hamdan, M. K.; Bagg, E. A.; Yeoh, K. K.; Lejeune, C.; Zhang, Z.; McDonough, M. A.; Schofield, C. J., Structural basis for inhibition of the fat mass and obesity associated protein (FTO). *J Med Chem* **2013,** *56* (9), 3680-8.

24. Falnes, P. O., Repair of 3-methylthymine and 1-methylguanine lesions by bacterial and human AlkB proteins. *Nucleic Acids Res* **2004,** *32* (21), 6260-7.

25. Duncan, T.; Trewick, S. C.; Koivisto, P.; Bates, P. A.; Lindahl, T.; Sedgwick, B., Reversal of DNA alkylation damage by two human dioxygenases. *Proc Natl Acad Sci USA* **2002,** *99* (26), 16660-5.

26. Westbye, M. P.; Feyzi, E.; Aas, P. A.; Vågbø, C. B.; Talstad, V. A.; Kavli, B.; Hagen, L.; Sundheim, O.; Akbari, M.; Liabakk, N.-B.; Slupphaug, G.; Otterlei, M.; Krokan, H. E., Human AlkB homolog 1 is a mitochondrial protein that demethylates 3-methylcytosine in DNA and RNA. *J Biol Chem* **2008,** *283* (36), 25046-56.

27. Li, M. M.; Nilsen, A.; Shi, Y.; Fusser, M.; Ding, Y. H.; Fu, Y.; Liu, B.; Niu, Y.; Wu, Y. S.; Huang, C. M.; Olofsson, M.; Jin, K. X.; Lv, Y.; Xu, X. Z.; He, C.; Dong, M. Q.; Rendtlew Danielsen, J. M.; Klungland, A.; Yang, Y. G., ALKBH4-dependent demethylation of actin regulates actomyosin dynamics. *Nat Commun* **2013,** *4*, 1832-45.

28. Fu, Y.; Dai, Q.; Zhang, W.; Ren, J.; Pan, T.; He, C., The AlkB domain of mammalian ABH8 catalyzes hydroxylation of 5-methoxycarbonylmethyluridine at the wobble position of tRNA. *Angew Chem* **2010,** *49* (47), 8885-8.

29. Delaney, J. C.; Smeester, L.; Wong, C.; Frick, L. E.; Taghizadeh, K.; Wishnok, J. S.; Drennan, C. L.; Samson, L. D.; Essigmann, J. M., AlkB reverses etheno DNA lesions caused by lipid oxidation in vitro and in vivo. *Nat Struct Mol Biol* **2005,** *12* (10), 855-60.

30. Falnes, P. O.; Johansen, R. F.; Seeberg, E., AlkB-mediated oxidative demethylation reverses DNA damage in Escherichia coli. *Nature* **2002,** *419* (6903), 178-82.

31. Mishina, Y.; Yang, C. G.; He, C., Direct repair of the exocyclic DNA adduct 1,N6-ethenoadenine by the DNA repair AlkB proteins. *J Am Chem Soc* **2005,** *127* (42), 14594-5.

32. Li, D.; Delaney, J. C.; Page, C. M.; Yang, X.; Chen, A. S.; Wong, C.; Drennan, C. L.; Essigmann, J. M., Exocyclic carbons adjacent to the N6 of adenine are targets for oxidation by the Escherichia coli adaptive response protein AlkB. *J Am Chem Soc* **2012,** *134* (21), 8896-901.

33. Zhu, C.; Yi, C., Switching Demethylation Activities between AlkB Family RNA/DNA Demethylases through Exchange of Active-Site Residues. *Angew Chem* **2014,** *53* (14), 3659-62.

34. Church, C.; Moir, L.; McMurray, F.; Girard, C.; Banks, G. T.; Teboul, L.; Wells, S.; Bruning, J. C.; Nolan, P. M.; Ashcroft, F. M.; Cox, R. D., Overexpression of Fto leads to increased food intake and results in obesity. *Nat Genet* **2010,** *42* (12), 1086-92.

35. Fischer, J.; Koch, L.; Emmerling, C.; Vierkotten, J.; Peters, T.; Bruning, J. C.; Ruther, U., Inactivation of the Fto gene protects from obesity. *Nature* **2009,** *458* (7240), 894-8.

36. Fustin, J. M.; Doi, M.; Yamaguchi, Y.; Hida, H.; Nishimura, S.; Yoshida, M.; Isagawa, T.; Morioka, M. S.; Kakeya, H.; Manabe, I.; Okamura, H., RNA-methylation-dependent RNA processing controls the speed of the circadian clock. *Cell* **2013,** *155* (4), 793-806.

Chapter 4

Biochemical studies on an FTO variant

Table of Contents

4.1. Introduction 151

4.2. Chapter Objectives 152

4.3. Production of FTO variants 153

4.4. Structural rationalisation 154

4.5. Circular dichroism (CD) 156

4.6. LC-MS demethylation assay 157

4.7. 2OG turnover assay by NMR 158

4.8. Discussion and future work 160

Acknowledgements **163**

References **164**

4. Biochemical studies on an FTO variant

4.1. Introduction

The fat mass and obesity-associated gene, *Fto,* encodes for the fat mass and obesity-associated protein (FTO). Studies have shown that single nucleotide polymorphisms (SNPs) in the first intron of the *Fto* gene correlated with an increased risk of childhood and adult obesity[1-2]. Subsequent studies in mice further support an important role of the *Fto* gene in energy homeostasis and fat mass regulation. Inactivation of FTO leads to reduction in the amount of adipose tissue and leaner body mass[3-4], and over-expression of FTO leads to increased food intake and results in obesity[5].

While the link between *Fto* SNPs and obesity seems to be robust, several studies suggest that rare variants in FTO alone do not appear to be related to risk of obesity in the studied populations[6-8]. By contrast, a homozygous loss-of-function (LOF) variant in FTO, p.(Arg316Gln), has been identified[9]. Affected individuals show severe growth retardation and multiple congenital malformations that include microcephaly, severe psychomotor delay, cardiomyopathy and characteristic facial features[9]. This finding suggests that FTO is required for the normal development of human central nervous and cardiovascular systems, at least at the developmental stage; and that homozygous LOF mutations in the *Fto* gene can lead to an autosomal recessive lethal disorder and multiple defects. A novel pathogenic mutation in *Fto*, p.(Ser319Phe), identified by next-generation sequencing (NGS) in a newborn human, has been identified[10]. The affected individual exhibits similar (but milder) clinical features as previously reported[9]. It was proposed that the cause is related to *Fto* gene mutation, hence a biochemical and biophysical investigation was carried out to assess the likelihood of a link between the observed pathogenic mutation and FTO enzyme activity. No other genetic disease-causing mutation in *Fto* has yet been reported prior to the work detailed in this chapter.

4.2. Objectives

A new pathogenic mutation has been identified in the *Fto* gene, termed p.(Ser319Phe)[10]. This shows severe clinical features, as does the loss of function p.(Arg316Gln3) mutation[9]. The p.(Arg316Gln3) mutation affects a catalytically important residue (Arg316), which is reported to be essential for 2-oxoglutarate (2OG) binding by FTO[9]. The p.(Ser319Phe) mutation affects a residue (Ser319) in a similar region to Arf316, possibly explaining the similar clinical features. The main objective of the work described in this chapter was to aid in functional assignment work on FTO, by identifying links between FTO (in)activity and physiology, through the kinetic/biochemical characterisation of wild-type FTO and the clinically observed FTO variant (Ser319Phe). Note this work was carried out before the development of the new FTO assays detailed in Chapter 2.

Please note that much of the work detailed in this chapter has been reported in the academic literature in: '*Identification of a pathogenic FTO mutation by next-generation sequencing in a newborn with growth retardation and developmental delay*', doi: 10.1136/jmedgenet-2015-103399.

4.3. Production of FTO variants

For biochemical characterisation of wild-type and clinical variants of FTO, mutational analyses were carried out on the Arg316 and Ser319 residues of FTO, respectively. The Ser319Phe and Arg316Gln FTO variants were produced by site-directed mutagenesis using standard methods as described in Chapter 6 (Materials and Methods).

Since the residues being substituted were not on the surface of the protein, it was proposed that the same protein preparation methods could be used for the two variants, hence expression trials were not necessary. The wild-type and two variant FTO proteins were prepared as described in Chapter 2 and Chapter 6, using Ni-affinity and heparin-affinity columns sequentially. At each stage in the purifications, protein purity was determined by sodium dodecyl sulphate-polyacrylamide gel electrophoresis (SDS-PAGE) (Figure 4.1). Once purification was complete, the molecular weights of the proteins were confirmed by electrospray ionisation-mass spectrometry (ESI-MS) (Figure 4.2).

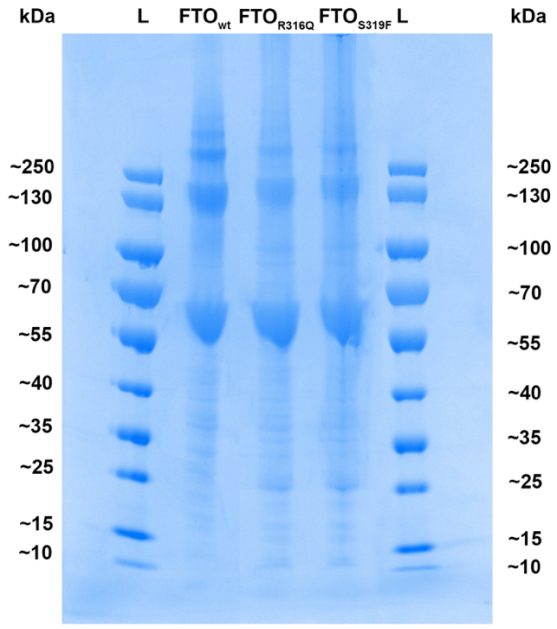
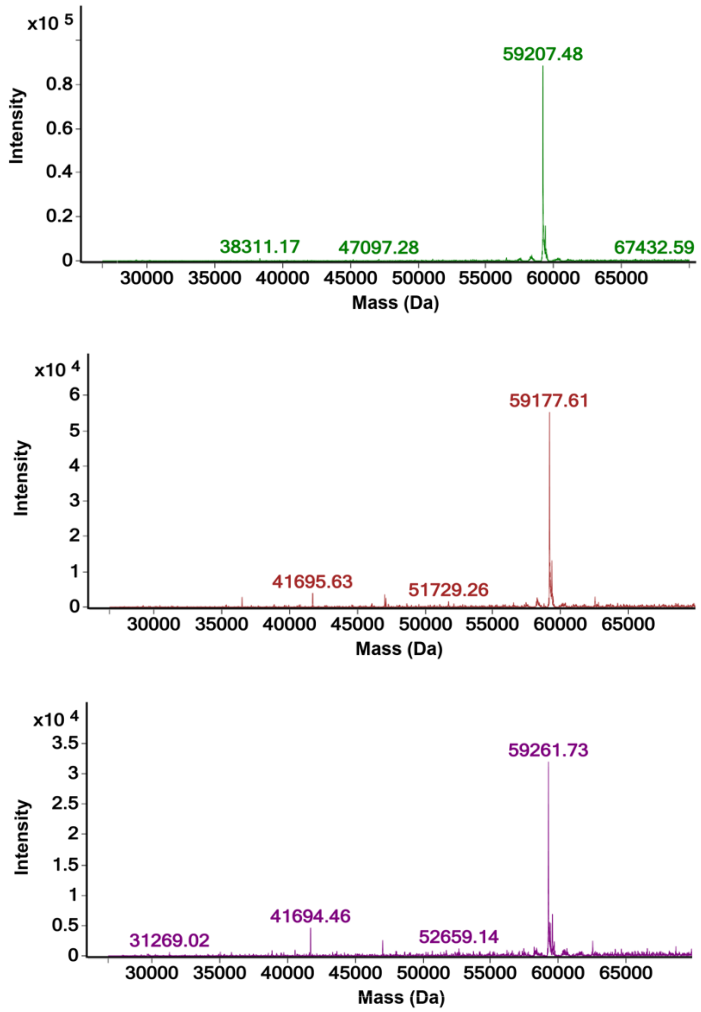


Figure 4.1: *SDS-PAGE Gel of wild-type, Ser319Phe, and Arg316Gln FTO, after metal-ion affinity purification by elution from an immobilised nickel column (HisTrap) with a gradient of 0-0.5 M imidazole, and heparin affinity purification by elution from an immobilised heparin column (Heparin) with a gradient of 0-2 M NaCl, at pH 7.5. All enzyme purification steps were carried out at 4 °C. FTO_{wt}: wild-type FTO; FTO_{S319F}: Ser319Phe FTO; FTO_{R316Q}: Arg316Gln FTO.*



Enzyme	Predicted mass (Da)	Measured mass (Da)
FTO_{wt}	59204.91	59207.48
FTO_{R316Q}	59176.85	59177.61
FTO_{S319F}	59265.01	59261.73

Figure 4.2: *Masses of enzymes newly purified for this study as determined by ESI-MS. Enzymes were assayed at c.a. 10 μM in 50 mM Tris buffer, pH 7.5. The predicted masses, based on amino acid sequences, are also provided. Green, wild-type FTO (FTO_{wt}); Brown, FTO_{R316Q}; Purple, FTO_{S319F}.*

4.4. Structural rationalisation

The genes of a 21-month-old girl who exhibited distinctive facial features, failure to thrive, global developmental delay, left ventricular cardiac hypertrophy, reduced vision and bilateral hearing loss, were investigated with Next Generation Sequencing (NGS)[10]. The results showed that a homozygous single nucleotide variant (c.956C>T) was located in exon 5 of the *Fto* gene (NM_001080432.2), leading to the substitution of serine by phenylalanine at codon 319. This

residue (Ser319) is located on the VIII β-strand of the distorted double-stranded β-helix (DSBH) core fold, which is conserved in 2OG-oxygenases, including FTO[11].

It seemed likely that the p.(Arg316Gln) substitution would affect catalysis by FTO, because Arg316 is essential for co-substrate (2OG) binding[9]. Due to its close proximity to the 2OG-binding site of FTO (Figure 4.3), it was proposed that the p.(Ser319Phe) substitution could hinder the FTO 2OG co-substrate binding, albeit possibly to a lesser extent than would be caused by p.(Arg316Gln) substitution. A crystal structure of wild-type FTO (PDB ID: 4IDZ) was used to model the effect of the p.(Ser319Phe) substitution on protein structure (modelling was performed by Dr Hwanho Choi). The residue Ser319 is located on the β-strand VIII, which is part of the double stranded β-helix (DSBH) core. However, the Ser319 side-chain faces away from of the active site. Since Ser319 is not directly involved in the binding of 2OG, it was proposed that p.(Ser319Phe) substitution might have had limited effect on FTO activity. However, the Ser319 residue forms polar interactions with its neighbouring residues (Figure 4.3 B), which may be important for stabilisation and proper folding of the protein. Substitution to a hydrophobic residue (i.e. Phe) may interrupt these polar interactions, and thus may affect 2OG binding.

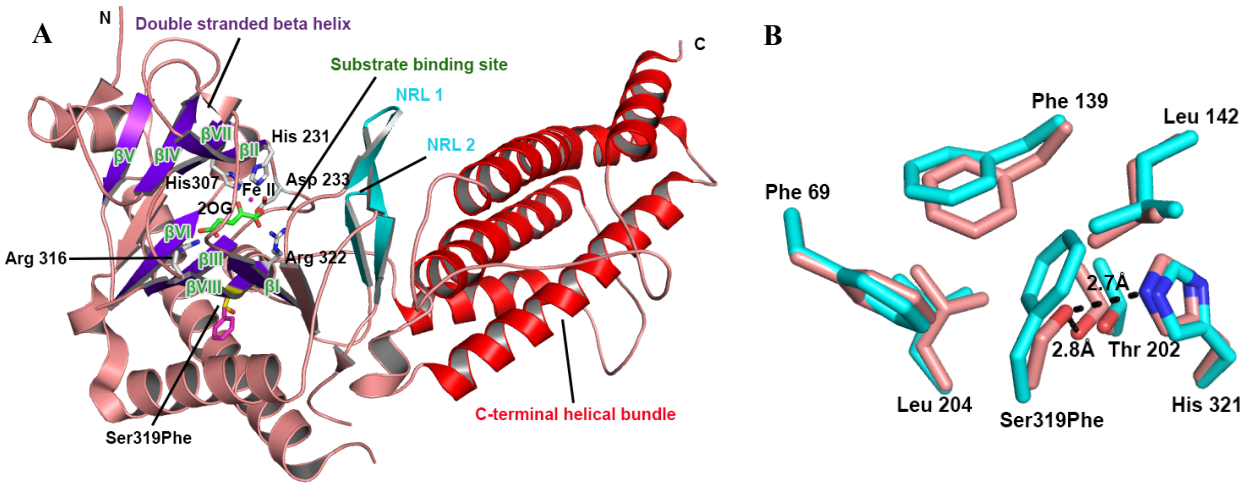


Figure 4.3: *Modelling of the three-dimensional structure of the p.(Ser319Phe) FTO substitution. (A) Ribbon representation of a crystal structure of FTO (PDB 4IDZ) with Fe(II), 2OG and a model of the p.(Ser319Phe) substitution. The core DSBH is in purple and the eight strands of the conserved DSBH core fold are labelled according to convention[12]. Substitution of either of two other residues positioned on DSBH strand β-VIII has been shown to affect activity. Arg316 plays a key role in binding the 2OG C-5 carboxylate: the Arg316Gln FTO is inactive. (B) Close-up sticks representation of the region around wild-type FTO Ser319 (salmon) and the modelled Phe319 (turquoise), indicating how neighbouring residues may accommodate the substitution. The p.(Ser319Phe) substitution results in the loss of two hydrogen bonds with Thr202 and His321. The bulky nature of the phenylalanine side chain appears to distort this region, which is positioned near the 2OG-binding site, and thus, may affect 2OG binding.*

4.5. Circular dichroism (CD)

To test whether protein stability was structurally affected by p.(Ser319Phe) substitution, circular dichroism (CD) spectroscopy was employed. This method can detect and quantify secondary structures in proteins, based on the interaction of circularly polarised light with the protein in solution[13]. The CD spectra of the wild-type and Ser319Phe FTO were the same, within limits of detection, which indicated the presence of highly similar secondary-structure characteristics of the same overall protein fold (Figure 4.4 A). To analyse potential stability differences, wild-type and Ser319Phe FTO were compared by CD measurements at 222 nm while increasing the temperature. The melting temperatures for wild-type and Ser319Phe FTO were almost indistinguishable, suggesting that the two proteins exhibited similar stabilities (Figure 4.4 B). However, the refolding results suggest that, unlike wild-type FTO (Figure 4.4 C), Ser319Phe FTO does not refold completely after thermal denaturation (Figure 4.4 D). This

could be due to hydrophobic aggregation caused by the exposed Phe319 residue (Figure 4.3 B).

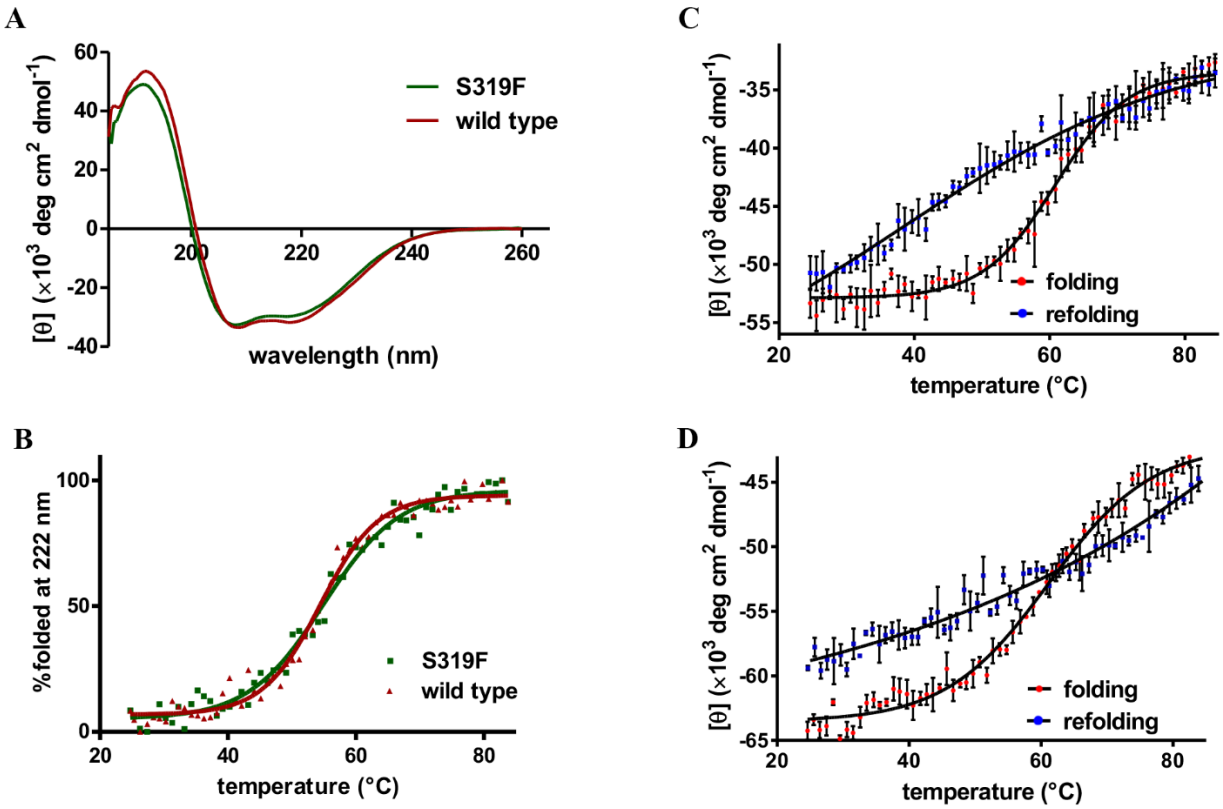


Figure 4.4: *(A) The CD spectra of wild-type (red) and Ser319Phe (green) FTO (measured at 0.2 mg/mL protein concentration) are similar, which suggests correct folding of the Ser319Phe FTO variant. (B) Thermal melting curves show Tm ~54.5 °C for both wild-type (red) and Ser319Phe (green) FTO (measured at 0.4 mg/mL protein concentration). The right-hand graphs show unfolding (red) and refolding (blue) of (C) wild-type and (D) Ser319Phe FTO; note that the Ser319Phe FTO variant appears not to re-fold as completely as wild-type FTO under these conditions.*

4.6. LC-MS demethylation assays

The demethylation activity of Ser319Phe FTO was next investigated by LC-MS, using 3-methylthymine (m^3T) nucleoside. Wild-type and Arg316Gln FTO were included for comparison studies. The m^3T substrate (70 μM) was incubated with the FTO proteins (3 μM), 2OG (160 μM), L-ascorbate (500 μM), and diammonium iron(II) sulphate (100 μM) in 50 mM Tris buffer, pH 7.5, at 25 ºC for 1 hour. Demethylation as catalysed by Ser319Phe FTO was observed, but at a much reduced level compared with wild-type FTO. Arg316Gln FTO completely ablated catalytic activity (Figure 4.5 A). Time-course experiments were carried out

on the Ser319Phe FTO at different enzyme concentrations; demethylation reactions were monitored over 70 minutes. Again the time courses showed reduced, but not ablated, enzyme activity of Ser319Phe FTO compared with wild-type FTO (Figure 4.5 B, C). The result in Figure 4.5 D shows that Arg316Gln FTO is inactive.

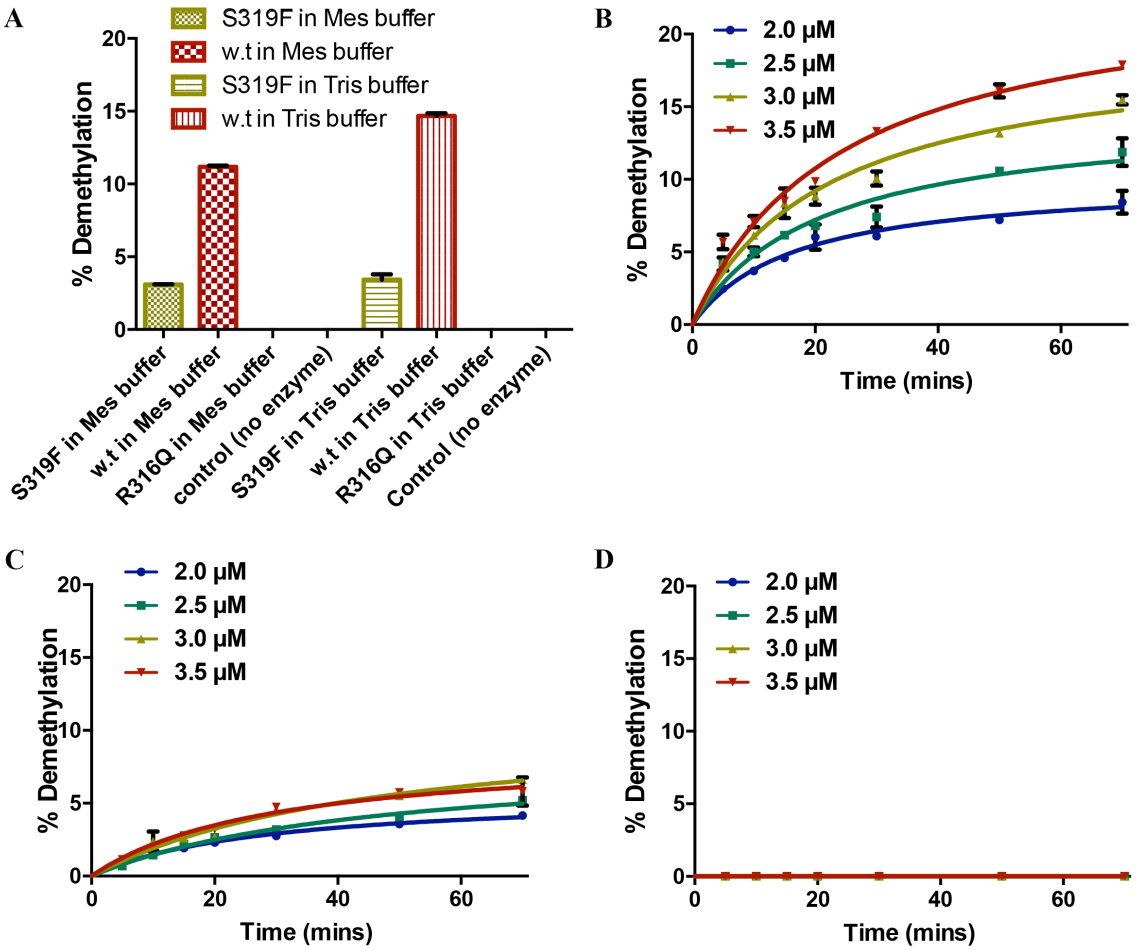


Figure 4.5: *(A) LC-MS analyses of demethylation of m^{3}T (70 µM) by wild-type, Ser319Phe, and Arg316Gln FTO (3 µM) after one-hour incubation at 25 ºC. . Time course of (B) wild-type, (C) Ser319Phe, and (D) Arg316Gln FTO at different enzyme concentrations. Key: w.t: wild-type; FTO$_{R316Q}$: Arg316Gln FTO; FTO$_{S319F}$: Ser319Phe.*

4.7. 2OG turnover assay by NMR

Analysis by ^{1}H NMR was performed to investigate whether Ser319Phe FTO could catalyse the oxidation of the co-substrate 2OG to the succinate product in the presence of m^{6}A primary substrate (2OG turnover, Figure 4.6 A). A reaction mixture that consisted of m^{6}A (4 µM), L-

ascorbate (1 mM), diammonium iron(II) sulphate (100 μM), and FTO proteins (20 μM) in 50 mM ammonium formate buffer (AFN) was prepared in an Eppendorf tube, and then immediately transferred to a 5 mm NMR tube (Table 4.1). Time-course data were collected over a period of 45 minutes. The 2OG turnover assay was carried out with wild-type and Ser319Phe FTO, in the presence and absence of m^6A, respectively. The results demonstrate apparent 2OG turnover activity for Ser319Phe FTO, though at a reduced level compared with wild-type FTO (Figure 4.6 B, C). Although further kinetic studies may reveal mechanistic details of the effect of the FTO p.(Ser319Phe) substitution, these results clearly reveal that the activity of recombinant Ser319Phe FTO is reduced compared with that of wild-type FTO, and its refolding ability is altered.

Table 4.1: NMR analysis conditions. AFN: ammonium formate.

	Stock *mM*	**Volume** *μL*	**Final conc.** *mM*
Enzyme	0.38	32	0.02
2OG	10	50	1
Ascorbate	10	50	1
Fe(II)	0.2 in D_2O	50	0.02
m^6A	10	200	4
AFN buffer		118	

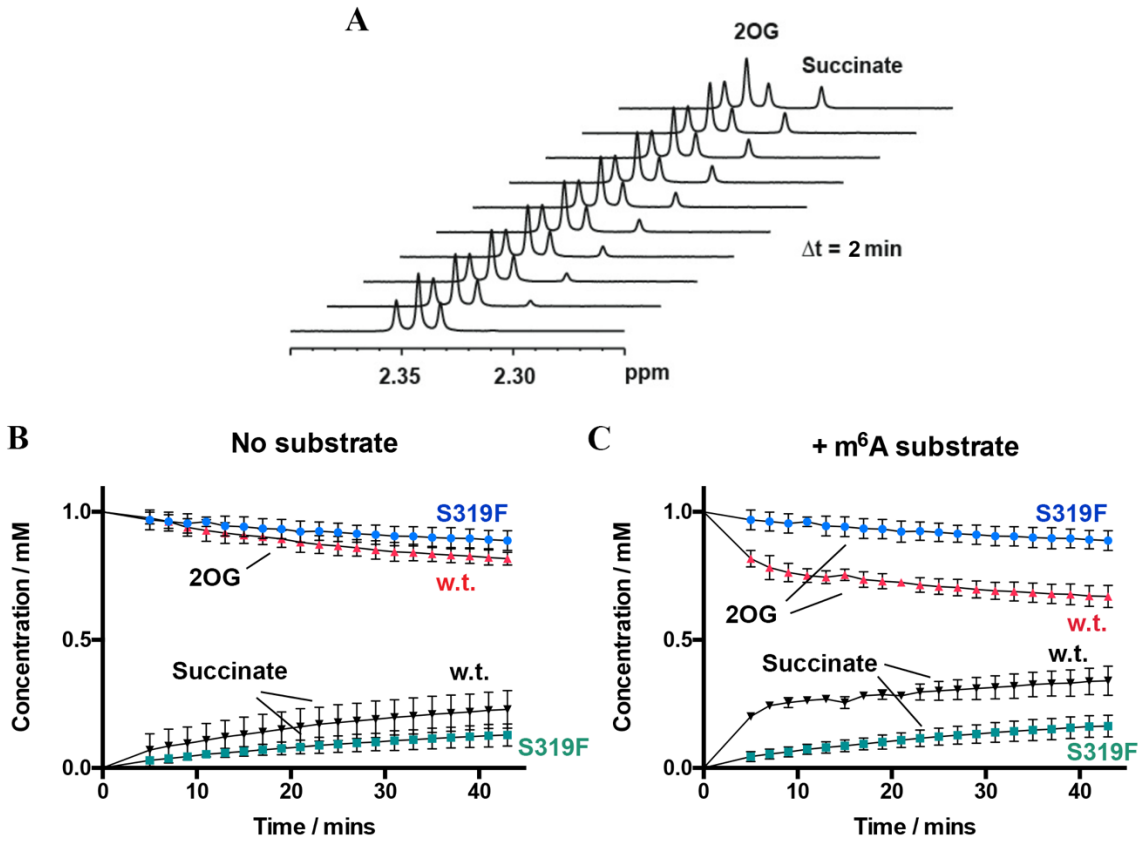


Figure 4.6: *Recombinant Ser319Phe FTO displays reduced 2OG-turnover activity compared with wild-type FTO as shown by ^{1}H NMR studies. (A) ^{1}H NMR analyses of wild-type and Ser319Phe FTO. Time-course NMR spectra demonstrate that wild-type FTO catalyses turnover of 2OG (triplet peak at 2.35 ppm) to succinate (single peak near 2.30 ppm) in the presence of m^{6}A substrate. Time course analysis of succinate production and 2OG depletion is shown (B) in the absence and (C) in the presence of m^{6}A substrate. The graphs show wild-type FTO depletion of 2OG (red), Ser319Phe FTO depletion of 2OG (blue), wild-type FTO production of succinate (black) and Ser319Phe FTO production of succinate (teal).*

4.8. Discussion and future work

A patient with novel pathogenic mutation in *Fto* was identified. The mutation revealed a FTO p.(Ser319Phe) substitution[10]. It was proposed that this substitution may have led to compromised (FTO) enzyme activity, which could result in dysregulation of RNA. Biochemical and biophysical characterisation was performed on the Ser319Phe FTO variant against its wild-type counterpart. It has been shown that the FTO p.(Ser319Phe) substitution affects a conserved residue (Ser319) located in the catalytic domain of the FTO protein (Figure

4.3), in which the affected residue is two amino acids away from the previously identified LOF substitution p.(Arg316Gln) that has been shown to ablate FTO activity[9].

Computational modelling suggests that although Ser319 is not directly involved in 2OG binding, the substitution to a hydrophobic Phe side chain may disrupt the polar interactions in the 2OG binding site, and hence destabilise the protein, which is likely to alter the 2OG binding modes. Results from LC-MS demethylation assay of the wild-type and Ser319Phe FTO support the proposal that p.(Ser319Phe) substitution affects FTO catalytic activity (Figure 4.5). The Ser319Phe substitution reduces, but does not ablate, FTO demethylation activity compared with that of wild-type FTO; in contrast, the p.(Arg316Gln) substitution inactivates FTO activity[9]. ^{1}H NMR analyses have also revealed that Ser319Phe FTO catalyses the oxidation of 2OG to succinate product, again showing reduced capacity compared with the wild-type FTO (Figure 4.6).

Arg316 is a strictly conserved 2OG binding residue in FTO[10], and is important for activity[9, 14]. Substitution of this residue causes severe growth retardation and malformations are ultimately lethal, while p.(Ser319Phe) substitution causes similar but milder symptoms. These observations strongly suggest that impaired FTO activity causes disease. FTO is highly expressed in the brain[15], and along with its subfamily member, ABH5, has been reported to demethylate m^{6}A[11, 16]. Modification of m^{6}A in mRNA plays an important role in the regulation of gene expression, mRNA splicing and transport[17-18]. The m^{6}A and its mRNA levels are regulated from early development through adulthood in a dynamic and tissue-specific manner[17-18]; mutations that affect the catalytic activity of FTO might alter the m^{6}A mRNA processing, which may affect gene expression and mRNA splicing.

FTO has also been reported to be involved in the coupling of amino acids to target rapamycin complex 1 (mTORC1) signalling in mammals. Prevention of FTO activity therefore reduces

the activation of the mTORC1 pathway and leads to an overall decrease in mRNA translation[19]. Interestingly, cells that express Arg316Gln FTO, which lack demethylase activity, have disrupted mTORC1 signalling, which suggests that FTO demethylation activity is crucial to its role in the cellular sensing of amino acids[19]. Together, results show that the Ser319Phe variant is less active than wild-type FTO, but it is still active. Therefore it is of interest to study this variant further in cellular and animal models.

In addition, mutations in FTO such as p.(Ser319Phe) substitution, which leads to severe developmental issues in the central nervous and cardiovascular systems in humans[10], may be caused by dysregulation of gene expression (perhaps *via* accumulation of m^6A). Identification of the downstream targets specifically regulated by FTO would shed more light on the pathophysiological mechanisms that lead to disease, and could open new avenues for therapeutic interventions.

Acknowledgements

The nucleoside substrate m^6A used in my work was kindly provided by Miss Shifali Shishodia.

Dr Hwanho Choi performed the modelling studies of the p.(Ser319Phe) FTO substitution.

References

1. Frayling, T. M.; Timpson, N. J.; Weedon, M. N.; Zeggini, E.; Freathy, R. M.; Lindgren, C. M.; Perry, J. R. B.; Elliott, K. S.; Lango, H.; Rayner, N. W.; Shields, B.; Harries, L. W.; Barrett, J. C.; Ellard, S.; Groves, C. J.; Knight, B.; Patch, A.-M.; Ness, A. R.; Ebrahim, S.; Lawlor, D. A.; Ring, S. M.; Ben-Shlomo, Y.; Jarvelin, M.-R.; Sovio, U.; Bennett, A. J.; Melzer, D.; Ferrucci, L.; Loos, R. J. F.; Barroso, I.; Wareham, N. J.; Karpe, F.; Owen, K. R.; Cardon, L. R.; Walker, M.; Hitman, G. A.; Palmer, C. N. A.; Doney, A. S. F.; Morris, A. D.; Smith, G. D.; Hattersley, A. T.; McCarthy, M. I., A common variant in the *FTO* gene is associated with body mass index and predisposes to childhood and adult obesity. *Science* **2007,** *316* (5826), 889-94.

2. Dina, C.; Meyre, D.; Gallina, S.; Durand, E.; Korner, A.; Jacobson, P.; Carlsson, L. M.; Kiess, W.; Vatin, V.; Lecoeur, C.; Delplanque, J.; Vaillant, E.; Pattou, F.; Ruiz, J.; Weill, J.; Levy-Marchal, C.; Horber, F.; Potoczna, N.; Hercberg, S.; Le Stunff, C.; Bougneres, P.; Kovacs, P.; Marre, M.; Balkau, B.; Cauchi, S.; Chevre, J. C.; Froguel, P., Variation in FTO contributes to childhood obesity and severe adult obesity. *Nat Genet* **2007,** *39* (6), 724-6.

3. Fischer, J.; Koch, L.; Emmerling, C.; Vierkotten, J.; Peters, T.; Bruning, J. C.; Ruther, U., Inactivation of the Fto gene protects from obesity. *Nature* **2009,** *458* (7240), 894-8.

4. McMurray, F.; Church, C. D.; Larder, R.; Nicholson, G.; Wells, S.; Teboul, L.; Tung, Y. C.; Rimmington, D.; Bosch, F.; Jimenez, V.; Yeo, G. S.; O'Rahilly, S.; Ashcroft, F. M.; Coll, A. P.; Cox, R. D., Adult onset global loss of the fto gene alters body composition and metabolism in the mouse. *PLoS Genet* **2013,** *9* (1), e1003166.

5. Church, C.; Moir, L.; McMurray, F.; Girard, C.; Banks, G. T.; Teboul, L.; Wells, S.; Bruning, J. C.; Nolan, P. M.; Ashcroft, F. M.; Cox, R. D., Overexpression of Fto leads to increased food intake and results in obesity. *Nat Genet* **2010,** *42* (12), 1086-92.

6. Meyre, D.; Proulx, K.; Kawagoe-Takaki, H.; Vatin, V.; Gutierrez-Aguilar, R.; Lyon, D.; Ma, M.; Choquet, H.; Horber, F.; Van Hul, W.; Van Gaal, L.; Balkau, B.; Visvikis-Siest, S.; Pattou, F.; Farooqi, I. S.; Saudek, V.; O'Rahilly, S.; Froguel, P.; Sedgwick, B.; Yeo, G. S., Prevalence of loss-of-function FTO mutations in lean and obese individuals. *Diabetes* **2010,** *59* (1), 311-8.

7. Deliard, S.; Panossian, S.; Mentch, F. D.; Kim, C. E.; Hou, C.; Frackelton, E. C.; Bradfield, J. P.; Glessner, J. T.; Zhang, H.; Wang, K.; Sleiman, P. M.; Chiavacci, R. M.; Berkowitz, R. I.; Hakonarson, H.; Zhao, J.; Grant, S. F., The missense variation landscape of FTO, MC4R, and TMEM18 in obese children of African ancestry. *Obesity (Silver Spring)* **2013,** *21* (1), 159-63.

8. Zheng, Z.; Hong, L.; Huang, X.; Yang, P.; Li, J.; Ding, Y.; Yao, R. E.; Geng, J.; Shen, Y.; Shen, Y.; Fu, Q.; Yu, Y., Screening for coding variants in FTO and SH2B1 genes in Chinese patients with obesity. *PLoS One* **2013,** *8* (6), e67039.

9. Boissel, S.; Reish, O.; Proulx, K.; Kawagoe-Takaki, H.; Sedgwick, B.; Yeo, G. S.; Meyre, D.; Golzio, C.; Molinari, F.; Kadhom, N.; Etchevers, H. C.; Saudek, V.; Farooqi, I. S.; Froguel, P.; Lindahl, T.; O'Rahilly, S.; Munnich, A.; Colleaux, L., Loss-of-function mutation in the dioxygenase-encoding FTO gene causes severe growth retardation and multiple malformations. *Am J Hum Genet* **2009,** *85* (1), 106-11.

10. Daoud, H.; Zhang, D.; McMurray, F.; Yu, A.; Luco, S. M.; Vanstone, J.; Jarinova, O.; Carson, N.; Wickens, J.; Shishodia, S.; Choi, H.; McDonough, M. A.; Schofield, C. J.; Harper, M. E.; Dyment, D. A.; Armour, C. M., Identification of a pathogenic FTO mutation by next-generation sequencing in a newborn with growth retardation and developmental delay. *J Med Genet* **2016,** *53* (3), 200-7.

11. Jia, G.; Fu, Y.; Zhao, X.; Dai, Q.; Zheng, G.; Yang, Y.; Yi, C.; Lindahl, T.; Pan, T.; Yang, Y.-G.; He, C., N6-Methyladenosine in nuclear RNA is a major substrate of the obesity-associated FTO. *Nat Chem Biol* **2011,** *7* (12), 885-887.

12. Clifton, I. J.; McDonough, M. A.; Ehrismann, D.; Kershaw, N. J.; Granatino, N.; Schofield, C. J., Structural studies on 2-oxoglutarate oxygenases and related double-stranded beta-helix fold proteins. *J Inorg Biochem* **2006,** *100* (4), 644-69.

13. Greenfield, N. J., Using circular dichroism spectra to estimate protein secondary structure. *Nature Protocols* **2006,** *1* (6), 2876-90.

14. Han, Z.; Huang, N.; Niu, T.; Chai, J., A loop matters for FTO substrate selection. *Protein Cell* **2010,** *1* (7), 616-20.

15. Gerken, T.; Girard, C. A.; Tung, Y. C.; Webby, C. J.; Saudek, V.; Hewitson, K. S.; Yeo, G. S.; McDonough, M. A.; Cunliffe, S.; McNeill, L. A.; Galvanovskis, J.; Rorsman, P.; Robins, P.; Prieur, X.; Coll, A. P.; Ma, M.; Jovanovic, Z.; Farooqi, I. S.; Sedgwick, B.; Barroso, I.; Lindahl, T.; Ponting, C. P.; Ashcroft, F. M.; O'Rahilly, S.; Schofield, C. J., The obesity-associated FTO gene encodes a 2-oxoglutarate-dependent nucleic acid demethylase. *Science* **2007,** *318* (5855), 1469-72.

16. Zheng, G.; Dahl, John A.; Niu, Y.; Fedorcsak, P.; Huang, C.-M.; Li, Charles J.; Vågbø, Cathrine B.; Shi, Y.; Wang, W.-L.; Song, S.-H.; Lu, Z.; Bosmans, Ralph P. G.; Dai, Q.; Hao, Y.-J.; Yang, X.; Zhao, W.-M.; Tong, W.-M.; Wang, X.-J.; Bogdan, F.; Furu, K.; Fu, Y.; Jia, G.; Zhao, X.; Liu, J.; Krokan, Hans E.; Klungland, A.; Yang, Y.-G.; He, C., ALKBH5 is a mammalian RNA Demethylase that Impacts RNA Metabolism and Mouse Fertility. *Mol Cell* **2013,** *49* (1), 18-29.

17. Meyer, K. D.; Saletore, Y.; Zumbo, P.; Elemento, O.; Mason, C. E.; Jaffrey, S. R., Comprehensive analysis of mRNA methylation reveals enrichment in 3' UTRs and near stop codons. *Cell* **2012,** *149* (7), 1635-46.

18. Dominissini, D.; Moshitch-Moshkovitz, S.; Schwartz, S.; Salmon-Divon, M.; Ungar, L.; Osenberg, S.; Cesarkas, K.; Jacob-Hirsch, J.; Amariglio, N.; Kupiec, M.; Sorek, R.; Rechavi, G., Topology of the human and mouse m6A RNA methylomes revealed by m6A-seq. *Nature* **2012,** *485* (7397), 201-206.

19. Gulati, P.; Cheung, M. K.; Antrobus, R.; Church, C. D.; Harding, H. P.; Tung, Y. C.; Rimmington, D.; Ma, M.; Ron, D.; Lehner, P. J.; Ashcroft, F. M.; Cox, R. D.; Coll, A. P.; O'Rahilly, S.; Yeo, G. S., Role for the obesity-related FTO gene in the cellular sensing of amino acids. *Proc Natl Acad Sci USA* **2013,** *110* (7), 2557-62.

Chapter 5

β-lactamases and their inhibition

Table of Contents

5.1. Introduction 170
5.1.1. The β-lactam antibiotics and their history 173
5.1.2. Mechanism of β-lactam antibiotics 181
5.1.3. Antibiotic resistance 182
5.1.4. Serine β-lactamases 186
5.1.5. Inhibition of serine β-lactamases 190
5.1.6. Metallo-β-lactamases 194
5.1.7. Mechanisms of metallo-β-lactamases 201
5.1.8. Inhibition of metallo-β-lactamases 208
5.1.9. Summary 211
5.2. Previous studies on rhodanines as MBL inhibitors 212
5.3. Chapter objectives 216
5.4. MBL inhibition 217
5.4.1. Design and synthesis of rhodanine and rhodanine-derivative inhibitors of MBLs 217
5.4.2. Protein production 224
5.4.3. Inhibition and structure activity relationship studies 224
5.4.4. Investigation of the binding/inhibiting motif 232
5.4.5. Synergistic inhibition studies 234
5.4.6. Structural studies 237
5.4.7. Susceptibility of clinical isolates to rhodanines and enethiols 243
5.4.8. Hydrolysis/degradation of rhodanine amides 245
5.5. SBL inhibition 249
5.6. A serendipitous finding 252

5.6.1. Emerging instability 252

5.6.2. Solvent screening 254

5.6.3. Product structure elucidation 257

5.7. Discussion and future work 269

Acknowledgements **272**

References **273**

5. Metallo-β-lactamases and their inhibition

5.1. Introduction

Antimicrobials arguably make up one of the most widely used and successful forms of chemotherapy in human history. Their significance is highlighted by their contribution to the control of infectious diseases and sepsis, which were the leading causes of morbidity and mortality before the 20th century[1]. Although the use of microorganisms or chemicals to alleviate infectious diseases had been documented in ancient China, Egypt, Greece and elsewhere[2], widely used purified antibiotics were only introduced in the early 20th century[3]. 'Antibiotics' were defined as metabolites produced by one microorganism that antagonised the growth of others[4]. Antibacterials are a subclass of antibiotics, along with antifungals and antiparasitics.

The modern antibiotic era has generally been considered to have started with the introduction in 1910 of Paul Ehrlich's 'magic bullet' arsphenamine (marketed as Salvarsan, Figure 5.1). His idea was to target only disease-causing microbes and not the host; he reasoned that through strategic reasoning and systemic screening of compounds, one would produce a perfect chemotherapy (antibiotic)[5]. In 1904, based on evidence that aniline and other synthetic dyes could stain specific microbes but not others, Ehrlich, Bertheim and Hata systematically synthesised and tested a vast number of compounds in search of a drug to treat syphilis. The 606th compound they screened was a hit, and it eventually became the 'magic bullet' in 1910[5]. In spite of toxicity issues, Salvarsan was the first clinically used synthetic antibiotic obtained from systematic screening and rational design; the only alternative available at the time to treat syphilis was inorganic mercury salts. Together with the less toxic Neosalvarsan, Salvarsan was the most frequently prescribed drug until benzylpenicillin (Figure 5.1) replaced it in the 1940s[6].

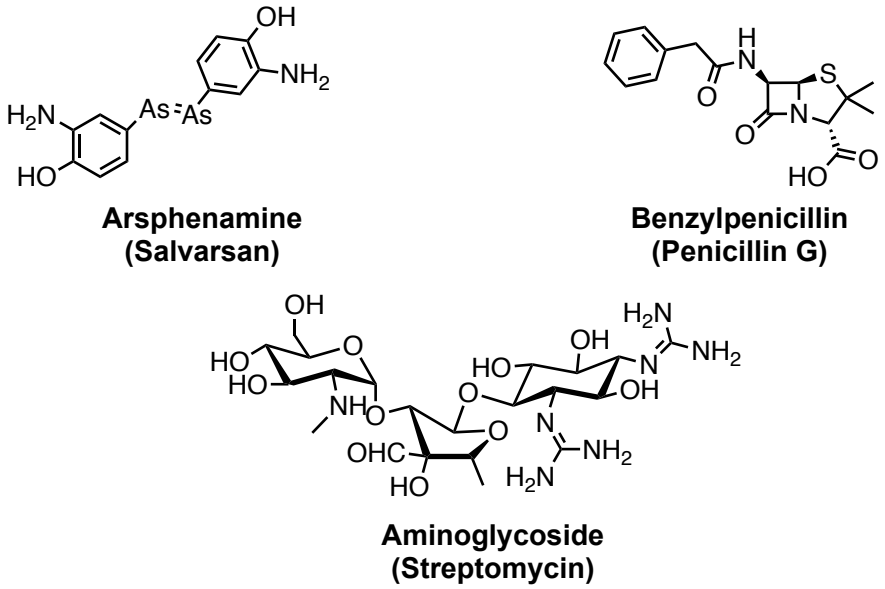


Figure 5.1: *Chemical structures of significant antibiotics (trade names are in brackets).*

The aminoglycoside streptomycin (Figure 5.1) was initially isolated in 1943 by Waksman *et al.*[7-8] and became the first effective antibiotic treatment for tuberculosis. Streptomycin binds to the 16S rRNA in the 30S subunit of the bacterial ribosome, and leads to codon misreading and inhibition of protein synthesis[9]. Streptomycin targets a range of Gram-negative and Gram-positive bacteria[10-14]. More importantly, streptomycin marked the start of the development of extensive clinical research into antibacterials. Indeed, streptomycin was the first drug used in a randomised controlled trial, for the treatment of pulmonary tuberculosis[15]. Inspired by Waksman's drug-discovery platform, the pharmaceutical industry quickly identified several new classes of antibacterials over the next 20 years. Since the 1940s, no fewer than 10 chemically distinct classes of antibacterials have been introduced to clinical use[15-31]. The structures of these antibacterials vary from very small molecules, such as nalidixic acid[25, 32] and the chloramphenicols[33-34], to the macrocyclic macrolides[35-39] (Figure 5.2). The molecular mechanisms by which they function range from inhibition of DNA/RNA synthesis to the inhibition of protein and cell wall biosynthesis[40].

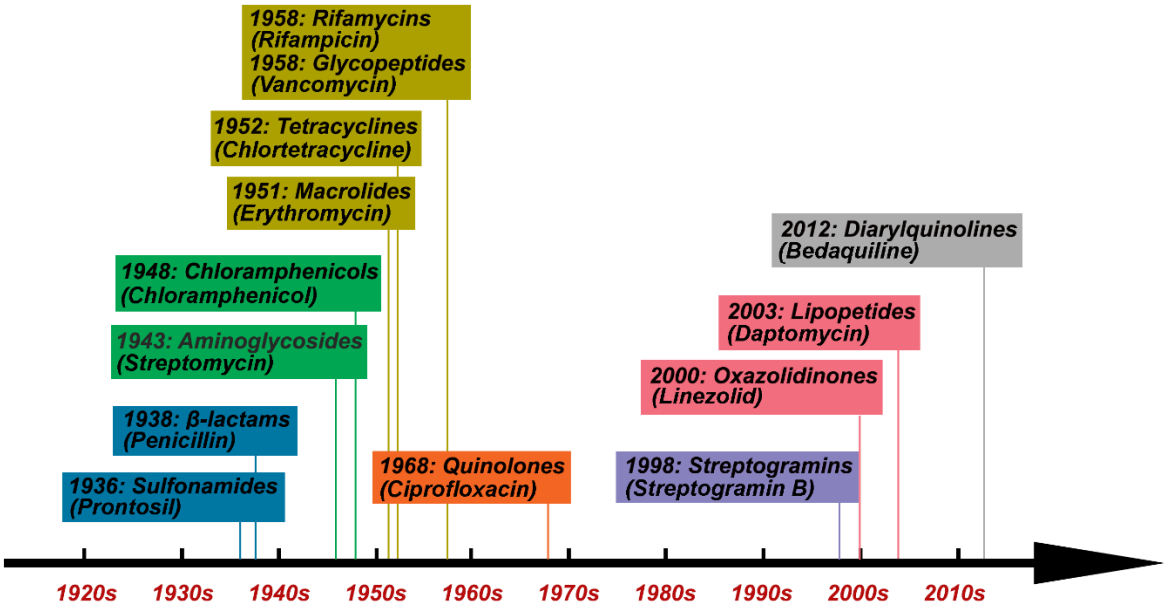


Figure 5.2: *Timeline of the clinical introduction of novel classes of antibiotic. The apparent absence of novel antibiotics between the 1970s and 1990s was a consequence of a shift by the pharmaceutical industry away from the antibiotic field, while the rejuvenation of antibiotic research was marked by the introduction of four new classes from 1998 to the present. Note that the streptogramins and oxazolidinones were in fact discovered before 1963 and daptomycin was discovered in the 1980s.*

The fruitful discoveries and clinical introduction of new antibacterials, along with new generations of semi-synthetic drugs, led to optimism that any infectious diseases could be managed, and it was time to '*close the book on infectious disease*'[41]. As humans declared victory over microbes, emphasis was redirected to chronic diseases such as cancer and heart disease[42]. Since the 1980s, most pharmaceutical companies seem to have considered that there is an overabundance of antibiotics and have sonsequently reduced their investment in the development of novel antibacterial drugs[43].

Antibiotic resistance among target microorganisms was observed very soon after antibiotics were introduced. The production of analogues of existing antibiotics was sufficient to keep pace with the spread of resistance[44]. Since the 1960s, no major new classes of broad-spectrum antibacterials have been discovered[45]. Probably the most recently discovered class of clinically useful antibiotics was that which includes daptomycin (in 1986)[46]. Daptomycin is a lipopeptide that acts against the bacterial cell membrane. It was approved for clinical use in 2003[29, 47].

However, it became obvious by the 1990s that human victory over bacterial pathogens was a false euphoria, as resistance spread faster than new antibiotics were being discovered. Reversion to the pre-antibiotic era has thus become a concern[48-49]. The pharmaceutical industry and the academic community have responded to the antibiotic resistance crisis by utilising novel approaches based on genomics, structure-based design, high-throughput screening (HTS), and combination therapeutics[50-51]. *In situ* cultivation of 'uncultured' soil bacteria, and the tapping of unusual bacterial ecosystems, in recent years[52-53] have suggested that there are new reservoirs of antibiotics and antibiotic classes which have yet to be exploited.

5.1.1. The β-lactam antibiotics and their history

Since the clinical introduction of the penicillins in the 1940s, β-lactam antibiotics rose to be, and remain, the most important medicines in use today, now constituting over 60% of all antibiotics used worldwide[54-55]. The β-lactam antibacterials constitute four major β-lactam subclasses: the penams (penicillins), cephems (cephalosporins), penems (carbapenems), and monobactams. Collectively, they are the most successful class of antibiotics developed so far. Their extraordinary longevity in spite of their early discovery has been attributed to their efficacy, low toxicity, and relative low cost of production[56-59].

The β-lactams are characterised by the presence a common four membered β-lactam ring (Figure 5.3), which is crucial for antibacterial activity. The penams, cephems and penems all exhibit a fused bicyclic core. In the case of the penicillin structure (or penams), the β-lactam is fused to a thiazolidine ring. In the case of the penems, the β-lactam is fused to a 2,3-dihydro-1H-pyrrole or 2,3-dihydrothiazole rings. These are named carbapenems or penems, respectively. Those that contain a dihydrothiazine ring comprise the cephalosporins and cephamycins[60].

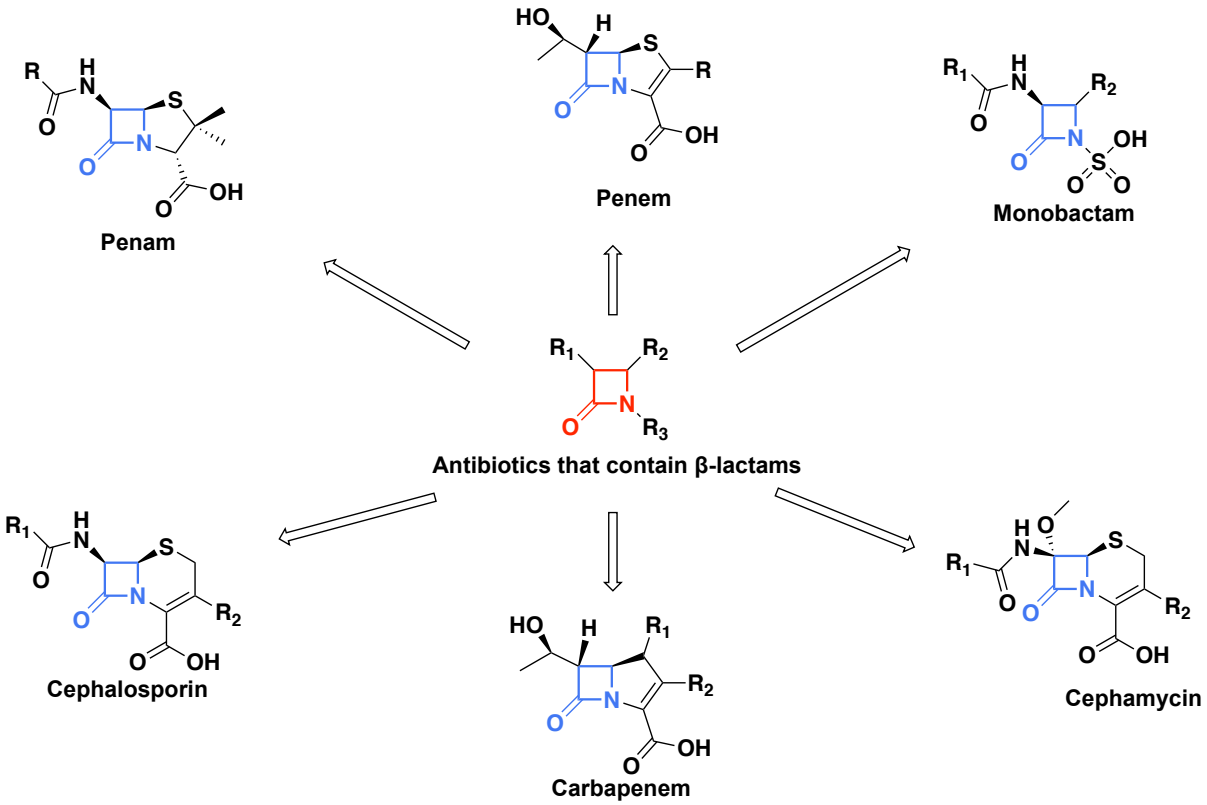


Figure 5.3: *General chemical structures of the main classes of β-lactam antibiotics. The characteristic four membered β-lactam ring is present in every class.*

Before Sir Alexander Fleming's serendipitous discovery of the activity of the penicillins[17], the concept that one organism could inhibit the growth of another had already been the subject of intense investigation in the late 19th century. Observations on the antagonism of fungi that belonged to the genus *Penicillium* against the growth of bacteria were recorded by well-known scientists including Burdon-Sanderson, Lister, Tyndall and Duchesne[3, 56, 61-63]. In 1871, Sir John Burdon-Sanderson observed that exposure to the *Penicillium* mould decreased the turbidity of cultured media, which was due to the inhibition of bacterial growth; he also documented the antagonistic effect of mould on bacterial growth in animal tissues (e.g., dissected guinea pig legs)[64]. However, he did not attribute the apparent antibacterial action to the fungus. Almost in parallel, Joseph Lister recorded that the presence of *Penicillium* mould caused abnormal growth of bacteria, and in some cases, a complete absence of bacteria, in urine samples[65]. Unlike Burdon-Sanderson, Lister fully realised the inhibitory effect of the

Penicillium on bacteria[66]. He may have successfully treated an infected patient with a crude extract of *Penicillium glaucum*[67], although he did not document this incident.

Inspired by Burdon-Sanderson and Lister's work, William Roberts validated such antagonistic effects, either of one bacterial species against another, or between a fungus and bacteria[68], and proposed the idea that became known as antibiosis[69]. While microbial antagonism had been previously observed, the theory that the phenomenon resulted from the production of a compound by one microorganism that could kill another was not obvious. For instance, Tyndall (in)famously reported that the bacterial growth inhibition observed in the presence of *Penicillium* was due to oxygen deprivation[70]. However, he did observe that a certain bacterial strain (almost certainly *Pseudomonas spp*.) was resistant to the antibiotic effect of *Penicillium;* this was probably the first recorded case of β-lactam antibiotic resistance[70]. Elsewhere, in France, Ernest Duschesne reported the antagonism between *Penicillium* and *Escherichia coli in vitro*[71]. He also discovered that co-injection of *Penicillium glaucum* and a normally lethal dose of *Salmonella typhi* prevented guinea pigs from contracting typhoid.

Apparently unaware of the considerable volume of prior relevant work on *Penicillium spp.*, as he cited none of the earlier publications, Fleming was to fascinate the world by his observation of the bactericidal effect of *Penicillium notatum*[17]. Arguably, he was the first to attribute the correct cause to the effect, i.e. the secretion of a toxic substance from the fungus, namely penicillins, which prevented bacterial growth by causing cell lysis.

Because Fleming and others were unable to extract enough penicillin for clinical evaluation, penicillin was not used as a therapeutic agent to treat infections until the 1940s (despite its discovery in 1928). The introduction of penicillin to clinical use was substantially due to the efforts of Howard Florey, Ernst Chain, and a team of researchers from Oxford University. They successfully devised methods to purify sufficient amounts of penicillin and demonstrated its

antibacterial activity against mice infected with *Streptomonas pyogenes*, *Staphylococcus aureus* and *Clostridium septique*[72]. In 1941, the (human) 'patient zero' improved swiftly from an unknown infection following treatment with penicillin, although this patient later deteriorated due to a lack of sufficient penicillin for continuous treatment. A year later, the first adult patient affected by septicaemia was successfully treated[73-74]. However, it was not possible in Florey's laboratory to manufacture the quantity of penicillin required. Hence, collaboration efforts that aimed for the mass production of penicillin were established with the US. The introduction of new large-scale fermentation techniques[75], the isolation of a novel high-yielding *Penicillium* strain (*Penicillium chrysogenum*, isolated from a mouldy cantaloupe)[76], and most importantly, substantial investments from pharmaceutical firms and governments[77-78], enabled the mass production of penicillins with hydrophobic side chains, e.g. penicillin G (Figure 5.4). After successful clinical trials, penicillin was finally brought to the market, after which it went on to save countless lives.

As work continued on penicillin, it was revealed that the British strain and the American strains produced different penicillin compounds. Thanks to the X-ray crystallography work of Dorothy Hodgkin (1949)[79], the structures of penicillin were elucidated. The penicillins produced from both the British strain (primarily 2-pentenylpenicillin) and the American strains (producing benzyl-penicillin or penicillin G) were shown to contain the same characteristic penam ring, as part of a 6-aminopenicillanic acid (6-APA, Figure 5.4) core[79-80]. Isolation of 6-APA from fermentation liquor[80-81], and the successful synthesis of penicillin V (Figure 5.4) by acylation of chemically synthesised 6-APA[82-83], led to the further development of novel β-lactam agents by introducing alternative side chains onto the C-6 amino group. Consequently, there was an eruption in production of semi-synthetic β-lactam compounds. In particular, methicillin (Figure 5.4) was the first semi-synthetic penicillin for clinical use that resisted hydrolysis by a

penicillinase β-lactamase[84]. Moreover, the penicillin analogue carbenicillin extended the spectrum of activity of the β-lactams, including activity against *Pseudomonas aeruginosa*[85].

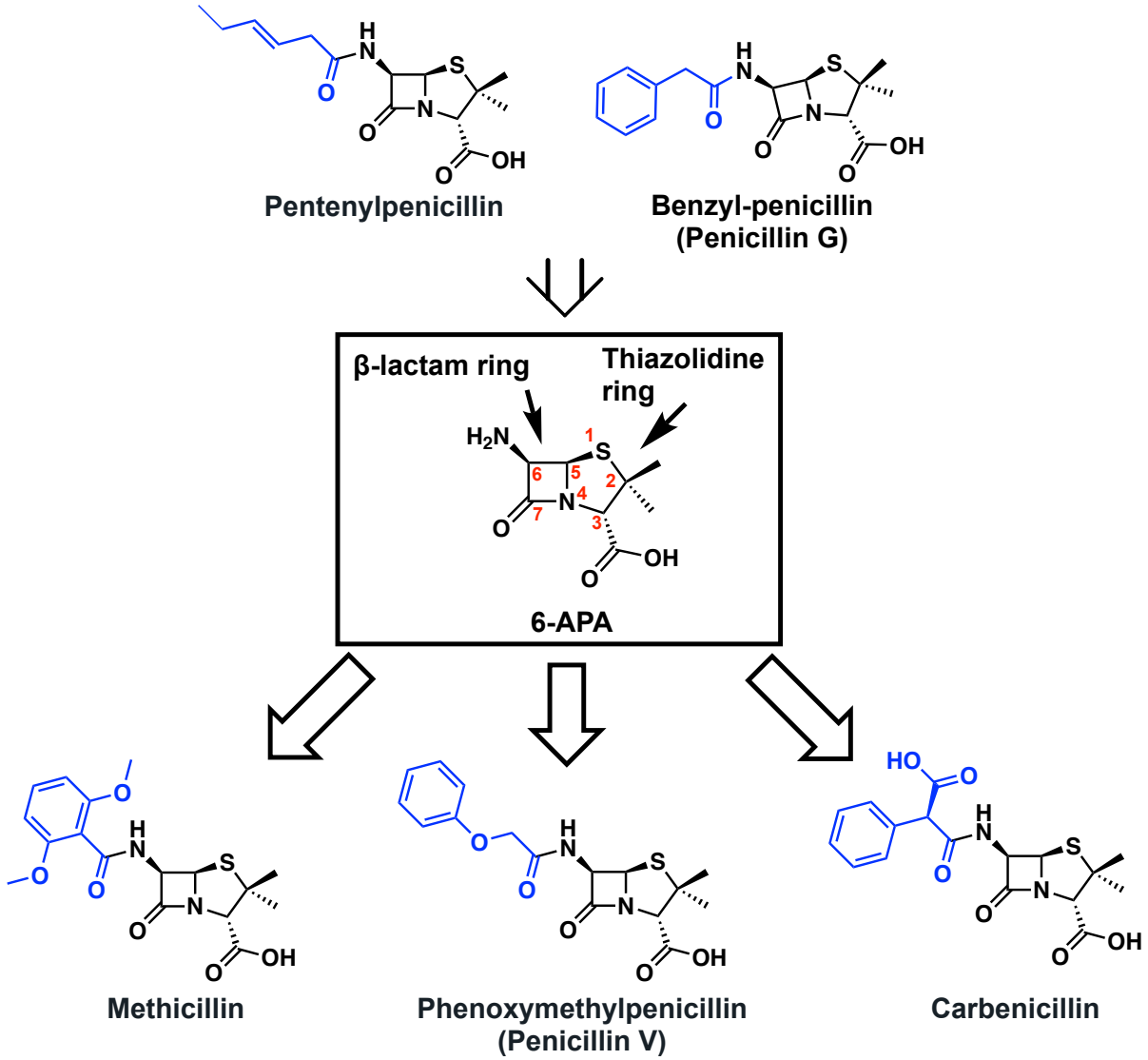


Figure 5.4: *Structure of 6-aminopenicillanic acid (6-APA), which is the core of the penicillins. Two examples of semi-synthetic penicillins, derived from the acylation of 6-APA, are shown: methicillin and carbenicillin. Penicillin V, a 'natural' penicillin, can also be made synthetically. Note: 6-APA is the hydrolysed product of a 'naturally' fermented penicillin, e.g., penicillin G.*

While the semi-synthetic penicillins provided a great resource, natural antibiotic sources of antibacterials continued to be explored. In 1945, Giuseppe Brotzu isolated *Cephalosporium acremonium* from sewage water following his observation that typhoid fever in the city of Cagliari seemed to occur less frequently than in the rest of Europe. The fungus was found to show inhibitory activity against a host of Gram-negative bacteria[86-87]. Unable to advance his

investigation, he passed on the sample to the University of Oxford, where Edward Abraham and Guy Newton took on the challenge. They quickly isolated cephalosporin P (which is active only against Gram-positive bacteria)[88]. Shortly thereafter, a molecule named cephalosporin N was isolated, which was active against both Gram-negative and Gram-positive bacteria[89]. Cephalosporin N was subsequently determined to be a penicillin with a d-α-aminoadipoyl side chain, and it was given the name penicillin N[89]. Further investigation on penicillin N led to the isolation and structural elucidation of cephalosporin C (Figure 5.5)[90-91]. Penicillin N and cephalosporin C have an identical side chain, i.e., the *D*-α-aminoadipicoyl side chain. Cephalosporin C has a six-membered dihydrothiazine ring fused to the β-lactam core, instead of the five-membered thiazolidine ring characteristic of the penicillins (Figure 5.5). The nucleus of cephalosporin C was named 7-aminocephalosporanic acid (7-ACA, Figure 5.5)[90-92]. Further industrial development of semi-synthetic cephalosporins based on modification of the α-aminoadipoyl side chain (at C-7, through N-acylation) from 7-ACA led to the first cephalosporin introduced for clinical use, cephalothin (cefalothin), although it could only be administered parenterally[93]. Since then, work on the synthesis of hundreds of semi-synthetic cephalosporin derivatives (including several generations) has enabled broad-spectrum antibacterial activities to be introduced. Cephalosporins are the largest β-lactam subfamily, and are among the most important clinically used antibiotics, based on their antibacterial spectrum, pharmacokinetics, side effects, and cost[94].

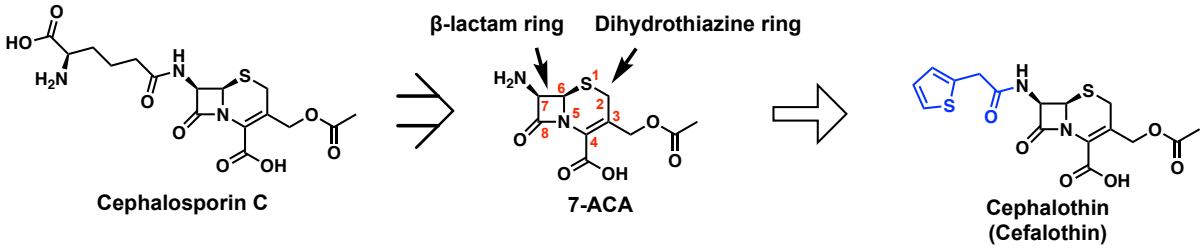


Figure 5.5: *Chemical structure of cephalosporin C, isolated from the fungus Cephalosporium acremonium. Its hydrolysis product, 7-aminocephalosporanic acid (7-ACA), and the semi-synthetic cephalosporin, cefalothin, are also shown.*

Monocyclic β-lactams contain a non-fused four-membered β-lactam ring that is not fused to another ring. The first monocyclic β-lactams to be discovered were the nocardicins, which were produced by bacterial strains of *Nocardia* and *Streptomyces*[95]. Later, the monocyclic β-lactam formadicin was isolated from *Flexibacter alginoliquefaciens* (Figure 5.6)[96-97]. Since these monobactams showed weak-to-moderate activity against Gram-negative bacteria and low activity against Gram-positive organisms, and resistance to enzymatic hydrolysis, they were never brought to the market. It was not until the synthesis of aztreonam (Figure 5.6), which contained a 2-oxo-azetidine-1-sulphonic acid core, that a commercial monobactam became available[98]. The introduction of aztreonam alleviated pressure on the penicillins, as aztreonam was stable to β-lactamase enzymatic hydrolysis[99], although the emergence of multidrug-resistant β-lactamase-producing organisms rendered it less effective[100].

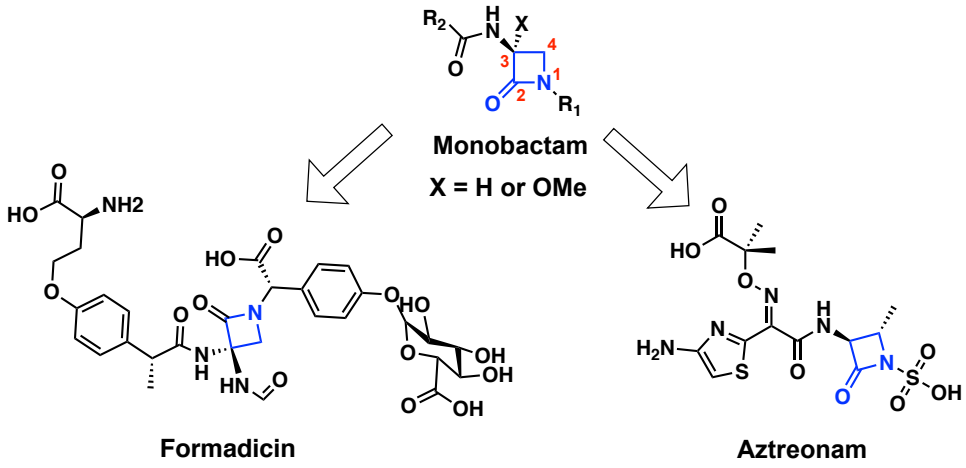


Figure 5.6: *Chemical structure of the 2-oxo-azetidine-1-sulphonic acid core of the monocyclic β-lactams; the first isolated monobactam, formadicin; and the first commercially available monobactam antibiotic, Aztreonam.*

The carbapenems, like the penicillins, have a β-lactam ring fused to a five-membered ring; however, the five-membered ring is unsaturated, and a carbon is present at position 1 instead of a sulphur. The first carbapenem, thienamycin (Figure 5.7), was isolated in the 1970s from the bacterium *Streptomyces cattleya*, and was marketed in the 1980s as a potent broad-spectrum antibiotic[101]. A little over 50 new natural carbapenem antibiotics have been isolated following

the discovery of thienamycin, with varied spectra of antibacterial activities[56]. A more potent and stable semi-synthetic derivative, N-formimidoylthienamycin (imipenem, Figure 5.7)[102], was developed due to the poor stability of thienamycin in aqueous solution. Although imipenem is highly resistant to microbial hydrolysis, it is hydrolysed by human renal dehydropeptidase-1 (DHP-1); hence it must be co-administered with cilastatin, a synthetic DHP inhibitor[103].

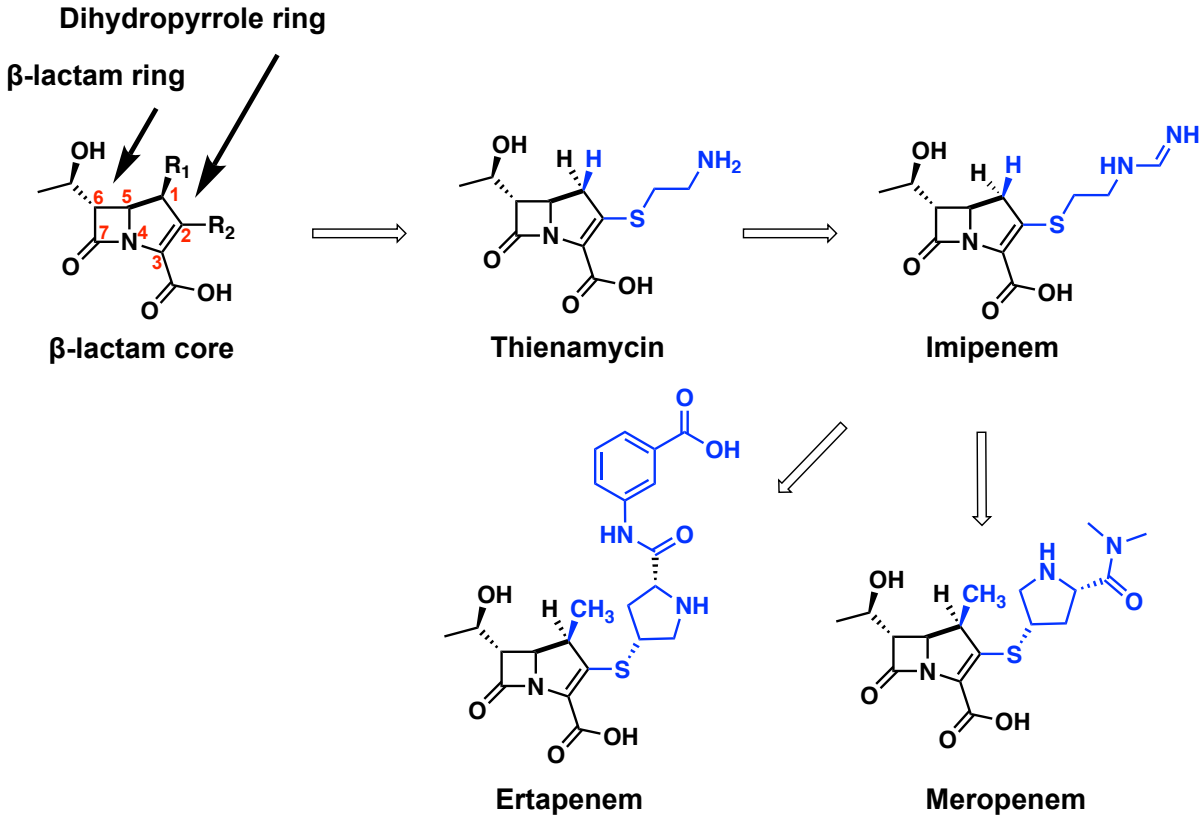


Figure 5.7: *General structures of the carbapenem subclass, the first isolated carbapenem thienamycin, and the subsequent derivative, imipenem. Stable form of carbapenems, i.e. ertapenem and meropenem, are given as examples.*

Further optimisation resulted in production of more stable and potent carbapenems, with modifications that included substitution of the hydrogen at the C-1 position with a 1β-methyl group[104], leading to meropenem, ertapenem, and doripenem[105]; additionally, these derivatives were not susceptible to DHP-mediated hydrolysis[104]. Carbapenems are often considered as antibiotics of last resort for resistant infections, due to their potency and broad-spectrum of activity against both Gram-positive and Gram-negative bacteria[104].

5.1.2. Mechanism of β-lactam antibiotics

β-Lactam antibiotics are bactericidal agents, which inhibit synthesis of bacterial cell wall synthesis by covalently binding to essential penicillin-binding proteins (PBPs)[106-107]. The β-lactam ring acts as an acylating agent that covalently reacts with catalytic serine residues in the active sites of PBPs[107]. PBPs are responsible for the final transpeptidation steps of peptidoglycan cross-linking. The transpeptidase initiates a cross-linking reaction, then a D-alanine carboxypeptidase catalyses the removal of the terminal D-alanine residue from non-crosslinked peptidoglycan as a means to regulate the amount of crosslinking present in the peptidoglycan[108-109]. Penicillin is essentially a cyclic dipeptide that consists of D-valine and L-cysteine. Structurally, the penicillin molecule is related to the backbone of the terminal D-alanyl-D-alanine dipeptide of the incoming peptidoglycan strand (Figure 5.8)[110]. It is proposed that the reactive amide bond in the β-lactam ring aligns with an amide bond in the peptidoglycan D-alanyl-D-alanine bond, which is the location of the bond cleaved during transpeptidation reaction. Thus, the penicillin molecule irreversibly binds to the catalytic serine that is required to react with the D-alanyl-D-alanine group in peptidoglycan[110], and generates a stable acyl-enzyme complex (Figure 5.8)[111]. It is also proposed that the penicillins may mimic the transition state of the initial acylation step of a PBP reacting with an incoming peptidoglycan strand (Figure 5.8)[111]. The antibiotic product with its opened lactam ring may then be slowly hydrolysed from the resulting inactive complex, though this process is thought to take longer than the lifetime of a bacterium (division cycle ~ 20 minutes)[112].

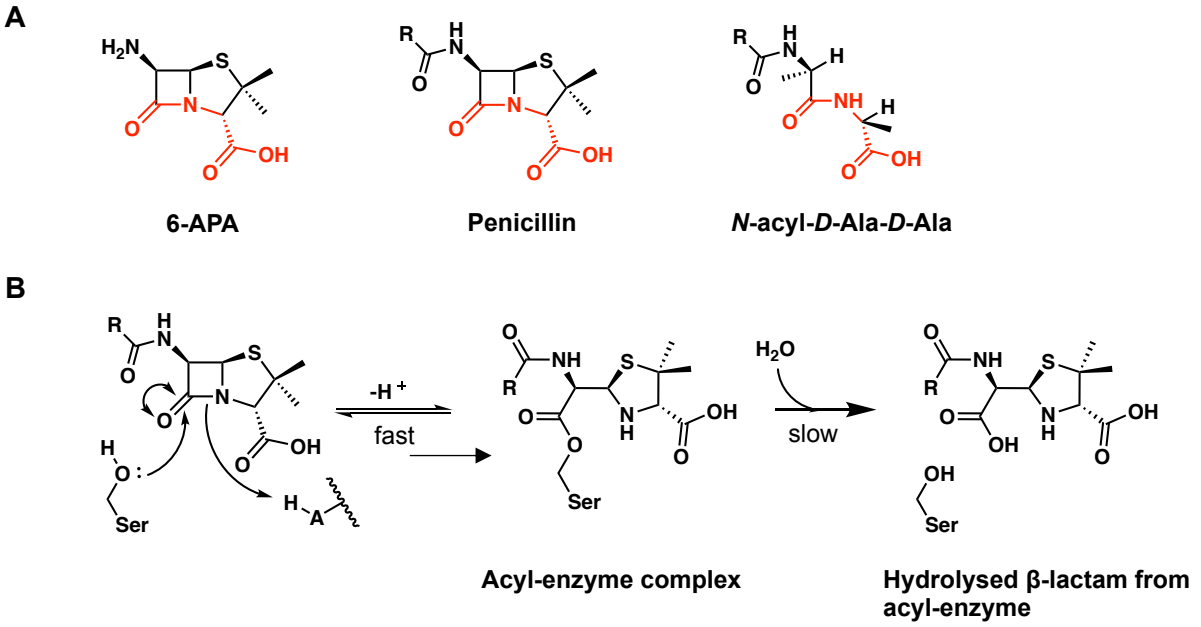


Figure 5.8: *(A) Structural similarities between penicillins and the D-Ala-D-Ala terminus of peptidoglycan strands, as highlighted in red, suggest that β-lactams may act as substrate analogues for PBPs. (B) Outline mechanism of PBP inhibition by β-lactam antibiotics. Generation of a stable acyl-enzyme complex prevents binding of peptidoglycan strands and hence disrupts the transpeptidation step of peptidoglycan synthesis during bacterial growth.*

Further details of the precise mechanisms of PBP inhibition by β-lactams remain to be elucidated, though it is certain that inhibition of the PBPs leads to interrupted cell wall formation, altered cell division, and ultimately lysis of the bacterial cell due to osmotic pressure[113-114]. There are no direct human homologues to the PBPs, which is a crucial reason for the apparent lack of toxicity that arises during use of β-lactam antibiotics; the selectivity of the β-lactams for their bacterial PBP targets limits unwanted side reactions with human enzymes.

5.1.3. Antibiotic resistance

Since almost all first-generation β-lactam antibiotics were isolated from soil-dwelling microorganisms[3, 62], it is reasonable to propose that microbial antibiotic resistance exists in natural habitats, independent of the clinical use of β-lactams. Antibiotics produced by fungi and bacteria in the biosphere have functions other than antibiosis. For example, low concentrations of antibiotics can trigger specific transcriptional changes and they are proposed

to act as signalling molecules that facilitate bacterial communication within microbial populations[115-116]. Similarly, antibiotic-producing microorganisms must have resistance mechanisms against the antibiotics they produce[117]. Indeed, genetic analyses suggest that antibiotic-resistance genes encoding for some serine β-lactamases have existed in bacterial plasmids for millions of years[118-121]. The lateral transmission of resistance genes to clinical pathogens contributes significantly to the evolution, maintenance, and transmission of virulence in pathogenic bacteria, and is a particular concern for antibiotic resistance[122].

The primary issue with antibiotic therapy is that resistance emerges quickly after the introduction of a new antibiotic[14, 44, 49, 55-56, 62, 123]. This scenario has sadly repeated on multiple occasions; thus there is a constant race between new antibiotic discovery and the emergence of resistance mechanisms in bacteria[124]. On the positive side, combination therapies, i.e. the use of two or more antibiotics/inhibitors from distinct classes that often exhibit different modes of action, has proven to be effective to slow the development of antibiotic resistance. This method may lead to a resurgence in the use of antibiotics that fail against resistant bacteria[125-127]. However, as stated above, the lack of antibiotic development from the 1970s to the present (barring the recent resurgence from academic groups) has resulted in depletion of available antibiotics that have not already been clinically exploited[128]. Efforts are urgently needed to tackle the ever-emerging resistance mechanisms in clinical frontiers alongside development of entirely new antibiotics. The old trick of chemical modification on the same core scaffold to create new generations of antibiotics can still be used, as it has successfully been applied for successive generations of penicillins and cephalosporins[129].

Over millions of years, and especially aided by human activities, bacteria have evolved mechanisms to avoid the antibacterial effects of molecules such as β-lactams, which may or may not be achieved simultaneously through multiple biochemical pathways (Figure 5.9)[130-

[133]. The main types of antibiotic resistance mechanisms manifested by bacteria are shown below.

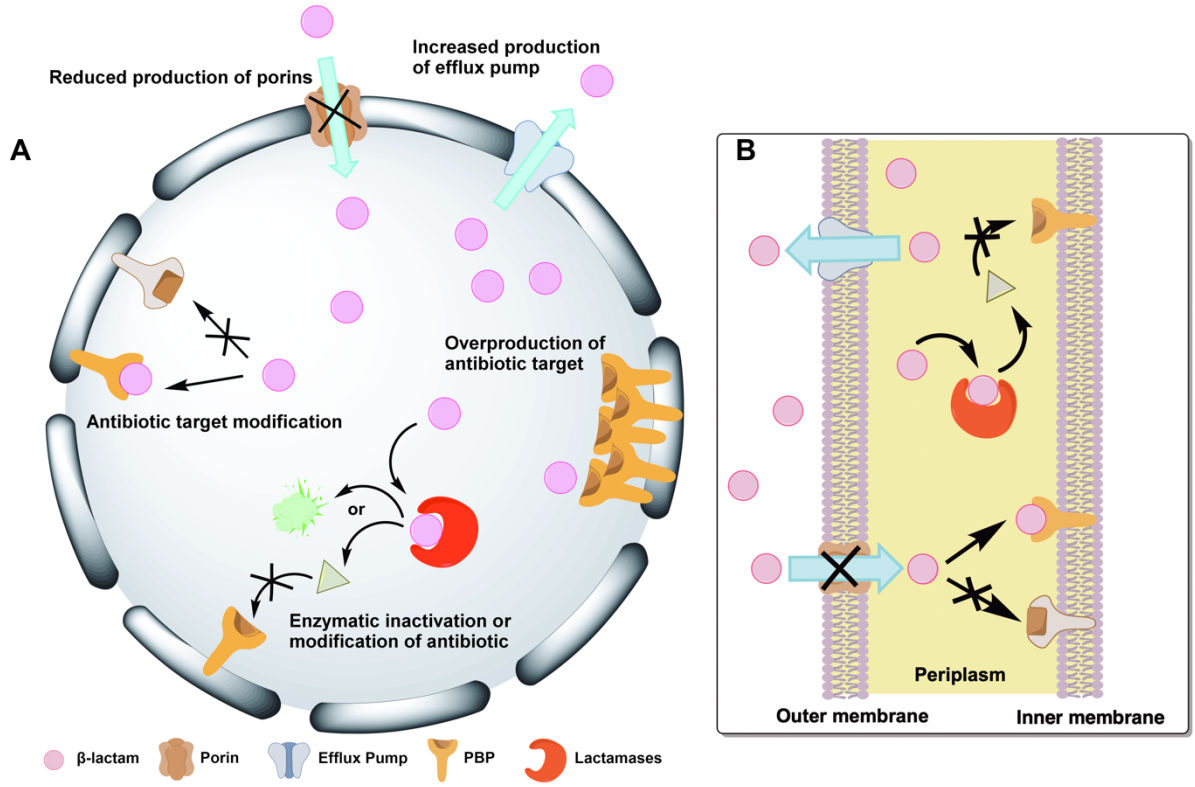


Figure 5.9: A. *Cartoon illustration showing the general mechanisms of antibiotic resistance in both Gram-positive and Gram-negative bacteria. These include target modification, overproduction of targets, destruction of antibiotics, and regulation of membrane permeability.* ***B.*** *Cartoon illustration showing the different cell wall/membrane composition in Gram-negative bacteria. Note: the outer membrane is only found in Gram-negative bacteria, though the general antibiotic resistance mechanisms are the same as those seen in Gram-positive bacteria.*

Regulation of membrane permeability. Many antibiotics need to penetrate the bacterial cell membranes to reach their targets. In the case of Gram-negative bacteria, which have two membranes, some targets are located within the inner cytoplasmic membrane, i.e., within the cell. Bacteria, especially Gram-negative bacteria, have developed mechanisms to down-regulate or to alter porin channels, and these mechanisms are particularly detrimental for hydrophilic molecules such as β-lactams, as they enter cells through these channels[134]. The abnormal production of the OprD protein in *Pseudomonas aeruginosa* is a classic example of porin-mediated resistance that leads to decreased efficacy of imipenem, a potent anti-pseudomonal carbapenem[135]. The production of efflux pumps capable of extruding toxic

compounds is another mechanism of antibiotic resistance; there are more than 20 genes that encode for the five major families of efflux systems, which affect a broad spectrum of antibiotics[136]. For example, the MexAB-OprM efflux system accepts a wide range of β-lactams as substrates for extrusion from *Pseudomonas aeruginosa*[137].

Modification of the antibiotic target sites. One way that bacteria exhibit antibacterial resistance is to reduce the activity of antibiotics, such as β-lactams, by modifying their targets. Bacteria have evolved tactics such as target protection (inhibiting the antibiotic from reaching its binding site) and target modifications, with the latter being the preferred resistance mechanism in bacteria. These modifications may be (i) point mutations in the genes that encode for the target protein, (ii) alterations of the binding site by enzymes (e.g. addition of methyl groups), and/or (iii) modification of original targets. Irrespective of the type of modification, the goal is to reduce the affinity of the antibiotic for the target site, resulting in loss of activity for the drug. In the case of β-lactams, for example, this is demonstrated by the acquisition of a foreign gene, *mecA*, which encodes for PBP2a, a PBP that has significantly reduced affinity for all β-lactams, including penicillins, cephalosporins and carbapenems[138]. The acquisition of *mecA* makes most β-lactams completely inactive against multi-drug resistant *Staphylococcus aureus* (MRSA), and is an important resistance mechanism of this bacterium[138].

Enzymatic modification of antibiotics. Arguably the most important resistance mechanism employed by bacteria, is the enzymatic (chemical) alteration of the structures of antibiotic molecules inactivates them, as they are no longer able to interact with their targets. In the case of β-lactam antibiotics, hydrolysis by β-lactamases renders them ineffective[123].

The β-lactams were the first antibiotics to be extensively studied from a resistance perspective[56]. Even before the clinical introduction of β-lactams in 1940, Abraham and Chain observed the enzymatic degradation of penicillin[139] by the first of the β-lactamases to be

identified. This enzyme, subsequently shown to be a serine β-lactamase (SBL), was given the name penicillinase. As the development of β-lactam antibiotics continued, cephalosporinase activity in *Bacillus cereus* was observed soon after the introduction of the cephalosporin drugs[140]. It was observed that treatment with ethylenediaminetetraacetic acid (EDTA) inhibited the cephalosporin hydrolysis[141]. This is thought to be the first reported observation of metallo-β-lactamase (MBL) activity . Although β-lactamases have probably existed in natural environments for millions of years before the human therapeutic use of antibiotics[120], penicillin-resistant *Staphylococcus aureus* established itself as a clinical threat in hospitals after penicillin became widely available[142]. The gene that encodes for this penicillinase was found to be readily transmitted between *S. aureus* strains, leading to rapid dissemination of β-lactamase mediated resistance[143]. Since the first observation of β-lactamase, over 1300 unique β-lactamases have been reported[144]. They can be categorised into families and sub-families[143]. Collectively, these enzymes are capable of hydrolysing/destroying all classes of β-lactam antibiotics.

5.1.4. Serine β-lactamases

There is evidence that the SBLs and the PBPs share a common ancestor[145-146]. Thus, it is perhaps unsurprising that they have similar enzymatic mechanisms. The formation of an acyl-enzyme complex in the SBLs is analogous to that in the PBPs, in which a nucleophilic serine residue attacks the β-lactam carbonyl. With the SBLs, water molecules have easy access to the active site and subsequently hydrolyse the acyl-enzyme complex, leading to recovery of the unmodified SBL (Figure 5.10)[145]. SBLs efficiently hydrolyse β-lactams into biologically inactive metabolites. For PBPs, the acyl-enzyme complex is stable and relatively hydrolytically inert, allowing β-lactam antibiotics to exert their antimicrobial activities[147].

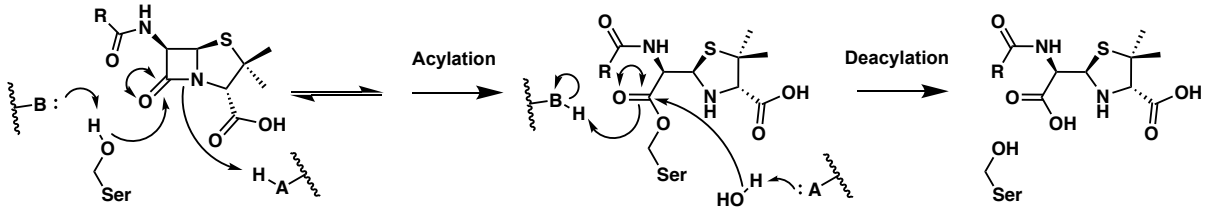


Figure 5.10: *Reaction scheme showing an outline mechanism of hydrolysis of a β-lactam catalysed by a serine-β-lactamase. Note that the acylation step resembles that seen for PBPs with β-lactams, but the deacylation step using water is exclusive to the serine-β-lactamases.*

Based on the spectrum of their substrate profile, enzyme inhibition profile, protein molecular weights, and sequence identities, the SBLs are classified into Ambler classes A (penicillinases), C (cephalosporinases), and D (oxacillinases).

5.1.4.1. Ambler class A serine β-lactamases

Class A SBLs, initially observed in Gram-positive bacteria as common plasmid-mediated penicillinases, are the most extensively studied SBLs, and display the highest levels of variation in terms of their sequence and kinetic properties[148]. Class A SBLs include the sulphydryl reagent variable β-lactamases (SHV)[149] and the Temoneira β-lactamase (TEM)[150] enzymes; they are, however, often effectively inhibited by clavulanic acid, tazobactam and sulbactam[151]. Class A β-lactamase inhibitor combination therapy relieve infections caused by organisms that carry a penicillinase. The extended-spectrum SBLs (ESBLs), initially described as variants of the SHV and TEM β-lactamases, have become a global threat as they exhibit broad-spectrum cephalosporin resistance. This is exemplified by the cefotaxime hydrolase from Munich (CTX-M) enzymes, which are currently the most prevalent ESBLs, and which are able to hydrolyse third-generation cephalosporins[152]. Carbapenemases, including imipenem-hydrolysing enzyme (IMI) and *Klebsiella pneumoniae* carbapenemase (KPC) enzymes, were first identified in the 1980s from *Enterobacteriaceae*. These bacteria showed not only high resistance to penicillins and cephalosporins, but also moderate resistance to carbapenems[153]. Furthermore, KPCs have been observed to display reduced inhibition to β-

lactamase inhibitors, such as clavulanic acid[154]. In particular, KPC-2 may hydrolyse avibactam, the latest approved inhibitor for class A β-lactamases[155-156].

The first crystallographic structure of a class A SBL to be solved was from *Bacillus licheniformis*[157]. Similar to the other classes of SBLs (classes C and D, respectively), the active site is located at the junction between an all-α domain and an α-β domain whose five-stranded β-sheet is protected by additional α-helices on both sides (Figure 5.11). In these enzymes, Glu166 is proposed to be the basic residue for deprotonating the serine nucleophile (Ser70) in the acylation step, as well as the hydrolytic water molecule in the deacylation step[158]. Lys73 and Ser130 have been reported to be important for proton shuttling during the reaction (Figure 5.11)[159-160].

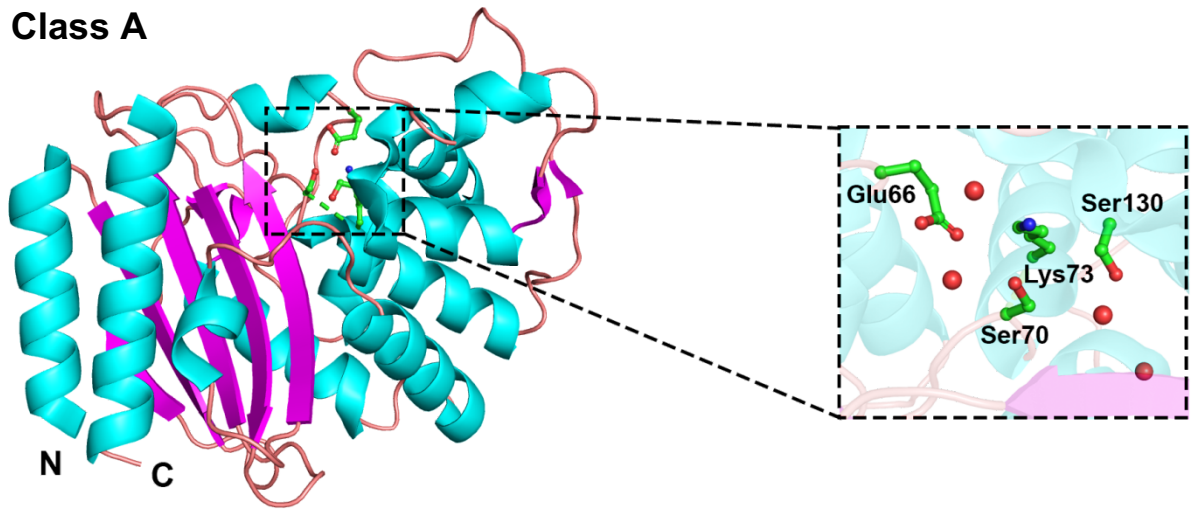


Figure 5.11: *View form a crystal structure of the class A serine β-lactamase TEM-1 (PDB ID: 1ERO)[161]. Amino acid residues involved in the hydrolysis reaction are illustrated as sticks and balls. Water molecules within hydrogen-bonding range are represented by red spheres.*

5.1.4.2. Ambler class C serine β-lactamases

Class C SBL (AmpC) enzymes are active against penicillins, and are known for their hydrolysing activity towards cephalosporins and cephamycins; hence they are known as cephalosporinases. AmpCs are among the most abundant β-lactamases based on the number of

bacteria that produce these enzymes, and are frequently identified in *Enterobacteriaciae* as chromosomal enzymes[162]. AmpC β-lactamases are generally not inhibited by typical SBL inhibitors such as clavulanic acid[163-164]. Extended spectrum AmpC (ESAC) enzymes with a broadened spectrum of hydrolytic activity towards cephalosporin substrates have also been reported[165]. Production of ESACs, combined with loss of membrane permeability, has been shown to significantly increase the resistance of *E. coli* towards carbapenems[166].

In class C SBLs, it is apparent that an extended hydrogen-bonding network exists at the active site. Instead of a single residue (Glu-166 in Class A β-lactamase) functioning as a general base (like in class A and class D SBLs), multiple residues are responsible for catalysis through a charge relay system[167]. Among these residues, both Lys67 (homologous to Lys73 in class A SBLs)[168-169] and Tyr150[170] have been proposed to be critical in the deacylation of the acyl-enzyme complex[171], although pK_a based modelling indicates that Tyr150 (for which the side chain exists in the form of a phenolate at neutral pH) may be responsible for activation of the nucleophilic serine (Figure 5.12)[172].

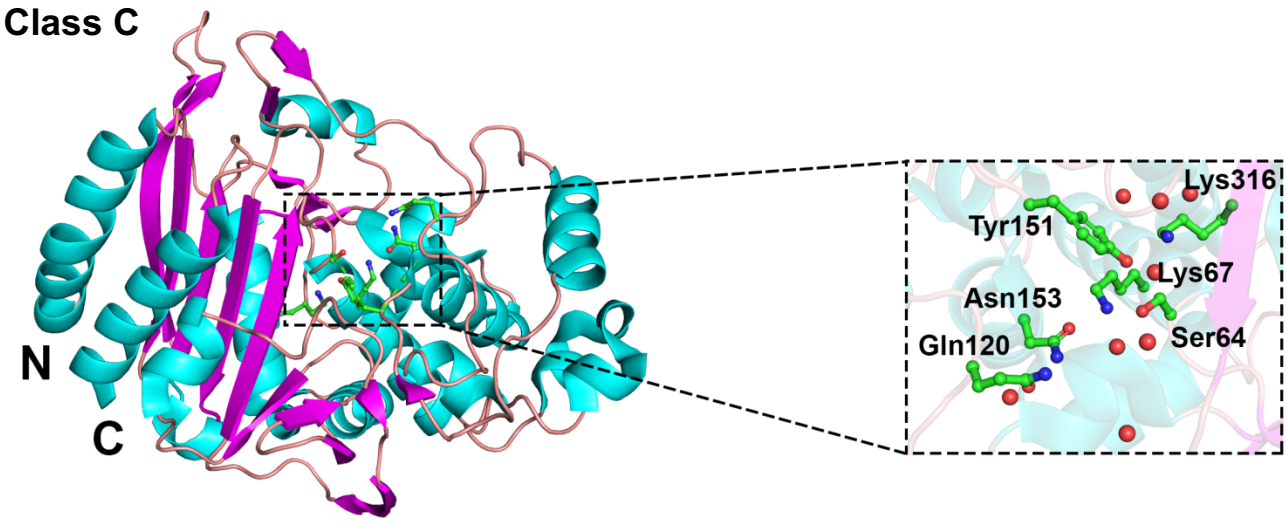


Figure 5.12: *View from a crystal structure of the class C serine β-lactamases AmpC from* P. aeruginosa *(PDB ID: 2ZJ9)[173]. Amino acid residues involved in the hydrolysis reaction are illustrated as sticks and balls. Water molecules within hydrogen-bonding proximity are represented by red spheres.*

5.1.4.3. Ambler class D serine-β-lactamases

Ambler class D SBLs are also known as oxacillinases (OXAs) because of their ability to hydrolyse isoxazolyl β-lactams, such as oxacillin[174]. Class D SBLs are readily inhibited by clavulanic acid[175]. Plasmid-mediated OXAs are commonly found in *Pseudomonas aeruginosa*, although chromosomally encoded OXA-50 was later identified from an AmpC mutation[176], which indicates that resistance is readily transmitted between pathogenic species. Distinctive from the other classes of SBLs, the OXA enzymes undergo an unusual carbamylation reaction (reacting with CO_2) at an active site lysine (Lys70) (Figure 5.13)[177]. The carbamylated lysine residue acts as a general base (and likely acid), activating the nucleophilic serine in the acylation step, and deprotonating a water molecule in the deacylation step, during the catalytic process of β-lactam hydrolysis[178].

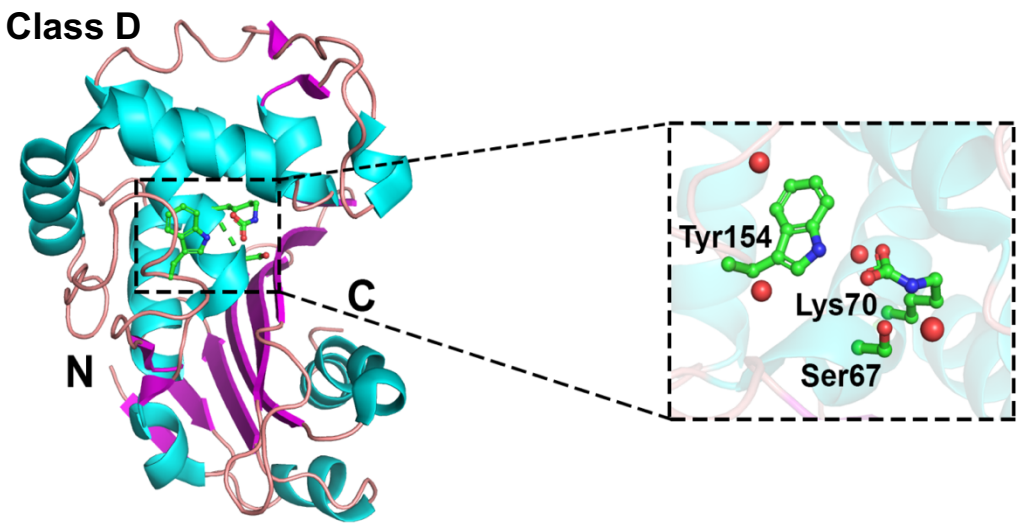


Figure 5.13: *View from a crystal structure of the class D serine β-lactamase OXA-10 (PDB ID: 5MMY)[179]. Amino acid residues involved in the hydrolysis reaction are illustrated as sticks and balls. Water molecules within hydrogen-bonding proximity are represented by red spheres. Note that the conserved all-α and α-β two-domain folds are present across the different SBL classes.*

5.1.5. Inhibition of serine β-lactamases

As mentioned earlier, although humans are in an 'arms race' with microorganisms, the development of β-lactam derivatives (penicillins and cephalosporins) has temporarily enabled

(partial) victory in combatting resistance[124]. When single antibiotic therapy failed, combination treatment that included use of a SBL inhibitor alongside a β-lactam antibiotic brought success, particularly against infections caused by pathogens that carry class A SBLs[125-127].

Clavulanic acid (Figure 5.14 A) was isolated from *Streptomyces clavuligerus* in the 1970s, as a result of attempts to screen natural products in the search for a TEM-1 Class A SBL inhibitor. Clavulanic acid then became the first clinically used broad-spectrum SBL inhibitor[180]. Clavulanic acid shares structural similarity with the penicillins, in which the characteristic system of a fused β-lactam and five-membered bicyclic ring is maintained. However, in clavulanic acid, the sulphur atom at the 1 position of the penicillins is replaced by an oxygen; the aminoacyl side chain is substituted with a hydrogen atom, and the dimethyl group found on the thiazolidine ring in the penicillins is replaced by a β-hydroxyethylidine group (Figure 5.14 A). Clavulanic acid has little antimicrobial activity, as it interacts poorly with PBPs; however, it is effective against many class A SBLs, including the prevalent CTX-M, TEM-1 and SHV-1 enzymes[181]. Clavulanic acid possesses an enol ether oxygen (as a good leaving group) at the 1-position of the oxazolidine ring, which enables the opening of this ring and inactivation of β-lactamase enzymes. Evidence from kinetic, mass spectrometric and X-ray crystallographic studies suggest that clavulanic acid undergoes complex rearrangements after the formation of the initial acyl-enzyme complex (Figure 5.14 B)[182-185]. The opening of the oxazolidine ring generates a transient imine intermediate, which then rearranges to form an enamine intermediate in either the *trans* or *cis* orientation[186-187]. Depending on the properties of the enzyme, the reaction eventually proceeds to irreversible inactivation as the enamine intermediate in the acyl-enzyme complex undergoes fragmentation[184] or decarboxylation[185] (Figure 5.14 C). Although not yet crystallographically observed, a MS study indicates that Ser130 at the active site is involved in cross-linking with the fragmented inhibitor, further preventing enzyme activity (Figure 5.14)[183].

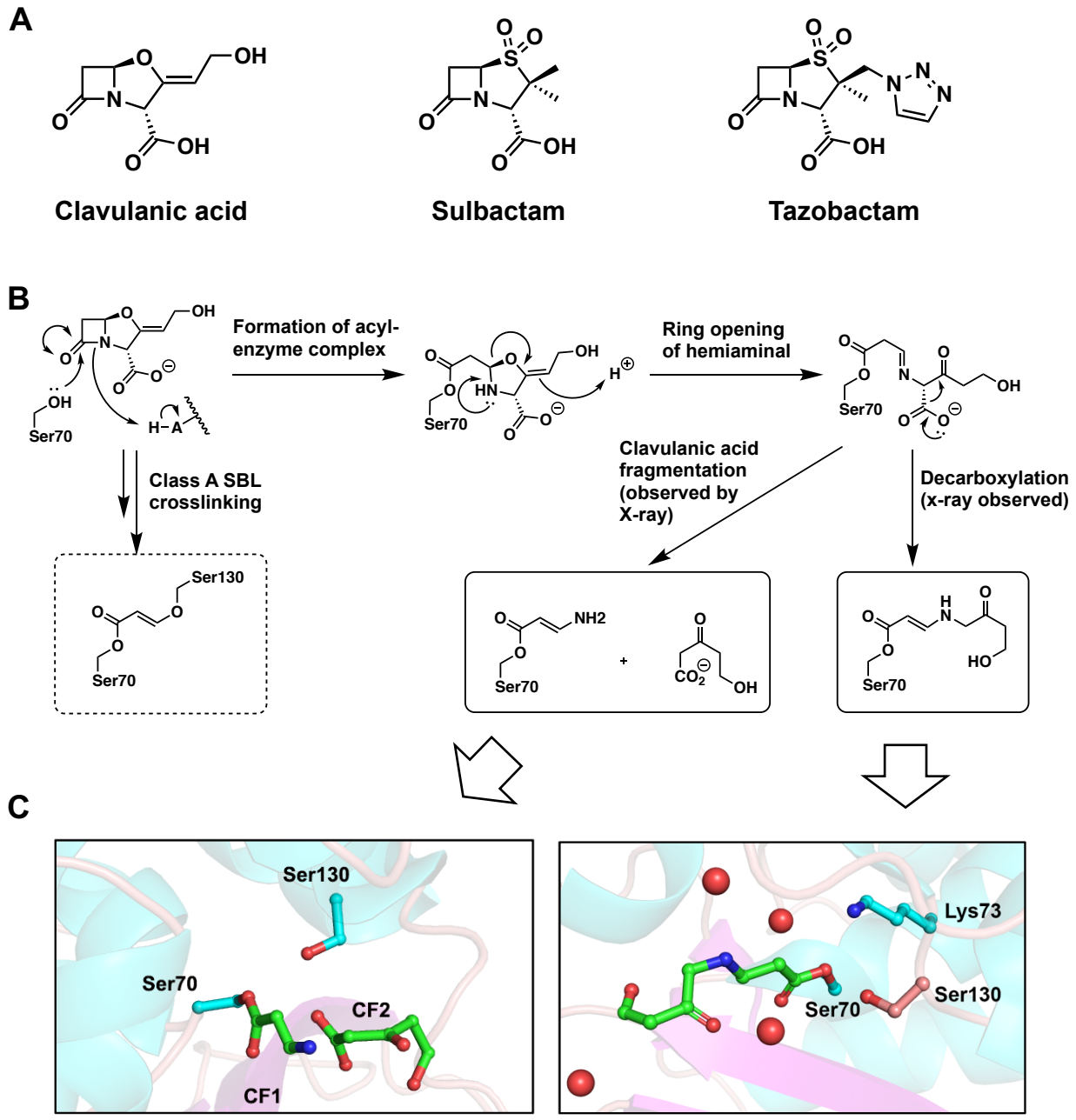


Figure 5.14: *A. Structures of clavulanic acid, sulbactam and tazobactam. B. Proposed general mechanisms of class A SBL inhibition by clavulanic acid, which acts as a covalent/suicide inhibitor. C. Detailed view at the active site of acyl-enzyme complex of* Bacillus licheniformis *BS3 (left, PDB ID: 2Y91), and SHV (right, PDB ID: 3CG5). Note, both fragmentation and decarboxylation of the imine/enamine have been observed by X-ray crystallography; however, there is no structural (i.e. crystallographic) evidence for the proposed active-site residue cross-linking of the inhibitor.*

The inhibitory activity of clavulanic acid enables the use of penicillins against SBL carrying pathogens. In β-lactam/β-lactamase inhibitor combination therapy, it is co-administered with amoxicillin and ticarcillin, as Augmentin[188] and Timentin[189], respectively, in order to expand

the antibacterial spectrum of penicillins to SBL-producing *K. pneumoniae*, *S. aureus*, *and E. coli* strains[190]. Development of synthetic derivatives of penams has led to sulbactam[191] and tazobactam[192], which are both penicillinate sulphones (Figure 5.14 A). Combination therapies that use these inhibitors have further extended the antibiotic activities of the β-lactams.

Although they are usually active against class A SBLs, class C and D β-lactamases are generally immune to the β-lactam-based SBL inhibitors[55]. The discovery of a bridged diazabicyclooctane (DBO) inhibitor, avibactam (Figure 5.15), brought much promise to the antibiotic world as it exhibited broad-spectrum inhibitory activity against class A, C and D SBLs, with KPC-2 as an exception (as KPC-2 slowly hydrolyses avibactam)[155, 193]. Unlike the β-lactam-based inhibitors, avibactam is a tight binding and reversible inhibitor, which can regenerate itself through recyclisation (Figure 5.15 B)[156]. The combination of avibactam and ceftazidime (β-lactamase inhibitor and β-lactam antibiotic, respectively) has been approved for clinical use for complicated urinary tract and intra-abdominal infections[127]. The other DBOs, such as relebactam (Figure 5.15), which has an additional 4-aminopiperidine sidechain, are in phase II clinical trials as combination therapy (with imipenem/cilastatin) for treatment of KPC-carrying pathogens (which are currently not treatable with the avibactam/ceftazidime combination)[194-195]. Similarly, vaborbactam (boronic acid, Figure 5.15)[196], also a synthetic non-β-lactam SBL inhibitor, works by forming reversible oxygen-boron covalent bonds that mimic the tetrahedral transition state of β-lactam hydrolysis in SBLs[197-198]. The combination therapy with meropenem has recently passed phase III clinical trials for class A carbapenemase-mediated resistant infections[199].

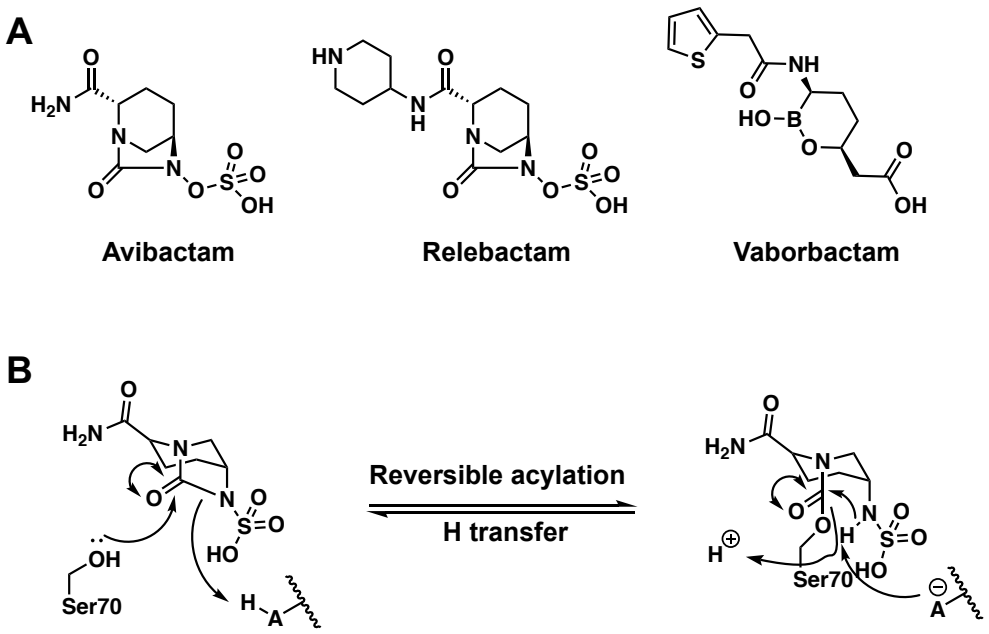


Figure 5.15: *A. Structures of avibactam, relebactam and vaborbactam. B. Outlined mechanism showing the reversible inhibition of SBLs by avibactam.*

5.1.6. Metallo-β-lactamases

The metallo-β-lactamase (MBL) superfamily contains >3500 identified members of mainly metallo-hydroxylases, ranging from small-molecule hydroxylases to DNA/RNA modifying/repairing enzymes. However, the metallo-β-lactamases of interest to the work described in this thesis are the so-called 'true' MBLs, which catalyse the hydrolysis of β-lactam antibiotics. While the class A, C and D SBLs utilise a nucleophilic serine in their catalytic activities, the class B β-lactamases require one or two zinc (Zn) ions to catalyse β-lactam hydrolysis, hence the name metallo-β-lactamase.

The first MBL to be purified, *Bacillus cereus* metallo-β-lactamase II (BcII), was identified by Sabbath and Abraham in 1966, when they revealed that the cephalosporinase activity exhibited by a *B. cereus* isolate was inhibited by addition of EDTA; they were able to restore the activity through addition of Zn(II) ions[140-141]. BcII was the only known MBL for the following two decades; since it was chromosomally encoded and only found in bacteria that seldom caused

serious infections; the first MBL was primarily considered to be a biological curiosity[200]. However, since the 1990s, the discovery of plasmid-mediated MBLs in nosocomial species such as *Bacteroides fragilis*[201], *Pseudomonas aeruginosa*[202], and *Elizabethkingia meningoseptica* (formerly *Chryseobacterium meningosepticum*)[203], means that they have become a serious clinical threat. These MBL genes have the ability to disseminate across different bacterial species, and this ability is probably responsible for the mounting reports of MBL-mediated antibiotic resistance in Gram-negative pathogens such as *Acinetobacter*, *Enterobacteriaciae* and *Pseudomonas* species[200, 204-205]. Moreover, many MBL-encoding genes are present in non-infectious bacterial species, so representing reservoirs of β-lactam resistance genes that are readily transmittable to infectious species[206-208].

Like the KPC enzymes, the MBLs are a major health risk as they can hydrolyse all classes of β-lactam antibiotics[209], with the exception of aztreonam[210], and are not inhibited by any clinically useful SBL inhibitors[48]. The MBLs are particularly worrisome as they also hydrolyse carbapenems – frequently regarded as the 'last-resort' antibiotics in drug-resistant bacterial infections[211]. Furthermore, the β-lactam-based SBL inhibitors, e.g. clavulanic acid, are readily hydrolysed by MBLs. Non-β-lactam SBL inhibitors, such as avibactam, are also MBL substrates, albeit poor ones at present[212]. Furthermore, many clinical pathogens co-produce SBLs and MBLs; although these bacteria are rare at the moment, their numbers are expected to increase in the near future[213].

Based on their structures, sequences alignments, and substrate profiles, MBLs are divided into three subgroups B1, B2, and B3[214].

5.1.6.1. Subclass B1 Metallo-β-lactamases

The B1 subclass MBLs contain the largest number of members, with over 14 distinct enzyme families that share approximately 30% sequence identity[214]. B1 MBLs are exemplified by the

first discovered MBL, BcII, as well as the MBL imipenemase (IMP), Verona integron-encoded metallo-β-lactamase (VIM), São Paulo metallo-β-lactamase (SPM) and New Delhi metallo-β-lactamase (NDM) variants[215]. B1 MBLs, such as VIM- and IMP-type enzymes, are encoded in integron machineries that are readily incorporated onto bacterial plasmids[216]. The integron allows horizontal transfer of plasmids that contain resistance genes (such as B1 MBLs) between pathogenic species, a powerful dissemination mechanism adopted by many bacteria[217]. Thus, the B1 MBLs are the most important MBLs from a clinical prospective.

The first MBL structure to be elucidated was that of BcII, which was initially solved as a mono-Zn(II), and later as a di-Zn(II), complex. The di-Zn(II) complex is generally accepted as the optimal form[218-219]. The X-ray structure revealed that BcII, like other B1 class MBLs solved later, has a characteristic αββα sandwich fold, with α-helices surrounding a β-sheet core. The active site is located in a solvent-exposed channel between two domains (Figure 5.16). The B1 MBLs have two zinc binding centres at the active site (Zn1 and Zn2). In the Zn1 binding site, also known as the 3H site, a Zn(II) ion is coordinated by three histidine residues, i.e. His116, His118 and His196. The Zn2 binding site, also known as the DCH site, is where the second Zn(II) ion is coordinated, by Asp120, Cys221 and His263 (Figure 5.16). These residues are apparently strictly conserved across the B1 MBLs. In the resulting enzyme, the two zinc ions are also coordinated by two water molecules: Zn1 coordinates Zn2 via the first water molecule (Wat1) in a 2μ bridging mode, while the 3H residues complete tetrahedral coordination. The Zn2 is coordinated by another water molecule (Wat2) as an apical ligand, while the DCH has a trigonal pyramidal coordination (Figure 5.16)[220].

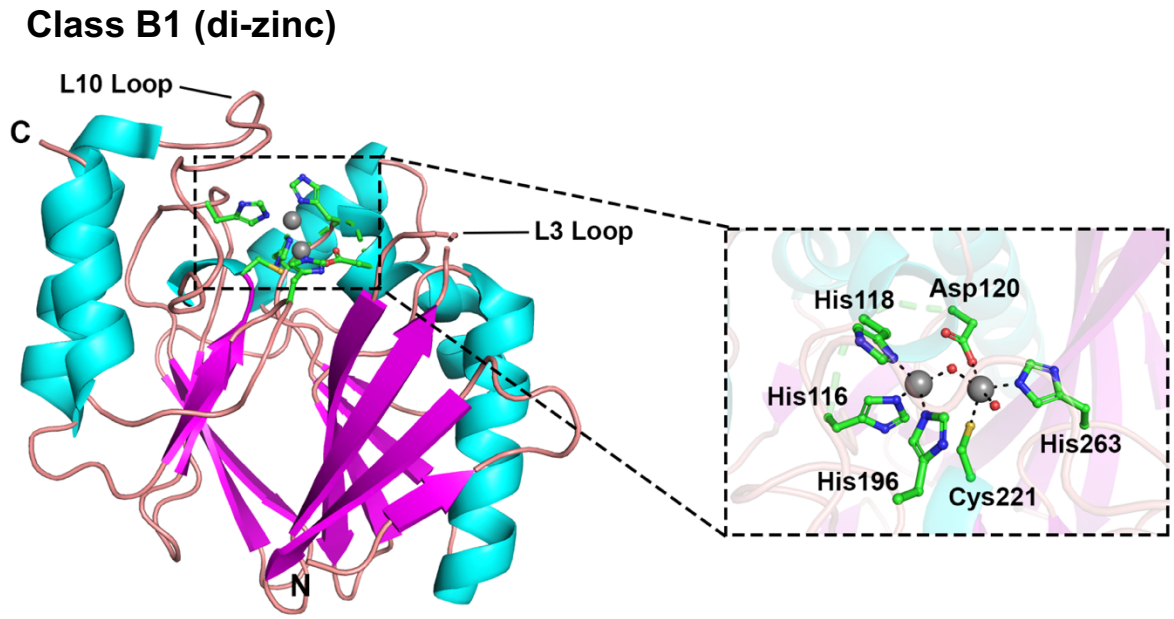


Figure 5.16: *View from a crystal structure of Ambler subclass B1 metallo-β-lactamase BcII[221]. Amino acid residues coordinated with the metal ions are represented as balls and sticks, while red spheres represent water molecules, and hydrogen bonds are illustrated by black dashed lines. Note the characteristic $\alpha\beta\beta\alpha$ fold, and the poor electron density of the L3 loop, which indicates that this region of the protein is highly flexible. (PDB ID: 4C09)*

The N-terminus of B1 MBLs contains a flexible loop, known as the L3 loop, which is located between β-sheets 3 and 4 (residues 61-65). The L10 loop is located between β-sheet 11 and α-helix 4 from residues 200-218 (Figure 5.16). These loops are important in substrate recognition and selectivity[221-223]. In the X-ray structure of MBLs, the electron density of the L3 loop is often poorly resolved, which implies high mobility for this loop even in a crystalline state. The L3 loop can move to 'close in' the substrate in the active site, which indicates that interactions occur between the hydrophobic residues on the loop (Trp64) and the hydrophobic side chain of the substrate[223]. Deletion of the L3 loop significantly reduces the enzyme activity as substrate binding is impaired[223]. The polar residues of the L10 loop, such as Lys224 or Arg228, hydrogen bond with the C3 or C4 carboxylates of β-lactam substrates and are important in binding[221].

5.1.6.2. Subclass B2 Metallo-β-lactamases

The B2 subclass MBLs have a much narrower activity profile than the B1 MBLs. The only B2 MBL members so far identified are a carbapenem hydrolysing enzyme from *Aeromonas hydrophila* (CphA), *Serratia fonticola* carbapenem hydrolase (Sfh-I) and imipenemase from *Aeromonas veronii bv. Sobria* (ImiS)[224-225]. The B2 MBLs are selective for carbapenem degradation over other β-lactams[226]. This is attributed to the distinct structure of B2 enzymes, in which the elongation of the α3 helix and a bend at Trp150 create a narrower groove at the active site. This structure is apparently well suited for carbapenems, as they lack the bulky side chains found in penicillins and cephalosporins[214]. Substitution of His116 (in B1 MBLs) to Asn116 (in B2 MBLs) (Figure 5.17) significantly reduces the affinity for Zn1 (as in B1 MBLs); thus the B2 enzymes only bind one zinc ion at the DHC site, which is sufficient for optimal enzyme activity[227]. Another Zn(II) ion can be forced into the active site by addition of excess Zn(II); however, this is inhibitory to B2 MBLs[228]. In B2 MBLs, the active site zinc ion is tetrahedrally coordinated with the DCH motif residues and a water molecule, and a second water molecule is hydrogen bonded between His118 and Asp120 (Figure 5.17).

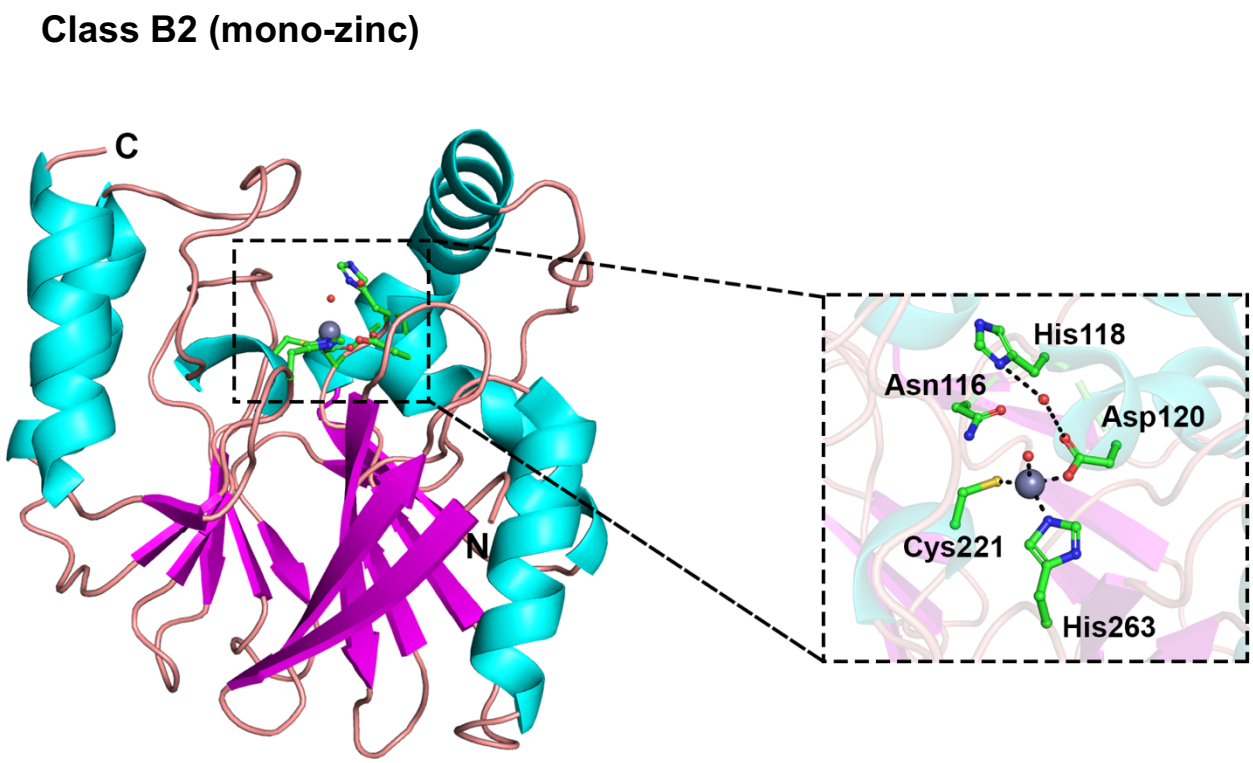


Figure 5.17: *View from a crystal structure of Ambler subclass B2 metallo-β-lactamase CphA (PDB ID: 1X8G)[229]. Amino-acid residues coordinated with the metal ion are represented as balls and sticks, red spheres represent water molecules, and hydrogen bonds are illustrated by black dashed lines. Note the characteristic αββα fold, the absence of a second Zn(II) ion, and the curved α3 helix.*

5.1.6.3. Subclass B3 Metallo-β-lactamases

The B3 subclass MBLs, in which some enzymes share only 13% sequence identity, are proposed to have evolved independently from the B1 and B2 classes (Figure 5.18)[230]. The B3 MBLs are exemplified by the *Chryseobacterium meningosepticum* β-lactamase (GOB-1), *Fluoribacter (Legionella) gormanii* endogenous zinc β-lactamase (FEZ-1), and labile enzyme from *Stenotrophomonas maltophilia* (L1)[231-233]. B3 MBLs utilise two zinc ions for their catalytic activities, except GOB-1, which is also fully active in a mono-zinc form[234]. The residues that interact with metal ions at the active site of B3 MBLs are different from those found in B1 and B2 enzymes. In the B3 MBLs, the Zn1 binds to the 3H site, as for B1 enzymes, but the Cys221 at the DCH motif is substituted by a serine residue in B3 enzymes, and Zn2 is ligated by Asp120, His121 and His263 (Figure 5.18). Although Ser221 is not directly involved

in metal binding, it is thought to interact with a water molecule in the active site and behave like a proton donor[231]. The characteristic αββα fold present in B3 enzymes is conserved across MBLs, and similar to B1 MBLs, there is a highly flexible loop between α3 and β7 that flanks the active site. This is thought to aid in substrate binding[231, 235]. L1 exists as a tetramer in solution, whereas all other MBLs are monomeric. The extended *N*-terminal regions from two L1 subunits are believed to interact to form the tetramer[231]. L1 and FEZ-1 form intra-molecular disulphide bonds, which are not observed in B1 and B2 MBLs[231, 235].

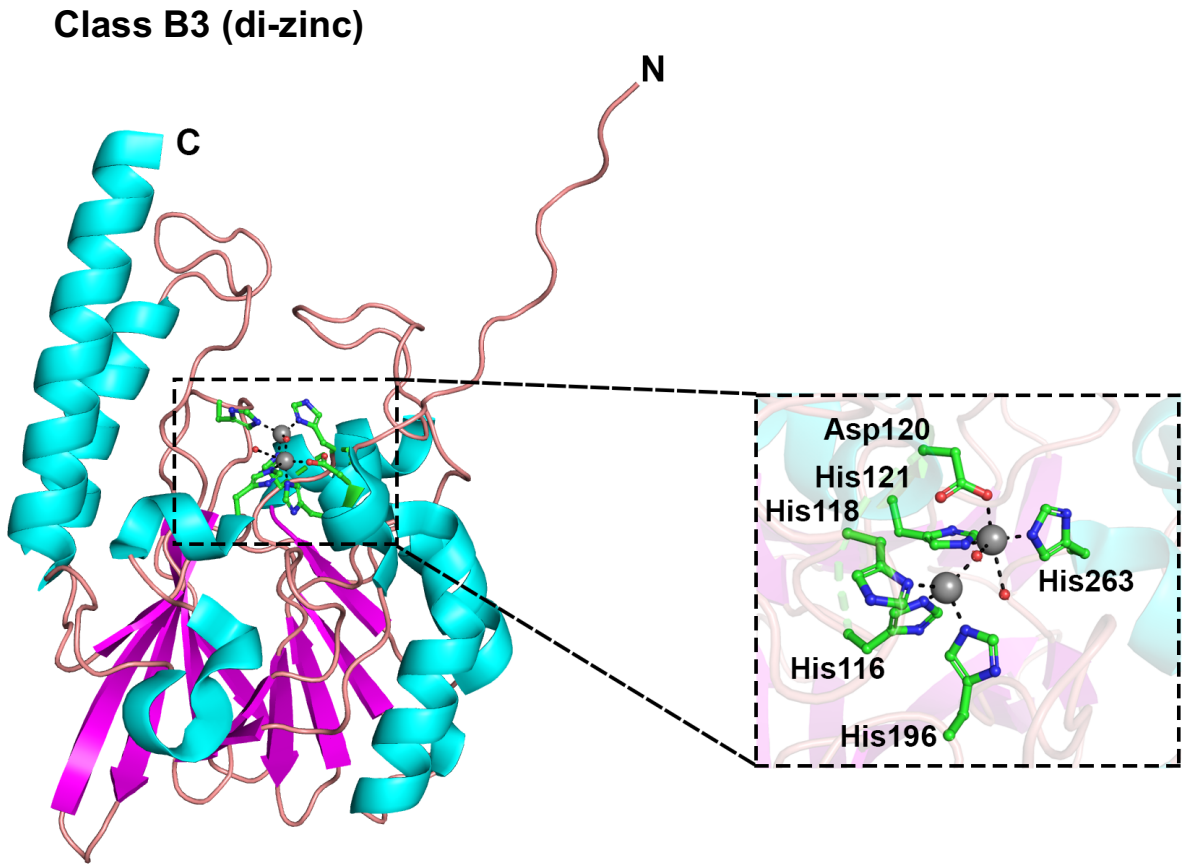


Figure 5.18: *View from a crystal structure of Ambler subclass B3 metallo-β-lactamase L1 (PDB ID: 2FM6)[231]. Amino acid residues coordinated with the metal ion are represented as balls and sticks, red spheres represent water molecules, and hydrogen bonds are illustrated by black dashed lines. Note the characteristic αββα fold, and the extended N-terminus, which is involved in oligomerisation.*

5.1.7. Mechanisms of metallo-β-lactamases

Zinc ions play a crucial role in MBL catalysis[236]. It is commonly understood that the zinc ions bound in the active site act as Lewis acids, coordinating to the carbonyl oxygen of β-lactams and polarising the C=O bond, thus facilitating nucleophilic attack on the carbon atom[236]. The resultant tetrahedral oxyanion is subsequently stabilised by the zinc ions, which also stabilise the anionic amine generated as the β-lactam ring is hydrolysed. The zinc ions directly coordinate to a water molecule, lowering the pK_a of the coordinated water, thus increasing the nucleophilicity of the resultant hydroxide ion compared with the hydroxide ions in the bulk solvent[236].

Although there is still dispute over the precise mechanism of the MBLs, it is generally agreed that the nucleophilic attack of a metal-bound water (hydroxide ion) onto the β-lactam carbonyl initiates the hydrolysis, followed by fission of the amide C-N bond, protonation of the negatively charged amine, and finally, the release of the hydrolysed product[236-240].

The initial hydrolysis mechanism was proposed based on the mono-zinc crystal structure of BcII, in which only one zinc was bound in the active site of the enzyme[218]. Upon binding of substrate, the zinc-bound water, which at neutral pH fully ionises to a hydroxide ion[237], attacks the β-lactam carbonyl group. The subsequent proton abstraction by Asp120, which acts as a general base/acid, generates a dianionic tetrahedral intermediate. This dioxyanion intermediate is stabilised by the zinc ion (via coordination), with Asp120 acting as proton donor, and this facilitates C-N bond cleavage (Figure 5.19). This mechanistic proposal has been questioned, as NMR, MS, and kinetic measurements now show that the hydrolytic activity of BcII is only optimal in the form of the di-zinc enzyme [241-242].

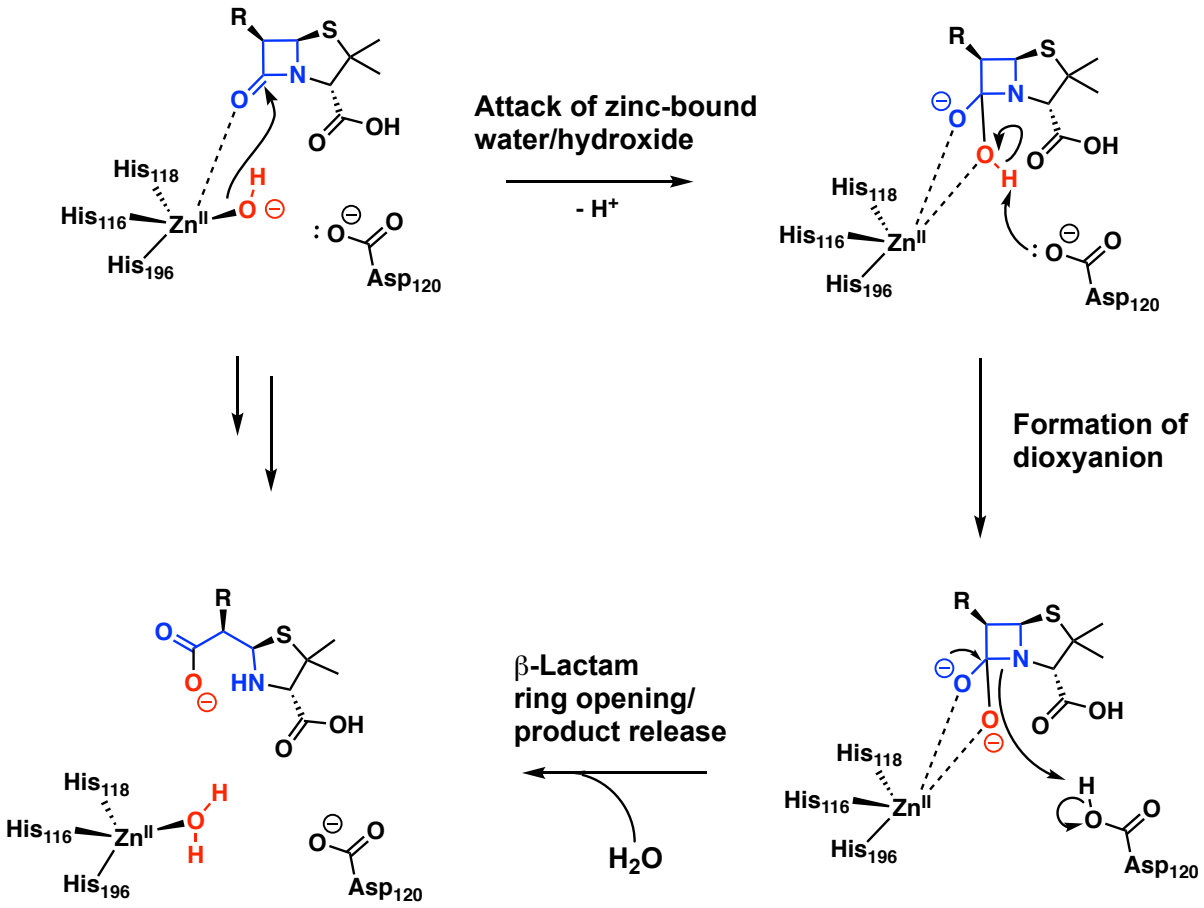


Figure 5.19: *Initial proposal of the mechanism of hydrolysis of β-lactam by metallo-β-lactamases, based on the first crystallographically observed structure of mono-zinc BcII.*

Extensive kinetic, spectroscopic and structural studies of B1 and B3 enzymes have revealed that they are di-zinc MBLs. The revised β-lactam hydrolysis mechanism begins *via* substrate binding at the metal centre. The substrate is coordinated to both zinc ions: the β-lactam carbonyl oxygen coordinates with Zn1, and the carboxylate (on the C-3 or C-4 position) interacts with Zn2. The zinc ions polarise the β-lactam carbonyl, facilitating nucleophilic attack from the μ2 bridging water molecule, which is fully ionised to a hydroxide ion at neutral pH due to stabilisation from the two zinc ions[237]. This hydroxide ion can then attack the carbonyl carbon, resulting in a transient tetrahedral intermediate (Figure 5.20).

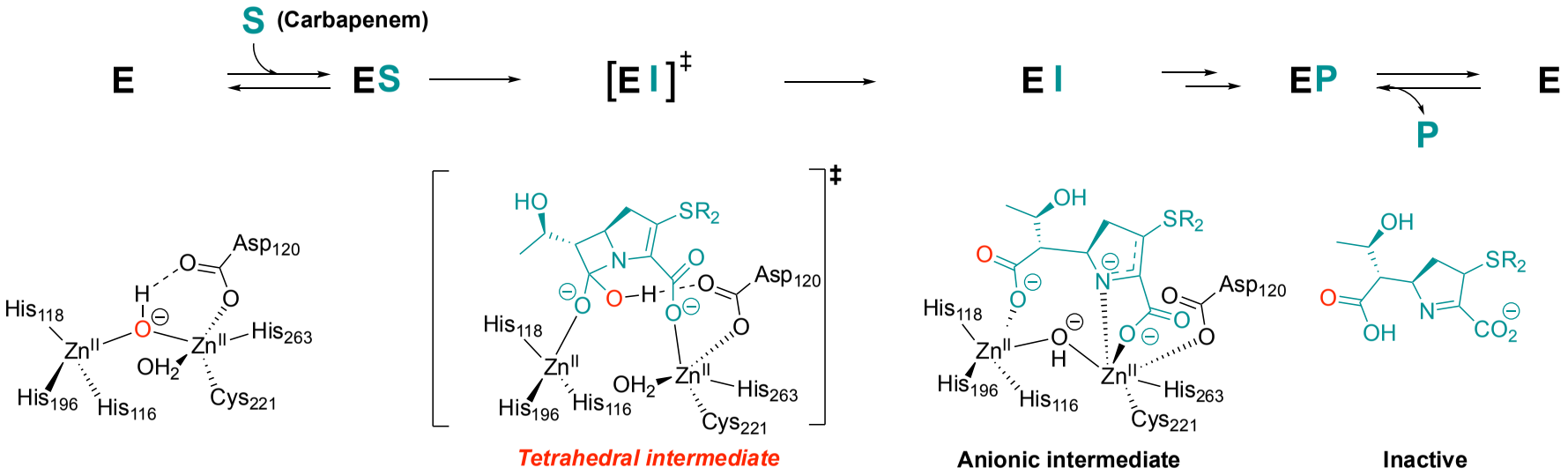


Figure 5.20: *Revised hydrolysis mechanism of B1 and B3 class metallo-β-lactamases as di-zinc enzymes, exemplified with a carbapenem. The anionic intermediate, but not the tetrahedral intermediate‡, has been observed spectroscopically. The substrate/product is shown in cyan and enzyme is shown in black. E: enzyme, S: substrate, ES: enzyme-substrate complex, [EI]‡: enzyme tetrahedral intermediate complex, EI: enzyme ionic intermediate complex, EP: enzyme-product complex, P: product.*

The mechanism through which the tetrahedral intermediate collapses and the C-N bond is subsequently cleaved is controversial. The C-N bond cleavage could be concomitant with protonation of the amine leaving group, or cleavage could occur without protonation of the negatively charged nitrogen atom, resulting in accumulation of an anionic species. Crystallographic and pre-steady state kinetic studies of cefoxitin- and carbapenem-resistant MBL (CcrA, B1) with a chromophoric β-lactam substrate, nitrocefin (Figure 5.21), have revealed accumulation of an enzyme-bound intermediate with a strong absorbance at 665 nm[239]. It has been suggested that the leaving nitrogen atom remains negatively charged during the C–N bond cleavage (Figure 5.21)[239]. A similar intermediate has been observed in stopped-flow analysis of the action of the B3 enzyme, L1, and this study has provided further evidence that protonation of the anionic intermediate is the rate-determining step[243]. However, no anionic intermediate accumulation has been observed for the reaction catalysed by BcII[244]. This apparent discrepancy may be due to the highly conjugated 2,4-dinitrostyryl substituent of nitrocefin (Figure 5.21), which is atypical compared with clinically used cephalosporins. The enhanced stabilisation of the negative charge on the nitrogen atom in this proposed system would cause protonation to be the rate-determining step. Studies of L1 with other substrates, e.g., cefaclor and meropenem, found no detectable intermediates, hence the C-N bond cleavage appears to be the rate-determining step[238]. In addition, several academic groups have reported conflicting results regarding nitrocefin hydrolysis by IMP-1; Griffin *et al*. reported accumulation of the anionic intermediate[245], whereas two other groups failed to detect any such species[246-247]. Although no intermediate has been detected during BcII hydrolysis of nitrocefin, stopped-flow studies show evidence that an intermediate does accumulate during hydrolysis of impenem[248]. These results suggest that the rate-limiting step, whether C–N bond cleavage or the subsequent protonation of the anionic nitrogen, is dependent on the specific substrate and enzyme involved.

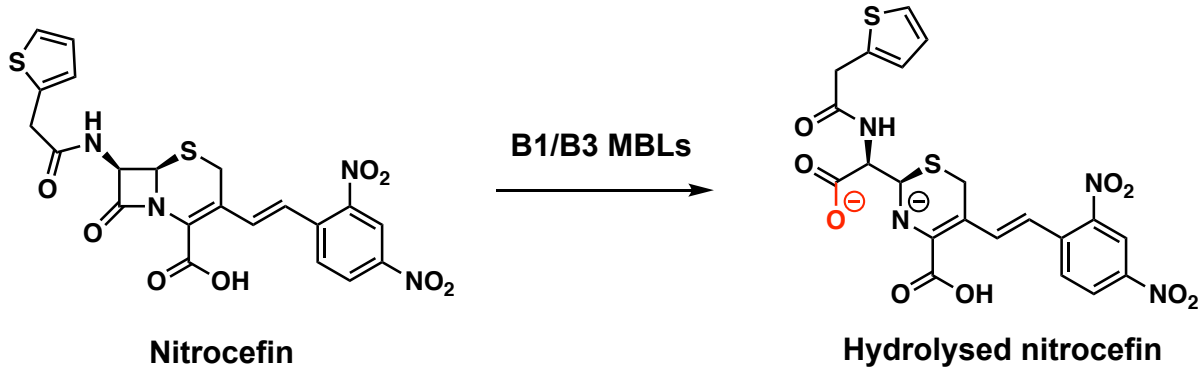


Figure 5.21: *Hydrolysis of the atypical substrate nitrocefin by subclass B1 and B3 MBLs. Note that in the anionic nitrogen intermediate, the negative charge is stabilised by the extensive conjugation of the 2,4-dinitrostyryl substituent at the 3 position of the dihydrothiazine ring.*

Mutational studies of BcII and L1 show that Asp120 is not essential for activating a nucleophile, nor does it behave as a proton donor for the anionic intermediate[249]. This finding suggests it does not have a role as a general acid/base catalysis. Rather, Asp120 is a strong ligand for Zn2, and is proposed to direct the zinc ion for optimal substrate binding[249-250]. Recent structural work on NDM-1 complexed with hydrolysed ampicillin has led to the proposal that the carboxylate formed during β-lactam hydrolysis (originally from the hydroxide ion) is responsible for protonation of the β-lactam derived nitrogen anion[240]. The apical water bound to Zn2 is optimally positioned to protonate the leaving nitrogen during the β-lactamase reaction[242]. This water molecule may then move to the Wat1 position, and then ionise, preparing the enzyme for further catalysis[242].

The subclass B2 MBLs show a somewhat different mechanism of catalysis compared with the B1 MBLs, as they are only active in mono-zinc form, with a zinc ion bound at the DCH site[251-252]. Structural work on CphA[251] and Sfh-I[253] has revealed a metal-bound water molecule, and another water molecule coordinated between His118 and Asp120 which possibly exists as a hydroxide ion, and may initiate the nucleophilic attack (Figure 5.22). The anionic nitrogen leaving group generated from the collapse of the tetrahedral intermediate is stabilised by zinc coordination, and the metal-bound water subsequently protonates the anionic nitrogen (Figure

5.22)[242]. This mechanism is supported by the apparent inhibition of B2 MBLs by a second zinc[252], since binding of the metal in the H3 site would require coordination with His196, (which has been proposed to activate the β-lactam carbonyl), and His118 (which is essential to deprotonate the hydrolytic water).

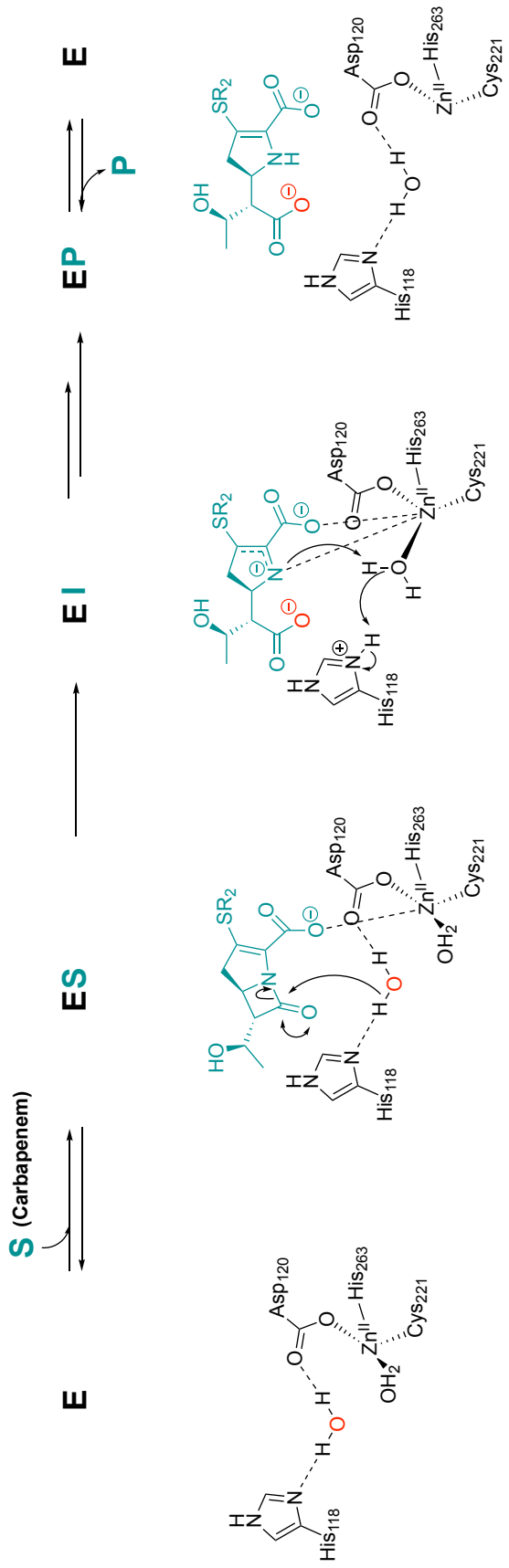


Figure 5.22: *Hydrolysis mechanism of B2 class metallo-β-lactamases as mono-zinc enzymes, exemplified with a carbapenem substrate. The substrate/product is shown in cyan and enzyme is shown in black. E: enzyme, S: substrate, ES: enzyme-substrate complex, EI: enzyme-intermediate complex, EP: enzyme-product complex, P: product.*

5.1.8. Inhibition of metallo-β-lactamases

Due to the variations in the sequences and mobile regions around the active sites of MBLs, it is challenging to develop MBL inhibitors with the breadth of activity required for clinical applications[254]. Distinct classes of MBL inhibitors have been developed[255], most of which are zinc/metal chelators; however, few if any of the reported inhibitors are able to inhibit the clinically widespread MBLs (e.g. NDMs, VIMs, and IMPs).

Zinc chelators:

The first MBL inhibitor, EDTA, was discovered serendipitously, and its finding led eventually to the identification of BcII. This opened the possibility for the development of inhibitors based on active site metal chelation, which typically contain one or more carboxylic acid groups or tetrazoles[255]. Substituted phthalic acids and succinic acids (Figure 5.23) show very good inhibition when optimised. Some of the most potent inhibitors act in the nanomolar range, and have been reported to potentiate carbapenems against IMP-1 producing *E. coli*[256-257]. Structural studies on IMP-1 have revealed that these inhibitors bind via the chelation of the carboxylate groups to the zinc ions at the active site, in a stoichiometric ratio, displacing the bridging water, and mimicking the binding of hydrolysed β-lactam products[258]. Succinic acids have also been reported to inhibit L1 through a similar binding mode[259]. Chelating inhibitors include the biphenyl tetrazoles (Figure 5.23), which, with considerable optimisation, can manifest IC_{50} values in the low micromolar range against IMP-1 and CcrA from *B. fragilis*[260]. Pyridine dicarboxylates and pyridine monothiocarboxylic acid analogues (Figure 5.23) exhibit low micromolar IC_{50} values against L1, CphA, and CcrA. It is proposed that they mimic hydrolysed cephalosporins[261-262]. Other zinc-chelating inhibitors include trifluoromethyl ketones/alcohols and hydroxamates (Figure 5.23), which are among the first synthetic MBL inhibitors to be developed[263-264].

Thiol derivatives:

The affinity of sulphur to zinc is well known; hence many inhibitors, such as the thiomandelic acids (Figure 5.23), show promising inhibition against MBLs[265]. Although these inhibitors exhibit a similar mode of action to that of the zinc chelators as discussed above, they distinguish themselves as the free sulphydryl group binds to both zinc ions, mimicking the hydrolytic water/hydroxide in the uninhibited enzyme (Figure 5.20)[265]. The thiol-based inhibitors may also contain carboxylate or phosphate groups, such as in 2,4-dichlorophenyl-mercaptomethyl-phosphonic acid (Figure 5.23), which is a potent subclass B2 MBL inhibitor[266]. The potent angiotensin-converting enzyme (ACE) inhibitor L-Captopril has been shown to inhibit all three subclasses of MBL, especially the di-zinc B1 and B3 subclasses[267]. The rhodanine compound ML302, and especially its hydrolysed fragment, the ene-thiol compound ML302F, has been reported as a broad-spectrum sub-micromolar inhibitor for subclass B1 MBLs (Figure 5.23)[268]. The slightly altered bond angle of the thiol and carboxylate enables an unusual binding mode, as the thiol replaces the bridging water/hydroxide between the two zinc ions while the carboxylate binds to the second zinc ion. This binding mode may be responsible for the potent inhibition. Spectroscopic studies on mercaptoacetic thiol esters with BcII have revealed that they may act as mechanism-based inhibitors[269]. These molecules are hydrolysed into mercaptoacetic acid *in situ*, reacting with Cys221 (from the DCH site) to form a disulphide linkage, which prevents the cysteine residue from coordinating with the second zinc ion.

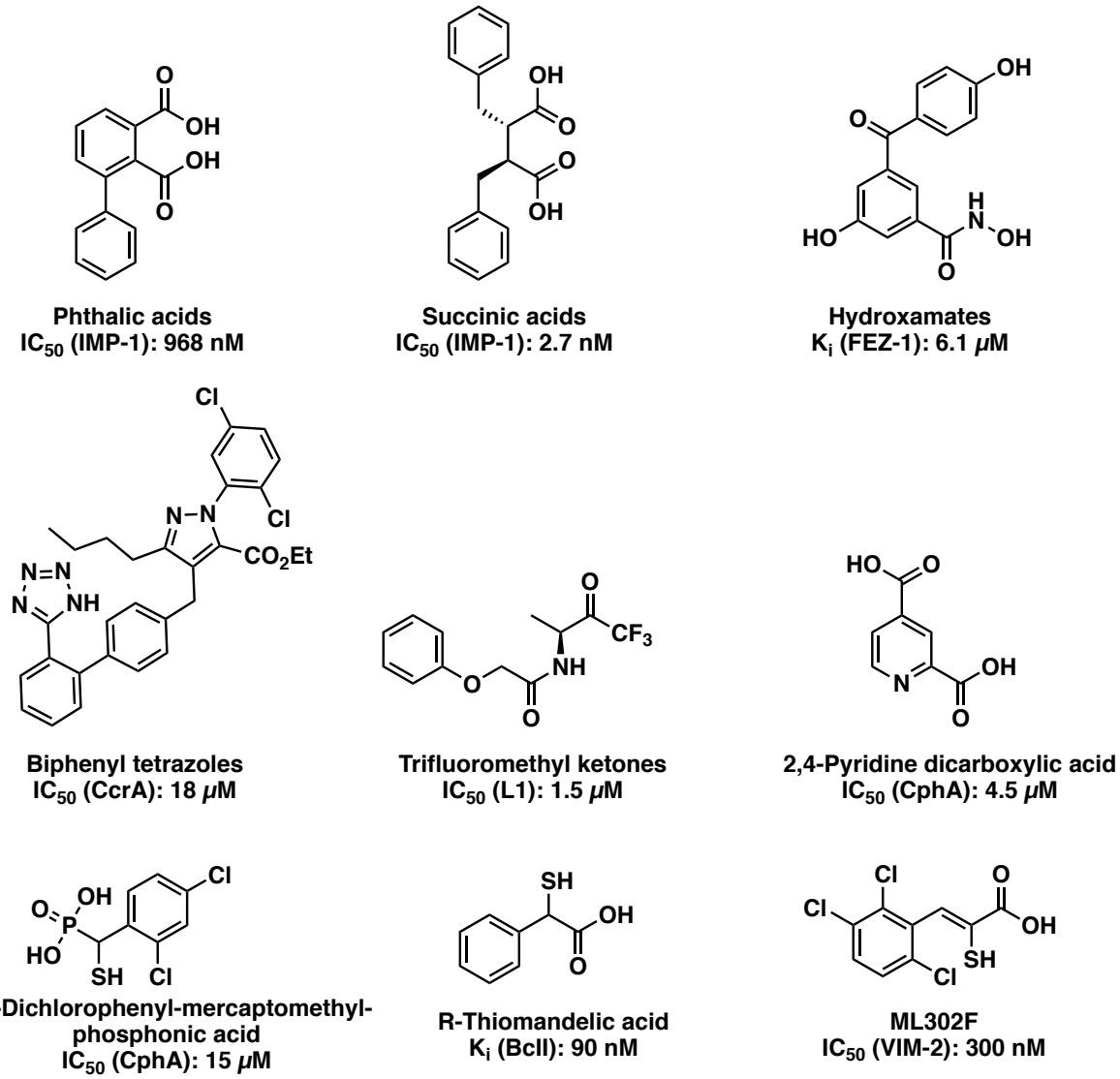


Figure 5.23: *Selected structures of the different classes of metallo-β-lactamase inhibitors. Reported IC_{50}/K_i values are also included.*

β-Lactam analogues as MBL inhibitors:

Since all classes of β-lactamases take the substrates with a β-lactam core, it is obvious to consider designing inhibitors that resemble their natural substrates. A carbapenem analogue, J-110,441, has been reported to inhibit simultaneously class A, B, and C β-lactamases, with K_i values of 0.83, 1.00, 0.23, and 0.0037 μM, for the BcII, L1, CcrA and IMP-1 MBLs, respectively[270].

5.1.9. Summary

The class of antibiotics known as β-lactams, since their discovery, have remained among the most important medicines in clinical use today. However, their remarkable longevity and efficacy to act as antibiotics is continuously challenged by multiple resistance mechanisms. Together, the SBLs and MBLs represent the most prevalent antibiotic resistance mechanism to β-lactams; these enzymes catalyse the hydrolysis of β-lactams to give (near) inactive β-amino acid products. Although they accept overlapping sets of substrates and exhibit conserved folds, the SBLs and MBLs show great variation in their active-site structures, metal requirements and hydrolysis mechanisms (particularly within the MBLs), and, importantly, in their inhibition. Although β-lactam antibiotics may ultimately lose their efficacy against resistant bacteria, continued research on β-lactamase enzymes and the development of inhibitors could preserve the β-lactams as effective drugs in the future.

While class A (and to some extent class C and D) SBL-mediated resistance can be managed by co-administration of SBL inhibitors, such as clavulanic acid and avibactam, alongside a β-lactam antibiotic, it is a major concern that to date there have been no clinically available MBL inhibitors. Although there are a number of inhibitors developed for MBLs, few, if any, have the required breadth of potency against the major clinically relevant subclass B1 MBLs. Combination therapy, which has been successful for SBL inhibition, could be useful for MBL inhibition; therefore, further understanding of MBLs and their mechanisms is required for the development of potent and broad inhibitors. There is also a growing need for 'dual-action' inhibitors that inhibit both SBLs and MBLs simultaneously, as the number of reports of resistant bacteria that co-produce both SBLs and MBLs continues to rise, and due to the ability of MBLs to degrade current SBL inhibitors, such as avibactam.

5.2. Previous studies on rhodanines as MBL inhibitors

Five-membered 'multiheterocyclic' (FMMH) ring molecules (Figure 5.24) are of considerable utility in medicinal chemistry. In particular, the rhodanine scaffold has been described both as a 'privileged scaffold'[271] and as a 'promiscuous binder'[272]. These apparently conflicting views reflect the potential of rhodanines to interact with multiple biological targets. This property can be regarded as an advantage in the field of antibiotics, since it can potentially enable interaction with several different targets in a biological pathway by a single inhibitor[273], or enable inhibition of a broad spectrum of targets, e.g. one inhibitor for all β-lactamases. Another reason why FMMHs, such as rhodanines, may have been considered 'privileged scaffolds' is that they can be readily functionalised. Knoevenagel condensation with aldehydes or ketones can be used to vary the α-carbon substituent. Electrophilic substitution at the amino group can be used to enable further variations (Figure 5.24)[274-279].

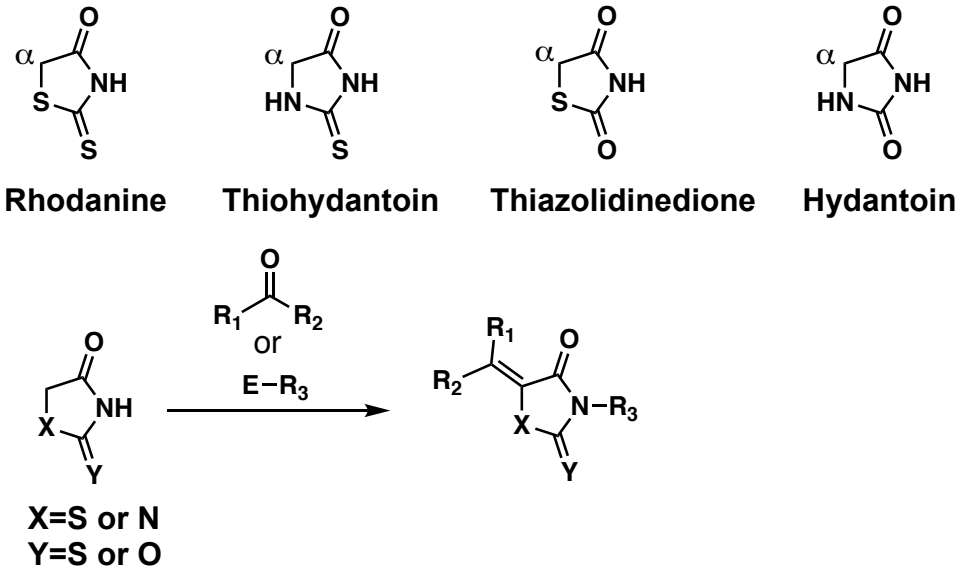


Figure 5.24: *General structures of five-membered multiheterocyclic rings and representative reaction schemes for functionalisation.*

One of the structural features of many FMMHs is the presence of an exocyclic double bond in conjugation with a ring group and carbonyl group. The αβ-unsaturated system (Michael acceptor) is prone to reactions with biological nucleophiles, which is a feature normally

avoided in medicinal chemistry. However, a systematic study of rhodanines and related FMMHs by Mendgen *et al*. reveals that compounds bearing these scaffolds do not necessarily show unspecific reactivity toward biological nucleophiles such as glutathione[271]. Powers *et al*. have described an unsaturated rhodanine that forms a covalent bond with a cysteine residue of hepatitis C virus polymerase. However, this reaction is reported to be highly specific for the target enzyme[280]. A study by Mendgen *et al*. argues against their use for inhibition in a promiscuous way; the binding properties of FMMHs, especially rhodanines, were proposed to be due to the ability of exocyclic double-bonded heavy atoms (sulphur in the case of rhodanines) to make multiple polar interactions[271].

(**I**) was the first reported rhodanine-derived β-lactamase inhibitor. It shows promising potency against TEM-1, from *E. coli* (class A), and β-lactamase from *E. cloacae* strain P99 (P99, class C) (Figure 5.25)[281]. After modification of the exocyclic side-chains, **II** was identified as a sub-micromolar inhibitor for P99, and was also found to be 200-fold more selective over TEM-1. Not only do these rhodanine compounds inhibit TEM-1 and P99, but they also show antibacterial activity toward bacterial strains that produce class A and C β-lactamases. Indeed, a number of studies have reported rhodanine or FMMH-derived compounds (**III-V**) as antimicrobial agents[273, 282-284]. Although these compounds were developed as standalone antimicrobials and compounds with the ability to target enzymes such as Mur ligases, they have also been found to have potential to inhibit β-lactamases. Rhodanine compounds (**VI**) have been reported to uncompetitively inhibit PBPs (PBP2 from *N. gonorrhoea*, and PBP2x from *S. pneumoniae*)[285]. The rhodanine **ML302** (**VII**) has been identified as a sub-micromolar potency (IC_{50}) broad-spectrum inhibitor of the class B1 MBLs, including IMP-1 and VIM-2[286].

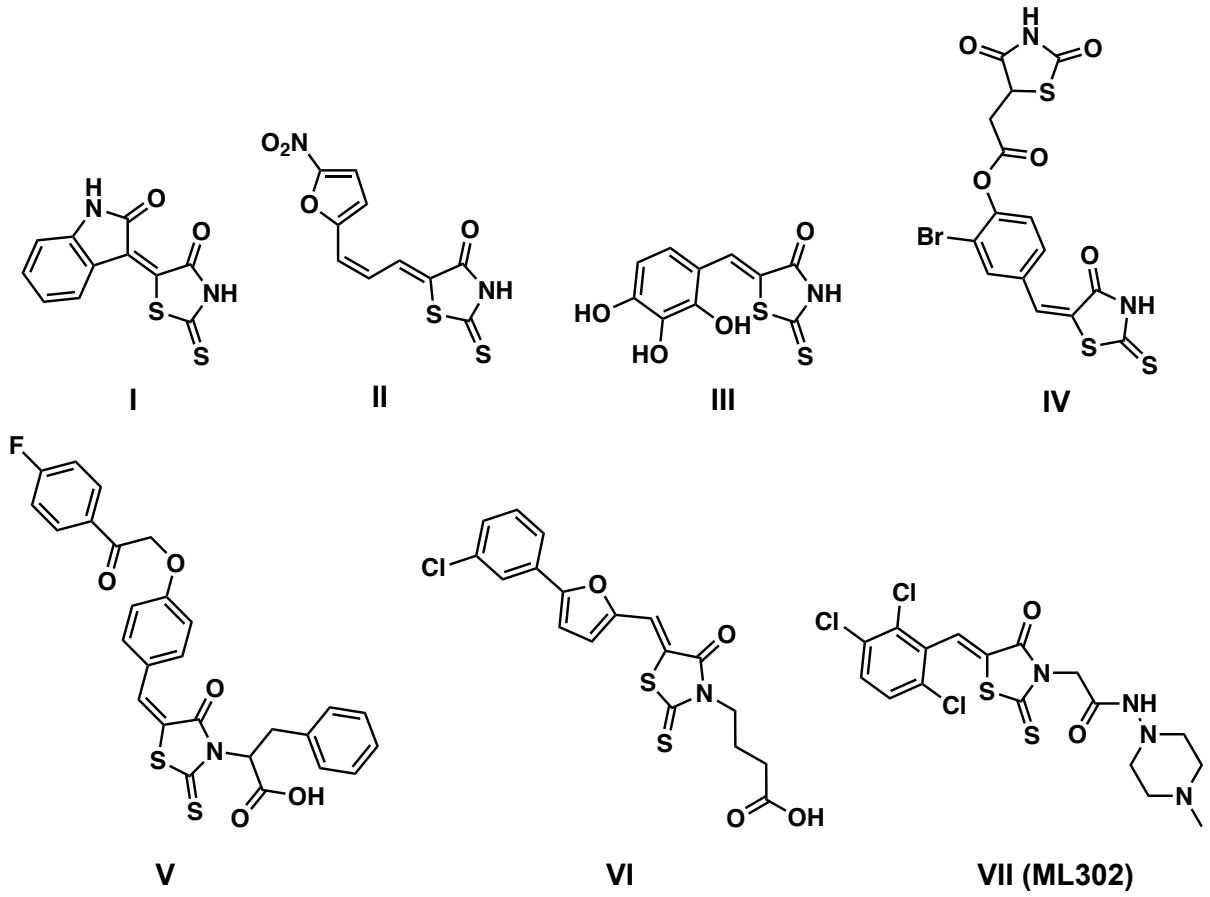


Figure 5.25: *Representative structures of reported antimicrobial agents that contain the rhodanine moiety.*

In 2014, researchers from the University of Oxford reported an unexpected observation[268] that **ML302** (Figure 5.26) underwent hydrolysis to produce the enethiol fragment, **ML302F** (Figure 5.26), which inhibited MBLs via Zn(II) ion chelation at the active site. In the case of VIM-2, the unusual formation of a ternary complex between the enzyme and two different ligands, **ML302** and **ML302F,** was observed. The mixture of the two molecules, **ML302M**, manifested greater inhibitory effect than either **ML302** or **ML302F** alone.

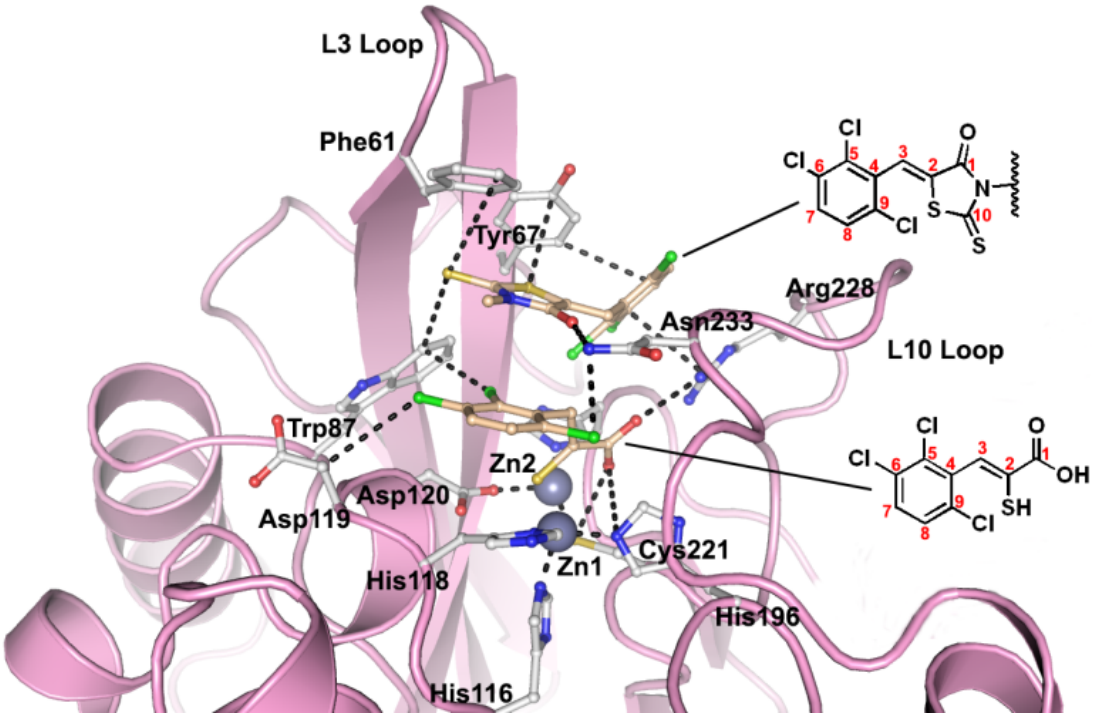


Figure 5.26: *Crystallographic analysis reveals that* ***ML302*** *undergoes fragmentation to form the enethiol inhibitor* ***ML302F*** *(PDB ID: 4PVO), which coordinates to the di-Zn(II)-containing active site of VIM-2*[268]*. The structure suggests possible synergistic inhibition of* ***ML302M*** *(****ML302****+****ML302F****) to VIM-2. All figures are labelled using the BBL numbering scheme*[287]*. Reprinted with permission from Elsevier B. V..*

Crystallographic studies of VIM-2 and the BcII in complex with **ML302F**, and in the case of VIM-2 and, **ML302** have been reported[268]. In the case of BcII, a single **ML302F** molecule was apparent at the active site. Unexpectedly, when **ML302** was co-crystallised with VIM-2, each of the two molecules in the asymmetric unit showed **ML302F** chelating Zn(II) at the active site. However, an additional molecule of **ML302** was apparent near the active site of chain A, but not chain B. The additional **ML302** was positioned to interact with **ML302F**, via staggered π-stacking between the rhodanine ring of **ML302** and the 2,3,6-trichlorophenyl ring of **ML302F** (Figure 5.26).

5.3. Chapter objectives

An assay platform for MBLs that employs a fluorogenic cephalosporin substrate has been developed at the University of Oxford[288]. Application of this assay has identified the rhodanine **ML302** (Figure 5.25) and its hydrolysed product, enethiol **ML302F** (Figure 5.23), as inhibitors of VIM-2 and IMP-1[268]. Following this initial report, the objective of the work described in this chapter was to investigate and develop rhodanine- and enethiol-derived MBL inhibitors. It was intended to carry out structure-activity relationship (SAR) and biophysical studies on identified inhibitors against MBLs and SBLs.

Please note, much of the work detailed in this chapter has been reported in the academic literature in: '*Structure activity relationship studies on rhodanines and derived enethiol inhibitors of metallo-β-lactamases*', https://doi.org/10.1016/j.bmc.2018.02.043.

In section 5.6, ^{1}H and ^{19}F NMR data acquisition for Figure 5.38-5.45 was performed by Mr Jos Kamps whom was also involved in figure preparation. 2D ^{1}H-^{13}C heteronuclear single quantum correlation (HSQC) and heteronuclear multiple bond correlation (HMBC) NMR experiments were conducted by Mr Jos Kamps including spectral characterisation. Mr Jos Kamps carried out data collection and data analysis for LC-MS experiments (Figure 5.48). Mr Jos Kamps also contributed in discussion on possible enethiol cyclisation/dimerization mechanism.

5.4. MBL inhibition

5.4.1. Design and synthesis of rhodanine and rhodanine-derivative inhibitors of MBLs

The hydrolysed product of rhodanine (i.e., the enethiol) has been reported to be a more potent MBL inhibitor than the parent rhodanine[268]. Thus, it was envisaged that inhibitors could be designed in which the thiolcarboxylate moiety was retained to secure zinc ion chelation, whilst the substituents on the phenyl ring could be varied to further increase binding to MBLs, whilst reducing off target inhibition (Figure 5.27). As the addition of the substituted phenyl group was the first step of the synthetic route to rhodanines/enethiols (Scheme 5.1), and various aromatic aldehydes were commercially available, this route was considered an attractive option to build analogues efficiently for use in SAR studies.

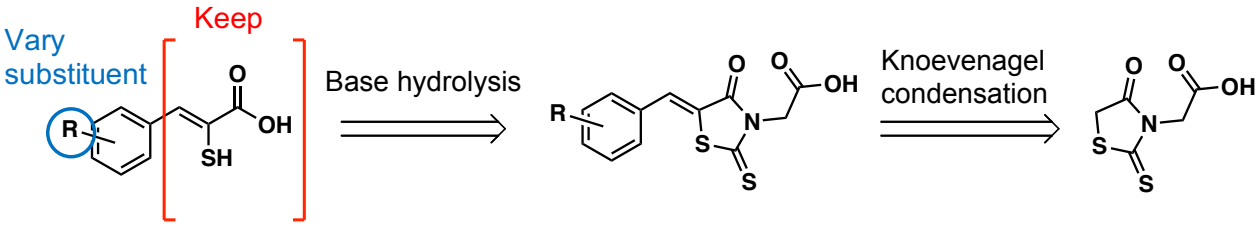
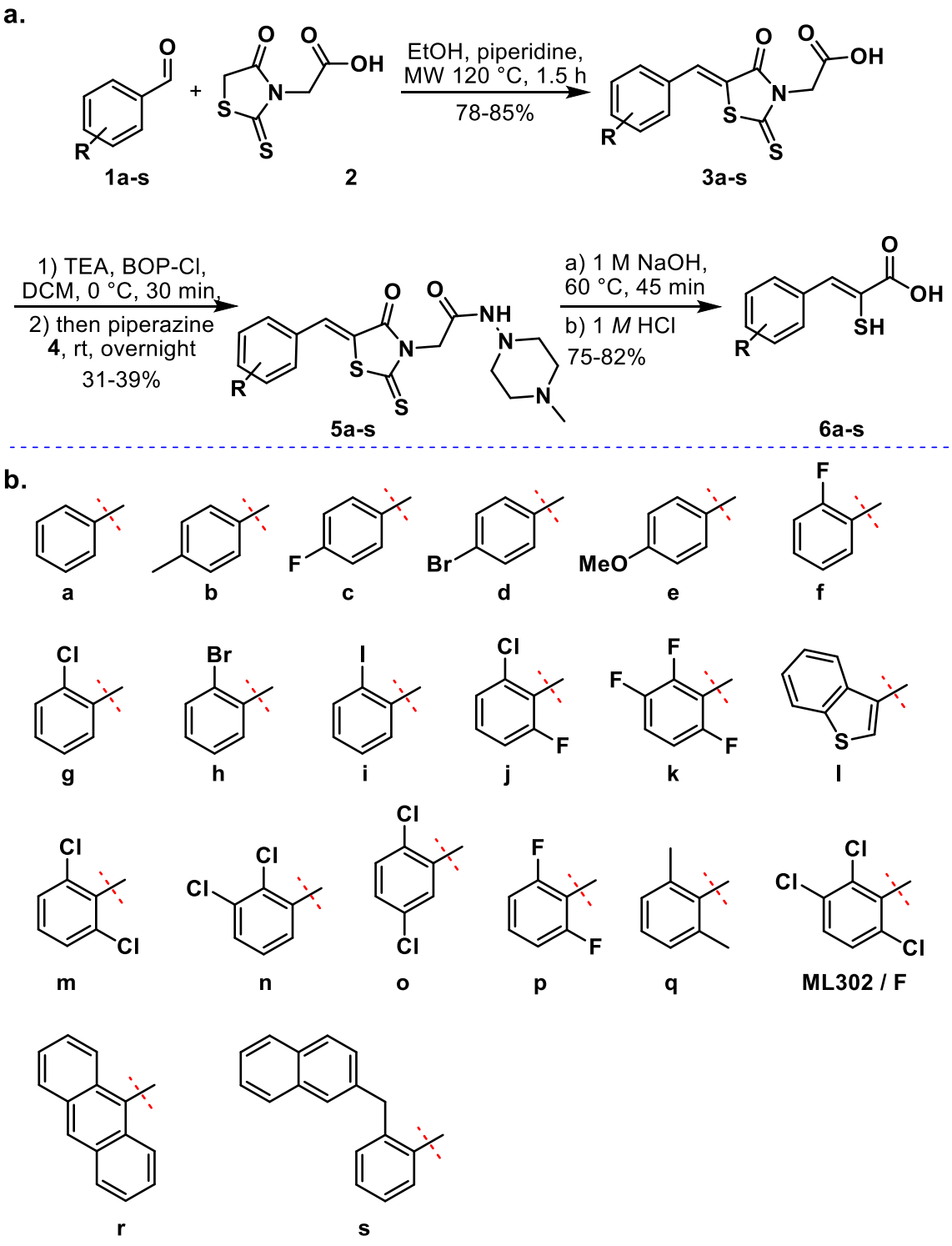


Figure 5.27: *Retrosynthetic analysis of the designed MBL inhibitors.*

The syntheses of **3a-s**, **ML302** analogues **5a-s**, and **ML302F** analogues **6a-s** (Scheme 5.1) were in general performed as previously described[268]. First, the Knoevenagel condensation of rhodanine-*N*-acetic acid **2** with aldehydes **1a-s** produced the stereoisomeric mixture of benzylidene-(4-oxo-2-thioxo-thiazolidin-3-yl)-acetic acid derivatives **3a-s**[289-290]. Next, amide coupling with 1-amino-4-methylpiperazine **4** gave the desired **ML302** analogues **5a-s** as a stereoisomeric mixture. Base hydrolysis with 1 M NaOH, followed by neutralisation with HCl gave the target enethiol **ML302F** and its analogues **6a-s** exclusively (as analysed by ^{1}H and ^{13}C NMR) as the Z-isomer. The molecule **1s**, which is the precursor of **3s**, was prepared by Suzuki coupling of naphthalene methyl bromide with 2-formylphenylboronic acid to give the desired aldehyde.



Scheme 5.1. *Synthesis of enethiol-based β-lactamase inhibitors. (a) Route used for preparation of the* ***ML302*** *analogues* ***5a-s*** *and the* ***ML302F*** *analogues* ***6a-s****. (b) R groups for* ***5a-s*** *and* ***6a-s****. MW: microwave irradiation.*

The Knoevenagel condensation reaction was relatively straightforward, giving the desired products (**3a-s**) in at least 80% yield. However, the subsequent amide couplings (to give **5a-s**) proved to be problematic. Initially, the reaction was performed as previously described, using bis(2-oxo-3-oxazolidinyl)phosphinic chloride (BOP-Cl)[268]; however, the resulting yields were unsatisfactory, averaging around 32%. Screening of other amide-coupling reagents did not lead to an improvement in the reaction yield (Table 5.1), hence BOP-Cl was used for further syntheses. The relatively low yield of coupling may in part be due to the conjugation of the aryl-rhodanine system, such that the carboxylic acid was less nucleophilic toward the coupling reagents.

Table 5.1: Reagents and conditions attempted for amide coupling. Substrates are **3a-s**, and products are **5a-s.**

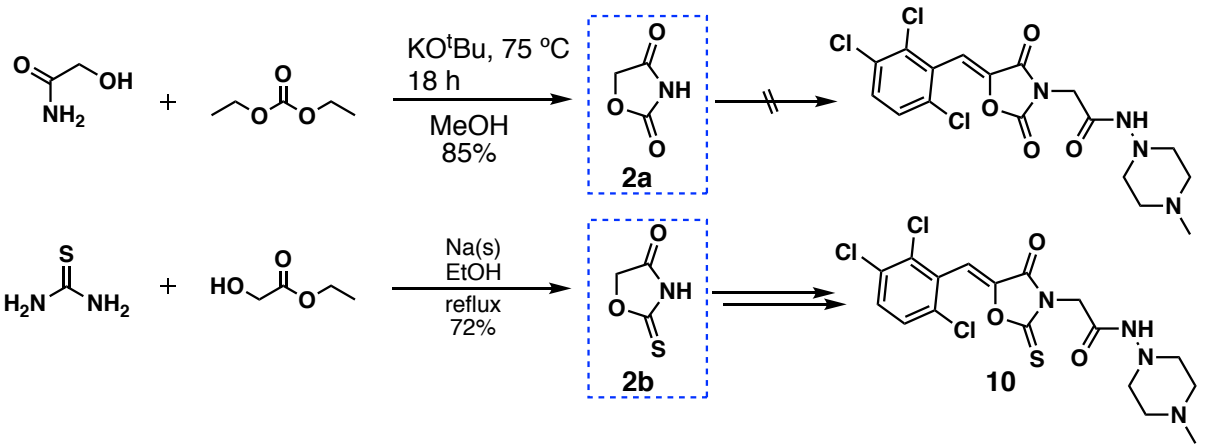
Reagents	Condition	Reaction	Yield
BOP-Cl	TEA, DCM, r.t., overnight	Yes	32%
PyBOP	DIPEA, DCM, r.t., overnight	Yes	31%
CDI	THF, r.t., overnight	Yes	23%
HATU	TEA, DCM, r.t., overnight	Yes	38%
T3P	DIPEA, DMA, r.t., overnight	Yes	29%

r.t.: room temperature, BOP-Cl: Bis(2-oxo-3-oxazolidinyl)phosphinic chloride, pyBOP: benzotriazol-1-yl-oxytripyrrolidinophosphonium hexafluorophosphate, CDI: carbonyldiimidazole, HATU: 1-[bis(dimethylamino)methylene]-1H-1,2,3-triazolo [4,5-b]pyridinium 3-oxid hexafluorophosphate, T3P: propylphosphonic anhydride, TEA: Triethylamine, DIPEA: N,N-diisopropylethylamine

The main issue encountered for this synthetic approach, however, was the reaction work-up and purification. The amide coupling products **5a-s** are tertiary amines with a piperazine moiety, so it was not possible to carry out standard aqueous work-up (to eliminate excess TEA) as the product would also be protonated and would enter the aqueous layer, and this would decrease the yield. As analysis by thin-layer chromatography (TLC) of the completed reaction showed clear separation between products and starting materials, purification by automated flash chromatography was an obvious choice. However, during flash chromatography TEA was observed to co-elute with **5a-s**, despite the fact that the compounds were well separated on

ninhydrin stained TLCs. LC-MS analyses revealed that the detected species were the amide products (**5a-s**) and TEA. Automated flash chromatography was repeated; however, no useful separation was achieved. Various other purification techniques were attempted, including azeotropic distillation with high boiling point solvents, overnight evaporation under high vacuum, and cation exchange chromatography. Recrystallisation using heated solvent was not an option as the compounds degrade at high temperature (see the compound characterisation section in Materials and Methods). Eventually, manual column chromatography (i.e. non-automated flash chromatography) successfully separated **5a-s** from the TEA contamination using DCM:MeOH 9:1, although the final yields of isolated product were only around 25%.

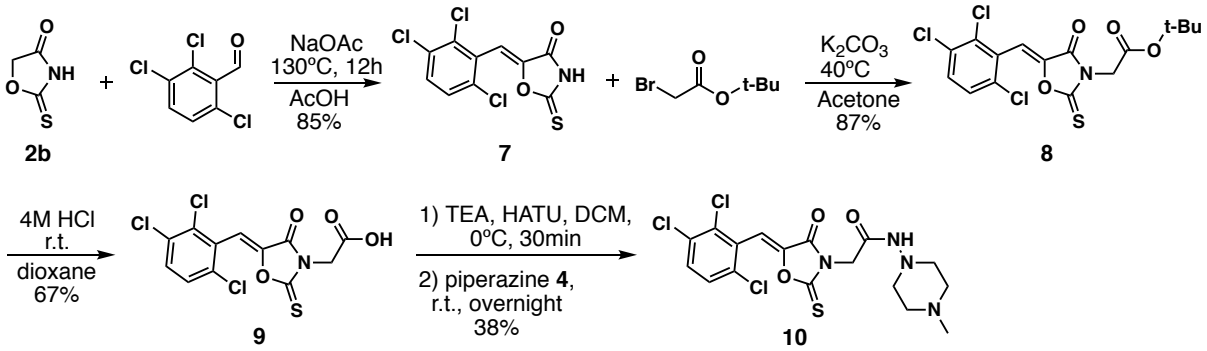
To investigate the effects on MBL inhibition of changing the electronic properties of the thiazolidine ring, two other FMMH ring compounds were prepared (**2a**, **2b**, Scheme 5.2).



Scheme 5.2: *Synthetic route to obtain the FMMH rings* ***2a*** *and* ***2b****.*

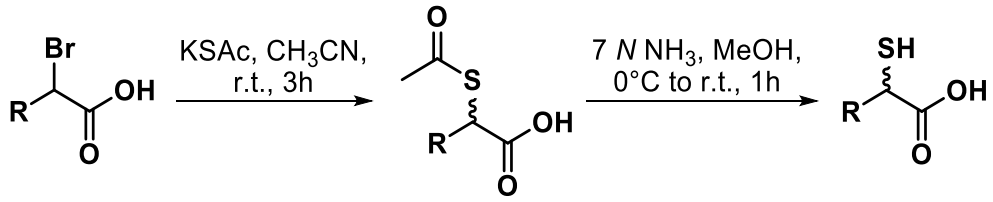
The **ML302** derivative, **10**, was initially prepared from **2b** in a similar manner to that used for the synthesis of the **ML302 5a-s** and **ML302F 6a-s** analogues (Scheme 5.1). However, after introduction of the *t*-butyl protected acetic acetyl chain via *N*-nucleophilic substitution, the Knoevenagel condensation occurred less readily than for the analogous 4-oxo-2-thioxo **2** (rhodanine) ring system. This reduced reactivity, coupled with the broad biological importance of these types of ring systems, has led to the development of catalytic protocols for their

synthesis (e.g. pyridine/EtOH, piperidine/EtOH/AcOH, NaOAc/AcOH, NH_4OAc/AcOH, NH_4OAc, NH_4OAc/toluene etc.)[274-278]. The above conditions were attempted without much success (yields of **8** were approximately 10%). Reversing the order of addition circumvented this problem (Scheme 5.3), as Knoevenagel condensation on the unsubstituted 2-thioxooxazolidin-4-one ring **2b** followed by *N*-nucleophilic addition gave a very good yield of **7** and **8**, over 85% in both steps. When the same procedure was attempted on compound **2a**, no reaction was observed, including reversing the reaction order. It was postulated that the poor orbital overlap and stronger electronegativity of the oxygen atom relative to the sulphur atom rendered the enolate relatively unreactive, hence the lack of reaction.



Scheme 5.3: *Synthesis of the* ***ML302*** *analogue,* ***10****. r.t.: room temperature.*

For comparison with the enethiols, α-mercaptocarboxylic acids **13a** and **13b** were prepared in two steps from the corresponding α-bromocarboxylic acids (**11a** and **11b**, respectively), following the procedure of Shaffer *et al.*[291] *via* nucleophilic substitution with potassium thioacetate followed by basic hydrolysis (Scheme 5.4). The α-hydroxycinnamic acid enol analogue **17** of **ML302F** was prepared from the corresponding aldehyde, *via* Erlenmeyer azlactone synthesis of **16** followed by acidic hydrolysis (these reactions were carried out by Dr Marios Markoulides) (Scheme 5.5).

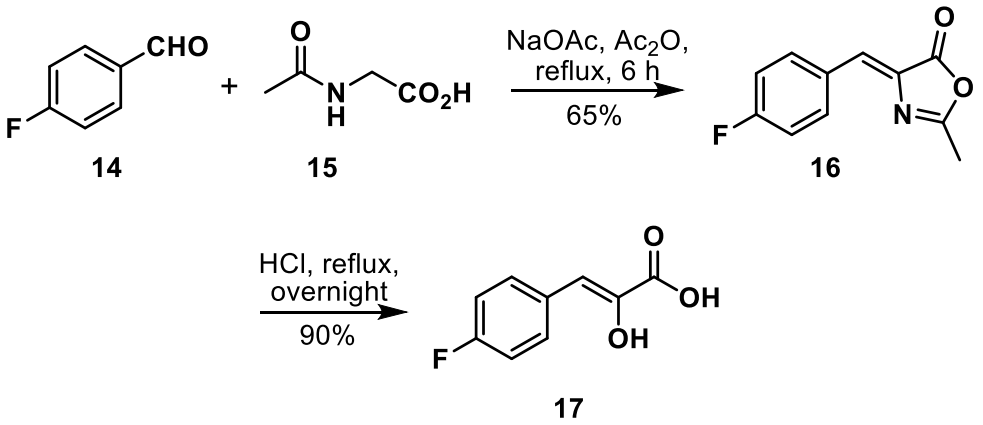


11a: R = Ph
11b: R = Bn

12a: 80%
12b: 85%

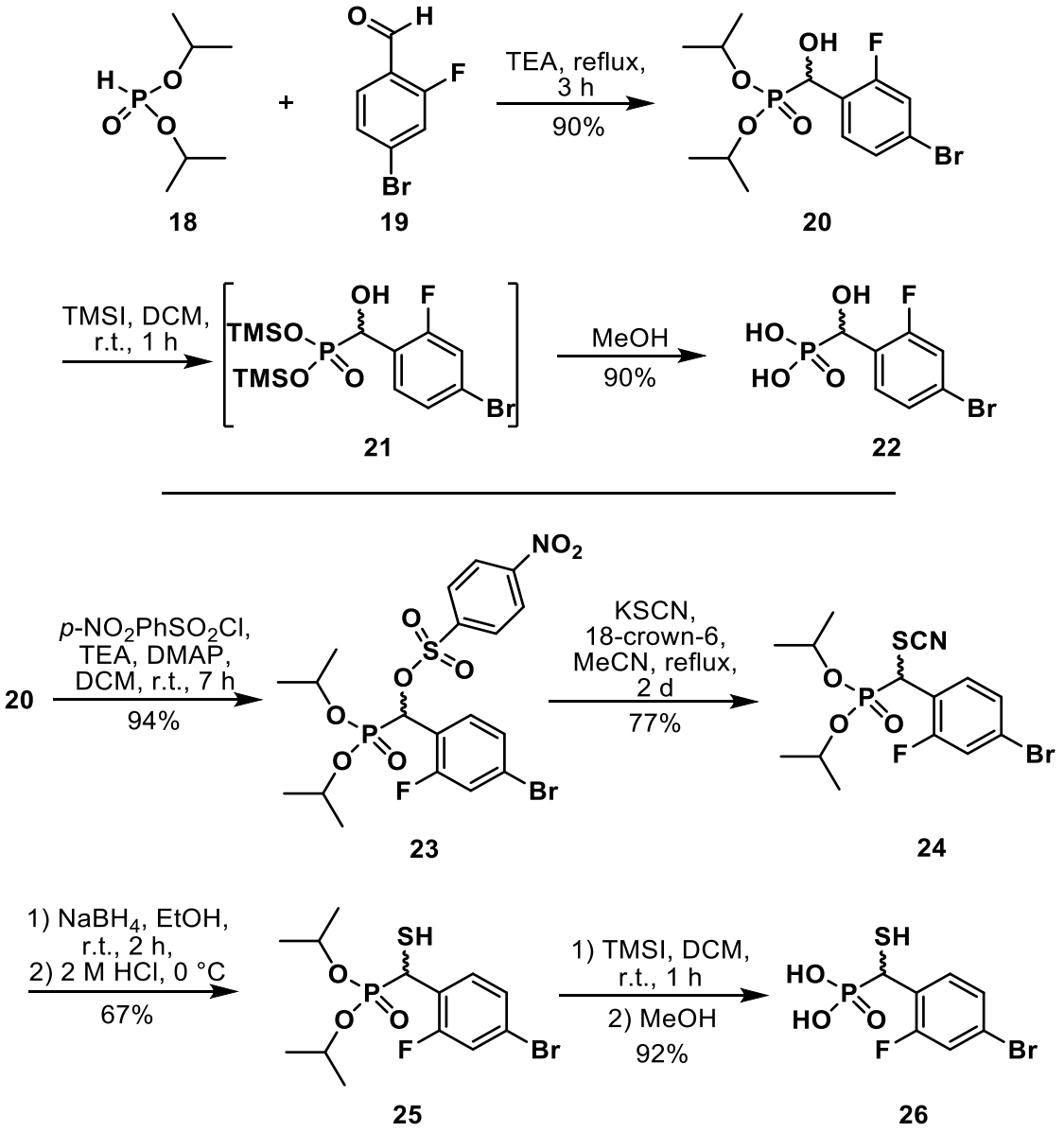
13a: 89%
13b: 92%

Scheme 5.4: *Synthesis of racemic α-mercaptocarboxylic acids **13a** and **13b**.*



Scheme 5.5: *Synthesis of α-hydroxycinnamic acid **17**.*

To investigate the importance of the carboxylate group for MBL inhibition[258-259, 292], α-sulphanyl phosphonic acid **26** was synthesised in five steps from diisopropyl phosphite with an overall yield of 40% (these reactions were carried out by Dr Marios Markoulides) (Scheme 5.6). Thus, 1,2-addition of diisopropyl phosphite **18** to 4-bromo-2-fluorobenzaldehyde **19** afforded α-hydroxy phosphonate **20**, which was then converted to the p-nitrobenzenesulphonate derivative **23**. Nucleophilic substitution using potassium thiocyanate gave the thiocyanate derivative **24**, which was reduced with sodium borohydride to afford α-sulphanyl phosphonate **25**. Treatment of α-sulphanyl phosphonate **25** with trimethylsilyliodide followed by methanolysis afforded the α-sulphanyl phosphonic acid **26**. The α-hydroxy phosphonic acid **22** was prepared in a similar way, by hydrolysis of the α-hydroxy phosphonate **20**.



Scheme 5.6: *Synthesis of α-hydroxy phosphonic acid* ***22*** *and α-sulphanyl phosphonic acid* ***26****.*

5.4.2. Protein production

The proteins used in this study were produced by Dr Samuel Cahill in conjunction with Dr Jürgen Brem.

5.4.3. Inhibition and structure activity relationship studies

The synthesised inhibitors were first screened against a representative set of MBLs, including those of clinical importance. The MBLs screened comprised B1 subclass enzymes, New Delhi MBL-1 (NDM-1); Verona integron–encoded MBL-2 (VIM-2); *Bacillus cereus* II MBL (BcII); São Paolo MBL-1 (SPM-1); imipenemase MBL-1 (IMP-1), a B2 subclass MBL which is a carbapenem-hydrolysing MBL from *Aeromonas hydrophila* (CphA); and a B3 subclass MBL labile enzyme from *Stenotrophomonas maltophilia* (L1). The B2 MBL (CphA) only utilises one active-site Zn(II) ion during catalysis, whilst the others normally use two Zn(II) ions[219, 227, 234]. The inhibitors were also screened against a representative panel of SBLs from different classes, Temoneira β-lactamase-1 (TEM-1), class A; cefotaxime-hydrolysing β-lactamase from Munich 15 (CTX-M-15), class A; extended spectrum β-lactamase (ESBL), class A; AmpC *Escherichia. coli*, class C, and oxacillinase-10 (OXA-10), class D.

The screening assay employed a fluorogenic platform previously developed at the University of Oxford[288]. When the cephalosporin derivative **FC5** (Figure 5.28) is used as a substrate, hydrolysis by MBLs or SBLs releases the umbelliferone (7-hydroxycoumarin) fluorophore, which absorbs strongly at λ_{ex} = 380 nm and emits at λ_{em} = 460 nm. The extent of inhibition was determined based on the intensity of the fluorescence signal. Subclass B1 and B3 (L1) MBLs and SBLs were screened using **FC5**, while the subclass B2 MBL CphA was screened using meropenem as the substrate. Note that CphA was screened in conjunction with Mr Samuel Cahill, while all SBL screening was performed by Mr Samuel Cahill.

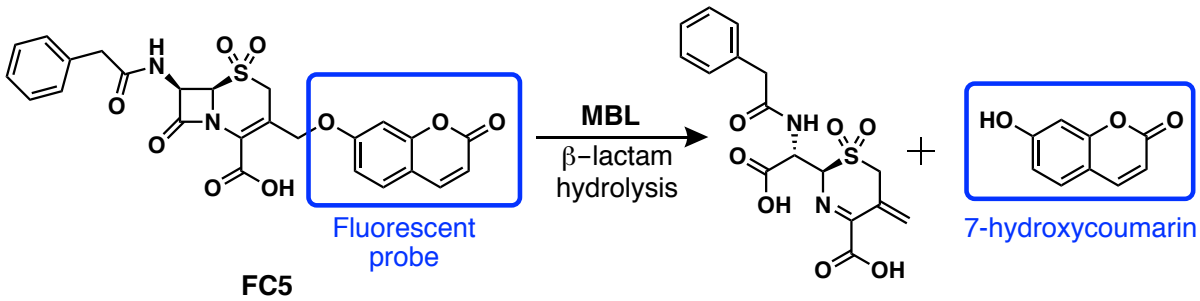


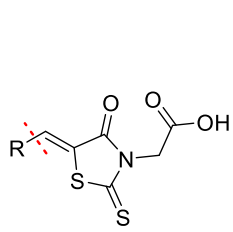
Figure 5.28: *Scheme showing hydrolysis of the fluorogenic substrate* ***FC5*** *by MBLs to release the umbelliferone fluorophore (7-hydroxycoumarin). An increased fluorescent signal is observed upon release of the fluorophore. Optimal wavelengths:* λ_{ex} *= 380 nm,* λ_{em} *= 460 nm.*[289]

The screening results for the clinically relevant class B1 MBLs (Table 5.2) revealed a number of trends for the rhodanine-derived inhibitors (compound series, **3a-l**, **5a-l**, and **6a-l**). Without exception, the enethiols (**6a-l**) were, by a significant margin, the most potent inhibitors within a given set of rhodanine/enethiol derivatives, indicating that the enethiol entity was indeed the probable main source of MBL inhibition. Except for in the cases of VIM-2 and an atypical subclass B1 MBL (SPM-1), the rhodanine-3-acetic acids (**3a-l**) were either inactive (at 50 μM) or only weakly active compared with the analogue enethiols (**6a-l**). A similar trend was observed for the amides (**ML302**, **5a-5l**) against certain MBLs, although the activity was slightly better in relation to the acids (e.g. **5i-l**). It is envisaged that, at least to some extent, the activities of the rhodanine-3-acetic acids (**3a-l**) and amides (**ML302**, **5a-5l**) may result from (partial) hydrolysis of the compounds to give their corresponding enethiols (**6a-l**).

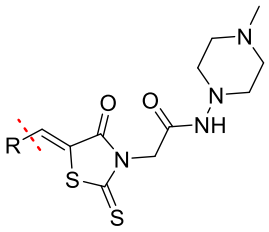
The differences in activities between rhodanine-3-acetic acids (**3a-l**) or amides (**ML302**, **5a-5l**) may in part reflect the extent of hydrolysis to give the enethiols. It is difficult to judge whether or not such hydrolysis is enzyme-catalysed, given the potency of the inhibition mediated by enethiol (**6a-l**). A similar trend was observed for the subclass B3 MBL, L1. In these experiments the rhodanine-3-acetic acids (**3a-l**) were significantly less active than the amides (**ML302**, **5a-5l**), which were again less active than their corresponding enethiols (**6a-l**).

The possibility of enzyme-mediated rhodanine hydrolysis is supported by the different levels of inhibition observed for the amides and enethiol analogues (with different enzymes). Thus, amide **ML302** manifested a similar level of inhibition compared with the enethiol **ML302F** for two of the tested B1 subclass MBLs (IMP-1 and VIM-2). For SPM-1, BcII and NDM-1, ML302 was ~five-, ~four- and ~15-fold less active than **ML302F**, respectively. For the subclass B2 MBL, CphA, **ML302** (IC_{50} value >50 μM) was also significantly less active than **ML302F** (IC_{50} 200 nM). Similarly, for the subclass B3 MBL, L1, **ML302** (IC_{50} 230 nM) was ~eight-fold less active than **ML302F** (IC_{50} 30 nM). Thus, the amides **5a-l** and **ML302** may be hydrolysed at different rates by the different MBLs.

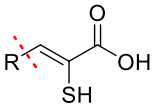
Table 5.2: Screening results for the inhibition of B1 and B3 subclass MBLs (di-zinc) by rhodanine-derived inhibitors.



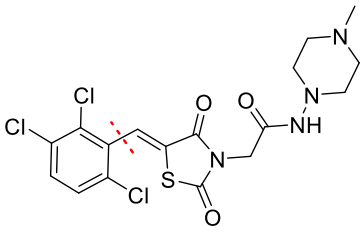
3a-q & ML302A



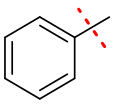
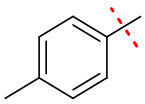
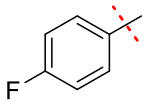
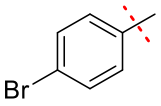
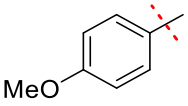
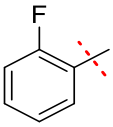
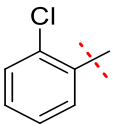
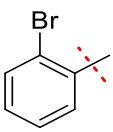
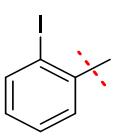
5a-q & ML302

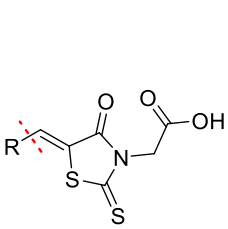


6a-s & ML302F

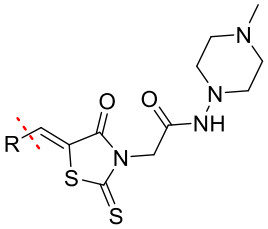


10

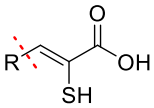
Compound	R	IC_{50} (μM) versus					
		SPM-1	IMP-1	BcII	VIM-2	NDM-1	L1
3a **5a** **6a**		>50 >50 0.3 ± 0.01	>50 22.7 ± 0.3 0.3 ± 0.03	>50 >50 0.7 ± 0.2	36.8 ± 0.3 16.4 ± 0.1 0.4 ± 0.02	>50 26.7 ± 1.0 7.9 ± 0.1	>50 6.2 ± 2.0 0.1 ± 0.02
3b **5b** **6b**		>50 >50 0.3 ± 0.01	>50 >50 0.2 ± 0.01	>50 >50 0.7 ± 0.05	32.0 ± 0.7 >50 0.4 ± 0.01	>50 28.0 ± 1.0 3.7 ± 0.1	>50 21.4 ± 2.1 0.2 ± 0.03
3c **5c** **6c**		>50 >50 4.1 ± 0.4	>50 >50 2.7 ± 0.1	>50 >50 8.2 ± 0.1	34.5 ± 0.6 >50 9.7 ± 0.3	>50 >50 5.0 ± 0.4	41.5 ± 2.1 24.8 ± 0.3 0.3 ± 0.01
3d **5d** **6d**		39.7 ± 0.8 >50 2.3 ± 0.3	>50 28.7 ± 1.2 3.3 ± 0.4	>50 >50 9.9 ± 0.2	>50 44.0 ± 0.4 9.4 ± 0.2	>50 >50 6.3 ± 0.2	47.3 ± 3.0 35.2 ± 4.1 0.3 ±0.05
3e **5e** **6e**		>50 >50 0.6 ± 0.1	>50 31.5 ± 3.2 0.8 ± 0.01	>50 >50 2.4 ± 0.1	>50 >50 0.4 ± 0.02	>50 48.9 ± 0.7 8.2 ± 0.3	30.7 ± 2.2 29.4 ± 1.7 0.08 ± 2×10^{-4}
3f **5f** **6f**		>50 42.7 ± 0.8 0.3 ± 0.01	>50 22.6 ± 0.3 1.4 ± 1.0	>50 26.3 ± 1.5 4.0 ± 0.1	17.6 ± 0.7 6.2 ± 0.2 3.3 ± 0.2	>50 >50 12.9 ± 0.4	18.6 ± 2.6 1.4 ± 0.8 0.1 ± 0.01
3g **5g** **6g**		25.1 ± 1.5 9.8 ± 0.4 0.1 ± 0.01	43.2 ± 2.1 7.6 ± 0.1 0.4 ± 0.01	>50 >50 0.9 ± 0.1	6.7 ± 0.2 2.0 ± 0.2 0.4 ± 0.02	>50 >50 5.1 ± 0.5	15.1 ± 0.9 1.4 ± 0.8 0.1 ± 0.02
3h **5h** **6h**		36.6 ± 0.8 8.1 ± 0.3 3.5 ± 0.3	32.5 ± 1.3 8.3 ± 0.2 0.8 ± 0.06	>50 14.6 ± 0.8 5.8 ± 0.1	>50 11.4 ± 1.0 2.7 ± 0.1	>50 >50 16.2 ± 0.3	23.1 ± 3.5 1.5 ± 0.7 0.2 ± 0.03
3i **5i** **6i**		2.0 ± 0.5 8.8 ± 0.3 1.4 ± 0.4	22.4 ± 0.4 37.1 ± 2.1 0.7 ± 0.02	31.7 ± 1.0 >50 6.3 ± 0.1	5.9 ± 0.1 37.6 ± 1.0 3.5 ± 0.1	>50 >50 5.0 ± 0.2	15.4 ± 4.0 17.1 ± 5.1 0.2 ± 0.06



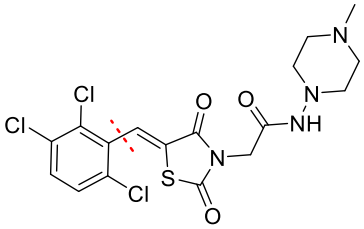
3a-q & ML302A



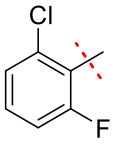
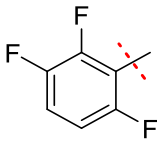
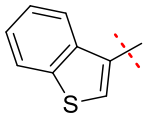
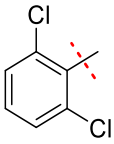
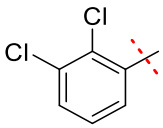
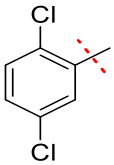
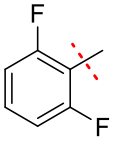
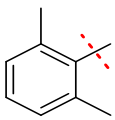
5a-q & ML302

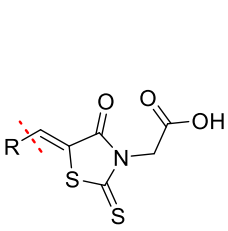


6a-s & ML302F

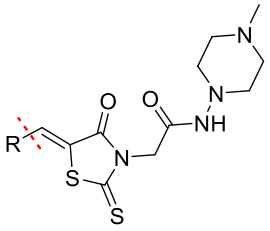


10

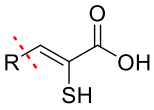
Compound	R	IC_{50} (μM) versus					
		SPM-1	IMP-1	BcII	VIM-2	NDM-1	L1
3j **5j** **6j**		1.2 ± 0.3 0.1 ± 4×10^{-3} 4.3×10^{-3} ± 3×10^{-4}	43.7 ± 0.5 0.3 ± 0.01 0.03 ± 1×10^{-3}	>50 2.0 ± 0.2 0.06 ± 2×10^{-3}	9.8 ± 2.8 0.8 ± 0.1 0.05 ± 1×10^{-3}	>50 >50 4.4 ± 0.2	2.5 ± 0.1 0.1 ± 0.02 9 ×10^{-3} ± 1×10^{-4}
3k **5k** **6k**		8.8 ± 0.3 1.5 ± 0.2 0.1 ± 0.01	46.5 ± 0.7 1.6 ± 0.4 0.4 ± 0.02	27.0 ± 2.2 3.5 ± 0.2 0.3 ± 0.01	47.6 ± 0.4 2.6 ± 0.1 0.3 ± 0.01	>50 40.1 ± 2.1 3.3 ± 0.1	28.5 ± 1.2 0.3 ± 0.02 0.7 ± 0.04
3l **5l** **6l**		13.9 ± 0.5 >50 0.4 ± 0.02	>50 >50 0.7 ± 0.05	21.7 ± 2.4 7.2 ± 3.3 3.1 ± 0.3	36.9 ± 0.2 41.8 ± 3.6 0.5 ± 0.03	>50 >50 11.1 ± 0.3	34.9 ± 3.1 16.7 ± 1.0 0.4 ± 0.02
3m **5m** **6m**		3.5 ± 0.4 0.2 ± 0.01 0.01 ± 1×10^{-3}	18.9 ± 0.8 0.2 ± 4×10^{-5} 0.01 ± 1×10^{-3}	41.8 ± 2.3 0.2 ± 0.3 0.07 ± 3×10^{-3}	0.6 ± 0.1 0.3 ± 0.01 0.03 ± 1×10^{-3}	>50 28.4 ± 0.4 0.6 ± 0.1	- - -
3n **5n** **6n**		1.0 ± 0.1 0.3 ± 0.01 0.2 ± 0.01	46.2 ± 1.4 0.6 ± 0.2 1.0 ± 2	22.1 ± 1.0 1.1 ± 0.3 1.0 ± 0.2	7.6 ± 0.3 39.5 ± 0.5 1.3 ± 0.2	>50 32.8 ± 0.8 46.5 ± 0.7	- - -
3o **5o** **6o**		16.6 ± 1.0 2.8 ± 0.2 0.8 ± 0.06	>50 7.0 ± 0.9 4.7 ± 0.2	>50 15.4 ± 1.0 1.6 ± 0.5	>50 >50 1.5 ± 0.2	>50 >50 45.3 ± 0.6	- - -
3p **5p** **6p**		32.1 ± 2.3 1.3 ± 0.2 0.06 ± 2×10^{-3}	>50 1.3 ± 0.2 0.2 ± 0.01	>50 3.0 ± 0.1 0.1 ± 0.01	6.8 ± 0.2 41.7 ± 1.9 0.2 ± 0.07	>50 >50 21.5 ± 0.8	- - -
3q **5q** **6q**		>50 0.2 ± 0.01 0.02 ± 1×10^{-3}	>50 2.7 ± 0.2 0.02 ± 2×10^{-3}	>50 27.0 ± 0.6 0.2 ± 0.01	18.7 ± 1.0 29.4 ± 1.0 0.07 ± 2×10^{-3}	>50 >50 4.9 ± 0.3	- - -



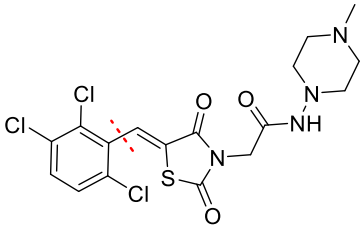
3a-q & ML302A



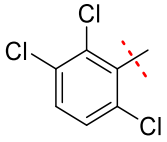
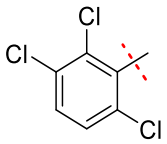
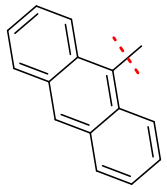
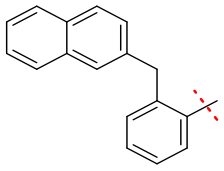
5a-q & ML302



6a-s & ML302F



10

Compound	R	IC_{50} (μM) versus					
		SPM-1	IMP-1	BcII	VIM-2	NDM-1	L1
ML302A **ML302** **ML302F**		4.8 ± 0.3 0.1 ± 0.01 0.02 ± 1×10^{-3}	9.6 ± 0.4 0.09 ± 2×10^{-3} 0.02 ± 1×10^{-3}	21.3 ± 0.5 0.3 ± 0.01 0.08 ± 2×10^{-3}	3.6 ± 0.7 0.06 ± 5×10^{-3} 0.04 ± 2×10^{-3}	>50 15.6 ± 0.7 2.4 ± 0.1	12.3 ± 1.1 0.2 ± 0.01 0.03 ± 1×10^{-3}
10		0.5 ± 0.04	3.2 ± 0.2	0.6 ± 0.05	0.2 ± 0.02	>50	0.5 ± 0.03
6r		3.2 ± 0.2	1.8 ± 0.01	>50	0.05 ± 1×10^{-3}	1.7 ± 0.6	- - -
6s		0.06 ± 3×10^{-3}	0.08 ± 2×10^{-3}	0.2 ± 0.03	0.1 ± 0.01	1.1 ± 1.7	- - -

Aside from the previously reported evidence for formation of a ternary complex in the case of VIM-2[268] (Figure 5.26), some of these results do suggest that intact rhodanines may exhibit inhibitory activity, as shown by the work of Spicer *et al.*[293]. Interestingly, despite the strong activity of the 2-thioxooxazolidin-4-one analogue **10** (or potentially a degradation product enethiol) of **ML302** against SPM-1, BcII, and VIM-2, **10** was less potent than **ML302** against all tested MBLs, being considerably less active against IMP-1 and particularly, NDM-1. Thus, the results support the proposal that electronic properties influence the potency of inhibitors. Replacement of the sulphur atom with oxygen would render the inhibitor less potent, based on

the observation that the sulphur atom makes more interactions than the oxygen atom[271]. The apparent decrease in potency of **10** compared with that of **ML302** may also be attributed to the electronic properties of the different ring systems, as the 2-thioxooxazolidin-4-one is likely to be more stable in hydrolysis reactions than the rhodanine[271], hence less enethiol is formed. Based on this trend, if the **ML302** analogue based on oxazolidine-2,4-dione (**2a**) had been prepared, it would have been expected to exhibit a further decrease in inhibition potency.

The results (Table 5.2) reveal further SAR trends. Some of the di-/tri-substituted (on the phenyl ring) amides and enethiols were markedly more active than the mono-substituted compounds. However, because the amides may undergo hydrolysis, and thus may inhibit *via* more than one mode of action, there are caveats when comparing the inhibition data for the two series. Notably, in most cases, amides **5a-5e** showed almost no inhibition against all the subclass B1 MBLs (IC_{50} values ~50 or >50 μM) when the *para*- position of the phenyl ring was functionalised with halogen or alkyl groups. By contrast, analogues such as mono-*ortho*-substituted **5f-5i** (IC_{50} values 2.0-52.1 μM), di-*ortho*-substituted **5j** (IC_{50} < 2.0 μM), and 2,3,6-trifluoro **5k** (IC_{50} < 3.5 μM) showed significant inhibition of all tested B1 subclass MBLs, with the exception of NDM-1. Interestingly, although similar activity was manifested by the subclass B3 MBL L1, amides **5a-5e** were moderately active (IC_{50} values 6.2-29.4 μM). In addition, as the size of substituent increased, the activity decreased. Mono-*ortho*-substituted **5f-5i** (IC_{50} values 1.4-17.1 μM) were also observed to be more active against B1 MBLs. Moreover, di-*ortho*-substituted **5j** (IC_{50} 0.1 μM), and 2,3,6-trifluoro **5k** (IC_{50} 0.3 μM) showed remarkable potency against L1, into the sub-micromolar range. The apparent inhibition profile of amides **5a-l** may in part be a result of the relatively narrow active site groove of L1[231], which enables the rhodanine motif to make more interactions, leading to tighter binding, and increased inhibition.

Comparable trends were observed for enethiols **6a-6l** against subclass B1 MBLs, although the IC_{50} values were mostly in the nanomolar range for all the tested B1 MBLs. The compound **6j** (IC_{50} values for SPM-1, IMP-1, BcII, VIM-2 and NDM-1 of 4.3 nM, 30 nM, 60 nM, 50 nM and 4.4 μM, respectively) showed a similar potency as compared with **ML302F** (IC_{50} values for SPM-1, IMP-1, BcII, VIM-2 and NDM-1 of 20 nM, 20 nM, 80 nM, 40 nM and 2.4 μM, respectively) across the panel of enzymes.

The results obtained with enethiols **6j** and **6l** led to further investigations regarding the role of aromatic substitutions. The di-*ortho*-substituted **6m** (IC_{50} values from 10 nM to 2.1 μM), **6p** (IC_{50} values from 60 nM to 41.5 μM) and **6q** (IC_{50} values from 20 nM to 4.9 μM) in general showed much better inhibition than the 2,3-substituted **6n** (IC_{50} values from 200 nM to >50 μM) or the 2,5-substituted **6o** (IC_{50} values from 800 nM to 46.9 μM) analogues. Thus, it was envisaged that compounds with increased steric bulk, especially at the *ortho* positions, would further improve inhibition. Substituents in the *meta*- positions appeared not to be essential for binding/inhibition. The compound **6r**, which was synthesised to investigate this hypothesis, manifested potent or moderately potent inhibition against most of the subclass B1 MBLs, with the exception of BcII (IC_{50} >50 μM). In the latter case, this molecule may not be able to access the active site due to its steric bulk. On the other hand, **6s**, which has only one *ortho*-substituted side-chain, showed potent inhibition against all the B1 MBLs tested, including BcII. The methylene naphthalene side-chain of **6s** is more flexible compared with the rigid tri-aromatic system in **6r**, hence it is expected to more easily access the active site, where it may interact hydrophobically with the L3 loop of B1 MBLs.

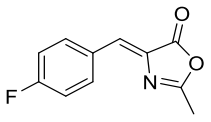
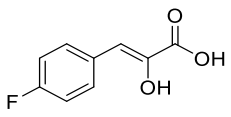
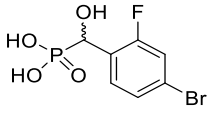
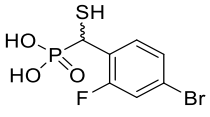
For the subclass B3 MBL L1, while all enethiols **6a-l** showed inhibition in the nanomolar range, **6j** was particularly potent (IC_{50} 9 nM), even compared with **ML302F** (IC_{50} 30 nM). L1 is produced by the clinically relevant *S. maltophilia*[231-233], which has strong links with lung

infection in patients with cystic fibrosis[294-296]. As **6j** is a promising lead inhibitor of L1, it was chosen for further investigation with clinical isolates. Due to potential conflict of interest, further SAR was not carried out with L1.

5.4.4. Investigation of the binding/inhibiting motif

A new set of analogues were synthesised and tested to investigate the importance for inhibition of the different functional groups present in the enethiol inhibitors (**6a-q**, **ML302F**). The hydroxyl analogue of **6c**, i.e. **17** (Table 5.3), was nearly inactive (at 100 μM), as was the 2-methyloxazol-5(4H)-one **16**, precursor of **17** (analogue of **3c**). These results support the proposal that the sulphur atom of the thiol group is important for binding and inhibition, even though **17** contains a carboxylic acid moiety. It is thus apparent that a potent inhibitor acting as a zinc chelator would require more than a single carboxylic acid moiety. This is exemplified by phthalic acid and succinic acid (Figure 5.23)[255]. The phosphonic acids **22** and **26** were found to be inactive, further supporting the importance of the carboxylate group to inhibition (Table 5.3). This suggests that both the carboxylic acid and thiol moieties (in enethiol) are required for binding/inhibition.

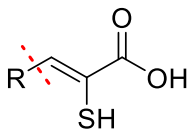
Table 5.3: Residual activities of metallo-β-lactamases (MBLs) upon incubation with selected rhodanine/thioenol derivatives (hydroxyl and phosphonate derivatives) at 100 μM.

 **16**	 **17**	 **22**	 **26**

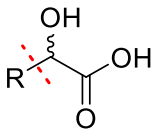
	% Residual activity versus				
Compound	**SPM-1**	**BcII**	**IMP-1**	**VIM-2**	**NDM-1**
16	87 ± 1	92 ± 2	100	100	97 ± 2
17	93 ± 2	90 ± 3	100	100	97 ± 4
22	92 ± 5	98 ± 2	100	100	100
26	95 ± 6	100	100	100	96 ± 3

To test this hypothesis, analogues that contained both carboxylic acid and thiol motifs (**13a**, **13b**) were synthesised and their activities compared with analogues that were missing one motif (i.e., mandelic acid and 3-phenyllactic acid). The saturated analogues of **6a**, i.e. **13a** (IC_{50} values for SPM-1, IMP-1, BcII, VIM-2 and NDM-1 of 50 nM, 70 nM, 100 nM, 40 nM and 12.9 μM, respectively) and **13b** (IC_{50} values for SPM-1, IMP-1, BcII, VIM-2 and NDM-1 of 70 nM, 50 nM, 1.4 μM, 70 nM and 38.7 μM, respectively) showed comparable or better potency against subclass B1 MBLs than **6a** (IC_{50} values for SPM-1, IMP-1, BcII, VIM-2 and NDM-1 of 3 nM, 30 nM, 700 nM, 400 nM and 7.9 μM, respectively) (Table 5.4). However, the hydroxyl analogues, i.e. mandelic acid and 3-phenylactic acid, were inactive at 100 μM (Table 5.4), again supporting the hypothesis that the sulphur/carboxylic acid combination was important for MBL inhibition. These observations support previous findings on the role of the α-mercaptocarboxylic acid motif in MBL binding/inhibition[297]. Although the relative acidity of the functional groups may be a factor, the increased inhibition observed for the (racemic) saturated α-mercaptocarboxylic acids (**13a**, **13b**) compared with the analogous enethiol (**6a**) could be a result of the different spatial relationship of the thiol and the carboxylate, which could enable improved binding of the saturated α-mercaptocarboxylic acids. However, **13a**/**13b** were much less active against the mono-zinc CphA (IC_{50} values for **6a**, **13a** and **13b** of 2.1 μM, 71.0 μM and 130.0 μM, respectively), suggesting that enethiol **6a** may bind differently compared with its saturated counterparts (**13a/13b**).

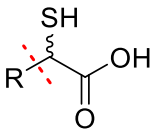
Table 5.4: *IC_{50} values for the inhibition of MBLs by α-mercapto and α-hydroxy carboxylic acids, and enethiols. NI: no observed inhibition at 100 μM inhibitor.*



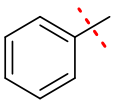
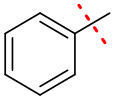
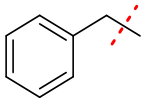
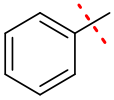
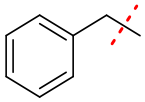
6a



Mandelic acid: R = Ph
3-Phenyllactic acid: R = $PhCH_2$



13a: R = Ph
13b: R = $PhCH_2$

		IC_{50} (μM)					
R	**Compound**	**SPM-1**	**IMP-1**	**BcII**	**VIM-2**	**NDM-1**	**CphA**
	**6a**	0.3 ± 0.01	0.3 ± 0.03	0.7 ± 0.2	0.4 ± 0.02	7.9 ± 0.1	2.1 ± 0.02
	**13a**	0.05 ± 1×10^{-3}	0.07 ± 3×10^{-3}	0.1 ± 0.01	0.04 ± 1×10^{-3}	12.9 ± 1.0	71.0 ± 1.0
	**13b**	0.07 ± 1×10^{-3}	0.05 ± 2×10^{-3}	1.4 ± 0.3	0.07 ± 2×10^{-3}	38.7 ± 4.7	130.0 ± 10
	**Mandelic acid**	*NI*	*NI*	*NI*	*NI*	*NI*	*NI*
	**3-Phenyllactic acid**	*NI*	*NI*	*NI*	*NI*	*NI*	*NI*

5.4.5. Synergistic inhibition studies

Since the mixture of **ML302** and **ML302F** (i.e., **ML302M**) showed significantly more inhibitory activity than either of the compounds alone against VIM-2[268], it was decided to test whether this synergistic inhibition was common to all enethiol compounds.

Selected enethiols with different aromatic substitutions were screened (**6a**, **6b**, **6g**, **6j**, **6k**, **6l**, **6m** and **ML302F** as control) in the presence of their amide analogues (**5a**, **5b**, **5g**, **5j**, **5k**, **5l**, **5m** and **ML302** as control) for potential inhibition *via* the formation of a ternary complex (Table 5.5). The use of a 1:1 mixture of **ML302** and **ML302F** (**ML302M**) manifested a >20-

fold increase in potency (IC_{50} = 1.8 nM) compared with the use of either **ML302** (IC_{50} = 60 nM) or **ML302F** (IC_{50} = 40 nM) individually against VIM-2, as observed previously[268]. The mixture **ML302M** was also moderately more active against IMP-1 (IC_{50} = 3 nM) and CphA (IC_{50} = 20 nM) than **ML302** (IC_{50} = 90 nM, >50 μM, for IMP-1 and ChpA, respectively) or **ML302F** alone (IC_{50} = 20 nM and 200 nM, for IMP-1 and ChpA, respectively). However, the increased inhibitory activity of the mixture was not observed for the other subclass B1 MBLs (BcII, SPM-1, NDM-1) tested, which suggests no formation of a ternary complex in these cases (Table 5.5). These observations are consistent with the results of a previous study[268], which suggested that a ternary complex could be accommodated by VIM-2 but not by BcII, indicating that different binding modes occur for these two enzymes. Further, no evidence for enhanced inhibition relative to the enethiols alone was observed for any of the other tested mixtures (**5a**, **5b**, **5g**, **5j**, **5k**, **5l**, and **6a**, **6b**, **6g**, **6j**, **6k**, **6l**). The only compound mixture that showed comparable results was **5m** with **6m**, a di-*ortho*-substituted analogue that was structurally almost identical to **ML302M**. Thus, the available evidence is that the formation of ternary complex is limited to specific combinations of enethiols and MBL. It is possible that the halogen substituents, especially chloride, on the aromatic system enhance the π-stacking effect on the enethiol with an additional rhodanine, and hence increase inhibition.

Table 5.5: Observed inhibition of MBLs by a 1:1 mixture of rhodanine amides (**5**) and enethiols (**6**), compared with their inhibition by **5** or **6** alone. Note that in most cases the mixture is of similar potency to the enethiol alone, but that in a few cases (notably **ML302**/**ML302F** and **5m**/**6m**) the mixture is more potent.

Compound/Mixture	Enzyme	IC_{50} when R = (μM)							
		a	b	g	J	k	l	m	ML302/F
Amide, **5**	**SPM-1**	>50	>50	9.8 ± 0.4	0.1 ± 0.01	1.5 ± 0.2	>50	0.2 ± 0.01	0.1 ± 0.01
Enethiol, **6**		0.3 ± 0.01	0.3 ± 0.01	0.1 ± 0.01	4×10^{-3} ± 1×10^{-4}	0.1 ± 0.01	0.4 ± 0.01	0.01 ± 1×10^{-3}	0.02 ± 2×10^{-3}
5+6 (1:1)		2.3 ± 0.01	42.4 ± 0.7	1.3 ± 0.2	0.1 ± 0.02	0. 4 ± 0.2	0.7 ± 0.3	0.02 ± 2×10^{-3}	0.02 ± 2×10^{-3}
Amide, **5**	**IMP-1**	22.7 ± 0.3	>50	7.6 ± 0.1	0.3 ± 0.01	1.6 ± 0.4	>50	0.2 ± 4×10^{-3}	0.09 ± 2×10^{-3}
Enethiol, **6**		0.3 ± 0.03	0.2 5×10^{-3}	0.4 ± 0.01	0.03 ± 3×10^{-3}	0.4 ± 0.1	0.7 ± 0.1	0.01 ± 6×10^{-5}	0.02 ± 3×10^{-4}
5+6 (1:1)		0.2 ± 0.01	0.1 3×10^{-3}	0.4 ± 0.01	0.02 ± 3×10^{-3}	0.2 ± 0.01	0.5 ± 0.1	7.0×10^{-3} ± 8×10^{-5}	3×10^{-3} ± 1×10^{-4}
Amide, **5**	**BcII**	>50	>50	>50	2.0 ± 0.2	3.5 ± 0.2	7.2 ± 3.3	1.5 ± 0.2	0.3 ± 0.01
Enethiol, **6**		0.7 ± 0.2	0.7 ± 0.2	0.9 ± 0.1	0.06 ± 2×10^{-3}	0.3 ± 0.01	3.1 ± 0.3	0.07 ± 3×10^{-3}	0.08 ± 2×10^{-3}
5+6 (1:1)		1.8 ± 0.3	1 ± 0.1	3.2 ± 0.06	0.1 ± 0.01	0.6 ± 0.4	6.3 ± 0.4	0.03 ± 1×10^{-3}	0.03 ± 1×10^{-3}
Amide, **5**	**VIM-2**	16.4 ± 0.1	>50	2.0 ± 0.2	0.8 ± 0.1	2.6 ± 0.1	41.8 ± 3.6	0.3 ± 0.01	0.06 ± 5×10^{-3}
Enethiol, **6**		0.4 ± 0.02	0.4 ± 0.01	0.4 ± 0.02	0.05 ± 1×10^{-3}	0.3 ± 0.01	0.5 ± 0.03	0.03 ± 2×10^{-4}	0.04 ± 2×10^{-3}
5+6 (1:1)		0.2 ± 0.01	0.3 ± 0.01	0.4 ± 0.02	0.05 ± 1×10^{-3}	0.2 ± 0.01	2.3 ± 0.2	0.02 ± 1×10^{-3}	1.8×10^{-3} ± 3×10^{-4}
Amide, **5**	**NDM-1**	26.7 ± 1.0	28.0 ± 1.0	>50	>50	40.1 ± 2.1	>50	28.4 ± 0.4	15.6 ± 0.7
Enethiol, **6**		7.9 ± 0.1	3.7 ± 0.1	5.1 ± 0.5	4.4 ± 0.2	3.3 ± 0.1	11.1 ± 0.3	0.6 ± 0.1	2.4 ± 0.1
5+6 (1:1)		18.5 ± 0.1	16.2 ± 0.5	33.8 ± 1.0	2.8 ± 0.4	28.6 ± 0.7	>50	1.7 ± 0.3	1.3 ± 0.4
Amide, **5**	**CphA**	>50	-	-	-	-	-	>50	>50
Enethiol, **6**		2.1 ± 0.02	-	-	-	-	-	0.8 ± 0.02	0.2 ± 4×10^{-3}
5+6 (1:1)		2.7 ± 0.04	-	-	-	-	-	0.4 ± 0.01	0.02 ± 1×10^{-3}

5.4.6. Structural studies

Previous crystallographic studies produced a structure of BcII in complex with **ML302F**, while an unexpected ternary structure of **ML302** + **ML302F** in complex with VIM-2 was also observed (Figure 5.26)[268]. In both of the molecules in the asymmetric unit, **ML302F** is positioned to chelate the two zinc ions at the active site of VIM-2. The thiol(ate) of **ML302F** replaces the μ2 nucleophilic hydroxide/water bridging system between the two zinc ions, whilst the carboxylate coordinates with the DCH zinc ion (Zn2, at a distance of 2.2 Å) and further interacts with Arg228. The phenyl ring is not coplanar, but rather is approximately orthogonal to the alkene and carboxylate, and therefore it is not conjugated; the observed conformation is likely to be caused by steric hindrance from the *ortho*-di-chloro substituents. This apparently enables the ring to form a π-stacking interaction with His118, while further hydrophobic interactions are aided by the (2-chloro) halogen substituent with the side-chain of Trp87 and the backbone carbons of Asp119 and Asn233 (Figure 5.26).

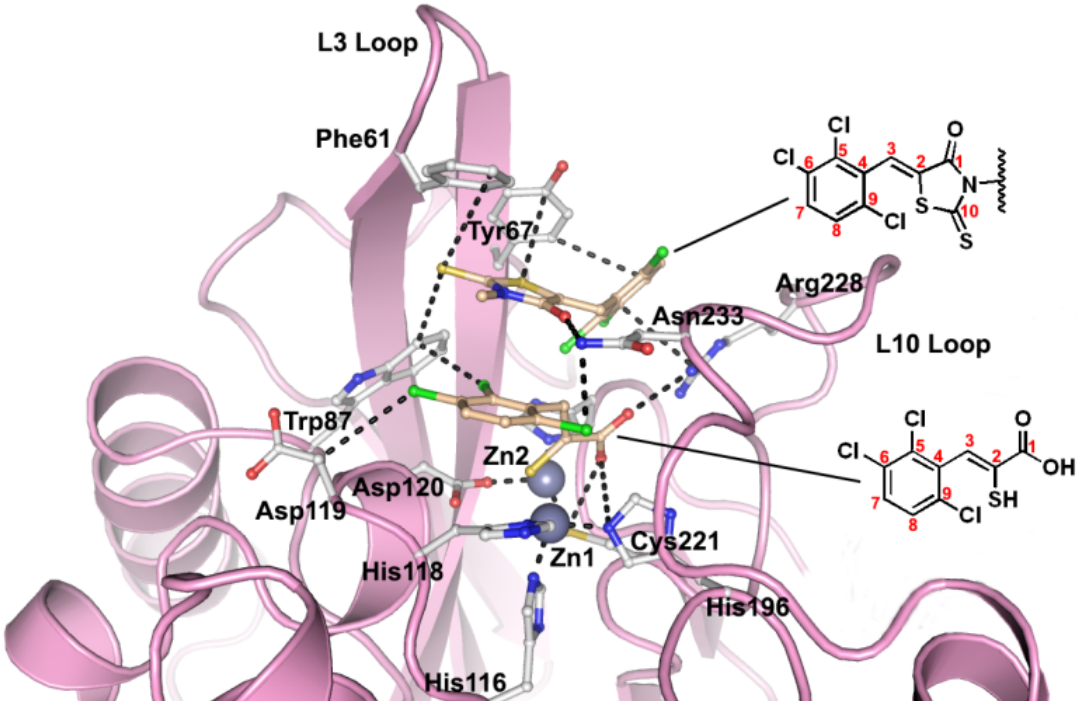


Figure 5.26: *Prior crystallographic analysis has revealed that **ML302** undergoes fragmentation to form the enethiol inhibitor **ML302F** (PDB ID: 4PVO), which coordinates with the di-Zn(II)-containing active site. The ternary structure reveals synergistic inhibition of **ML302M** (**ML302**+**ML302F**) to VIM-2. All figures are labelled using the BBL numbering scheme. Reprinted with permission from Elsevier B. V..*

An additional molecule of **ML302** that was apparent only near the active site of chain A (and not chain B) was positioned to interact with **ML302F**, *via* a staggered π-stacking between the rhodanine ring of **ML302** and the 2,3,6-trichlorophenyl ring of **ML302F** (Figure 5.26). In order to further investigate the mode of enethiol binding to MBLs in relation to the SAR results, four additional crystal structures of BcII co-crystallised with enethiols **6c** (Figure 5.29 A, PDB ID: 5JMX), **6k** (Figure 5.29 B, PDB ID: 6EUM), **6l** (Figure 5.29 C, PDB ID: 6EWE), and **6s** (Figure 5.29 D, PDB ID: 6F2N) were obtained. A new structure of VIM-2 in complex with **ML302F** (Figure 5.30, PDB ID: 6EW3) was also obtained for comparison. Please note, the production and refinement of crystal structures were carried out by Mr Dmitrijs Stepanovs under the supervision of Dr Michael McDonough.

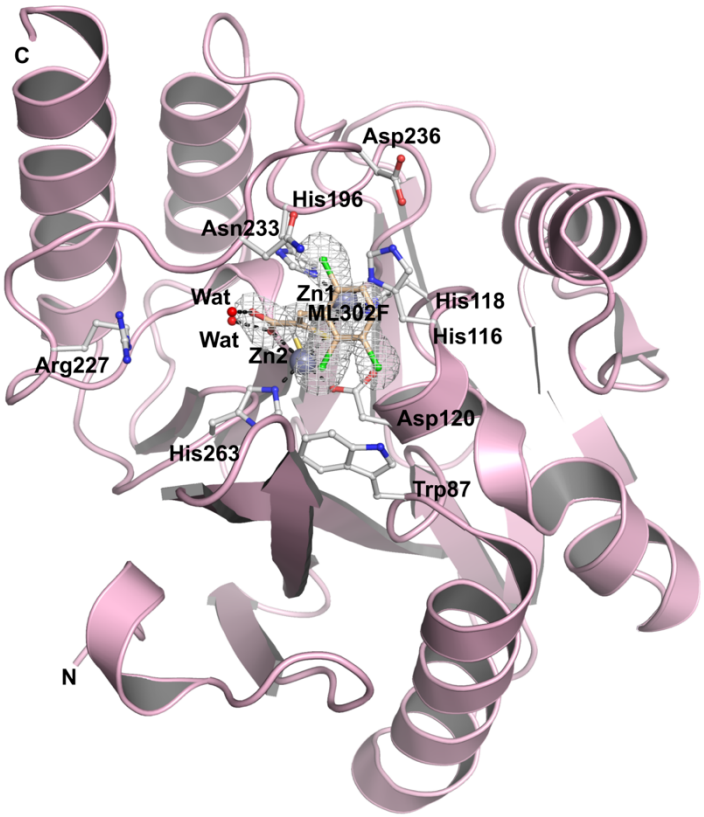


Figure 5.30: *View from a crystal structure of VIM-2 (pink) in complex with* ***ML302F*** *(wheat) (PDB ID: 6EW3). Active site residues are shown as balls and sticks with atoms coloured white representing C, red representing O, blue representing N, grey spheres representing Zn, and red spheres representing water. Ligand interactions are indicated by black dashed lines. Ligand mFo-DFc OMIT maps contoured to 3.0 σ are shown as light grey mesh. Reprinted with permission from Elsevier B. V..*

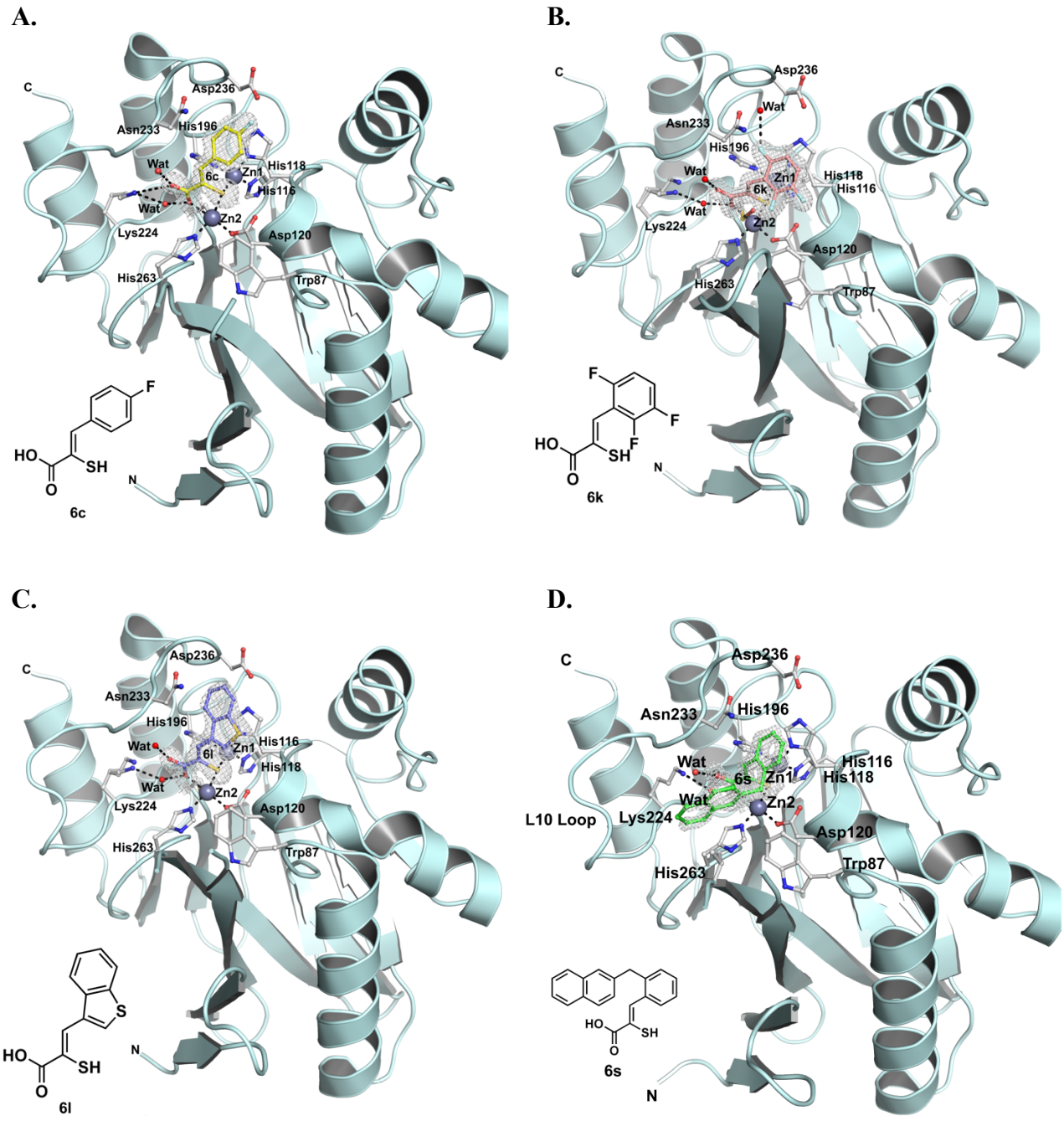


Figure 5.29: *View from crystal structures of BcII (turquoise) in complex with enethiols. A:* ***6c*** *(yellow, PDB ID: 5JMX); B:* ***6k*** *(salmon, PDB ID: 6EUM); C:* ***6l*** *(purple, PDB ID: 6EWE); and D:* ***6s*** *(green, PDB ID: 6F2N). Active site residues are shown as ball-and-stick models with atoms coloured white (C), red (O), blue (N), grey spheres (Zn), and red sphere (water). Ligand interactions are indicated by black dashed lines. Ligand mFo-DFc OMIT maps contoured to 3.0 σ are shown as light grey mesh. Reprinted with permission from Elsevier B. V..*

Comparison of the BcII structures in complex with the different enethiols (**6c, 6k, 6l, 6s,** respectively) reveals that the core of enethiols has a remarkably similar binding mode to that observed for **ML302F**[268]; the thiol(ate) displaces the bridging water molecule normally located between the two Zn(II) ions and the inhibitor carboxylate ligates to Zn2. The enethiol-linked phenyl rings of the inhibitors all occupy the same region of the active site (Figure 5.31). One of the oxygens of the enethiol carboxylate is positioned to interact with Zn2. The other oxygen is positioned to interact with the N^{ε} amino group of Lys-224 (Figure 5.29). As observed in the VIM-2:**ML302F** complex structure[268], the plane of the phenyl side-chain on all the enethiol inhibitors is rotated about the C3–C4 bond such that it is not co-planar with the enethiol alkene, and is therefore likely to hinder conjugation. For **ML302F**, the skewed arrangement was thought to be caused, at least partially, by steric hindrance due to the *ortho*-di-chloro substituents on the phenyl ring, as proposed previously[268]. However, enethiols without *ortho*-substituents are also observed to retain similar conformations (as evidenced by a crystal structure of BcII in complex with **6c**, Figure 5.29), which indicates that the *ortho*- substitution may not be an essential factor. Instead, the hydrophobic interactions with the surrounding residues, especially π-stacking with His118, may be the principal cause of the skewed arrangement of inhibitors.

Superimposition of the structure of BcII in complex with **6s** with that of VIM-2 in complex with **ML302F** (Figure 5.31) implies that there may be a steric clash between the naphthalene side chain of **6s** with Tyr67 on the L3 loop of VIM-2, which disfavours binding. However, the IC_{50} values for **6s** with BcII and VIM-2 are comparable (IC_{50} = 0.2 μM and 0.1 μM, respectively), which indicates that **6s** might adopt a different conformation when binding to VIM-2 and/or that it induces a conformational change of the L3 loop.

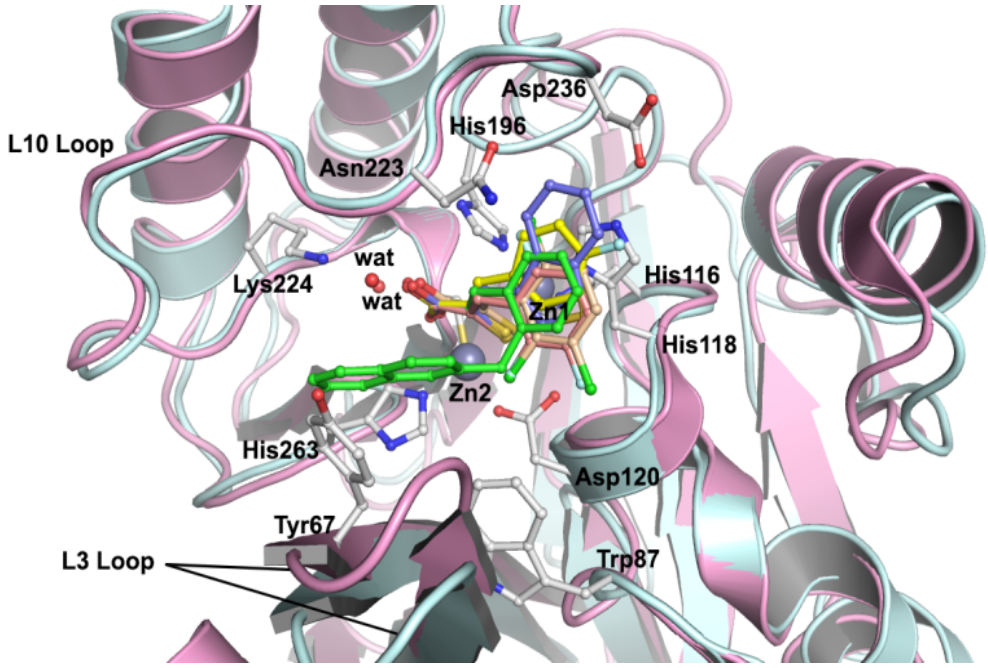


Figure 5.31: *Superimposition of structures of BcII (turquoise; PDB ID: 5JMX, 6EUM, 6EWE, 6F2N) with VIM-2 (pink; PDB ID: 6EW3) showing the similarity in binding modes for compounds* ***6c*** *(yellow),* ***6k*** *(salmon),* ***6l*** *(purple),* ***6s*** *(green) and* ***ML302F*** *(wheat). With both MBLs, the thiolate interacts with both Zn(II) ions and the inhibitor carboxylate interacts with Zn2 and Lys-224 of BcII or Arg233 of VIM-2. Note that the L3 loop on VIM-2 is positioned differently from that of BcII, indicating an unfavourable interaction with the naphthalene group of* ***6s****. Thus a conformational change is likely. Reprinted with permission from Elsevier B. V..*

The binding mode of enethiols to BcII shares some important similarities with the binding of hydrolysed β-lactam product intermediates with NDM-1 (PDB ID: 4EYF)[220] (Figure 5.32, represented by **6s**). The thiol(ate) of **6s** bridges the two zinc ions, while the carboxylate coordinates with Zn2 in the DCH site; analogously, the newly formed β-amino group from β-lactam hydrolysis (in benzylpenicillin, penicillin G) is also positioned between the two zinc ions while the adjacent carboxylate coordinates with the Zn2. Furthermore, the carboxylate of **6s** interacts with Lys201, in an almost identical fashion to the interaction between the hydrolysed penicillin product C-3 carboxylate and the analogous Lys211 in NDM-1, though in this case water may also be involved as a bridging molecule. Finally, **6s** interacts hydrophobically with Val69 and Trp89 in a similar manner to the interactions observed for

Val73 and Trp93 of NDM-1 with hydrolysed benzylpenicillin. Although not exemplified in this case by **6s**, enethiols with *ortho*-substitutions, e.g. **6k** and **ML302F,** are positioned to make a further interaction with Asn233. This interaction is similar to the hydrogen bonding between Asn220 and the newly formed carboxylate group of hydrolysed benzylpenicillin in complex with NDM-1[220]. Hence, it is likely that enethiols inhibit MBLs in a manner that mimics the β-lactam hydrolysis product complexes. Given the strong affinity of sulphur atoms for Zn metal centres, the binding of enethiols at the active site of MBLs is likely to be strong. This strong link would stop the enzymes from turning over their β-lactam substrates (e.g. penicillin G).

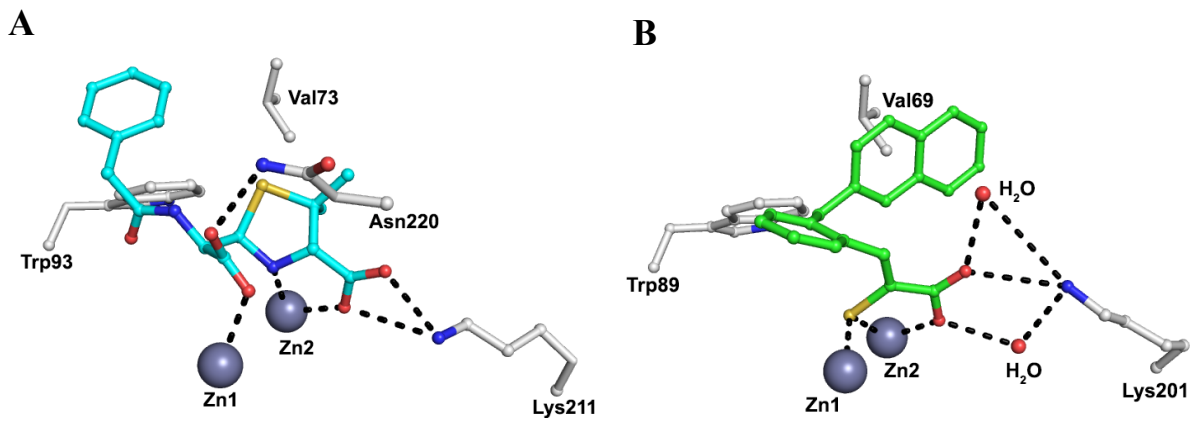


Figure 5.32: *Crystallographic analysis reveals that the binding modes of the enethiol carboxylates are similar to those of the MBL β-lactam antibiotic hydrolysis products.* ***A.*** *Binding mode of hydrolysed benzylpenicillin (penicillin G, cyan) with NDM-1 (PDB code: 4EYF)[258],* ***B.*** *Binding mode of* ***6s*** *(green) obtained by co-crystallisation of* ***6s*** *with BcII (PDB ID:6F2N).*

5.4.7. Susceptibility of clinical isolates to rhodanines and enethiols

Table 5.6: Minimum inhibitory concentration (MIC) values of enethiols **6j** and **ML302F**, and their parent rhodanine amides **5j** and **ML302**. MIC values of meropenem are shown in the absence and presence of the MBL inhibitors against a panel of clinical isolates that produce L1 and/or multiple other β-lactamases. A clinically relevant MIC, i.e. susceptible to given chemical, is classed as ≤ 2 mg L^{-1} according to current CLSI/EUCAST breakpoints [221]. MIC values in black indicate resistance and those in red indicate susceptibility. MEM: meropenem.

	Resistance	Inhibitor MIC (mg L^{-1})				MEM MIC in *absence* of the inhibitor (mg L^{-1})	MEM in *presence* of the inhibitor (mg L^{-1})			
		6j	5j	M302F	M302		6j	5j	M302F	M302
							Inhibitor at 10 mg L^{-1}			
***Smlt* K279a**	Basal L1, L2	>128	>128	>128	>128	**16**	0.25	0.25	0.5	0.5
***Clinical Isolate* 29**		>128	128	>128	64	**32**	0.25	0.25	0.5	0.25
***Clinical Isolate* 31**	IS *ampDI*	>128	>128	>128	>128	**256**	4	2	4	4
***Clinical Isolate* 20**		128	128	128	64	**16**	0.25	0.25	0.25	0.25
***Clinical Isolate* 24**		128	128	128	64	**2**	1	1	1	1
5CAZ	*ampR* single point mutation	>128	>128	>128	>128	**128**	0.5	0.5	1	1
10AMP	*ampD* deletion	>128	>128	>128	128	**128**	1	1	1	2
14FEP	*mpl* deletion	>128	>128	>128	128	**64**	1	1	2	2
Kami32	Over-expression SmeYZ	>128	>128	>128	>128	**8**	0.25	0.5	0.5	0.5
Kmox8	Over-expression SmeF	>128	>128	>128	>128	**8**	0.25	0.5	1	1

During the *in vitro* screening of enethiols against the B3 MBL L1, **6j** (IC_{50} 9 nM) was observed to be the most potent inhibitor, even compared with the benchmark compound **ML302F** (IC_{50} 30 nM). Given that the L1-producing *S. maltophilia* is strongly linked to lung infections in patients with cystic fibrosis[294-296], and considering the promising *in vitro* inhibition results of the enethiol **6j** and its parent rhodanine amide **5j**, it was decided to test their inhibitory efficacy against clinically relevant bacterial isolates. Thus, **5j** and **6j** (10 mg L^{-1}) were tested against a variety of clinical isolates that expressed L1 or multiple β-lactamase enzymes (including L1) (Table 5.6-5.7), while **ML302** and **ML302F** were tested as controls. In this assay, the efficacy

of the inhibitors was measured by their capacity to potentiate the activity of the carbapenem meropenem[221]. Please note, cell-based screening was carried out by Ms Karina Calvopina from the University of Bristol as part of collaboration work.

It is evident that the enethiols (**6k**, **ML302F**) and rhodanine amides (**5k**, **ML302**) alone were not inhibitory, having MIC values >128 mg L^{-1} (Table 5.6). This observation indicates that these compounds are not toxic to bacterial cells (assuming that they penetrate the cell wall). This finding supports the argument that (at least under the tested conditions) rhodanine-based inhibitors are not 'promiscuous binders'. However, it was exciting to discover that all clinical isolates tested were significantly affected by the presence (10 mg L^{-1}) of the enethiols (**6k**, **ML302F**) and rhodanine amides (**5k**, **ML302**), as compared with meropenem alone. While clinical isolate 24 is already susceptible to meropenem, all other tested clinical isolates were resistant to meropenem (MIC ≥ 8 mg L^{-1}), yet supplementation with the MBL inhibitors (10 mg L^{-1}) completely restored the susceptibility of these isolates to meropenem. The isolate 5CAZ, which carries a single-point mutation in the *ampR* gene, was affected the most, showing a 256-fold increase in its susceptibility (MIC value from 128 to 0.5 mg L^{-1}) to meropenem. The unprecedented level of potentiation to a given β-lactam antibiotic agent by enethiols is largely attributed to their intrinsic inhibition of MBLs, especially L1, and/or their ability to penetrate the bacterial cell wall.

Further susceptibility testing was carried out with meropenem against the subclass B1 MBLs produced by *Enterobacteriaceae* (e.g., *E. coli*), IMP and VIM-1 (Table 5.7). Again, the enethiol inhibitors potentiated meropenem, such that the MIC was considered to be in the susceptible range.

Figure 5.7: Minimum inhibitory concentration (MIC) values of enethiols **6k** and **ML302F**, and their parent rhodanine amides **5k** and **ML302**. MIC values are shown for meropenem in the absence and presence of the MBL inhibitors against clinical *E. coli* isolates that produce IMP or VIM-1. A clinically relevant MIC, i.e. susceptibility to the given antibiotic, is classed as ≤1 mg L^{-1} according to current CLSI/EUCAST breakpoints for *Enterobacteriaceae*[221]. MIC values in black indicate resistance and those in red indicate susceptibility.

	Resistance	Inhibitor MIC (mg L^{-1})				MEM MIC in *absence* of the inhibitor (mg L^{-1})	MEM in *presence* of the inhibitor (mg L^{-1})			
		6k	5k	M302F	M302		6k	5k	M302F	M302
							Inhibitor at 10 mg L^{-1}			
E. coli	-	>256	>256	>256	256	**0.25**	0.25	0.25	0.25	0.25
E. coli	IMP	>256	>256	>256	>256	**64**	1	1	0.25	1
E. coli	VIM-1	>256	>256	>256	>128	**8**	2	2	1	2

5.4.8. Hydrolysis/degradation of rhodanine amides

As discussed above, the apparent activity of **ML302**, and indeed **10**, is likely to be the result of hydrolysis to produce the primary active agent, i.e. the enethiol **ML302F**. To investigate whether this hydrolysis was catalysed by MBL enzymes, NMR time courses were performed. A ^{1}H NMR (700 MHz) time course was set up to monitor the rate of decomposition/hydrolysis of **10** in two different buffers, tris(hydroxymethyl)aminomethane (Tris) and ammonium bicarbonate (NH_4HCO_3). The clinically relevant subclass B1 MBL NDM-1 was used to investigate the extent of enzyme-mediated hydrolysis. A stock solution of **10** (50 mM in DMSO-d_6) was diluted in either freshly prepared NH_4HCO_3 (50 mM, pH 7.50) or Tris-d_{11} (50 mM, pH 7.50) both with NaCl (100 mM) in D_2O, to give a final concentration of 200 μM. When specified, NDM-1 was added to a final concentration of 1 μM. The reaction was monitored at 1 hour intervals over 18 hours. (The experiments were performed in conjunction with Mr Jos Kamps) Results are shown in Figure 5.33.

It is clear from the NMR analyses that **10** is hydrolysed to form **ML302F**. As the signals associated with **10** diminished, new peaks corresponding to the enethiol (**ML302**) emerged at different chemical shifts over the duration of the time course. The peak integrals were used to calculate the compound concentrations, and plotted against time (Figure 5.34). The rate of hydrolysis was faster in NH_4HCO_3 compared with the rate in Tris (in the presence and absence of NDM-1), which demonstrated that assay buffers can affect stability of test rhodanine compounds. Nevertheless, the hydrolysis of **10** was not observed by NMR on the timescale of the inhibition studies; the compounds were incubated at room temperature with enzymes for 10 minutes, followed by 15 minutes of measurements (i.e., 25 minutes of total assay time). In addition, the rate of hydrolysis/degradation of **10** was almost identical in the presence or absence of NDM-1 MBL, which suggests that there was no observable enzyme-catalysed hydrolysis of the compound (note the NDM-1 is inhibited by enethiol product). Although the hydrolysis of **10** to form **ML302F** at low levels cannot be ruled out, these results suggest that further SAR studies on the intact rhodanine scaffold, or preferably on more stable analogues, are of interest. One possibility is that the intact rhodanines can bind to the active site in a manner that does not involve metal chelation, as recently reported for another series of MBL inhibitors[298].

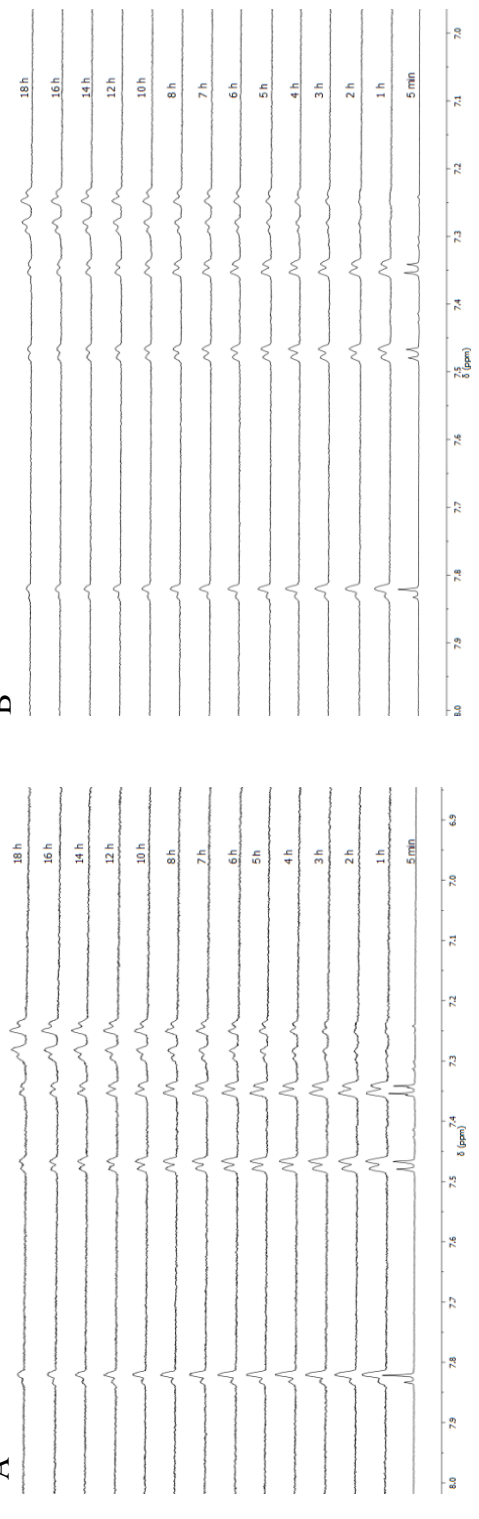


Figure 5.33: *^{1}H NMR (700MHz) stability test for compound **10**. A: **10** (200 µM) in NH_4HCO_3 (50 mM, pH 7.5 in D_2O) in the absence of NDM-1 over 18 hours; B: **10** (200 µM) in NH_4HCO_3 (50 mM, pH 7.5 in D_2O) in the presence of NDM-1 (1 µM) over 18 hours; C: **10** (200 µM) in Tris-d_{11} (50 mM, pH 7.5 in D_2O) in the absence of NDM-1 over 18 hours; D: **10** (200 µM) in Tris-d_{11} (50 mM, pH 7.5 in D_2O) in the presence of NDM-1 (1 µM) over 18 hours. Reprinted with permission from Elsevier B. V.,*

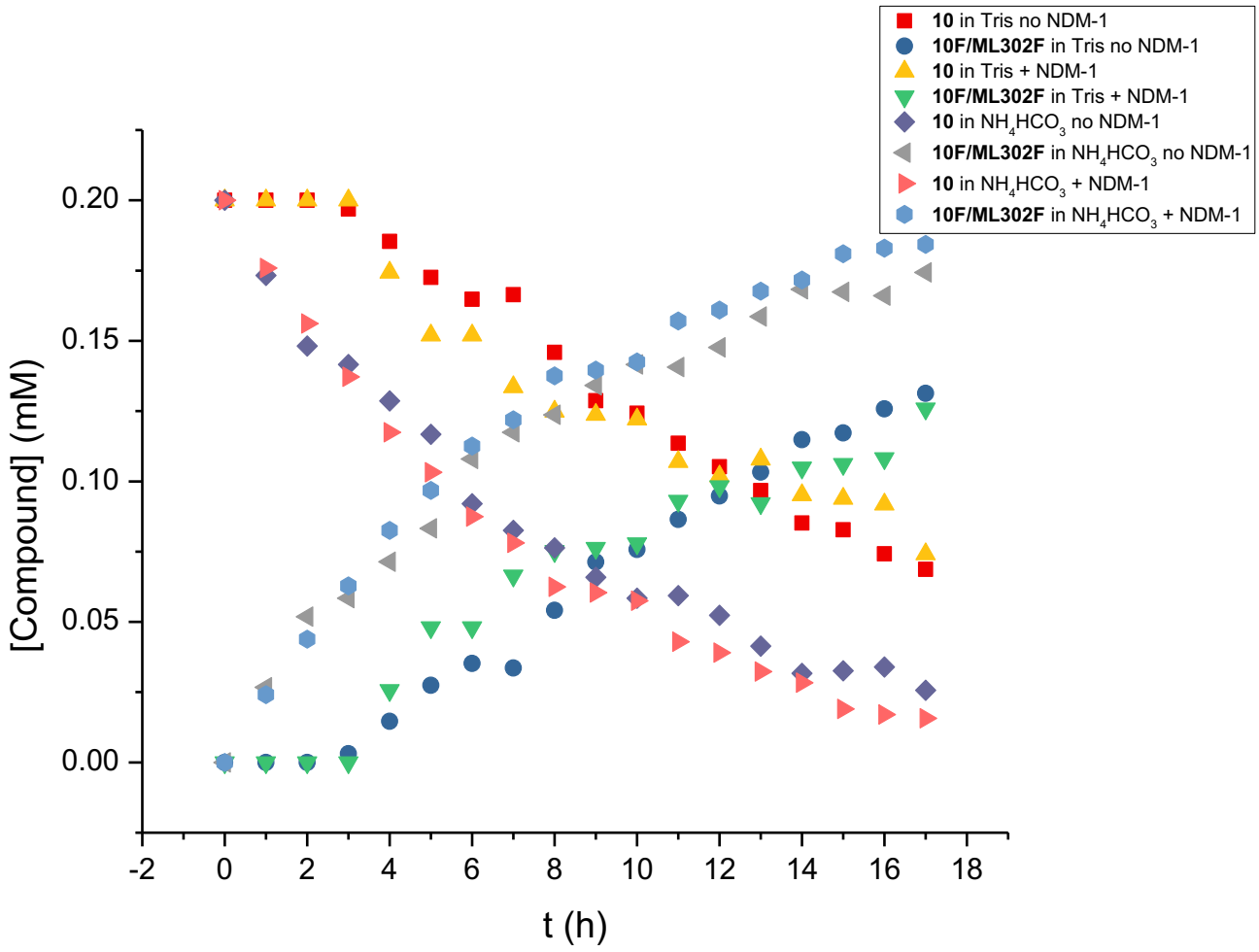


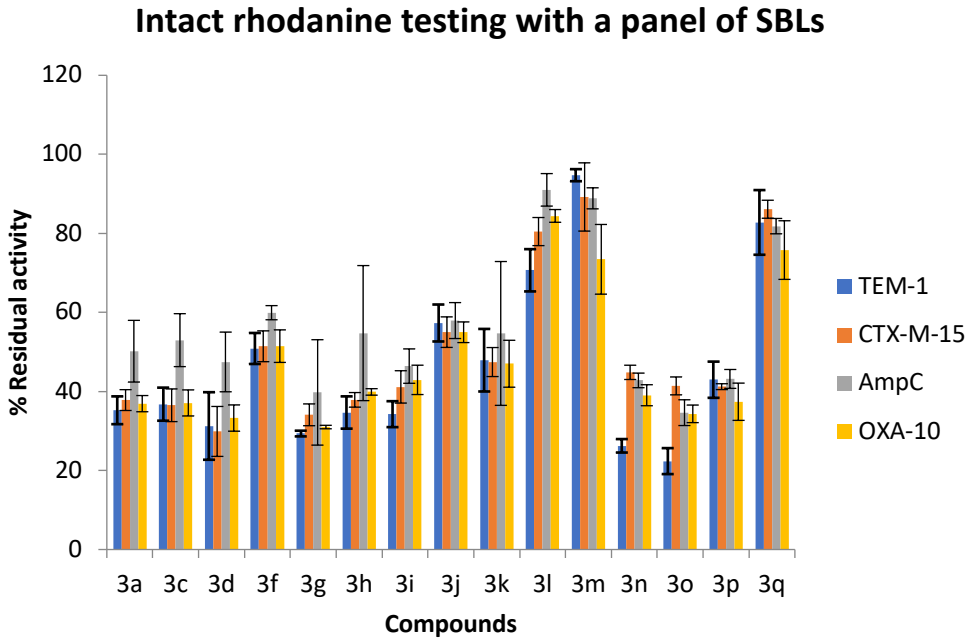
Figure 5.34: *Degradation of compound **10** (200 μM initial concentration) monitored over 18 hours by ^{1}H NMR (700 MHz) in (A) Tris-d_{11} (50 mM, pH 7.5, D_2O solution) in the absence of NDM-1 (**10** red squares, **10F/ML302F** blue circles), (B) Tris-d_{11} (50 mM, pH 7.5, D_2O solution) in the presence of NDM-1 (1 μM) (**10** yellow triangles, **ML302F** green triangles), (C) in NH_4HCO_3 (50 mM, pH 7.5, D_2O solution) in the absence of NDM-1 (**10** purple diamonds, **10F/ML302F** grey triangles), and (D) in NH_4HCO_3 (50 mM, pH 7.5, D_2O solution) in the presence of NDM-1 (1 μM) (**10** red triangles, **10F/ML302F** blue hexagons). Reprinted with permission from Elsevier B. V..*

5.5. SBL inhibition

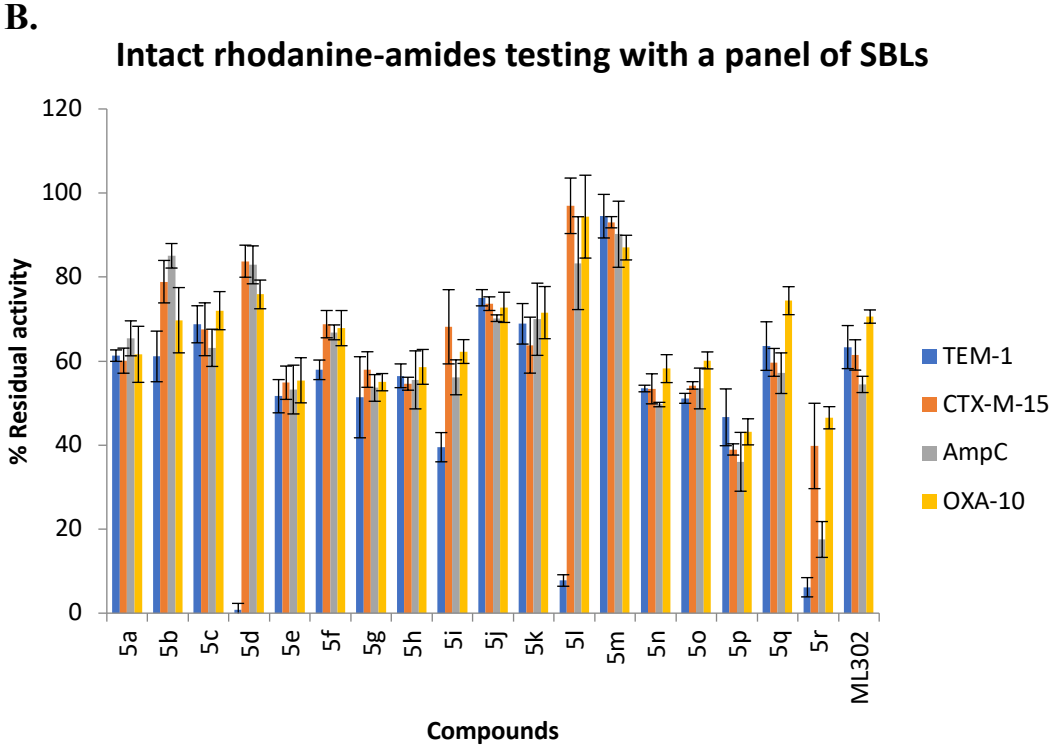
The enethiols may inhibit MBLs by mimicking the binding of the hydrolysed β-lactam product intermediates; analogue complexes could be present during SBL catalysis. It was thus envisaged that the enethiols might also inhibit SBLs.

Residual activities for rhodanine acetic acids (**3a-q**), rhodanine amides (**5a-r**, **ML302**) and enethiols (**6a-r**, **ML302F**) against class A SBLs TEM-1 and CTX-M-15, class C SBL AmpC, and class D SBL OXA-10 are shown in Figure 5.35. All the enethiols, except **6r** (and rhodanine amides **5d** and **5r**), were nearly inactive (at 200 μM) against the panel of tested SBLs. The observed SBL inhibition by **5r** (residual activities at 200 μM for TEM-1, CTX-M-15, AmpC and OXA-10 of ~6%, ~40%, ~18%, respectively) and **6r** (residual activities at 200 μM for TEM-1, CTX-M-15, AmpC and OXA-10 of ~47%, and ~1%, ~65%, ~41% and ~47%, respectively) may be due to active site hydrophobic interactions involving the tri-aromatic ring system. Intriguingly, the initially tested compound **ML302F** manifested little to no inhibition against the tested enzymes, while the 2,3-dichloro and 2,5-dichloro-substituted enethiols **6n** and **6o** showed greater potency, although they were poor MBL inhibitors. The rhodanine acetic acids were the most active inhibitors in a given set, which was the reverse of the MBL inhibition results. The weakest activity by enethiols was against the ESBL CTX-M-15; no inhibitor tested decreased the residual activity below ~60%. Remarkably, although both TEM-1 and CTX-M-15 are class A SBLs, **6r** potently inhibited TEM-1 but not the other enzyme. This observation exemplifies diversity in the biochemistry of the SBLs, even within the same class. The α-hydroxycarboxylic acids and phosphates (**16**, **17**, **22**, **26**) showed almost no inhibition against SBLs (Figure 5.35 D), consistent with the MBL inhibition results.

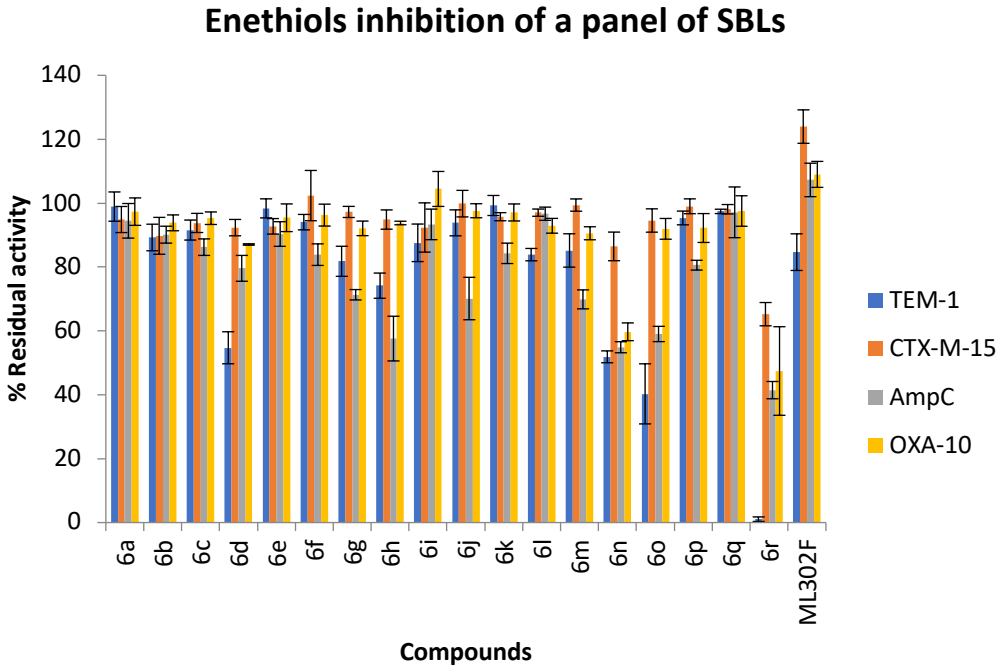
A.


Intact rhodanine testing with a panel of SBLs
% Residual activity
120
100
80
60
40
20
0
3a 3c 3d 3f 3g 3h 3i 3j 3k 3l 3m 3n 3o 3p 3q
Compounds
TEM-1
CTX-M-15
AmpC
OXA-10

B.


Intact rhodanine-amides testing with a panel of SBLs
% Residual activity
120
100
80
60
40
20
0
5a 5b 5c 5d 5e 5f 5g 5h 5i 5j 5k 5l 5m 5n 5o 5p 5q 5r ML302
Compounds
TEM-1
CTX-M-15
AmpC
OXA-10

C.



D.

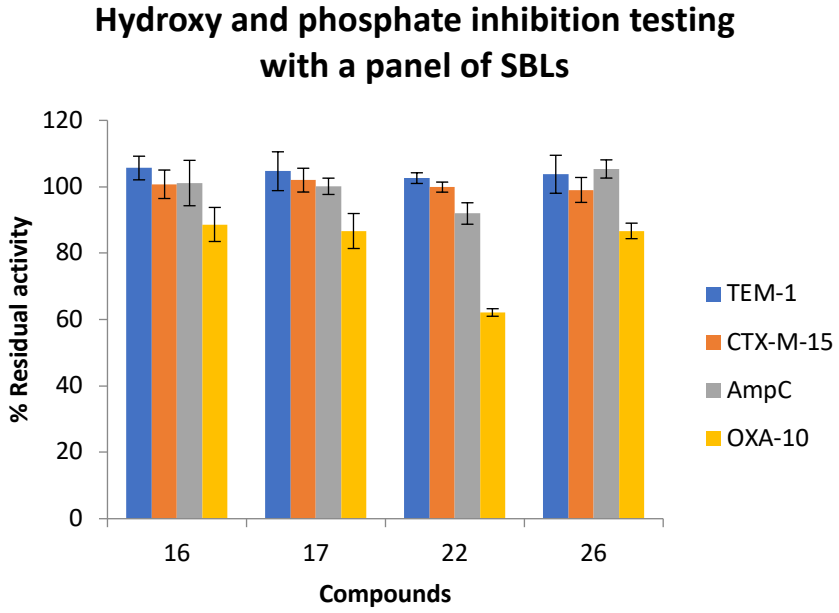


Figure 5.35: Residual activities of serine-β-lactamases (SBLs) in the presence of **A)** rhodanine acetic acids (**3a-q**), **B)** rhodanine amides (**5a-r**), **C)** enethiols (**6a-r**) and **D)** other analogues, all at 200 μM.

5.6. A serendipitous finding

5.6.1. Emerging instability

During the studies on the synthesis of the enethiols from their parent rhodanines (*via* base hydrolysis), it was observed that the product spot on TLC turned black, which indicated possible degradation on silica. Although LC-MS analysis manifested a single clear peak, the ^{1}H NMR spectra showed a different story (Figure 5.36).

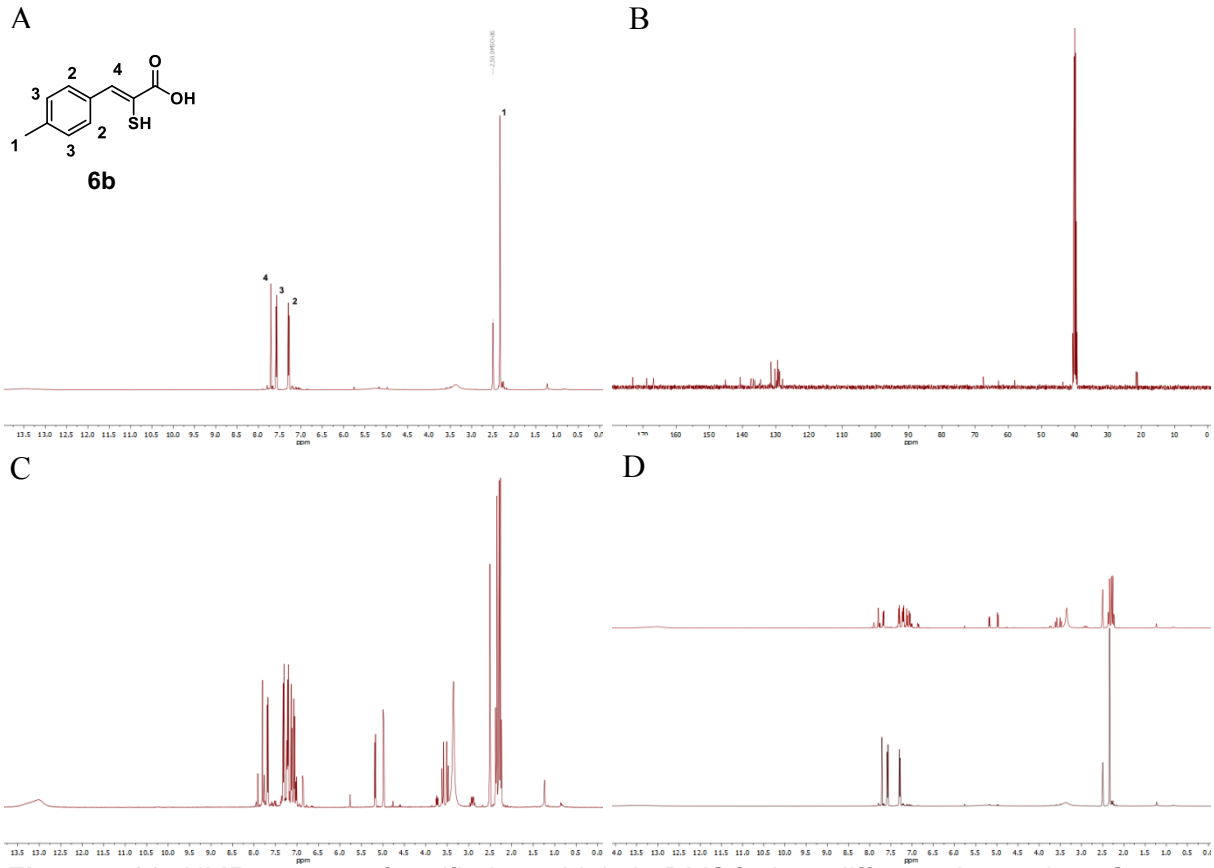


Figure 5.36: *NMR spectra of purified enethiols in DMSO-d_6 at different time points. Spectra are shown for* ***6b*** *as a representative example, but the phenomenon was common to all enethiols tested (**6a-6q**). A, ^{1}H NMR (400 MHz) spectrum of* ***6b*** *in DMSO-d_6; data were acquired within 10 minutes of sample solution preparation. B, ^{13}C NMR (101 MHz) spectrum of* ***6b*** *in DMSO-d_6; data were acquired eight hours after the initial ^{1}H NMR spectrum. C, ^{1}H NMR spectrum of* ***6b*** *in DMSO-d_6 16 hours after the initial ^{1}H NMR spectrum. D, overlay of ^{1}H NMR spectra of* ***6b*** *at t = 10 min (bottom), and t = 16 h (top), indicating that the compound is unstable.*

Initially, ^{1}H NMR data were acquired soon after sample solutions had been prepared (10 min, in DMSO-d_6); the resultant spectra showed good purity. Due to the automated NMR service, ^{13}C NMR spectra were normally acquired overnight, and so the **6b** sample had been in DMSO-d_6 for over eight hours when its ^{13}C NMR spectrum was acquired. Surprisingly, the number of peaks in the ^{13}C NMR spectrum did not match the structure of **6b**, despite the apparently consistent assignment in the ^{1}H NMR spectrum collected earlier. A new ^{1}H NMR spectrum, acquired for the same sample 16 hours after the initial acquisition (Figure 5.36 C), showed significant degradation/decomposition, consistent with the apparent inconsistency between the ^{1}H and ^{13}C NMR spectra. The enethiols were thus proposed to be unstable. This reflected their behaviour on TLC and the observation that their melting point measurements ended in decomposition. A previous sample of **6b** in MeOH that had been used for LC-MS was then re-analysed. Only one peak for the assigned mass that was observed for **6b** was observed for this MeOH sample. Hence it was envisaged that DMSO might be involved in the degradation of **6b**.

The hydrolysis of rhodanines, including enethiols, to produce 'complex' products has been reported in the literature[299-300]. It has been proposed that enethiols can potentially oligomerise (Figure 5.37), although no such products have been isolated[301]. Recrystallisation using heated solvents has been used by other researchers to purify the enethiols. Hence it was decided to attempt to recrystallise all the enethiols (**6a-6s**).

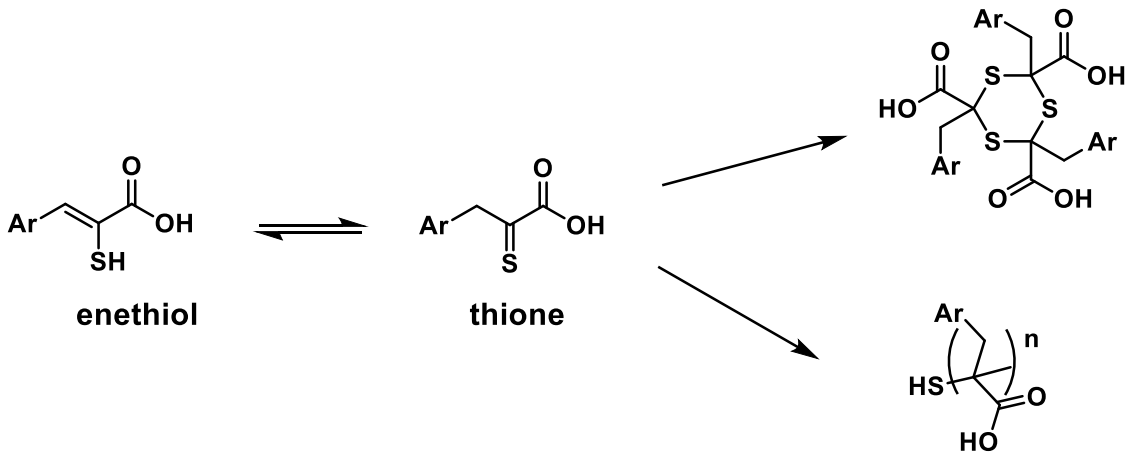


Figure 5.37: *Enethiol/thione tautomerisation and the proposed (but not yet observed) polymerisation/trimerisation products from thione*[301].

5.6.2. Solvent screening

Enethiols (**6a-6s**) were recrystallised from toluene at 110 °C, leading to production of needle-like crystals, for which the spectroscopic data were supportive of the original enethiol structures. The stability of the enethiols (**6a** is shown as an example) was then tested in different deuterated solvents, i.e. acetone-d_6, dioxane-d_8, DMSO-d_6, DMF-d_7, and MeOD-d_4 (Figures 5.38-5.42). As shown in these figures, **6a** was apparently stable in acetone-d_6, dioxane-d_8, and MeOD-d_4 over the time course, and was relatively stable in DMF for approximately half of the time course (five hours). However, **6a** was clearly unstable in DMSO. Thus, use of DMSO should be avoided for biological assays with enethiols/rhodanines. It is also clear that the enethiols can be relatively stable compounds under certain conditions. In order to circumvent this problem, fresh solids were used for each biological assay; stock solutions were prepared by dissolving enethiols in 0.1 M $NaHCO_3$. It should be noted that the thione tautomer was not observed (Figures 5.38-5.40), as the integration of all ^{1}H NMR signals corresponded to enethiol. Thus, the enethiol appears to be the dominant tautomer in solution. ^{1}H NMR data collection was done by Mr Jos Kamps.

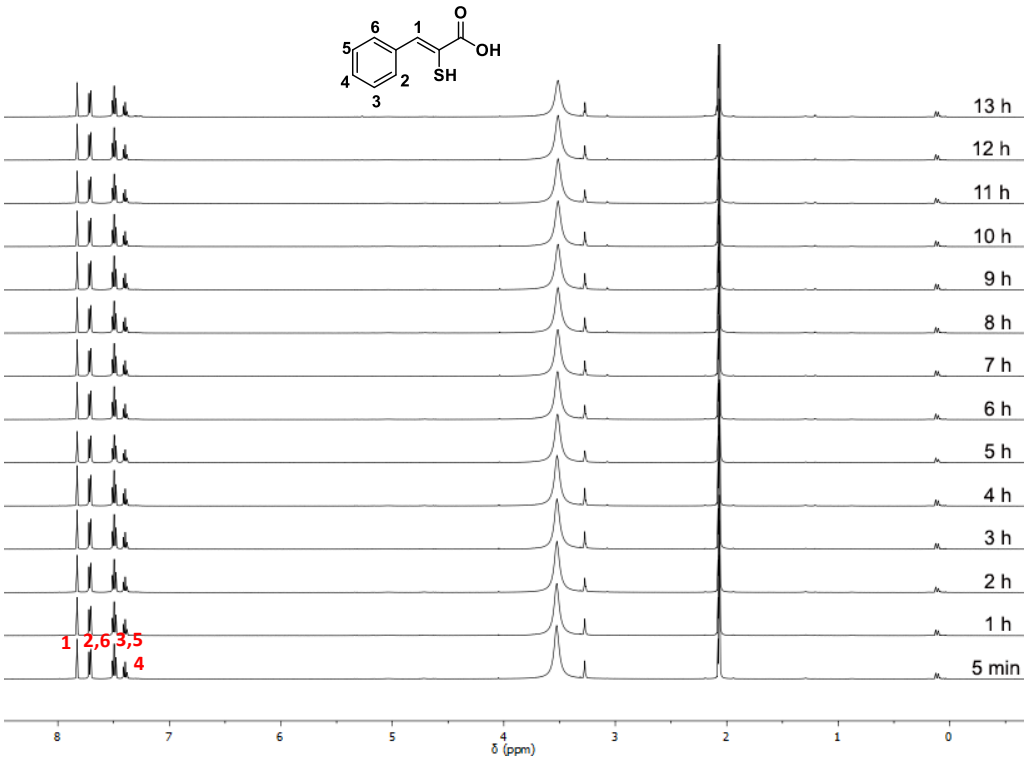


Figure 5.38: *^{1}H NMR (500 MHz) stability test for compound* ***6a*** *in acetone-d_6 over 13 hours. Data acquired by Mr Jos Kamps.*

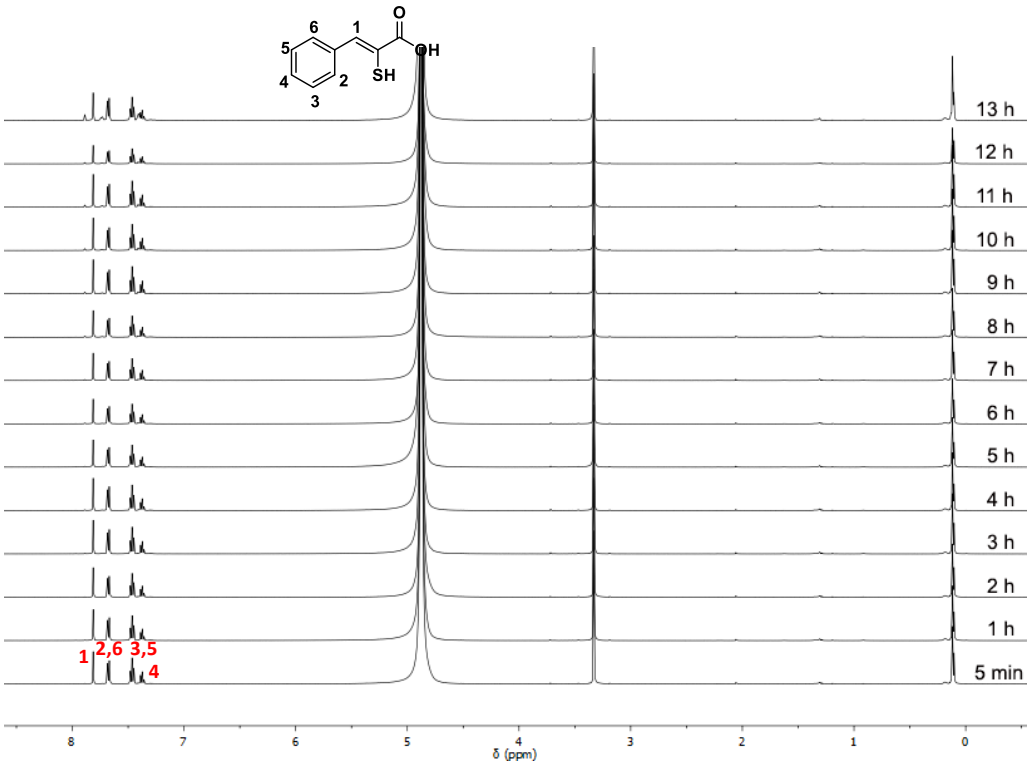


Figure 5.39: *^{1}H NMR (500 MHz) stability test for compound* ***6a*** *in MeOD-d_4 over 13 hours. Data acquired by Mr Jos Kamps.*

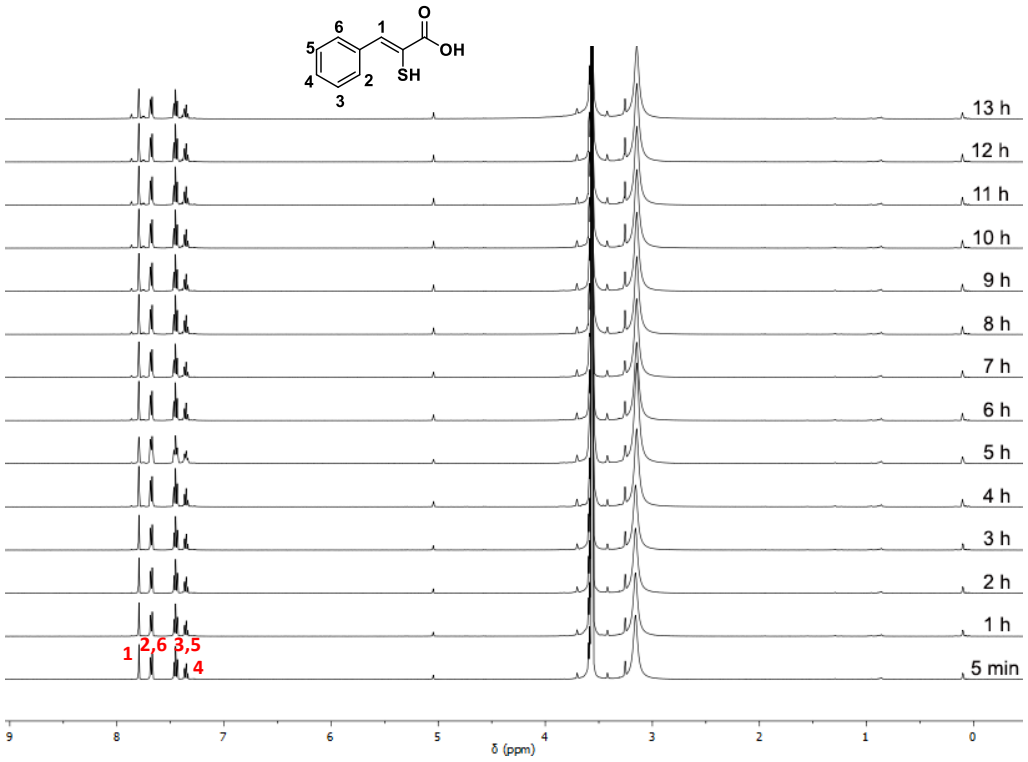


Figure 5.40: *^{1}H NMR (500 MHz) stability test for compound* ***6a*** *in dioxane-d_8 over 13 hours. Data acquired by Mr Jos Kamps.*

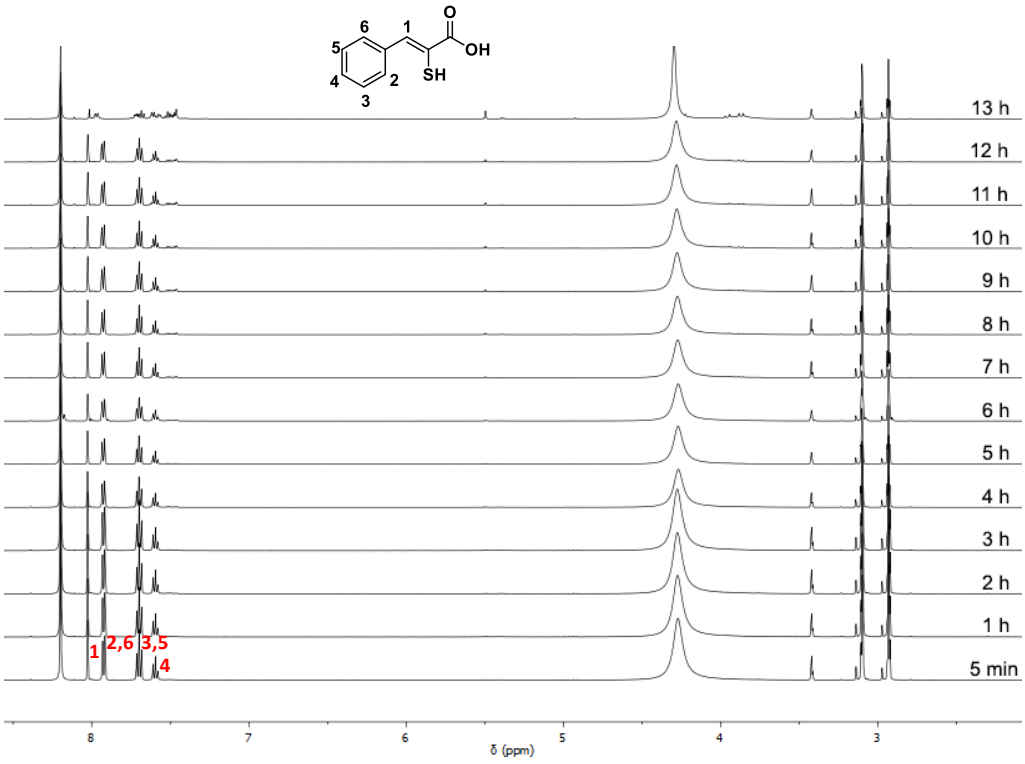


Figure 5.41: *^{1}H NMR (500 MHz) stability test for compound* ***6a*** *in DMF-d_7 over 13 hours. Data acquired by Mr Jos Kamps.*

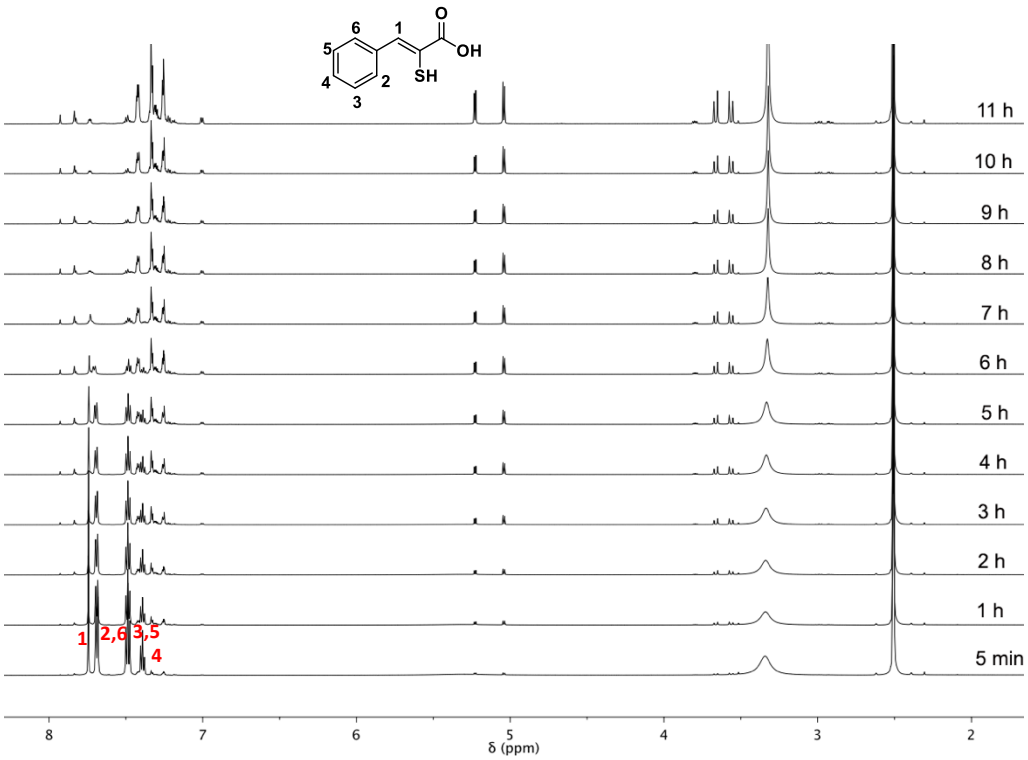


Figure 5.42: *^{1}H NMR (500 MHz) stability test for compound **6a** in DMSO-d_6 over 11 hours. Data acquired by Mr Jos Kamps.*

5.6.3. Product structure elucidation

Enethiol **6j** was further investigated with respect to elucidation of the degradation product. This was because **6j** contains a fluoride substituent which enabled observation of the newly evolving species by ^{19}F NMR. Hence, ^{1}H and ^{19}F time courses in DMSO-d_6 were performed to monitor its reaction (Figures 5.43 and 5.44). Despite the structural similarities of **6j** and **6a**, the halogen substituents on **6j** appear to make **6j** more prone to degradation (Figure 5.43), i.e. the rate of new product formation for **6j** was faster than for **6a** (Figure 5.42). The ^{19}F NMR time-course experiments manifested appearance of two new signals simultaneously as the **6j** signal disappeared. Integration of the new signals shows they are in an ~1:1 ratio, suggesting that the new product could be a dimer (rather than a trimer or polymer). ^{1}H and ^{19}F NMR data collection was done by Mr Jos Kamps.

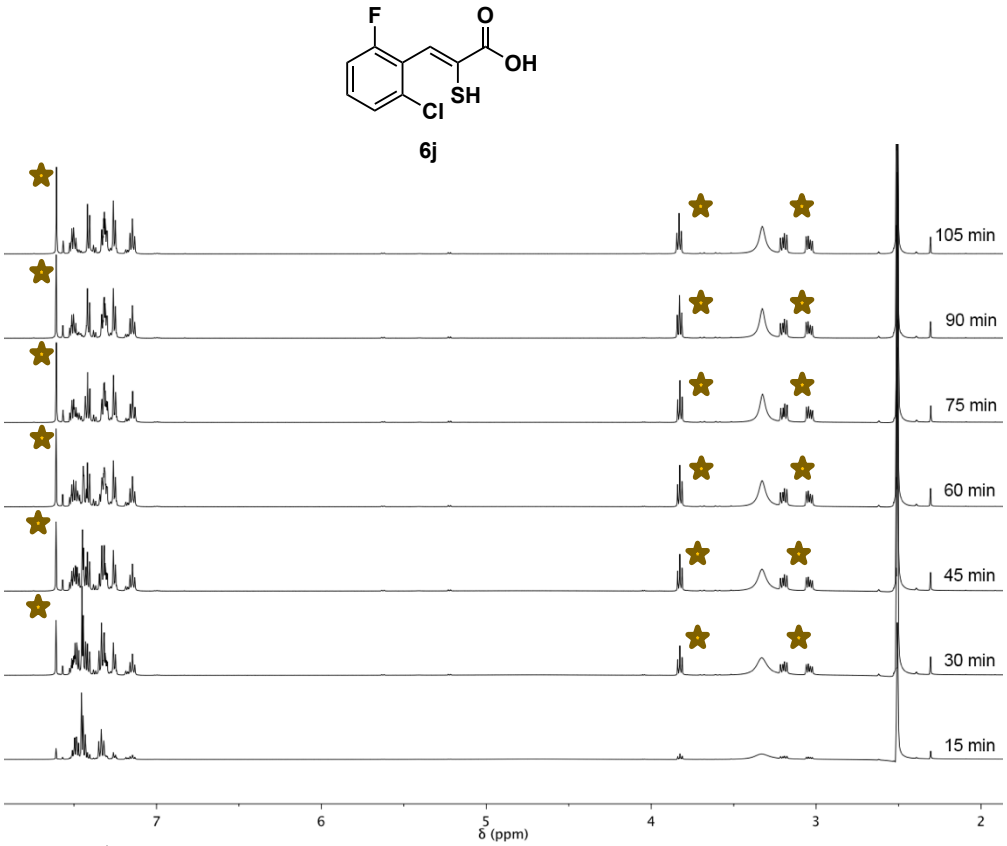


Figure 5.43: *^{1}H NMR (600 MHz) time course for compound **6j** in DMSO-d_6 over 105 mins. Note the new product formation (signals shown as stars). Data acquired by Mr Jos Kamps.*

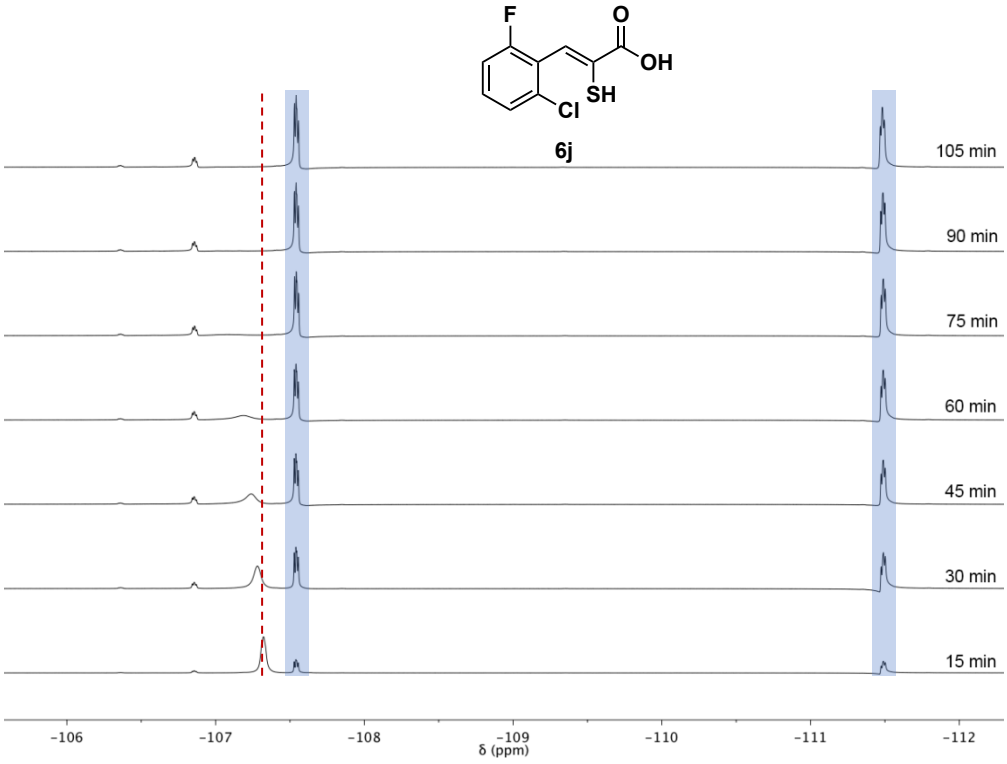


Figure 5.44: *^{19}F NMR (600 MHz) time course for compound **6j** in DMSO-d_6 over 105 mins. **6j** appears to degrade over time, with two new signals appearing (highlighted in a blue box) simultaneously in an ~1:1 ratio. Data acquired by Mr Jos Kamps.*

Enethiol degradation in deuterated and protiated DMSO was then investigated further by ^{1}H NMR analysis (Figure 5.45). If DMSO was directly involved in the reaction, it might be expected that protiated or deuterated DMSO solutions would give different spectra, i.e. protiated DMSO should give more signals than the deuterated counterpart. However, the obtained ^{1}H NMR spectra were almost identical, which suggested that there was no incorporation of DMSO into the degradation products, though a role for DMSO as a catalyst/initiator could not be ruled out.

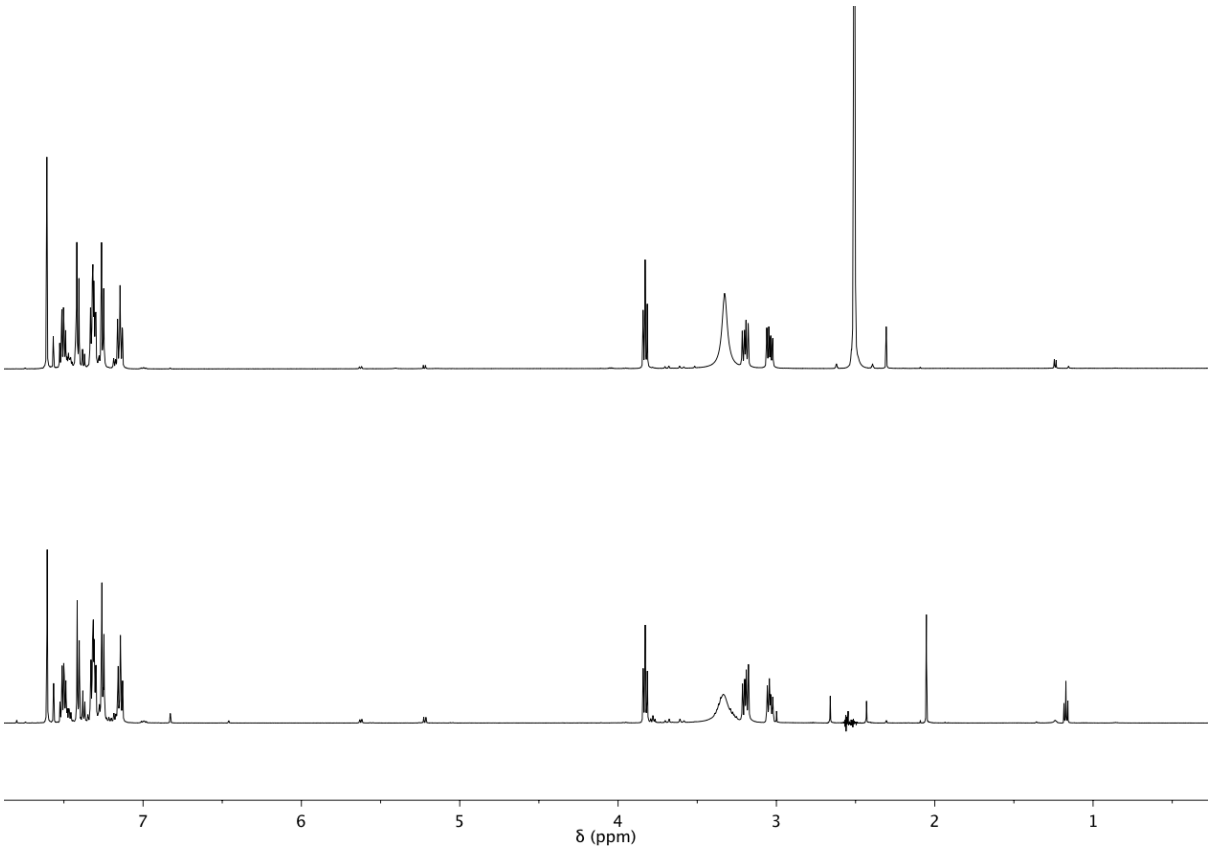
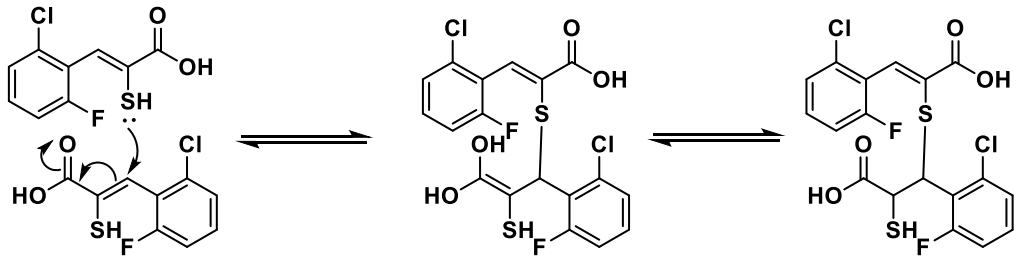


Figure 5.45: *Comparison of ^{1}H NMR spectra after reaction of* ***6j*** *(12 hours) in DMSO-h_6 (top) and DMSO-d_6 (bottom). Data acquired by Mr Jos Kamps.*

To identify the structure of the product from **6j**, 2D ^{1}H-^{13}C heteronuclear single quantum correlation (HSQC) and heteronuclear multiple bond correlation (HMBC) NMR experiments were carried out two hours after sample preparation in DMSO-d_6 (Figure 5.46, NMR data

collection and spectral characterisation was performed by Mr Jos Kamps). Two distinct sets of resonances were identified. One corresponded to aliphatic protons at δ_H 3.04 ppm and δ_H 3.20 ppm, and the other corresponded to a proton in the 'aromatic region' at δ_H 7.61 ppm (Figure 5.46). Integration of the ^{1}H NMR signals shows that all signals correspond to one proton. Thus it was proposed that all the observed signals arose from a single compound, possibly a dimer. One possible reaction to produce an asymmetric dimer is via a Michael addition (Scheme 5.7).



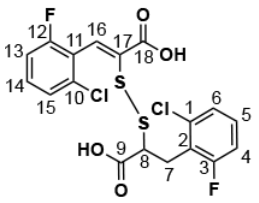
Scheme 5.7: *Proposed dimerisation product **6j*** from enethiol **6j** via Michael addition.*

However, the proposed product **6j*** does not explain the observed triplet at δ_H 3.82 ppm (J = 8.0 Hz, 1 H) (Figure 5.46). Instead the product was proposed to have structure **27j** (Table 5.8, Figure 5.46). This structure is consistent with the spectrum findings that the triplet is clearly connected to a tertiary carbon (C-8, $R_1R_2R_3C$-***H***, represented as red spots in the HSQC spectrum in Figure 5.46) and is coupled to aliphatic protons (on C-7 of **27j**, a $R_1R_2C\boldsymbol{H_aH_b}$ environment is illustrated as blue spots in the HSQC spectrum in Figure 5.46) at δ_H 3.04 ppm (dd, J = 14.0, 8.0 Hz, 1 H) and 3.20 ppm (dd, J = 14.0, 8.0 Hz, 1 H). The aliphatic protons at C-7 have an apparent doublet of doublets/ABX splitting pattern, consistent with coupling with a proton on a tertiary carbon (C-8). The HMBC analyses show that the aliphatic protons (C-7) and the proton on the tertiary carbon (C-8) correlate to a carbonyl carbon (C-9) at δ_C 171.85 ppm and a quaternary carbon (C-2) at δ_C 123.64 ppm. The aliphatic protons on C-7 show a correlation to two further aromatic carbons, with one of the carbon (C-3) signals is split into a doublet (d, J = 248.0 Hz), which is typical of ^{19}F-^{13}C coupling. The observed ^{1}H and ^{13}C NMR signals and assignments are summarised in Table 5.8.

One part of **27j** thus resembles the enethiol precursor, where the benzylic vinyl proton (on C-16) appears as a singlet at δ_H 7.61 ppm (on C-16, $R_1R_2R_3C$-***H***, represented as red spots in the HSQC spectrum in Figure 5.46); the proton on C-16 makes five further correlations, as observed on the enethiol precursor. Since there is no ^1H-^{13}C correlation between the two parts of the molecule, it was proposed that the product is an asymmetric dimer linked *via* a disulphide bridge, with one of the enethiols having been reduced (**27j**, Figure 5.46).

Table 5.8: ^1H and ^{13}C NMR assignments for enethiol **6j** degradation product **27j**.

Position number	δ_H (ppm)	Multiplicity	Coupling constant, *J* (Hz)	δ_C (ppm)	Multiplicity	Coupling constant, *J* (Hz)
1				134.99	d	6.0
2				123.36	d	18.5
3				161.49	d	248.0
4	7.14	t	9.0	114.77	d	22.5
5						
6	7.25	d	8.0	125.83	s	
7	3.04 3.20	dd	14.0, 8.5	29.41	s	
8	3.83	t	8.0	53.27	s	
9				171.52	s	
10				133.76	d	4.1
11				122.11	d	18.5
12				159.25	d	248.5
13	7.31	m		115.11	d	22.5
14						
15	7.41	d		125.83	s	
16	7.61	s		134.32	s	
17						
18				165.22	s	



27j

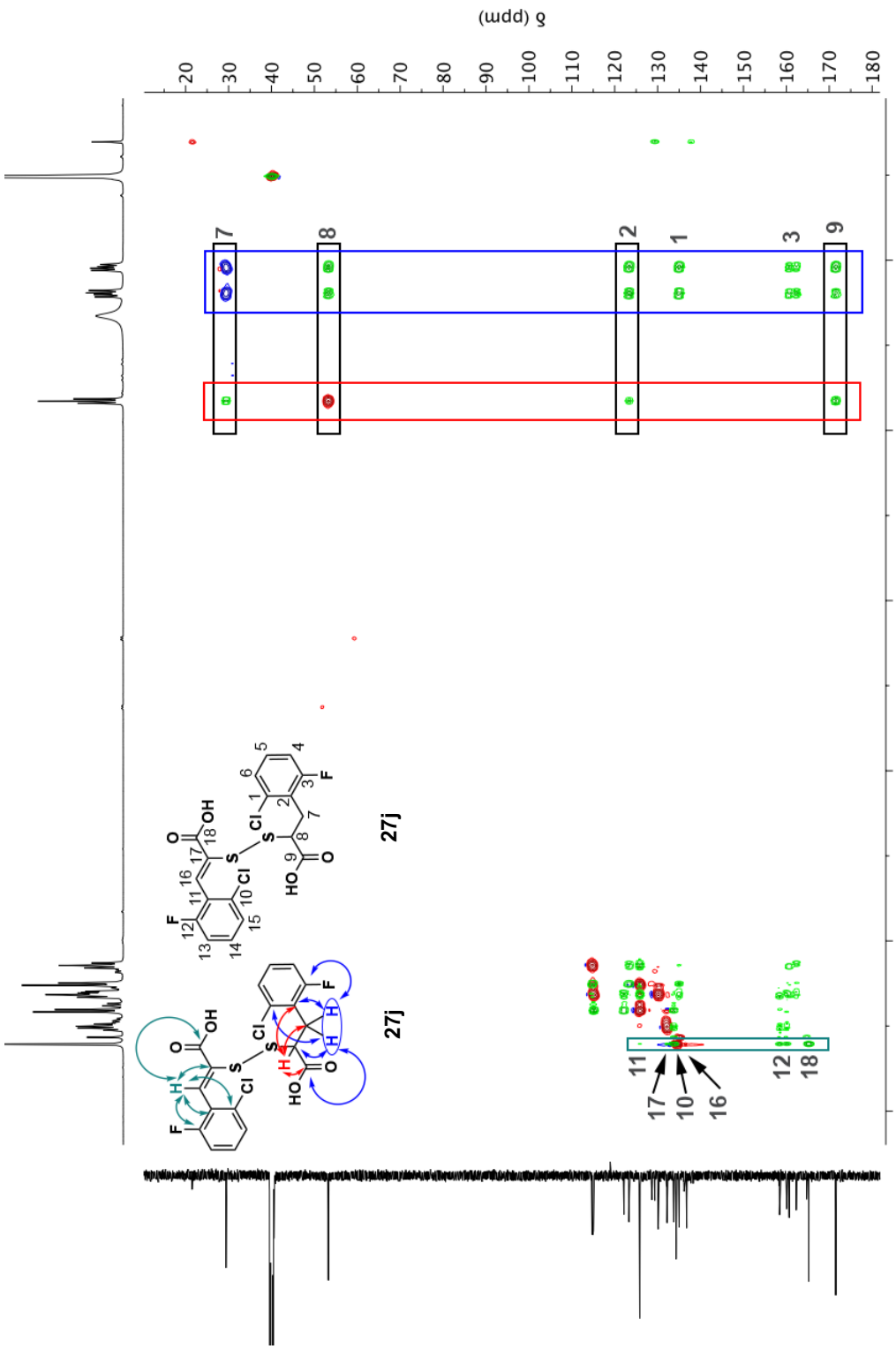


Figure 5.46: *Overlaid 2D HSQC (blue and red) and HMBC (green) NMR spectra (600 MHz) of the dimerisation reaction of **6j** in DMSO-d_6 after 2 h. Cross-peaks highlighted in the blue box correspond to correlations between the aliphatic protons (on C7) to C1, C2, C3, C7, C8 and C9. Multiple-bond correlations are represented by blue arrows. Cross-peaks highlighted in the red box correspond to correlations between the proton on the tertiary carbon (C8) to C2, C7, C8 and C9. Multiple-bond correlations are represented by red arrows. Cross-peaks highlighted in the teal box correspond to correlations between the vinyl proton (on C16) to C10, C11, C12, C16, C17 and C18. Multiple-bond correlations are represented by teal arrows. The black boxes show protons from the reduced enethiol. Data acquisition and interpretation were done by Mr Jos Kamps.*

After compound **6a** had been kept in DMSO-d_6 for an extended period of time, closer inspection of the ^{1}H NMR spectrum revealed new signals at δ_H 5.22 ppm (d, J = 8.0 Hz, 1 H) and 5.63 ppm (d, J = 8.0 Hz, 1 H) (Figure 5.47), a distinctive sign of vicinal coupling [302]. The two newly formed doublets at δ_H 3.60 ppm (J = 15.0 Hz) and 3.69 ppm (J = 15.0 Hz) are characteristic of benzylic CH_2 protons (Figure 5.47). These differed from the signals observed for **27j** (dd, J = 14.1, 8.0 Hz) as they do not couple with the proton on the C-8 tertiary carbon, consistent with formation of a cyclised molecule (**28j**) (Scheme 5.8).

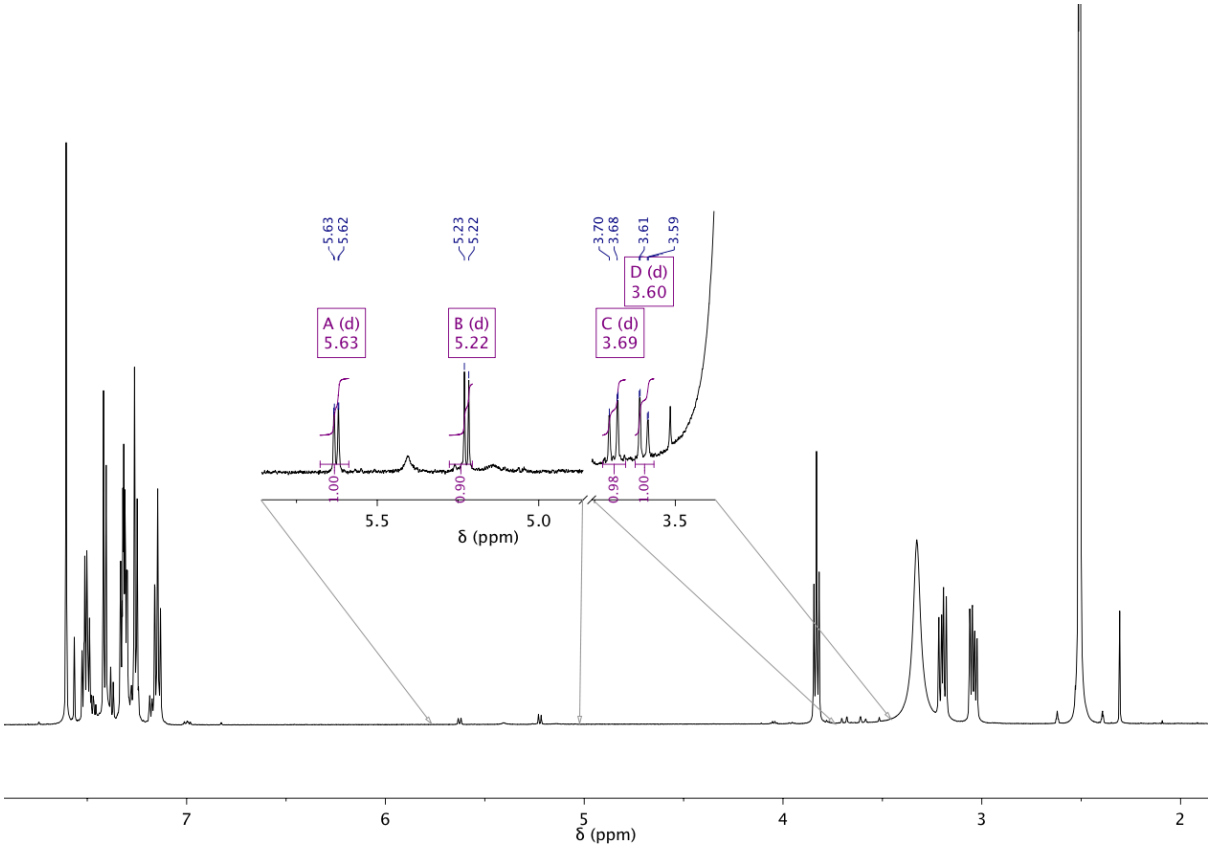
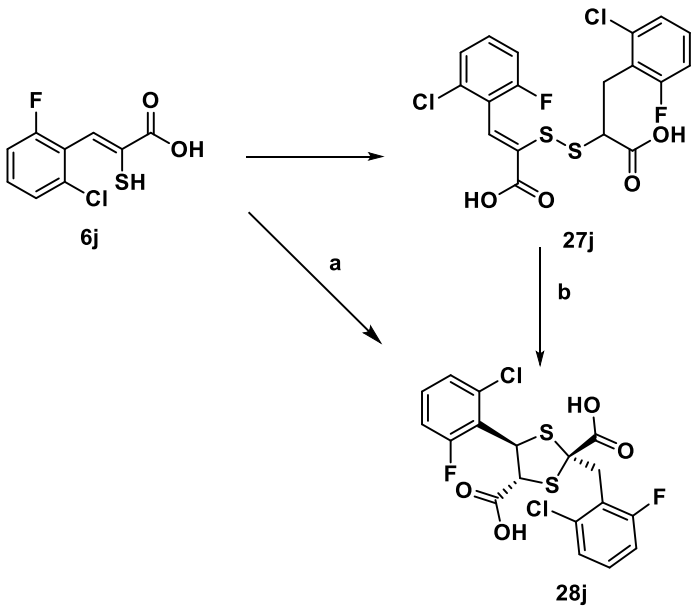


Figure 5.47: *^{1}H NMR (600 MHz) spectrum of **6j** after two hours, showing the newly formed vicinal proton signals at δ_H 5.22 ppm (d, J = 8.2 Hz, 1 H) and 5.63 ppm (d, J = 8.2 Hz, 1 H), which do not couple with the benzylic proton signals at δ_H 3.60 ppm (J = 15.2 Hz) and 3.69 ppm (J = 15.2 Hz). Data acquisition was performed by Mr Jos Kamps.*



Scheme 5.8: *Observed product (**28j**) of enethiol (**6j**) dimerisation reaction via **a)** reduced disulphide intermediate (**27j**) or **b),** directly from enethiol (more likely).*

The formation of the reduced disulphide **27j** and/or cyclised product **28j** was further supported by LC-MS analysis (Figure 5.48, LC-MS data collection was performed by Mr Jos Kamps). Two peaks were observed at the beginning of the reaction, with the peak at RT = 4.60 min consistent with the enethiol disulphide species, **6j** (m/z = 463). The peak at RT = 4.80 min that appears to correspond to the reduced disulphide **27j** (m/z = 465). The reaction was monitored again after 35 min, showing that the peak corresponding to **6j** had diminished (RT = 4.60 min, m/z = 463) and that corresponding to **27j** (RT = 4.80 min, m/z = 465) had increased. As the reaction advanced (65 min), the peak for **6j** disappeared within limits of detection (RT = 4.60 min, m/z = 463), and that for **27j** (RT = 4.80 min, m/z = 465) appears to develop a shoulder, which could be due to the cyclised product **28j**.

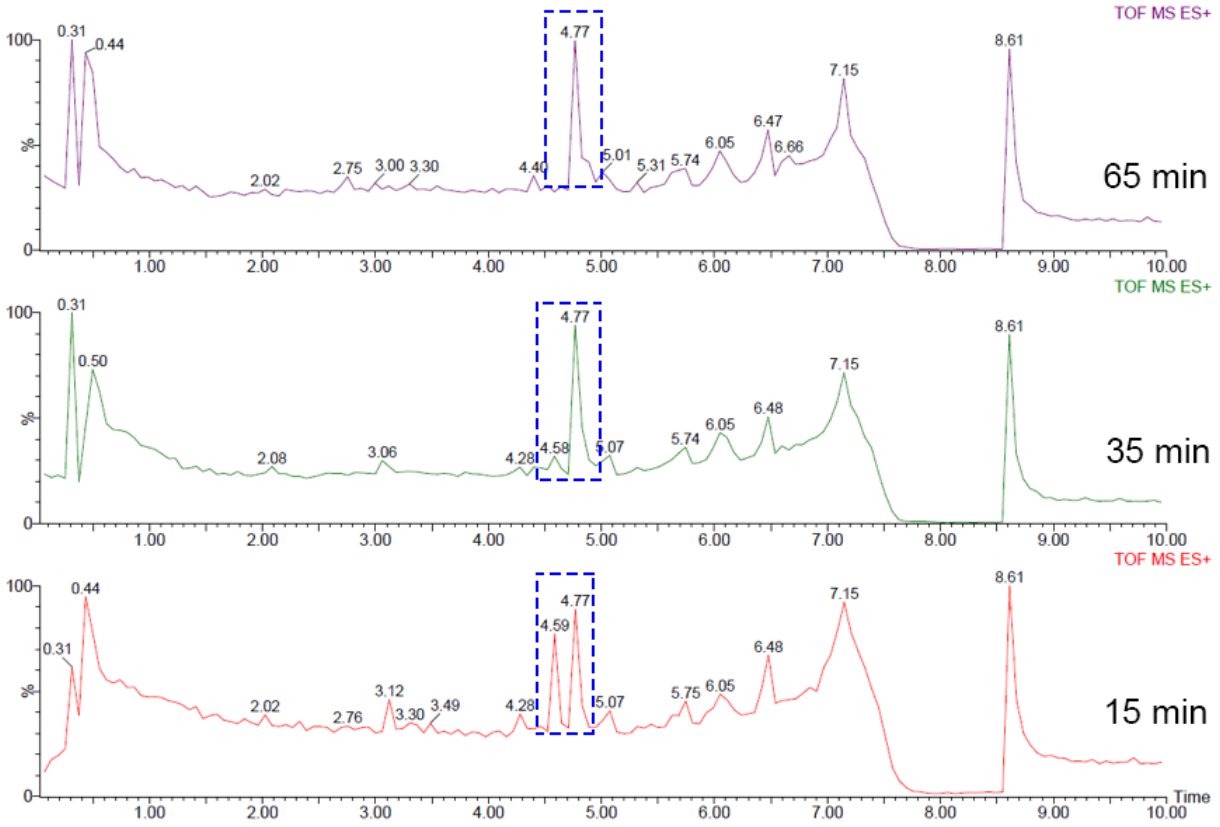


Figure 5.48: *LC-MS chromatograms of the* ***6j*** *dimerisation reaction in DMSO. The peak at 4.60 min is enethiol* ***6j*** *observed as a disulphide (m/z = 463), while the peak at 4.80 min appears to be the reduced disulphide product* ***27j*** *(m/z = 465). Data acquisition and interpretation were done by Mr Jos Kamps.*

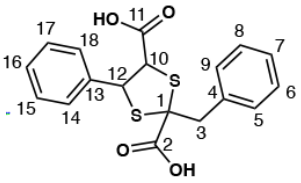
It was proposed that **6a** may degrade differently to **6j**, since the ^{1}H NMR time-course experiment of **6a** (Figure 5.42) gave a different result to that of **6j** (Figure 5.43), which indicated that the products might be different. To test this hypothesis, 2D HSQC and HMBC NMR analyses were carried out to investigate the potential product of **6a** degradation (Figure 5.49, NMR data collection and spectral characterisation was performed by Mr Jos Kamps). NMR spectra were recorded after formation of the degradation product (12 hrs). The ^{1}H and ^{13}C NMR assignments are summarised in Table 5.9.

The characteristic triplet (for **27j**, Figure 5.46) at δ_H 3.82 ppm (J = 8.0 Hz, 1 H) and the two doublet of doublets at δ_H 3.04 ppm (dd, J = 14.1, 8.0 Hz, 1 H) and 3.20 ppm (dd, J = 14.1, 8.0 Hz, 1 H) are not present for **28a** (Figure 5.49). Instead, the doublet of doublets signal (on C-3,

$R_1R_2C\boldsymbol{H_aH_b}$, illustrated as blue spots in the HSQC spectrum in Figure 5.49) at δ_H 3.56 ppm (d, J = 14.0 Hz, 1 H) and 3.66 ppm (d, J = 14.0 Hz, 1 H) is characteristic of a benzylic ABX splitting pattern. The vicinal protons (on C-10 and C-12, $R_1R_2R_3C$-***H***, represented as red spots in Figure 5.49, from HSQC) appear as two doublets at δ_H 5.04 ppm (J = 6.5 Hz, 1 H) and 5.23 ppm (J = 6.5 Hz, 1 H), respectively. These signals support the proposed cyclic structure **28a**.

Table 5.9: ^{1}H and ^{13}C NMR assignments for enethiol **6a** degradation to (cyclised) product **28a**.

Position number	δ_H (ppm)	Multiplicity	Coupling constant, J (Hz)	δ_C (ppm)	Multiplicity	Coupling constant, J (Hz)
1				67.44	s	
2				173.04	s	
3	3.56, 3.66	d	14.0	43.84	s	
4				137.52	s	
5	7.33	m		130.44	s	
6						
7						
8						
9	7.33	m		130.44	s	
10	5.04	d	6.5	63.03	s	
11				168.81	s	
12	5.23	d	6.5	58.25	s	
13				139.41	s	
14	7.42	m		129.43	s	
15						
16						
17						
18	7.42	m		129.43	s	



28a

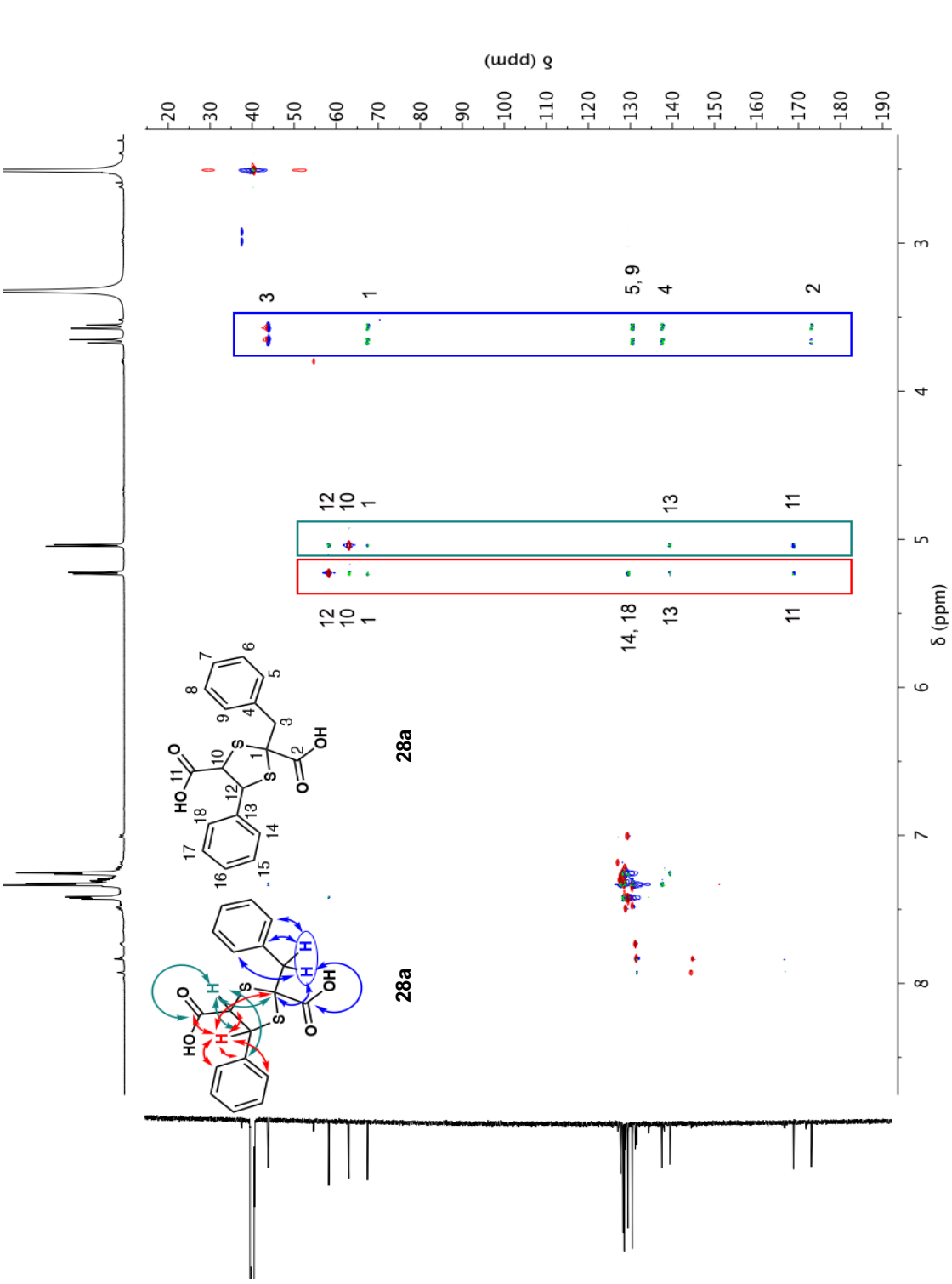


Figure 5.49: *Overlaid 2D HSQC (blue and red) and HMBC (green) NMR spectra (600 MHz) of the dimerisation reaction of* ***6a*** *in DMSO-d_6 after 12 h. Cross-peaks highlighted in the blue box correspond to correlations between the aliphatic protons (on C3) to C1, C2, C3, C4, C5 and C9. Multiple-bond correlations are represented by blue arrows. Cross-peaks highlighted in the red box correspond to correlations between the vicinal proton (on C12) and C1, C10, C11, C12, C13, C14 and C18. Multiple-bond correlations are represented by red arrows. Cross-peaks highlighted in the teal box correspond to correlations between the vicinal proton (on C10) and C1, C10, C11, C12 and C13. Multiple bond correlations are represented by teal arrows. Data acquisition and interpretation were done by Mr Jos Kamps.*

There is precedent for the proposed dimerisation of enethiols [303]. A crystal structure of a cyclic product derived from an enethiol has been reported[303], although the NMR assignments described in that study appear to have been misinterpreted, i.e. the ^{13}C chemical shifts for C-1, C-10 and C-12 were assigned to aromatic carbons (above 120 ppm). The authors also proposed a mechanism for the dimerisation, initially *via* Michael addition. However, the NMR data obtained as part of the work for this thesis strongly suggest formation of a reduced disulphide (Figure 5.46).

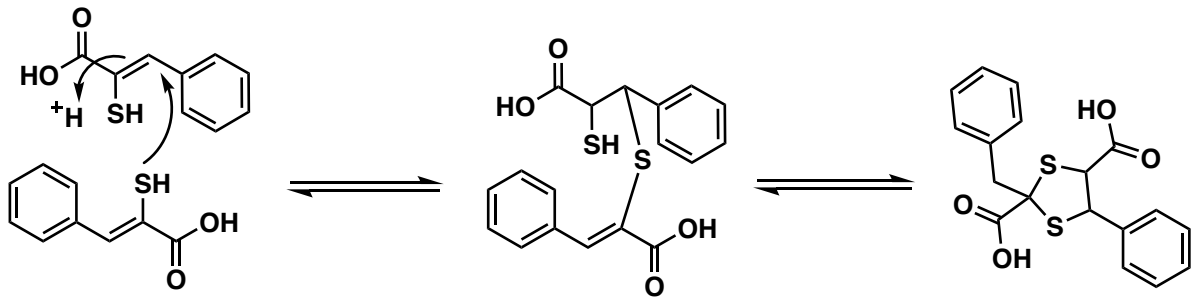
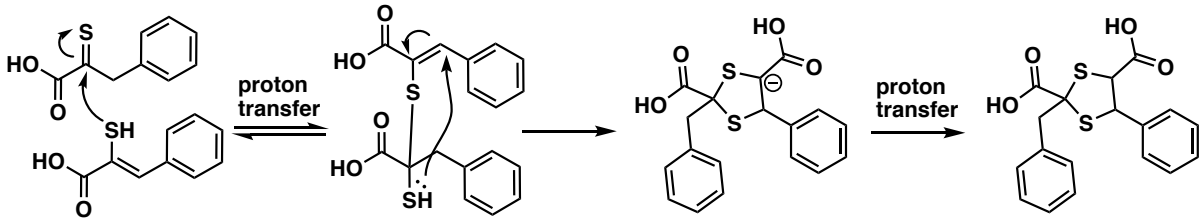


Figure 5.50: Proposed mechanism from the literature[304].

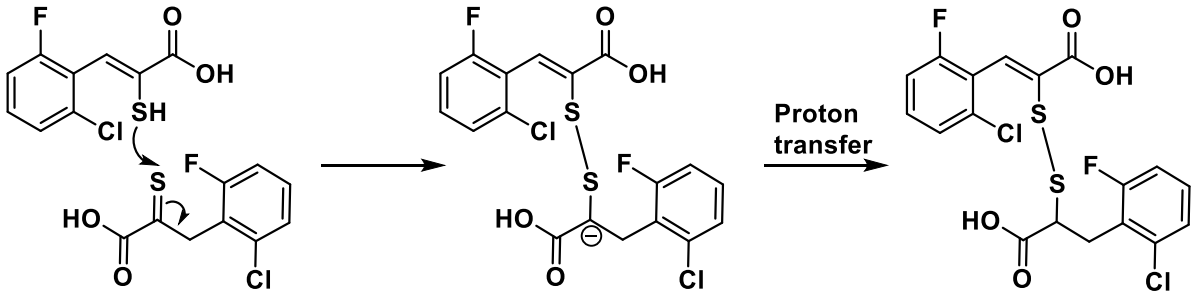
Enethiols undergo tautomerisation to give their thione form in equilibrium in solution[304]. However, the thione tautomer was not observed in NMR time-course studies using different solvents (Figures 5.38-5.42). A possible mechanism of the reaction is *via* nucleophilic attack of an enethiol thiol (**6a**) on the thione carbon. Subsequent intramolecular cyclisation followed by proton transfer to gives **28a** (Figure 5.49, Scheme 5.9).



6a **6a*** **28a**

Scheme 5.9: *Possible alternative mechanism of enethiol dimerisation to give the cyclised product.*

The results imply different substrates produce different reaction outcomes, e.g. **6a** produces mainly **28a** and **6j** produces mainly **27j**. Thus, the *ortho*-chloro substituent on the phenyl ring of **6j** may hinder attack of the enethiol on the thione carbon, favouring formation of **27j** (Scheme 5.10). In the case of **6a**, which is less sterically hindered, formation of **28a** is favoured.



6j **27j**

Scheme 5.10: *Proposed mechanism of enethiol dimerisation with steric hindrance.*

5.7. Discussion and future work

The overall results reveal that rhodanine-derived species have potential as broad-spectrum MBL inhibitors. Their activity may reflect the mimicking of the binding of β-lactam hydrolysis products by enethiol carboxylates (Figure 5.32). The ability of enethiols to inhibit SBLs appears more limited, at least among those tested in this study[268, 305]. Although the enethiols **6a-6q**, which are derived by rhodanine hydrolysis, are the most potent of the series identified, the SAR studies of compounds with intact rhodanine ring structures suggest that rhodanine-related heterocycles that do not chelate via a thiol/sulphur may also have potential as MBL inhibitors. Recent work on another series suggests that such compounds have potential to inhibit without active site metal chelation[271]. The proposal that the enethiols **6a-6l** and rhodanine amides **5a-5l** undergo different binding modes is supported by the observation that the SAR trends for the two series only partially overlapped.

Structural evidence that ML302/ML302F can form a ternary complex with VIM-2 has been previously reported[268]. However, the SAR results obtained here suggest that formation of such a ternary complex is not a general feature of rhodanine-derived MBL inhibition. Hence, ternary complex formation, although interesting, is unlikely to be a productive path for the development of broad-spectrum MBL inhibitors.

Rhodanines have been characterised as 'difficult to progress' and 'promiscuous' compounds[271-273]. Despite their complex nature, one rhodanine is clinically approved for use in nerve damage due to diabetes mellitus (Epalrestat®, an aldose reductase inhibitor)[306], and other rhodanine-related heterocycles are in development[307]. The overall results presented here contribute to our understanding of the potential complexities involved in the interpretation of the results of assays that involve rhodanines.

The results presented here support the proposal that rhodanines have potential as promiscuous enzyme inhibitors/protein binders, in part owing to their tendency to undergo hydrolysis to products, including enethiols, which have potential to inhibit the multiple metallo-enzymes present in cells, including related MBL-fold enzymes. These metallo-enzymes have important biological roles beyond antibiotic resistance, which include nucleic acid repair and metabolism[308]. These results also imply that any medicinal chemistry studies that employ rhodanine inhibitors should, as a matter of course, include testing of their degradation products. Further, it is recommended that rhodanines/enethiols are not stored/assayed in DMSO in which they undergo degradation.

The results also indicate that the reaction outcomes of rhodanine derived enethiol degradation depends on the substitution pattern of the enethiols, with steric hindrance determining the extent of formation of the **27j-**type product compared with the **28a** cyclic-type product. The more sterically hindered **6j** degrades to asymmetrical disulphide product **27j**, while the less

hindered **6a** degrades to cyclic product **28a**, probably through different reaction pathways. It would be interesting to test whether different substitutions would affect the reaction rate.

Acknowledgements

Proteins used in my work were kindly provided by Mr Samuel Cahill and Dr Jürgen Brem. I would also thank Mr Samuel Cahill for helping me to run inhibition assays with CphA. SBL screening was carried out solely by Mr Samuel Cahill. Compounds **16**, **17**, **22** and **26** were synthesised by Dr Marios Markoulides. Special thanks to Mr Jos Kamps for helping with and running NMR time-course experiments for rhodanine stability tests. He carried out the ^{1}H and ^{19}F NMR time courses, 1D and 2D characterisation experiments, and ran the LC-MS experiments for the enethiol dimerization. Professor Timothy Claridge offered guidance on interpretation of NMR data. Mr Dmitrijs Stepanovs obtained crystals and refined structures under the supervision of Dr Michael McDonough, who also carried out the refinement of some crystal structures.

References

1. Finch, C. E., Evolution of the human lifespan and diseases of aging: Roles of infection, inflammation, and nutrition. *P Natl Acad Sci USA* **2010,** *107*, 1718-24.

2. Böttcher, H. M., *Miracle drugs; a history of antibiotics*. Heinemann: London, **1963**; p ix, 285 p.

3. Zaffiri, L.; Gardner, J.; Toledo-Pereyra, L. H., History of antibiotics. from salvarsan to cephalosporins. *J Invest Surg* **2012,** *25* (2), 67-77.

4. Sengupta, S.; Chattopadhyay, M. K.; Grossart, H. P., The multifaceted roles of antibiotics and antibiotic resistance in nature. *Front Microbiol* **2013,** 4-6.

5. Williams, K. J., The introduction of 'chemotherapy' using arsphenamine - the first magic bullet. *J Roy Soc Med* **2009,** *102* (8), 343-8.

6. Mahoney, J. F.; Arnold, R. C.; Harris, A., Penicillin treatment of early syphilis-a preliminary report. *Am J Public Health* **1943,** *33* (12), 1387-91.

7. Spotts, C. R.; Stanier, R. Y., Mechanism of streptomycin action on bacteria - unitary hypothesis. *Nature* **1961,** *192* (480), 633-8.

8. Comroe, J. H., Jr., Pay dirt: the story of streptomycin. Part I. From Waksman to Waksman. *Am Rev Respir Dis* **1978,** *117* (4), 773-81.

9. Simon, H. J., Streptomycin, Kanamycin, Neomycin and Paromomycin. *Pediatr Clin North Am* **1968,** *15* (1), 73-83.

10. Bayram, Y.; Korkoca H Fau - Aypak, C.; Aypak C Fau - Parlak, M.; Parlak M Fau - Cikman, A.; Cikman A Fau - Kilic, S.; Kilic S Fau - Berktas, M.; Berktas, M., Antimicrobial susceptibilities of Brucella isolates from various clinical specimens. *Int J Med Sci* **2011**, 8, 198-202.

11. Enderlin, G.; Morales, L.; Jacobs, R. F.; Cross, J. T., Streptomycin and alternative agents for the treatment of tularemia - review of the literature. *Clin Infect Dis* **1994,** *19* (1), 42-7.

12. Richens, J., The diagnosis and treatment of donovanosis (Granuloma Inguinale). *Genitourin Med* **1991,** *67* (6), 441-52.

13. Thornsberry, C.; Baker, C. N.; Facklam, R. R., Antibiotic susceptibility of Streptococcus bovis and other group D streptococci causing endocarditis. *Antimicrob Agents Chemother* **1974,** *5* (3), 228-33.

14. Chow, J. W., Aminoglycoside resistance in enterococci. *Clin Infect Dis* **2000,** *31* (2), 586-9.

15. Pfuetze Kh Fau - Pyle, M. M.; Pyle Mm Fau - Hinshaw, H. C.; Hinshaw Hc Fau - Feldman, W. H.; Feldman, W. H., The first clinical trial of streptomycin in human tuberculosis. *Am Rev Tuberc* **1955,** *71* (5), 572-4.

16. Silver, L. L., Challenges of antibacterial discovery. *Clin Microbiol Rev* **2011,** *24* (1), 71-5.

17. Fleming, A., On the antibacterial action of cultures of a Penicillium, with special feference to their use in the isolation of B. influenzæ. *Br J Exp Pathol*. **1929,** *10* (3), 226-36.

18. Smadel, J. E., Chloramphenicol (Chloromycetin) in the treatment of infectious diseases. *Am J Med* **1949,** *7* (5), 671-85.

19. Harris, H. J., Aureomycin and Chloromycetin in Brucellosis - with special feference to chronic brucellosis. *B New York Acad Med* **1949,** *25* (7), 458-9.

20. Geraci, J. E.; Heilman, F. R.; Nichols, D. R.; Wellman, W. E.; Ross, G. T., Some laboratory and clinical experiences with a bew antibiotic, vancomycin. *J Lab Clin Med* **1956,** *48* (5), 809-10.

21. Griffith, R. S.; Black, H. R., Comparative in vitro antistreptococcal activity of Penicillin V, propionyl erythromycin, tetracycline, and vancomycin. *Curr Ther Res Clin E* **1963,** *5* (2), 57-8.

22. Sensi P Fau - Margalith, P.; Margalith P Fau - Timbal, M. T.; Timbal, M. T., Rifomycin, a new antibiotic; preliminary report. *Farmaco Sci* **1959,** *14* (2), 146-7.

23. Noall, E. W. P.; Sewards, H. F. G.; Waterworth, P. M., Successful treatment of a case of proteus septicaemia. *Brit Med J* **1962,** (5312), 1101-2.

24. Lesher, G. Y.; Gruett, M. D.; Froelich, E. J.; Brundage, R. P.; Bailey, J. H., 1,8-Naphthyridine derivatives - a new class of chemotherapeutic agents. *J Med Pharmaceut Ch* **1962,** *5* (5), 1063-5.

25. Smart Jg Fau - Heughan, C.; Heughan, C., A clinical trial of naldixic acid (Negram) in urinary infections. *Br J Clin Pract* **1965,** (19), 269-73.

26. Orecchio, R. M.; Mischler, T. W., A Double-blind multiclinic comparative trial of mupirocin topical and its vehicle in the treatment of bacterial skin infections. *Curr Ther Res Clin E* **1986,** *39* (1), 82-6.

27. Bonfiglio, G.; Furneri, P. M., Novel streptogramin antibiotics. *Expert Opin Inv Drug* **2001,** *10* (2), 185-98.

28. Plouffe, J. F., Emerging therapies for serious gram-positive bacterial infections: A focus on linezolid. *Clin Infect Dis* **2000,** *31*, S144-S9.

29. Steenbergen, J. N.; Alder, J.; Thorne, G. M.; Tally, F. P., Daptomycin: a lipopeptide antibiotic for the treatment of serious Gram-positive infections. *J Antimicrob Chemoth* **2005,** *55* (3), 283-8.

30. Jacobs, M. R., Retapamulin: a semisynthetic pleuromutilin compound for topical treatment of skin infections in adults and children. *Future Microbiol* **2007,** *2* (6), 591-600.

31. Novak, R.; Shlaes, D. M., The pleuromutilin antibiotics: A new class for human use. *Curr Opin Invest Dr* **2010,** *11* (2), 182-191.

32. Hooper, D. C., Emerging mechanisms of fluoroquinolone resistance. *Emerg Infect Dis* **2001,** *7* (2), 337-41.

33. Greaves Ab Fau - Hilleman, M. R.; Hilleman Mr Fau - Taggart, S. R.; Taggart Sr Fau - Bankhead, A. B.; Bankhead Ab Fau - Feld, M.; Feld, M., Chemotherapy in bubonic lymphogranuloma venereum: a clinical and serological evaluation. *B World Health Organ* **1957,** *16* (2), 277-89.

34. Lantin, P. T.; Gamboa, E. L.; Sadili, F., Studies on chloramphenicol in the treatment of typhoid fever. *Am J Med Sci* **1951,** *222* (3), 285-291.

35. Zuckerman, J. M.; Qamar, F.; Bono, B. R., Review of macrolides (Azithromycin, Clarithromycin), ketolids (Telithromycin) and glycylcyclines (Tigecycline). *Med Clin N Am* **2011,** *95* (4), 761-78.

36. Annotations, Spiramycin. *Brit Med J* **1956,** *1* (4967), 621.

37. Mills, W. H.; Thompson, G. W.; Beagrie, G. S., Clinical evaluation of Spiramycin and Erythromycin in control of periodontal disease. *J Clin Periodontol* **1979,** *6* (5), 308-16.

38. Jones, R. N.; Biedenbach, D. J., Antimicrobial activity of RU-66647, a new ketolide. *Diagn Micr Infec Dis* **1997,** *27* (1-2), 7-12.

39. Yamaguchi, T.; Hirakata, Y.; Izumikawa, K.; Miyazaki, Y.; Maesaki, S.; Tomono, K.; Yamada, Y.; Kamihira, S.; Kohno, S., In vitro activity of telithromycin (HMR3647), a new ketolide, against clinical isolates of Mycoplasma pneumoniae in Japan. *Antimicrob Agents Chemother* **2000,** *44* (5), 1381-2.

40. Coates, A.; Hu, Y. M.; Bax, R.; Page, C., The future challenges facing the development of new antimicrobial drugs. *Nat Rev Drug Discov* **2002,** *1* (11), 895-910.

41. Mann, J. M.; Tarantola, D.; Netter, T. W., *AIDS in the world*. Harvard University Press: Cambridge, Mass., 1992; p xiv, 1037 p.

42. Cohen, M. L., Changing patterns of infectious disease. *Nature* **2000,** *406* (6797), 762-7.

43. Culotta, E., Science policy - funding crunch hobbles antibiotic-resistance research. *Science* **1994,** *264* (5157), 362-3.

44. Aminov, R. I., A brief history of the antibiotic era: lessons learned and challenges for the future. *Front Microb* **2010,** *1* (134), 1-7

45. Lewis, K., Platforms for antibiotic discovery. *Nat Rev Drug Discov* **2013,** *12* (5), 371-87.

46. Eliopoulos, G. M.; Willey, S.; Reiszner, E.; Spitzer, P. G.; Caputo, G.; Moellering, R. C., In vitro and in vivo activity of LY 146032, a new cyclic lipopeptide antibiotic. *Antimicrob Agents Chemother* **1986,** *30* (4), 532-5.

47. Raja, A.; LaBonte, J.; Lebbos, J.; Kirkpatrick, P., Daptomycin. *Nat Rev Drug Discov* **2003,** *2* (12), 943-4.

48. Bush, K., Alarming beta-lactamase-mediated resistance in multidrug-resistant Enterobacteriaceae. *Curr Opin Microbiol* **2010,** *13* (5), 558-64.

49. Neu, H. C., The crisis in antibiotic-resistance. *Science* **1992,** *257* (5073), 1064-73.

50. Payne, D. J.; Gwynn, M. N.; Holmes, D. J.; Pompliano, D. L., Drugs for bad bugs: confronting the challenges of antibacterial discovery. *Nat Rev Drug Discov* **2007,** *6* (1), 29-40.

51. Garber, K., A beta-lactamase inhibitor revival provides new hope for old antibiotics. *Nat Rev Drug Discov* **2015,** *14* (7), 445-U88.

52. Ling, L. L.; Schneider, T.; Peoples, A. J.; Spoering, A. L.; Engels, I.; Conlon, B. P.; Mueller, A.; Schaberle, T. F.; Hughes, D. E.; Epstein, S.; Jones, M.; Lazarides, L.; Steadman, V. A.; Cohen, D. R.; Felix, C. R.; Fetterman, K. A.; Millett, W. P.; Nitti, A. G.; Zullo, A. M.; Chen, C.; Lewis, K., A new antibiotic kills pathogens without detectable resistance. *Nature* **2015,** *517* (7535), 455-9.

53. Zipperer, A.; Konnerth, M. C.; Laux, C.; Berscheid, A.; Janek, D.; Weidenmaier, C.; Burian, M.; Schilling, N. A.; Slavetinsky, C.; Marschal, M.; Willmann, M.; Kalbacher, H.; Schittek, B.; Brotz-Oesterhelt, H.; Grond, S.; Peschel, A.; Krismer, B., Human commensals producing a novel antibiotic impair pathogen colonization. *Nature* **2016,** *535* (7613), 511-6.

54. Versporten, A.; Bolokhovets, G.; Ghazaryan, L.; Abilova, V.; Pyshnik, G.; Spasojevic, T.; Korinteli, I.; Raka, L.; Kambaralieva, B.; Cizmovic, L.; Carp, A.; Radonjic, V.; Maqsudova, N.; Celik, H. D.; Payerl-Pal, M.; Pedersen, H. B.; Sautenkova, N.; Goossens, H.; Grp, W. E.-E. P., Antibiotic use in eastern Europe: a cross-national database study in coordination with the WHO Regional Office for Europe. *Lancet Infect Dis* **2014,** *14* (5), 381-7.

55. Bush, K.; Bradford, P. A., Beta-lactams and beta-lactamase inhibitors: an overview. *Cold Spring Harb Perspect Med* **2016,** *6* (8), 1-22.

56. Demain, A. L.; Elander, R. P., The beta-lactam antibiotics: past, present, and future. *Antonie Van Leeuwenhoek* **1999,** *75* (1-2), 5-19.

57. Elander, R. P., Industrial production of beta-lactam antibiotics. *Appl Microbiol Biotechnol* **2003,** *61* (5-6), 385-92.

58. Stewart, G. T., Toxicity of the penicillins. *Postgrad Med J* **1964,** *40*, SUPPL:160-9.

59. Toshkov, A., Toxicity of semisynthetic penicillins applied to guinea pigs. *C R Acad Bulg Sci* **1965,** *18* (6), 569-72.

60. Dalhoff, A.; Janjic, N.; Echols, R., Redefining penems. *Biochem Pharmacol* **2006,** *71* (7), 1085-95.

61. Brunel, J., Antibiosis from Pasteur to Fleming. *J Hist Med Allied Sci* **1951,** *6* (3), 287-301.

62. Kong, K. F.; Schneper, L.; Mathee, K., Beta-lactam antibiotics: from antibiosis to resistance and bacteriology. *APMIS* **2010,** *118* (1), 1-36.

63. Selwyn, S., Pioneer work on the 'penicillin phenomenon', 1870-6. *J Antimicrob Chemother* **1979,** *5* (3), 249-55.

64. Burdon-Sanderson, J. S. *Appendix No. 5 - Further Report of Researches Concerning the Intimate Pathology of Contagion. The Origin and Distribution of Microzymes (Bacteria) in Water, and the Circumstances which Determine Their Existence in the Tissue and Liquids of the Living Body* Her Majesty's Stationery Office: London, 1871; pp 56-66.

65. Lister, J., XVI.—A Contribution to the Germ Theory of Putrefaction and other Fermentative Changes, and to the Natural History of Torulæ and Bacteria. *Trans R Soc Edinburgh* **2013,** *27* (3), 313-44.

66. Lister, J., In Correspondence with Arthur Lister (Cited by W. Fraser-Moodie, 1971). 1872.

67. Fraser-Moodie, W., Struggle against infection. *Proc R Soc Med* **1971,** *64* (1), 87-94.

68. Roberts, W., Studies on Biogenesis. *Philos Trans Royal Soc* **1874,** *164*, 457-477.

69. Ward, H. M., Symbiosis. *Annals of Botany* **1899,** *13*, 549-62.

70. Tyndall, J., II. The optical deportment of the atmosphere in relation to the phenomena of putrefaction and infection. *Philos Trans Royal Soc* **1876,** *166*, 27-74.

71. Duchesne, E. Contribution à l'étude de la concurrence vitale chez les micro-organismes: antagonisme entre les moisissures et les microbes. l'Ecole du Service de Santé Militaire de Lyon, Lyon, 1897.

72. Chain, E.; Florey, H. W.; Adelaide, M. B.; Gardner, A. D.; Heatley, N. G.; Jennings, M. A.; Orr-Ewing, J.; Sanders, A. G.; Peltier, L. F., Penicillin as a chemotherapeutic agent. *Lancet* **1940,** *236* (6104), 226-28.

73. Florey, H. W.; Chain, E.; Heatley, N. G.; Jennings, M. A.; Sanders, A. G.; Abraham, E. P.; Florey, M.; Ary, E., *Antibiotics. A survey of penicillin, streptomycin, and other antimicrobial substances from fungi, actinomyeetes, bacteria, and plants. Volume II*. London, Oxford University Press: 1949; p vii, 1774 pp.

74. Abraham, E. P.; Chain, E.; Fletcher, C. M.; Gardner, A. D.; Heatley, N. G.; Jennings, M. A.; Florey, H. W., Further observations om penicillin. *The Lancet* **1941,** *238* (6155), 177-189.

75. Henderson, J. W., The yellow brick road to penicillin: a story of serendipity. *Mayo Clin Proc* **1997,** *72* (7), 683-7.

76. Maiti, S. N.; Phillips, O. A.; Micetich, R. G.; Livermore, D. M., Beta-lactamase inhibitors: agents to overcome bacterial resistance. *Curr Med Chem* **1998,** *5* (6), 441-56.

77. Richards, A. N., Statement released by the committee on medical research. *J Am Med Assoc* **1943**, 122.

78. Richards, A. N., Production of penicillin in the United States (1941-1946). *Nature* **1964,** *201*, 441-5.

79. Crowfoot, D.; Bunn, C. W.; Rogers-Low, B. W.; Turner-Jones, A., *The X-ray Crystallographic Investigation of the Structure of Penicillin*. Princeton University Press: Penicillin, 1949.

80. Batchelor, F. R.; Doyle, F. P.; Nayler, J. H.; Rolinson, G. N., Synthesis of penicillin: 6-aminopenicillanic acid in penicillin fermentations. *Nature* **1959,** *183* (4656), 257-8.

81. Huang, H. T.; English, A. R.; Seto, T. A.; Shull, G. M.; Sobin, B. A., Enzymatic hydrolysis of the sdie chain of penicillins. *J Am Chem Soc* **1960,** *82* (14), 3790-1.

82. Sheehan, J. C.; Logan, K. R. H., A general synthesis of the penicillins. *J Am Chem Soc* **1959,** *81* (21), 5838-9.

83. Sheehan, J. C.; Henery-Logan, K. R., The total and partial general syntheses of the penicillins. *J Am Chem Soc* **1962,** *84* (15), 2983-90.

84. Fairbrother, R.; Taylor, G., Sodium methicillin in routine therapy. *Lancet* **1961,** *1* (717), 473-6.

85. Acred, P.; Brown, D. M.; Knudsen, E. T.; Rolinson, G. N.; Sutherland, R., New semi-synthetic penicillin active against pseudomonas pyocyanea. *Nature* **1967,** *215* (5096), 25-30.

86. Brotzu, G., Ricerche su di un Nuovo Antibiotico. *Lavori dell'Instituto d'Igiene di Cagliari* **1948**, 1-11.

87. Sader, H. S.; Jones, R. N., Historical overview of the cephalosporin spectrum: Four generations of structural evolution. *Antimicrobic Newsletter* **1992,** *8* (12), 75-82.

88. Burton, H. S.; Abraham, E. P., Isolation of antibiotics from a species of Cephalosporium; cephalosporins P1, P2, P3, P4, and P5. *Biochem J* **1951,** *50* (2), 168-74.

89. Newton, G. G.; Abraham, E. P., Degradation, structure and some derivatives of cephalosporin N. *Biochem J* **1954,** *58* (1), 103-11.

90. Abraham, E. P.; Newton, G. G., The structure of cephalesporin C. *Biochem J* **1961,** *79* (2), 377-93.

91. Hodgkin, D. C.; Maslen, E. N., The x-ray analysis of the structure of cephalosporin C. *Biochem J* **1961,** *79*, 393-402.

92. Abraham, E. P.; Trown, P. W., Structure and synthesis of cephalosporidine, a degradation product of cephalosporin C. *Biochem J* **1963,** *86*, 271-7.

93. Loder, B.; Newton, G. G.; Abraham, E. P., The cephalosporin C nucleus (7-aminocephalosporanic acid) and some of its derivatives. *The Biochem J* **1961,** *79* (2), 408-16.

94. Donowitz, G. R.; Mandell, G. L., Drug therapy. Beta-lactam antibiotics (2). *N Engl J Med* **1988,** *318* (8), 490-500.

95. Aoki, H.; Sakai, H.; Kohsaka, M.; Konomi, T.; Hosoda, J., Nocardicin A, a new monocyclic beta-lactam antibiotic. I. Discovery, isolation and characterization. *J Antibiot (Tokyo)* **1976,** *29* (5), 492-500.

96. Katayama, N.; Nozaki, Y.; Okonogi, K.; Ono, H.; Harada, S.; Okazaki, H., Formadicins, new monocyclic beta-lactam antibiotics of bacterial origin. I. Taxonomy, fermentation and biological activities. *J Antibiot (Tokyo)* **1985,** *38* (9), 1117-27.

97. Hida, T.; Tsubotani, S.; Katayama, N.; Okazaki, H.; Harada, S., Formadicins, new monocyclic beta-lactam antibiotics of bacterial origin. II. Isolation, characterization and structures. *J Antibiot (Tokyo)* **1985,** *38* (9), 1128-40.

98. Sykes, R. B.; Bonner, D. P., Aztreonam: the first monobactam. *Am J Med* **1985,** *78* (2A), 2-10.

99. Sykes, R. B.; Bonner, D. P.; Bush, K.; Georgopapadakou, N. H., Azthreonam (SQ 26,776), a synthetic monobactam specifically active against aerobic gram-negative bacteria. *Antimicrob Agents Chemother* **1982,** *21* (1), 85-92.

100. Wang, X.; Zhang, F.; Zhao, C.; Wang, Z.; Nichols, W. W.; Testa, R.; Li, H.; Chen, H.; He, W.; Wang, Q.; Wang, H., In vitro activities of ceftazidime-avibactam and aztreonam-avibactam against 372 Gram-negative bacilli collected in 2011 and 2012 from 11 teaching hospitals in China. *Antimicrob Agents Chemother* **2014,** *58* (3), 1774-8.

101. Kahan, J. S.; Kahan, F. M.; Goegelman, R.; Currie, S. A.; Jackson, M.; Stapley, E. O.; Miller, T. W.; Miller, A. K.; Hendlin, D.; Mochales, S.; Hernandez, S.; Woodruff, H. B.; Birnbaum, J., Thienamycin, a new beta-lactam antibiotic. I. Discovery, taxonomy, isolation and physical properties. *J Antibiot (Tokyo)* **1979,** *32* (1), 1-12.

102. Kesado, T.; Hashizume, T.; Asahi, Y., Antibacterial activities of a new stabilized thienamycin, N-formimidoyl thienamycin, in comparison with other antibiotics. *Antimicrob Agents Chemother* **1980,** *17* (6), 912-7.

103. Kahan, F. M.; Kropp, H.; Sundelof, J. G.; Birnbaum, J., Thienamycin: development of imipenen-cilastatin. *J Antimicrob Chemother* **1983,** *12 Suppl D*, 1-35.

104. Zhanel, G. G.; Wiebe, R.; Dilay, L.; Thomson, K.; Rubinstein, E.; Hoban, D. J.; Noreddin, A. M.; Karlowsky, J. A., Comparative review of the carbapenems. *Drugs* **2007,** *67* (7), 1027-52.

105. Baughman, R. P., The Use of Carbapenems in the Treatment of Serious Infections. *J Intensive Care Med* **2009,** *24* (4), 230-41.

106. Wise, E. M., Jr.; Park, J. T., Penicillin: its basic site of action as an inhibitor of a peptide cross-linking reaction in cell wall mucopeptide synthesis. *P Natl Acad Sci USA* **1965,** *54* (1), 75-81.

107. Yocum, R. R.; Rasmussen, J. R.; Strominger, J. L., The mechanism of action of penicillin. Penicillin acylates the active site of Bacillus stearothermophilus D-alanine carboxypeptidase. *J Biol Chem* **1980,** *255* (9), 3977-86.

108. Araki, Y.; Shimada, A.; Ito, E., Effect of penicillin on cell wall mucopeptide synthesis in a Escherichia coli particulate system. *Biochem Biophys Res Commun* **1966,** *23* (4), 518-25.

109. Izaki, K.; Matsuhashi, M.; Strominger, J. L., Biosynthesis of the peptidoglycan of bacterial cell walls. 8. Peptidoglycan transpeptidase and D-alanine carboxypeptidase: penicillin-sensitive enzymatic reaction in strains of Escherichia coli. *J Biol Chem* **1968,** *243* (11), 3180-92.

110. Tipper, D. J.; Strominger, J. L., Mechanism of action of penicillins: a proposal based on their structural similarity to acyl-D-alanyl-D-alanine. *P Natl Acad Sci USA* **1965,** *54* (4), 1133-41.

111. Lee, B., Conformation of penicillin as a transition-state analog of the substrate of peptidoglycan transpeptidase. *J Mol Biol* **1971,** *61* (2), 463-9.

112. Frere, J. M.; Joris, B., Penicillin-sensitive enzymes in peptidoglycan biosynthesis. *Crit Rev Microbiol* **1985,** *11* (4), 299-396.

113. Chung, H. S.; Yao, Z.; Goehring, N. W.; Kishony, R.; Beckwith, J.; Kahne, D., Rapid beta-lactam-induced lysis requires successful assembly of the cell division machinery. *Proc Natl Acad Sci USA* **2009,** *106* (51), 21872-7.

114. de Pedro, M. A.; Holtje, J. V.; Schwarz, H., Fast lysis of Escherichia coli filament cells requires differentiation of potential division sites. *Microbiology* **2002,** *148* (Pt 1), 79-86.

115. Fajardo, A.; Martínez, J. L., Antibiotics as signals that trigger specific bacterial responses. *Curr Opin Microbiol* **2008,** *11* (2), 161-7.

116. Linares, J. F.; Gustafsson, I.; Baquero, F.; Martinez, J. L., Antibiotics as intermicrobial signaling agents instead of weapons. *P Natl Acad Sci USA* **2006,** *103* (51), 19484-9.

117. Martinez, J. L., Antibiotics and antibiotic resistance genes in natural environments. *Science* **2008,** *321* (5887), 365-7.

118. Aminov, R. I., The role of antibiotics and antibiotic resistance in nature. *Environmental Microbiology* **2009,** *11* (12), 2970-88.

119. Hall, B. G.; Barlow, M., Evolution of the serine beta-lactamases: past, present and future. *Drug Resist Updat: reviews and commentaries in antimicrobial and anticancer chemotherapy* **2004,** *7* (2), 111-23.

120. Barlow, M.; Hall, B. G., Phylogenetic analysis shows that the OXA b-Lactamase genes have been on plasmids for millions of years. *J Mol Biol Evol* **2002,** *55* (3), 314-21.

121. Aminov, R. I.; Mackie, R. I., Evolution and ecology of antibiotic resistance genes. *FEMS Microbiol Lett* **2007,** *271* (2), 147-61.

122. Forsberg, K. J.; Reyes, A.; Wang, B.; Selleck, E. M.; Sommer, M. O.; Dantas, G., The shared antibiotic resistome of soil bacteria and human pathogens. *Science* **2012,** *337* (6098), 1107-11.

123. Frére, J. M.; Joris, B.; Granier, B.; Matagne, A.; Jacob, F.; Bourguignonbellefroid, C., Diversity of the mechanisms of resistance to beta-lactam antibiotics. *Res Microbiol* **1991,** *142* (6), 705-10.

124. Hede, K., Antibiotic resistance: An infectious arms race. *Nature* **2014,** *509* (7498), S2-3.

125. Bush, L. M.; Johnson, C. C., Ureidopenicillins and beta-lactam/beta-lactamase inhibitor combinations. *Infect Dis Clin North Am* **2000,** *14* (2), 409-33.

126. Sensakovic, J. W.; Smith, L. G., Beta-lactamase inhibitor combinations. *Med Clin North Am* **1995,** *79* (4), 695-704.

127. Zhanel, G. G.; Lawson, C. D.; Adam, H.; Schweizer, F.; Zelenitsky, S.; Lagace-Wiens, P. R.; Denisuik, A.; Rubinstein, E.; Gin, A. S.; Hoban, D. J.; Lynch, J. P., 3rd; Karlowsky, J. A., Ceftazidime-avibactam: a novel cephalosporin/beta-lactamase inhibitor combination. *Drugs* **2013,** *73* (2), 159-77.

128. Conly, J.; Johnston, B., Where are all the new antibiotics? The new antibiotic paradox. *Can J Infect Dis Med Microbiol* **2005,** *16* (3), 159-60.

129. Buynak, J. D., The discovery and development of modified penicillin- and cephalosporin-derived beta-lactamase inhibitors. *Curr Med Chem* **2004,** *11* (14), 1951-64.

130. Munita, J. M.; Arias, C. A., Mechanisms of antibiotic resistance. *Microbiol Spectr* **2016,** *4* (2), 1-24.

131. Blair, J. M.; Webber, M. A.; Baylay, A. J.; Ogbolu, D. O.; Piddock, L. J., Molecular mechanisms of antibiotic resistance. *Nat Rev Microbiol* **2015,** *13* (1), 42-51.

132. Lin, J.; Nishino, K.; Roberts, M. C.; Tolmasky, M.; Aminov, R. I.; Zhang, L., Mechanisms of antibiotic resistance. *Front Microbiol* **2015,** *6*, 34-7.

133. Tenover, F. C., Mechanisms of antimicrobial resistance in bacteria. *Am J Med* **2006,** *119* (6 Suppl 1), S3-10; discussion S62-70.

134. Pages, J. M.; James, C. E.; Winterhalter, M., The porin and the permeating antibiotic: a selective diffusion barrier in Gram-negative bacteria. *Nat Rev Microbiol* **2008,** *6* (12), 893-903.

135. Farra, A.; Islam, S.; Stralfors, A.; Sorberg, M.; Wretlind, B., Role of outer membrane protein OprD and penicillin-binding proteins in resistance of Pseudomonas aeruginosa to imipenem and meropenem. *Int J Antimicrob Agents* **2008,** *31* (5), 427-33.

136. Piddock, L. J., Clinically relevant chromosomally encoded multidrug resistance efflux pumps in bacteria. *Clin Microbiol Rev* **2006,** *19* (2), 382-402.

137. Li, X. Z.; Ma, D.; Livermore, D. M.; Nikaido, H., Role of efflux pump(s) in intrinsic resistance of Pseudomonas-Aeruginosa - Active efflux as a contributing factor to beta-lactam resistance. *Antimicrob Agents Chemother* **1994,** *38* (8), 1742-52.

138. Ubukata, K.; Nonoguchi, R.; Matsuhashi, M.; Konno, M., Expression and inducibility in Staphylococcus-Aureus of the Meca gene, which encodes a methicillin-resistant S Aureus specific penicillin-binding protein. *J Bacteriol* **1989,** *171* (5), 2882-5.

139. Abraham, E. P.; Chain, E., An enzyme from bacteria able to destroy penicillin. 1940. *Rev Infect Dis* **1988,** *10* (4), 677-8.

140. Sabath, L. D.; Abraham, E. P., Cephalosporinase and penicillinase activity of Bacillus cereus. *Antimicrob Agents Chemother (Bethesda)* **1965,** *5*, 392-7.

141. Sabath, L. D.; Abraham, E. P., Zinc as a cofactor for cephalosporinase from Bacillus cereus 569. *Biochem J* **1966,** *98* (1), 11C-3C.

142. Barber, M.; Rozwadowska-Dowzenko, M., Infection by penicillin-resistant staphylococci. *Lancet* **1948,** *2* (6530), 641-4.

143. Bush, K., Proliferation and significance of clinically relevant beta-lactamases. *Ann N Y Acad Sci* **2013,** *1277*, 84-90.

144. Bush, K.; Palzkill, T.; Jacoby, G. β-Lactamase Classification and Amino Acid Sequences for TEM, SHV and OXA Extended-Spectrum and Inhibitor Resistant Enzymes, http://www.lahey.org/Studies/webt.asp, accessed on 01 Oct 2018. http://www.lahey.org/Studies/webt.asp (accessed 01 October).

145. Ghuysen, J. M., Serine beta-lactamases and penicillin-binding proteins. *Annu Rev Microbiol* **1991,** *45*, 37-67.

146. Massova, I.; Mobashery, S., Structural and mechanistic aspects of evolution of beta-lactamases and penicillin-binding proteins. *Curr Pharm Des* **1999,** *5* (11), 929-37.

147. Hata, M.; Fujii, Y.; Tanaka, Y.; Ishikawa, H.; Ishii, M.; Neya, S.; Tsuda, M.; Hoshino, T., Substrate deacylation mechanisms of serine-beta-lactamases. *Biol Pharm Bull* **2006,** *29* (11), 2151-9.

148. Matagne, A.; Misselyn-Bauduin, A. M.; Joris, B.; Erpicum, T.; Granier, B.; Frere, J. M., The diversity of the catalytic properties of class A beta-lactamases. *Biochem J* **1990,** *265* (1), 131-46.

149. Bush, K., Bench-to-bedside review: The role of beta-lactamases in antibiotic-resistant Gram-negative infections. *Crit Care* **2010,** *14* (3), 224-32.

150. Perine, P. L.; Thornsberry, C.; Schalla, W.; Biddle, J.; Siegel, M. S.; Wong, K. H.; Thompson, S. E., Evidence for two distinct types of penicillinase-producing Neisseria gonorrhoeae. *Lancet* **1977,** *2* (8046), 993-5.

151. Bush, K.; Jacoby, G. A.; Medeiros, A. A., A functional classification scheme for beta-lactamases and its correlation with molecular structure. *Antimicrob Agents Chemother* **1995,** *39* (6), 1211-33.

152. Cartelle, M.; Tomas, M. D.; Molina, F.; Moure, R.; Villanueva, R.; Bou, G., High-level resistance to ceftazidime conferred by a novel enzyme, CTX-M-32, derived from CTX-M-1 through a single Asp240-Gly substitution. *Antimicrob Agents Chemother* **2004,** *48* (6), 2308-13.

153. Queenan, A. M.; Bush, K., Carbapenemases: the versatile beta-lactamases. *Clin Microbiol Rev* **2007,** *20* (3), 440-58.

154. Papp-Wallace, K. M.; Bethel, C. R.; Distler, A. M.; Kasuboski, C.; Taracila, M.; Bonomo, R. A., Inhibitor resistance in the KPC-2 beta-lactamase, a preeminent property of this class A beta-lactamase. *Antimicrob Agents Chemother* **2010,** *54* (2), 890-7.

155. Ehmann, D. E.; Jahic, H.; Ross, P. L.; Gu, R. F.; Hu, J.; Durand-Reville, T. F.; Lahiri, S.; Thresher, J.; Livchak, S.; Gao, N.; Palmer, T.; Walkup, G. K.; Fisher, S. L., Kinetics of avibactam inhibition against Class A, C, and D beta-lactamases. *J Biol Chem* **2013,** *288* (39), 27960-71.

156. Choi, H.; Paton, R. S.; Park, H.; Schofield, C. J., Investigations on recyclisation and hydrolysis in avibactam mediated serine beta-lactamase inhibition. *Org Biomol Chem* **2016,** *14* (17), 4116-28.

157. Moews, P. C.; Knox, J. R.; Dideberg, O.; Charlier, P.; Frère, J.-M., β-Lactamase of Bacillus licheniformis 749/C at 2 Å resolution. *Proteins* **1990,** *7* (2), 156-71.

158. Hermann, J. C.; Ridder, L.; Mulholland, A. J.; Höltje, H.-D., Identification of Glu166 as the general base in the acylation reaction of class A β-lactamases through QM/MM modeling. *J Am Chem Soc* **2003,** *125* (32), 9590-1.

159. Hata, M.; Fujii, Y.; Ishii, M.; Hoshino, T.; Tsuda, M., Catalytic mechanism of class A beta-lactamase. I. The role of Glu166 and Serl30 in the deacylation reaction. *Chem Pharm Bull (Tokyo)* **2000,** *48* (4), 447-53.

160. Ishiguro, M.; Imajo, S., Modeling study on a hydrolytic mechanism of class A beta-lactamases. *J Med Chem* **1996,** *39* (11), 2207-18.

161. Ness, S.; Martin, R.; Kindler, A. M.; Paetzel, M.; Gold, M.; Jensen, S. E.; Jones, J. B.; Strynadka, N. C., Structure-based design guides the improved efficacy of deacylation transition state analogue inhibitors of TEM-1 beta-lactamase. *Biochemistry* **2000,** *39* (18), 5312-21.

162. Jacoby, G. A., AmpC β-Lactamases. *Clin Microbiol Rev* **2009,** *22* (1), 161-82.

163. Monnaie, D.; Frere, J. M., Interaction of clavulanate with class C beta-lactamases. *FEBS letters* **1993,** *334* (3), 269-71.

164. Galleni, M.; Amicosante, G.; Frere, J. M., A survey of the kinetic parameters of class C beta-lactamases. Cephalosporins and other beta-lactam compounds. *Biochem J* **1988,** *255* (1), 123-9.

165. Mammeri, H.; Nordmann, P.; Berkani, A.; Eb, F., Contribution of extended-spectrum AmpC (ESAC) β-lactamases to carbapenem resistance in Escherichia coli. *FEMS Microbiology Letters* **2008,** *282* (2), 238-40.

166. Adler, M.; Anjum, M.; Andersson, D.; Sandegren, L., Influence of acquired -lactamases on the evolution of spontaneous carbapenem resistance in Escherichia Coli. *J Antimicrob Chemother,* **2012**, *68* (1), 51-59.

167. Goldberg, S. D.; Iannuccilli, W.; Nguyen, T.; Ju, J.; Cornish, V. W., Identification of residues critical for catalysis in a class C beta-lactamase by combinatorial scanning mutagenesis. *Protein Sci* **2003,** *12* (8), 1633-45.

168. Tripathi, R.; Nair, N. N., Mechanism of acyl-enzyme complex formation from the Henry-Michaelis complex of class C beta-lactamases with beta-lactam antibiotics. *J Am Chem Soc* **2013,** *135* (39), 14679-90.

169. Chen, Y.; McReynolds, A.; Shoichet, B. K., Re-examining the role of Lys67 in class C beta-lactamase catalysis. *Protein Sci* **2009,** *18* (3), 662-9.

170. Dubus, A.; Ledent, P.; Lamotte-Brasseur, J.; Frere, J. M., The roles of residues Tyr150, Glu272, and His314 in class C beta-lactamases. *Proteins* **1996,** *25* (4), 473-85.

171. Chen, Y.; Minasov, G.; Roth, T. A.; Prati, F.; Shoichet, B. K., The deacylation mechanism of AmpC β-lactamase at ultrahigh resolution. *J Am Chem Soc* **2006,** *128* (9), 2970-2976.

172. Lamotte-Brasseur, J.; Dubus, A.; Wade, R. C., pKa calculations for class C β-lactamases: The role of tyr-150. *Proteins* **2000,** *40* (1), 23-28.

173. Yamaguchi, Y.; Sato, G.; Yamagata, Y.; Doi, Y.; Wachino, J.; Arakawa, Y.; Matsuda, K.; Kurosaki, H., Structure of AmpC beta-lactamase (AmpCD) from an Escherichia coli clinical isolate with a tripeptide deletion (Gly286-Ser287-Asp288) in the H10 helix. *Acta Crystallogr Sect F Struct Biol Cryst Commun* **2009,** *65* (Pt 6), 540-3.

174. Evans, B. A.; Amyes, S. G., OXA beta-lactamases. *Clin Microbiol Rev* **2014,** *27* (2), 241-63.

175. Medeiros, A. A.; Cohenford, M.; Jacoby, G. A., Five novel plasmid-determined beta-lactamases. *Antimicrob Agents Chemother* **1985,** *27* (5), 715-9.

176. Kong, K. F.; Jayawardena, S. R.; Del Puerto, A.; Wiehlmann, L.; Laabs, U.; Tummler, B.; Mathee, K., Characterization of poxB, a chromosomal-encoded Pseudomonas aeruginosa oxacillinase. *Gene* **2005,** *358*, 82-92.

177. Li, J.; Cross, J. B.; Vreven, T.; Meroueh, S. O.; Mobashery, S.; Schlegel, H. B., Lysine carboxylation in proteins: OXA-10 beta-lactamase. *Proteins* **2005,** *61* (2), 246-57.

178. Golemi, D.; Maveyraud, L.; Vakulenko, S.; Samama, J. P.; Mobashery, S., Critical involvement of a carbamylated lysine in catalytic function of class D beta-lactamases. *Proc Natl Acad Sci USA* **2001,** *98* (25), 14280-5.

179. Lohans, C. T.; Wang, D. Y.; Jorgensen, C.; Cahill, S. T.; Clifton, I. J.; McDonough, M. A.; Oswin, H. P.; Spencer, J.; Domene, C.; Claridge, T. D. W.; Brem, J.; Schofield, C. J., ^{13}C-Carbamylation as a mechanistic probe for the inhibition of class D β-lactamases by avibactam and halide ions. *Org Biomol Chem***2017,** *15* (28), 6024-32.

180. Reading, C.; Cole, M., Clavulanic acid: a beta-lactamase-inhiting beta-lactam from Streptomyces clavuligerus. *Antimicrob Agents Chemother* **1977,** *11* (5), 852-7.

181. Bush, K., Beta-lactamase inhibitors from laboratory to clinic. *Clin Microbiol Rev* **1988,** *1* (1), 109-23.

182. Fisher, J.; Charnas, R. L.; Knowles, J. R., Kinetic studies on the inactivation of Escherichia coli RTEM β-lactamase by clavulanic acid. *Biochemistry* **1978,** *17* (11), 2180-4.

183. Brown, R. P. A.; Aplin, R. T.; Schofield, C. J., Inhibition of TEM-2 β-lactamase from Escherichia coli by clavulanic acid: observation of intermediates by rlectrospray ionization mass spectrometry. *Biochemistry* **1996,** *35* (38), 12421-32.

184. Power, P.; Mercuri, P.; Herman, R.; Kerff, F.; Gutkind, G.; Dive, G.; Galleni, M.; Charlier, P.; Sauvage, E., Novel fragments of clavulanate observed in the structure of the class A β-lactamase from Bacillus licheniformis BS3. *J Antimicrob Chemoth* **2012,** *67* (10), 2379-87.

185. Tremblay, L. W.; Hugonnet, J.-E.; Blanchard, J. S., Structure of the covalent adduct Formed between mycobacterium tuberculosis β-lactamase and clavulanate. *Biochemistry* **2008,** *47* (19), 5312-6.

186. Kalp, M.; Totir, M. A.; Buynak, J. D.; Carey, P. R., Different intermediate populations formed by tazobactam, sulbactam, and clavulanate reacting with SHV-1 β-lactamases: raman crystallographic evidence. *J Am Chem Soc* **2009,** *131* (6), 2338-47.

187. Padayatti, P. S.; Helfand, M. S.; Totir, M. A.; Carey, M. P.; Carey, P. R.; Bonomo, R. A.; van den Akker, F., High resolution crystal structures of the trans-enamine intermediates formed by sulbactam and clavulanic acid and E166A SHV-1 β-lactamase. *J Biol Chem* **2005,** *280* (41), 34900-7.

188. Leigh, A., Augmentin (amoxycillin and clavulanic acid) in the treatment of urinary tract infections. *Scott Med J* **1982,** *27 Spec No.*, S28-34.

189. Blumer, J. L., Ticarcillin/clavulanate for the treatment of serious infections in hospitalized pediatric patients. *Pediatr Infect Dis J* **1998,** *17* (12), 1211-5.

190. Brown, A. G., Clavulanic acid, a novel beta-lactamase inhibitor – a case study in drug discovery and development. *Drug Des Deliv* **1986,** *1* (1), 1-21.

191. English, A. R.; Retsema, J. A.; Girard, A. E.; Lynch, J. E.; Barth, W. E., CP-45,899, a beta-lactamase inhibitor that extends the antibacterial spectrum of beta-lactams: initial bacteriological characterization. *Antimicrob Agents Chemother* **1978,** *14* (3), 414-9.

192. Fisher, J.; Belasco, J. G.; Charnas, R. L.; Khosla, S.; Knowles, J. R., β-Lactamase inactivation by mechanism-based reagents. *Philos Trans Royal Soc B, Biol Sci* **1980,** *289* (1036), 309-19.

193. Papp-Wallace, K. M.; Winkler, M. L.; Taracila, M. A.; Bonomo, R. A., Variants of β-lactamase KPC-2 that are resistant to inhibition by avibactam. *Antimicrob Agents Chemother* **2015,** *59* (7), 3710-7.

194. Lucasti, C.; Vasile, L.; Sandesc, D.; Venskutonis, D.; McLeroth, P.; Lala, M.; Rizk, M. L.; Brown, M. L.; Losada, M. C.; Pedley, A.; Kartsonis, N. A.; Paschke, A., Phase 2, dose-ranging study of relebactam with imipenem-cilastatin in subjects with complicated intra-abdominal infection. *Antimicrob Agents Chemother* **2016,** *60* (10), 6234-43.

195. Lob, S. H.; Hackel, M. A.; Kazmierczak, K. M.; Young, K.; Motyl, M. R.; Karlowsky, J. A.; Sahm, D. F., In vitro activity of imipenem-relebactam against gram-negative ESKAPE pathogens isolated by clinical laboratories in the United States in 2015 (results from the SMART global surveillance program). *Antimicrob Agents Chemother* **2017,** *61* (6), e02209-16.

196. Hecker, S. J.; Reddy, K. R.; Totrov, M.; Hirst, G. C.; Lomovskaya, O.; Griffith, D. C.; King, P.; Tsivkovski, R.; Sun, D.; Sabet, M.; Tarazi, Z.; Clifton, M. C.; Atkins, K.; Raymond, A.; Potts, K. T.; Abendroth, J.; Boyer, S. H.; Loutit, J. S.; Morgan, E. E.; Durso, S.; Dudley, M. N., Discovery of a cyclic boronic acid β-lactamase inhibitor (RPX7009) with utility vs class A Serine carbapenemases. *J Med Chem* **2015,** *58* (9), 3682-92.

197. Bull, S. D.; Davidson, M. G.; van den Elsen, J. M.; Fossey, J. S.; Jenkins, A. T.; Jiang, Y. B.; Kubo, Y.; Marken, F.; Sakurai, K.; Zhao, J.; James, T. D., Exploiting the reversible covalent bonding of boronic acids: recognition, sensing, and assembly. *Acc Chem Res* **2013,** *46* (2), 312-26.

198. Crompton, I. E.; Cuthbert, B. K.; Lowe, G.; Waley, S. G., Beta-lactamase inhibitors. The inhibition of serine beta-lactamases by specific boronic acids. *Biochem J* **1988,** *251* (2), 453-9.

199. Castanheira, M.; Rhomberg, P. R.; Flamm, R. K.; Jones, R. N., Effect of the β-lactamase inhibitor vaborbactam combined with meropenem against serine carbapenemase-producing Enterobacteriaceae. *Antimicrob Agents Chemother* **2016,** *60* (9), 5454-8.

200. Walsh, T. R.; Toleman, M. A.; Poirel, L.; Nordmann, P., Metallo-beta-lactamases: the quiet before the storm? *Clin Microbiol Rev* **2005,** *18* (2), 306-25.

201. Rasmussen, B. A.; Gluzman, Y.; Tally, F. P., Cloning and sequencing of the class B beta-lactamase gene (ccrA) from Bacteroides fragilis TAL3636. *Antimicrob Agents Chemother* **1990,** *34* (8), 1590-2.

202. Watanabe, M.; Iyobe, S.; Inoue, M.; Mitsuhashi, S., Transferable imipenem resistance in Pseudomonas aeruginosa. *Antimicrob Agents Chemother* **1991,** *35* (1), 147-51.

203. Rossolini, G. M.; Franceschini, N.; Riccio, M. L.; Mercuri, P. S.; Perilli, M.; Galleni, M.; Frere, J. M.; Amicosante, G., Characterization and sequence of the Chryseobacterium (Flavobacterium) meningosepticum carbapenemase: a new molecular class B beta-lactamase showing a broad substrate profile. *Biochem J* **1998,** *332 (Pt 1)*, 145-52.

204. Grundmann, H.; Livermore, D. M.; Giske, C. G.; Canton, R.; Rossolini, G. M.; Campos, J.; Vatopoulos, A.; Gniadkowski, M.; Toth, A.; Pfeifer, Y.; Jarlier, V.; Carmeli, Y.; Group, C. W., Carbapenem-non-susceptible Enterobacteriaceae in Europe: conclusions from a meeting of national experts. *Euro Surveill* **2010,** *15* (46).

205. Diene, S. M.; Rolain, J. M., Carbapenemase genes and genetic platforms in Gram-negative bacilli: Enterobacteriaceae, Pseudomonas and Acinetobacter species. *Clin Microbiol Infect* **2014,** *20* (9), 831-8.

206. Simm, A. M.; Higgins, C. S.; Pullan, S. T.; Avison, M. B.; Niumsup, P.; Erdozain, O.; Bennett, P. M.; Walsh, T. R., A novel metallo-beta-lactamase, Mbl1b, produced by the environmental bacterium Caulobacter crescentus. *FEBS letters* **2001,** *509* (3), 350-4.

207. Rossolini, G. M.; Condemi, M. A.; Pantanella, F.; Docquier, J. D.; Amicosante, G.; Thaller, M. C., Metallo-beta-lactamase producers in environmental microbiota: new molecular class B enzyme in Janthinobacterium lividum. *Antimicrob Agents Chemother* **2001,** *45* (3), 837-44.

208. Saavedra, M. J.; Peixe, L.; Sousa, J. C.; Henriques, I.; Alves, A.; Correia, A., Sfh-I, a subclass B2 metallo-beta-lactamase from a Serratia fonticola environmental isolate. *Antimicrob Agents Chemother* **2003,** *47* (7), 2330-3.

209. Frère, J. M., Beta-lactamases and bacterial resistance to antibiotics. *Mol Microbiol* **1995,** *16* (3), 385-95.

210. Felici, A.; Amicosante, G.; Oratore, A.; Strom, R.; Ledent, P.; Joris, B.; Fanuel, L.; Frere, J. M., An overview of the kinetic parameters of class B beta-lactamases. *Biochem J* **1993,** *291 (Pt 1)*, 151-5.

211. Papp-Wallace, K. M.; Endimiani, A.; Taracila, M. A.; Bonomo, R. A., Carbapenems: past, present, and future. *Antimicrob Agents Chemother* **2011,** *55* (11), 4943-60.

212. Abboud, M. I.; Damblon, C.; Brem, J.; Smargiasso, N.; Mercuri, P.; Gilbert, B.; Rydzik, A. M.; Claridge, T. D.; Schofield, C. J.; Frere, J. M., Interaction of Avibactam with Class B Metallo-beta-Lactamases. *Antimicrob Agents Chemother* **2016,** *60* (10), 5655-62.

213. Rafiee, R.; Eftekhar, F.; Tabatabaei, S. A.; Minaee Tehrani, D., Prevalence of Extended-Spectrum and Metallo beta-Lactamase Production in AmpC beta-Lactamase Producing Pseudomonas aeruginosa Isolates From Burns. *Jundishapur J Microbiol* **2014,** *7* (9), e16436.

214. Bebrone, C., Metallo-β-lactamases (classification, activity, genetic organization, structure, zinc coordination) and their superfamily. *Biochem Pharmacol* **2007,** *74* (12), 1686-701.

215. Palzkill, T., Metallo-β-lactamase structure and function. *Ann N Y Acad Sci* **2013,** *1277*, 91-104.

216. Cornaglia, G.; Giamarellou, H.; Rossolini, G. M., Metallo-β-lactamases: a last frontier for β-lactams? *Lancet Infect Dis* **2011,** *11* (5), 381-393.

217. Bennett, P. M., Plasmid encoded antibiotic resistance: acquisition and transfer of antibiotic resistance genes in bacteria. *Br J Pharmacol* **2008,** *153 Suppl 1* (Suppl 1), S347-S357.

218. Carfi, A.; Pares, S.; Duée, E.; Galleni, M.; Duez, C.; Frère, J. M.; Dideberg, O., The 3-D structure of a zinc metallo-beta-lactamase from Bacillus cereus reveals a new type of protein fold. *EMBO J* **1995,** *14* (20), 4914-21.

219. Carfi, A.; Duee, E.; Galleni, M.; Frere, J.-M.; Dideberg, O., 1.85 A resolution structure of the zincII [beta]-lactamase from Bacillus cereus. *Acta Crystallogr Sect D Biol Crystallogr* **1998,** *54* (3), 313-23.

220. King, D. T.; Worrall, L. J.; Gruninger, R.; Strynadka, N. C. J., New Delhi metallo-β-lactamase: structural insights into β-lactam recognition and inhibition. *J Am Chem Soc* **2012,** *134* (28), 11362-5.

221. Brem, J.; van Berkel, S. S.; Zollman, D.; Lee, S. Y.; Gileadi, O.; McHugh, P. J.; Walsh, T. R.; McDonough, M. A.; Schofield, C. J., Structural basis of metallo-β-lactamase inhibition by captopril stereoisomers. *Antimicrob agents and chemother* **2015,** *60* (1), 142-50.

222. Brem, J.; Struwe, W. B.; Rydzik, A. M.; Tarhonskaya, H.; Pfeffer, I.; Flashman, E.; van Berkel, S. S.; Spencer, J.; Claridge, T. D. W.; McDonough, M. A.; Benesch, J. L. P.; Schofield, C. J., Studying the active-site loop movement of the São Paolo metallo-β-lactamase-1. *Chem Sci* **2015,** *6* (2), 956-63.

223. Moali, C.; Anne, C.; Lamotte-Brasseur, J.; Groslambert, S.; Devreese, B.; Van Beeumen, J.; Galleni, M.; Frère, J. M., Analysis of the importance of the metallo-beta-lactamase active site loop in substrate binding and catalysis. *Chem Biol* **2003,** *10* (4), 319-29.

224. Rossolini, G. M.; Zanchi, A.; Chiesurin, A.; Amicosante, G.; Satta, G.; Guglielmetti, P., Distribution of cphA or related carbapenemase-encoding genes and production of carbapenemase activity in members of the genus Aeromonas. *Antimicrob Agents Chemother* **1995,** *39* (2), 346-9.

225. Fonseca, F.; Arthur, C. J.; Bromley, E. H.; Samyn, B.; Moerman, P.; Saavedra, M. J.; Correia, A.; Spencer, J., Biochemical characterization of Sfh-I, a subclass B2 metallo-beta-lactamase from Serratia fonticola UTAD54. *Antimicrob Agents Chemother* **2011,** *55* (11), 5392-5.

226. Segatore, B.; Massidda, O.; Satta, G.; Setacci, D.; Amicosante, G., High specificity of cphA-encoded metallo-beta-lactamase from Aeromonas hydrophila AE036 for carbapenems and its contribution to beta-lactam resistance. *Antimicrob Agents Chemother* **1993,** *37* (6), 1324-8.

227. Hernandez Valladares, M.; Felici, A.; Weber, G.; Adolph, H. W.; Zeppezauer, M.; Rossolini, G. M.; Amicosante, G.; Frere, J. M.; Galleni, M., Zn(II) dependence of the Aeromonas hydrophila AE036 metallo-beta-lactamase activity and stability. *Biochemistry* **1997,** *36* (38), 11534-41.

228. Costello, A. L.; Sharma, N. P.; Yang, K. W.; Crowder, M. W.; Tierney, D. L., X-ray absorption spectroscopy of the zinc-binding sites in the class B2 metallo-beta-lactamase ImiS from Aeromonas veronii bv. sobria. *Biochemistry* **2006,** *45* (45), 13650-8.

229. Garau, G.; Bebrone, C.; Anne, C.; Galleni, M.; Frere, J. M.; Dideberg, O., A metallo-beta-lactamase enzyme in action: crystal structures of the monozinc carbapenemase CphA and its complex with biapenem. *J Mol Biol* **2005,** *345* (4), 785-95.

230. Hall, B. G.; Salipante, S. J.; Barlow, M., Independent origins of subgroup Bl+B2 and subgroup B3 metallo-β-lactamases. *J Mol Biol Evol* **2004,** *59* (1), 133-41.

231. Ullah, J. H.; Walsh, T. R.; Taylor, I. A.; Emery, D. C.; Verma, C. S.; Gamblin, S. J.; Spencer, J., The crystal structure of the L1 metallo-β-lactamase from Stenotrophomonas maltophilia at 1.7 å resolution11Edited by K. Nagai. *J Mol Biol* **1998,** *284* (1), 125-36.

232. Boschi, L.; Mercuri, P. S.; Riccio, M. L.; Amicosante, G.; Galleni, M.; Frere, J. M.; Rossolini, G. M., The Legionella (Fluoribacter) gormanii metallo-beta-lactamase: a new member of the highly divergent lineage of molecular-subclass B3 beta-lactamases. *Antimicrob Agents Chemother* **2000,** *44* (6), 1538-43.

233. Bellais, S.; Aubert, D.; Naas, T.; Nordmann, P., Molecular and biochemical heterogeneity of class B carbapenem-hydrolyzing beta-lactamases in Chryseobacterium meningosepticum. *Antimicrob Agents Chemother* **2000,** *44* (7), 1878-86.

234. Moran-Barrio, J.; Lisa, M. N.; Larrieux, N.; Drusin, S. I.; Viale, A. M.; Moreno, D. M.; Buschiazzo, A.; Vila, A. J., Crystal structure of the metallo-beta-lactamase GOB in the periplasmic dizinc form reveals an unusual metal site. *Antimicrob Agents Chemother* **2016,** *60* (10), 6013-22.

235. Garcia-Saez, I.; Mercuri, P. S.; Papamicael, C.; Kahn, R.; Frere, J. M.; Galleni, M.; Rossolini, G. M.; Dideberg, O., Three-dimensional structure of FEZ-1, a monomeric subclass B3 metallo-beta-lactamase from Fluoribacter gormanii, in native form and in complex with D-captopril. *J Mol Biol* **2003,** *325* (4), 651-60.

236. Page, M. I.; Badarau, A., The mechanisms of catalysis by metallo beta-lactamases. *Bioinorg Chem Appl* **2008**, 1-14.

237. Bounaga, S.; Laws, A. P.; Galleni, M.; Page, M. I., The mechanism of catalysis and the inhibition of the Bacillus cereus zinc-dependent beta-lactamase. *Biochem J* **1998,** *331 (Pt 3)*, 703-11.

238. Spencer, J.; Clarke, A. R.; Walsh, T. R., Novel mechanism of hydrolysis of therapeutic beta-lactams by Stenotrophomonas maltophilia L1 metallo-beta-lactamase. *J Biol Chem* **2001,** *276* (36), 33638-44.

239. Wang, Z.; Fast, W.; Benkovic, S. J., On the mechanism of the metallo-beta-lactamase from Bacteroides fragilis. *Biochemistry* **1999,** *38* (31), 10013-23.

240. Zhang, H.; Hao, Q., Crystal structure of NDM-1 reveals a common beta-lactam hydrolysis mechanism. *FASEB J* **2011,** *25* (8), 2574-82.

241. Rasia, R. M.; Vila, A. J., Exploring the role and the binding affinity of a second zinc rquivalent in B. cereus metallo-β-lactamase. *Biochemistry* **2002,** *41* (6), 1853-60.

242. Meini, M. R.; Llarrull, L. I.; Vila, A. J., Overcoming differences: The catalytic mechanism of metallo-beta-lactamases. *FEBS letters* **2015,** *589* (22), 3419-32.

243. McManus-Munoz, S.; Crowder, M. W., Kinetic mechanism of metallo-beta-lactamase L1 from Stenotrophomonas maltophilia. *Biochemistry* **1999,** *38* (5), 1547-53.

244. Rasia, R.; Vila, A., *Mechanistic study of the hydrolysis of nitrocefin mediated by B. cereus metallo-β-lactamase*. 2003; Vol. 2003, p 507-516.

245. Griffin, D. H.; Richmond, T. K.; Sanchez, C.; Moller, A. J.; Breece, R. M.; Tierney, D. L.; Bennett, B.; Crowder, M. W., Structural and kinetic studies on metallo-β-lactamase IMP-1. *Biochemistry* **2011,** *50* (42), 9125-34.

246. Yamaguchi, Y.; Kuroki, T.; Yasuzawa, H.; Higashi, T.; Jin, W.; Kawanami, A.; Yamagata, Y.; Arakawa, Y.; Goto, M.; Kurosaki, H., Probing the role of Asp-120(81) of metallo-β-lactamase (IMP-1) by site-directed mutagenesis, kinetic studies, and x-ray crystallography. *J Biol Chem* **2005,** *280* (21), 20824-32.

247. Moali, C.; Anne, C.; Lamotte-Brasseur, J.; Groslambert, S.; Devreese, B.; Van Beeumen, J.; Galleni, M.; Frère, J.-M., Analysis of the importance of the metallo-β-lactamase active site loop in substrate binding and catalysis. *Chem Biol* **2003,** *10* (4), 319-29.

248. Tioni, M. F.; Llarrull, L. I.; Poeylaut-Palena, A. A.; Martí, M. A.; Saggu, M.; Periyannan, G. R.; Mata, E. G.; Bennett, B.; Murgida, D. H.; Vila, A. J., Trapping and characterization of a reaction intermediate in carbapenem hydrolysis by B. cereus metallo-β-lactamase. *J Am Chem Soc* **2008,** *130* (47), 15852-63.

249. Garrity, J. D.; Carenbauer, A. L.; Herron, L. R.; Crowder, M. W., Metal binding Asp-120 in metallo-beta-lactamase L1 from Stenotrophomonas maltophilia plays a crucial role in catalysis. *J Biol Chem* **2004,** *279* (2), 920-7.

250. Llarrull, L. I.; Fabiane, S. M.; Kowalski, J. M.; Bennett, B.; Sutton, B. J.; Vila, A. J., Asp-120 locates Zn2 for optimal metallo-beta-lactamase activity. *J Biol Chem* **2007,** *282* (25), 18276-85.

251. Garau, G.; Bebrone, C.; Anne, C.; Galleni, M.; Frere, J. M.; Dideberg, O., A metallo-beta-lactamase enzyme in action: Crystal structures of the monozinc carbapenemase CphA and its complex with biapenem. *J Mol Biol* **2005,** *345* (4), 785-95.

252. Bebrone, C.; Delbrück, H.; Kupper, M. B.; Schlömer, P.; Willmann, C.; Frère, J.-M.; Fischer, R.; Galleni, M.; Hoffmann, K. M. V., The structure of the dizinc subclass B2 metallo-β-lactamase CphA reveals that the second inhibitory zinc bon Binds in the histidine site. *Antimicrob Agents Chemother* **2009,** *53* (10), 4464.

253. Fonseca, F.; Bromley, E. H.; Saavedra, M. J.; Correia, A.; Spencer, J., Crystal structure of Serratia fonticola Sfh-I: activation of the nucleophile in mono-zinc metallo-beta-lactamases. *J Mol Biol* **2011,** *411* (5), 951-9.

254. Gonzalez, J. M.; Buschiazzo, A.; Vila, A. J., Evidence of adaptability in metal coordination geometry and active-site loop conformation among B1 metallo-beta-lactamases. *Biochemistry* **2010,** *49* (36), 7930-8.

255. Faridoon; Ul Islam, N., An Update on the Status of Potent Inhibitors of Metallo-beta-Lactamases. *Scientia pharmaceutica* **2013,** *81* (2), 309-27.

256. Moloughney, J. G.; D. Thomas, J.; Toney, J. H., Novel IMP-1 metallo-β-lactamase inhibitors can reverse meropenem resistance in Escherichia coli expressing IMP-1. *FEMS Microbiology Letters* **2005,** *243* (1), 65-71.

257. Hiraiwa, Y.; Morinaka, A.; Fukushima, T.; Kudo, T., Metallo-beta-lactamase inhibitory activity of phthalic acid derivatives. *Bioorg Med Chem Lett* **2009,** *19* (17), 5162-5.

258. King, D. T.; Worrall, L. J.; Gruninger, R.; Strynadka, N. C., New Delhi metallo-beta-lactamase: structural insights into beta-lactam recognition and inhibition. *J Am Chem Soc* **2012,** *134* (28), 11362-5.

259. Nauton, L.; Kahn, R.; Garau, G.; Hernandez, J. F.; Dideberg, O., Structural Insights into the Design of Inhibitors for the L1 Metallo-β-lactamase from Stenotrophomonas maltophilia. *J Mol Biol* **2008,** *375* (1), 257-269.

260. Toney, J. H.; Fitzgerald, P. M. D.; Grover-Sharma, N.; Olson, S. H.; May, W. R.; Sundelof, J. G.; Vanderwall, D. E.; Cleary, K. A.; Grant, S. K.; Wu, J. S. K.; Kozarich, J. W.; Pompliano, D. L.; Hammond, G., Antibiotic sensitization using biphenyl tetrazoles as potent inhibitors of Bacteroides fragilis metallo-beta-lactamase. *Chem Biol* **1998,** *5* (4), 185-96.

261. Horsfall, L. E.; Garau, G.; Lienard, B. M.; Dideberg, O.; Schofield, C. J.; Frere, J. M.; Galleni, M., Competitive inhibitors of the CphA metallo-beta-lactamase from Aeromonas hydrophila. *Antimicrob Agents Chemother* **2007,** *51* (6), 2136-42.

262. Roll, D. M.; Yang, Y.; Wildey, M. J.; Bush, K.; Lee, M. D., Inhibition of metallo-beta-lactamases by pyridine monothiocarboxylic acid analogs. *J Antibiot (Tokyo)* **2010,** *63* (5), 255-7.

263. Walter, M. W.; Felici, A.; Galleni, M.; Soto, R. P.; Adlington, R. M.; Baldwin, J. E.; Frère, J.-M.; Gololobov, M.; Schofield, C. J., Trifluoromethyl alcohol and ketone inhibitors of metallo-β-lactamases. *Bioorg Med Chem Lett* **1996,** *6* (20), 2455-2458.

264. Lienard, B. M.; Horsfall, L. E.; Galleni, M.; Frere, J. M.; Schofield, C. J., Inhibitors of the FEZ-1 metallo-beta-lactamase. *Bioorg Med Chem Lett* **2007,** *17* (4), 964-8.

265. Damblon, C.; Jensen, M.; Ababou, A.; Barsukov, I.; Papamicael, C.; Schofield, C. J.; Olsen, L.; Bauer, R.; Roberts, G. C. K., The inhibitor thiomandelic acid binds to both metal ions in metallo-β-lactamase and induces positive cooperativity in metal binding. *J Biol Chem* **2003,** *278* (31), 29240-51.

266. Lassaux, P.; Hamel, M.; Gulea, M.; Delbrück, H.; Mercuri, P. S.; Horsfall, L.; Dehareng, D.; Kupper, M.; Frère, J.-M.; Hoffmann, K.; Galleni, M.; Bebrone, C., Mercaptophosphonate compounds as broad-spectrum inhibitors of the metallo-β-lactamases. *J Med Chem* **2010,** *53* (13), 4862-76.

267. Yusof, Y.; Tan, D. T. C.; Arjomandi, O. K.; Schenk, G.; McGeary, R. P., Captopril analogues as metallo-β-lactamase inhibitors. *Bioorg Med Chem Lett* **2016,** *26* (6), 1589-93.

268. Brem, J.; van Berkel, S. S.; Aik, W.; Rydzik, A. M.; Avison, M. B.; Pettinati, I.; Umland, K. D.; Kawamura, A.; Spencer, J.; Claridge, T. D.; McDonough, M. A.; Schofield, C. J., Rhodanine hydrolysis leads to potent thioenolate mediated metallo-beta-lactamase inhibition. *Nat Chem* **2014,** *6* (12), 1084-90.

269. Payne, D. J.; Bateson, J. H.; Gasson, B. C.; Proctor, D.; Khushi, T.; Farmer, T. H.; Tolson, D. A.; Bell, D.; Skett, P. W.; Marshall, A. C.; Reid, R.; Ghosez, L.; Combret, Y.; Marchand-Brynaert, J., Inhibition of metallo-beta-lactamases by a series of mercaptoacetic acid thiol ester derivatives. *Antimicrob Agents Chemother* **1997,** *41* (1), 135-40.

270. Nagano, R.; Adachi, Y.; Imamura, H.; Yamada, K.; Hashizume, T.; Morishima, H., Carbapenem derivatives as potential inhibitors of various beta-lactamases, including class B metallo-beta-lactamases. *Antimicrob Agents Chemother* **1999,** *43* (10), 2497-503.

271. Mendgen, T.; Steuer, C.; Klein, C. D., Privileged scaffolds or promiscuous binders: a comparative study on rhodanines and related heterocycles in medicinal chemistry. *J Med Chem* **2012,** *55* (2), 743-53.

272. Baell, J. B.; Holloway, G. A., New Substructure Filters for Removal of Pan Assay Interference compounds (PAINS) from screening libraries and for their exclusion in bioassays. *J Med Chem* **2010,** *53* (7), 2719-40.

273. Tomašić, T.; Zidar, N.; Kovač, A.; Turk, S.; Simčič, M.; Blanot, D.; Müller-Premru, M.; Filipič, M.; Grdadolnik, S. G.; Zega, A.; Anderluh, M.; Gobec, S.; Kikelj, D.; Peterlin Mašič, L., 5-Benzylidenethiazolidin-4-ones as multitarget inhibitors of bacterial Mur ligases. *ChemMedChem* **2010,** *5* (2), 286-95.

274. Zvarec, O.; Polyak, S. W.; Tieu, W.; Kuan, K.; Dai, H.; Pedersen, D. S.; Morona, R.; Zhang, L.; Booker, G. W.; Abell, A. D., 5-benzylidenerhodanine and 5-benzylidene-2-4-thiazolidinedione based antibacterials. *Bioorg Med Chem Lett* **2012,** *22* (8), 2720-2.

275. Khodair, A. I.; Gesson, J. P., A new approach for the N- and S-galactosylation of 5-arylidene-2-thioxo-4-thiazolidinones. *Carbohydr Res* **2011,** *346* (18), 2831-7.

276. Ramesh, V.; Ananda Rao, B.; Sharma, P.; Swarna, B.; Thummuri, D.; Srinivas, K.; Naidu, V. G.; Jayathirtha Rao, V., Synthesis and biological evaluation of new rhodanine analogues bearing 2-chloroquinoline and benzo[h]quinoline scaffolds as anticancer agents. *Eur J Med Chem* **2014,** *83*, 569-80.

277. Maccari, R.; Del Corso, A.; Giglio, M.; Moschini, R.; Mura, U.; Ottana, R., In vitro evaluation of 5-arylidene-2-thioxo-4-thiazolidinones active as aldose reductase inhibitors. *Bioorg Med Chem Lett* **2011,** *21* (1), 200-3.

278. Chen, Z. H.; Zheng, C. J.; Sun, L. P.; Piao, H. R., Synthesis of new chalcone derivatives containing a rhodanine-3-acetic acid moiety with potential anti-bacterial activity. *Eur J Med Chem* **2010,** *45* (12), 5739-43.

279. Meyer, T.; Ogermann, D.; Pankrath, A.; Kleinermanns, K.; Muller, T. J., Phenothiazinyl rhodanylidene merocyanines for dye-sensitized solar cells. *J Org Chem* **2012,** *77* (8), 3704-15.

280. Powers, J. P.; Piper, D. E.; Li, Y.; Mayorga, V.; Anzola, J.; Chen, J. M.; Jaen, J. C.; Lee, G.; Liu, J.; Peterson, M. G.; Tonn, G. R.; Ye, Q.; Walker, N. P.; Wang, Z., SAR and mode of action of novel non-nucleoside inhibitors of hepatitis C NS5b RNA polymerase. *J Med Chem* **2006,** *49* (3), 1034-46.

281. Grant, E. B.; Guiadeen, D.; Baum, E. Z.; Foleno, B. D.; Jin, H.; Montenegro, D. A.; Nelson, E. A.; Bush, K.; Hlasta, D. J., The synthesis and SAR of rhodanines as novel class C β-lactamase inhibitors. *Bioorg Med Chem Lett* **2000,** *10* (19), 2179-2182.

282. Tomasic, T.; Zidar, N.; Mueller-Premru, M.; Kikelj, D.; Masic, L. P., Synthesis and antibacterial activity of 5-ylidenethiazolidin-4-ones and 5-benzylidene-4,6-pyrimidinediones. *Eur J Med Chem* **2010,** *45* (4), 1667-1672.

283. Trotsko, N.; Kosikowska, U.; Paneth, A.; Wujec, M.; Malm, A., Synthesis and antibacterial activity of new (2,4-dioxothiazolidin-5-yl/ylidene)acetic acid derivatives with thiazolidine-2,4-dione, rhodanine and 2-thiohydantoin moieties. *Saudi Pharm J* **2018,** *26* (4), 568-577.

284. Song, M.-X.; Zheng, C.-J.; Deng, X.-Q.; Wang, Q.; Hou, S.-P.; Liu, T.-T.; Xing, X.-L.; Piao, H.-R., Synthesis and bioactivity evaluation of rhodanine derivatives as potential anti-bacterial agents. *Eur J Med Chem* **2012,** *54*, 403-412.

285. Zervosen, A.; Lu, W.-P.; Chen, Z.; White, R. E.; Demuth, T. P., Jr.; Frère, J.-M., Interactions between penicillin-binding proteins (PBPs) and two novel classes of PBP inhibitors, arylalkylidene rhodanines and arylalkylidene iminothiazolidin-4-ones. *Antimicrob Agents Chemother* **2004,** *48* (3), 961-969.

286. Bethesda, *Probe Reports from the NIH Molecular Libraries Program [Internet]*. National Center for Biotechnology Information: US, 2010.

287. Garau, G.; Garcia-Saez, I.; Bebrone, C.; Anne, C.; Mercuri, P.; Galleni, M.; Frere, J. M.; Dideberg, O., Update of the standard numbering scheme for class B beta-lactamases. *Antimicrob Agents Chemother* **2004,** *48* (7), 2347-9.

288. van Berkel, S. S.; Brem, J.; Rydzik, A. M.; Salimraj, R.; Cain, R.; Verma, A.; Owens, R. J.; Fishwick, C. W.; Spencer, J.; Schofield, C. J., Assay platform for clinically relevant metallo-beta-lactamases. *J Med Chem* **2013,** *56* (17), 6945-53.

289. Harada, K.; Kubo, H.; Abe, J.; Haneta, M.; Conception, A.; Inoue, S.; Okada, S.; Nishioka, K., Discovery of potent and orally bioavailable 17beta-hydroxysteroid dehydrogenase type 3 inhibitors. *Bioorg Med Chem* **2012,** *20* (10), 3242-54.

290. Fresneau, P.; Cussac, M.; Morand, J. M.; Szymonski, B.; Tranqui, D.; Leclerc, G., Synthesis, activity, and molecular modeling of new 2, 4-dioxo-5-(naphthylmethylene)-3-thiazolidineacetic acids and 2-thioxo analogues as potent aldose reductase inhibitors. *J Med Chem* **1998,** *41* (24), 4706-15.

291. Shaffer, J. E.; Thomson, S. A. Oxathi(SIV)azol-5-one compounds. 5,087,631. U.S. Patent, 1992.

292. Skagseth, S.; Akhter, S.; Paulsen, M. H.; Muhammad, Z.; Lauksund, S.; Samuelsen, Ø.; Leiros, H.-K. S.; Bayer, A., Metallo-β-lactamase inhibitors by bioisosteric replacement: Preparation, activity and binding. *Eur J Med Chem* **2017,** *135*, 159-173.

293. Spicer T, et. al. *ML302: A Novel Beta-lactamase (BLA) Inhibitor*; National Center for Biotechnology Information: 2010.

294. Amin, R.; Waters, V., Antibiotic treatment for Stenotrophomonas maltophilia in people with cystic fibrosis. *Cochrane Database Syst Rev* **2016,** *7* (7), 1-9.

295. Hansen, C. R., Stenotrophomonas maltophilia: to be or not to be a cystic fibrosis pathogen. *Curr Opin Pulm Med* **2012,** *18* (6), 628-31.

296. Barsky, E. E.; Williams, K. A.; Priebe, G. P.; Sawicki, G. S., Incident Stenotrophomonas maltophilia infection and lung function decline in cystic fibrosis. *Pediatric Pulmonology* **2017,** *52* (10), 1276-82.

297. Liénard, B. M.; Garau, G.; Horsfall, L.; Karsisiotis, A. I.; Damblon, C.; Lassaux, P.; Papamicael, C.; Roberts, G. C.; Galleni, M.; Dideberg, O.; Frére, J. M.; Schofield, C. J., Structural basis for the broad-spectrum inhibition of metallo-beta-lactamases by thiols. *Org Biomol Chem***2008,** *6* (13), 2282-94.

298. Li, G. B.; Abboud, M. I.; Brem, J.; Someya, H.; Lohans, C. T.; Yang, S. Y.; Spencer, J.; Wareham, D. W.; McDonough, M. A.; Schofield, C. J., NMR-filtered virtual screening leads to non-metal chelating metallo-beta-lactamase inhibitors. *Chem Sci* **2017,** *8* (2), 928-937.

299. Gränacher, C.; Gerö, M.; Ofner, A.; Klopfenstein, A.; Schlatter, E., Über die Verwendung des Rhodanins zu organischen Synthesen II. Aminosäuren und Ketosäuren. *Helvetica Chimica Acta* **1923,** *6* (1), 458-467.

300. Crowe, B. F.; Nord, F. F., Studies in the thipohene series. VI. Azlactones and rhodanines prepared from 2-thenaldehyde and some substituted 2-thenaldehydes1. *J Org Chem* **1950,** *15* (1), 81-8.

301. Campaigne, E.; Cline, R. E., Preparation and absorption spectra of some -aryl – mercaptoacrylic acids and related disulfides. *J Org Chem* **1956,** *21* (1), 32-8.

302. Karplus, M., Vicinal proton coupling in nuclear magnetic resonance. *J Am Chem Soc* **1963,** *85* (18), 2870-1.

303. Castineiras, A.; Gil, M. J.; Sevillano, P., Synthesis, spectroscopic characterization and X-ray crystal structure of 2-(4-methylpyridinium)-5-(4-pyridinium)-1,3-dithiolane-2,4-dicarboxylic acid dithiocyanate monohydrate. *J Mol Struct* **2000,** *522*, 193-9.

304. Kresge, A. J.; Meng, Q., 2,4,6-Trimethylthioacetophenone and Its Enol. The first quantitative characterization of a simple thiocarbonyl system in aqueous solution. *J Am Chem Soc* **1998,** *120* (45), 11830-1.

305. Cahill, S. T.; Cain, R.; Wang, D. Y.; Lohans, C. T.; Wareham, D. W.; Oswin, H. P.; Mohammed, J.; Spencer, J.; Fishwick, C. W.; McDonough, M. A.; Schofield, C. J.; Brem, J., Cyclic boronates inhibit all classes of beta-lactamases. *Antimicrob Agents Chemother* **2017,** *61* (4), e02260-16.

306. Ramirez, M. A.; Borja, N. L., Epalrestat: an aldose reductase inhibitor for the treatment of diabetic neuropathy. *Pharmacotherapy* **2008,** *28* (5), 646-55.

307. Kaminskyy, D.; Kryshchyshyn, A.; Lesyk, R., Recent developments with rhodanine as a scaffold for drug discovery. *Expert Opin Drug Deliv* **2017,** *12* (12), 1233-1252.

308. Pettinati, I.; Brem, J.; Lee, S. Y.; McHugh, P. J.; Schofield, C. J., The Chemical Biology of Human Metallo-beta-Lactamase Fold Proteins. *Trends Biochem Sci* **2016,** *41* (4), 338-55.

Chapter 6

Summary

6. Summary

Methylation on N^6 adenosine (m^6A) is the most prevalent modification on messenger RNA[1-2] and is proposed to play a key role in regulating expression, mRNA splicing, and mRNA transporting[3-4]. The discovery of the first m^6A demethylase, the Fat mass and obesity-associated protein (FTO), suggests that the m^6A modification on RNA may be dynamically regulated[5-6]. Dysregulation of FTO correlates with diseases, e.g. overexpression of FTO is involved in dopaminergic neuronal death, which is a reported biological marker for Parkinson's disease[7]. The FTO protein is a member of the Fe(II) and 2-oxoglutrate dependent oxygenase superfamily[8], and specifically a member of (nucleic acid modifying) AlkB subfamily. The m^6A demethylase activity of FTO overlaps with another member of the AlkB subfamily, ABH5. Studies on FTO were the main focus of the work described in the first half of this thesis.

The work described in Chapter 2 concerned the development of FTO inhibitors and the optimisation of FTO inhibition assays. New generations of FTO (small molecule) inhibitors were designed based on previously discovered pyridinyl scaffold[9]. Following successful synthetic work, these new inhibitors showed moderate potency and selectivity. Initial inhibition data obtained from MALDI-TOF MS based assays were insufficient to obtain IC_{50} values. The previously developed LC-MS based assay was revised in hope that enzyme concentration could be lowered. Although the IC_{50} value decreased two-fold (IC_{50} from 3.2 ± 0.4 μM to 1.45 ± 0.5 μM), the assay was deemed not suitable for high-throughput screening. A new RF-MS based assay was then developed. Following successful assay optimisation, the RF-MS based assay proved to be suitable for high-throughput and reliable compound screening. In addition, new enzyme kinetic parameters were determined using RF-MS. A potent and (at least) partially selective FTO inhibitor (**34**, IC_{50} 0.08 ± 0.005 μM) was identified.

During assay optimisation using RF-MS, it was observed that the RNA oligonucleotide (m^6A) substrate underwent FTO-catalysed hydroxylation rather than reported demethylation[10]. Chapter 3 describes comparative investigations on the FTO mechanism. Potential FTO catalysed hydroxylation was compared with analogous reactions catalysed by related enzymes, i.e. AlkB and ABH5, and mouse homologue (mFTO). Using RF-MS FTO was observed to apparently convert m^6A to a hydroxymethyl hemiaminal (hm^6A) product, while ABH5 apparently demethylated the same substrate. Further investigations revealed that, under tested conditions, hm^6A is not a substrate for FTO, contrasting with previous reports[11]. NMR analyses supported the proposal that hm^6A is an end product of FTO catalysed reaction. Although fragmentation of the (hm^6A) hemiaminal to the demethylated product and formaldehyde was observed, it was shown to proceed *via* a non-enzyme catalysed manner.

Chapter 4 describes work concerning the biochemical and biophysical characterisation of a clinical variant of FTO, i.e. p.(Ser319Phe). A new-born baby with growth retardation and malformations was identified and was shown to carry a mutation on the *fto* gene, this mutation results in residue Ser319 being substituted with a phenylalanine[12]. Using modelling the Ser319Phe substitution is predicted to affect co-substrate (2OG) binding, because of its close proximity to the catalytically important residue Arg316, which is involved in 2OG binding. Circular dichroism analyses revealed that the Ser319Phe FTO has the same overall secondary structure as the wildtype FTO; however, Ser319Phe FTO does not refold completely after thermal denaturation (Figure 4.4). This could be due to hydrophobic aggregation caused by the exposed Phe319 residue. LC-MS assays demonstrated that Ser319Phe FTO has reduced, but not ablated, catalytic activity compared to that of wildtype FTO. NMR analyses show that Ser319Phe FTO does not turnover 2OG as effectively as wildtype FTO. The physiological significance of FTO is strongly supported by the observed clinical mutation, which further understanding on RNA regulation.

Chapter 5 introduces the Zn(II) ion dependent β-lactamases (metallo-β-lactamases, MBLs), which are involved in antibacterial resistance. The MBLs employ one or two Zn(II) ions to catalyse the hydroxylation of nearly all classes of β-lactam antibiotics, including the carbapenems which are often considered antibiotics of last resort. Following an inhibition report showing that rhodanine derived enethiols can be potent MBL inhibitors[13], extensive SAR studies were carried out on rhodanines and enethiols as MBL inhibitors. Highly potent enethiol based MBL inhibitors were identified, though some evidence from rhodanine based inhibition was accrued. The results support the proposal that rhodanines have potential as promiscuous enzyme inhibitors/protein binders, in part owing to their tendency to undergo hydrolysis to products, including enethiols, which have potential to inhibit the multiple metallo-enzymes present in cells, including related MBL fold enzymes, which have important biological roles beyond antibiotic resistance including in nucleic acid repair and metabolism. These results also imply that any medicinal chemistry studies employing rhodanine inhibitors should, as a matter of course, include testing of their degradation products.

Overall, the work described in this thesis has provided biochemical insight into the mechanism of FTO, and its physiological significance is highlighted by the clinical mutation. The high-throughput screening assay developed for inhibition studies provideds a solid platform for future inhibitor developments. Detailed SAR studies on metallo-β-lactamases revealed that broad-spectrum MBL inhibition is possible with relatively simple small molecule inhibitors, although the stability and potential degradation products should also be considered in future inhibitor development programs.

References

1. Narayan, P.; Rottman, F. M., An in vitro system for accurate methylation of internal adenosine residues in messenger RNA. *Science* **1988,** *242* (4882), 1159-62.

2. Horowitz, S.; Horowitz, A.; Nilsen, T. W.; Munns, T. W.; Rottman, F. M., Mapping of N6-methyladenosine residues in bovine prolactin mRNA. *Proc Natl Acad Sci USA* **1984,** *81* (18), 5667-71.

3. Meyer, K. D.; Saletore, Y.; Zumbo, P.; Elemento, O.; Mason, C. E.; Jaffrey, S. R., Comprehensive analysis of mRNA methylation reveals enrichment in 3' UTRs and near stop codons. *Cell* **2012,** *149* (7), 1635-46.

4. Dominissini, D.; Moshitch-Moshkovitz, S.; Schwartz, S.; Salmon-Divon, M.; Ungar, L.; Osenberg, S.; Cesarkas, K.; Jacob-Hirsch, J.; Amariglio, N.; Kupiec, M.; Sorek, R.; Rechavi, G., Topology of the human and mouse m6A RNA methylomes revealed by m6A-seq. *Nature* **2012,** *485* (7397), 201-6.

5. Liu, N.; Pan, T., RNA epigenetics. *Transl Res* **2015,** *165* (1), 28-35.

6. Roundtree, I. A.; He, C., RNA epigenetics--chemical messages for posttranscriptional gene regulation. *Curr Opin Chem Biol* **2016,** *30*, 46-51.

7. Chen, X.; Yu, C.; Guo, M.; Zheng, X.; Ali, S.; Huang, H.; Zhang, L.; Wang, S.; Huang, Y.; Qie, S.; Wang, J., Down-regulation of m6A mRNA methylation is involved in dopaminergic neuronal death. *ACS Chem Neurosci* **2019,** *10* (5), 2355-63.

8. Loenarz, C.; Schofield, C. J., Expanding chemical biology of 2-oxoglutarate oxygenases. *Nat Chem Biol* **2008,** *4* (3), 152-6.

9. Aik, W.; Demetriades, M.; Hamdan, M. K.; Bagg, E. A.; Yeoh, K. K.; Lejeune, C.; Zhang, Z.; McDonough, M. A.; Schofield, C. J., Structural basis for inhibition of the fat mass and obesity associated protein (FTO). *J Med Chem* **2013,** *56* (9), 3680-8.

10. Jia, G.; Fu, Y.; Zhao, X.; Dai, Q.; Zheng, G.; Yang, Y.; Yi, C.; Lindahl, T.; Pan, T.; Yang, Y.-G.; He, C., N6-Methyladenosine in nuclear RNA is a major substrate of the obesity-associated FTO. *Nat Chem Biol* **2011,** *7*, 885-7.

11. Fu, Y.; Jia, G.; Pang, X.; Wang, R. N.; Wang, X.; Li, C. J.; Smemo, S.; Dai, Q.; Bailey, K. A.; Nobrega, M. A.; Han, K.-L.; Cui, Q.; He, C., FTO-mediated formation of N6-

hydroxymethyladenosine and N6-formyladenosine in mammalian RNA. *Nat Commun* **2013,** *4*, 1798-801.

12. Daoud, H.; Zhang, D.; McMurray, F.; Yu, A.; Luco, S. M.; Vanstone, J.; Jarinova, O.; Carson, N.; Wickens, J.; Shishodia, S.; Choi, H.; McDonough, M. A.; Schofield, C. J.; Harper, M. E.; Dyment, D. A.; Armour, C. M., Identification of a pathogenic FTO mutation by next-generation sequencing in a newborn with growth retardation and developmental delay. *J Med Genet* **2016,** *53* (3), 200-7.

13. Brem, J.; van Berkel, S. S.; Aik, W.; Rydzik, A. M.; Avison, M. B.; Pettinati, I.; Umland, K. D.; Kawamura, A.; Spencer, J.; Claridge, T. D.; McDonough, M. A.; Schofield, C. J., Rhodanine hydrolysis leads to potent thioenolate mediated metallo-beta-lactamase inhibition. *Nat chem* **2014,** *6* (12), 1084-90.

Chapter 7

Materials and Methods

Table of Contents

7.1. Sourcing of materials……..312

7.2. Competent Cells…….313

7.3. pH Measurement for Buffer Solutions…….....313

7.4. Determination of DNA Concentration…….....313

7.5. Determination of Protein Concentration…….313

7.6. Cell Density Measurements…….....314

7.7. Centrifugation of Samples……..314

7.8. Buffer Exchange…….....314

7.9. Media and Antibiotic Plate Preparation…….315

7.9.1. 1000x Antibiotic Stocks for Cell Growth and Agar Plates……315

7.9.2. Preparation of 2TY Medium……..315

7.9.3. Preparation of Super Optimal Catabolite Repression (SOC) Outgrowth Medium…315

7.10. SDS-PAGE Electrophoresis…….....316

7.10.1. SDS-PAGE Gel Preparation……...316

7.10.2. Running of SDS-PAGE Experiments…….317

7.11. Site Directed Mutagenesis……..318

7.12. DNA Digests……..319

7.13. Plasmid Purification……...320

7.14. Protein Production and Purification……320

7.14.1. Competent Cell Transformations……320

7.14.2. Starter Cultures……...321

7.14.3. Large Scale Cell Growths……...321

7.14.4. Cell Lysate Preparation……...322

7.14.5. Fast Protein Liquid Chromatography (FPLC)…….322

7.15. Denaturing Mass-Spectrometry……..323

7.16. In Vitro Biochemical Assays for 2OG oxygenases……324

7.16.1. LC-MS Based Demethylation Assays……324

7.16.2. MALDI-MS Based Assays…….325

7.16.3. RapidFire-MS (RF-MS) Based Assays……...326

7.16.4. K_M Determination……...327

7.16.5. Inhibition Assays……327

7.17. MBL Inhibition assays……328

7.18. Standard Error Calculation…….329

7.19. Circular Dichroism (CD) Analyses……329

7.20. Computational Modelling of the Ser319Phe FTO Substitution…….330

7.21. Nuclear Magnetic Resonance Spectroscopy……..330

7.21.1. NMR time course for 2OG Turnover Assays……..331

7.21.2. NMR (^{1}H-^{13}C-HSQC) Time Course on FTO catalysis Product Degradation……331

7.21.3. NMR Time Course for Rhodanine Degradation…….332

7.22. Organic synthesis……332

7.22.1. Synthesis and compound characterisation……..333

References……..359

7. Materials and Methods

7.1. Sourcing of materials

Reagents Where possible, and unless otherwise stated, all materials were obtained from Sigma-Aldrich Ltd., New England Biolabs, or Invitrogen, and of the highest purity available. Bacto tryptone, yeast extract and agar for cell growth media and antibiotic plates were obtained from Fisher Scientific Ltd. Isopropyl β-D-1-thiogalactopyranoside (IPTG) was obtained from Apollo Scientific Ltd.

Milli-Q water refers to water purified using a Millipore Elix Reverse Osmosis system followed by filtration through a 0.22 μm Millipore Milli-Q filter. Sterilisation of non-sterile media and equipment was conducted *via* autoclaving in at 121°C for 20 minutes either a LTE TouchClave® II benchtop autoclave (LTE Scientific) or a LTE Falcon benchtop autoclave (LTE Scientific).

Solvents (including dry solvents) for chemical transformations, work-up and chromatography were from Sigma-Aldrich (Dorset, UK) at HPLC grade, and used without further purification.

Column chromatography was performed using prepacked SNAP columns on a Biotage SP1 Purification system (Uppsala, Sweden).

Thin-layer chromatography (TLC) was carried out using Merck aluminium plates coated with $HF_{254/366}$ silica gel. Visualization was performed with a 254 nm ultraviolet (UV) light source and/or by immersion in potassium permanganate or phosphomolybdic acid (PMA) solutions.

Microwave assisted reactions were performed using a Biotage Initiator^{TM} microwave synthesizer in sealed vials.

Deuterated solvents were from Cambridge Isotopes, Apollo Scientific Ltd, and/or Sigma-Aldrich.

7.2. Competent Cells

The following strains of *E. coli* cells were used for cloning and protein expression:

XL10-GOLD competent cells

BL21(DE3)

7.3. pH Measurement for Buffer Solutions

The pH of solutions was determined using a Jenway pH Meter 3305, equipped with an Aldrich glass/calomel combination electrode. Calibration was carried out prior to all measurements with buffer solutions of phthalate (pH 4.0), phosphate (pH 7.0) and borate (pH 10.0) (Fisher Scientific), with the former two used for calibration in the range of 4.0-7.0, and the latter two in the range of 7.0-10.0. Electrodes were stored in a 4 M saturated potassium chloride solution when not in use.

7.4. Determination of DNA Concentration

DNA concentrations were determined by monitoring absorbance at λ = 260 nm using a NanoDrop ND-1000 Spectrophotometer (NanoDrop Technologies Inc.); DNA concentration was determined using the 'Nucleic Acid' software module, with the absorbance of sterile ddH_2O being set to 0.

7.5. Determination of Protein Concentration

Protein concentrations were determined using a NanoDrop ND-1000 spectrophotometer by monitoring the absorbance at 280 nm, using the 'Protein A280' module of the controlling

software. The absorbance was normalised to that of sample buffer to zero and the absorption coefficient, ε, of the protein of interest was calculated using the ExPASy Protparam online application (http://www.expasy.org/).

7.6. Cell Density Measurements

Cell density was measured by assessing the optical density of culture medium at λ = 600 nm (OD600). This was carried out by measuring the absorbance of a 1 mL sample in a cuvette (Fisher Scientific) using an Amersham Biosciences Novaspec III visible spectrophotometer; with the absorbance of the uninoculated growth medium being set to 0.

7.7. Centrifugation of Samples

Samples with a volume less than 1.5 mL, and suitable for handling room temperature, were centrifuged using a 1-14 microfuge (Sigma). Samples with a volume less than 1.5 mL requiring cold handling were centrifuged using a Microfuge 22R bench top centrifuge (Beckman Coulter Ltd.) at 4 °C. Pelleting of small scale cell growth cultures and protein concentration was performed using a Beckmann Allegra X-30R at 4 °C. Large scale cell growth cultures and cell lysates were centrifuged in a Beckmann Avanti J-25 at 4 °C.

7.8. Buffer Exchange

Samples were buffer exchanged using either a PD10 column (GE healthcare), Micro BioSpin column (BioRad) or Slide-A-Lyzer dialysis cassette (ThermoFisher Scientific), following the manufacturer's instructions.

7.9. Media and Antibiotic Plate Preparation

7.9.1. 1000x Antibiotic Stocks for Cell Growth and Agar Plates

For the preparation of ampicillin or kanamycin stock solutions, 500 mg or 340 mg, respectively, of antibiotic was dissolved in 10 mL Milli-Q water and the resultant solution was passed through a 0.22 μM filter before storage as aliquots at -20 °C. For chloramphenicol, 340 mg of antibiotic was dissolved in 10 mL of ethanol and stored as aliquots at -20 °C.

7.9.2. Preparation of 2TY Medium

2TY Medium was made according to the following protocol. Solid components were dissolved in 900 mL of Milli-Q water and the pH was adjusted to 7.0 by addition of 1 M NaOH. The solution volume was then adjusted to 1 L before autoclaving.

Table 7.1: Composition of 2TY medium

Reagent	Concentration
Bacto Tryptone	16 g L^{-1}
Yeast Extraction	10 g L^{-1}
NaCl	5 g L^{-1}

7.9.3. Preparation of Super Optimal Catabolite Repression (SOC) Outgrowth Medium

SOC Outgrowth Medium was prepared according to the following recipe. SOC medium was made fresh in sterile Eppendorf tubes when required.

Table 7.2: Composition of SOC outgrowth medium

Reagent	Volume
2 TY medium	970 μL
2 M glucose (sterile)	20 μL
1 M $MgCl_2$ (sterile)	10 μL

7.10. SDS-PAGE Electrophoresis

7.10.1. SDS-PAGE Gel Preparation

SDS-PAGE gels were made according to the following recipes. Polyacrylamide gels were made using the Mini-PROTEAN Tetra Cell system (Bio-Rad). In both running and stacking gel preparation, tetramethyleneethylenediamine (TEMED) was added as the last component. During production, the running buffer was covered with a layer of propan-2-ol to prevent it from drying out whilst setting. This was subsequently removed before pouring and setting of the stacking gel layer. SDS-PAGE gels were covered in wet tissue and stored at 4 °C until required.

Running Gel Recipe

Figure 7.3: Composition of running gel

Reagent	Volume
ddH_2O	0.79 mL
1.5 M Tris-HCl pH 8.8	6.00 mL
30% (w/v) Acrylamide	5.00 mL
10% (w/v) SDS	0.12 mL
10% (w/v) Ammonium Persulfat	0.10 mL
Tetraethylenediamine	0.01 mL

Stacking Gel Recipe

Figure 7.4: Composition of stacking gel

Reagent	Volume
ddH_2O	2.30 mL
0.5 M Tris-HCl pH 6.8	0.40 mL
30% (w/v) Acrylamide	0.32 mL
10% (w/v) SDS	0.032 mL
10% (w/v) Ammonium Persulfat	0.06 mL
Tetraethylenediamine	0.01 mL

7.10.2. Running of SDS-PAGE Experiments

10 μL of protein sample were mixed with 10 μL of 2x SDS-PAGE Gel Loading Buffer. The samples were then heated at 100 °C on a hot block for 2 min before loading of up to 10 μL of each sample per well. Electrophoresis was carried out at a constant voltage of 160 V for 10 min followed by 180 V for 50 min using SDS-PAGE Running Buffer. Gels were subsequently stained for 10 minutes in SDS-PAGE Staining Solution and transferred into water. The gels were heated by microwaving until bands were visible before destaining overnight in water.

2x SDS-PAGE Gel Loading Buffer Recipe

2x SDS-PAGE gel loading buffer was made according to the following recipe. The components were combined and the solution was adjusted to 50 mL by addition of Milli-Q water. The final solution was stored at room temperature for future use.

Table 7.5: Composition of 2x SDS-PAGE Gel Loading Buffer

Reagent	Mass/Volume
SDS	6 g
Dithiothreitol	4.65 g
Bromophenol blue	30 mg
Glycerol	23.5 mL
1 M Tris-HCl pH 6.8	3 mL

10x SDS-PAGE Running Buffer Recipe

10x SDS-PAGE running buffer was made according to the following recipe. Components were dissolved in 900 mL before adjusting the final volume to 1 L. The solution was stored at room temperature for future use.

Table 7.6: Composition of 10x SDS-PAGE Running Buffer

Reagent	Mass/Volume
Glycine	144 g
Tris base	30 g
SDS	10 g

SDS-PAGE Staining Solution Recipe

The SDS-PAGE staining solution was made according to the following recipe. The solution was stored in a foil-wrapped bottle, to protect it from sources of light, and kept at room temperature for future use.

Table 7.6: Composition of 10x SDS-PAGE Running Buffer

Reagent	Mass/Volume
Coomassie brilliant blue G250	0.4 g
Milli-Q water	800 mL
Ethanol	50 mL
70% perchloric acid	34 mL

7.11. Site Directed Mutagenesis

Primers containing the desired mutation were designed following the protocols outlined in the QuikChange™ site-directed mutagenesis kit (Agilent), and used to amplify the full vector and insert sequence. A reaction mixture was set up as outlined in Table 7.7 and the mutagenesis reaction was run in a BioRad MJ Mini thermal cycler.

Table 7.7: Reaction mixture for typical mutagenesis PCR

Reagent	Volume
ddH_2O	8.50 µL
Q5 Reaction Buffer (5 x stock, New England Biolabs)	5.00 µL
Q5 High GC Enhancer (5 x stock, New England Biolabs)	5.00 µL
Forward Primer, 10 µM	1.25 µL
Reverse Primer, 10 µM	1.25 µL
Template DNA	1.00 µL (approx. 50 ng)
dNTP mix (New England Biolabs)	2.50 µL
Q5 DNA Polymerase (New England Biolabs)	0.50 µL

Typical Mutagenesis PCR Samples were heated to 94°C for 120 s to denature the template DNA. 18 cycles then followed:

i. Denaturing at 94°C for 45 s

ii. Annealing at 5°C below the lowest primer Tm for 60 s

iii. Extension at 68°C for 1 min per kb of plasmid

Following these cycles, reactions were held at 68 °C for a 20 min final extension prior to holding at 4 °C.

Following this, 1 µL of DpnI (New England Biolabs) was added to the mixture to digest any supercoiled DNA; the digest was conducted for 12 hours at 25 °C. 5 µL of the resultant mixture was used in a transformation and colonies selected on LB agar plates that were treated with the appropriate antibiotic.

7.12. DNA Digests

DNA was digested using restriction enzymes purchased from New England Biolabs. When possible, a double digest (i.e. simultaneous digestion with two different restriction enzymes) was conducted using the conditions recommended by New England Biolabs. The digest was

set up and conducted at 25 °C for 12 hours; standard double digest conditions are detailed in the table 7.8. Products were not purified and stored at -20°C.

Table 7.8: Typical Conditions for an Enzymatic Double Digest

Reagent	Mass/Volume
DNA for digestion	8.50 µL
Restriction Enzyme 1	1.00 µL
Restriction Enzyme 2	1.00 µL
10 x Buffer (New England Biolabs)	2.50 µL
ddH_2O	To a total volume of 25 µL

7.13. Plasmid Purification

From an overnight 100 mL culture, plasmid DNA was extracted by pelleting 5 mL of culture followed by purification using a Miniprep kit (ThermoFisher Scientific), following the manufacturer's instructions. When larger quantities of DNA were required for downstream uses, 50 mL of culture was pelleted followed by the use of a Midiprep kit (ThermoFisher Scientific). Autoclaved ddH_2O was used as a direct substitute for elution buffer in all instances.

7.14. Protein Production and Purification

7.14.1. Competent Cell Transformations

Competent cells (Stratagene) were thawed on ice. 1 µl of plasmid DNA was then added to 35 µl of the competent cells in pre-chilled 1.5 ml Eppendorf tubes. The tubes were left on ice for 20 minutes before placement into a water bath at 42 ºC ('heat shocked') for 45s. The tubes were then returned to ice for 2 min. Super Optimal Broth, Catabolite Repressing (SOC) medium (200 µl) was added to each tube which were then incubated at 37 ºC for 30 min before 100 µl of the transformation mixture was spread on kanamycin agar plates. After the plates were dry, they were inverted and incubated at 37 ºCC overnight. All agar plates were poured

and streaked in a laminar flow hood (HeraSafe® Model KS12 Class II Biosafety Cabinet (Thermo Fisher Scientific) using sterile media and equipment.

7.14.2. Starter Cultures

Starter cultures were initiated in antibiotic treated 2TY (100 mL medium in a 500 mL conical flask) via inoculation with a single colony from an agar plate, or from a single scraping from a glycerol stock. The culture was then incubated overnight at 37°C with 180 rpm shaking in a New Brunswick Scientific G25 environmental shaker.

7.14.3. Large Scale Cell Growths

A 100 ml culture of BL21 (DE3) *E. coli*, transformed 2TY media, was produced to act as a starter culture for large scale cell growths. Large scale recombinant protein expression was performed using 2000 ml PYREX® narrow-mouth graduated Erlenmeyer flasks containing either 600 ml 2-TY, containing kanamycin (600 µl). Flasks containing growth medium were inoculated with the bacterial starter culture (7 ml) and grown at 37 ºC with vigorous stirring (180 rpm) until they reached an OD_{600} according to the table 7.9. At this point, the cultures were induced with 0.1 or 0.5 M IPTG (600 µl), and further incubated at 18 or 16 ºC for a further 12 hours. After this time, the cultures were centrifuged and the resulting bacterial pellet frozen in a sealable plastic bag at -80 ºC.

Table 7.9: Induction conditions for large scale cell growth.

Protein	Inducing Agent	[Inducing Agent] / mM	OD_{600} at Induction	Post-Induction Temp /°C
hFTO	IPTG	0.5	0.6-0.8	18
$hFTO_{\Delta 1\text{-}31}$	IPTG	0.5	0.8-1.0	16
$hFTO_{S319F}$	IPTG	0.5	0.6-0.8	18
$hFTO_{R316Q}$	IPTG	0.5	0.6-0.8	18
mFTO	IPTG	0.5	0.6-0.8	18
$ABH5_{88\text{-}262}$	IPTG	0.1	0.6-0.8	18

7.14.4. Cell Lysate Preparation

Between 15 g to 20 g of thawed cells, which had been stored at -80 ºC, were re-suspended in 120 ml binding buffer (50 mM Tris-HCl pH 7.5, 500 mM NaCl, 20 mM Imidazole). 1 M MgCl2 (120 µl) and approximately 1 mg of DNAseI (Roche Diagnostics) were added to the suspension and the mixture was stirred at 4 ºC until homogeneous. The cells were lysed by sonication (4 - 45 second bursts with 45 seconds rest between) using a Vibra Cell VCX 500 with a 13 mm probe at 60 % intensity, on ice. Cell debris was removed by centrifugation using a JLA-16.25 rotor at 15,000 rpm for 20 minutes and then a JA-25.5 rotor at 21,000 rpm for 10 mins at 4 ºC in a Beckman Avanti J25 centrifuge, with the supernatant (cell lysate) being decanted from the resulting pellet. The supernatant was then filtered using a 0.2 µM Omnipore^{TM} filter (Millipore U.K.).

7.14.5. Fast Protein Liquid Chromatography (FPLC)

FPLC for protein purification was carried out using ÄktaTM FPLC systems (GE Healthcare) at 4 ºC. Buffers were freshly prepared in Milli-Q water, degassed and filtered through a 0.22 µm filter before use. Purification procedures were followed by monitoring absorbance at 280 nm with a UPC-900 monitor on the FPLC and by SDS-PAGE. Sample fractions were collected using a Frac-920 fraction collector.

Nickel ion Affinity Chromatography (HisTrap)

Cell pellets were resuspended in 50 mM Tris-HCl pH 7.5, 500 mM NaCl, 20 mM imidazole, prior to the addition of 1 mg DNAseI (bovine pancreas, grade II, Roche) and one tablet of protease cocktail inhibitors (GE Healthcare). Cells were lysed via sonication, centrifuged at 50,000 xg for 25 minutes and the supernatant was then collected and subjected to filtration through a 0.45 µm syringe filter. The filtered lysate was then loaded onto a pre-equilibrated HisTrap HP 5 mL column (GE Healthcare) before being washed with 50 mM Tris-HCl pH 7.5,

500 mM NaCl, 40 mM imidazole for 10 column volumes. The bound protein was eluted with 50 mM Tris-HCl pH 7.5, 500 mM NaCl, 250 mM imidazole.

Heparin Affinity (HiTrap Heparin)and Anion Exchange (MonoQ) Chromatography

The fractions eluted from the HisTrap column was buffer exchanged using a PD-10 desalting column (GE Healthcare) to 25 mM Tris-HCl pH 7.5. The sample was then loaded onto a pre-equilibrated HiTrap Heparin HP column (GE Healthcare) prior to elution, which was achieved via a gradient of 25 mM Tris- HCl pH 7.5, 1M NaCl in 25 mM Tris-HCl pH 7.5 (0-80 % over 25 minutes, elution of FTO protein occurs at approximately 12 %). The protein was again buffer exchanged into 25 mM Tris-HCl pH 7.5 with a PD- 10 desalting column, prior to loading onto a MonoQ column (GE Healthcare), which was run in 25 mM Tris-HCl pH 7.5. Product fractions were pooled and concentrated to 20 mg mL-1. Protein was then divided into aliquots were stored at -80 °C.

7.15. Denaturing Mass-Spectrometry

Molecular masses of purified proteins were verified by denaturing mass spectrometry. Data were collected using an LCT Premier mass spectrometer (Waters) coupled to an Agilent 1100 Series HPLC using a Chromolith® FastGradient RP-18 endcapped column equipped with a 50-2 monolithic silica HPLC column (C18, 2 x 50 mm, 1.6 µm diameter macropores, Merck). Samples were diluted to 0.01 mg mL-1 before injection via a CTC-autosampler inlet system. Proteins were separated using a multi-step gradient over 10 min (Solvent A 94.9% (v/v) H^2O, 5% (v/v) CH3CN, 0.1% (v/v) formic acid; Solvent B 99.9% (v/v) CH3CN, 0.1% (v/v) formic acid; 0-1 min 5% B, 1-5 min linear gradient to 100% B, 5-8 min 100% B, 8-10 min linear gradient to 5% B) with a flow rate of 0.4 mL min-1. The ionisation source used a capillary voltage of 3.2 kV and cone voltage of 25 V. Nitrogen was used as the nebulizer desolvation

gas at a flow rate of 600 L hour-1. Calculated masses were determined from amino acid sequence using the ExPASy Protparam online application (http://www.expasy.org/).

7.16. *In Vitro* Biochemical Assays for 2OG oxygenases

7.16.1. LC-MS Based Demethylation Assays

Oligonucleotide Demethylation

For demethylation assays, a 25µL reaction mixture containing final concentrations of 1.2 µM hFTO; 22 µM 5-mer oligonucleotide [GG(m^6A)CU]; 10 µM 2OG; 500 µM L-ascorbate; 10µ M diammonium iron(II) sulphate; and 25 mM Tris-HCl, pH 7.5, was incubated at room temperature for 30 min. After incubation the reaction mixture was quenched with methanol (25 µL) then centrifuged (14000 rpm, 10 min) to remove precipitated protein. The supernatant was then dried using an Eppendorf Speedvac machine, then re-suspended in (25 µL) MilliQ purified water. 1,1,1,3,3,3-Hexafluoro-2-propanol (HFIP) and 8 triethylamine were used as ion paring buffer for better separation and retention of my 5-mer oligo.23 Buffer A: 200mM HFIP, 8.15 mM TEA buffer, 5% methanol, buffer B: 20% buffer A + 80% methanol. Separation of oligonucleotides was monitored by UV and 255-292nm. Initially, the LC conditions were set at a gradient from 98% buffer A (2% buffer B) to 80% buffer A (20% buffer B) in 6 minutes, then to 30% buffer A (70% buffer B) at 8 minutes. The product [GGACU] and substrate [GG(m^6A)CU] were separated using a Waters Acquity UPLC Oligonucleotide BEH C-18 column (130 Å,1.7µm, 2.1 mm×50 mm) with a gradient of 98% buffer to 70% buffer B over 8 min, at room temperature. The UV detection wavelength was set to 265-292 nm. Retention time for [GGACU] and [GG(m^6A)CU] is 2.5 min and 3.0 min, respectively. The masses for each peak were confirmed by electrospray ionisation-time of flight (ESI-TOF) mass spectrometry (Bruker Daltonos, micrOTOF instrument). The area under the curve of the substrate ([GG(m^6A)CU]) and product ([GGACU]) peaks were integrated using Data Analysis

Software (Bruker) in the negative ion mode, and the percentage conversion of [GG(m^6A)CU] to [GGACU] was used to quantify the demethylation activity of FTO.

Nucleoside Demethylation

For enzyme activity assays, a 25 μL reaction mixture containing final concentrations of 3 μM hFTO; 70 μM 3-methyl thymidine (m^3T) nucleoside; 160 μM 2OG; 500 μM L-ascorbate; 100 μM diammonium iron(II) sulphate; and 25 mM Tris-HCl, pH 7.5, was incubated at room temperature for 1 h. After incubation the reaction mixture was quenched with methanol (25 μL) then centrifuged (14000 rpm, 10 min) to remove precipitated protein. The supernatant was then dried using an Eppendorf Speedvac machine, then re-suspended in (25 μL) MilliQ purified water. The product (thymidine) and substrate (m^3T) were separated using a Waters Acquity Ultra Performance Liquid Chromatography (UPLC) Atlantis C-18 column (130 Å,1.7μm, 2.1 mm×100 mm) with a gradient of 95% A (H2O with 1% formic acid) to 80% B (methanol with 0.1% formic acid) over 6 min, at room temperature. The UV detection wavelength was set to 266 nm. Retention time for thymidine and m^3T is 3.4 min and 3.9 min, respectively. The masses for each peak were confirmed by Orbitrap liquid chromatography mass spectrometry (Waters EXACTIVE instrument). The area under the curve of the substrate (m^3T) and product (thymidine) peaks were integrated using XcaliburTM Software (Thermo Scientific) in the positive ion mode, and the percentage conversion of m^3T to thymidine was used to quantify the activity of wildtype, Ser319Phe, and Arg316Gln variant FTO. To determine the optimal enzyme concentration, assays were carried out in triplicate with a range of enzyme concentrations (2, 2.5, 3, 3.5 μM) assuming they would be similar to those previously reported[1].

7.16.2. MALDI-MS Based Assays

For enzyme activity assays, a 25 μL reaction mixture containing final concentrations of 1.3 μM hFTO; 20 μM 5-mer oligonucleotide [GG(m^6A)CU]; 10 μM 2OG; 500 μM L-ascorbate; 10

μM diammonium iron(II) sulphate; and 25 mM Tris-HCl, pH 7.5, was incubated at room temperature for 30 min. After incubation the reaction mixture was quenched with 1 mM EDTA at the desired time points. 1 μL quenched solution was mixed with 1 μL of 0.5 M 2,4,6-trihydroxyacetophenone in EtOH with 0.1 M ammonium citrate in H_2O on a MALDI plate. Each 96- well MALDI plate was analysed using positive reflection mode using a Water MALDI Micro MX instrument. All reagents were freshly made prior to the experiments. For KM value determinations, assays were carried out in 96-well clear PCR plates.

7.16.3. RapidFire-MS (RF-MS) Based Assays

A reaction mixture containing RNA oligonucleotide [AUUGUGG(m^6A)CUGCAGC] or [GG(m^6A)CU], 1 μM), 2OG (10 μM), ascorbic acid (100 μM), diammonium iron(II) sulphate (10 μM) and FTO (100 nM) in 50 mM Tris buffer in H2O at pH 7.5 was prepared in a 2 mL 96-well plate (Greiner) and reaction progression was monitored by MS using an Agilent RapidFire RF360 high throughput system paired with an Agilent quad time of flight (Q-TOF) mass spectrometer. Aliquots from the mixture were periodically subjected to MS analysis (at 1 minute intervals over the first 14 minutes after mixing, then at 23 minutes and 33 minute after mixing). The sample was passed through an Agilent C8 RapidFire cartridge, which isolated the oligonucleotides; the oligonucleotides were then eluted from the cartridge with 600mM octyl ammonium acetate (OAA) (20 %) and acetonitrile (80 %), and injected into the spectrometer. The RapidFire RF360 system was operated using RapidFire RF360 integrated software, and the mass spectrometer was operated using Agilent MassHunter Workstation Data Acquisition software. Signal intensities were quantified as the total ion count, and analysed using RapidFire integrator software (Agilent).

7.16.4. K_M Determination

The concentration of only one component was varied whilst the other concentrations were maintained at those detailed in Table 7.10. Reactions were conducted at 25°C on a 500 µL (for RF-MS) or 25 µL (for MALDI-MS) scale in a 96 well plate in triplicate and against a no enzyme control. Reactions were initiated by combining a mix of 2OG (disodium salt), ascorbic acid and oligonucleotide with enzyme and $(NH_4)_2Fe(SO_4)_2$. For MALDI-MS based assays, reactions were quenched after 30 minutes via the addition of 10 mM EDTA prior to analysis by MALDI-TOF MS. For RF-MS based assays, reactions were monitored real-time without quenching. Percent hydroxylation / demethylation was calculated by comparing the ion intensities of peaks corresponding to (for RF-MS based assay) $[M-H]^{3-}$ and to $[M+OH]^{3-}$, or (for MALDI-MS based assay) $[M+H]^+$ and to $[M-CH_3]^+$. Initial rates of product formation were calculated and plotted using GraphPad Prism, indicating the mean and standard error, before fitting a Michaelis-Menten curve.

Table 7.10: Optimised conditions of FTO for RF-MS and MALDI-MS assay based on the K_m of reagents.

Reagent	MALDI (µM)	RapidFire (µM)
L-ascorbic acid	500	200
2OG	10	1
$(NH_4)_2Fe(SO_4)_2 \cdot 6H_2O$	10	0.5
Substrate	ssRNA-GG(m^6A)CU / 20	15-mer ssRNA / 0.6
FTO	1.3	0.1
Buffer	Tris 25mM pH 7.5	Tris 25mM pH 7.5
Incubation time/T	30min / r.t	10min / r.t
Final Volume	25 µL	25 µL

7.16.5. Inhibition Assays

Compounds 29-35 were synthesised by Miss Shifali Shishodia.

The final reaction concentrations used are indicated in Table 7.11. Inhibitor and enzyme were incubated for 5 minutes prior to the addition of a solution of 2OG, ascorbic acid, Fe(II) and 15-mer oligonucleotide. Reactions were conducted in triplicate at room temperature and quenched after 10 minutes *via* the addition of 10 mM $MgCl_2$. Reactions were analysed by RF-MS; percent hydroxylation was calculated by comparing the ion intensities of peaks corresponding to $[M-H]^{3-}$ to $[M+OH]^{3-}$. The percentage response was then calculated by comparing the reaction mixture to a no inhibitor control. Data were fitted using GraphPad Prism.

Table 7.11: Reaction composition of FTO inhibition assay.

Reagent	RapidFire (μM)
L-ascorbic acid	200
2OG	1
$(NH_4)_2Fe(SO_4)_2 \cdot 6H_2O$	0.5
Substrate	15-mer ssRNA / 0.6
FTO	0.1
Buffer	Tris 25mM pH 7.5
Incubation time/T	10min / r.t
Inhibitor	Varied for IC_{50} determination (100-0.02)
Final Volume	25 μL

7.17. MBL Inhibition assays

Inhibition assays were performed by monitoring the initial rate of **FC5** hydrolysis via fluorescence at a range of inhibitor concentrations. Inhibitors were stored as solids and made fresh either with DMSO or 0.1 M $NaHCO_3$ (for **6a-s** only) to 100 mM stock solutions, these were diluted to appropriate concentrations in the assay buffer. Typically inhibition assays were carried out using black 384 well format μclear® plates (Griener Bio-One) with a final assay volume of 25 μL. Enzyme concentrations were chosen to give a linear rate of **FC5** hydrolysis over the first 5 min of the assay time with an **FC5** concentration of 5 μM. Components were added in the following order and volumes:

Table 7.12: Reaction composition of MBL inhibition assay.

Reagent	Inhibited enzyme volume (µL)	Free enzyme volume (µL)	Background hydrolysis volume (µL)
Inhibitor solution	**1**	**-**	**-**
Assay buffer	14	15	20
5x enzyme solution	5	5	-
25 µM FC5	5	5	5

Unless otherwise stated, the enzymes were incubated with the inhibitor for 10 min prior to initiation of the reaction by the addition of the substrate. The residual activities were calculated using the following formula:

$$\%RA = \frac{100 \times \left(V_{inhibited} - V_{background}\right)}{\left(V_{uninhibited} - V_{background}\right)}$$

7.18. Standard Error Calculation

Non-linear regression fitting of IC_{50} curves was carried out using a three-parameter dose-response curve in GraphPad Prism 5 software. Errors in IC_{50} values are expressed as:

$$\frac{\sigma(\log IC_{50})}{\log IC_{50}} \times IC_{50}$$

7.19. Circular Dichroism (CD) Analyses

CD measurements were carried out using a Chirascan™ CD Spectrometer (Applied Photophysics) equipped with a Peltier temperature-controlled cell holder. Experiments were performed at 25 °C in a 0.1 cm pathlength cuvette using 0.4 mg/mL protein in 10 mM sodium phosphate buffer (pH 8.0). Data were recorded from 185 to 260 nm at 0.5 nm intervals; each data point was averaged for 1 s. Spectra were baseline corrected and smoothed using the Savitzky–Golay filter. Thermal denaturation profiles were produced by monitoring ellipticity [θ] at 222 nm, with data recorded every 1 °C from 25 to 85 °C at a ramp-rate of 1 °C/min. Data

were fitted to a Boltzmann sigmoidal curve using GraphPad Prism® 5.01 to determine protein melting and refolding profiles.

7.20. Computational Modelling of the Ser319Phe FTO Substitution

Energy minimisation modelling was carried out by Dr. Hwanho Choi. In brief, crystal structure of wildtype FTO (PDB ID: 4IDZ) was used to model the effect of the Ser319Phe substitution on protein structure. Bond orders and all hydrogen atoms were regenerated. The protonation states for Asp, Glu, His and Lys residues were assigned followed by geometric optimisation of the positions of the hydrogen atoms by restrained energy minimisation using the OPLS-2005 force-field[2]. Protonation states were predicted for pH 7.2 (range +/- 2.0) using PROPKA[3]. Steric clashes were resolved with convergence of RMSD to 0.3Å. Energy minimisation was then performed using an all atom model with the OPLS-2005 force-field after assigning partial charges and force-field parameters. The GB/SA effective water model[4] was used as the solvation model and non-bonded electrostatic interactions were truncated with a cutoff distance of 20 Å. The convergence process of energy minimisation was terminated after 1000 iteration cycles and 0.05 kcal/mol Å gradient thresholds.

7.21. Nuclear Magnetic Resonance Spectroscopy

Routine Nuclear Magnetic Resonance (NMR) spectra were obtained using either a Bruker AVIII400 HD spectrometer or a Bruker AVANCE 400 spectrometer. Variable temperature NMR experiments were conducted on a Bruker DRX500 spectrometer.

NMR spectroscopy of enzyme samples was conducted with the help of Dr Richard Hopkinson, Dr Martine Abboud and Dr Christopher Lohans. NMR spectra were obtained using either:

− A Bruker AVIII 600 MHz NMR spectrometer equipped with a broad band BB-$^{19}F/^{1}H$ Prodigy N_2 cryoprobe controlled by Topspin 3.2 software (Bruker).

Or

− A Bruker AVIII 700 MHz NMR Spectrometer equipped with an inverse TCI cryoprobe optimised for ^{1}H observation, controlled by Topspin 3 software (Bruker). Data were analysed using Topspin 3.1 software (Bruker).

7.21.1. NMR time course for 2OG Turnover Assays

NMR spectra were recorded using Topspin 3.1 interfaced to a Bruker Avance AVIII 700 MHz instrument, optimized for ^{1}H observation (experiments were carried out in triplicate). Samples (50 µl) were prepared in Eppendorf tubes before transferring to 5 mm NMR tubes (Norell); time course data were then collected over a period of 45 min at 2 min intervals. The solvent deuterium signal was used as an internal lock signal, and the solvent signal was reduced by presaturation during a 2 s recovery delay. Samples were prepared in ammonium formate buffer (AFN), as adopted from a previously reported procedure[5].

Enzyme stocks were in protiated 25 mM Tris buffer pH 7.5, which was diluted with AFN buffer according to Table 7.13.

Table 7.13. NMR conditions for 2OG turnover assay.

	Stock (mM)	Volume (µL)	Final concentration (mM)
Enzyme	0.38	32	0.02
2OG	10	50	1
Ascorbic Aicd	10	50	1
Fe(II)	0.2 in D_2O	50	0.02
m^6A	10	200	4
AFN Buffer	5	118	

7.21.2. NMR (^{1}H-^{13}C-HSQC) Time Course on FTO catalysis Product Degradation

FTO catalysis was monitored using both ^{1}H NMR and the gradient-selected 1 dimensional heteronuclear single quantum correlation (^{1}H-^{13}C-HSQC) method, performed by Miss Shifali Shishoudia. Samples were prepared containing FTO (prepared as reported[1], with a final

concentration of 20 μM), the nucleoside selectively ^{13}C-labelled of the methyl group (400 μM), 2OG, (5 mM), sodium ascorbate (1 mM), ferrous iron (20 μM) in ammonium formate (AFN) buffer in D^{2}O pH* 7.5. The samples were then transferred to 3 mM MATCH NMR tubes (Hilgenberg) and monitored by NMR. ^{1}H analyses employed NOESY water presaturation, while the 1 dimensional heteronuclear single quantum correlation (1D-^{1}H-^{13}C-HSQC) method was derived from the standard 2D ^{1}H-^{13}C-HSQC pulse sequence to remove both the variable t1 period and ^{13}C decoupling during data acquisition. The $1/2J_{CH}$ delays were optimised for 145 Hz.

7.21.3. NMR Time Course for Rhodanine Degradation

NMR experiments were carried out using a Bruker Avance III 700 MHz machine equipped with a TCI inverse cryoprobe or a Bruker Avance III HD 600 MHz spectrometer equipped with a Prodigy cryoprobe at 298 K. Data were analysed using Bruker Topspin 3.5. Processing of spectra was done with a Lorentzian line broadening of 0.3 Hz. Chemical shifts (δ) are given as parts per million (ppm) relative to the residual HDO signal (δ_H 4.70 ppm for ^{1}H NMR).

For rhodanine stability studies, the following conditions were used:

The solutions were buffered in either freshly prepared NH_4HCO_3 (50 mM, pH 7.50) or Tris-d_{11} (50 mM, pH 7.50) both with NaCl (100 mM) in D_2O. **10** stock solution (50 mM in DMSO-d_6) was added to a sample to give a final concentration of 200 μM. When specified, NDM-1 was added to a final concentration of 1 μM. The reaction was followed at 1 hour intervals over 18 hours.

7.22. Organic synthesis

^{1}H and **^{13}C NMR** spectra were recorded either using a Bruker Avance III HD NanoBay 400 spectrometer, Bruker Avance III HD 600 spectrometer, or using a Bruker Avance II 500 with

^{13}C cryoprobe spectrometers. Residual non-deuterated solvent was used as the internal standard for ^{1}H NMR spectra, and a carbon signal of the solvent was used as the internal standard for ^{13}C NMR spectra. Chemical shifts (δ) are given in parts per million (ppm) downfield from tetramethylsilane (TMS). The resonance multiplicity patterns are described as singlet (s), broad singlet (br s), doublet (d), triplet (t), quartet (q), quintet (quin), multiplet (m), or a combination of these. Coupling constants (*J*) are quoted in hertz (Hz) to the nearest 0.5 Hz. Peak assignments were aided by COSY, HMQC, and/or HMBC whenever necessary.

High-resolution mass spectra were recorded either using a Bruker MicroTOF instrument using an ESI source and Time of Flight (TOF) analyser.

IR spectra were recorded on a Bruker Tensor 27 Attenuated Total Reflection (ATR) FT-IR spectrometer, and absorbance bands are quoted in cm^{-1}.

7.22.1. Synthesis and compound characterisation

General Procedure A: Rhodanine-3-acetic acid coupling

A 20-mL microwave vial was charged with aldehyde **1** (**a-s**) and rhodanine-3-acetic acid **2**. Ethanol (10mL) was added followed by piperidine (2 drops). The vial was sealed and submitted to microwave irradiation at 120 °C for 90 min. The solvent was removed *in vacuo* and the crude product purified by column chromatography (DCM/MeOH 9:1) to yield a yellow solid **3** (**a-s**).

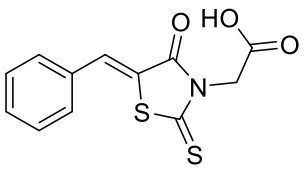
General Procedure B: 1-Methylpiperazine coupling

A solution of **3** (**a-s**) and 1.2 equivalents Bis(2-oxo-3-oxazolidinyl)phosphinic chloride (BOP-Cl) in DCM was cooled to 0 °C using an ice/water bath under an inert atmosphere. Freshly distilled triethylamine (TEA) was added and the solution was kept at 0 °C for 30 min. 1-

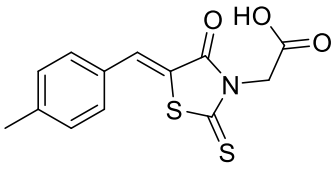
Methylpiperazine (1.2 equiv) was added and the temperature was raised to r.t. after which the reaction was stirred overnight. The crude product, obtained by removal of DCM *in vacuo*, was than purified by flash chromatography (DCM/MeOH 9:1) to give inseparable mixture of *E/Z* isomer of **5 (a-s**) as a yellow solid.

General Procedure C: Rhodanine hydrolysis

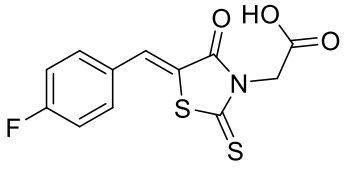
Compounds **5** (**a-s**) was dissolved in 1M NaOH upon which a colour change to orange was observed. The clear reaction mixture was warmed to 60 °C and stirred for 45 min (the reaction colour changes from orange to yellow), subsequent consumption of starting material was observed. The reaction mixture was cooled to r.t. and subsequently carefully acidified with 1M HCl to ~ pH 7. A white precipitate was formed, which was collected by centrifugation (4000g/10min). After removal of the liquid phase the white solid was resuspended in H_2O and again collected by centrifugation. This process was repeated twice more. The obtained solid was dried in a freeze drier overnight. The product was obtained as an inseparable mixture of E/Z isomers as an off-white solid **6** (**a-s**).



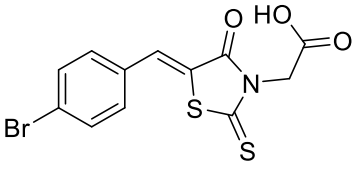
(5-Benzylidene-4-oxo-2-thioxothiazolidin-3-yl)acetic acid 3a: isolated as a yellow solid (85%). **mp** 217-236 °C. $\boldsymbol{R_f}$= 0.60 (CH_2Cl_2 : MeOH, 9 : 1). **IR** ν_{max} (ATR)/cm^{-1}: 3160 (COO-H), 1731 (HOC=O), 1683 (NC=O), 1588 (SC=C). **HRMS** (ESI−): calculated for $C_{12}H_8NO_3S_2$ $[M - H]^-$ requires 277.9951; found 277.9955. **^{1}H NMR** (400 MHz, DMSO-d_6): δ_H 7.89 (s, 1H), 7.68 (d, J = 7.0 Hz, 2H), 7.47-7.63 (m, 3H), 4.68 (s, 2H). **^{13}C NMR** (100 MHz, DMSO-d_6) δ_C 193.77, 167.81, 166.95, 134.11, 133.35, 131.63, 131.22, 130.03, 122.55, 46.14.



(5-(4-Methylbenzylidene)-4-oxo-2-thioxothiazolidin-3-yl)acetic acid 3b: isolated as a yellow solid (79%). **mp** 247-359 °C. R_f = 0.55 (CH_2Cl_2 : MeOH, 9 : 1). **IR** ν_{max} (ATR)/cm^{-1}: 3095 (COO-H), 1699 (HOC=O), 1656 (NC=O), 1594 (SC=C). **HRMS** (ESI−): calculated for $C_{13}H_{10}NO_3S_2$ $[M - H]^-$ requires 292.0108; found 292.0114. **^{1}H NMR** (400 MHz, DMSO-d_6) δ_H 7.70 (s, 1H), 7.53 (d, J = 9.0 Hz, 2H), 7.23 (d, J = 9.0 Hz, 2H), 4.71 (s, 2H), 2.55 (s, 3H). **^{13}C NMR** (100 MHz, DMSO-d_6) δ_C 193.41, 166.42, 165.76, 163.00, 134.14, 132.93, 132.13, 125.89, 123.23, 55.81, 45.88.

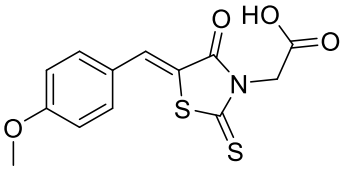


(5-(4-Fluorobenzylidene)-4-oxo-2-thioxothiazolidin-3-yl)acetic acid 3c: isolated as a yellow solid (82%). **mp** 225-235 °C. R_f = 0.55 (CH_2Cl_2 : MeOH, 9 : 1). **IR** ν_{max} (ATR)/cm^{-1}: 3172 (COO-H), 1732 (HOC=O), 1676 (NC=O), 1581 (SC=C). **HRMS** (ESI−): calculated for $C_{12}H_8FNO_3S_2$ $[M]^-$ requires 295.9857; found 295.9861. **^{1}H NMR** (400 MHz, DMSO-d_6) δ_H 7.91 (s, 1 H), 7.77 (dd, J = 8.7, 5.0 Hz, 2H), 7.43 (t, J = 8.5 Hz, 2H), 4.68 (s, 2H). **^{13}C NMR** (100 MHz, DMSO-d_6) δ_C 193.59, 167.70, 166.90, 163.75 (d, J = 251.5 Hz), 133.79 (d, J = 9.0 Hz), 133.00, 130.07 (d, J = 3.0 Hz), 122.23, 117.24 (d, J = 22.0 Hz), 46.14.

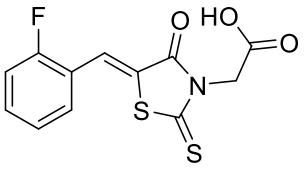


(5-(4-Bromobenzylidene)-4-oxo-2-thioxothiazolidin-3-yl)acetic acid 3d: isolated as a yellow solid (84%). **mp** 239-253 °C. R_f = 0.50 (CH_2Cl_2 : MeOH, 9 : 1). **IR** ν_{max} (ATR)/cm^{-1}: 3090 (COO-H), 1709 (HOC=O), 1589 (NC=O), 1587 (SC=C). **HRMS** (ESI−): calculated for $C_{12}H_7BrNO_3S_2$ $[M - H]^-$ requires 355.9056; found 355.9062. **^{1}H NMR** (400 MHz, DMSO-d_6) δ_H 7.85 (s, 1H), 7.76 (d, J = 8.5 Hz, 2H), 7.60 (d, J = 8.5 Hz, 2H), 4.72 (s, 2H); **^{13}C NMR** (100

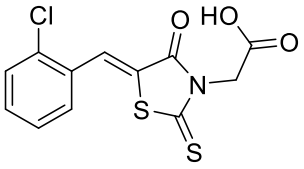
MHz, DMSO-d_6) δ_C 193.38, 167.73, 166.81, 133.00, 132.94, 132.48, 125.37, 123.17, 45.75, 44.14.



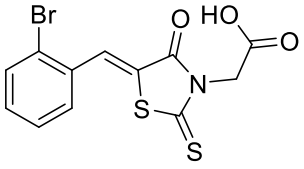
(5-(4-Methoxybenzylidene)-4-oxo-2-thioxothiazolidin-3-yl)acetic acid 3e: isolated as a yellow solid (80%). **mp** 187-243 °C. R_f = 0.50 (CH_2Cl_2 : MeOH, 9 : 1). **IR** ν_{max} (ATR)/cm^{-1}: 2963 (COO-H), 1679 (HOC=O), 1586 (NC=O), 1564 (SC=C). **HRMS** (ESI−): calculated for $C_{13}H_{10}NO_4S_2$ $[M - H]^-$ requires 308.0057; found 308.0062. **^{1}H NMR** (400 MHz, DMSO-d_6) δ_H 7.82 (s, 1H), 7.63 (d, J = 9.0 Hz, 2H), 7.12 (d, J = 9.0 Hz, 2H), 4.68 (s, 2H), 3.85 (s, 3H). **^{13}C NMR** (100 MHz, DMSO-d_6) δ_C 193.54 167.86, 166.99, 162.15, 134.33, 133.53, 125.89, 119.10, 115.66, 56.08, 45.96.



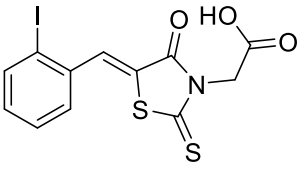
(5-(2-Fluorobenzylidene)-4-oxo-2-thioxothiazolidin-3-yl)acetic acid 3f: isolated as an orange solid (76%). **mp** 230-249 °C. R_f = 0.50 (CH_2Cl_2 : MeOH, 9 : 1). **IR** ν_{max} (ATR)/cm^{-1}: 2993 (COO-H), 1713 (HOC=O), 1604 (NC=O), 1397 (SC=C). **HRMS** (ESI−): calculated for $C_{12}H_7FNO_3S_2$ $[M - H]^-$ requires 295.9857; found 295.9860. **^{1}H NMR** (400 MHz, DMSO-d_6) δ_H 7.82 (s, 1 H), 7.60 (t, J = 7.0 Hz, 2H), 7.37-7.47 (m, 2H), 4.69 (s, 2H). **^{13}C NMR** (100 MHz, DMSO-d_6) δ_C 193.46, 167.70, 166.71, 161.12 (d, J = 253.0 Hz), 134.02 (d, J = 9.0 Hz), 130.19, 126.15 (d, J = 3.5 Hz), 125.72-124.28 (m), 121.19 (d, J = 12.0 Hz), 116.84 (d, J = 21.5 Hz), 46.09.



(5-(2-Chlorobenzylidene)-4-oxo-2-thioxothiazolidin-3-yl)acetic acid 3g: isolated as a yellow solid (77%). **mp** 234-237 °C. R_f = 0.55 (CH_2Cl_2 : MeOH, 9 : 1). **IR** ν_{max} (ATR)/cm^{-1}: 2926 (COO-H), 1708 (HOC=O), 1594 (NC=O), 1433 (SC=C). **HRMS** (ESI−): calcualted for $C_{12}H_7ClNO_3S_2$ $[M - H]^-$ requires 311.9561; found 311.9567. **^{1}H NMR** (400 MHz, DMSO-d_6) δ_H 7.95 (s, 1 H), 7.66 (dd, J = 6.0, 3.5 Hz, 1H), 7.58-7.62 (m, 1H), 7.52-7.57 (m, 1H), 4.72 (s, 2H). **^{13}C NMR** (100 MHz, DMSO-d_6) δ_C 193.54, 167.70, 166.58, 135.38, 132.99, 131.16, 130.99, 130.02, 128.83, 125.99, 45.86.

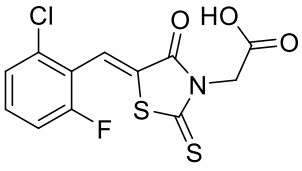


(5-(2-Bromobenzylidene)-4-oxo-2-thioxothiazolidin-3-yl)acetic acid 3h: isolated as a yellow solid (83%). **mp** 235-249 °C. R_f = 0.55 (CH_2Cl_2 : MeOH, 9 : 1). **IR** ν_{max} (ATR)/cm^{-1}: 3028 (COO-H), 1706 (HOC=O), 1594 (NC=O), 1429 (SC=C). **HRMS** (ESI−) calculated for $C_{12}H_7BrNO_3S_2$ $[M - H]^-$ requires 355.9056; found 355.9060. **^{1}H NMR** (400 MHz, DMSO-d_6) δ_H 8.00 (s, 1H), 7.57 (d, J = 8.0 Hz, 1H), 7.33 (m, 3H), 4.27 (s, 2H). **^{13}C NMR** (100 MHz, DMSO-d_6) δ_C 193.20, 167.94, 165.43, 141.02, 137.48, 136.99, 130.14, 130.55, 129.98, 126.23, 105.01, 45.73.

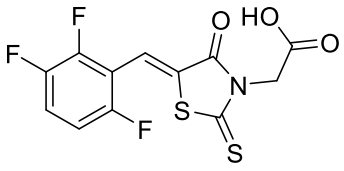


(5-(2-Iodobenzylidene)-4-oxo-2-thioxothiazolidin-3-yl)acetic acid 3i: isolated as a yellow solid (75%). **mp** 229-240 °C. R_f = 0.55 (CH_2Cl_2 : MeOH, 9 : 1). **IR** ν_{max} (ATR)/cm^{-1}: 2938 (COO-H), 1703 (HOC=O), 1588 (NC=O), 1393 (SC=C). **HRMS** (ESI−): calculated for $C_{12}H_7NO_3S_2$ $[M - H]^-$ requires 403.8918; found 403.8925. **^{1}H NMR** (400 MHz, DMSO-d_6) δ_H 8.06 (d, J = 8.0 Hz, 1H), 7.82 (s, 1H), 7.51-7.62 (m, 2H), 7.20-7.28 (m, 1H), 4.71 (s, 2H). **^{13}C NMR** (100 MHz,

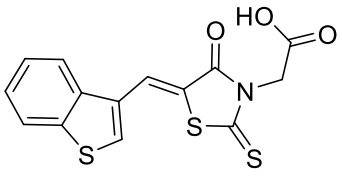
DMSO-d_6) δ_C 193.69, 167.74, 166.43, 140.73, 136.71, 136.16, 132.87, 129.83, 129.49, 125.73, 104.00, 45.90.



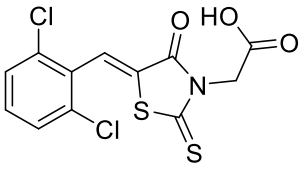
(5-(2-Chloro-6-fluorobenzylidene)-4-oxo-2-thioxothiazolidin-3-yl)acetic acid 3j: isolated as a yellow solid (84%). **mp** 237-250 °C. R_f = 0.50 (CH_2Cl_2 : MeOH, 9 : 1). **IR** ν_{max} (ATR)/cm^{-1}: 3026 (COO-H), 1717 (HOC=O), 1598 (NC=O), 1393 (SC=C). **HRMS** (ESI−): calculated for $C_{12}H_6ClFNO_3S_2$ $[M - H]^-$ requires 329.9467; found 329.9473. **^{1}H NMR** (400 MHz, DMSO-d_6) δ_H 13.54 (br s, 1H), 7.79 (s, 1H), 7.56-7.66 (m, 1H), 7.48-7.55 (m, 1H), 7.41 (t, J = 9.5 Hz, 1H), 4.74 (s, 2H). **^{13}C NMR** (100 MHz, DMSO-d_6) δ_C 193.38 (d, J = 6.5 Hz), 167.70, 165.99, 159.44 (d, J = 253.0 Hz), 134.86 (d, J = 5.0 Hz), 133.84 (d, J = 10.0 Hz), 129.74 (d, J = 1.5 Hz), 126.83 (d, J = 3.0 Hz), 125.18, 120.22 (d, J = 18.0 Hz), 115.94 (d, J = 22.0 Hz), 45.63.



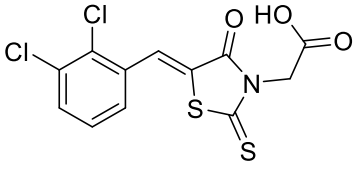
(4-Oxo-2-thioxo-5-(2,3,6-trifluorobenzylidene)thiazolidin-3-yl)acetic acid 3k: isolated as an orange solid (78%). **mp** 195-228 °C. R_f = 0.50 (CH_2Cl_2 : MeOH, 9 : 1). **IR** ν_{max} (ATR)/cm^{-1}: 3212 (COO-H), 1709 (HOC=O), 1681 (NC=O), 1602 (SC=C). **HRMS** (ESI−): calculated for $C_{12}H_5F_3NO_3S_2$ $[M - H]^-$ requires 331.9668; found 331.9669. **^{1}H NMR** (400 MHz, DMSO-d_6) δ_H 7.72 (s, 1H), 7.76 (m, 1H), 7.38 (m, 1H), 4.75 (s, 2H). **^{13}C NMR** (100 MHz, DMSO-d_6) δ_C 193.31, 167.71, 166.22, 155.25 (d, J = 249.5 Hz), 148.96-146.01 (m), 148.48-145.33 (m), 130.05, 120.83 (dd, J = 19.5, 10.5 Hz), 119.90, 112.91 (dd, J = 24.5, 4.0 Hz), 112.75-112.28 (m), 46.23.



(5-(Benzo[b]thiophen-3-ylmethylene)-4-oxo-2-thioxothiazolidin-3-yl)acetic acid 3l: isolated as a yellow solid (76%). **mp** 242-266 °C. R_f = 0.60 (CH_2Cl_2 : MeOH, 9 : 1). **IR** ν_{max} (ATR)/cm^{-1}: 3132 (COO-H), 1703 (HOC=O), 1702 (NC=O), 1587 (SC=C). **HRMS** (ESI−): calculated for $C_{14}H_8NO_4S_2$ $[M - H]^-$ requires 333.9672; found 333.9678. **^{1}H NMR** (400 MHz, DMSO-d_6) δ_H 7.95 (s, 1H), 7.49-7.71 (m, 4H), 7.55 (s, 1H), 4.72 (s, 2H). **^{13}C NMR** (100 MHz, DMSO-d_6) δ_C 193.54, 167.70, 166.58, 135.38, 132.99, 131.16, 130.99, 130.02, 128.83, 125.99, 45.86.

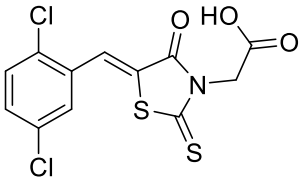


(5-(2,6-Dichlorobenzylidene)-4-oxo-2-thioxothiazolidin-3-yl)acetic acid 3m: isolated as a yellow solid (83%). **mp** 235-237 °C. R_f = 0.50 (CH_2Cl_2 : MeOH, 9 : 1). **IR** ν_{max} (ATR)/cm^{-1}: 2931 (COO-H), 1710 (HOC=O), 1600 (NC=O), 1442 (SC=C). **HRMS** (ESI+): calculated for $C_{12}H_7Cl_2NO_3S_2Na$ $[M + Na]^+$ requires 369.9137; found 369.9137. **^{1}H NMR** (400 MHz, DMSO-d_6) δ_H 7.86 (s, 1H), 7.71-7.60 (m, 2H), 7.54 (ddd, J = 9.0, 7.3, 0.7 Hz, 1H), 4.68 (s, 3H). **^{13}C NMR** (100 MHz, DMSO-d_6) δ_C 193.23, 167.66, 165.45, 133.43, 132.74, 131.37, 131.20, 129.41, 129.32, 46.27.

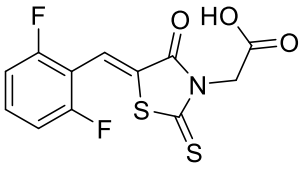


(5-(2,3-Dichlorobenzylidene)-4-oxo-2-thioxothiazolidin-3-yl)acetic acid 3n: isolated as a yellow solid (81%). **mp** 236-237 °C. R_f = 0.50 (CH_2Cl_2 : MeOH, 9 : 1). **IR** ν_{max} (ATR)/cm^{-1}: 2930 (COO-H), 1708 (HOC=O), 1598 (NC=O), 1440 (SC=C). **HRMS** (ESI−): calculated for $C_{12}H_6Cl_2NO_3S_2$ $[M - H]^-$ requires 345.9172; found 345.9167. **^{1}H NMR** (400 MHz, DMSO-d_6) δ_H 7.83 (s, 1H), 7.70 (d, J = 8.5 Hz, 1H), 7.61 (dd, J = 8.5, 2.5 Hz, 1H), 7.55 (d, J = 2.5 Hz,

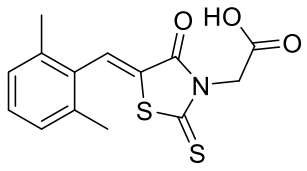
1H), 4.69 (s, 2H). **^{13}C NMR** (100 MHz, DMSO-d_6) δ_C 193.01, 167.63, 166.34, 133.67, 133.16, 132.52, 132.38, 129.02, 127.81, 127.47, 46.10.



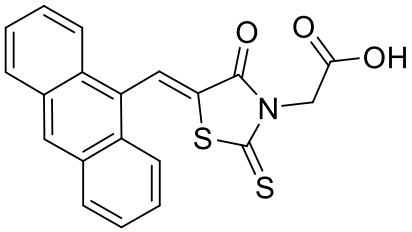
(5-(2,5-Dichlorobenzylidene)-4-oxo-2-thioxothiazolidin-3-yl)acetic acid 3o: isolated as a yellow solid (80%). **mp** 237-238 °C. $\boldsymbol{R_f}$ = 0.50 (CH_2Cl_2 : MeOH, 9 : 1). **IR** ν_{max} (ATR)/cm^{-1}: 2933 (COO-H), 1705 (HOC=O), 1595 (NC=O), 1447 (SC=C). **HRMS** (ESI−): calculated for $C_{12}H_6Cl_2NO_3S_2$ $[M - H]^-$ requires 345.9172; found 345.9167. **^{1}H NMR** (400 MHz, DMSO-d_6) δ_H 13.59 (br s, 1H), 7.92 (s, 1H), 7.78 (dd, J = 7.5, 2.0 Hz, 1H), 7.59-7.50 (m, 2H), 4.75 (s, 2H). **^{13}C NMR** (100 MHz, DMSO-d_6) δ_C 193.35, 167.65, 166.35, 133.68, 133.59, 132.97, 132.90, 129.57, 128.84, 128.51, 127.27, 45.56.



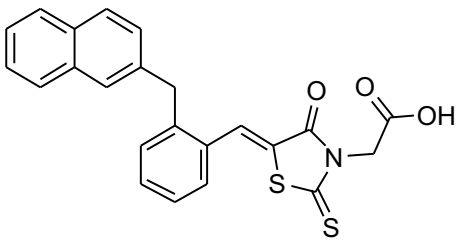
(5-(2,6-Difluorobenzylidene)-4-oxo-2-thioxothiazolidin-3-yl)acetic acid 3p: isolated as an orange solid (79%). **mp** 238-240 °C. $\boldsymbol{R_f}$ = 0.55 (CH_2Cl_2 : MeOH, 9 : 1). **IR** ν_{max} (ATR)/cm^{-1}: 2924 (COO-H), 1700 (HOC=O), 1575 (NC=O), 1438 (SC=C). **HRMS** (ESI−): calculated for $C_{12}H_6F_2NO_3S_2$ $[M - H]^-$ requires 313.9763; found 313.9760. **^{1}H NMR** (400 MHz, DMSO-d_6) δ_H 7.71 (s, 1H), 7.66 (ddd, J = 8.5, 6.5, 2.0 Hz, 1H), 7.30 (t, J = 9.0 Hz, 2H). **^{13}C NMR** (100 MHz, DMSO-d_6) δ_C 193.58, 167.74, 166.32, 159.98 (d, J = 253.0 Hz), 158.60 (d, J = 252.5 Hz), 134.55 (t, J = 11.0 Hz), 128.64, 121.09, 113.37-112.76 (m), 110.69 (t, J = 17.5 Hz), 45.92.



(5-(2,6-Dimethylbenzylidene)-4-oxo-2-thioxothiazolidin-3-yl)acetic acid 3q: isolated as a pale yellow solid (82%). **mp** 240-242 °C. R_f = 0.55 (CH_2Cl_2 : MeOH, 9 : 1). **IR** ν_{max} (ATR)/cm^{-1}: 2932 (COO-H), 1710 (HOC=O), 1588 (NC=O), 1449 (SC=C). **HRMS** (ESI−): calculated for $C_{14}H_{12}NO_3S_2$ $[M - H]^-$ requires 306.0264; found 306.0261. **^{1}H NMR** (400 MHz, DMSO-d_6) δ_H 13.53 (br s, 1H), 8.03 (s, 1H), 7.25 (m, 1H), 7.14 (d, J = 7.5 Hz, 2H), 4.73 (s, 2H), 2.22 (s, 6H). **^{13}C NMR** (100 MHz, DMSO-d_6) δ_C 194.17, 167.79, 165.13, 135.69, 135.63, 133.39, 129.64, 129.03, 128.33, 45.54, 20.17.

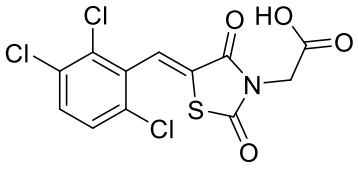


2-(5-(anthracen-9-ylmethylene)-4-oxo-2-thioxothiazolidin-3-yl)acetic acid 3r: isolated as an orange solid (90%). **mp** 240-242 °C. R_f = 0.55 (CH_2Cl_2 : MeOH, 9 : 1). **IR** ν_{max} (ATR)/cm^{-1}: 2967 (COO-H), 1707 (HOC=O), 1611(NC=O), 1401 (SC=C). **^{1}H NMR** (400 MHz, DMSO-d_6) δ_H 8.81 (s, 2 H), 8.22 (d, J=7.65 Hz, 2 H), 8.05 (d, J=8.55 Hz, 2 H), 7.59 - 7.71 (m, 5 H), 4.74 (s, 2 H) ppm. **^{13}C NMR** (101 MHz, DMSO-d_6) δ_C 194.0, 167.8, 132.3, 131.5, 131.2, 129.7, 128.5, 127.9, 127.4, 126.4, 125.4.

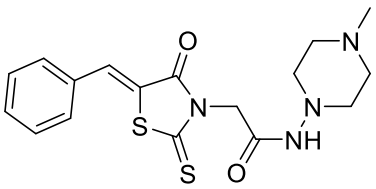


2-(5-(2-(naphthalen-2-ylmethyl)benzylidene)-4-oxo-2-thioxothiazolidin-3-yl)acetic acid 3s: isolated as an off white solid (88%). **mp** 251-259 °C. R_f = 0.55 (CH_2Cl_2 : MeOH, 9 : 1). **IR** ν_{max} (ATR)/cm^{-1}: 2899 (COO-H), 1721 (HOC=O), 1600 (NC=O), 1476 (SC=C). **HRMS** (ESI−): calculated for $C_{23}H_{16}NO_3S_2$ $[M - H]^-$ requires 418.0577; found 418.0570. **^{1}H NMR** (400 MHz, DMSO-d_6) δ_H 13.46 (s, 1H), 8.09 (s, 1H), 7.88 – 7.74 (m, 3H), 7.64 – 7.26 (m, 8H), 4.69 (s, 2H), 4.36 (s, 2H). **^{13}C NMR** (101 MHz,

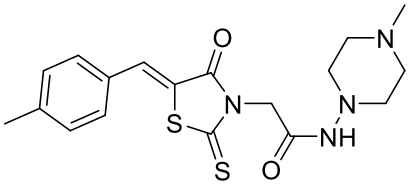
DMSO-d_6) δ_C 193.55, 167.21, 165.85, 141.94, 137.69, 133.06, 131.96, 131.79, 131.62, 131.43, 131.28, 128.28, 128.12, 127.66, 127.48, 127.39, 127.15, 126.59, 126.22, 125.59, 123.80, 44.95.



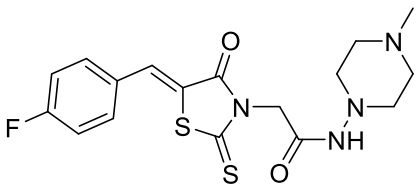
2-(2,4-Dioxo-5-(2,3,6-trichlorobenzylidene)thiazolidin-3-yl)acetic acid 9: isolated as a pale yellow solid (82%). **mp** 150-153 °C. R_f = 0.50 (CH_2Cl_2 : MeOH, 9 : 1). **IR** ν_{max} (ATR)/cm^{-1}: 2947 (COO-H), 1711 (HOC=O), 1600 (NC=O), 1458 (SC=C). **HRMS** (ESI+): calculated for $C_{12}H_5Cl_3NO_4S$ $[M - H]^-$ requires 363.9010; found 363.9008. **^{1}H NMR** (400 MHz, CD_3OD) δ_H 7.85 (s, 1H), 7.64 (dd, J = 9.0, 0.7 Hz, 1H), 7.52 (d, J = 9.0 Hz, 1H), 4.33 (s, 2H). **^{13}C NMR** (100 MHz, CD_3OD) δ_C 169.69, 167.53, 165.25, 134.62, 133.46, 133.30, 133.20, 132.90, 132.24, 130.50, 130.02, 43.21.



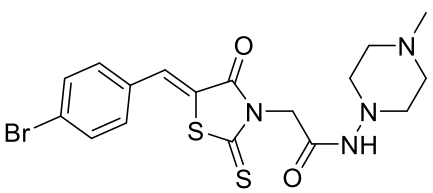
(5-Benzylidene-4-oxo-2-thioxothiazolidin-3-yl)-N-(4-methylpiperazin-1-yl)acetamide 5a: isolated as a yellow solid (35%). **mp** >255 °C (dec.). R_f = 0.40 (CH_2Cl_2 : MeOH, 9 : 1). **IR** ν_{max} (ATR)/cm^{-1}: 3215 (NH), 1713 (HNC=O), 1671 (NC=O), 1597 (SC=C). **HRMS** (ESI+): calculated for $C_{17}H_{21}N_4O_2S_2$ $[M + H]^+$ requires 377.1100; found 377.1100. **^{1}H NMR** (400 MHz, $CDCl_3$) δ_H 7.76 (s, 1H), 7.53 – 7.41 (m, 5H), 4.94 (s, 2H), 3.61 – 3.39 (m, 5H), 1.69 (5H). **^{13}C NMR** (100 MHz, $CDCl_3$) δ_C 193.80, 167.58, 162.23, 133.71, 133.43, 130.85, 130.71, 129.42, 123.12, 46.18, 45.07, 43.63, 26.42, 25.48, 24.49.



(5-(4-Methylbenzylidene)-4-oxo-2-thioxothiazolidin-3-yl)-N-(4-methylpiperazin-1-yl)acetamide 5b: isolated as a yellow solid (37%). **mp** >248 °C (dec.). R_f = 0.40 (CH_2Cl_2 : MeOH, 9 : 1). **IR** ν_{max} (ATR)/cm^{-1}: 3209 (NH), 1712 (HNC=O), 1670 (NC=O), 1595 (SC=C). **HRMS** (ESI+): calculated for $C_{18}H_{23}N_4O_2S_2$ $[M + H]^+$ requires 391.1257; found 391.1256. **^{1}H NMR** (600 MHz, DMSO-d$_6$) δ_H 9.07 (s, 1H), 7.84 (s, 1H), 7.58 (d, J = 8.0 Hz, 2H), 7.40 (d, J = 8.0 Hz, 2H), 4.93 (s, 2H), 3.20-2.57 (m, 8H), 2.39 (s, 3H), 2.22 (s, 3H). **^{13}C NMR** (150 MHz, DMSO-d$_6$) δ_C 193.21, 167.03, 166.66, 141.70, 133.77, 133.59, 130.83, 130.78, 130.19, 129.29, 129.09, 54.97, 54.18, 45.18, 44.91, 21.16.

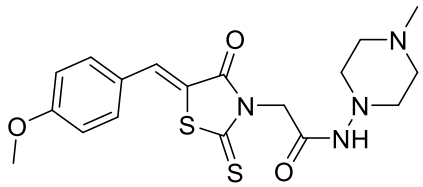


(4-Fluorobenzylidene)-4-oxo-2-thioxothiazolidin-3-yl)-N-(4-methylpiperazin-1-yl)acetamide 5c: isolated as an orange solid (35%). **mp** >266 °C (dec.). R_f = 0.35 (CH_2Cl_2 : MeOH, 9 : 1). **IR** ν_{max} (ATR)/cm^{-1}: 3213 (NH), 1712 (HNC=O), 1669 (NC=O), 1585 (SC=C). **HRMS** (ESI+): calculated for $C_{17}H_{20}FN_4O_2S_2$ $[M + H]^+$ requires 395.1006; found 395.1004. **^{1}H NMR** (600 MHz, DMSO-d$_6$) δ_H 9.06 (s, 1H), 7.89 (s, 1H), 7.79-7.75 (m, 2H), 7.46-7.40 (m, 2H), 4.93 (s, 2H), 3.12-2.30 (m, 8H), 2.18 (s, 3H). **^{13}C NMR** (150 MHz, DMSO-d$_6$) δ_C 193.83, 167.08, 166.56, 162.56 (d, J = 105.0 Hz), 133.73 (d, J = 9.0 Hz), 132.84, 130.11, 122.42 (d, J = 2.5 Hz), 117.25 (d, J = 22.0 Hz), 55.64, 54.80, 45.87, 45.45.

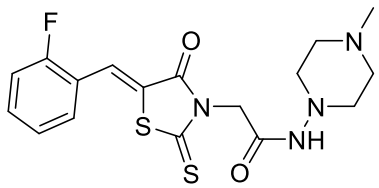


(5-(4-Bromobenzylidene)-4-oxo-2-thioxothiazolidin-3-yl)-N-(4-methylpiperazin-1-yl)acetamide 5d: isolated as a pale yellow solid (36%). **mp** >267 °C (dec.). R_f = 0.35 (CH_2Cl_2 : MeOH, 9 : 1). **IR** ν_{max} (ATR)/cm^{-1}: 3212 (NH), 1712 (HNC=O), 1670 (NC=O), 1598

(SC=C). **HRMS** (ESI+): calculated for $C_{17}H_{20}BrN_4O_2S_2$ $[M + H]^+$ requires 455.0206; found 455.0202. **^{1}H NMR** (600 MHz, $CDCl_3$) δ_H 7.69 (s, 1H), 7.62 (d, J = 8.5 Hz, 2H), 7.37 (d, J = 8.5 Hz, 2H), 6.36 (s, 1H), 5.08 (s, 2H), 3.27 – 2.55 (m, 8H), 2.32 (s, 3H). **^{13}C NMR** (150 MHz, $CDCl_3$) δ_C 193.10, 167.54, 166.99, 132.82, 132.36, 132.25, 131.94, 125.61, 123.99, 56.56, 54.62, 45.77, 45.05.

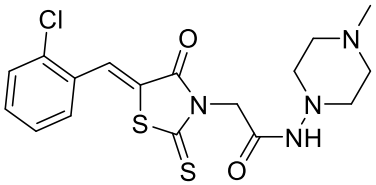


(5-(4-Methoxybenzylidene)-4-oxo-2-thioxothiazolidin-3-yl)-N-(4-methylpiperazin-1-yl)acetamide 5e: isolated as a yellow solid (31%). **mp** >253 °C (dec.). R_f = 0.35 (CH_2Cl_2 : MeOH, 9 : 1). **IR** ν_{max} (ATR)/cm^{-1}: 3215 (NH), 1708 (HNC=O), 1667 (NC=O), 1583 (SC=C). **HRMS** (ESI+): calculated for $C_{18}H_{23}N_4O_3S_2$ $[M + H]^+$ requires 407.1206; found 407.1201. **^{1}H NMR** (600 MHz, CD_2Cl_2) δ_H 7.71 (s, 1H), 7.49 (d, J = 9.0 Hz, 2H), 7.01 (d, J = 9.0 Hz, 2H), 5.03 (s, 2H), 3.86 (s, 3H), 3.11-2.58 (m, 8H), 2.24 (s, 3H). **^{13}C NMR** (150 MHz, CD_2Cl_2) δ_C 194.34, 168.03, 167.38, 162.43, 134.06, 133.29, 126.51, 120.37, 115.44, 56.65, 56.10, 55.09, 45.96, 45.53.

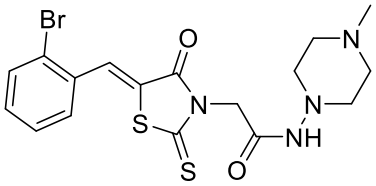


(5-(2-Fluorobenzylidene)-4-oxo-2-thioxothiazolidin-3-yl)-N-(4-methylpiperazin-1-yl)acetamide 5f: isolated as an orange solid (31%). **mp** >269 °C (dec.). R_f = 0.35 (CH_2Cl_2 : MeOH, 9 : 1). **IR** ν_{max} (ATR)/cm^{-1}: 3211 (NH), 1717 (HNC=O), 1670 (NC=O), 1605 (SC=C). **HRMS** (ESI+): calculated for $C_{17}H_{20}FN_4O_2S_2$ $[M + H]^+$ requires 395.1006; found 395.1003. **^{1}H NMR** (600 MHz, DMSO-d_6) δ_H 9.13 (s, 1H), 7.81 (s, 1H), 7.61 (ddt, J = 10.5, 6.0, 1.5 Hz, 2H), 7.42 (td, J = 8.5, 8.0, 3.0 Hz, 2H), 4.95 (s, 2H), 3.06-2.57 (m, 8H), 2.27 (s, 3H). **^{13}C NMR** (150 MHz, DMSO-d_6) δ_C 193.22, 167.30, 166.08, 160.63 (d, J = 253.0 Hz), 133.52 (d, J = 9.0

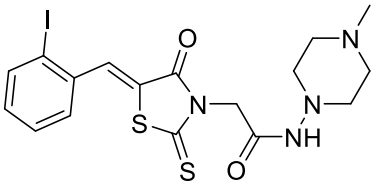
Hz), 129.69, 125.68, 124.84 (d, J = 10.5 Hz), 124.42 (d, J = 6.0 Hz), 120.75 (d, J = 12.0 Hz), 116.38 (d, J = 21.5 Hz), 54.58, 53.84, 46.28, 45.01.



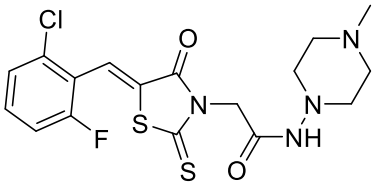
(5-(2-Chlorobenzylidene)-4-oxo-2-thioxothiazolidin-3-yl)-N-(4-methylpiperazin-1-yl)acetamide 5g: isolated as a yellow solid (36%). **mp** >267 °C (dec.). R_f = 0.35 (CH_2Cl_2 : MeOH, 9 : 1). **IR** ν_{max} (ATR)/cm^{-1}: 3219 (NH), 1721 (HNC=O), 1672 (NC=O), 1600 (SC=C). **HRMS** (ESI+): calculated for $C_{17}H_{20}ClN_4O_2S_2$ $[M + H]^+$ requires 411.0711; found 411.0707. **^{1}H NMR** (600 MHz, DMSO-d$_6$) δ_H 9.10 (s, 1H), 7.96 (s, 1H), 7.71-7.66 (m, 1H), 7.65-7.60 (m, 1H), 7.59-7.53 (m, 2H), 4.94 (s, 2H), 3.01-2.63 (m, 8H), 2.21 (s, 3H). **^{13}C NMR** (150 MHz, DMSO-d$_6$) δ_C 193.78, 166.79, 166.51, 135.27, 132.95, 131.24, 130.99, 129.99, 128.87, 128.58, 126.27, 55.49, 54.68, 45.70, 45.49.



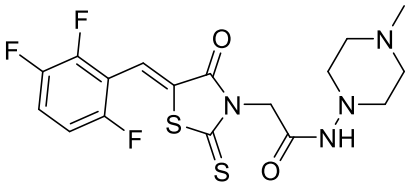
(5-(2-Bromobenzylidene)-4-oxo-2-thioxothiazolidin-3-yl)-N-(4-methylpiperazin-1-yl)acetamide 5h: isolated as a pale yellow solid (32%). **mp** >259 °C (dec.). R_f = 0.40 (CH_2Cl_2 : MeOH, 9 : 1). **IR** ν_{max} (ATR)/cm^{-1}: 3210 (NH), 1710 (HNC=O), 1659 (NC=O), 1591 (SC=C). **HRMS** (ESI+): calculated for $C_{17}H_{20}BrN_4O_2S_2$ $[M + H]^+$ requires 455.0206; found 455.0204. **^{1}H NMR** (600 MHz, DMSO-d$_6$) δ_H 9.64 (s, 0H), 7.66 (d, J = 5.0 Hz, 1H), 7.60 (d, J = 7.4 Hz, 1H), 7.40 – 7.31 (m, 2H), 7.22 (d, J = 6.6 Hz, 1H), 4.77 (s, 1H), 3.46 – 2.62 (m, 11H), 2.26 (s, 2H). **^{13}C NMR** (150 MHz, DMSO-d$_6$) δ_C 193.32, 166.18, 162.07, 133.74, 132.37, 130.85, 129.55, 128.85, 125.84, 125.67, 125.62, 51.92, 50.66, 45.30, 44.83.



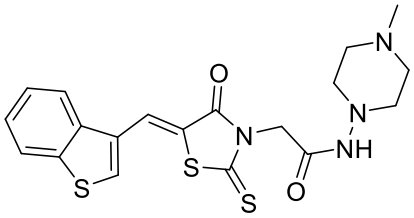
(5-(2-Iodobenzylidene)-4-oxo-2-thioxothiazolidin-3-yl)-N-(4-methylpiperazin-1-yl)acetamide 5i: isolated as a yellow solid (39%). **mp** >250 °C (dec.). R_f = 0.40 (CH_2Cl_2 : MeOH, 9 : 1). **IR** ν_{max} (ATR)/cm^{-1}: 3215 (NH), 1711 (HNC=O), 1672 (NC=O), 1592 (SC=C). **HRMS** (ESI+): calculated for $C_{17}H_{20}IN_4O_2S_2$ $[M + H]^+$ requires 503.0067; found 503.0062. **^{1}H NMR** (600 MHz, DMSO-d_6) δ_H 9.08 (s, 1H), 8.08 (t, J = 7.5 Hz, 1H), 7.76 (s, 1H), 7.64-7.51 (m, 1H), 7.26 (m, 2H), 4.94 (s, 2H), 3.02-2.58 (m, 8H), 2.18 (s, 3H). **^{13}C NMR** (150 MHz, DMSO-d_6) δ_C 193.70, 166.83, 166.53, 140.68, 136.43, 135.35, 132.60, 129.81, 129.39, 126.64, 103.69, 55.63, 54.79, 45.86, 45.49.



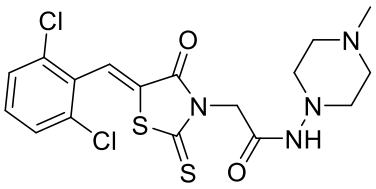
(5-(2-Chloro-6-fluorobenzylidene)-4-oxo-2-thioxothiazolidin-3-yl)-N-(4-methylpiperazin-1-yl)acetamide 5j: isolated as a yellow solid (35%). **mp** >261 °C (dec.). R_f = 0.35 (CH_2Cl_2 : MeOH, 9 : 1). **IR** ν_{max} (ATR)/cm^{-1}: 3211 (NH), 1723 (HNC=O), 1675 (NC=O), 1599 (SC=C). **HRMS** (ESI+): calculated for $C_{17}H_{19}ClFN_4O_2S_2$ $[M + H]^+$ requires 429.0616; found 429.0610. **^{1}H NMR** (600 MHz, DMSO-d_6) δ_H 9.09 (s, 1H), 7.78 (s, 1H), 7.59-7.65 (m, 1H), 7.54 (d, J = 8.0 Hz, 1H), 7.45 (t, J = 9.0 Hz, 1H), 4.92 (s, 2H), 2.91 (br s, 4H), 2.71 (br s, 4H), 2.18 (s, 3H). **^{13}C NMR** (150 MHz, DMSO-d_6) δ_C 193.16 (d, J = 6.2 Hz), 166.03, 165.74, 160.75 (d, J = 287.4 Hz), 134.27 (d, J = 5.0 Hz), 133.32 (d, J = 10.1 Hz), 129.67, 126.37 (d, J = 3.1 Hz), 124.26, 119.88 (d, J = 18.0 Hz), 115.50 (d, J = 22.1 Hz), 55.13, 54.28, 45.35, 45.13.



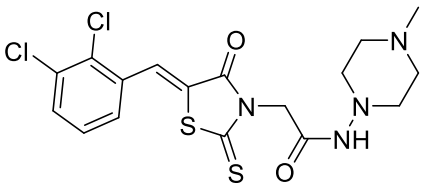
(4-Methylpiperazin-1-yl)-2-(4-oxo-2-thioxo-5-(2,3,6-trifluorobenzylidene)thiazolidin-3-yl)acetamide 5k: isolated as an orange solid (35%). **mp** >259 °C (dec.). R_f = 0.35 (CH_2Cl_2 : MeOH, 9 : 1). **IR** ν_{max} (ATR)/cm^{-1}: 3209 (NH), 1717 (HNC=O), 1668 (NC=O), 1596 (SC=C). **HRMS** (ESI+): calculated for $C_{17}H_{18}F_3N_4O_2S_2$ $[M + H]^+$ requires 431.0818; found 431.0815. **^{1}H NMR** (600 MHz, DMSO-d_6) δ_H 9.10 (s, 1H), 7.75 (qd, J = 9.5, 5.0 Hz, 1H), 7.68 (s, 1H), 7.37 (tdd, J = 9.5, 4.0, 2.0 Hz, 1H), 4.93 (s, 2H), 3.00-2.33 (m, 8H), 2.19 (s, 3H). **^{13}C NMR** (150 MHz, DMSO-d_6) δ_C 193.56, 166.46, 162.15, 157.08-154.13 (m), 147.49 (ddd, J = 254.5, 15.5, 7.5 Hz), 147.12 (ddd, J = 243.5, 12.5, 3.5 Hz), 130.31, 120.80 (dd, J = 19.5, 10.5 Hz), 119.85, 112.91 (ddd, J = 24.0, 7.0, 4.0 Hz), 112.63 (dd, J = 20.0, 14.0 Hz), 55.56, 54.74, 45.78, 45.65.



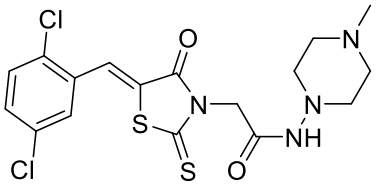
5-(Benzo[b]thiophen-3-ylmethylene)-4-oxo-2-thioxothiazolidin-3-yl)-N-(4-methylpiperazin-1-yl)acetamide 5l: isolated as a yellow solid (31%). **mp** >271 °C (dec.). R_f = 0.40 (CH_2Cl_2 : MeOH, 9 : 1). **IR** ν_{max} (ATR)/cm^{-1}: 3216 (NH), 1708 (HNC=O), 1674 (NC=O), 1598 (SC=C). **HRMS** (ESI+): calculated for $C_{19}H_{21}N_4O_2S_3$ $[M + H]^+$ requires 433.0821; found 433.0815. **^{1}H NMR** (600 MHz, DMSO-d_6) δ_H 9.08 (s, 1H), 8.28 (s, 1H), 8.24-8.20 (m, 1H), 8.16-8.12 (m, 1H), 8.11 (s, 1H), 7.58-7.50 (m, 2H), 4.96 (s, 2H), 3.04-2.59 (m, 8H), 2.20 (s, 3H). **^{13}C NMR** (150 MHz, DMSO-d_6) δ_C 193.66, 166.81, 166.63, 139.61, 138.09, 133.19, 129.68, 126.23, 125.93, 123.82, 123.74, 123.69, 122.30, 55.57, 54.75, 45.81, 45.45.



(5-(2,6-Dichlorobenzylidene)-4-oxo-2-thioxothiazolidin-3-yl)-N-(4-methylpiperazin-1-yl)acetamide 5m: isolated as a yellow solid (33%). **mp** >267 °C (dec.). R_f = 0.35 (CH_2Cl_2 : MeOH, 9 : 1). **IR** ν_{max} (ATR)/cm^{-1}: 3220 (NH), 1723 (HNC=O), 1675 (NC=O), 1603 (SC=C). **HRMS** (ESI+): calculated for $C_{17}H_{19}Cl_2N_4O_2S_2$ $[M + H]^+$ requires 445.0321; found 445.0315. **^{1}H NMR** (400 MHz, DMSO-d_6) δ_H 9.38 (s, 1H), 7.83 (s, 1H), 7.65-7.60 (d, J = 7.5 Hz, 2H), 7.52 (t, J = 9.0 Hz, 1H), 4.98 (s, 2H), 3.41-2.86 (m, 8H), 2.68 (s, 3H). **^{13}C NMR** (100 MHz, DMSO-d_6) δ_C 193.47, 166.79, 165.68, 133.45, 132.72, 131.22, 129.41, 128.87, 120.67, 52.90, 51.53, 46.02, 45.49.

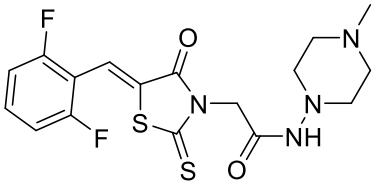


(5-(2,3-Dichlorobenzylidene)-4-oxo-2-thioxothiazolidin-3-yl)-N-(4-methylpiperazin-1-yl)acetamide 5n: isolated as a yellow solid (37%). **mp** >260 °C (dec.). R_f = 0.35 (CH_2Cl_2 : MeOH, 9 : 1). **IR** ν_{max} (ATR)/cm^{-1}: 3225 (NH), 1720 (HNC=O), 1677 (NC=O), 1599 (SC=C). **HRMS** (ESI+): calculated for $C_{17}H_{19}Cl_2N_4O_2S_2$ $[M + H]^+$ requires 445.0321; found 445.0315. **^{1}H NMR** (400 MHz, DMSO-d_6) δ_H 9.41 (s, 1H), 7.83 (s, 1H), 7.70 (d, J = 8.5 Hz, 1H), 7.62 (dd, J = 8.5, 2.5 Hz, 1H), 7.56 (d, J = 2.5 Hz, 1H), 5.02 (s, 2H), 3.27-2.95 (m, 8H), 2.77 (s, 3H). **^{13}C NMR** (100 MHz, DMSO-d_6) δ_C 192.83, 166.11, 166.06, 162.20, 133.18, 132.72, 132.09, 131.95, 128.58, 127.62, 127.03, 120.72, 52.12, 50.77, 45.41, 44.95.

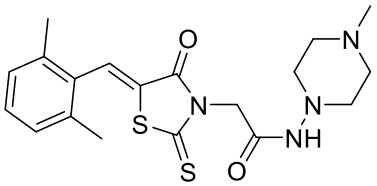


(5-(2,5-Dichlorobenzylidene)-4-oxo-2-thioxothiazolidin-3-yl)-N-(4-methylpiperazin-1-yl)acetamide 5o: isolated as a yellow solid (34%). **mp** >260 °C (dec.). R_f = 0.35 (CH_2Cl_2 :

MeOH, 9 : 1). **IR** ν_{max} (ATR)/cm^{-1}: 3220 (NH), 1723 (HNC=O), 1681 (NC=O), 1597 (SC=C). **HRMS** (ESI+): calculated for $C_{17}H_{19}Cl_2N_4O_2S_2$ [M + H]$^+$ requires 445.0321; found 445.0315. **^{1}H NMR** (400 MHz, DMSO-d$_6$) δ_H 9.41 (s, 1H), 7.91 (s, 1H), 7.79 (d, J = 7.0 Hz, 1H), 7.61-7.50 (m, 2H), 5.02 (s, 2H), 3.19-2.91 (m, 8H), 2.78 (s, 3H). **^{13}C NMR** (100 MHz, DMSO-d$_6$) δ_C 193.62, 166.75, 166.64, 162.73, 133.67, 132.90, 129.62, 128.56, 128.50, 127.74, 127.59, 53.10, 52.65, 45.85, 45.36.

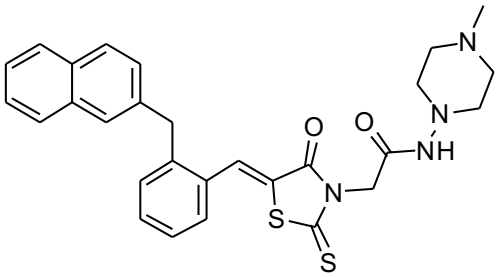


(5-(2,6-Difluorobenzylidene)-4-oxo-2-thioxothiazolidin-3-yl)-N-(4-methylpiperazin-1-yl)acetamide 5p: isolated as an orange solid (35%). **mp** >268 °C (dec.). ***R*$_f$** = 0.35 (CH_2Cl_2 : MeOH, 9 : 1). **IR** ν_{max} (ATR)/cm^{-1}: 3229 (NH), 1731 (HNC=O), 1696 (NC=O), 1602(SC=C). **HRMS** (ESI+): calculated for $C_{17}H_{19}F_2N_4O_2S_2$ [M + H]$^+$ requires 413.0912; found 413.0907. **^{1}H NMR** (400 MHz, DMSO-d$_6$) δ_H 9.87 (s, 1H), 7.72 (s, 1H), 7.71-7.62 (m, 1H), 7.32 (td, J = 9.0, 1.0 Hz, 2H), 4.99 (s, 2H), 3.49-2.89 (m, 8H), 2.69 (s, 3H). **^{13}C NMR** (100 MHz, DMSO-d$_6$) δ_C 193.79, 166.81, 166.54, 160.67 (d, J = 393.0 Hz), 134.40, 129.03 (d, J = 19.0 Hz), 120.88 (d, J = 14.8 Hz), 113.03 (d, J = 24.5 Hz), 110.75, 52.53, 51.36, 45.95, 45.51.

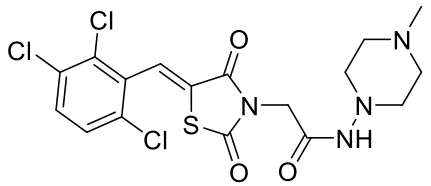


(5-(2,6-Dimethylbenzylidene)-4-oxo-2-thioxothiazolidin-3-yl)-N-(4-methylpiperazin-1-yl)acetamide 5q: isolated as a pale yellow solid (31%). **mp** >265 °C (dec.). ***R*$_f$** = 0.40 (CH_2Cl_2 : MeOH, 9 : 1). **IR** ν_{max} (ATR)/cm^{-1}: 3218 (NH), 1715 (HNC=O), 1677 (NC=O), 1586 (SC=C). **HRMS** (ESI+): calculated for $C_{19}H_{25}N_4O_2S_2$ [M + H]$^+$ requires 405.1413; found 405.1410. **^{1}H NMR** (400 MHz, DMSO-d$_6$) δ_H 9.30 (s, 1H), 8.00 (s, 1H), 7.25 (t, J = 7.5 Hz, 1H), 7.15 (d, J = 7.5 Hz, 2H), 4.98 (s, 2H), 3.27-2.73 (m, 8H), 2.55 (s, 3H). **^{13}C NMR** (100 MHz, DMSO-

d_6) δ_C 194.43, 166.74, 165.40, 135.59, 135.08, 133.43, 129.53, 128.27, 120.66, 53.61, 52.93, 45.73, 45.32, 20.05.

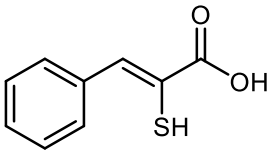


***N*-(4-methylpiperazin-1-yl)-2-(5-(2-(naphthalen-2-ylmethyl)benzylidene)-4-oxo-2-thioxothiazolidin-3-yl)acetamide 5s:** isolated as a yellow solid (38%). **mp** >257 °C (dec.). R_f = 0.40 (CH_2Cl_2 : MeOH, 9 : 1). **IR** ν_{max} (ATR)/cm^{-1}: 3228 (NH), 1726 (HNC=O), 1680 (NC=O), 1591 (SC=C). **HRMS** (ESI+): calculated for $C_{28}H_{29}N_4O_2S_2$ $[M + H]^+$ requires 517.1732; found 517.1740. **^{1}H NMR** (400 MHz, DMSO-d_6) δ_H 9.37 (s, 1H), 8.08 – 8.01 (m, 1H), 7.89 – 7.74 (m, 3H), 7.59 (d, J = 1.5 Hz, 1H), 7.54 – 7.41 (m, 6H), 7.32 (dd, J = 8.5, 1.5 Hz, 1H), 4.94 (s, 1H), 4.56 (s, 1H), 4.35 (s, 2H), 3.33 – 2.90 (m, 8H), 2.70 (s, 3H). **^{13}C NMR** (100 MHz, DMSO-d_6) δ_C 194.19, 171.51, 162.68, 142.34, 138.16, 133.53, 132.45, 132.09, 131.94, 131.81, 131.67, 128.72, 128.60, 128.16, 127.97, 127.87, 127.61, 127.05, 126.71, 126.08, 124.64, 124.48, 52.03, 51.17, 50.04, 42.24.

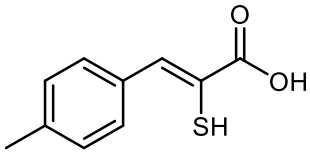


2-(2,4-Dioxo-5-(2,3,6-trichlorobenzylidene)thiazolidin-3-yl)-*N*-(4-methylpiperazin-1-yl)acetamide 10: isolated as an off white solid (40%). **mp** >245 °C (dec.). R_f = 0.35 (CH_2Cl_2 : MeOH, 9 : 1). **IR** ν_{max} (ATR)/cm^{-1}: 3220 (NH), 1712 (HNC=O), 1668 (NC=O), 1591 (SC=C). **HRMS** (ESI+): calculated for $C_{19}H_{18}Cl_3N_4O_3S$ $[M + H]^+$ requires 463.0165; found 463.0173. **^{1}H NMR** (400 MHz, CD_3OD) δ_H 7.85 (s, 1H), 7.64 (d, J = 9.0 Hz, 1H), 7.52 (d, J = 9.0 Hz, 1H), 4.72 (s, 1H), 4.35 (s, 1H), 3.31 (s, 2H), 3.22 – 2.59 (m, 8H), 2.51 (s, 3H). **^{13}C**

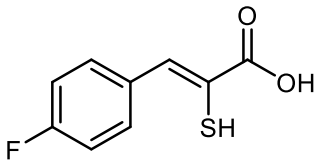
NMR (101 MHz, CD_3OD) δ_C 168.43, 166.49, 164.67, 133.38, 132.11, 131.96, 131.83, 131.58, 129.18, 128.64, 128.49, 54.00, 53.94, 53.52, 52.87, 43.42, 42.05.



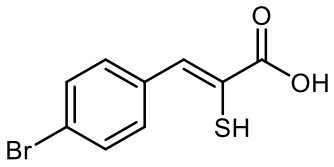
Mercapto-3-phenylacrylic acid 6a: isolated as off white crystals (79%). **mp** >300 ºC. **IR** ν_{max} (ATR)/cm^{-1}: 1574 (OC=O), 1387 (HSC=C). **HRMS** (ESI−): calculated for $C_9H_7O_2S$ $[M - H]^-$ requires 179.0172; found 179.0158. **^{1}H NMR** (400 MHz, CD_3OD) δ_H 7.81 (s, 1H), 7.72-7.58 (m, 2H), 7.49-7.41 (m, 2H), 7.39-7.31 (m, 1H). **^{13}C NMR** (100 MHz, CD_3OD) δ_C 166.77, 135.29, 134.12, 129.53, 128.46, 128.21, 123.67.



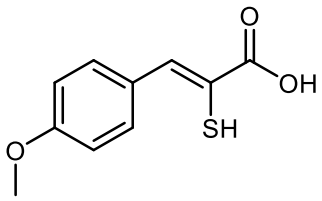
Mercapto-3-(p-tolyl)acrylic acid 6b: isolated as yellow crystals (77%). **mp** >300 ºC. **IR** ν_{max} (ATR)/cm^{-1}: 1615 (OC=O), 1378 (HSC=C). **HRMS** (ESI−): calculated for $C_{10}H_9O_2S$ $[M - H]^-$ requires 193.0329; found 193.0325. **^{1}H NMR** (400 MHz, CD_3OD) δ_H 7.66 (s, 1H), 7.45 (d, J = 8.0 Hz, 2H), 7.15 (d, J = 8.0 Hz, 2H), 2.26 (s, 3H). **^{13}C NMR** (100 MHz, CD_3OD) δ_C 166.89, 138.94, 134.20, 132.47, 129.64, 128.85, 122.35, 20.01.



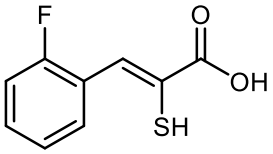
(4-Fluorophenyl)-2-mercaptoacrylic acid 6c: isolated as yellow crystals (82%). **mp** >300 ºC. **IR** ν_{max} (ATR)/cm^{-1}: 1601 (OC=O), 1364 (HSC=C). **HRMS** (ESI−): calculated for $C_9H_6FO_2S$ $[M - H]^-$ requires 197.0078; found 197.0075. **^{1}H NMR** (400 MHz, CD_3OD) δ_H 7.68 (s, 1H), 7.64-7.56 (m, 2H), 7.13-7.04 (m, 2H). **^{13}C NMR** (100 MHz, CD_3OD) δ_C 168.03, 163.92 (d, J = 249.0 Hz), 134.24, 133.08 (d, J = 8.5 Hz), 124.88, 116.51 (d, J = 22.0 Hz).



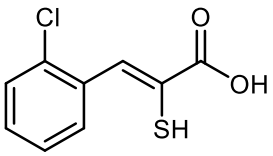
(4-Bromophenyl)-2-mercaptoacrylic acid 6d: isolated as yellow crystals (76%). **mp** >300 ºC. **IR** ν_{max} (ATR)/cm^{-1}: 1589 (OC=O), 1383 (HSC=C). **HRMS** (ESI−): calculated for $C_9H_6BrO_2S$ $[M - H]^-$ requires 256.9277; found 256.9281. **^{1}H NMR** (400 MHz, CD_3OD) δ_H 77.75 (s, 1H), 7.63-7.55 (m, 4H). **^{13}C NMR** (100 MHz, CD_3OD) δ_C 166.46, 134.38, 132.59, 131.40, 131.14, 124.82, 122.29.



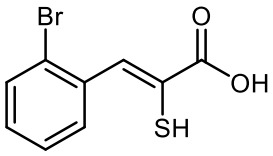
Mercapto-3-(4-methoxyphenyl)acrylic acid 6e: isolated as yellow crystals (81%). **mp** >300 ºC. **IR** ν_{max} (ATR)/cm^{-1}: 1589 (OC=O), 1389 (HSC=C). **HRMS** (ESI−): calculated for $C_9H_9O_3S$ $[M - H]^-$ requires 209.0278; found 209.0276. **^{1}H NMR** (400 MHz, CD_3OD) δ_H 7.78 (s, 1H), 7.66 (d, J = 9.0 Hz, 2H), 7.01 (d, J = 9.0 Hz, 1H), 3.85 (s, 3H). **^{13}C NMR** (100 MHz, CD_3OD) δ_C 167.07, 160.20, 134.14, 131.44, 127.78, 120.44, 113.63, 54.42.



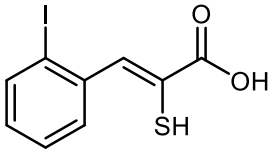
(2-Fluorophenyl)-2-mercaptoacrylic acid 6f: isolated as pale yellow crystals (76%). **mp** >300 ºC. **IR** ν_{max} (ATR)/cm^{-1}: 1619 (OC=O), 1330 (HSC=C). **HRMS** (ESI−): calculated for $C_9H_6FO_2S$ $[M - H]^-$ requires 197.0078; found 197.0081. **^{1}H NMR** (400 MHz, CD_3OD) δ_H 7.91 (s, 1H), 7.89 (dd, J = 8.0, 1.5 Hz, 1H), 7.45-7.36 (m, 1H), 7.28 (td, J = 7.5, 1.0 Hz, 1H), 7.18 (ddd, J = 10.5, 8.0, 1.0 Hz, 1H). **^{13}C NMR** (100 MHz, CD_3OD) δ_C 166.28, 160.40 (d, J = 250.5 Hz), 130.50 (d, J = 8.5 Hz), 129.18 (d, J = 2.5 Hz), 126.45, 125.37 (d, J = 6.5 Hz), 123.86 (d, J = 4.0 Hz), 123.17 (d, J = 12.5 Hz), 115.09 (d, J = 22.0 Hz).



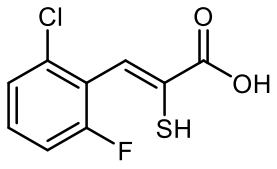
(2-Chlorophenyl)-2-mercaptoacrylic acid 6g: isolated as pale yellow crystals (81%). **mp** >300 ºC. **IR** ν_{max} (ATR)/cm^{-1}: 1588 (OC=O), 1360 (HSC=C). **HRMS** (ESI−): calculated for $C_9H_6ClO_2S$ $[M - H]^-$ requires 212.9783; found 212.9781. **^{1}H NMR** (400 MHz, CD_3OD) δ_H 7.84 (s, 1H), 7.72-7.61 (m, 1H), 7.38 (dd, J = 8.0, 1.5 Hz, 1H), 7.32-7.19 (m, 2H). **^{13}C NMR** (100 MHz, CD_3OD) δ_C 166.17, 133.80, 133.56, 130.42, 129.75, 129.47, 129.43, 127.04, 126.56.



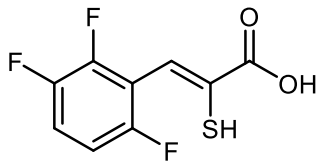
(2-Bromophenyl)-2-mercaptoacrylic acid 6h: isolated as pale yellow crystals (75%). **mp** >300 ºC. **IR** ν_{max} (ATR)/cm^{-1}: 1575 (OC=O), 1358 (HSC=C). **HRMS** (ESI−): calculated for $C_9H_6BrO_2S$ $[M - H]^-$ requires 256.9277; found 256.9280. **^{1}H NMR** (400 MHz, CD_3OD) δ_H 7.77 (s, 1H), 7.65 (dd, J = 7.8, 1.5 Hz, 1H), 7.58 (dd, J = 8.0, 1.0 Hz, 1H), 7.33 (td, J = 7.5, 1.0 Hz, 1H), 7.15 (td, J = 7.5, 1.5 Hz, 1H). **^{13}C NMR** (100 MHz, CD_3OD) δ_C 166.12, 135.44, 133.04, 132.73, 129.91, 129.59, 127.15, 126.97, 123.94.



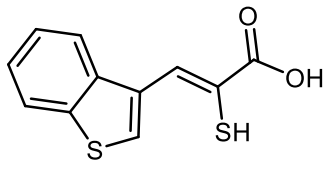
(2-Iodophenyl)-2-mercaptoacrylic acid 6i: isolated as light green crystals (78%). **mp** >300 ºC. **IR** ν_{max} (ATR)/cm^{-1}: 1577 (OC=O), 1385 (HSC=C). **HRMS** (ESI−): calculated for $C_9H_6IO_2S$ $[M - H]^-$ requires 304.9139; found 304.9143. **^{1}H NMR** (400 MHz, CD_3OD) δ_H 9.60 7.85 (dd, J = 8.0, 1.0 Hz, 1H), 7.63 (d, J = 1.0 Hz, 1H), 7.56 (dd, J = 8.0, 1.5 Hz, 1H), 7.35 (td, J = 7.5, 1.0 Hz, 1H), 6.97 (td, J = 7.5, 1.5 Hz, 1H). **^{13}C NMR** (100 MHz, CD_3OD) δ_C 166.06, 139.33, 139.08, 137.74, 129.82, 128.97, 127.90, 126.77, 99.35.



(2-Chloro-6-fluorophenyl)-2-mercaptoacrylic acid 6j: isolated as a white solid (81%). **mp** >300 ºC. **IR** ν_{max} (ATR)/cm^{-1}: 1578 (OC=O), 1370 (HSC=C). **HRMS** (ESI−): calculated for $C_9H_6FClO_2S$ $[M - H]^-$ requires 230.9688; found 230.9690. **^{1}H NMR** (400 MHz, CD_3OD) δ_H 7.53 (s, 1H), 7.40 (td, *J* = 8.0, 6.0 Hz, 1H), 7.33 (d, *J* = 8.0 Hz, 1H), 7.16 (t, *J* = 8.0 Hz, 1H). **^{13}C NMR** (100 MHz, CD_3OD) δ_C 165.26, 159.38 (d, *J* = 250.5 Hz), 133.86 (d, *J* = 5.0 Hz), 131.88, 130.52 (d, *J* = 9.5 Hz), 126.02, 125.11 (d, *J* = 3.5 Hz), 122.82 (d, *J* = 19.0 Hz), 114.21 (d, *J* = 22.5 Hz).

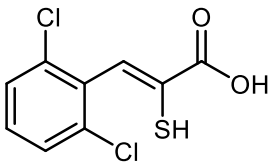


Mercapto-3-(2,3,6-trifluorophenyl)acrylic acid 6k: isolated as yellow crystals (79%). **mp** >300 ºC. **IR** ν_{max} (ATR)/cm^{-1}: 1622 (OC=O), 1371 (HSC=C). **HRMS** (ESI−): calculated for $C_9H_4F_3O_2S$ $[M - H]^-$ requires 232.9890; found 232.9892. **^{1}H NMR** (400 MHz, CD_3OD) δ_H 7.69 (s, 1H), 7.34 (ddt, *J* = 9.5, 5.0, 2.5 Hz, 1H), 7.09 (dddd, *J* = 10.5, 8.0, 6.5, 3.0 Hz, 1H). **^{13}C NMR** (100 MHz, CD_3OD) δ_C 166.91, 160.15 (dd, *J* = 11.1, 3.4 Hz), 148.08 – 147.28 (m), 145.95 – 144.50 (m), 131.33, 127.83 – 126.93 (m), 124.11, 111.66 (dd, *J* = 25.7, 3.6 Hz), 106.68 (dd, *J* = 28.4, 21.6 Hz).

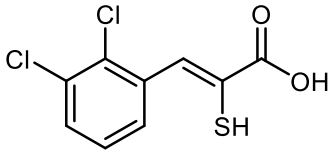


(Benzo[b]thiophen-3-yl)-2-mercaptoacrylic acid 6l: isolated as a yellow solid (75%). **mp** >300 ºC. **IR** ν_{max} (ATR)/cm^{-1}: 1672 (OC=O), 1381 (HSC=C). **HRMS** (ESI−): calculated for $C_{11}H_7O_2S$ $[M - H]^-$ requires 234.9893; found 234.9893. **^{1}H NMR** (400 MHz, CD_3OD) δ_H 9.60 (s, 1H),

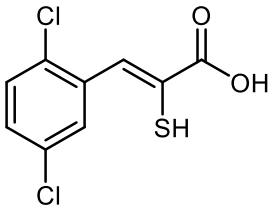
7.95 (s, 1H), 7.92 (dd, J =7.5 Hz, 2H), 7.27-7.52 (m, 2H). **^{13}C NMR** (100 MHz, CD_3OD) δ_C 169.03, 14.38, 139.63, 139.02, 134.70, 124.73, 124.46, 123.46, 123.30, 121.23, 115.15.



(2,6-Dichlorophenyl)-2-mercaptoacrylic acid 6m: isolated as yellow crystals (80%). **mp** >300 ºC. **IR** ν_{max} (ATR)/cm^{-1}: 1593 (OC=O), 1368 (HSC=C). **HRMS** (ESI−): calculated for $C_9H_6Cl_2O_2S$ $[M - H]^-$ requires 246.9393; found 246.9392. **^{1}H NMR** (400 MHz, CD_3OD) δ_H 7.44 (s, 1H), 7.39-7.32 (m, 2H), 7.28-7.20 (m, 1H). **^{13}C NMR** (100 MHz, CD_3OD) δ_C 165.23, 133.74, 133.36, 131.56, 130.08, 129.93, 128.00.

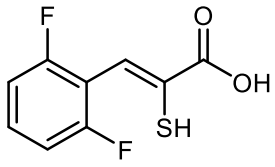


(2,3-Dichlorophenyl)-2-mercaptoacrylic acid 6n: isolated as yellow crystals (77%). **mp** >300 ºC. **IR** ν_{max} (ATR)/cm^{-1}: 1594 (OC=O), 1364 (HSC=C). **HRMS** (ESI−): calculated for $C_9H_5Cl_2O_2S$ $[M - H]^-$ requires 246.9393; found 246.9394. **^{1}H NMR** (400 MHz, CD_3OD) δ_H 7.74 (s, 1H), 7.70 (d, J = 2.5 Hz, 1H), 7.39 (d, J = 8.5 Hz, 1H), 7.27 (dd, J = 8.5, 2.5 Hz, 1H). **^{13}C NMR** (100 MHz, CD_3OD) δ_C 165.83, 135.22, 132.40, 132.18, 130.80, 129.45, 128.99, 128.88, 128.77.

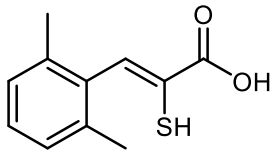


(2,5-Dichlorophenyl)-2-mercaptoacrylic acid 6o: isolated as yellow crystals (75%). **mp** >300 ºC. **IR** ν_{max} (ATR)/cm^{-1}: 1582 (OC=O), 1367 (HSC=C). **HRMS** (ESI−): calculated for $C_9H_6Cl_2O_2S$ $[M - H]^-$ requires 246.9393; found 246.9393. **^{1}H NMR** (400 MHz, CD_3OD) δ_H 7.79 (s, 1H), 7.62 (dd, J

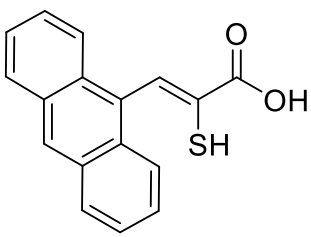
= 8.0, 1.5 Hz, 1H), 7.45 (dd, *J* = 8.0, 1.5 Hz, 1H), 7.29 (t, *J* = 8.0 Hz, 1H). **^{13}C NMR** (100 MHz, CD_3OD) δ_C 165.96, 136.08, 133.12, 131.51, 128.66, 127.86, 127.33.



(2,6-Difluorophenyl)-2-mercaptoacrylic acid 6p: isolated as yellow crystals (82%). **mp** >300 ºC. **IR** ν_{max} (ATR)/cm^{-1}: 1580 (OC=O), 1355 (HSC=C). **HRMS** (ESI−): calculated for $C_9H_6F_2O_2S$ $[M - H]^-$ requires 214.9984; found 214.9984. **^{1}H NMR** (400 MHz, CD_3OD) δ_H 7.43 (s, 1H), 7.34 (tt, *J* = 8.5, 6.5 Hz, 1H), 6.94 (t, *J* = 8.0 Hz, 2H). **^{13}C NMR** (100 MHz, CD_3OD) δ_C 165.35, 159.67 (d, *J* = 250.5 Hz), 132.04, 130.75 (t, *J* = 10.5 Hz), 122.21, 112.65 (m), 111.26 (m).

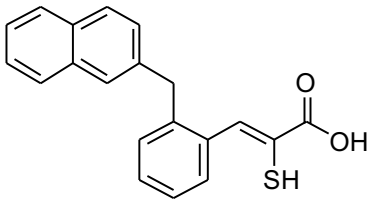


(2,6-Dimethylphenyl)-2-mercaptoacrylic acid 6q: isolated as pale yellow crystals (79%). **mp** >300 ºC. **IR** ν_{max} (ATR)/cm^{-1}: 1599 (OC=O), 1370 (HSC=C). **HRMS** (ESI−): calculated for $C_{11}H_{11}O_2S$ $[M - H]^-$ requires 207.0485; found 207.0484. **^{1}H NMR** (400 MHz, CD_3OD) δ_H 7.60 (s, 1H), 7.04 (dd, *J* = 8.5, 6.5 Hz, 1H), 6.97 (d, *J* = 7.0 Hz, 2H), 2.10 (s, 6H). **^{13}C NMR** (100 MHz, CD_3OD) δ_C 165.84, 135.08, 134.95, 134.55, 128.49, 127.79, 127.29, 18.52.

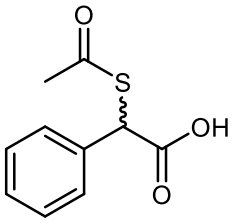


3-(Anthracen-9-yl)-2-mercaptoacrylic acid 6r: isolated as yellow solid (33%). **mp** 252-254 ºC. **IR** ν_{max} (ATR)/cm^{-1}: 1676 (OC=O), 1223 (HSC=C). **HRMS** (ESI−): calculated for $C_{17}H_{12}O_2NaS$ $[M + Na]^+$: 303.0450, found: 303.0452. **^{1}H NMR** (400 MHz, CD_3OD) δ_H 8.63 (s, 1H), 8.29 (s, 1H), 8.12 - 8.18 (m, 2 H), 7.95 - 8.02 (m, 2 H), 7.52 - 7.59 (m, 4 H). **^{13}C**

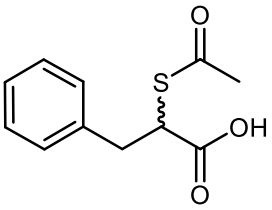
NMR (100 MHz, CD_3OD) δ_C 180.7, 137.7, 132.9, 131.5, 129.2, 128.9, 128.3, 126.4, 126.0, 124.4.



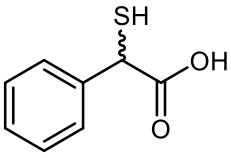
2-Mercapto-3-(2-(naphthalen-2-ylmethyl)phenyl)acrylic acid 6s: isolated as white solid ().**mp** 250-256 ºC. **IR** ν_{max} (ATR)/cm^{-1}: 1690 (OC=O), 1245 (HSC=C). **HRMS** (ESI−): calculated for $C_{20}H_{15}O_2S$ $[M - H]^-$: 320.0871, found: 320.0866. **^{1}H NMR** (400 MHz, CD_3OD) δ_H 7.90 (s, 1H), 7.83 – 7.66 (m, 3H), 7.61 – 7.51 (m, 2H), 7.46 – 7.21 (m, 6H), 4.15 (s, 2H). **^{13}C NMR** (100 MHz, CD_3OD) δ_C 167.75, 140.98, 139.03, 136.34, 135.02, 134.91, 133.57, 131.66, 129.96, 129.64, 128.95, 128.54, 128.28, 128.07, 127.64, 127.53, 126.95, 126.36, 101.38, 40.63.



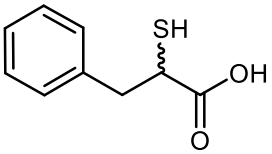
2-(Acetylthio)-2-phenylacetic acid 12a: isolated as an off white solid (80%). **mp** 136-139 °C. R_f= 0.45 (C_6H_{12}/EtOAc 6:4). **IR** ν_{max} (ATR)/cm^{-1}: 2946 (COO-H), 1711 (HOC=O), 1650 (SC=O). **HRMS** (ESI+): calculated for $C_{10}H_{10}O_3SNa$ $[M + Na]^+$ requires 233.0243; found 233.0244. **^{1}H NMR** (400 MHz, DMSO-d_6) δ_H 13.16 (br., s, 1H), 7.57-7.11 (m, 5H), 5.20 (s, 1H), 2.36 (s, 3H). **^{13}C NMR** (100 MHz, DMSO-d_6) δ_C 194.40, 170.98, 135.90, 129.29, 128.69, 51.41, 30.36.



2-(Acetylthio)-3-phenylpropanoic acid 12b: isolated as pale yellow oil (85%). R_f = 0.50 (C_6H_{12}/EtOAc 6:4). **IR** ν_{max} (ATR)/cm^{-1}: 295 (COO-H), 1710 (HOC=O), 1648 (SC=O). **HRMS** (ESI+): calculated for $C_{11}H_{12}O_3SNa$ $[M + Na]^+$ requires 247.0399; found 247.0400. **^{1}H NMR** (400 MHz, DMSO-d_6) δ_H 12.96 (s, 1H), 7.33-7.27 (m, 2H), 7.23 (td, J = 6.0, 1.5 Hz, 3H), 4.25 (t, J = 8.0, 1H), 3.18 (dd, J = 14.0, 8.0 Hz, 1H), 2.94 (dd, J = 14.0, 7.5 Hz, 1H), 2.33 (s, 3H). **^{13}C NMR** (100 MHz, DMSO-d_6) δ_C 193.97, 172.07, 138.05, 129.45, 128.78, 127.23, 47.46, 37.68, 30.66.



2-Mercapto-2-phenylacetic acid 13a: isolated as pale yellow oil (89%). **IR** ν_{max} (ATR)/cm^{-1}: 2946 (COO-H), 1711 (HOC=O). **HRMS** (ESI+): calculated for $C_8H_7O_2S$ $[M - H]^-$ requires 167.0172; found 167.0163. **^{1}H NMR** (400 MHz, DMSO-d_6) δ_H 13.00 (br s, 1H), 7.47-7.25 (m, 5H), 4.80 (d, J = 7.5 Hz, 1H), 3.52 (d, J = 7.5 Hz, 1H). **^{13}C NMR** (100 MHz, DMSO-d_6) δ_C 172.92, 140.00, 128.89, 128.31, 128.06, 45.44.



2-Mercapto-3-phenylpropanoic acid 13b: isolated as pale yellow oil (92%). **IR** ν_{max} (ATR)/cm^{-1}: 2952 (COO-H), 1719 (HOC=O). **HRMS** (ESI+): calculated for $C_9H_9O_2S$ $[M - Na]^-$ requires 181.0329; found 181.0325. **^{1}H NMR** (400 MHz, DMSO-d_6) δ_H 12.68 (s, 1H), 7.58-7.01 (m, 5H), 3.62 (td, J = 9.0, 6.5 Hz, 1H), 3.13 (dd, J = 14.0, 8.5 Hz, 1H), 3.12 (d, J = 9.0 Hz, 1H), 2.91 (dd, J = 14.0, 6.5 Hz, 1H). **^{13}C NMR** (100 MHz, DMSO-d_6) δ_C 174.16, 138.81, 129.49, 128.69, 127.00, 41.92, 41.45.

References

1. Aik, W.; Demetriades, M.; Hamdan, M. K.; Bagg, E. A.; Yeoh, K. K.; Lejeune, C. ; Zhang, Z.; McDonough, M. A.; Schofield, C. J., Structural basis for inhibition of the fat mass and obesity associated protein (FTO). *J Med Chem* **2013,** *56* (9), 3680-8.

2. Banks, J. L.; Beard, H. S.; Cao, Y.; Cho, A. E.; Damm, W.; Farid, R. ; Felts, A. K.; Halgren, T. A.; Mainz, D. T.; Maple, J. R.; Murphy, R.; Philipp, D. M.; Repasky, M. P.; Zhang, L. Y.; Berne, B. J.; Friesner, R. A.; Gallicchio, E.; Levy, R. M., Integrated Modeling Program, Applied Chemical Theory (IMPACT). *J Comput Chem* **2005,** *26* (16), 1752-80.

3. Li, H.; Robertson, A. D.; Jensen, J. H., Very fast empirical prediction and rationalization of protein pKa values. *Proteins* **2005,** *61* (4), 704-21.

4. Greenidge, P. A.; Kramer, C.; Mozziconacci, J.-C.; Wolf, R. M., MM/GBSA Binding Energy Prediction on the PDBbind Data Set: Successes, Failures, and Directions for Further Improvement. *J. Chem. Inf. Model.* **2013,** *53* (1), 201-9.

5. Hopkinson, R. J.; Hamed, R. B.; Rose, N. R.; Claridge, T. D.; Schofield, C. J., Monitoring the activity of 2-oxoglutarate dependent histone demethylases by NMR spectroscopy: direct observation of formaldehyde. *Chembiochem* **2010,** *11* (4), 506-10.